TECHNISCHE UNIVERSITÄT MÜNCHEN

Fakultät für Chemie

Electrochemical and Spectroscopic Investigation of Lithium-Ion Battery Cathode Active Materials

Johannes Sicklinger

Vollständiger Abdruck der von der Fakultät für Chemie der Technischen Universität München zur Erlangung des akademischen Grades eines

Doktors der Naturwissenschaften (Dr. rer. nat.)

genehmigten Dissertation.

Vorsitzender:	Prof. Dr. Jürgen Hauer
Prüfer der Dissertation:	1. Prof. Dr. Hubert A. Gasteiger
	2. Prof. Dr. Tom Nilges

Diese Dissertation wurde am 11.07.2022 bei der Technischen Universität München eingereicht und durch die Fakultät für Chemie am 27.07.2022 angenommen.

"Our world will change dramatically."

Akira Yoshino, December 9th 2019, Nobel speech in Stockholm

"It's great to see all the changes."

M. Stanley Whittingham, October 9th 2019, Telephone Interview by Adam Smith

"We need better batteries."

John B. Goodenough, October 15th, 2019, Press Conference, University of Texas at Austin

Abstract

Electrolyte stability and surface reactivity of cathode active materials strongly affect the aging and thus the lifetime of Li-ion battery cells. Both topics are addressed by this thesis. The oxidative and the reductive stability of the electrolyte components vinylene carbonate (VC), ethylene carbonate (EC), and $LiPF_6$ were investigated by combining infrared spectroscopy with electrochemical potential scans. On that account, an *operando* method involving diffuse reflectance infrared Fourier transform spectroscopy (DRIFTS) method has been developed. By using this method, the formation of gaseous POF_3, PF_5, and CO_2 from the oxidative decomposition of $LiPF_6$ in VC could be observed. The stability of electrolyte formulations is a crucial factor to enable the application of cathode materials such as Ni-rich lithium nickel cobalt manganese oxide (NCM) or lithium- and manganese-rich NCM (LMR-NCM). Upon exposure to ambient air, both layered oxides tend to form reactive surface species that accelerate parasitic side reactions with the electrolyte. As a major part of this thesis, quantity and nature of surface contaminants on Ni-rich NCM and LMR-NCM have been studied before and after exposure to moisture and CO_2. This was achieved by a detailed analysis involving DRIFTS, thermogravimetric analysis coupled with mass spectrometry (TGA-MS), on-line mass spectrometry (OMS), and full-cell cycling. It could be demonstrated that thermal treatment with the reactive gas SO_3 makes LMR-NCM more robust towards CO_2 and moisture. During this treatment surface sulfates were formed, as shown by X-ray photoelectron spectroscopy (XPS). In addition, the modification of LMR-NCM via gaseous SO_2 and Ni-rich NCM with pure F_2 were studied to enhance the electrochemical performance of these cathode active materials (CAMs).

Kurzfassung

Elektrolytstabilität und Oberflächenreaktionen von Kathodenaktivmaterialien haben einen starken Einfluss auf die Alterung und damit auf die Lebensdauer von Lithium-Ionen-Batterien. Beide Themen werden in dieser Arbeit behandelt. Die oxidative und reduktive Stabilität der Elektrolytkomponenten Vinylencarbonat (VC), Ethylencarbonat (EC) und $LiPF_6$ wurden durch eine Kombination von Infrarotspektroskopie mit elektrochemischen Potentialscans untersucht. Dafür wurde eine *operando* Methode entwickelt, die diffusive Reflexions-Fouriertransformations-Infrarotspektroskopie (DRIFTS) verwendet. Durch den Einsatz dieser Methode konnte die Bildung von POF_3, PF_5 und CO_2 durch die oxidative Zersetzung von $LiPF_6$ in VC beobachtet werden. Die Stabilität von Elektrolytformulierungen ist ein entscheidender Faktor, um die Anwendung von Kathodenaktivmaterialien wie Ni-reiches Lithium-Nickelkobaltmanganoxid (NCM) oder Lithium- und Manganreiches NCM (LMR-NCM) zu ermöglichen. Im Kontakt mit Luft neigen beide Schichtoxide zur Bildung reaktiver Spezies auf der Oberfläche, welche parasitäre Nebenreaktionen mit dem Elektrolyten beschleunigen. Ein großer Teil dieser Arbeit beschreibt die Untersuchung von Umfang und Art der Oberflächenverunreinigungen auf Ni-reichem NCM und LMR-NCM vor und nach der Exposition gegenüber Feuchtigkeit und CO_2. Dieses wurde durch eine ausführliche Analyse erreicht, die DRIFTS, thermogravimetrische Analyse gekoppelt mit Massenspektrometrie (TGA-MS), on-line Massenspektrometrie (OMS) und Vollzellzyklisierung beinhaltet. Es konnte gezeigt werden, dass thermische Behandlung mit dem Reaktivgas SO_3 das LMR-NCM robuster gegen CO_2 und Feuchte macht. Während der Behandlung kommt es zur Bildung von Sulfaten auf der Oberfläche der CAM-Partikel, die durch Röntgenphotoelektronenspektroskopie (XPS) nachgewiesen wurden. Zusätzlich wurde die Modifikation von LMR-NCM mittels gasförmigem SO_2 und die von Ni-reichem NCM mit reinem F_2 untersucht, um die elektrochemische Leistungsfähigkeit dieser Kathodenaktivmateralien zu steigern.

Acknowledgements

First of all, I want to thank my supervisor **Prof. Hubert A. Gasteiger** for the great opportunity to be part of the Technical Electrochemistry (TEC) group for six years. I am grateful for your incentive, encouragement and dedication to convey science with passion, clarity and precision, but also with all the patience required to give guidance through ambitious and challenging projects. It was great to profit from many resources for experimental work in the labs. At the same time, you supported the scientific exchange by letting us participate at conferences, during our TEC winter and summer seminars. In our group seminars you encouraged everyone to be an active part of the discussion. In the lab and in our projects you paid great attention to team work and mutual support within the group. All this has created an atmosphere of vivid and inspiring scientific exchange, which made it scientifically and personally enriching to work with you.

Many thanks go to **Veronika Pichler** for keeping the chair running every day, for taking care of every problem with friendliness and cordiality, with skill and helpfulness. It was amazing how you always found a solution for administrative problems. Your moral support throughout all these years was incredible and I am still sad that we are not working next door any more since I moved away from TEC!

I would like to thank **Dr. Uta Schwenke** for teaching me Li-O_2 and DRIFTS techniques when I started my thesis. You supported me whenever needed, gave honest and constructive feedback and taught me how to accurately evaluate DRIFT spectra. I am especially grateful that you were always open for discussion and feedback on my *operando* DRIFTS projects even quite a long time after you had left TEC. Speaking of *operando* DRIFTS, I have to send many thanks to **Dr. Nina Zensen** who had worked on this topic within her M.Sc. thesis. You were a diligent, creative and hard-working student, really pushing forward the project. Apart from that, it was personally enriching to have you in the team!

I express my gratitude to **Dott. Ric. Michele Piana** and **Dr. Hans Beyer** for supporting me with scientific and personal advice from the perspective of experienced team members. Special thanks go to you, Hans, for elaborating a detailed XPS study to support the "surface modification" projects after just having gone through all the adventures of installing the device in our lab. The TGA-MS techniques developed by you were a central piece of several studies. Without your support, it would have been quite hard to get the contact process for SO_3 generation running. In addition, I am really grateful to **Prof. Michael Metzger** who has been an amazing partner in getting the "surface contamination" project started, especially when it came down to gassing analysis. Special thanks go to **Anna Freiberg** for involving me in the Li_2CO_3 project, but also for constantly sharing great scientific ideas, and for making TEC labs a better place. Thanks to **Benjamin, Sophie, Daniel, Stefan, Franzi and Tobi** for being congenial team mates in all the BASF-related projects! I would like to thank the colleagues from the BASF for fruitful discussions during their visits and during the BASF battery network events, especially

Dr. Heino Sommer, Dr. Pascal Hartmann and Dr. Manuel Mendez. I want to thank our cooperation partners within the battery network, Prof. Doron Aurbach's group at Bar-Ilan University (BIU), Israel and Prof. Ingo Krossing's group at the University of Freiburg. Special thanks go to **Dr. Boris Markovsky** and to **Dr. Hadar Sclar** for driving the scientific cooperation between TUM and BIU on SO_2-treatment of LMR-NCM. Apart from the scientific collaboration, I am grateful for the personal connection that has been established! The same holds absolutely true for **Dr. Ulf Breddemann** from Ingo Krossing's group. Without doubt, you are my favorite fluorine chemist!

Many thanks go to my hard-working students **Felix Riewald, Korbinian Huber and Maximilian Pöverlein** for being a great support to the scientific projects. I especially thank **Louis Hartmann** and **Christian Sedlmeier**, who were eager to absorb all the theoretical and practical knowledge in no time and convert it into innumerate O-MS trials, coin cells, thermal gas treatments, TGA-MS measurements and last but not least you helped to apply the legendary *operando* DRIFTS device for *ex situ* studies. Thanks, Christian, for joining me in the *in situ* DRIFTS adventure! And to you, Louis, for helping with the XPS once Hans had found a new job outside TEC. Both of you really brought me a big step forward by supporting the projects with lots of dedication and skill. I am more than happy that both of you continued to stay at TEC as PhD students. It was great to discuss papers and thesis-related questions together with you, and it is really nice to have you as friends within the TEC group!

I would like to thank the **whole TEC group** for the open and inspiring atmosphere at the chair, for great scientific and non-scientific discussions and adventures inside and outside the chair. I like to remember the trip in Yucatán (2018) after the conference in Cancún, together with **Alex, Anna and Max**. Thanks for being great travel mates! Bike trips were another opportunity to connect with scientists from inside and outside of TEC. The same is true about the already mentioned Winter and Summer Seminars. Many thanks to **Prof. Gessie Brisard** and **Dr. Alexander Ogrodnik** for lifting my spirits whenever discussing about science, thesis problems and many other fields of interest. Thanks to my TEC colleagues, especially **Sophie, Pankaj, Armin, Dominik, Freddie, Cyril, Irmi**, but also to the undergrads, especially **Ela and Vio**, for having a great time in the group! Last but not least, thanks to **Heiko Juranowitsch** for taking care of our lab infrastructure.

My heartfelt thanks go to **friends and family**, without their support I would not have made it here. Above all I want to thank my **twin brother Michael**!

Table of Contents

List of Actronyms

ASSB	all-solid state battery
ATR	attenuated total reflection
BET	Brunauer-Emmett-Teller
BEV	battery electric vehicle
CAM	cathode active material
CE	coulombic efficiency
DCIR	direct current internal resistance
DEC	diethyl carbonate
DEMS	differential electrochemical mass spectrometry
DMC	dimethyl carbonate
DRIFTS	diffuse reflectance infrared Fourier transform spectroscopy
DTA	differential thermal analysis
EC	ethylene carbonate
EMC	ethyl methyl carbonate
FEC	fluoro-etylene carbonate
FSE	fluorine-selective electrode
FTIR	Fourier transform infrared spectroscopy
HEV	hybrid electric vehicle
HVC	high-temperature reaction chamber
HR-TEM	high resolution transmission electron microscopy
ICP-MS	inductively coupled plasma mass spectrometry
IR	infrared spectroscopy
KM	Kubelka-Munk
LCO	lithium cobalt oxide ($LiCoO_2$)
LCP	lithium cobalt phosphate ($LiCoPO_4$)
LEDC	lithium ethylene dicarbonate
LFP	lithium iron phosphate ($LiFePO_4$)
LGPS	lithium germanium thiophosphate ($Li_{10}GeP_2S_{12}$)
LIB	lithium-ion battery
LLZO	lithium lanthanum zirconium oxide ($Li_7La_3Zr_2O_{12}$)

LMR-NCM	lithium- and manganese-rich nickel cobalt manganese oxide ($x\ Li_2MnO_3 \cdot (1\text{-}x)\ Li[Ni_xCo_yMn_{1\text{-}x\text{-}y}]O_2$)
LNMO	lithium nickel manganese spinel ($LiNi_{0.5}Mn_{1.5}O_4$)
LNO	lithium nickel oxide ($LiNiO_2$)
LTO	lithium titanate ($Li_4Ti_5O_{12}$)
MCMB	microporous carbon microbeads
MCT	mercury cadmium telluride
NCA	lithium nickel cobalt aluminum oxide ($LiNi_{0.8}Co_{0.15}Al_{0.05}O_2$)
NCBH	basic nickel carbonate hydrate ($NiCO_3 \cdot 2Ni(OH)_2 \cdot x\ H_2O$)
NCM	lithium nickel cobalt manganese oxide ($LiNi_xCo_yMn_{1\text{-}x\text{-}y}O_2$)
NiMH	nickel metal hydride
NMP	*N*-methyl-2-pyrrolidone
OCV	open circuit voltage
OEMS	on-line electrochemical mass spectrometry
OMS	on-line mass spectrometry
PEEK	polyether ether ketone
PHEV	plug-in hybrid electric vehicle
SEI	solid-electrolyte interphase
SiG	silicon-graphite
SNIFTIRS	subtractively normalized interfacial Fourier transform infrared spectroscopy
SOC	state of charge
TGA-MS	thermogravimetric analysis coupled to mass spectrometry
VC	vinylene carbonate
XPS	X-ray photoelectron spectroscopy
XRD	X-ray diffractometry

1. Introduction

Nowadays, at the beginning of the 21st century, lithium-ion batteries (LIBs) have become indispensable in the field of consumer electronics such as smartphones and laptops.[1,2] This technological advancement clearly has transformed our daily communication and our working lives. Furthermore, lithium-ion batteries serve as energy storage devices for power tools such as cordless screwdrivers and an increasing number of machine tools from power saws to small excavators.[3,4] More and more of those machines are being equipped with an electric power train instead of an internal combustion engine.[4]

For an increasing number of people, the comfort of their own personal mobility has been lifted by the market introduction of battery driven "e-bikes", "e-scooters", and similar vehicles. In 2019, almost every 3rd bike sold in Germany was an e-bike,[5] e.g., enabling employees to ride to their office without sweating or making it possible for pensioners to go on mountain bike tours. In the larger German cities, several thousands of e-scooters have been cruising on sidewalks and streets since their legalization in 2019.[6] This new field of micromobility has become an increasingly important supplement to public transport.[7] But also conventional means of transport such as cars or even buses currently are at the start of a transformation themselves.[8] The development of large battery packs makes the replacement of combustion engines by electrical drive trains more and more attractive. Every big car manufacturer either has battery electric vehicles (BEVs) or hybrid electric vehicles (HEVs) in their portfolio or is currently developing such models.[1] While in case of BEVs the car is exclusively driven by the electricity stored in the battery pack, HEVs use the combined power of electric motors and an internal combustion engine. The battery pack of hybrid cars can be partially re-charged during slowdown of the car by converting kinetic to electrical energy. This recuperation process allows to save a significant amount of fuel. Plug-in hybrid electric vehicles (PHEVs) are primarily powered by the battery pack and have an internal combustion engine only serving as a range extender.[9]

While in 2008 less than half a million all-electric cars were sold world-wide, the number has risen to almost 1.5 million in 2018. In the same year, more than six hundred thousand HEVs were sold. The number of EV sales per year has been continuously rising and is expected to keep rising in the upcoming years.[10] The development of electric cars was largely inspired by the release of the Toyota Prius Hybrid in 1997 and the all-electric Tesla Roadster in 2008.[11,12] Tesla and most of the other car manufacturers soon decided for the Li-Ion-Battery technology,[1] Toyota held on quite long to the nickel metal hydride (NiMH) technology for HEVs.[13]

Tesla has become famous for his Model S with an all-electric range of up to 632 km for the long-range version of the current generation (released in 2017).[14] Inspired by this initially small Silicon-Valley startup and by advancements in battery technology, government bonuses and more and more strict regulations for reducing exhaust fumes from ICE cars, traditional car companies started to offer

HEVs and BEVs within their product portfolio.[15] However, the driving ranges of competing BEV models are typically lower compared to the Tesla Model S. For instance, the premium versions of Tesla's model 3 and Volkswagen's new ID.3 have driving ranges above 500 km,[16,17] while the latest version of the VW e-up (2019) and the BMW i3 (2018) only have a practical driving range of up to 260 km according to the manufacturers.[18,19] However, for the next decade an increase of energy density of the battery pack as well as more economic prices are forecast. Taking into account government bonuses, already today the total cost of ownership of BEVs can be competitive to conventional gasoline cars depending on the choice of car and the usage profile.[20] Besides, the emergence of electric cars surely helps to reduce local emissions in big cities, thus reducing air pollution and raising the quality of life for a large number of people.[21]

However, it must be mentioned that the electrification of cars is just a small piece in the big context of energy transformation, the aim of which is to minimize CO_2 emission, fossil fuel consumption, and nuclear energy use. Not surprisingly, this transformation comes with a number of challenges, such as the increase of energy production from renewable sources such as wind and solar as well as the extension of the energy transport infrastructure – from long-range power transmission lines to a much wider spreading of charging stations for electric cars. To refurbish the power grid, new stationary storage facilities must be installed. While hydropower is the classic grid storage technology, stationary batteries offer a new option to decentralize energy storage and thus stabilize the grid in times of more fluctuating consumption due to, e.g., the charging of electric cars and in times of unsteady supply of energy from renewables such as wind and solar power. An impressive example is the Li-ion battery power station in Hornsdale, Australia, built by Tesla with an electric storage capacity of 129 MWh[1,22]

It is crucial to notice that battery storage is not the only new emerging technology in the field of energy storage but that innovations in the field of fuel cells, hydrogen storage and water electrolysis offer new tools in power-to-gas conversion and are subject to increasing research and development activities at present.[23] While conversion efficiency and hydrogen cost as well as the high prices for fuel cells currently make them lag behind especially in the competition of fuel cell vs. battery cars, on the larger scale they most probably will become increasingly important in the future.[1,24] Examples in which fuel cells can be more advantageous than batteries are the sector of heavy-duty transport or large-scale stationary storage.[25,26] However, even if every car were a fuel cell car, this would still cause a huge demand for efficient battery packs, as every fuel cell car needs a buffer battery to provide peak power to the drive train while the fuel cell itself can operate within quite a steady intermediate output power range.[27]

For all of the above-mentioned battery applications, the Li-ion technology is and probably will remain the dominant type of cell chemistry. Other secondary battery technologies such as the traditional lead-acid battery, nickel-metal hydride (NiMH) or nickel-cadmium cells are outperformed in terms of cost, volumetric and gravimetric energy density as well as longevity by Li-ion cells.[1,2] This fact makes it worth to have a closer look inside such Li-ion cells. Before doing so, it is now time to get back to the three scientists whose quotes were given at the very beginning of this introductory chapter: Akira Yoshino, M. Stanley Whittingham and John B. Goodenough were awarded the Nobel prize in chemistry in 2019 for their groundbreaking discoveries leading to the development of today's Li-Ion batteries.[28] Back in the 1970s, Whittingham found the intercalation compound lithium titanate TiS_2 to be promising as a cathode active material for batteries, with a potential of 2.5 V versus lithium.[29] By pairing this cathode with a lithium-aluminium alloy as anode, Wittingham and his group at the Exxon Research Laboratory developed a new 2 V battery system.[30] Not much later, with Goodenough's discovery of lithium cobalt oxide $LiCoO_2$ (LCO) as a cathode active material, the voltage versus lithium could be almost doubled.[31] An additional breakthrough was achieved by the third Nobel laureate Akiro Yoshino, who created the first prototype of lithium-ion battery with a carbonaceous anode in 1985.[32,33] Six years later, Sony started to sell the first commercial lithium ion battery (LIB) with LCO as cathode, graphite as anode, and $LiPF_6$ in an aprotic solvent mixture as electrolyte.[2,34] Some of the present-day LIBs still use LCO as cathode material, e.g., LIBs for portable electronics applications. In the field of electric mobility, lithium nickel cobalt manganese oxide (NCM), i.e., $LiNi_xCo_yMn_{1-x-y}O_2$ and lithium nickel cobalt aluminium oxide (NCA), i.e., $LiNi_{0.8}Co_{0.15}Al_{0.05}O_2$ (NCA) are the preferred choice of cathode materials.[2,35]

With the increasing spread of lithium-ion batteries in mobile and stationary storage applications, new questions and problems arise. The state-of-the-art lithium-ion battery requires a large amount of costly and critical resources such as cobalt or lithium.[36,37] In addition, the energy required to prepare electrode materials for lithium-ion cells is immense. This is a strong driving force to minimize the use of the most critical raw materials such as cobalt,[37] and to increase the energy density of electrode materials while making battery life longer.[1,2] In 2019, Jessie E. Harlow *et al.* from Jeff Dahn's group presented a benchmark study on the "million-mile battery" in the Journal of the Electrochemical Society, setting new standards for improved cell performance and lifetime in the battery research community.[38] In order to better understand how this was achieved, why batteries age and which material combination seems most promising in the future, the following chapters will give more insights and a broader overview over the cell chemistries and material choices for present and future LIBs.

1.1. Lithium-Ion Battery Cell Chemistry

Typical examples of cell components and materials have already been mentioned in the previous section: lithium cobalt oxide (LCO) as cathode active material, graphite as anode material, and $LiPF_6$ as a conductive salt in an electrolyte based on aprotic solvents.[1,2] Before laying out the varieties of electrode materials and electrolyte components applied in state-of-the-art battery manufacturing, we shall first have a closer look at the working principle of a lithium-ion battery cell:

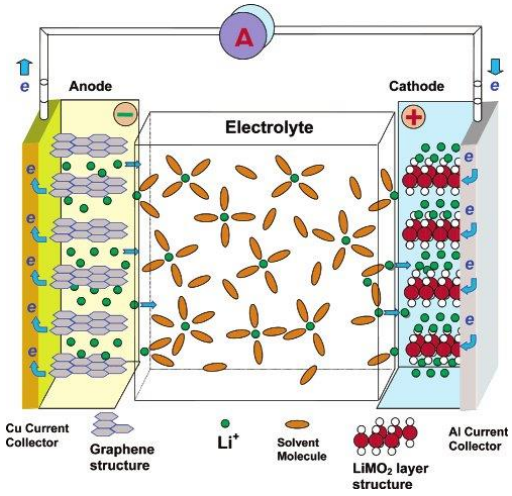

Figure 1: Scheme of the discharge process for a lithium-ion battery containing a carbonaceous anode material such as graphite and a layered oxide ($LiMO_2$) cathode such as NCM (nickel-cobalt-manganese oxide). The electrolyte consists of aprotic solvents such as the cyclic ethylene carbonate (EC) or the linear dimethyl carbonate (DMC), diethylcarbonate (DEC) and ethyl methyl carbonate (EMC). $LiPF_6$ serves as conductive salt and the Li^+ ion loses its solvation shell when intercalating into the cathode. While Li^+ ions are conducted internally in the battery, electrons are travelling on the external electric circuit providing power to the consumer load. Reprinted with permission from Kang Xu, *Chemical Reviews*, **104**, 4303–4418 (2004). Copyright (2004) American Chemical Society.[39]

The scheme in Figure 1 depicts the "rocking-chair" model as the operational principle of lithium-ion batteries.[39,40] The name "rocking-chair" derives from the fact that the lithium-ions go back and forth between the intercalation cathode and the intercalation anode during charge and discharge. During charge, the lithium ions in the initially fully lithiated cathode active material travel to the anode (equations 1 and 2): [39,40]

$$\text{Cathode: } LiCoO_2 \rightarrow Li_{1-x}CoO_2 + x\ Li^+ + x\ e^- \qquad \text{(equation 1)}$$

$$\text{Anode: } 6\ C + x\ Li^+ + x\ e^- \rightarrow Li_xC_6 \qquad \text{(equation 2)}$$

The reverse reactions take place during discharge.[39,40] In case of $Li_{1-x}CoO_2$ (equation 1), the charge must be limited to ca. 0.5 Li in order to ensure stable cycling. This limits the practical LCO capacity to roughly 140 mAh/g.[41] While the lithium ions travel internally inside the battery cell between cathode and anode, the electrons are conducted externally via an electric circuit supplying the consuming device with

electric current and power. It should be noted that there is a discrepancy between the thermodynamic terms for anode and cathode and the conventional designations[39] of "anode" and "cathode" for the two electrodes of a lithium-ion battery. From a thermodynamic point of view, the anode is defined as the electrode where the oxidation half-reaction of the redox-reaction in an electrochemical cell takes place.[42] In case of the discharge of a lithium-ion battery cell, Li_xC_6 is oxidized by the ongoing delithiation, i.e., the term "anode" holds true thermodynamically. In case of charge, the graphite electrode is thermodynamically speaking a cathode, but is still referred to as "anode" in the lithium-ion battery convention.

For both charge and discharge, the cell voltage during operation is determined by the thermodynamic voltage V_{OC}, usually referred to as open circuit voltage (OCV) of the battery cell, and by the overpotential η (equations 3 and 4). The OCV results from the difference of anode and cathode potential and is influenced by the lithiation degree and structural changes of the active materials during lithiation and delithiation. The overpotential η depends on the state of charge q and the current I.[43]

$$V_{\mathrm{dis}} = V_{\mathrm{oc}} - \eta(q, I_{\mathrm{dis}}) \qquad \text{(equation 3)}$$

$$V_{\mathrm{ch}} = V_{\mathrm{oc}} + \eta(q, I_{\mathrm{ch}}) \qquad \text{(equation 4)}$$

The energy E_{dis} that a cell can provide to the consuming device during discharge is determined by the discharge voltage and the capacity Q_{dis} of the cell, as specified by equation 5:

$$E_{\mathrm{dis}} = \int_0^{Q_{\mathrm{dis}}} V_{\mathrm{dis}}(q)dq \qquad \text{(equation 5)}$$

The mean discharge potential $\overline{V_{\mathrm{dis}}}$ can deliver useful insights, e.g., into thermodynamic and kinetic properties of anode and cathode. From cycling data it can be determined as follows (equation 6):

$$\overline{V_{\mathrm{dis}}} = \frac{\int_0^{Q_{\mathrm{dis}}} V_{\mathrm{dis}}(q)dq}{\Delta Q} \qquad \text{(equation 6)}$$

The specific discharge energy of a battery cell is an important figure of merit for practical application. However, in the Li-ion battery research community, publications usually focus on the discharge capacity, which relates to the number of Coulombs exchanged during discharge (equation 7). The specific discharge capacity q_{dis}, which, e.g., normalizes the capacity by the active material mass m, is usually displayed in units of mAh/g (equation 8).

$$Q_{\mathrm{dis}} = \int_0^{\Delta t} I(t)dt \qquad \text{(equation 7)}$$

$$q_{\mathrm{dis}} = \frac{Q_{\mathrm{dis}}}{m} \qquad \text{(equation 8)}$$

The charge capacity is determined analogously. In terms of reversibility of a charge and discharge cycle, the coulombic efficiency (CE, equation 9) comes into play. The CE is a vital factor determining the longevity of Li-ion cells.

$$CE = \frac{Q_{dis}}{Q_{cha}} \cdot 100\% \qquad \text{(equation 9)}$$

For prolonged cycling, a CE value close to 100% is essential. For 1,000 cycles, a CE of at least 99.98% would be needed or 99.998% for 10,000 cycles. Several thousand cycles are required in case of the previously mentioned "million mile battery" as shown by Jeff Dahn's group.[38]

Having discussed the operational principle of Li-ion cells, the most frequently used materials will be introduced. There is a large variety of such materials and material combinations applied in the manufacturing of state-of-the-art lithium-ion battery cells. Graphite has already been introduced as classical anode material. It should be noted that Sony used petroleum coke in their first commercial cell in 1991, but this was soon replaced by graphite due to its higher capacity.[39,44]

An intercalation material alternative to graphite is lithium titanate $Li_4Ti_5O_{12}$ (LTO),[45] which has a much lower theoretical capacity than graphite (175 vs. 372 mAh/g). However, LTO is a so-called "zero-strain" material and thus does not show any volume expansion or contraction during cycling in contrast to graphite.[45,46] In addition, the operating potential of LTO (1.55 V vs. Li/Li^+) is much higher than that of graphite, which operates close to the lithium potential. LTO with its Ti^{IV}/Ti^{III} redox couple can reversibly accommodate three Li^+ ions per formula unit. During lithiation, the following reaction (equation 10) takes place:[46]

$$Li_4Ti_5O_{12} + 3\ Li^+ + 3\ e^- \rightarrow Li_7Ti_5O_{12} \qquad \text{(equation 10)}$$

Despite its low specific energy density, LTO is the material of choice in certain cases, especially for high-power applications such as buffer battery packs for fuel-cell electric buses.[8]

With respect to cathode active materials, LCO has already been mentioned as the first cathode active material applied in commercial lithium-ion cells. Later, mixed layered oxide components such as $LiNi_{1/3}Co_{1/3}Mn_{1/3}O_2$ (NCM111) have been developed. This substitution of cobalt by nickel and manganese allows the extraction of much more Li^+ as compared to LCO.[41] More details about the NCM chemistry and strategies to increase the energy density will be discussed in the next chapter. NCM[47] is often referred to as NMC[48] in the literature; both abbreviations refer to the same material.

While NCM and LCO belong to the class of layered oxides, $LiFePO_4$ (LFP) is an olivine. The first study on LFP has been reported by Goodenough and his coworkers in 1997.[49] During lithiation or delithiation, Fe switches between an oxidation state of $+_{III}/+_{II}$, exemplarily depicted for the charge reaction (equation 11): [50]

$$LiFe^{III}PO_4 \rightarrow Fe^{II}PO_4 + Li^+ + e^- \qquad \text{(equation 11)}$$

The advantage of LFP compared to LCO or NCM is its flat voltage profile at 3.4 V vs. Li/Li^+, low cost raw materials and eco friendliness. In addition, LFP is beneficial in terms of thermal stability and power capability. The drawbacks are a high processing cost due to the required carbon coating as well as a lower capacity and energy density. All this makes LFP a less ideal candidate for EV energy storage solutions, but an attractive cathode material for power tools and stationary energy storage systems.[2,50]

Typical Li-ion battery electrolytes are composed of a 1 M solution of $LiPF_6$ in organic solvents, usually a mixture of cyclic carbonates such as ethylene carbonate (EC) and linear carbonates such as dimethyl carbonate (DMC), ethyl methyl carbonate (EMC) or diethyl carbonate (DEC) as depicted in Figure 2. The reduction of electrolyte components at the graphite anode leads to the formation of a solid-electrolyte interphase (SEI). Typically, the organic carbonates are reduced at ≈ 0.8 V vs. Li/Li^+ leading to the formation of inorganic compounds such as LiF and Li_2CO_3 as well as organic species such as lithium ethylene dicarbonate (LEDC).[51–54] The SEI is a Li^+ conducting but electronically insulating film on the electrode/electrolyte interface of the graphite anode.[51,52] This passivating film is crucial to enable long-term cycling of lithium-ion batteries with graphite as anode by preventing ongoing electrolyte reduction.[52] Additives, i.e., small quantities of solvents such as vinylene carbonate (VC) can be beneficial for the formation of the SEI on graphite.[55–57]

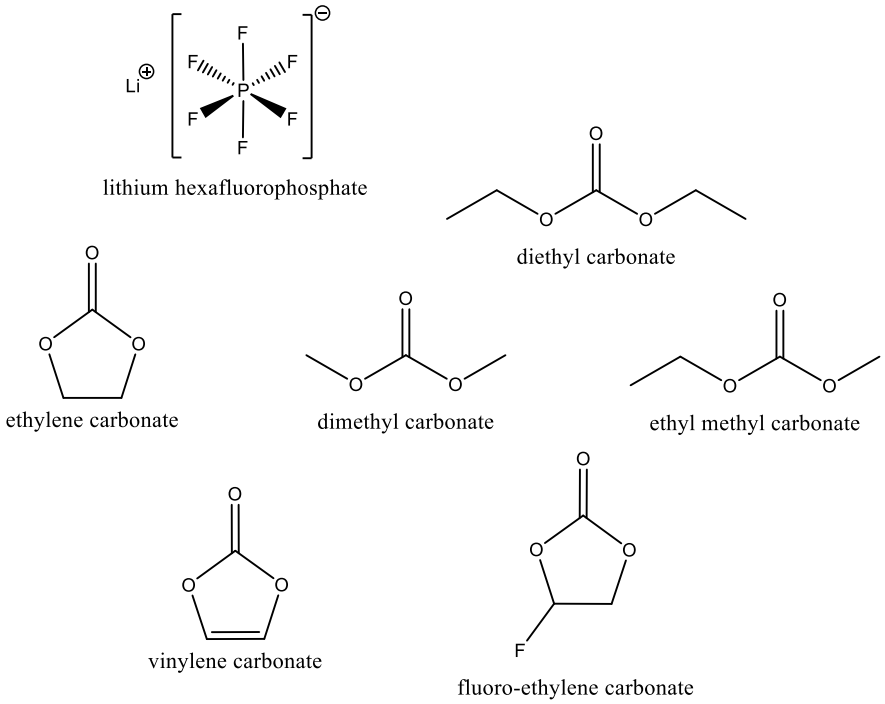

Figure 2: The typical lithium-ion battery solvent molecules ethylene carbonate (EC), dimethyl carbonate (DMC), ethyl methyl carbonate (EMC), and diethyl carbonate (DEC) as well as the SEI-forming additive vinylene carbonate (VC) and the co-solvent fluoro-ethylene carbonate (FEC) as well as the conductive salt $LiPF_6$.

In case of commercial cell chemistries such as NCM111//graphite, which typically operate at full-cell potentials up to 4.2 V, examples of characteristic electrolyte formulations are LP30 (1.0 M $LiPF_6$ in EC/DMC = 50/50 (v/v)), LP57 (1.0 M $LiPF_6$ in EC/EMC = 30/70 (v/v)), and LP572 (LP57 with 2 vol.-% VC).[58–60] The well-established electrolyte additive VC and the co-solvent fluoro-ethylene carbonate (FEC), which is beneficial for silicon-containing anodes, are known to form CO_2 during reduction.[61–63] The CO_2 itself is converted to Li_2CO_3, lithium formate (Li(HCOO)), and lithium oxalate ($Li_2(COO)_2$) and thereby positively impacts SEI formation.[57,64] In case of novel high-voltage CAMs, which will be discussed in the next chapter, fluorinated molecules such as FEC were found to positively impact the cycle-life of CAMs that tend to release oxygen upon delithiation, such as lithium- and manganese-rich NCM (LMR-NCM). [65–67] In contrast, classical electrolyte components such as EC and VC were found to hamper cell performance and cycle-life of such cathode materials.[68–70] VC is oxidatively unstable above ≈ 4.5 V vs. Li/Li^+, EC is decomposed by singlet oxygen released from layered oxides at high degrees of delithiation (> 80%), e.g., in case of Ni-rich NCMs and LMR-NCM.[66,67,71–73] However, FEC was not found to positively impact the cycle-life of high-voltage CAMs that do not release oxygen such as the "high-voltage spinel" $LiNi_{0.5}Mn_{1.5}O_4$ (LNMO).[74,75] In contrast, side reaction of FEC with $LiPF_6$ can lead to thermal instabilities of the electrolyte.[74,76] Taken together, the electrolyte formulation must be well adjusted to the specific choices made for anode and cathode active materials as well as the resulting operating potential of the battery cell. Within this thesis, an *operando* infrared spectroscopic method was developed to investigate the oxidative and reductive

stability of model electrolytes consisting of $LiPF_6$ in VC and $LiPF_6$ in EC, as will be discussed in chapters 2.1 and 3.1.

1.2. Strategies to Increase the Energy Density

In the following, approaches to further increase the energy density on the active material level will be discussed. With respect to the anode, lithium metal and silicon offer improvements to the conventional cell chemistry in terms of specific energy density, however they suffer from severe degradation phenomena due to the lack of a stable interphase with the electrolyte.[77–81] Even before graphite was used, lithium metal had been investigated as anode material.[39,77] However, instead of forming a stable SEI as is the case for graphite, lithium metal tends to form dendrites and "mossy lithium" during charge at the lithium side.[78] This continuous surface area increase leads to a continuous electrolyte consumption, which negatively affects the coulombic efficiency.[77] As a result, a rather thick SEI is formed, leading to drastic impedance build-up that is particularly detrimental at high rates.[79] In addition, the dendrites can, in the worst case, grow through the electrolyte and penetrate the separator between anode and cathode, thus leading to electric shortcuts. This is a detrimental failure mechanism for Li-ion half-cells, leading to very limited cycle-life and in the worst case even to fire or explosion of battery cells.[77] Solid electrolytes such as, e.g., the garnet ceramic $Li_7La_3Zr_2O_{12}$ (LLZO)[82] or the thiophosphate $Li_{10}GeP_2S_{12}$ (LGPS)[83] and many other Li-ion conductive solids were suggested to enable the use of lithium metal anodes in the future.[84] Yet under some conditions, dendrite formation was reported to occur in all-solid state batteries (ASSB) with lithium metal anodes as well.[84] A rather different field of application of lithium metal anodes are Li-O_2 batteries. This type of battery typically consists of said lithium metal anode, a non-aqueous electrolyte, and a positive electrode out of porous carbon to allow the formation of solid Li_2O_2 from gaseous O_2.[85–87] This topic has been intensely investigated in the early 2010s, however it became more and more clear that this approach has many drawbacks on a system level, including the high-risk of incorporating a metal anode.[88]

In the field of conventional LIBs with liquid electrolyte, silicon-based anodes offer a true alternative to lithium metal electrodes.[35,80,89] In contrast to graphite or LTO, no intercalation takes place when silicon is lithiated but an alloy is formed instead. On the one hand, silicon offers a much lower average voltage (ca. 0.4 V vs. Li/Li^+) as compared to LTO (1.55 V vs. Li/Li^+) and a much higher theoretical capacity than graphite (3580 mAh/g for the $Li_{15}Si_4$ phase vs. 372 mAh/g for graphite).[59,89] However, silicon-based anodes suffer from mechanical stress due to the large volume-expansion of silicon upon lithiation.[81,90] This causes a severe mechanical instability which can lead to a disintegration of the electrode. Silicon nanoparticles had been studied as an alternative to micron-sized particles in order to solve the volume-expansion problem, however their large surface area leads to enhanced side reactions with the electrolyte[90,91] These side reactions are concomitant to active lithium loss and a low

coulombic efficiency.[90,92] In addition, the practical application of pure silicon anodes is complicated by a large voltage hysteresis of up to 0.35 V after the first cycle.[93,94] Silicon-graphite (SiG) composite might alleviate some of these problems. By optimizing its morphology and the silicon:graphite ratio, one can profit from a capacity increase by using silicon while enhancing stability and lifetime via the graphite component.[59,89] Especially when combining SiG composite electrodes with novel cathode active materials such as LMR-NCM, the energy density of battery systems could be raised compared to the state-of-the-art LIB chemistry.[35,89,95,96] The scheme in Figure 3 illustrates this opportunity based on a spreadsheet calculation by R. Schmuch et al.[96] by comparing volumetric and gravimetric energy densities for various cell chemistries on the level of an electrode stack for automotive batteries.

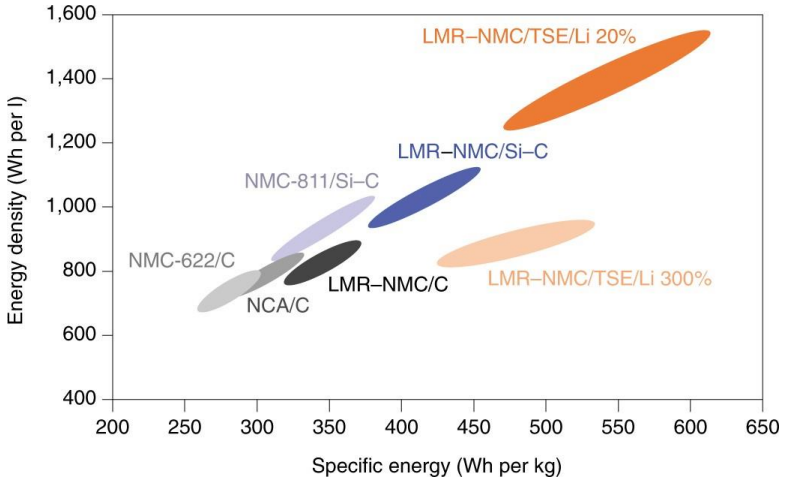

Figure 3: Scheme by R. Schmuch et al.[96] to compare various Li-ion full-cell chemistries with regards to energy content by volume and by weight at electrode stack level (taking into account anode, cathode, separator and electrolyte). The scheme was reprinted by permission from Springer Nature (R. Schmuch, R. Wagner, G. Hörpel, T. Placke and M. Winter: Performance and cost of materials for lithium-based rechargeable automotive batteries, Nature Energy, Copyright 2018). According to the authors of this study, the values are based on the calculation of the energy content of a cell stack by varying positive electrode thicknesses between 50 and 150 µm and using physical and electrochemical material properties as input parameters for a spreadsheet calculation. "TSE" refers to a thiophosphate solid electrolyte such as $Li_7P_3S_{11}$, either with 20 or 300% Li excess of the lithium metal anode, all other anode/cathode combinations refer to state-of-the art liquid electrolytes. "C" refers to graphite anodes, "Si-C" to a silicon-carbon composite anode with 20% Si. "LMR-NCM", "NCA" and "NCM622" refer to the same cathode materials as described in this thesis: Li-and Mn-rich nickel cobalt manganese oxides (LMR-NCM, $x\ Li_2MnO_3 \cdot (1\text{-}x)\ Li[Ni_xCo_yMn_{1-x-y}]O_2$), nickel cobalt aluminum oxide (NCA, $LiNi_{0.8}Co_{0.15}Al_{0.05}O_2$) and lithium nickel cobalt manganese oxide (NCM622, $LiNi_{0.6}Co_{0.2}Mn_{0.2}O_2$ and NCM811, $LiNi_{0.8}Co_{0.1}Mn_{0.1}O_2$).

In general, cathode active materials can be optimized by either raising the operating potential of the cathode active material or by increasing its capacity. Both pathways will lead to an enhanced energy density of the battery cell.[43] For example, the spinel $LiNi_{0.5}Mn_{1.5}O_4$ (LNMO) and the olivine $LiCoPO_4$ (LCP) offer a comparatively high operating potential.[97–100] Alternatively, LMR-NCM as well as stoichiometric Ni-rich NCM, NCA, and doped LNO offer higher capacities than the conventional NCM111 discussed in chapter 1.1.[101,102]

To start with the more detailed discussion of novel CAMs, the olivine LCP offers a theoretical capacity of 167 mAh/g and a rather high mean potential of 4.8 V vs. Li/Li^+, much higher than LFP with

3.4 V vs. Li/Li^+ or NCM111 with 3.8 V vs. Li/Li^+.[2,97,98] However, similar to LFP, LCP requires a carbon coating to enable cycling. In case of LCP, the thermal stability of such a carbon coating is not ensured, especially at high states of charge.[97] In addition, the carbon coating is prone to anodic oxidation at the high operating potential of LCP, which is a clear drawback regarding the cycle-life.[58] On the other hand, Fe substitution and various doping and coating strategies were demonstrated to optimize the practical capacity as well as the cycling stability of LCP and these approaches might open at least some perspective towards practical application in the future.[98] Not only olivines such as LCP, but also spinels such as $LiNi_{0.5}Mn_{1.5}O_4$ (LNMO) have been investigated as active materials for high-voltage cathodes. LNMO operates at 4.7 V vs. Li/Li^+ and offers a theoretical capacity of 146 mAh/g.[35,99,100] In contrast to NCM-based layered oxide materials, the spinel LNMO does not release oxygen at high states of charge.[72] However, the practical cycling performance of LNMO still has to be optimized by adjusting electrolyte formulations as well as the surface chemistry of LNMO. For instance, parasitic side reactions such as manganese dissolution must be mitigated in order to ensure a sufficiently long cycle-life of LNMO-containing full-cells.[100,103]

Similar to LNMO, LMR-NCM is a Mn-rich material, which makes it economically attractive.[96] In the literature, LMR-NCM is considered a promising candidate for reducing the Ni- and the Co-content compared to stoichiometric NCM.[104] Even Co-free versions of LMR-NCM are being discussed.[105] The use of Mn-rich CAMs such as LNMO or LMR-NCM could help to reduce the cost of CAMs drastically and would alleviate socio-economic problems associated to Co mining.[106] However, the structural properties are quite different, with LNMO being a spinel and LMR-NCM being a layered oxide.[97,100] The stoichiometric formula of LMR-NCM is $x\ Li_2MnO_3 \cdot (1\text{-}x)\ Li[Ni_xCo_yMn_{1-x-y}]O_2$, with the Li_2MnO_3 part representing the additional Li- and Mn-content compared to stoichiometric NCM materials with the formula $Li[Ni_xCo_yMn_{1-x-y}]O_2$.[95] Due to its high practical capacity of ca. 250 mAh/g, LMR-NCM is seen as a promising candidate for future Li-ion technology.[95] However, on an electrode stack level, LMR-NCM does not raise the volumetric and gravimetric energy density drastically, unless matched with innovative anode chemistries such as silicon-carbon composite electrodes according to R. Schmuch et al. (compare Figure 3).[96] A recent study by Schreiner et al. report a ca. 5 – 10% higher energy density for LMR-NCM//graphite cells compared to NCA//graphite cells in a comparative evaluation in multilayer pouch cells, despite a 30% higher CAM-specific capacity of LMR-NCM.[107] In order to access reversible capacities as high as 250 mAh/g, LMR-NCM must undergo an electrochemical "activation" plateau at $\approx$ 4.5 V vs. Li/Li^+ during the first delithiation, i.e. charge half-cycle.[108–110] During the activation, oxygen gas is released, which was initially ascribed to structural changes in the bulk, but later found to be part of a structural rearrangement of the active material surface.[111–115] While the origin of the extra-capacity of LMR-NCM compared to stoichiometric NCMs has been the object of vivid discussions within the scientific literature, there is increasing evidence that anionic oxygen redox within the bulk of LMR-NCM gives rise to high reversible capacities without any oxygen loss from the bulk

itself.[111,116–121] However, regarding the practical application of LMR-NCM, several obstacles still have to be overcome. First, LMR-NCM comes along with a large coulombic inefficiency in the activation cycle, and second, the impedance build-up is more severe compared to stoichiometric NCM.[122,123] In addition, LMR-NCM suffers from a large hysteresis between charge and discharge voltage as well as a constant decrease of the mean discharge voltage over cycling, the so-called "voltage fade".[102,104] In the literature, transition metal dissolution from the particle surface is reported to be problematic for both stoichiometric as well as overlithiated NCM. The dissolved transition metal ions are re-deposited on the graphite anode of a full-cell, which triggers gassing and causes resistance build-up.[124–127] Strategies to tackle these problems involve an optimization of the Li_2MnO_3 content,[128] bulk doping,[129–131] reactive gas and/or thermal treatment,[132–136] surface coating[137–139] as well as creating core-shell particles.[140,141] Examples for surface treatments of active materials will be presented in greater detail in the results section of this thesis (chapter 3.3).

Having discussed various research approaches for cathode active materials above, we shall now consider the already mentioned class of Ni-rich layered oxides. Some of these materials, e.g., NCM622 ($LiNi_{0.6}Co_{0.2}Mn_{0.2}O_2$) or NCA (e.g., $LiNi_{0.8}Co_{0.15}Al_{0.05}O_2$) can be already found in present-day commercial batteries, while some others such as doped $LiNiO_2$ (LNO) are still in the development phase.[2,142,143] Figure 3 illustrates that the higher Ni-content of NCM811 allows for a higher energy density than NCM622 on an electrode stack level. On a material level, within the group of NCM-based materials, increasing the Ni content typically means increasing the capacity.[144] The Ni-rich NCM chemistry is already being used in commercial cells for high-energy applications such as electric cars.[2,35,89] The same holds true for NCA materials, being among else Tesla's choice of cathode material for EV battery packs.[2,35]

Regarding the NCM electrochemistry, for all $LiNi_xCo_yMn_zO_2$ stoichiometries with $x + y + z = 1$, the theoretical capacity defined by the Li^+ content per formula unit is rather similar, i.e., ca. 275 mAh/g.[71,145,146] However, an increased nickel content lowers the potential profile in such way that higher states of charge are accessible within the stability window of typical LIB electrolytes. For instance, NCM111 and NCM622 would have to be charged to 4.7 V vs. Li/Li^+ to extract ca. 80 – 90% of the Li^+ contained in the $LiMO_2$ stoichiometry, which clearly exceeds the oxidative stability limit of electrolyte components such as VC. In contrast, NCM811 reaches the same SOC already at 4.3 V vs. Li/Li^+ as demonstrated by Jung et al.[147] It should be noted that none of the mentioned NCMs can be charged much beyond 80% SOC, since then O_2 is evolved from the layered oxide itself, leading to rapid aging of the cathode active material and in addition to further side reactions with the electrolyte.[147] Depending on material quality, potential cut-off, C-rate, and electrolyte choice, the class of NCM materials moves towards a practical specific capacity slightly above 200 mAh/g, clearly exceeding the practical NCM111 capacity of ca. 150 – 160 mAh/g [38,41,144,147] Both, Ni-rich NCM such as NCM811 and

NCA can be seen as derivatives of LNO.[142,148] The drawback of Ni-rich layered oxides is the lower thermal stability compared to, e.g., NCM111.[144,149] In the future, surface-stabilized $LiNiO_2$ doped with a small percentage of Al, Co, Mn, or Mg might be an option for future high-energy CAMs, provided that the structural stability and the cycling performance of such high-Ni materials can be optimized.[37] To achieve such a goal, structural instabilities of Ni-rich layered oxides during electrochemical cycling have to be tackled. For instance, nickel is prone to disorder within the layered oxide structure, which makes the structures of bulk and surface less stable.[37,127] The high crystallographic volume change during lithiation/delithiation of Ni-rich layered oxides is challenging in terms of structural integrity during extended cycling and gives rise to particle cracking.[150–152] However, the destabilizing effect also appears to be connected to the higher Li^+ utilization of Ni-rich NCMs or NCA compared to, e.g., NCM111 as pointed out in Jeff Dahn's group by the work of Li et al.[148] As mentioned above, a very high degree of delithiation can destabilize the structure of Ni-rich layered oxides. Typically, at SOCs above 80% or at high temperature, O_2 is released from the surface, thereby transforming the shell of the active material particles to a NiO rocksalt layer.[144,153–155] While uncontrolled gassing in general can lead to cell bulging, O_2 is particularly dangerous because it vividly reacts with the organic electrolyte solvents at elevated temperature. In the worst case, this can lead to a thermal runaway leading to fire or explosion of the whole cell.[156,157] Putting aside safety questions, the SOC-dependent oxygen loss accelerates the aging of battery cells.[68,147,155] It should be noted that highly reactive singlet oxygen is set free during such degradation reactions as experimentally proven by Freiberg et al.[158] The singlet oxygen decomposes electrolyte components such as EC, while the linear carbonate DMC was found to be stable.[159] This is consistent with the finding that EC-free electrolytes containing FEC and EMC enable a more stable cycling of Ni-rich layered oxides.[68,160] Various strategies have been reported to optimize the stability of Ni-rich NCMs, such as thermal treatment,[47,161] reactive gas treatment,[162,163] surface-coating[138,164] as well as the development of core-shell particles.[165,166] Doping, e.g., with Mg, Ti, or Zr cations, has been reported to optimize bulk as well as surface properties of Ni-rich layered oxides during electrochemical cycling.[149,167,168] In the end, by finding the best strategies to stabilize Ni-rich layered oxide, electrochemical performance and lifetime characteristics of these CAMs are likely to be increased and foster their application in commercial batteries, e.g., for electric vehicles.

Regarding surface properties, the chemical reactivity of Ni-rich oxides is a major challenge not only regarding the lifetime of full-cells, but also in the context of electrode manufacturing. Due to its high basicity, the active material surface is prone to react with CO_2 and moisture, e.g. from ambient air, which leads to the formation of surface hydrates, hydroxides, carbonates, and mixtures thereof (Figure 4).[47,48,161,169] These surface contaminants can be formed during CAM handling and electrode manufacturing if the surrounding atmosphere is not sufficiently dry, which will be discussed in greater detail in chapter 3.2.2. Not only Ni-rich NCM, but also LMR-NCM suffers from similar degradation phenomena when exposed to moisture and CO_2 due to its typically high specific surface area compared

to stoichiometric NCMs, as will be pointed out in chapter 3.2.1. Two major problems caused by the surface contaminants are, first, the gelation of NMP(*N*-methyl-2-pyrrolidone)-based slurries prepared for electrode manufacturing and, second, side reactions with the electrolyte leading to accelerated aging and severe gassing inside the cell.[48,161,170] Within this thesis, the surface reactivity of Ni-rich NCM and LMR-NCM exposed to atmospheric CO_2 and moisture has been investigated qualitatively and quantitatively (cf. chapter 3.2). In case of LMR-NCM, a thermal treatment with SO_3 was developed in order to make the material more robust versus humid ambient air (cf. chapter 3.3.1 and Figure 4). Besides, thermal treatments of LMR-NCM with SO_2[135] and Ni-rich NCM with F_2[163] were found to positively impact the electrochemical performance of the respective CAM (cf. chapters 3.3.2 and 3.3.4, respectively).

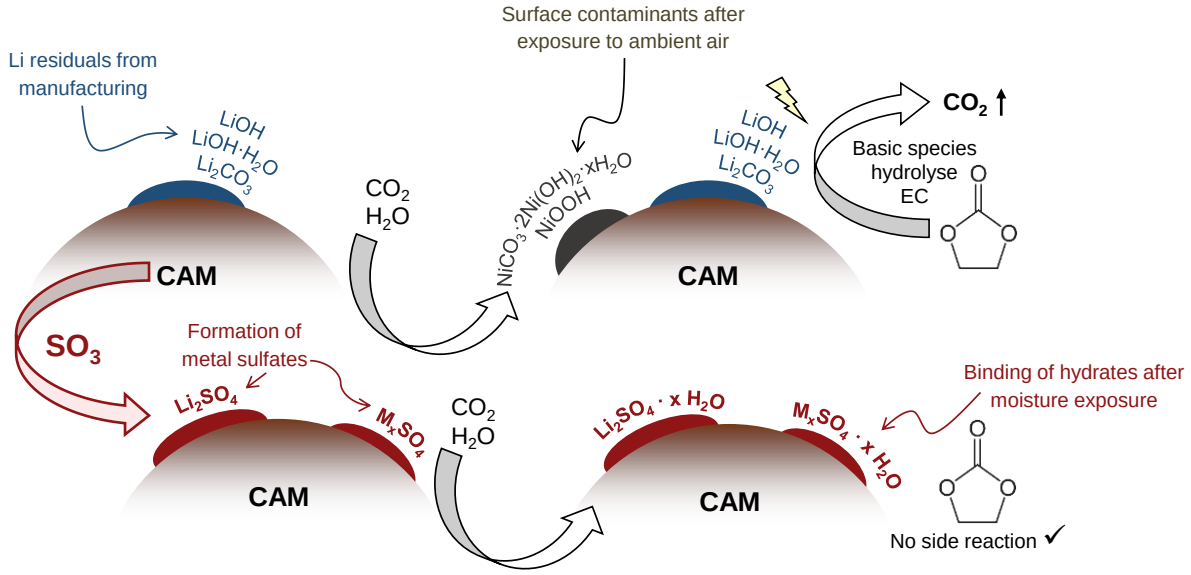

Figure 4: Scheme of two central topics within this thesis: (i) the formation of surface contaminants on CAMs after exposure to CO_2 and moisture from ambient air (top part) and (ii) surface sulfation by SO_3 treatment (bottom part). Hydroxides within the surface contaminants and lithium residues from CAM manufacturing decompose EC and lead to severe CO_2 gassing (top part). In contrast, after SO_3 treatment (bottom part), metal sulfates can still bind water in the form of hydrates, however they do not form carbonates when exposed to CO_2. Most importantly the formation of basic surface species is mitigated, thus EC is not hydrolysed and CO_2 gassing is prevented.

2. Materials and Methods

2.1. *Operando* Diffuse Reflectance Infrared Fourier Transform Spectroscopy

There exist multiple tools to assess surface properties of electrode materials as well as electrolyte decomposition reactions, *ex situ* as well as *in situ*/*operando*. E.g., gassing analysis via on-line or differential electrochemical mass spectrometry (OEMS/DEMS) of battery cells is a powerful tool to get insights into parasitic reaction mechanisms. In case of graphite, CO_2, CO, and ethylene evolution were found to occur concomitant to SEI formation when using EC based electrolytes.[64,171–173] *Ex situ* surface analysis via X-ray photoelectron spectroscopy (XPS) or Fourier transform infrared spectroscopy (FTIR) allows to characterize electrolyte decomposition products on the surface of active material particles. While inorganic materials such as Li_2O or LiF are well accessible by XPS analysis,[61] FTIR helps to identify organic species such as lithium ethylene dicarbonate (LEDC)[174] as well as inorganic SEI decomposition compounds such as lithium carbonate (Li_2CO_3).[57,124] One can choose between various sampling techniques for infrared spectroscopy such as attenuated total reflection (ATR),[174,175] transmission FTIR[176] or diffuse reflectance infrared Fourier transform spectroscopy (DRIFTS).[177–179] The advantage of DRIFTS is its high surface sensitivity for rough substrates[180] such as typical LIB electrodes. A special technique developed for *operando* studies on lithium-ion battery electrolytes is substractively normalized interfacial FTIR spectroscopy (SNIFTIRS). In SNIFTIRS, the spectral intensity is calculated according to equation 12, with R_n being the reflectance of the n^{th} spectrum in a consecutive measurement of spectra:[181,182]

$$\Delta R = \frac{R_{n+1} - R_n}{R_n} \qquad \text{(equation 12)}$$

This technique has been used, for example, to study (i) the oxidation of carbonate based electrolyte formulations via external reflection FTIR spectroscopy on a polished nickel metal electrode[181] or (ii) signal changes ascribed to SEI formation on graphite from an EC-based electrolyte using an *operando* cell designed for ATR-FTIR spectroscopy.[182] These literature studies on SNIFTIRS reveal on the one hand a certain sensitivity towards spectral changes during *operando* studies, however at the same time the discussed spectra appear to have only poor signal-to-noise-ratios, and random fluctuations from electrolyte signals are also possible.

A different technique was introduced by Yohannes et al.[177] from the group of Shawn D. Lin in Taiwan, who recently published a study of the SEI formed on mesoporous carbon microbeads (MCMB) by $LiPF_6$ based electrolytes containing ethylene carbonate (EC), vinylene carbonate (VC), and fluoroethylene carbonate (FEC) via an *in situ* DRIFTS method which was developed in the same group.[183]

Within this thesis, the *operando* DRIFT spectra were evaluated in reflectance units using a gold background without subtracting or normalizing the spectra of a measurement sequence from each other (equation 13) in order to avoid the above mentioned artefacts from the literature studies:

$$\% R = \frac{R_{\text{sample}}}{R_{\text{reference}}} \cdot 100\% \qquad \text{(equation 13)}$$

The DRIFT spectra in chapter 3.1 are displayed in reflectance unit according to equation 13.

2.1.1. IR Spectrometer

Infrared spectra were recorded with a Cary 670 FTIR spectrometer (Agilent Technologies, USA) equipped with a liquid nitrogen cooled MCT (mercury cadmium telluride) detector with high sensitivity in the mid-IR region from 6000 to 450 cm^{-1}. The spectrometer was constantly purged with dried compressed air using an adsorption dryer (FST GmbH, Germany).

2.1.2. Electrode Preparation

Lithium iron phosphate (LFP, $LiFePO_4$) electrodes were prepared by mixing 93 wt.-% LFP (LFP-400, BASF, BET surface area: 23 m^2/g) with 4 wt.-% PVDF (Kynar® HSV 900, Arkema, France), and 3 wt.-% conductive carbon (C-NERGY Super C65 Carbon Black Additive, TIMCAL, Switzerland). The solids were mixed at 2000 rpm for 1 min in a planetary orbital mixer (Thinky, Japan). After addition of NMP (*N*-methyl-2-pyrrolidone, Aldrich, USA, anhydrous, 99.5% purity) resulting in a solid content of 60%, the obtained slurry was mixed at 2000 rpm for 2 min. The next NMP addition step resulted in 55% solid content, the slurry was mixed for 2 min at 2000 rpm, yielding a highly viscous ink. Coatings were made on a woven steel wire mesh with 26 µm aperture and 25 µm wire diameter (from stainless steel 316, Mesh500, TheMeshCompany, United Kingdom). The use of a mesh as electrode substrate instead of an aluminum foil was necessary to allow the penetration of the electrolyte through the current collector, which is illustrated by the scheme of the cell setup in Figure 5. A doctor blade driven by an automatic coating machine (RK print, Germany, speed mode 1, i.e., 25 mm/s) served to prepare coatings with 100 µm wet film thickness. After drying at 50 °C, electrodes were punched and further dried under vacuum overnight in a glass oven at 120 °C. The resulting loading was ≈20 mg_{LFP}/cm^2.

LTO electrodes (SAFT, USA, BET surface area 5.5 m^2/g) were prepared in the same way as the LFP electrodes (NMP-based slurry with LTO/PVDF/C65 in a 93:4:3 ratio), resulting in loadings around 7 mg_{LTO}/cm^2.

NMP-based Graphite slurries were mixed using graphite (TIMREX SLP30 Primary Synthetic Potato® Shape, TIMCAL, Switzerland, BET surface area: 7.5 m²/g) and PVDF (Kynar® HSV 900, Arkema, France) as binder material (wt.%-ratio: 90:10, solid content 30 wt.%). The slurries were mixed for 5 min at 2000 rpm under partial vacuum (5 kPa total pressure) in the planetary orbital mixer. Blade-coating was carried out with wet film thickness of 250 µm with the automatic coater at a speed of 25 mm/s (RK print, Germany).

2.1.3. Cell Assembly and Mounting in the Spectrometer

The cell illustrated in Figure 5 was tailor-made for the *operando* DRIFTS study. The first version of the *operando* DRIFTS cell is described in Uta Schwenke's PhD thesis.[179] It has been designed for Li-O_2 research. The modified version of the cell described in the following offers more space for a slightly bigger lithium counter electrode and additional space for thicker separators – glass fiber instead of polyolefin. The compressibility of the glass fiber separators served to improve the mechanical contact between separator and working electrode compared to the previously used[179] polyolefin separators. This effect was enhanced by coating the working electrode on a steel mesh and not on polyolefin separators as had been done for the Li-O_2 studies.[179] In addition, the aluminum wire connecting the working electrode to the potentiostat has been replaced by copper in the thesis at hand, since aluminum is less stable at negative potentials.[184,185] Figure 6 explains the cell assembly, as well as the mounting inside the DRIFTS chamber. It should be noted that in Figure 6 the insertion of a gold background with a rough surface (gold sputtered silica paper) is depicted instead of the cell stack described in the following.

For the cell stack (Figure 5), we used an electrically insulating polyether ether ketone (PEEK) body (part C in Figures 5 and 6) with a steel plate at the bottom as current collector (D) equipped with a thread to be tightly fixed with a screw-nut at the bottom (E). The DRIFTS cell was assembled inside an Ar-filled glovebox (< 0.1 ppm O_2 and H_2O). On top of the steel plate (D), a lithium electrode was placed (Rockwood lithium, USA, > 99.9% pure, 0.45 mm thick, punched to 7 mm diameter and compressed manually with a plastic stamp to extend to 8 mm on the steel plate), followed by 9 mm separators (VWR glass fiber filter, grade 691, dried under vacuum prior to cell assembly at 120 °C) and an 8 mm working electrode (coated on a woven wire mesh, details see above). In between, 20 µL electrolyte was added in two steps (see Figure 5 for details). The electrolyte consisted of 1.5 M $LiPF_6$ in pure vinylene carbonate (VC) or 1.5 M $LiPF_6$ in pure ethylene carbonate (EC). EC, VC, and $LiPF_6$ were provided by BASF. The specified purities (w/w) were 99.9 – 99.99% in case of VC, 99 – 100% for EC, and 100% for $LiPF_6$. These "EC-only" and "VC-only" electrolytes were used to avoid volatile components such as EMC, which is contained in commercial electrolyte formulations such as LP57. In pre-tests it was found that volatile solvents evaporate quickly from the working electrode, which has a large uncovered surface in order to allow the access of the IR beam to the electrode (cf. Figure 5). For

electrical contacting of the working electrode, a steel ring and M1 screws were used (A and B in Figures 5 and 6), going to threads inside the PEEK body (C). PEEK was chosen as a material because it is chemically stable and mechanically strong enough for mounting these tiny screws. These PEEK threads typically were worn out after twenty times of cell assembly and disassembly. The last screw was used to connect a copper wire (panel 3.3 in Figure 6) after placing the cell inside the stainless steel chamber. The copper wire is surrounded by an electrically insulating heat-shrink sleeve (HST28T, Adtech Polymer Engineering Ltd., United Kingdom). For improving the electrical contact between the nut (E) at the bottom of the lithium electrode with the housing, a copper foil was used (panel 3.2 in Figure 6). After mounting the cell inside the chamber, it was capped with a dome (panel 4 in Figure 6) with two IR-transparent windows (KBr, Korth Kristalle GmbH, Germany) and one silica viewing glass (the lower one in panel 4.2). Chamber and dome were adapted and modified after purchase from Harrick Scientific Products Inc., USA. For the sealing of the dome, a Viton® O-Ring is used, while the KBr windows and the viewing glass are equipped with FEP-O-Seal® O-rings (Angst+Pfister, Switzerland).

For comparison, a Swagelok® T-cell was assembled with a Li counter electrode of 10 mm diameter, one 11 mm glass fiber separator, 50 µL EC with 1.5 M $LiPF_6$ ("EC-only") electrolyte added in one step, and a 10 mm working electrode (LFP on woven wire mesh, electrode preparation see chapter 2.1.2).

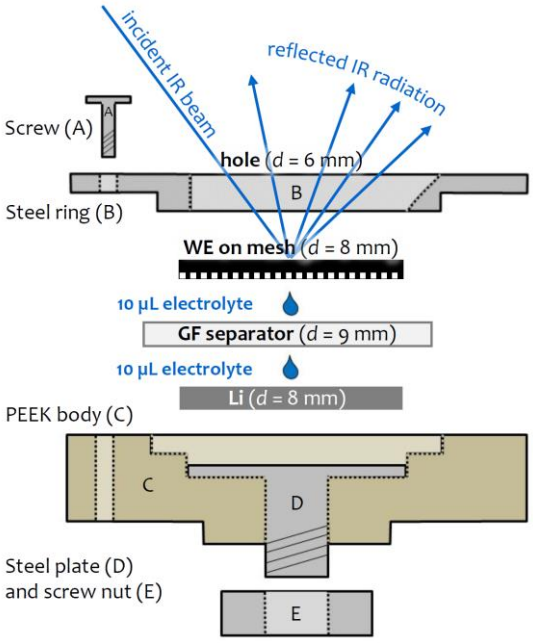

Figure 5: Sketch of the *operando* DRIFTS cell (adapted and modified from Uta Schwenke's thesis[179]) with LFP coated on woven wire mesh as working electrode (WE), 20 µL of 1.5 M $LiPF_6$ in EC as electrolyte, and Li as counter electrode. Three screws (A) are used to mount the stainless steel ring which serves as current collector for the WE (B) on the PEEK body (C). The Li counter electrode (CE) is placed on top of the current collector, i.e., a steel plate (D) fixed with a screw nut (E).

After DRIFTS cell assembly in the glovebox (< 0.1 ppm O_2 and H_2O), it was flushed with 10% CO_2 in Ar for 90 s at 15 Nl/h, if experiments were carried out in presence of CO_2. Otherwise, the

cell was flushed with pure Ar for 90 s at 15 Nl/h in order to remove trace amounts of CO_2 and N_2 contained in the glovebox atmosphere.

The Harricks chamber with the cell inside is then mounted in the DRIFTS mirror optics (Figure 6, Praying Mantis™ by Harricks Scientific Products Inc., USA). After mounting the chamber and adjusting the height (see next chapter 2.1.4), the spectrometer (panel 6.3) was closed and a rest of 15 min was allowed to flush out ambient air from the sampling compartment and letting it be replaced by dried and CO_2-free compressed air provided by the air dryer (6.2). The potentiostat (6.1) is connected via (i) the chamber steel housing in case of the lithium counter electrode (blue cable in panel 5.2) and (ii) the copper wire welded to a pin, which is connected to the red cable in panel 5.2.

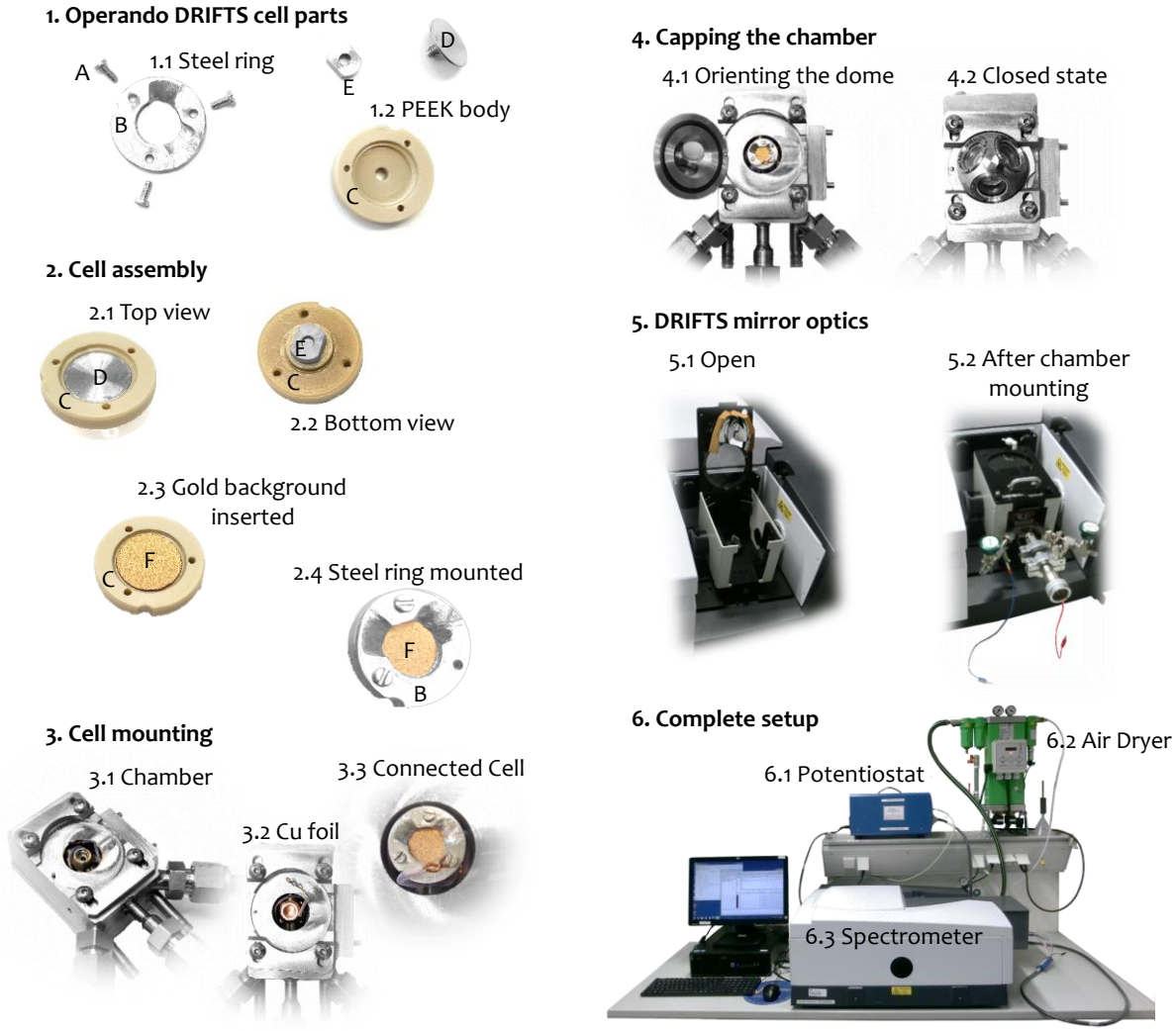

Figure 6: *Operando* DRIFTS cell parts and assembly (1, 2). Parts A-E are specified in Figure 5. Instead of the cell stack (CE, separator, WE), the insertion of the coarse gold background (F) is demonstrated here. Panel (3) illustrates the cell mounting inside the Harricks chamber and the gas-tight sealing with a dome (4) comprising two IR-transparent KBr windows and one viewing glass window. The DRIFTS chamber is mounted inside the Harricks Praying Mantis™ mirror optics (5). Panel (6) depicts the complete *operando* DRIFTS measurement setup with a Bio-Logic SP-200 potentiostat (6.1) connected to the cell inside the Agilent Cary 670 IR spectrometer (6.3), which is constantly purged with dried compressed air (6.2).

Figure 7 illustrates how the IR beam passes the DRIFTS mirror optics (Praying Mantis™, panel (a)) and how the *operando* DRIFTS cell is placed inside the modified high temperature reaction chamber (panel(b)).

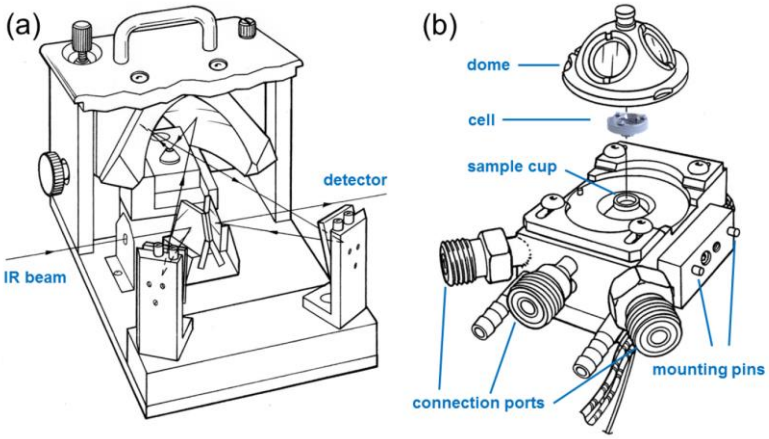

Figure 7: The Praying Mantis™ accessory designed for DRIFTS by Harrick Scientific Products, Inc. (modified scheme from the user manual, reprinted from Uta Schwenke's thesis[179], with permission from Harrick Scientific Products, Inc.). (a) Sketch of the infrared beam path. (b) High temperature reaction chamber by Harricks modified for placing the electrochemical cell (Figure 5) inside.

2.1.4. DRIFTS Measurement and Evaluation

After mounting the chamber in the DRIFTS accessory (Figures 6 and 7), the height of the cell was adjusted to maximize the intensity of a live-monitored interferogram (detector signal intensity as a function of the optical path difference generated between two mirrors in the interferometer). As mentioned above, the cell was allowed to rest 15 min after closing the spectrometer housing to remove CO_2 and moisture from the measurement compartment.

First, instead of the cell stack, a gold background, i.e., a gold sputtered abrasive paper with granulation 400 was mounted in the cell to obtain a background spectrum (360 scans, 1 cm^{-1} resolution, recording time of 2 min per spectrum). This was then used as reference to convert the intensity of each sample spectrum into reflectance units $\%\,R = \frac{R_{\text{sample}}}{R_{\text{reference}}} \cdot 100\,\%$ (cf. equation 13 in $\%\,R = \frac{R_{\text{sample}}}{R_{\text{reference}}} \cdot 100\,\%$). A sample in this case refers to an *operando* cell with the working electrode being measured.

The rationale behind choosing this specific type of gold background was (i) to maximize diffuse reflectance by using a rough surface and (ii) having a fully reflective surface, i.e., gold. Thus, the sample intensity (e.g., graphite electrode coating) will always have a lower intensity than the gold background, resulting in reflectance values smaller than 100%.

2.1.5. Electrochemical Cell Cycling Procedure for *operando* DRIFTS Cells

In case of graphite/EC + 1.5 M $LiPF_6$/Li, negative potential scans were performed with a rate of 0.5 mV/s from OCV to 0 V vs. lithium and positive scans to 1.5 V, using an SP-200 potentiostat (Bio-Logic, France). Galvanostatic cycling of graphite was carried out at a rate of C/10 (37.2 $mA/g_{graphite}$) with 0 V vs. lithium as lower and 1.5 V as the upper cutoff.

One LFP/EC + 1.5 M $LiPF_6$/Li cell was cycled at C/2 (85 mA/g_{LFP}) with 4 V as upper and 1.5 V as lower cut-off. Subsequently a potential scan was performed with 0.5 mV/s from OCV to 0 V vs. lithium. An LTO/ VC + 1.5 M $LiPF_6$/Li cell was swept from OCV to 5 V vs. lithium with 0.5 mV/s.

2.2. Formation of Surface Contaminants on Cathode Active Materials

When NCM811 is exposed to moisture and CO_2, hydroxides, carbonates, and hydrates are formed on the surface, often referred to as surface contaminants, as mentioned at the end of the introduction (chapter 1.2) and discussed in more detail in the publication[47] in chapter 3.2.2. Some of these species have IR active vibrations such as the carbonate band[186–188] at 1470 cm^{-1} and can be characterized by DRIFTS. A new setup was developed to monitor the formation of surface contaminants on NCM811 powder while it is exposed to a CO_2 and moisture containing gas mixture (Figure 8). The characterization of surface contaminants was complemented by TGA-MS and NCM811//graphite full-cell cycle-life tests. The results of the *in situ* DRIFTS study on surface contaminants are described in section 3.2.3 of this thesis.

The *in situ* DRIFTS setup (Figure 8) consisted of a gas cylinder with 1000 ppm CO_2 in Ar (99.9% CO_2 in 99.999% Ar, Westfalen, Germany), a flowmeter with the gas flow set to 10 ml/min, and a self-made humidifier system consisting of a modified and tightly sealed glass vial (DURAN®, Schott, Germany). The humidifier temperature was kept at 0°C in order to avoid moisture saturation of the carrier gas. The humidified carrier gas feeds the DRIFTS sample chamber inside the spectrometer, which operates at room temperature. All gas linings were connected with stainless steel tubes, valves, and fittings from *Swagelok* (USA). The humidifier was connected to a bypass tube via two valves in order to allow flushing of dry gas without moisture input. A gas-tight chamber (high-temperature reaction Chamber (HVC), Harrick Scientific Products Inc., USA, same as described in chapter 2.1.3) with IR-transparent windows was connected to the gas line. Between the gas line and the chamber, an outlet valve was mounted to allow flushing of the whole line before connecting the chamber to the gas feed. The gas-tight sample chamber was the same as used for the *operando* DRIFTS study described in chapter 2.1.3. However, instead of an electrochemical cell, a small steel pot was placed and filled with the

powder sample in an Ar-filled glovebox (< 0.1 ppm O_2 and H_2O). The sealed chamber was mounted in the Praying Mantis™ accessory, as described in chapter 2.1.3.

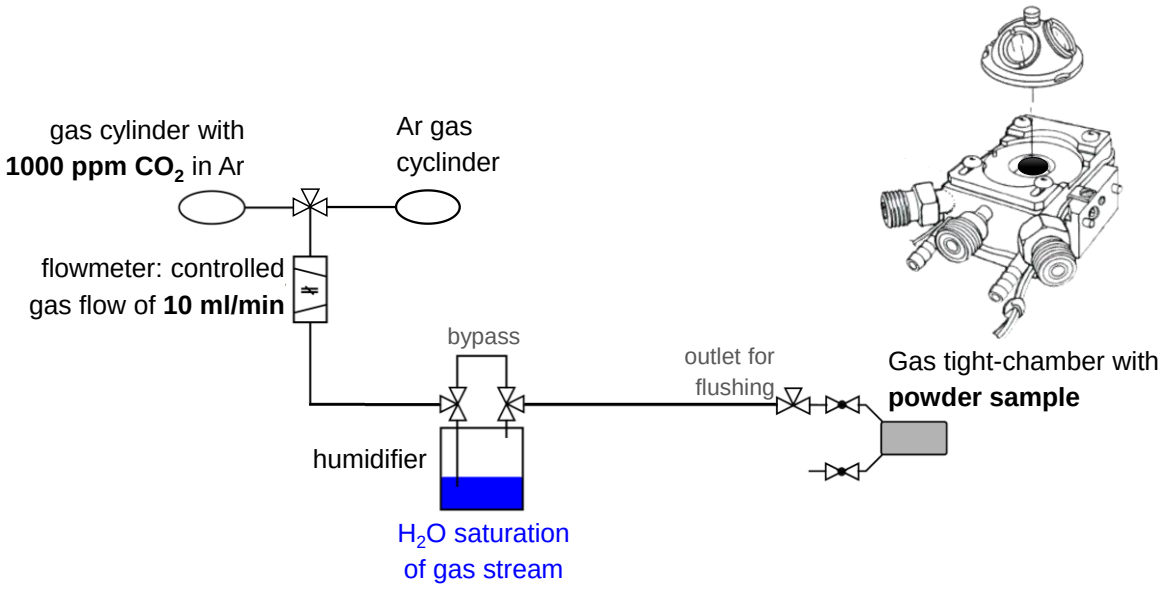

Figure 8: Setup for *in situ* DRIFTS measurements exposing CAM powders to various gas mixtures containing Ar as carrier gas and CO_2, H_2O vapor, or both as reactants. The humidifier was immersed in a water/ice bath to be kept at a temperature of 0°C in order to control the water vapor content of the humidified Ar. The DRIFTS chamber where the sample is placed operates at room temperature. The sketch was adapted from Christian Sedlmeier's Master's thesis.[189]

Typically, one would prepare a small fraction of sample, e.g., 1% in a dilution medium such as KBr in order to achieve a good signal quality and high sensitivity for surface species.[180] Consequently, KBr dilutions were used for the *ex situ* DRIFTS measurements of CAM samples presented in the articles[47,134] in chapters 3.2.2 and 3.3.1, respectively. However, it was found that the dilution media such as KBr react with moisture. Thus, for the *in situ* DRIFTS study, pure NCM811 powder was characterized without any dilution medium in order to avoid artefacts from reactions between moisture and the dilution medium. Even less hygroscopic dilution media than KBr, such as AgBr, SiC, CaF_2, or Al_2O_3 were found to react with moisture (data not shown).

For undiluted samples, DRIFT spectra are displayed in reflectance units R_{CAM}, which are defined by the ratio of sample intensity (I_{CAM}) versus the intensity of gold sputtered sand paper (I_{gold}) as background (equation 14). Spectra were recorded with a resolution of 1 cm^{-1}. Further details on the IR spectrometer are given in chapter 2.1.1. The gold background is explained in chapter 2.1.4.

$$R_{CAM} = \frac{I_{CAM}}{I_{gold}} \qquad \text{(equation 14)}$$

Kubelka-Munk units (equation 15) were used as recommended by textbook literature[180] for CAM samples measured in KBr dilutions (1 wt% CAM in KBr), i.e., for the *ex situ* DRIFT spectra

discussed in the papers[47,134] in chapters 3.2.2 and 3.3.1. Since the KM normalization can lead to baseline fluctuations,[190] it was not used for the undiluted samples for the *in situ* experiment. Instead, reflectance units were used as explained above (equation 14) in order to avoid artefacts from normalization.

$$\mathrm{KM} = \frac{(1 - R_{\mathrm{CAM}})^2}{2R_{\mathrm{CAM}}} \qquad \text{(equation 15)}$$

For the *in situ* DRIFTS measurements, NCM811 powder (BASF, Germany) was exposed to several gas atmospheres containing moisture, CO_2, or a combination of both, using the setup depicted in Figure 8. Before this, NCM811 was calcined at 525°C for 1 h under Ar flow (1 l/min; 99.999% purity, Westfalen, Germany) in a tube furnace (Carbolite, Germany) in order to remove a major fraction of the typically present surface contaminants. This calcined NCM811 was deliberately exposed to CO_2 and moisture for several days in order to maximize the signal intensities of potentially formed surface contaminants (compare Table 5). The detailed experimental procedure was: First, the CAM powder was placed in the Harricks chamber and mounted inside the Praying Mantis™. The spectrometer was then closed with a custom-made housing and continuously fed with dry air as described in chapter 2.1.1. The settings for data collection were 360 scans per spectrum, 1 cm^{-1} resolution, i.e., a recording time of 2 min per spectrum, in other words the same as explained for the *operando* DRIFTS study described in chapter 2.1.4. The gas tubes of the *in situ* DRIFTS setup passed through the housing to connect the Harricks chamber to the gas line depicted in Figure 8. Several gas mixes containing moisture, CO_2, or a combination of both with a total gas flow 10 ml/min were tested in sequence, as will be explained in more detail in the results part in chapter 3.2.3.

Along with the NCM811 powder, electrodes were exposed under the same conditions inside the HVC chamber to enable accompanying electrochemical tests. The electrodes were placed in such a way that they did not interfere with the incoming and outgoing IR beam.

NCM811 electrodes were prepared in an Ar-filled glovebox under the same conditions as described in the article[47] in chapter 3.2.2 (experimental part, electrode preparation and cycling). The manufacturing of graphite anodes is described therein as well. Swagelok T-cells were tested at 25°C with 80 µL LP572 electrolyte (1 M $LiPF_6$ in EC:EMC 3:7 (w:w) plus 2 vol% VC, BASF, Germany). Anode and cathode were separated by two glass fiber separators (glass microfiber filter #691, VWR, Germany) with 11 mm diameter. Lithium metal foil (Rockwood Lithium, USA) was used as reference electrode in a 3-electrode T-cell setup. Cycling was carried out as follows: The cells were charged to 4.2 V vs. graphite in constant current mode followed by a constant voltage hold (CCCV) until the current would drop below C/20 or for a maximum time of 1 h; they were discharged to 3.0 V vs. graphite in constant current (CC) mode. The cycling was started with two C/10 cycles, followed by 48 1C cycles

(same rates for charge and discharge). This 50 cycle-segment (three C/10 rate checks followed by extended 1C cycling) was repeated 4 times, summing up to 200 cycles in total.

The findings from the *in situ* DRIFTS measurements and the electrochemical cycling were supported by a TGA measurement of the NMC811 powder before starting the *in situ* DRIFTS measurement, i.e., taking NMC811 directly after calcination at 525°C as well as after completing the *in situ* DRIFTS experiment, which will be described later in the results part (cf. chapter 3.2.3). Experimental details for TGA-MS measurements are consistent with the procedure described in the article[47] in chapter 3.2.2. As discussed therein in more detail, TGA allows to characterize the amount of surface contaminants via the TGA weight loss. The coupling to mass spectrometry was not available when the TGA experiments for the *in situ* DRIFTS study were carried out.

2.3. Thermal Treatment of Cathode Active Materials with SO_2 and SO_3

2.3.1. Furnace Setup

As will be discussed in chapter 3.3.1, a tube furnace setup was applied to treat CAM powder samples with the reactive gas SO_3. The specifications of the components, gases and gas mixtures used in the setup are mentioned in detail in the experimental part of the journal article[134] presented in chapter 3.3.1, together with a functional scheme of the setup (Figure 3 therein). This furnace setup also allowed the use of SO_2 in Ar instead of SO_3 in Ar and O_2 as a reactive gas. The results of thermal treatment of LMR-NCM with SO_2 have been published, too, and are presented in chapter 3.3.2.[135] Therein, the SO_2 treatment method developed within this thesis at the Technical University of Munich (TUM) is compared against a different set of experiments performed at Bar-Ilan University (BIU).

Figure 9 further illustrates how the same tube furnace setup can be either used for SO_3 or SO_2 treatment of CAM samples by controlling the activity of a V_2O_5 catalyst inside a separate ceramic tube (reactor) connected to the tube furnace. A photograph of this tube furnace setup is shown in Figure 10. The catalyst activity is controlled via temperature and by choosing between the presence and absence of oxygen in the gas mixture. In both cases, all surface contaminants, i.e., hydroxides, carbonates and hydrates are removed by a calcination step under 30% O_2 in Ar at 625°C (total gas flow 1 l/min, compare step I in Figure 9a and b) before the reactive gas treatment (step II(a) in Figure 9a and b) with the exception of lithium carbonate, which has a higher temperature stability as discussed in the publication[47] in chapter 3.2.2. The “cleaned” oxide surface is exposed to SO_3 or SO_2. In case of SO_3 treatment (Figure 9a and c), the industrially well-established contact process was applied to convert small concentrations of SO_2 (0.5%) in Ar as carrier gas into SO_3 in the presence of an oxygen excess. The final concentrations

of SO_2, Ar and O_2 were adjusted by regulating the gas flow of the reactor feed gases SO_2 (in Ar), pure Ar and pure O_2 feed gases to reach final concentrations of 0.5% SO_3 and 30% O_2 in Ar to react with the sample. The conversion of SO_2 to SO_3 in the presence of the obvious oxygen excess was catalyzed by crushed V_2O_5 pellets inside a ceramic tube preheated to 430°C (see Figure 9c). As explained in the above mentioned publication,[134] the conversion efficiency from SO_2 to SO_3 is > 97% according to the catalyst manufacturer under the applied conditions with a space velocity of 11/h and a total flow rate of 1 l/min inside the ceramic tube.

For the SO_2 treatment of CAM samples within the same setup (compare Figure 9b and d), 0.5% SO_2 in Ar as carrier gas (without oxygen) was supplied to the tube furnace, as described in the experimental part of the publication in chapter 3.3.2.[135] In this case, the conversion of SO_2 to SO_3 can be excluded for two reasons: first, the catalyst temperature was not heated to its activation temperature and second, no oxygen was present in the feed gas to the catalyst. The ceramic tube containing the crushed V_2O_5 catalyst pellets was kept at 100°C as a precautionary step in order to exclude any adsorption of SO_2 on the V_2O_5 surface.

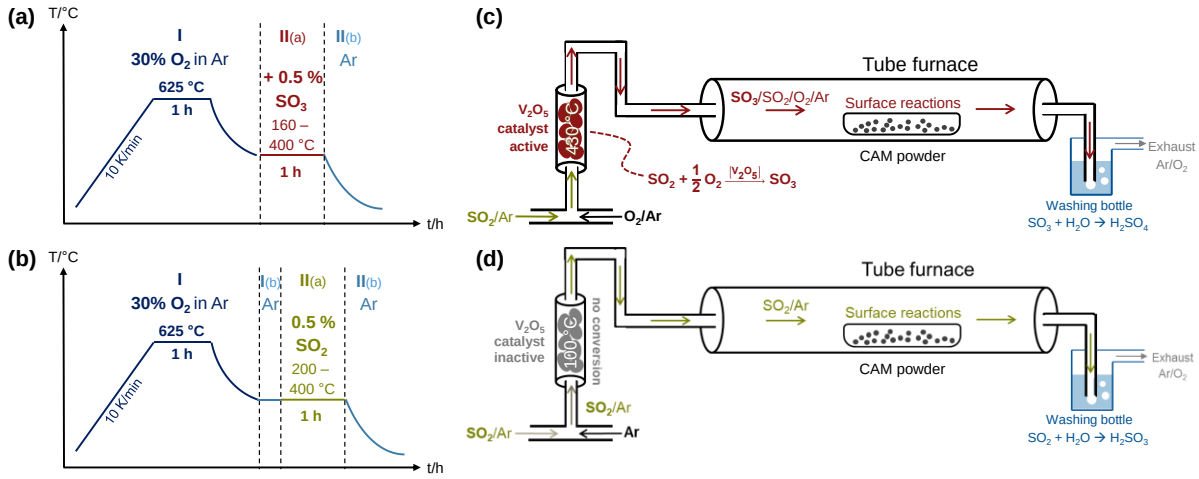

Figure 9: Experimental parameters for the thermal treatment of CAM powder with SO_2 (a, c) or SO_3 (b, d). Temperature profile and protocol for (a) SO_3 and (b) SO_2 treatment. Scheme of the tube furnace setup for (c) SO_3 and (d) SO_2 treatment. The total gas flow in the ceramic tube containing the V_2O_5 catalyst as well as in the tube furnace containing the CAM samples was adjusted to 1 l/min. The washing bottles at the tube furnace exhaust (depicted in panels b and d) served to quench leftover SO_2 or SO_3 to ensure safe operation of the furnace setup. Scheme (c) was adapted from Figure 3 in the article[134] by J. Sicklinger, H. Beyer, L. Hartmann, F. Riewald, C. Sedlmeier, and H. A. Gasteiger, *J. Electrochem. Soc.*, 167, 130507 (2020), published September 18, 2020, © The Electrochemical Society. Reproduced by permission of IOP Publishing. All rights reserved. In this publication some more details such as the manufacturer's data can be found (compare chapter 3.3.1).

In addition, the SO_2 and SO_3 treatment procedures were adapted to the Ni-rich NCM851005 (results are presented in chapter 3.3.3). In a first set of experiments, almost the same treatment conditions as described above for LMR-NCM were applied. The only difference was a lower calcination temperature of 525°C instead of 625°C in the calcination step before the SO_3 or SO_2 treatment (referring to step I in Figure 9a and b). This lower temperature was chosen due to the lower temperature stability

of Ni-rich NCM as compared to LMR-NCM, thus being consistent with the experimental study on surface contaminants presented in chapter 3.2.2.[47] In a second set of experiments with NCM851005, the samples were heated to either 300 °C or 400 °C at a rate of 10 K min^{-1} and kept at this temperature for 1 h. Then the gas feed was changed to 0.5% SO_2 in Ar or 0.5% SO_3 and 30% O_2 in Ar for SO_2 and SO_3 treatment, respectively, thereby using the same gas mixtures as described above for LMR-NCM. A baseline experiment was performed containing the annealing step for 2 h under Ar at 400 °C.

Figure 10: Photograph of the tube furnace setup for the SO_2 and SO_3 treatment of LMR-NCM samples. A detailed description and scheme can be found in Figure 3 in the experimental part of the publication[134] presented in chapter 3.3.1. A mixture of 1% SO_2 in Ar was provided by a 10 L gas cylinder (1). Ar, O_2, and SO_2 in Ar were mixed via flowmeters (2) to reach a resulting flow of 1.0 l/min in the ceramic tube filled with the V_2O_5 catalyst (3). The resulting SO_3-containg gas mix then entered the glass tube (4) of the split tube furnace (5). The exhaust gases were then quenched by water in a washing bottle (6).

In all cases, after cool down to room temperature under Ar (1 l/min, compare step II(b) in Figure 9a and b), the samples were transferred to the glovebox under inert conditions to avoid any air exposure of the LMR-NCM or Ni-rich NCM samples after thermal and reactive gas treatment.

2.3.2. Electrochemical Characterization

The assembly of full-cells with LMR-NCM versus graphite is described in the experimental section (Table I) of the study[134] presented in chapter 3.3.1. In case of NCM851005, half-cells versus lithium were assembled. In addition, the cycling protocol was modified with regards to cut-off voltage

and formation procedure. In both cases, stainless-steel CR2032 type coin cells were used (Hohsen Corp., Japan).

NCM851005 cathodes were manufactured in inert conditions by coating an NMP-based slurry on aluminum foil, similar to the study on surface contaminants[47] and the study on LMR-NCM.[134] 96% of the CAM were first mixed with 2% carbon black (Super C65, Timcal, Switzerland) and 2% polyvinylidene difluoride binder (PVDF, Kynar® HSV, France) in dry state at 1000 rpm for 2 min with a planetary orbital mixer (ARC-310, Thinky, USA). *N*-methyl-2-pyrrolidone (NMP, anhydrous, 99.5%, Sigma-Aldrich) was then added in two steps to reach a final solid content of 61%. The slurry was mixed for 5 min at 2000 rpm after each NMP addition step. The NMP amount had been adjusted to achieve a viscous, lump-free slurry. Weighing and mixing were carried out in a mixing vessel inside an Ar-filled glovebox (O_2, H_2O > 0.1 ppm, MBraun, Germany), which was sealed and transferred out of the glovebox for every mixing step inside the planetary orbital mixer. Carbon black and PVdF had been vacuum dried at 120 °C for three days before transfer into the glovebox. After the final mixing step, the slurry was manually coated on the aluminum (18 µm, MTI corporation, USA) foil using the 100 µm side of a four-edge-blade inside the glovebox and then dried there overnight. Disc-shaped electrodes with 14 mm in diameter were punched out of the foil and compressed at 1 t for 20 s outside the glovebox. The compression tool was wrapped with plastic bags before transfer out of the glovebox in order to minimize the exposure to moisture and CO_2 from ambient air. The compressed electrodes where weighed inside the glovebox and finally dried at 120 °C under vacuum overnight. The electrode loading was 8.0 ±0.5 $mg_{NCM851005}/cm^{-2}$, corresponding to an areal capacity of 1.6±0.1 mAh/cm² when referring to a reversible capacity of 200 $mAh/g_{NCM851005}$.

Table 1: Cycling protocol for NCM851005/LP572/Li coin cells at 25 °C with 80 µl of electrolyte and two glass fiber separators (VWR glass fiber filter, grade 691). All segments are repeated 4 times to reach 200 cycles in total for the lifetime test and C-rates are referenced to 200 $mAh/g_{NCM851005}$. CC refers to constant-current and CCCV to constant-current constant-voltage with C/10 lower current limit. The DCIR test is carried out in segment 2: direct current internal resistance measurement at 40% state-of-charge (SOC), with 100% SOC referring to the last discharge capacity of segment 1. The partial charge and discharge cycle directly before/after the DCIR pulse was carried out at C/10. Before the pulse, the cell was allowed to rest for 1 h in OCV mode. The 10 s DCIR discharge pulse corresponded to a current to C/5.

	Segment	Potential range [V vs. Li/Li^+]	Charge rate	Discharge rate	Cycles	Repeats
1	Slow cycling	4.3 – 3.0	C/10 (CC)	C/10 (CC)	3	4 (start of loop)
2	DCIR	After C/10 charge to 40% SOC and 1 h OCV	C/5	C/5 pulse (10 s)	1	4
3	Fast cycling	4.3 – 3.0	C/2 (CCCV)	3 C (CC)	3	4
4	Standard cycling	4.3 – 3.0	C/2 (CCCV)	1 C (CC)	33	4 (end of loop)

CR 2032 type coin cells were assembled inside the glovebox. The cell contained a disc shaped lithium metal anode with 15 mm diameter that was punched inside the glovebox from a lithium foil

(Rockwood lithium, USA, > 99.9% pure, 0.45 mm thick), two glass fiber separators with 16 mm diameter (VWR glass fiber filter, grade 691, dried under vacuum prior to cell assembly at 120 °C), and 80 µL LP572 electrolyte (1 M $LiPF_6$ in EC:EMC 3:7 (w:w) plus 2 vol% VC, BASF, Germany). Electrochemical cycling was carried out at 25 °C with a battery cycler. The cycling protocol is summarized in Table 1 and contains the following sequence, similar to the study on LMR-NCM (chapter 3.3.1):[134] i) three cycles at C/10, ii) a direct current internal resistance (DCIR) pulse test (10 s discharge at C/5) at 40% SOC, iii) three cycles at 3 C, and iv) 33 standard cycles with C/2 CCCV charging and 1 C CC discharging. All segments are repeated until the end of the lifetime test.

3. Results and Discussion

3.1. Development of an *Operando* DRIFTS Cell

The formation of a stable solid-electrolyte interphase from electrolyte reduction products, e.g., on graphite electrodes, is one of the key phenomena occurring in state-of the art lithium-ion batteries and it is one of the prerequisites for a long cycle-life of commercial full-cells.[174,178,191] At the same time, especially in the context of novel high-voltage materials such as the Li- and Mn-rich NCM (LMR-NCM, x Li_2MnO_3 · (1-x) $Li[Ni_xCo_yMn_{1-x-y}]O_2$) or the "high-voltage spinel" LNMO ($LiNi_{0.5}Mn_{1.5}O_4$), oxidative stability of LIB electrolytes and chemical stability of cathode active materials against electrolyte oxidation products such as protons becomes crucial. Protons lead to HF formation and thereby leach out transition metals from the cathode material, which is detrimental for the cycle-life of LIBs, especially when the dissolved transition metal ions are deposited on the anode.[124,192–194] In general, reactions at the electrode-electrolyte interface are crucial for the lifetime and performance of a battery cell.[195]

In the thesis at hand, an *operando* DRIFTS cell is described that serves to monitor infrared (IR) active gases as well as the active material particle surface with the surrounding electrolyte layer. The two central aims were (i) to assess the surface sensitivity of the method with regards to SEI formation on graphite from EC-based electrolytes and (ii) decomposition mechanisms of the anode SEI forming additive VC on the cathode side at oxidative potentials. For this purpose, an *operando* DRIFTS cell was designed, enabling the electrochemical cycling of a custom-made cell inside a gas-tight Ar-filled chamber with IR-transparent windows. The major fraction of the working electrode surface was accessible to the IR beam as well as the head space above the working electrode, which allows to collect the gases evolved during electrochemical measurements. For typical composite LIB electrodes such as graphite anodes or LFP cathodes that have rough surfaces, infrared spectroscopy in diffuse reflectance mode (DRIFTS) is very well-suited.[180] Within this thesis, graphite, LFP, and LTO were taken as working electrodes and $LiPF_6$ in VC or EC as electrolyte to carry out oxidative and reductive potential scans or to perform a galvanostatic charge and discharge experiments.

3.1.1. Electrochemical Performance of the *Operando* DRIFTS cell

To validate the electrochemical performance of the developed cell setup (cf. chapter 2.1.3, Figure 5), an LFP electrode (coated on woven wire mesh) was charged and discharged at C/2 in a LFP//lithium *operando* DRIFTS cell and compared to a Swagelok® T-cell (Figure 11). After one galvanostatic cycle, a potential scan was performed (cf. chapter 3.1.3, Figure 16). With regards to the galvanostatic experiment, the C/2 charge delivered 97.1% of the theoretical capacity (170 mAh/g), a coulombic efficiency of 94.4%, and 97 mV polarization between charge and discharge at Q_{theo} = 50% SOC. Accordingly, the cell setup allows to perform *operando* DRIFTS studies when avoiding too high

C-rates or in potential scan mode at moderate scan rates. For comparison, a T-cell test was made with a 10 mm LFP electrode that was punched out from the same coating as the LFP electrode in the DRIFTS cell. The T-cell tests delivered only 89.8% of the theoretical LFP capacity (Figure 11), which is even less than the 97.1% achieved with the *operando* DRIFTS cell. This 7.3% discrepancy in capacity might be caused by an inaccuracy during electrode punching, since both electrodes were obtained from two different punching tools (8 mm diameter for the T-cell vs. 10 mm for the *operando* DRIFTS cell). A deviation of 3.7 % from the target diameter of only one of the electrodes (e.g., a 0.37 mm too small diameter for the T cell) would lead to a 7.3 % deviation in the geometric electrode area and thus in a 7.3% deviation of the obtained capacity. Such a deviation would not be acceptable for standard cell tests with cathodes coated on aluminium foil. However, cutting the electrodes was challenging, since the punching tool had to cut through electrodes coated on an a rather hard substrate, i.e., woven steel wire mesh with a wire diameter of 25 µm. The same punching tools are normally used for electrodes coated on aluminium foil, which is much thinner (typically 10-15 µm) and softer than the woven steel wire mesh. The punching was done manually with a hollow punch and a hammer, which is not as precise as special tools such as handheld or machine-driven punches would be. For future studies with electrodes coated on steel mesh it might certainly help to optimize the punching procedure and to double-check the obtained electrode diameter, to be aware of geometrical deviations.

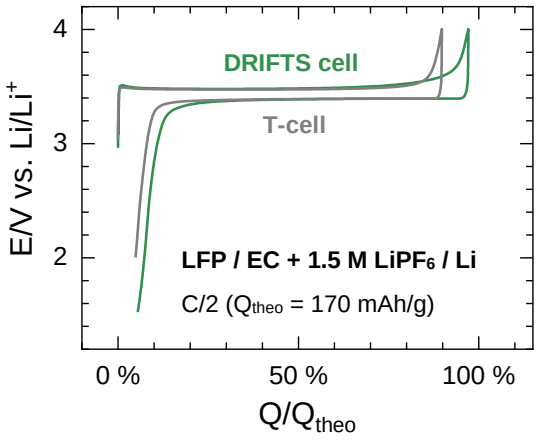

Figure 11: *Operando* DRIFTS cell with LFP/EC+1.5 M $LiPF_6$/Li. One glass fiber separator was put in the DRIFTS cell, two in the Swagelok® T-cell. In case of the DRIFTS cell, 20 µL electrolyte were used and 60 µL for the T-cell. In both cases, galvanostatic charge and discharge were performed with a rate of C/2. The lower cut-off is 2 V for the T-cell and 1.5 V for the DRIFTS cell.

3.1.2. *Operando* DRIFT Spectra of Graphite Lithiation

With the intention to study SEI formation, a graphite working electrode was monitored during a reductive scan from OCV to 0 V vs. lithium. In more detail, the scan was carried out at 0.5 mV/s in a graphite/EC+1.5 M $LiPF_6$/Li *operando* DRIFTS cell (Figure 12a). The current-voltage profile reveals

the onset of graphite lithiation below 1.6 V, with the reduction current continuously increasing toward 0 V. In additon, a shoulder at 0.8 V is observed, which can be clearly assigned to EC reduction.[60,196]

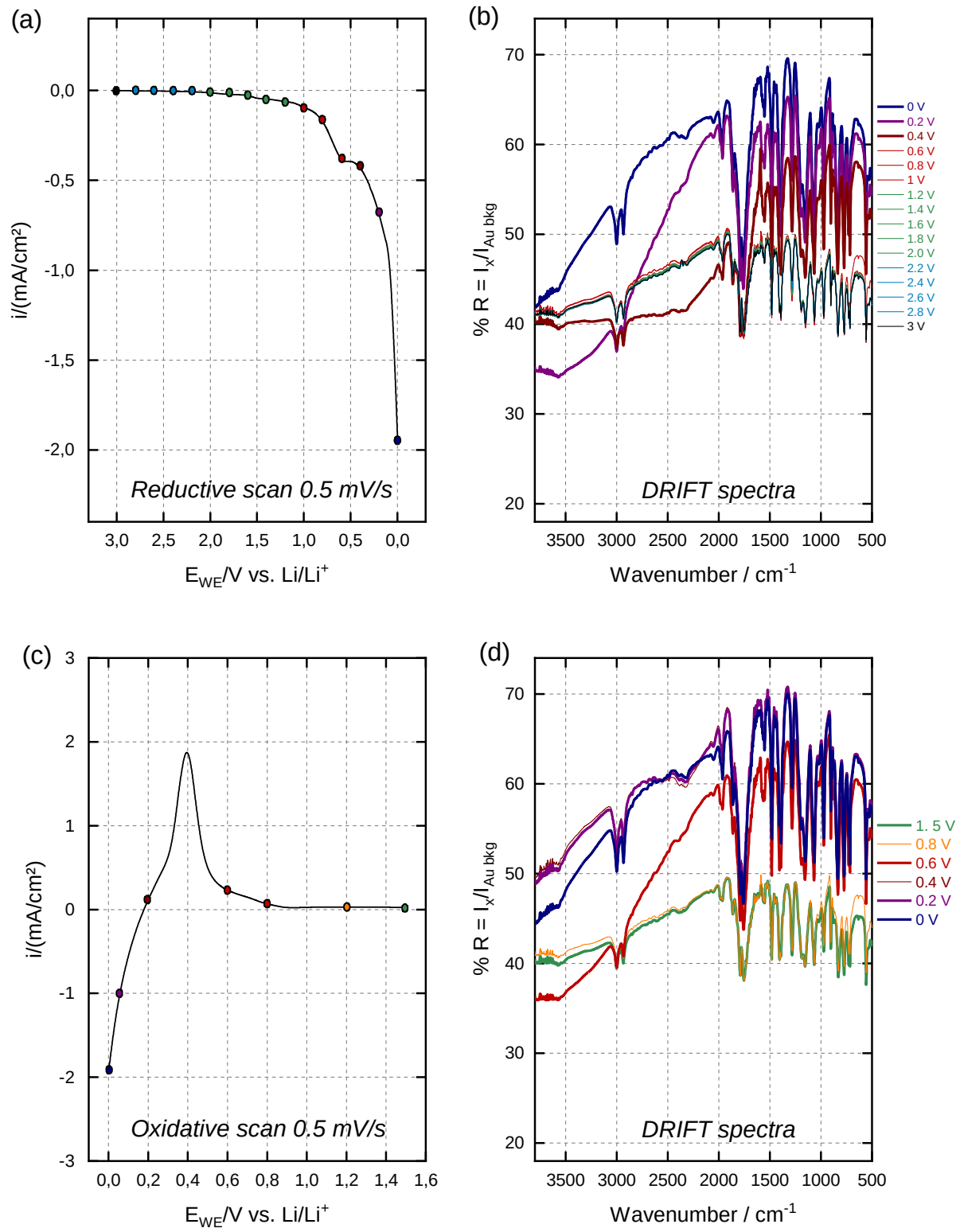

Figure 12: Reductive scan of graphite/1.5 M $LiPF_6$ in EC/Li obtained in the *operando* DRIFTS cell from OCV to 0 V, displaying (a) the geometric current density in mA/cm^2 and (b) the corresponding DRIFT spectra. The DRIFT spectra in panel (b) are assigned to the potential curves in panel (a) by dot markers that have the same color as the corresponding lines in panel (b). Analogously, panels (c) and (d) show the current density and the DRIFTS spectra during a subsequent oxidative scan to from 0 V back to 1.5 V. To clearly demonstrate the impact of baseline distortion of the DRIFT spectra during the potential scans, the spectra are all referenced to the same gold background and plotted in reflectance units without any offset.

The DRIFT spectra recorded during the reductive scan are depicted in Figure 12b. First, multiple downward pointing bands can be observed in all the spectra. These bands are created by infrared absorption bands from the electrolyte, which is explained in more detail by the band assignments in Table 2.

Table 2: Comparison of electrolyte signals (1.5 M $LiPF_6$ in EC) from the spectra in Figure 12 (left column) to the corresponding experimental frequencies of EC as well as the vibration modes reported in the literature (middle and right column).[197] The wavenumbers (unit: cm^{-1}) for the C=O stretching are strongly affected by Li^+ solvation. According to a computational study by Masia et al. based on ab ignition calculations of isolated EC molecules and $[Li(EC)_n]^+$ complexes,[197] the C=O stretching of solvated EC, i.e., $[Li(EC)_n]^+$ (n = 1 - 4) is shifted by -88 cm^{-1} when compared to EC. This computational result is reflected by the strong absorption bands at 1793/1756 cm^{-1} for 1.5 M $LiPF_6$ in EC that might both correspond to the signal of 1868 cm^{-1} for pure EC, corresponding to a redshift of -75/-112 cm^{-1} due to Li^+ solvation.

1.5 M $LiPF_6$ in EC	Pure EC	Assignment
2998	3004	CH_2 stretching
2925	2925	CH_2 stretching
1793	1868	(C=O stretching)
1756	1868	(C=O stretching)
1481	1483	CH_2 scissoring
1393	1386	CH_2 wagging
1204	1218	CH_2 twisting
1155	1157	CH_2 twisting
1065	1087	ring stretching
974	960	ring stretching
902	881	ring breathing
771	768	CH_2 rocking
715	715	ring bending
556	527	C=O bending

During the reductive scan (cf. Figure 12b), all DRIFT spectra from OCV (3 V) to 0.8 V are almost identical. However, at 0.6 V the first small changes can be observed, i.e. a slightly higher intensity around 700 cm^{-1}. At 0.4 V and 0.2 V, the intensity above 1500 cm^{-1} increases while the one below 2000 cm^{-1} gets smaller. At the end of the scan (0 V), the intensity has increased over the entire wavenumber range. The maximum intensity of the whole spectrum increases from R = 50% at OCV to R = 70% at 0 V, accompanied by a stretch of the electrolyte bands. At the same time, no additional bands

emerge and no bands disappear during the scan. While all the electrolyte bands grow in intensity, the band positions remain unchanged. There are no additional bands emerging during the scan.

Within a typical SEI on graphite anodes, lithium ethylene dicarbonate (LEDC) and lithium carbonate (Li_2CO_3) are the most prominent IR active species discussed in the literature.[51–54] Even if these species had been formed during the *operando* DRIFTS experiment, the Li_2CO_3 main band[188,198] around 1470 cm^{-1} as well as the LEDC main bands[53] at 1663/1652 cm^{-1} and 1318/1302 cm^{-1} would be overshadowed by intense electrolyte signals. Especially the C=O stretch of ethylene carbonate doublet at 1793/1756 cm^{-1} (cf. Table 2) causes a very strong and rather broad signal, with a tail even below 1700 cm^{-1}. This demonstrates how challenging it can be to detect SEI species buried underneath the highly absorbing electrolyte layer.

During the oxidative scan (Figure 12c and d), the spectra at 0 V and 0.2 V differ only slightly in the high wavenumber region above 2500 cm^{-1} and the ones at 0.2 V and 0.4 V are nearly identical. The spectra recorded at 0.4 V, 0.6 V and 0.8 V show baseline distortions similar to the reductive scan. The spectrum at 0.8 V it is rather similar to the initial one recorded at OCV before the first reductive scan. In the further course of the oxidative scan, i.e. from 0.8 V and 1.5 V, no significant changes can be observed.

Taken together, the baseline distortion and the overall signal intensity are a function of the graphite lithiation degree and they change reversibly during the oxidative and the reductive scan. The baseline distortion of the DRIFT spectra can be rationalized by the increasingly metallic properties of graphite during the lithiation process. In general, metals have stronger infrared reflective properties than non-metals.[199] Besides, graphite is known to change its optical colour during lithiation, from black (unlithiated graphite) to blue (LiC_{18}), red (LiC_{12}) and golden (LiC_6)[200]. However, the lithiation degree was only 16% at the end of the reductive potential scan. Apparently this is sufficient for strong baseline distortions. A follow-up experiment was designed to investigate a graphite working electrode during a full galvanostatic lithiation and delithiation cycle (cf. Figure 13).

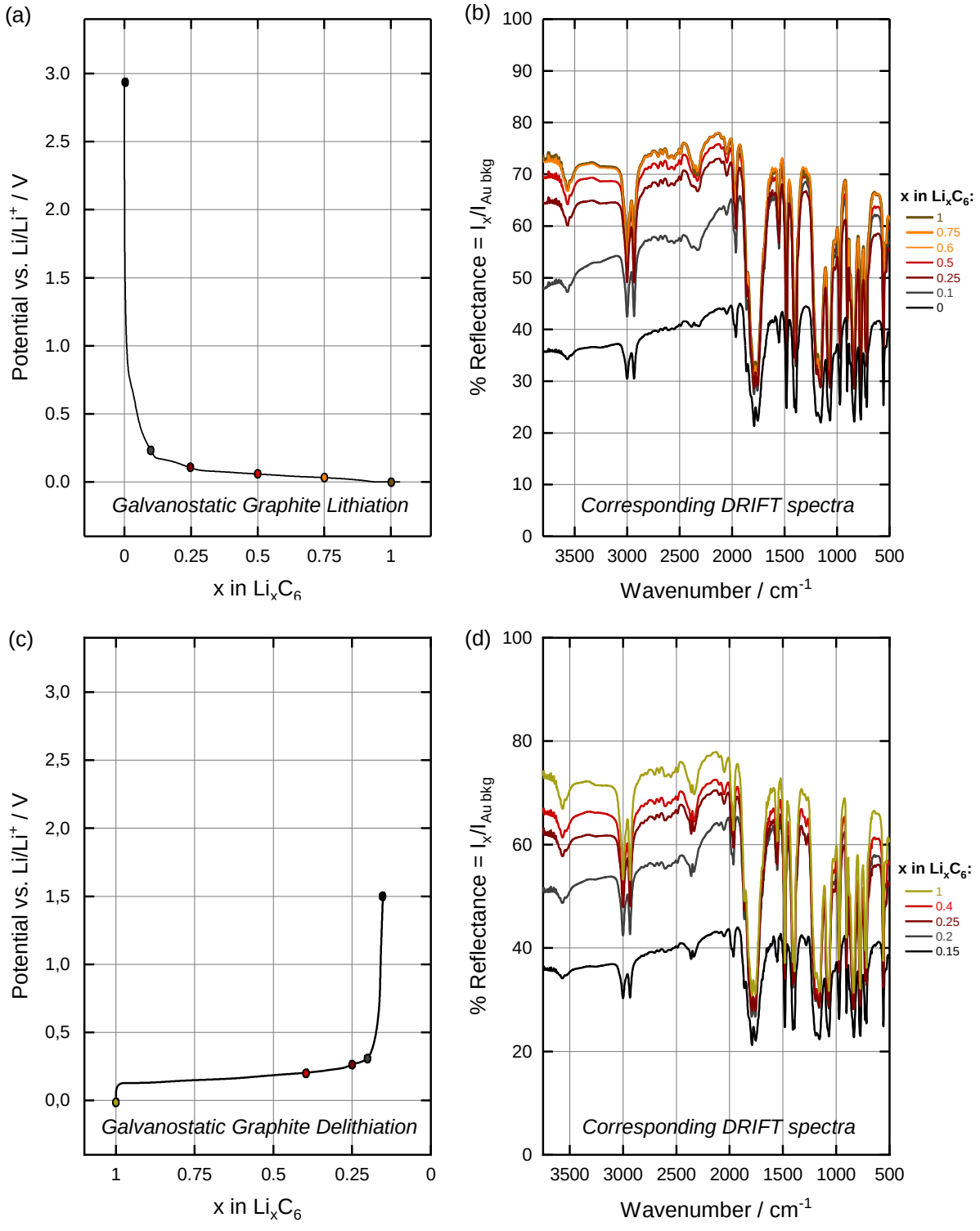

Figure 13: (a) Potential curves of a galvanostatic charge at C/10 with a graphite/1.5 M $LiPF_6$ in EC/Li *operando* DRIFTS cell; (b) corresponding DRIFT spectra. (c, d) Subsequent discharge at C/10. The DRIFT spectra in panels (b) and (d) are assigned to the corresponding lithiation states by dot markers in panels (a) and (c) that have the same color as the lines in panels (b) and (d). To clearly demonstrate the impact of baseline distortion of the DRIFT spectra during the potential scans, the spectra are all referenced to the same gold background and plotted in reflectance units without any offset.

The galvanostatic lithiation and delithiation of graphite was performed at C/10 with a graphite/1.5 M $LiPF_6$ in EC/Li *operando* DRIFTS cell (Figure 13). At the end of the lithiation scan (0 V vs. Li/Li^+, Figure 13a), 104% of the theoretical capacity are reached. This indicates that a significant fraction of the current applied went into electrolyte decomposition, i.e., SEI formation and possibly further reductive side reactions. Due to these irreversible reactions, the delithiation capacity (Figure 13b) is much smaller (85% of the theoretical capacity) than the lithiation capacity, leading to a coulombic efficiency of only 82%.

In case of the lithiation half cycle (Figure 13a and b), a drastic baseline distortion is observed for the infrared spectra. In more detail, the overall infrared signal intensity at a lithiation degree of 10% (grey line) is roughly 1.5 times higher than the one at the initial state (0% lithiation). The further IR signal intensity increase up to 25% lithiation is less pronounced, at 50% and 60% lithiation the change becomes smaller and smaller, and between 60 and 100% the spectra remain unchanged. Accordingly, the initial changes when starting the lithiation of graphite have a bigger impact on the baseline distortion of the DRIFT spectra compared to the changes at the end of charge.

All these effects are reversible, as demonstrated by the subsequent delithiation half cycle (Figure 13c and d). While the spectra for 100%, 40% and even 25% lithiation are rather comparable, a drastic signal intensity decrease and baseline change is observed between 25%, 20%, and 15%.

While the SOC range of CV and galvanostatic cycle are drastically different, one observation is similar: the spectral intensity and the baseline change reversibly with lithiation and delithiation. Analogous to the potential scans (Figure 12), only a stretching of the electrolyte band intensity was observed in the galvanostatic cycle (Figure 13), but no additional signals which would be expected due to SEI formation. This, unfortunately, confirms the hypothesis that the coverage of graphite by electrolyte leads to a too low sensitivity for detecting SEI species by *operando* DRIFTS.

As a next step, alternatives to graphite as working electrode were tested. The aim was to avoid lithiation or delithiation during the potential scans, since in case of graphite this was shown to lead to a baseline distortion. Within the following *operando* DRIFTS experiments, LFP and LTO were used as working electrodes.

3.1.3. EC reduction on an LFP Working Electrode

To avoid any change of the lithiation degree of the working electrode, a completely lithiated LFP electrode was examined for use as a working electrode for reductive scans. Before discussing the *operando* DRIFTS data measured with a LFP working electrode, it is worth considering the infrared spectrum of the LFP itself. In contrast to graphite, the LFP ($LiFePO_4$) bulk exhibits characteristic IR active vibrations, i.e., the ones of the phosphate (PO_4^{3-}) anion. In case of a dry LFP electrode (cf. Figure

14a), the phosphate bands can be clearly identified below 1140 cm^{-1}. However, if the solid composite electrode is wetted by the "EC only" electrolyte solution, the LFP signals become very weak (cf. Figure 14b). The strong LFP bands at 1139 and 1096 cm^{-1} are distorted due to the overlap with electrolyte bands and the weaker LFP bands below 650 cm^{-1} have almost disappeard. PVdF features would be expected around ≈840, ≈900, ≈1200, and ≈1400 cm^{-1}, with precise wavenumbers depending on the crystallinity of the polymer.[179,201,202] From the spectrum of the dry LFP electrode with 4 wt% PVdF (cf. Figure 14a) it gets clear that these features cannot be distinguished within the depicted spectrum, since the PVdF bands are missing even though there are no strong LFP bands in the same region. Apparently, the thin binder layer around the active material particles is not detected in the DRIFTS measurement at hand.

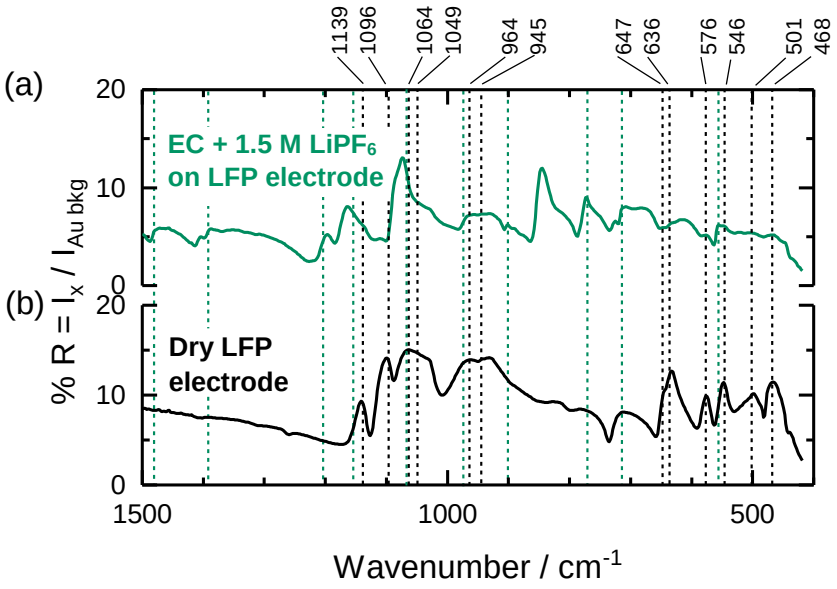

Figure 14: DRIFT spectra of the "EC-only" electrolyte (1.5 M $LiPF_6$ in EC) on an electrolyte wetted LFP electrode (a) compared to a dry LFP electrode (b). Black dashed lines mark LFP bands with the wavenumbers according to the literature,[203–205] specified on top. Green dashed lines indicate the position of the electrolyte bands, that have been listed in detail before (cf. Table 2).

The scheme in Figure 15 illustrates three different possibilities, how the incident IR beam in the *operando* DRIFTS cell interacts with the LFP working electrode: (i) the surface of the electrolyte layer reflects the IR beam; (ii) it penetrates the electrolyte and is then reflected at the LFP particle surface, and/or (iii) the IR beam interacts with the LFP bulk after crossing the electrolyte layer. The final spectra are most probably the sum of all three processes. Accordingly, it can be assumed that the formation of interphases between active material and electrolyte can only be observed if the formed layer is thick enough and contains a high amount of IR active species. This might be very challenging, since even the PVdF layer around the LFP active material has not been detected in the present example. Assuming a density of 1.78 g/cm³ (according to the technical datasheet for Kynar® HSV 900 by ARKEMA, France) and an electrode loading of 20 mg_{LFP}/cm^2, a BET surface area of 23 m^2/g_{LFP} as well as the electrode composition of 93 % LFP and 4 % PVDF, it can be estimated that a hypothetical conformal PVDF layer

surrounding the LFP particles would only be 1 nm thick. This rough calculation neglects the interaction with the conductive carbon in the electrode and it neglects the fact that PVDF is typically present as fibers rather than covering the cathode active material particles homogeneously. However, it still allows to demonstrate that surface layers with a thickness in the nanometer range cannot be resolved by the *operando* DRIFTS technique developed within this thesis. This makes it very unlikely to resolve the SEI formation on graphite, confirming the findings from the previous chapter.

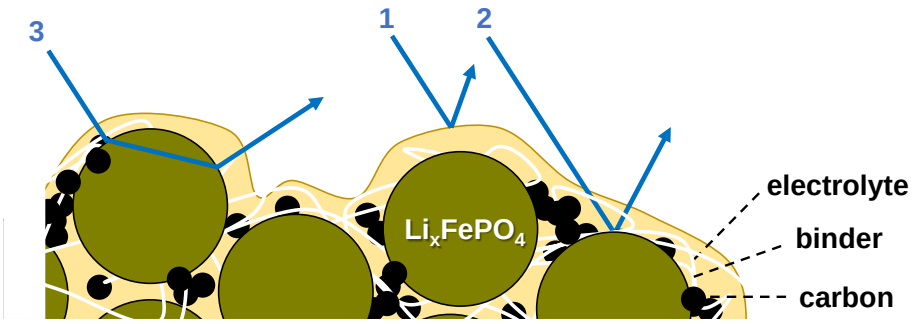

Figure 15: Scheme of potential diffuse reflection processes for IR radiation inside the *operando* DRIFTS cell with an LFP working electrode: (i) reflection by the electrolyte layer at its surface, (ii) complete penetration of the electrolyte layer and reflection at the LFP/electrolyte interface, and/or (iii) complete penetration of the electrolyte layer and interaction with the LFP bulk.

In summary, as already indicated by the results from *operando* DRIFTS with graphite as a working electrode, IR active species within thin interphases such as the SEI on graphite are not necessarily detected (cf. chapter 3.1.2). This might become plausible when assuming that the electrolyte layer covers several µm around the active material particles, while the SEI is only a few nm thick.

In order to monitor the electrolyte reduction without interference from the observed baseline distortion, the next experiment was carried out on LFP as working electrode (Figure 16). For this purpose, an LFP/EC + 1.5 M $LiPF_6$/Li *operando* DRIFTS cell (Figure 16a) was assembled to do a potential scan from OCV to 0 V vs. lithium. Two separate experiments were performed: the first one with Ar atmosphere inside the DRIFTS cell ("EC reduction" experiment, Figure 16c) and the second one with a mixture of 10 vol.-% CO_2 in Ar ("EC + CO_2 red." experiment, Figure 16d). Considering recent studies, Li_2CO_3 is the main SEI compound formed from CO_2 reduction.[57,64] This would be potentially helpful for benchmarking an *operando* DRIFTS method, since Li_2CO_3 has a strong signal at 1470 cm^{-1}.[186] It should be noted that the cell without CO_2 had been used for a galvanostatic cycle before the reductive potential scan was performed. Figure 16c depicts the OCV spectrum (2.98 V vs. Li/Li^+), which had been recorded before the galvanostatic charge/discharge was started(cf. Figure 11). Since the

DRIFTS spectra did not change significantly during this one galvanostatic cycle, they were omitted from the graph in Figure 16c. During the discharge half cycle, the LFP working electrode was galvanostatically lithiated until a potential of 1.5 V vs. Li/Li^+ had been reached. A linear sweep from 1.5 V to 0 V was directly attached without allowing the cell to relax to an OCV potential. Figure 16c contains the DRIFT spectra recorded during the potential scan from 1.5 V to 0 V vs. Li/Li^+. In contrast, the cell with CO_2 had not been cycled prior to the potential scan and the reductive potential scan covers the whole range from 3.2 V (OCV) vs. Li/Li^+ to 0 V vs. Li/Li^+. (cf. Figure 16a).

To facilitate the interpretation of the o*perando* DRIFT spectra, we first consider the IR signals of the "EC-only" (1.5 M $LiPF_6$ in EC) electrolyte (cf. ATR-FTIR spectrum in Figure 16b). The most prominent band are typical carbonate signals, e.g., the very strong C=O stretching vibration below 1800 cm^{-1}. A detailed assignment of the bands can be found in Table 2. In Figure 16c, the DRIFT spectra of the "EC reduction" recorded during the reductive scan are compared to the initial (OCV) spectrum (2.98 V). Again, the spectra are dominated by strong electrolyte signals, which do not change during electrochemical cycling. For both the ATR-FTIR spectrum in transmission units (panel b) and the DRIFTS in reflectance units (panel c), the absorptive electrolyte bands lead to downward pointing signals. In case of DRIFTS, especially the strong bands such as the C=O stretching doublet at 1793/1756 cm^{-1} have a derivative shape, which typically occurs when the surface concentration of IR active species is high,[180] which is clearly the case for the electrolyte layer on top of the active material in our working electrode setup.

By zooming in the region 1750 to 1250 cm^{-1} (Figure 16e-f), it is possible to have a closer look at potential EC reduction products such as LEDC or Li_2CO_3. The LEDC main bands that have been reported in the literature[174] would be expected at 1663/52 and 1318/1302 cm^{-1} and are marked as green dashed lines. However, these LEDC signals do not emerge during the reductive scan. The formation of Li_2CO_3 would give rise to a strong doublet[186] at ≈1470 cm^{-1}, but no such signals can be observed (Figure 16f). Taken together, there are no clearly distinguishable changes in the spectra during the reductive scan. Similar observations have been made for an analogous experiment in a LFP/VC + 1.5 M $LiPF_6$/Li *operando* DRIFTS cell (data not shown).

Figure 16g depicts the enlarged spectra for the cell with "EC-only" electrolyte in the presence of CO_2. During the reductive scan, extremely weak positive signals emerge at 1346 and 1296 cm^{-1} at a potential of 1.8 V vs. Li/Li^+. These bands might be assigned to the LEDC doublet above 1300 cm^{-1}, however, the other LEDC signal above 1650 cm^{-1} are simply missing. If LEDC were formed, all of the main bands would have to be present. Since this is not the case, the presence of LEDC cannot be proven. Similarly, there is no indication for a significant change around ≈1470 cm^{-1} that would be expected when Li_2CO_3 is formed, e.g., from CO_2 reduction.

In all cases so far, EC reduction products that must have been formed during the reductive scans as indicated by the *i*/V curves, are masked by strongly absorbing electrolyte bands. Thus, the *operando* DRIFTS cells neither with graphite nor with LFP as working electrode served to detect electrolyte reduction products. As a final test run for the *operando* DRIFTS method, an oxidative scan was performed using an LTO electrode and a "VC only" electrolyte, i.e. VC + 1.5 M $LiPF_6$. The following section will demonstrate how the formation of IR active gases can be detected via *operando* DRIFTS.

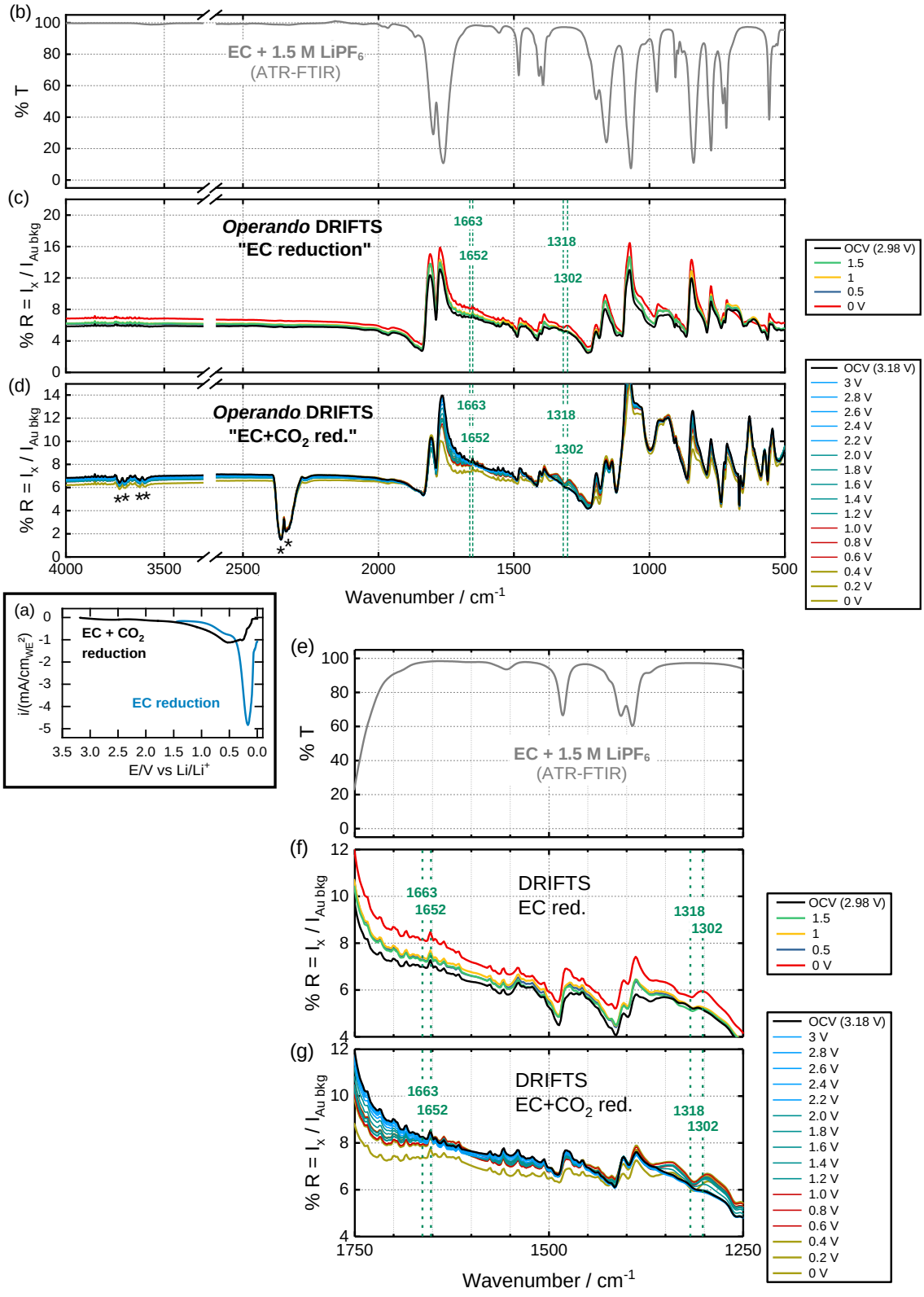

Figure 16: *Operando* DRIFTS cells with LFP/1.5 M $LiPF_6$ in EC/Li filled with Ar (labelled "EC reduction") as well as 10% CO_2 in Ar (labelled "EC + CO_2 red.") with (a) the corresponding current-voltage profiles. The reductive scan with 0.5 mV/s from OCV to 0 V vs. Li/Li^+ has been performed on a LFP/C working electrode (93% LFP/C, 4% carbon, 3% binder). (b) ATR-FTIR reference spectrum of the EC + 1.5 M $LiPF_6$ electrolyte displayed in transmittance units. (c) *Operando* DRIFT spectra of the "EC reduction" cell as well as (d) the "EC + CO_2 red." cell. CO_2 signals are marked with asterisks. All DRIFT spectra are displayed in reflectance units without any offset in order to clearly see even small signal changes within the spectra. The spectra are color coded and can be assigned to specific potentials via the legend on the right. Panels (e) – (g) are enlarged views of (b) – (d). Green dashed lines: LEDC main bands according to the literature.[206]

3.1.4. Oxidation of $LiPF_6$ in Vinylene Carbonate Electrolyte on LTO Working Electrode

The VC/$LiPF_6$ oxidation experiment was performed in an LTO/1.5 M $LiPF_6$ in VC/Li *operando* DRIFTS cell. Again, the experiment was performed in such way that the lithiation degree of the working electrode remained unchanged. Figure 17a depicts the current-voltage curve of the oxidative scan with LTO. The onset of electrolyte oxidation is detected above 4.4 V by the onset of a positive current. Figure 17b correlates the ATR spectrum of the "VC-only" electrolyte solution (1.5 M $LiPF_6$ in VC) to DRIFT spectra recorded during the LSV scan (Figure 17c). Similar to the "EC-only" case (see section 3.1.3), strong bands in the "VC-only" electrolyte give rise to intense derivative shaped bands in the DRIFT spectra. Table 3 lists all the wavenumber positions of the "vibration bands and compares them to literature data for pure VC. Similar to the "EC-only" electrolyte discussed in chapters 3.1.2 and 3.1.3, also the "VC-only" electrolyte exhibits a multitude of strong absorption bands.

Changes in DRIFT spectra are only observed at potentials above 4.6 V, thus the spectra between OCV and 4.6 V are omitted in Figure 17c. All of the emerging signals are downward pointing, i.e., are absorptive bands (given that reflectance units are used). By referring to the literature,[205] these bands can be assigned to IR active gases, i.e., CO_2 (2360/30 cm^{-1}), POF_3 (1416 and 989 cm^{-1}) and PF_5 (1022, 944, 574 and 532 cm^{-1}). The gas evolution will be discussed in more detail with the help of an enlarged view of the lower wavenumber region (Figure 18). While almost all of all the evolving signals can be clearly assigned to the formation of either CO_2, POF_3, and PF_5, the feature at 830 cm^{-1} is a bit ambiguous. It might be associated to a weak PF_5 band at 848 cm^{-1} according to the literature[207] Alternatively, it might be created by a weak POF_3 signal at 830 cm^{-1} that was reported Gutowsky et al.[208] Very close to this, a strong POF_3 signal should have been obtained with a maximum at 871 cm^{-1} (P-F stretching) according to a study by Yang et al.[205] Taken together, the overlap of several expected signals impedes a clear assignment of the signal observed at 830 cm^{-1} within the spectra depicted in Figure 17.

Table 3: Comparison of electrolyte signals to VC vibrations according to the literature[209]

1.5 M $LiPF_6$ in VC	Pure VC	Vibration mode
3168	3170	Symmetrical C-H stretch
1829	1831	C=O stretch
1348	1347	C-H in-plane bend
1160	1160	C-H in-plane bend
1078	1081	Skeletal stretch
748	740	Skeletal bend
704	711	C-H out-of-plane
556	564	C=O in-plane bend

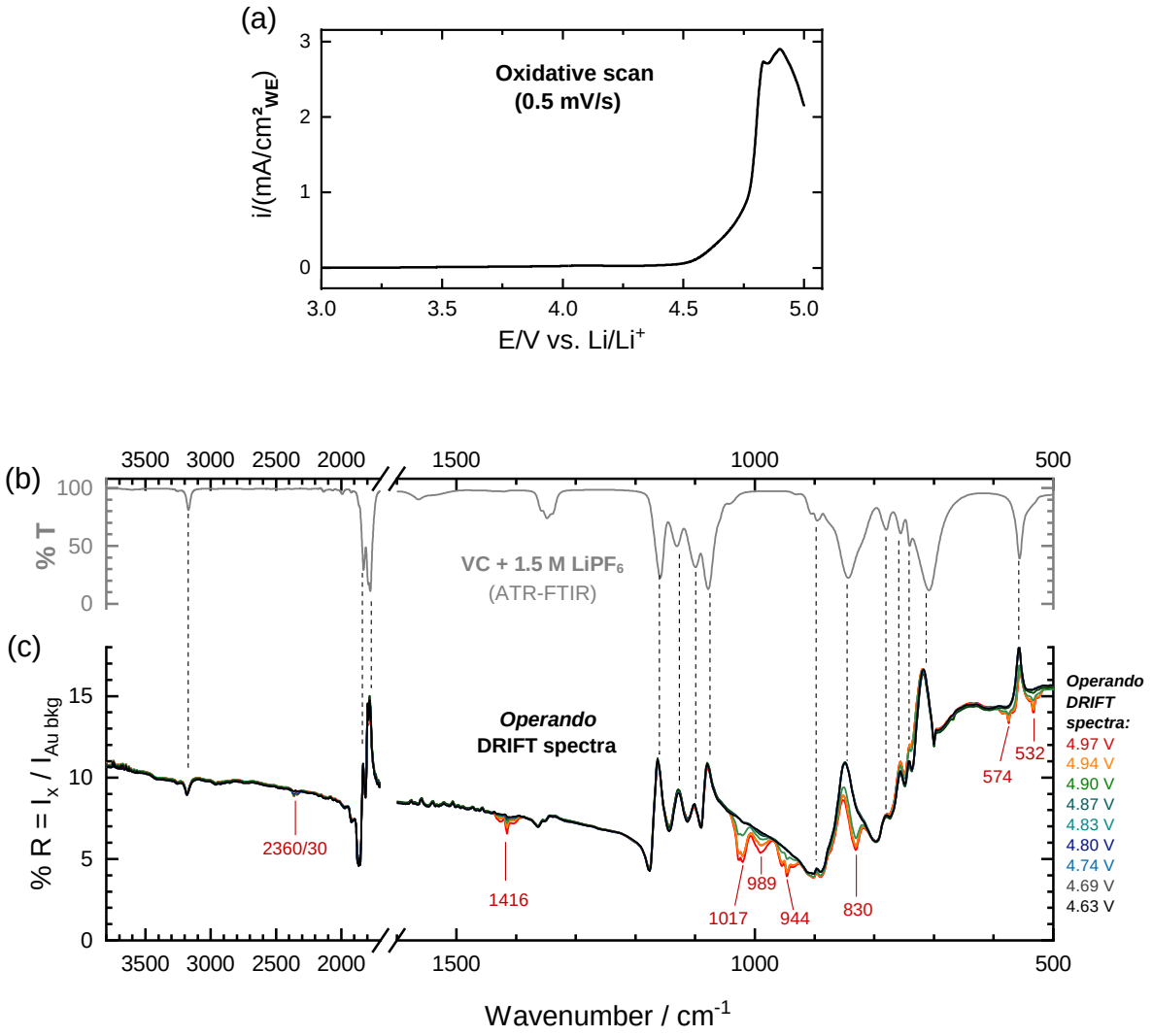

Figure 17: Oxidation of 1.5 M $LiPF_6$ in VC studied by *operando* DRIFTS. (a) Current-voltage profile of the oxidative scan from OCV to 5 V vs. Li/Li^+. (b) ATR FTIR spectrum of the electrolyte solution of 1.5 M $LiPF_6$ in VC shown in transmittance units (ATR corrected). (c) *Operando* DRIFT spectra of the oxidative scan. Vertical dashed lines correlate the electrolyte bands in the DRIFT spectra to the ATR reference spectrum. Bands formed during oxidation are labelled with the respective wavenumber. Spectra between OCV and below 4.63 V are omitted since they are identical to each other and the one at 4.63 V. All DRIFT spectra are plotted in reflectance units, without any offset (i.e., partially covering each other) to clearly demonstrate that additional signals were emerging during the oxidative scan while there was no baseline distortion in the spectra. Wave numbers of emerging signals during the oxidative scan are shown in red and are assigned in Table 4.

The experimental and literature values for the infrared absorption bands of POF_3, PF_5 and CO_2 are assigned to vibrational modes of the gas molecules in Table 4. The same signals can be seen in Figures 18 and 20. These gas signals grow with increasing potential indicating continuous gas evolution during electrolyte oxidation above 4.6 V. The normalized values of the integrated absorption bands are correlated to the working electrode potential, at which the corresponding spectra were measured (Figure 18a-d). From this, gas evolution onsets have been determined being 4.6 V for CO_2, 4.7 V for POF_3 and 4.8 V in case of PF_5.

Table 4: POF_3, PF_5, and CO_2 experimental frequencies (wavenumbers in cm^{-1})

Oxidation of $LiPF_6$ in VC	Literature values[205,210]	Vibration mode
(a) Bands assigned to POF_3		
1416	1416	P=O stretching
989	989	P-F asymetric stretching
(b) Bands assigned to PF_5		
1022	1018	P-F stretching
944	945	P-F stretching
574	574	P-F bending
532	534	P-F bending
(c) Bands assigned to CO_2		
2360/2330	2349	O=C=O asymmetrical stretch
670	667	Bending

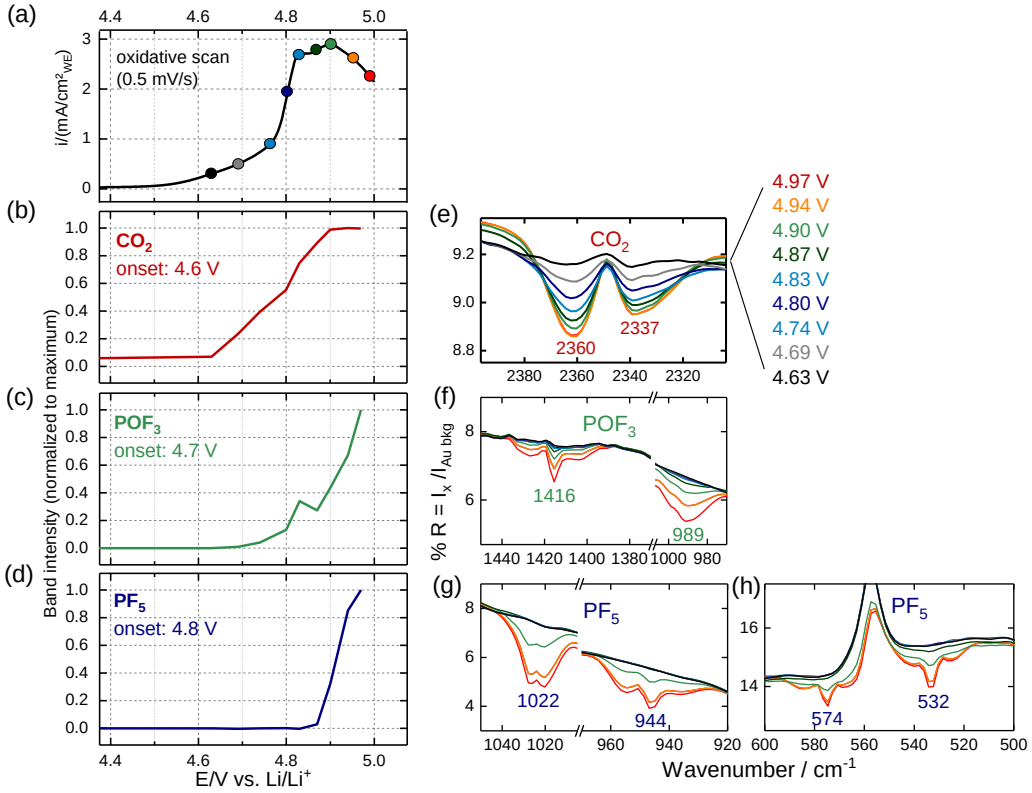

Figure 18: Gas formation during oxidation of 1.5 M $LiPF_6$ in VC studied by *operando* DRIFTS. (a) Current-voltage profile (same data as in Figure 17a) with colored dots marking the potentials were DRIFT spectra (line colors of the spectra match the dot colors of the potential curves) have been recorded. (b) – (d) Normalized band intensities vs. potential vs. Li/Li^+ for (b) CO_2, (c) POF_3 and (d) PF_5. (e) – (h) Absorption bands (same data as in Figure 17c) of CO_2, POF_3 and PF_5, assigned according to literature.[206,211]

The evolution of CO_2, POF_3, and PF_5 at high potentials from the decomposition of a VC/$LiPF_6$ electrolyte is consistent with on-line electrochemical mass (OEMS) spectroscopy data from our group.[212] The major advantage of DRIFTS, however, is the possibility to differentiate between PF_5 and POF_3. In case of OEMS this is complicated by the hydrolysis of PF_5 taking place on the way to the detector through the capillary either due to reaction with water traces in the tubing system of the OEMS or with native oxide on the surface of steel components. For conventional OEMS measurements, these reactions lead to a quantitative conversion of PF_5 to POF_3.[212] In contrast, the gas spectra in Figure 18 clearly demonstrate that PF_5 and POF_3 can be detected simultaneously via *operando* IR measurements.

Having demonstrated that PF_5, POF_3, and CO_2 can be detected via DRIFTS measurements, the amount of gaseous oxidation products formed at the end of the VC oxidation experiment shall be roughly estimated. To do this for CO_2, the signal with maximum intensity (compare Figure 18e) is compared to a calibration gas measurement. Before doing so, it will be briefly discussed how infrared absorption by gas molecules in the head space of the DRIFTS dome can be used to determine the gas concentration via Lambert-Beer's law. Figure 19 schematically depicts the various stages at which the intensity of the incoming infrared radiation is decreased step by step. The incoming signal from the infrared source I_0 is slightly decreased when passing the first KBr window yielding the intensity value I_1. On the way from

the KBr window to the working electrode surface, absorption by gas molecules further decreases the intensity to I_2. After complex trans-flection processes at the working electrode surface, the intensity is represented by I_3 and then again, absorption by gas molecules takes places leading to I_4. After passing the second KBr window, the final intensity I_5 is obtained. The attenuation is described by an absorptive process for every of these steps:

$$A_1 = -\lg\left(\frac{I_1}{I_0}\right) \rightarrow I_1 = I_0 \cdot e^{-A_1} \qquad \text{(equation 16)}$$

$$I_2 = I_1 \cdot e^{-A_2};\ I_3 = I_2 \cdot e^{-A_3};\ I_4 = I_3 \cdot e^{-A_4};\ I_5 = I_4 \cdot e^{-A_5} \qquad \text{(equation 17)}$$

Thus the final intensity I_5 is:

$$I_5 = I_0 \cdot e^{-(A_1+A_2+A_3+A_4+A_5)} \qquad \text{(equation 18)}$$

In case there is no infrared absorptive gas in the head space of the cell, $A_2 = 0$ and $A_4 = 0$ leading to the simplified equation:

$$I'_5 = I_0 \cdot e^{-(A_1+A_3+A_5)} \qquad \text{(equation 19)}$$

Comparing the intensity before (I'_5) and after gas evolution (I_5), A_{gas} can be calculated as the sum of A_2 and A_4:

$$\frac{I_5}{I'_5} = \frac{I_{\text{after gas evolution}}}{I_{\text{before gas evolution}}} = e^{-(A_2+A_4)} = e^{-A_{\text{gas}}} \qquad \text{(equation 20)}$$

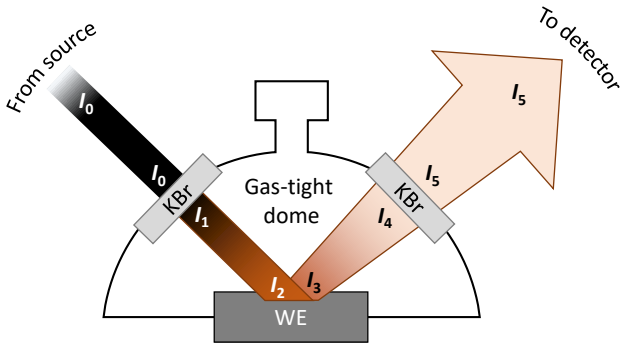

Figure 19: Scheme of gas absorption inside the DRIFTS dome. Simplifications have been made and only the cell components are depicted which contribute to the infrared signal at the detector, i.e., KBr windows, the working electrode, and the head space of the cell inside the gas-tight dome of the Harricks™ chamber.

Of course, equation 20 is only correct when changes in the working electrode are negligible in terms of IR reflectivity. This seems to be the case for the VC/$LiPF_6$ oxidation experiment, since the overall intensity and baseline of all the DRIFT spectra remain constant during the whole scan (cf. Figure 17c). Accordingly, Lambert-Beer's law can be applied to quantify the gas amount. Lambert-Beer's law

describes the connection between the absorbance A_{gas} to the absorptivity ε_{gas}, the gas concentration c_{gas}, and the pathlength l of the IR beam:

$$A_{\text{gas}} = -\lg\left(\frac{I}{I^0}\right) = \varepsilon_{\text{gas}} \cdot c_{\text{gas}} \cdot l \qquad \text{(equation 21)}$$

First, a calibration factor $k_{gas} = \varepsilon_{gas} \cdot l$ can serve to simplify equation 21. To avoid confusion between mol/l and ppm as concentration units, k_{gas} is used when referring to c_{gas} in units of mol/l and k_{gas}^{ppm} is used as a calibration factor for the gas concentration c_{gas}^{ppm} in units of ppm:

$$A_{\text{gas}} = \varepsilon_{\text{gas}} \cdot c_{\text{gas}} \cdot l = k_{gas} \cdot c_{gas} = k_{gas}^{\text{ppm}} \cdot c_{gas}^{\text{ppm}} \qquad \text{(equation 22)}$$

Equation 23 demonstrates how the calibration factor $k_{\text{gas}}^{\text{ppm}}$ for concentration units in ppm can be calculated from the DRIFT spectra displayed in reflectance units:

$$A_{\text{gas}} = -\lg\left(\frac{I_{\text{gas}}}{I_{\text{gas}}^0}\right) = -\lg\left(\frac{\frac{I_{\text{gas}}}{I_{\text{gold bkg.}}}}{\frac{I_{\text{gas}}^0}{I_{\text{gold bkg.}}}}\right) = -\lg\left(\frac{R_{gas}}{R_{gas}^0}\right) = k_{\text{gas}}^{\text{ppm}} \cdot c_{\text{gas}}^{\text{ppm}} \qquad \text{(equation 23)}$$

The calibration gas contained 2000 ppm CO_2 in Ar and was used to fill a DRIFTS cell with gold background (cf. Figure 20a). The calibration factor k_{CO2} for the CO_2 concentration $c(CO_2)$ is determined from the absorbance of the calibration gas A_{cal} at 2360 cm^{-1}, i.e., from the signal intensity after gas filling R_{cal} (2360 cm^{-1}) and the baseline value (cf. Figure 20a) R^0_{cal} (2360 cm^{-1}) as follows:

$$A_{\text{CO}_2}(2360\ \text{cm}^{-1}) = -\lg\left(\frac{R_{\text{cal}}(2360\text{cm}^{-1})}{R_{\text{cal}}^0(2360\text{cm}^{-1})}\right) = k_{\text{CO}_2}^{\text{ppm}} \cdot 2000\ \text{ppm} \qquad \text{(equation 24)}$$

With R_{cal} (2360 cm^{-1}) = 107.4% and R^0_{cal} (2360 cm^{-1}) = 125.1% (see Figure 20), the calibration factor for the CO_2 concentration inside the *operando* DRIFTS cell is obtained:

$$k_{\text{CO}_2}^{\text{ppm}} = -\frac{\lg\left(\frac{R_{\text{cal}}(2360\text{cm}^{-1})}{R_{\text{cal}}^0(2360\text{cm}^{-1})}\right)}{2000\ \text{ppm}} = -\frac{\lg\left(\frac{107.4\%}{125.1\%}\right)}{2000\ \text{ppm}} = 3.31 \cdot 10^{-5}\ \text{ppm}^{-1} \qquad \text{(equation 25)}$$

With the help of $k_{\text{CO}_2}^{\text{ppm}}$, one can now calculate the CO_2 concentration inside the *operando* DRIFTS cell after the VC oxidation. To do so, the signal intensity at 2360 cm^{-1} of the spectrum at 4.97 V (final spectrum recorded during the VC/$LiPF_6$ oxidation experiment) is inserted in equation 23:

$$c^{\text{ppm}}(\text{CO}_2) = -\frac{\lg\left(\frac{I_{4.97\ \text{V}}(2360\text{cm}^{-1})}{I_{4.97\ \text{V}}^0(2360\text{cm}^{-1})}\right)}{k_{\text{CO}_2}^{\text{ppm}}} = -\frac{\lg\left(\frac{8.86\%}{9.31\%}\right)}{3.31 \cdot 10^{-5}\ \text{ppm}^{-1}} = 650\ \text{ppm} \qquad \text{(equation 26)}$$

In order to calculate the moles of CO_2, one needs the total volume of the *operando* DRIFT cell. In a pressure transducer experiments analogous to a previous study from our group,[213] it was found to be 37 ml. In addition, the molar volume at 25°C and 1,013 bar ambient pressure is needed for the calculation:

$$pV = nRT \rightarrow \frac{V}{n} = V_{molar} = \frac{RT}{p} = \frac{8.314\ \frac{\text{J}}{\text{K}\cdot\text{mol}} \cdot 298.15\ \text{K}}{1{,}013 \cdot 10^5\ \text{Pa}} = 22.5\ \frac{\text{l}}{\text{mol}} \qquad \text{(equation 27)}$$

The moles of CO_2 can then be calculated as follows:

$$n(CO_2) = \frac{c^{ppm}(CO_2) \cdot V_{CO_2}}{V_{molar}} = \frac{650\ \text{ppm} \cdot 37\ \text{ml}}{22.5\ \frac{l}{mol}} = 1.07\ \mu\text{mol} \qquad \text{(equation 28)}$$

With an LTO amount of 2.3 mg (93% of the total electrode coating weight of 2.5 mg) and a carbon black amount of 0.075 g (3% of the coating weight), a combined electrode surface area of $1.74 \cdot 10^{-2}$ m^2 is obtained from the BET surface areas of LTO (5.5 m^2/g) and the carbon black Super C65 (62 m^2/g). The moles of CO_2 can be referenced to this combined surface area of the electrode yielding a value of 61 $\mu mol/m^2_{BET}$. This indicates that a really large fraction of the VC contained in the cell must have been oxidized. The electrolyte volume of 20 µl contains ≈300 µmol VC (estimated from a molar mass of 86 g/mol and a density of 1.35 g/cm^3 for pure VC).[214]

It must be mentioned, however, that such a one-point calibration only serves to roughly estimate the evolved gas amount, not for precisely quantifying it. In case of CO_2, there might be a small CO_2 signal (with an intensity that is typically much smaller than 10 % of the CO_2 depicted signals) caused by fluctuations in the dry air feed to the spectrometer. Since these fluctuations are random, they cannot be corrected for. However, they do not explain why an unexpected high CO_2 amount of 61 $\mu mol/m^2_{BET}$ was obtained in the *operando* DRIFTS experiment. In an OEMS study by Pritzl et al.[66], 1 M $LiPF_6$ in VC was oxidized on a ^{13}C carbon electrode; at 5 V, ≈0.6 $\mu mol/m^2_{BET}$ CO_2 had been formed. There are several major differences between the OEMS and the *operando* DRIFTS study, which might create this discrepancy. It is obvious that two different cell setups and two different types of working electrode were used. For the OEMS study, a sealed two-compartment cell was utilized, which prevents cross-talk between the working electrode and the lithium counter electrode.[215] Another influencing factor might be the over-estimation of the BET surface area of the working electrodes, especially in case of the ^{13}C carbon electrode. PVdF is likely to cover the carbon in the electrode and thus reduce the surface area accessible to the electrolyte. In addition, the salt concentration in the OEMS study was lower (1 M $LiPF_6$) compared to the operando DRIFTS experiment (1.5 M $LiPF_6$). Furthermore, the scan speeds were different, with 0.1 mV/s for the OEMS experiment and 0.5 mV/s in the *operando* DRIFTS study. The most decisive factors, however, are most likely the use of a 2-compartment cell and a carbon black electrode for the OEMS study.

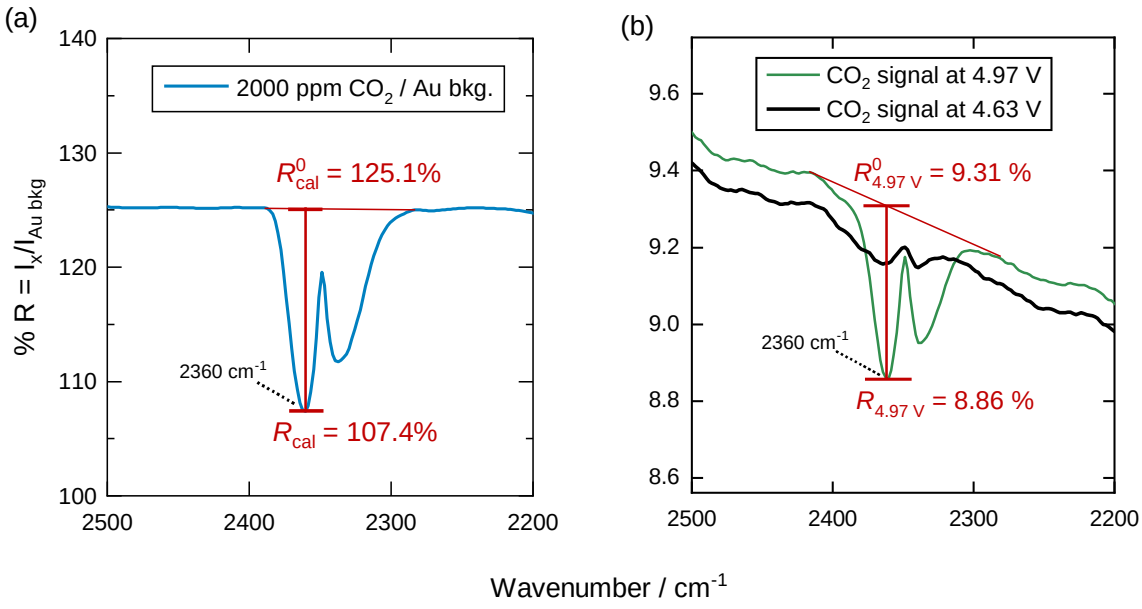

Figure 20: Comparison of the CO_2 signal intensities of (a) calibration gas containing 2000 ppm CO_2 in the DRIFTS cell with a rough gold substrate and (b) maximum CO_2 signal after VC oxidation (oxidative scan to 5 V) in the *operando* DRIFTS cell (cf. Figure 18e). In panel (a), the reflectance exceeds 100% because the height of the cell within the Praying Mantis was readjusted after gas filling, leading to a slightly different vertical position of the cell. The mounting of the cell inside the spectrometer is described in detail in the experimental part (chapter 2.1.3). The linear interpolation of the R_0 values was preferred to reading the R^0 value for CO_2, e.g., from the spectrum at 4.63 V, since the reflectance typically fluctuates about 0.1 % during extended measurement periods, which would lead to a significant error when determining the band intensity.

Having demonstrated how the CO_2 concentration can be estimated from the final spectrum of the VC/$LiPF_6$ oxidation experiment, POF_3 shall be quantified in the same way. In contrast to CO_2, no POF_3 calibration gas was available at the time the experiments were performed. Thus the calibration factor for POF_3 is determined with the help of a literature value for the absorptivity of POF_3, which was reported to be $\varepsilon^{\mathrm{ppm}}_{\mathrm{POF_3}}$ (1416 cm^{-1}) = 0.0014 ppm^{-1} m^{-1} in a study by Andersson et al.[211] Given that the total optical path length of the IR radiation is 1.4 cm in the head space of the *operando* DRIFTS cell, the literature value of $\approx 0.0014\ \mathrm{ppm^{-1}\ m^{-1}}$ can be converted to a calibration factor for the POF_3 concentration in the *operando* DRIFTS cell:

$$k^{\mathrm{ppm}}_{\mathrm{POF_3}} = \varepsilon^{\mathrm{ppm}}_{\mathrm{POF_3}} \cdot l_{\mathrm{DRIFTS\ cell}} = 0.0014\ \mathrm{ppm^{-1}\ m^{-1}} \cdot 1.4 \cdot 10^{-2}\ \mathrm{m} = 1.96 \cdot 10^{-5}\ \mathrm{ppm^{-1}} \quad \text{(equation 29)}$$

Analogous to CO_2, the POF_3 concentration can be calculated from the intensity at 1416 cm^{-1} (cf. Figure 18f) of the spectrum at 4.97 V, which yields the final POF_3 concentration after the oxidative scan:

$$c^{\mathrm{ppm}}(\mathrm{POF_3}) = -\frac{\lg\left(\frac{I_{4.97\ \mathrm{V}}(1416\ \mathrm{cm^{-1}})}{I^0_{4.63\ \mathrm{V}}(1416\ \mathrm{cm^{-1}})}\right)}{k^{\mathrm{ppm}}_{\mathrm{POF_3}}} = -\frac{\lg\left(\frac{6.54\%}{7.76\%}\right)}{1.96 \cdot 10^{-5}\ \mathrm{ppm^{-1}}} = 3790\ ppm \approx 4000\ \mathrm{ppm} \quad \text{(equation 30)}$$

The moles of POF_3 can be calculated as follows:

$$n(\mathrm{POF_3}) = \frac{c^{\mathrm{ppm}}(\mathrm{POF_3}) \cdot V_{\mathrm{POF_3}}}{V_{\mathrm{molar}}} = \frac{3790\ \mathrm{ppm} \cdot 37\ \mathrm{ml}}{22.5\ \frac{\mathrm{l}}{\mathrm{mol}}} = 6.23\ \mu\mathrm{mol} \approx 6\ \mu\mathrm{mol} \qquad \text{(equation 31)}$$

With the electrode surface area of $1.74 \cdot 10^{-2}$ m^2, the specific gas generation is ≈ 360 $\mu mol_{POF3}/ m^2_{BET}$.

In case of PF_5, Andersson et al. reported challenges when trying to calibrate their gas transmission FTIR spectrometer for quantitative measurements. PF_5 has an extremely high reactivity with moisture. Even when minimizing trace water inside the equipment as much as possible, the authors did not succeed to avoid partial decomposition of PF_5 to POF_3 and HF as well as unknown decomposition products. For this reason, the absorptivity of PF_5 cannot be calculated reliably from the literature data.[211,216]

Similarly, in the present study on the oxidation of VC and $LiPF_6$, the highly reactive PF_5 might be partially detected as POF_3 due to reactions with steel components inside the *operando* DRIFTS cell. A similar effect was reported for OEMS experiments as discussed above.[212]

3.1.5. Conclusion

Using our *operando* DRIFTS setup, we studied the reductive and oxidative stability of electrolyte solvents such as EC and VC and the commonly used electrolyte salt $LiPF_6$. Interestingly, the overall signal intensity was found to be drastically impacted by the lithiation degree of graphite, thus LFP was used for a second set of experiments to avoid baseline distortions of the IR spectra. Regarding reductive stability, we could not detect any infrared signals belonging to surface species such as LEDC that typically are formed during the reduction of EC-based electrolytes.[206] Due to the dominant electrolyte signals, the sensitivity of the method appears to be too low to differentiate between fluctuations of electrolyte signals and the formation of electrolyte reduction products.

However, one can study the evolution of infrared active gases such as POF_3, CO_2, and PF_5 from the oxidative decomposition of a VC/$LiPF_6$ electrolyte. In case of POF_3 and PF_5, the gas quantities can be estimated by absorption coefficients from the literature and in case of CO_2 additionally via a calibration gas measurement. The VC oxidation experiments are consistent with literature reports on the instability of VC at high potentials[66] and the formation of gaseous oxidation products.[217] Classic electrolyte additives such as VC can potentially be problematic for high-voltage cathode active materials such as LMR-NCM or LNMO. For this reason, VC-free electrolytes are commonly used for high-voltage cathode active materials, taking into account that VC is not stable at potentials above 4.3 V.[66,74]

3.2. Surface Stability of Layered Oxide Cathode Active Materials

Both, CAMs with high specific surface area such as LMR-NCM and CAMs with high nickel content such as NCM811 suffer from high reactivity towards CO_2 and H_2O when they are exposed to ambient air. As a result, hydrates, hydroxides, carbonates, and mixtures of those are formed on the surface.[48,136,161] Surface contaminants on LMR-NCM are discussed in chapter 3.2.1 by comparing two materials with different lithium content on the basis of full-cell cycling data and TGA-MS analysis.

Surface contaminants on NCM811 are discussed in chapter 3.2.2, presenting an article from 2019 on ambient storage-derived surface contamination of NCM811 and NCM111.[47] In order to induce surface contaminants, CAMs were deliberately exposed to atmospheric atmosphere at high humidity. Calcination at 525°C was demonstrated to remove most of the formed contaminants and was thus suggested as a mitigation strategy. In a combined analysis approach, first the nature and quantity of surface contaminants is assessed for the different pre-treatments via surface spectroscopy (DRIFTS, XPS) and thermal characterization (TGA-MS). Side reactions with the electrolyte and the impact on gassing is investigated by storing CAMs with electrolyte at 60°C and recording the gassing via on-line mass spectrometry (O-MS). The impact of "wet" storage and calcination on the electrochemical performance is monitored by full-cell cycling experiments.

Having discussed the formation of surface contaminants on NCM811 in chapter 3.2.2, the same material will finally be used to evaluate the applicability of *in situ* DRIFTS as a potential method for monitoring the reaction between NCM811 and CO_2, H_2O, or a combination of both (cf. chapter 3.2.3).

3.2.1. Impact of the Li Content on the Surface Reactivity of LMR-NCM

As explained above, LMR-NCM potentially forms a significant amount of surface contaminants due to its comparatively large BET surface area. To investigate the reactivity of LMR-NCM towards CO_2 and H_2O, it was exposed to ambient air with high moisture content (≈85% relative humidity at 25°C) and atmospheric CO_2 concentration for one week. This "wet storage" experiment has been described in more detail in the study on the surface contamination of NCM111 and NCM811 (chapter 3.2.2)[47] as well as in the study of LMR-NCM modified by SO_3 treatment (chapter 3.3.1).[134] In the following, the "wet storage" experiment will be used to discuss the different impact of CO_2 and H_2O on two different LMR-NCM stoichiometries with the general formula $x\ Li_2MnO_3 \cdot (1-x)\ LiNi_xCo_yMn_zO_2$. In one case, $x = 1.33$ for the composition $0.33\ Li_2MnO_3 \cdot 0.66\ LiNi_{0.4}Co_{0.2}Mn_{0.4}O_2$, referred to as $Li_{1.33}$-LMR-NCM. In a second case, $x = 1.42$ for the composition $0.42\ Li_2MnO_3 \cdot 0.58\ LiNi_{0.4}Co_{0.2}Mn_{0.4}O_2$, referred to as $Li_{1.42}$-LMR-NCM.

The full-cell cycling data of both CAMs are compared in Figure 21 for the same pre-treatments that are described in the article[134] on $Li_{1.42}$-LMR-NCM presented in chapter 3.3.1: (i) the CAM powders were processed as received ("dry"), (ii) after a one week long storage at ambient air with ≈85% humidity ("wet"), and (iii) after calcination for 1 h in an atmosphere containing 30% O_2 in Ar ("calcined"). In case of $Li_{1.33}$-LMR-NCM, the cycle-life is similar for all three pre-treatments (cf. Figure 21a-d): the deviation in capacity is within the error bars for all tested discharge rates (1C, C/10, and 3C, panels a-c) as well as in case of the DCIR pulse test (panel d). In case of $Li_{1.42}$-LMR-NCM, a completely different picture is obtained (panel e-h). While the "dry" and "calcined" sample do not significantly differ in rate performance, cycle-life, and DCIR resistance, the one week long "wet" storage drastically deteriorates the 1C cycling performance (panel e) and leads to a worse 3C rate capability (panel g). This is consistent with an accelerated full-cell resistance growth (panel h) of "wet" $Li_{1.42}$-LMR-NCM compared to "dry" and "calcined" $Li_{1.42}$-LMR-NCM, as already described in the above mentioned article[134] (compare chapter 3.3.1). In contrast, the C/10 capacity is only slightly affected by the "wet" storage, indicating that the strongest impact of the degradation of $Li_{1.42}$-LMR-NCM during "wet" storage is an increased resistance along with reduced rate performance.

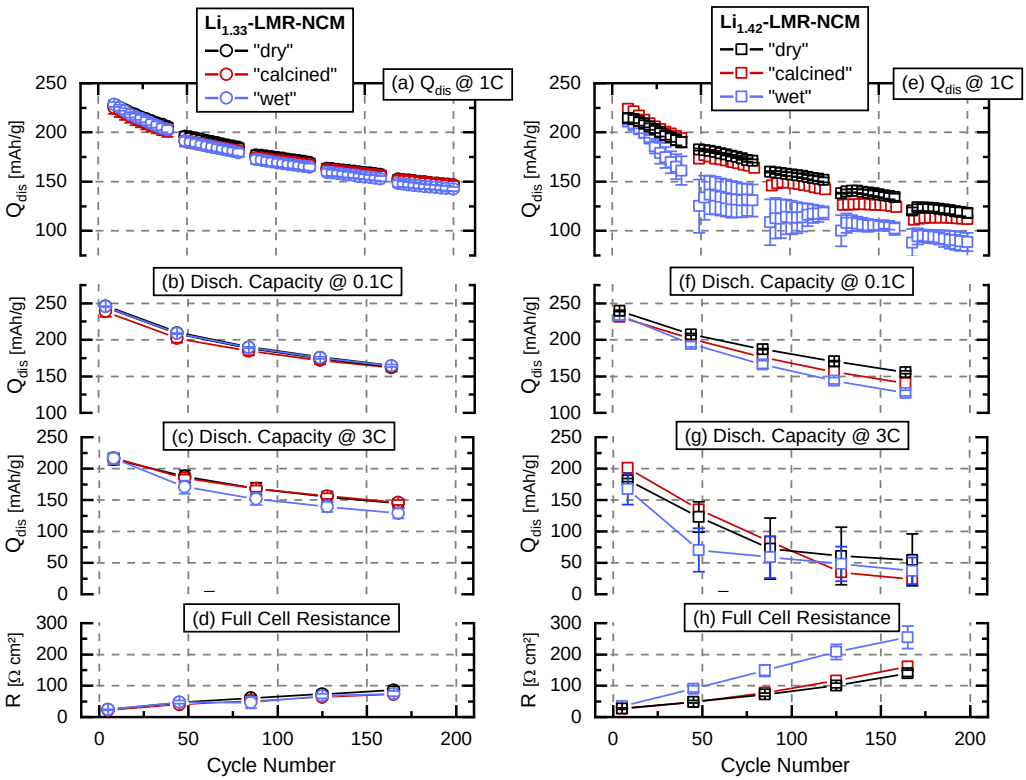

Figure 21: Full-cell cycle-life data of LMR-NCM//graphite coin cells at 45°C (average of two cells each, with error bars representing maximum and minimum values) with different pre-treatments of two different LMR-NCM (x $Li_2MnO_3 \cdot (1-x)$ $LiNi_xCo_yMn_zO_2$) compositions: **(a) – (d)** $x = 1.33$ ("$Li_{1.33}$-LMR-NCM", i.e., 0.33 $Li_2MnO_3 \cdot$ 0.66 $LiNi_{0.4}Co_{0.2}Mn_{0.4}O_2$); **(e) – (h)** $x = 1.42$ ("$Li_{1.42}$-LMR-NCM", i.e., 0.42 $Li_2MnO_3 \cdot$ 0.58 $LiNi_{0.4}Co_{0.2}Mn_{0.4}O_2$). The detailed cell setup and cycling protocol can be found in the Experimental section of the article[134] presented in chapter 3.3.1. The following pre-treatments were tested: (i) as received ("dry"), (ii) effect of one week storing at ambient air with high humidity ("wet"), and (iii) heating at 625°C under Ar for 1 h ("calcined"). The "dry" and "wet" data in panels (e) - (h) are identical to Figure 10 in the mentioned publication.[134] In more detail, the cycling data depicted here comprise **(a, e)** the discharge capacity (Q_{dis}) at 1C (only every third cycle is displayed for the sake of better visibility); **(b, f)** the discharge capacity at intermittent cycles at C/10 (the last one of the three cycles for every rate is displayed); **(c, g)** at 3C (again, the last one of the three cycles for every rate is displayed); **(d, h)** DCIR pulse resistance (R) after charge to 40% SOC.

Apart from the different sensitivity to CO_2 and H_2O, it is apparent that the $Li_{1.33}$-LMR-NCM (Figure 21a) has a significantly better 1C cycle-life performance than $Li_{1.42}$-LMR-NCM (Figure 21e). When comparing the "dry" samples, for instance, the $Li_{1.33}$-LMR-NCM starts with a discharge capacity of 228 mAh/g (cycle 9) and fades down to 146 mAh/g after 200 cycles. The "dry" $Li_{1.42}$-LMR-NCM has a significantly lower initial 1C discharge capacity of 215 mAh/g in cycle 9 and a more pronounced capacity fading (only 118 mAh/g after 200 cycles). It should be noted that both materials have roughly the same BET surface area of ≈6.5 m²/g,[128,134] consequently the different lithium content of $Li_{1.33}$-LMR-NCM and $Li_{1.42}$-NCM seems to be the most important factor to explain the different reactivity with CO_2 and moisture. Apparently, the higher overlithiation degree is challenging in terms of electrochemical aging properties and chemical robustness of the $Li_{1.42}$-LMR-NCM towards CO_2 and H_2O. In this context, Teufl et al.[128] demonstrated that $Li_{1.42}$-LMR-NCM releases much more oxygen in the first activation charge as compared to $Li_{1.33}$-LMR-NCM, namely ≈180 $\mu mol_{oxygen}/g_{CAM}$ for $Li_{1.42}$-LMR-NCM as opposed to ≈6 $\mu mol_{oxygen}/g_{CAM}$ for $Li_{1.33}$-LMR-NCM. It was confirmed that after oxygen release, the resulting oxygen-deficient surface layers are converted to resistive spinel layers.[71,111,128] Since $Li_{1.42}$-

LMR-NCM clearly releases more oxygen, a faster resistance build-up accompanied by faster aging is well expected, as observed from the cycle-life data in Figure 21. To further elucidate the different reactivity of $Li_{1.33}$- and $Li_{1.42}$-LMR-NCM with CO_2 and moisture, TGA-MS analysis was performed to reveal the impact of "wet" storage on the amount of surface contaminants (Figure 22).

As demonstrated in the article[47] on surface contaminants (cf. chapter 3.2.2), the amount of surface carbonates, hydroxides and hydrates can be well characterized by the weight-loss between 125 and 525°C. In the present study (Figure 22), a slightly different range was chosen (120 – 450°C) in order to achieve better comparability with the $Li_{1.33}$-LMR-NCM data (panels a, b) that were collected with an optimized TGA-MS procedure with a temperature ramp including plateaus at 120 and 450°C. In this way, all the relevant surface contaminants such as $NiCO_3 \cdot 2Ni(OH)_2 \cdot x\ H_2O$, LiOH, NiOOH, etc. can be assessed,[47,218] with the exception of Li_2CO_2 that decomposes only above 700°C.[47] The comparison between "calcined" and "wet" $Li_{1.33}$-LMR-NCM (Figure 22 a, b) reveals only a small difference of 0.06% weight loss for the "calcined" material and 0.16% for the "wet" stored powder. In contrast, "dry" $Li_{1.42}$-LMR-NCM loses 0.32% in weight in the same temperature range and "wet" $Li_{1.42}$-LMR-NCM as much as 0.75% (Figure 22 c, d). This clearly proves that the worse cycling performance of "wet" $Li_{1.42}$-LMR-NCM was in fact caused by a higher amount of surface contaminants.

While the TGA data allow the quantitative discussion of surface contaminants, the MS traces give a hint on the nature of those. While an enhancement of H_2O (m/z = 18) indicates the desorption of water (up to 120°C) as well as the decomposition of hydrates and hydroxides (above 120°C), the CO_2 trace (m/z = 44) goes typically along with the decomposition of carbonates. In contrast to the quantitative information obtained from the TGA weight loss, the accompanying MS measurement gives qualitative information only, as explained in the study[47] on surface contaminants (cf. chapter 3.2.2). From Figure 22 it gets clear that all samples exhibit the characteristic CO_2 signal between 120°C and 450°C, indicating the decomposition of carbonate-based surface impurities. In the same temperature region, the H_2O signal rises as well in case of $Li_{1.42}$-LMR-NCM, being consistent with the presence of larger fractions of hydroxides and hydrates. In contrast, for $Li_{1.33}$-LMR-NCM, the H_2O signals are much weaker and unfortunately overshadowed by the kinks in the MS signals induced by switching between a temperature ramp and the temperature holds at 120°C and 450°C. Still, the small increase of the H_2O signal between 120°C and 450°C would be consistent with a tiny amount of hydroxides and hydrates, which is consistent with the comparatively small weight losses for $Li_{1.33}$-LMR-NCM even after "wet" storage. In summary, it becomes once more clear how robust $Li_{1.33}$-LMR-NCM is towards CO_2 and moisture, in great contrast to $Li_{1.42}$-LMR-NCM. This was clearly reflected by the above discussed cycling data.

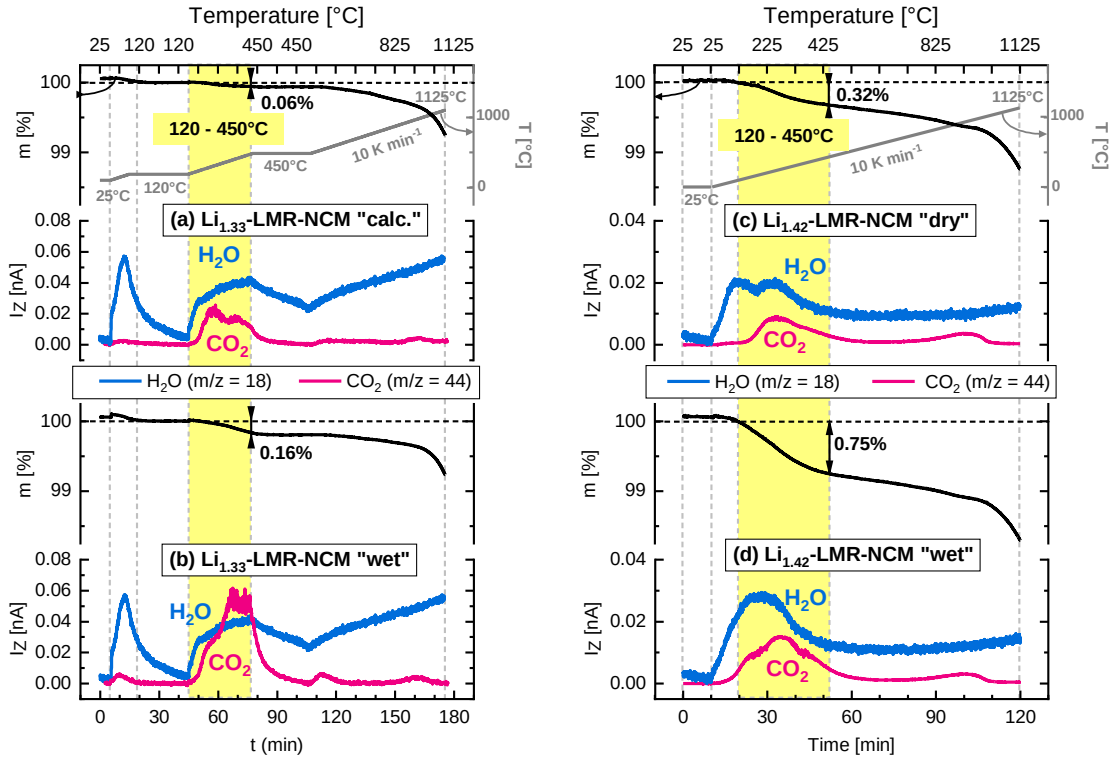

Figure 22: TGA-MS analysis of LMR-NCM with the composition $x\ Li_2MnO_3 \cdot (1-x)\ LiNi_xCo_yMn_zO_2$: **(a, b)** $x = 1.33$ ($Li_{1.33}$-LMR-NCM, i.e., $0.33\ Li_2MnO_3 \cdot 0.66\ LiNi_{0.4}Co_{0.2}Mn_{0.4}O_2$); **(c, d)** $x = 1.42$ ($Li_{1.42}$-LMR-NCM, i.e. $0.42\ Li_2MnO_3 \cdot 0.58\ LiNi_{0.4}Co_{0.2}Mn_{0.4}O_2$). **(a, c)** "Calcined" $Li_{1.33}$-LMR-NCM and "dry" $Li_{1.42}$-LMR-NCM, both with limited amount of surface contaminants ("dry" $Li_{1.33}$-LMR-NCM data were not recorded so that the "calcined" sample is depicted instead). **(b, d)** Impact of "wet" storage, i.e., a one week long storage at ambient air with high humidity. The TGA-MS analysis was carried out under Ar with a 10 K/min temperature ramp from 25 to 1125°C. The yellow area marks the temperature range from 125 to 450°C, where a mass loss due to the thermal decomposition of surface contaminants accompanied by CO_2 and H_2O signals in the MS is observed (similar analysis as that shown in Figure 3 of the study[47] on surface contaminants (cf. chapter 3.2.2)). In panels (a) and (b), a slighlty different procedure is used with intermittent plateaus at 120°C and 450°C (30 min each). The sample weights m [%] are normalized to the value at 120°C. The MS signals are depicted without any baseline manipulation, only with a simple offset correction (the last value at 25°C is set to $I_z = 0$).

In the publication[134] in chapter 3.3.1, $Li_{1.42}$-LMR-NCM is used to showcase the positive impact of SO_3 treatment on this CAM, making it much more robust to CO_2 and moisture. In the following section, NCM111 and NCM811 will be discussed in the context of ambient storage derived surface contaminants.

3.2.2. Ambient Storage Derived Surface Contamination of NCM811 and NCM111: Performance Implications and Mitigation Strategies

The manuscript entitled “Ambient Storage Derived Surface Contamination of NCM811 and NCM111: Performance Implications and Mitigation Strategies” was first submitted to the peer-reviewed Journal of the Electrochemical Society on April 3, 2019. A revised version was submitted on May, 28, 2019 and published online on July, 2, 2019. The article is published “open access” under the terms of the Creative Commons Attribution 4.0 License (CC BY, http://creativecommons.org/licenses/by/4.0/), which permits unrestricted reuse of the work in any medium, provided the original work is properly cited. A permanent link to this article can be found under https://doi.org/10.1149/2.0011912jes.

The formation of surface contaminants due to improper storage and handling of CAMs were first discussed in the patent literature,[219–224] before the scientific community became more and more interested in investigating the nature of the surface contaminants and the mechanisms of their formation.[47,48,161,225] The chemical reactivity of Ni-rich oxides with moisture and CO_2 from ambient air can cause serious problems during electrode manufacturing. Surface contaminants such as hydrates, hydroxides, carbonates, and mixtures of those can be formed during material handling and electrode manufacturing, which creates a challenge for designing industrial electrode manufacturing processes.[47,48,161] Surface contaminants can cause the gelation of NMP-based slurries. In addition, the basic surface species trigger side reactions with the electrolyte and potentially harmful gassing inside the cell.[48,161,170]

Within the article presented in this chapter, the surface reactivity of the Ni-rich NCM811 is compared to NCM111 after exposure to atmospheric CO_2 and moisture. Quantity and nature of the surface contaminants are revealed by a combinatory analysis using TGA-MS, DRIFTS, on-line mass spectrometry (OMS), and NCM811//graphite full-cell cycling experiments. Thereby it was demonstrated that NCM811 is much more prone to surface contaminants than NCM111. The TGA-MS analysis of NCM811 compared to reference samples allowed to identify basic nickel carbonate hydrate $NiCO_3 \cdot 2Ni(OH)_2 \cdot x\,H_2O$ (NCBH) as the major surface contaminant, consistent with a pronounced carbonate (CO_3^{2-}) signal accompanied by OH^-/H_2O vibrations in the infrared spectra. DRIFTS turned out to be much more sensitive towards surface species on NCM powders than ATR-FTIR and transmission FTIR. The reactions of electrolyte with surface contaminants was investigated by storing CAM powder wetted by electrolyte at 60°C. The formed CO_2 was quantified via mass spectrometry (OMS). It was found that a high amount of surface contaminants leads to increased CO_2 gassing, faster resistance growth, and shorter full-cell cycle-life. Finally, it was demonstrated that a thermal treatment under Ar serves to remove most of the surface contaminants formed after exposure to CO_2 and moisture, which mitigates gassing problems and enables improved full-cell cycle-life.

Author contributions

J. S. and M. M. performed the surface area measurements. H. B. and M. M. carried out the detailed TGA-MS analysis of NCM and reference samples. J.S. performed the FTIR analysis comparing DRIFTS to transmission and ATR-FTIR. M. M. developed the OMS method and carried out the experiments. J. S. prepared electrodes and J.S. and D.P. assembled full-cells and performed the electrochemical cycling tests. J. S., M. M., H. B., and H. A. G wrote the manuscript. All authors discussed the data and commented on the manuscript.

Ambient Storage Derived Surface Contamination of NCM811 and NCM111: Performance Implications and Mitigation Strategies

Johannes Sicklinger,[=,*] Michael Metzger,[=] Hans Beyer,[z] Daniel Pritzl,[*] and Hubert A. Gasteiger[**]

Chair of Technical Electrochemistry, Department of Chemistry and Catalysis Research Center, Technische Universität München, D-85748 Garching, Germany

The quality of metal oxide-based battery active materials is compromised by surface contamination from storage and handling at ambient conditions. We present a detailed analysis of the true nature and the quantity of the surface contaminants on two different cathode active materials, the widely used $LiNi_{1/3}Co_{1/3}Mn_{1/3}O_2$ (NCM111) and the Ni-rich $LiNi_{0.8}Co_{0.1}Mn_{0.1}O_2$ (NCM811). We process these materials in three distinct conditions "wet" (excessive exposure to moisture), "dry" (standard drying of as-received materials), and "calcined" (heat-treatment of cathode powders). Surface contaminants are then quantified by thermogravimetric analysis coupled with mass spectrometry (TGA-MS), and their reactivity with an ethylene carbonate-based electrolyte is evaluated using on-line mass spectrometry (OMS). We demonstrate that not only the commonly assumed LiOH and Li_2CO_3 residues account for NCM performance deterioration upon storage in moisture and CO_2 containing atmosphere, but also basic transition metal hydroxides/carbonates formed on the material surface. Eventually, we showcase a thermal treatment that removes these transition metal based surface contaminants and leads to superior cycling stability.

 [DOI: 10.1149/2.0011912jes]

Manuscript submitted April 3, 2019; revised manuscript received May 28, 2019. Published July 2, 2019.

State-of-the-art cathode active materials (CAMs) for lithium-ion batteries range from the classic $LiCoO_2$ (LCO) and $LiMn_2O_4$ (LMO), which are still at the heart of nearly all portable electronic devices, to mixed metal oxides, such as $LiNi_aMn_bCo_cO_2$ (a+b+c = 1) with various compositions, where the most widespread representative is $LiNi_{1/3}Mn_{1/3}Co_{1/3}O_2$ (NCM111).[1] For NCM111, the general understanding is that Ni provides high capacity but poor thermal stability, that Mn maintains good cycle life and safety, and that Co offers structural stability and high electronic conductivity resulting in a better rate capability.[2,3] To boost the energy density and minimize the dependence on Co, current development focuses on Ni-rich compositions, e.g., NCM523, which is already a commercial commodity and expected to be replaced by NCM622 soon. Nowadays, considerable research effort is devoted to the Li- and Mn-rich version of NCM, viz., (1-x) $Li_2MnO_3 \cdot xLi[Ni_aMn_bCo_c]O_2$ (HE-NCM), and the Ni-rich material NCM811, which are being envisaged as potential CAMs for high-energy battery packs in the next generation of electric cars,[4,5] and which are considered to be competitive alternatives to Ni-rich NCA ($LiNi_{0.80}Co_{0.15}Al_{0.05}O_2$).[1,5]

In the synthesis of these materials (see Figure 1 for a simple scheme), transition metal precursors are obtained from precipitation of aqueous transition metal sulfate or nitrate solutions by increasing the pH.[6,7] The obtained transition metal hydroxides are then mixed with the lithium precursor, viz., Li_2CO_3 or a technical grade $LiOH \cdot H_2O$ containing typically 1 wt% of Li_2CO_3.[7,8] The mixture is subsequently calcined under O_2-rich atmosphere, e.g., in a pusher kiln (step 1 in Figure 1) to form the desired layered transition metal oxide cathode active material. In the case of Ni-rich materials ((e.g., NCM811), the calcination step can only be done at rather moderate temperatures (<700°C), since the thermal stability of the product is inversely proportional to the Ni content;[3] in this case, $LiOH \cdot H_2O$ is preferred due to its lower decomposition temperature,[9] but the Li_2CO_3 impurities remain in the resulting CAM powder, especially on its surface.[6,7] Additionally, any residual LiOH after calcination can react with CO_2 in air to form Li_2CO_3. This could already happen during the cooldown (step 2 in Figure 1), if CO_2 and H_2O released from the precursors during calcination are not entirely removed. Both, LiOH and Li_2CO_3 were reported to trigger electrolyte decomposition and thus deteriorate the cell cycling performance.[10–13]

In addition to these known Li_2CO_3 and LiOH residues, metal oxide-based cathode materials are highly prone to contamination from improper storage and handling (step 3 in Figure 1), a fact that was so far mainly discussed in the patent literature.[6–8,14–16] As of yet, the mechanism of these weathering phenomena and the nature of the resulting surface contaminants have not been clearly resolved. Ni-rich materials are particularly sensitive to moisture exposure.[17–19] Long air exposure of the CAM powder typically results in a high content of soluble base,[7] which makes it difficult to fabricate good electrodes due to gelation of the cathode slurry caused by the increased pH.[3] Further, a deterioration of cycling performance is observed for batteries made from surface contaminated cathode active materials.[17,20,21]

Out of the few scientific publications that deal with the storage of cathode active materials, the article by Shkrob et al.[22] presents evidence for a bulk H^+/Li^+ exchange during long-term exposure (several months) of NCM materials to humid air. While these bulk changes are not the focus of our current study, also Liu et al. have reported Li^+ cations and oxygen atoms migrating toward the surface of layered oxide particles and recombining with water and CO_2 to yield LiOH, $LiHCO_3$, and Li_2CO_3.[19,23] Recently, Faenza et al.[24] conducted a study on NCA proposing to remove those contaminants via thermal treatment. However, similar to Liu et al.,[19,23] they interpreted surface species that could be removed between 150 and 350°C as $LiHCO_3$. Although thermodynamic data on $LiHCO_3$ is scarce, there is some consensus that it can be formed by the reaction of CO_2 with aqueous Li_2CO_3 and is only stable in solution.[25] More specifically, CO_2 capture by aqueous Li_2CO_3 has been predicted by DFT to take place at $T \leq 300K$, $p_{H_2O} = 1$ bar and $p_{CO_2} \geq 0.1$ bar, but no experimental evidence was provided.[26] To the best of our knowledge, solid $LiHCO_3$ has not been observed at ambient conditions and there is no known or experimentally determined crystal structure. In short, its existence as a solid contaminant on metal oxide surfaces at temperatures up to 150°C appears unlikely. The formation of lithium carbonate impurities from synthesis or improper storage can, in principle, be mitigated by washing the affected oxide in water[18] or alcohol.[27] To our knowledge, only two articles reported surface contaminants other than the above-mentioned lithium compounds: The first is a paper by Moshtev et al.,[28] suggesting a reaction of overlithiated $LiNiO_2$ with water to nickel (+III) oxide hydroxide (NiOOH) and surface LiOH due to Li^+ de-intercalation. The second is a study on the ambient storage NCM811 based electrodes which was conducted within our group in parallel to the present work.[29] Therein, the appearance of a voltage spike in the first charge of electrodes stored over extended times in ambient air as well as a significant performance loss in full-cell

[=]These authors contributed equally to this work.
[*]Electrochemical Society Member.
[**]Electrochemical Society Fellow.
[z]E-mail: hans.beyer@tum.de

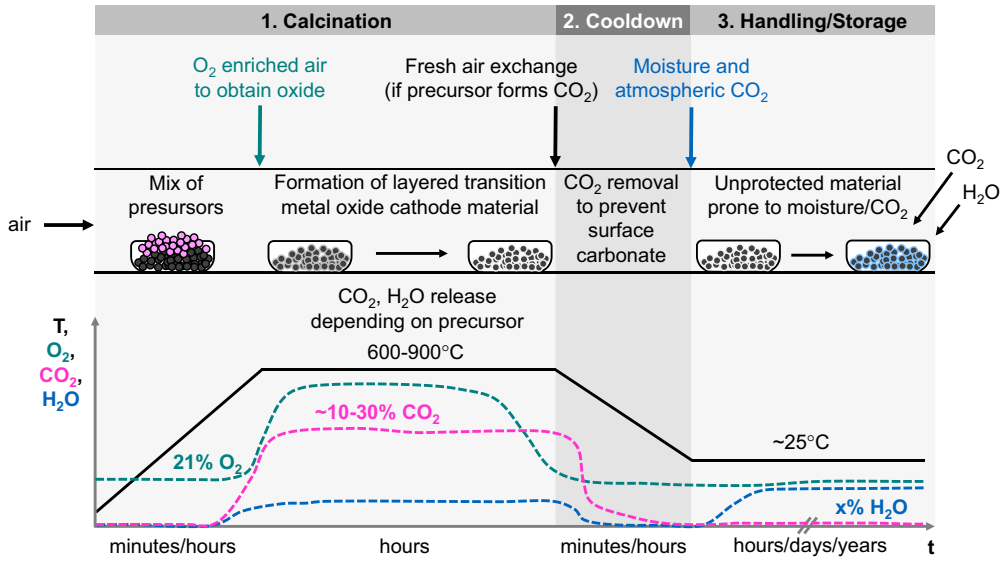

Figure 1. Scheme of the synthesis process to obtain a metal oxide-based cathode active material (CAM), exemplarily shown for a pusher kiln setup where a saggar moves through various furnace compartments (upper panel) at different temperatures, and showing also the approximate variation in the surrounding gas environment (lower panel). Transition metal precursors and lithium precursor are mixed and heated to 600–900°C during calcination in O_2 enriched air (step 1). During the subsequent cooldown (step 2), fresh air is supplied to remove H_2O and CO_2 released from the precursors, which would otherwise lead to the formation of surface hydroxides and carbonates. During improper storage and handling (step 3), the metal oxide surface is prone to contamination in moisture and CO_2 containing atmosphere.

cycling is described. Both effects increase with the time of exposure to ambient air (3 and 12 months). Raman spectroscopy demonstrated that hydrated nickel carbonate-hydroxides (referred to as $(NiCO_3)_2{\cdot}(Ni(OH)_2)_3{\cdot}4\ H_2O$ in that work) are crucial surface contaminants produced upon ambient air storage, rather than only the commonly reported Li_2CO_3 and LiOH surface contaminants.

In a recent study,[30] we added discrete amounts of H_2O or TBAOH x 30 H_2O as hydroxide ion (OH^-) sources in order to study the hydrolysis of electrolytes based on ethylene carbonate (EC). At high temperature ($\geq$ 60°C), both the H_2O- and the OH^--induced EC hydrolysis generated large amounts of CO_2. The decisive finding, however, was that the OH^--induced reaction has a lower activation energy and is thus already relevant at typical battery operating conditions ($\leq$ 40°C). These results have important implications for cell manufacturing and cathode active materials synthesis. On the one hand, trace amounts of water and OH^- could easily be introduced into lithium-ion cells by improper drying of cell components, as pointed out in previous studies with regard to gas evolution at the cathode[31,32] and the anode.[33,34] On the other hand, alkaline surface contaminants originating from the synthesis and/or the storage of transition metal oxide based CAMs in moisture and CO_2 containing atmosphere (i.e., ambient air) would likely attack carbonate-based electrolytes in a similar manner as described above. In the literature, spinel coating has been demonstrated to overcome chemical instability of layered oxides.[35] In principle, bulk doping might increase or decrease the reactivity of layered oxides with CO_2 and H_2O by altering the basicity of the oxide surface. The NCM samples described in the article at hand were neither modified by surface coating nor by bulk doping.

In this study, two different metal oxide-based cathode active materials are investigated in terms of their susceptibility to surface contamination: the widely used $LiNi_{1/3}Mn_{1/3}Co_{1/3}O_2$ (NCM111) and the Ni-rich $LiNi_{0.8}Mn_{0.1}Co_{0.1}O_2$ (NCM811). The samples are preconditioned under carefully controlled conditions (see Experimental Section for details), leading to "wet" (after extended exposure to wet air), "dry" (standard drying of as-received CAMs), and "calcined" samples (heat-treatment of CAMs). These are subjected to detailed TGA-MS and DRIFTS (diffuse reflectance infrared Fourier transform spectroscopy) analyses, and their reactivity with EC-based electrolyte is tested by on-line mass spectrometry (OMS) of heated mixtures of EC and differently conditioned CAMs. In this work, we also explore a strategy to reverse surface contamination from improper storage conditions. Finally, we demonstrate that the condition of the CAM surface strongly affects the cycling stability of NCM811//graphite full-cells.

Experimental

Treatment of cathode active materials.—To investigate the formation and the effect of surface impurities, the two CAM samples, NCM111 and NCM811 (all BASF, Germany) are treated in three distinct ways as graphically summarized in Figure 2.

The "wet" samples are obtained by storing the CAM powder for one week in ambient air over an open water bath held at 25°C, thus exposing them to moisture (relative humidity of 85 $\pm$ 5%) and the typical concentration of ~400 ppm CO_2 in air (step 1a in Figure 2). The vessel contining the water bath was covered with a lid which contained a small hole to allow CO_2 diffusion from the ambient into the vessel, so that CO_2 could be supplied continuously. The samples are then dried in a glass oven (Büchi, Switzerland) for 6 h at 70°C under dynamic vacuum to remove physisorbed H_2O (step 1b in Figure 2), and subsequently stored in an Ar-filled glove box (<0.1 ppm O_2 and H_2O, MBraun, Germany) without exposure to ambient air after drying. We strive to demonstrate the effect of surface contaminants on cell cycling behavior and thus wanted to ensure not to decompose any surface contaminants. For this reason, we chose the unusually low drying temperature of 70°C for the "wet" samples.

The simultaneous presence of CO_2 and H_2O during "wet" storage facilitates the formation of carbonates, hydroxides, and their hydrates. Without moisture, no hydroxides or hydrates can be formed, which also might impede the formation of carbonates (this was demonstrated by DRIFTS measurements for materials stored for several days in pure but dry CO_2; data not shown). The higher the moisture content, the faster the formation of contaminants and the higher the amount of contaminants being formed.

The "dry" samples are taken from the as-received CAM powders that were shipped under inert gas packaging and stored in an Ar-filled glove box (step 2a in Figure 2). These samples are dried at the standard conditions for electrodes in our lab, viz., 12 h at 120°C under dynamic vacuum in a glass oven (step 2b in Figure 2), before returning them into the glove box without exposure to ambient air. Note that these samples were not necessarily handled under inert atmosphere

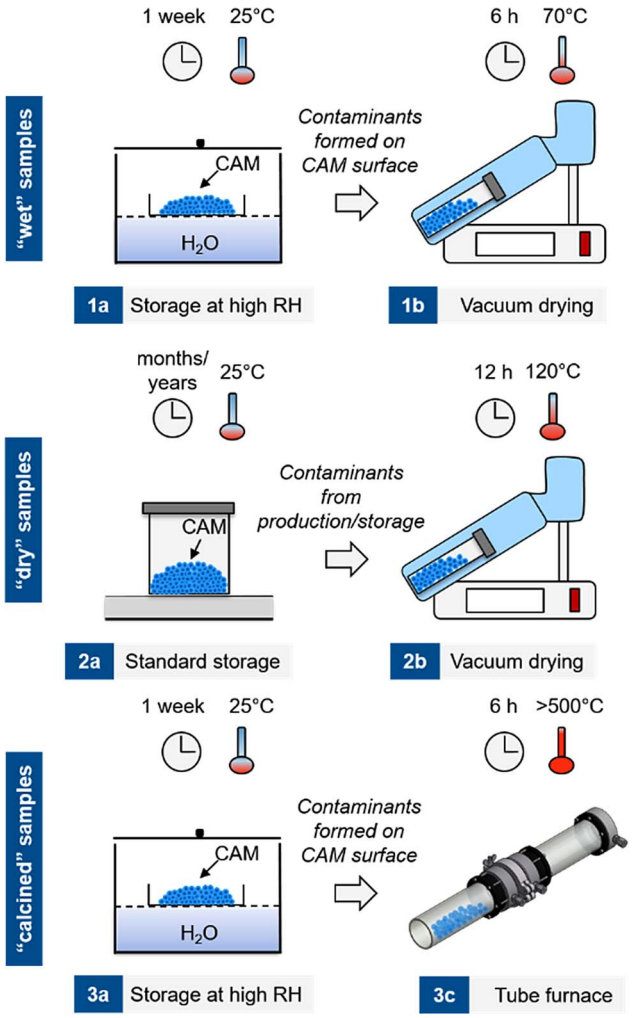

Figure 2. Storage conditions for the two CAM samples, NCM111 (standard material) and NCM811 (Ni-rich material). The "wet" condition is obtained by storing the CAMs under high relative humidity (RH) for one week, followed by mild drying under dynamic vacuum (6 h at 70°C) to remove physisorbed water (upper panel); the "dry" condition refers to the as-received CAMs stored in an Ar-filled glove box and dried under standard electrode fabrication conditions (12 h at 120°C under dynamic vacuum) prior to use (middle panel); the "calcined" condition refers to "wet" storage, followed by a high temperature treatment (6 h at >500°C in a pure argon flow) to remove surface contaminants (lower panel).

before shipping, such that a surface contamination prior to handling in our labs cannot be excluded. Finally, the "calcined" samples are preconditioned in the same way as the "wet" samples. After one-week of exposure to moisture and CO_2, the samples are heat treated in a tube furnace (Carbolite, Germany) under argon flow (1 l/min; 99.999% purity, Westfalen, Germany) for 6 h at 625°C in case of NCM111 and at 525°C in case of NCM811 due to its lower thermal stability (step 3b in Figure 2). Afterwards, the "calcined" samples are transferred into the glove box without exposure to ambient conditions.

Surface area measurements.—The surface area of the "dry" and "calcined" CAMs is determined by Brunauer–Emmett–Teller (BET) N_2 adsorption in the relative pressure range of $0.05 \leq (p/p_0) \leq 0.30$, using an Autosorb-iQ instrument (Quantachrome, Germany). Prior to the measurement, all samples are degassed under dynamic vacuum at 200°C for 12 h. This relatively low degassing temperature is chosen to stay well below the calcination temperature, since the purpose of the BET measurements is to see if any sintering of the particles occurs during calcination. Table I shows the calcination temperature for the different CAMs and the BET surface area before and after calcination, as well as the absolute (in m^2/g) and the relative change upon calcination (in %). For both, the NCM111 and the NCM811 sample, the surface area decreases somewhat upon calcination, i.e., by 23% in the case of NCM111 and by 17% in the case of NCM811. Note that no harm is done to the crystal structure of the materials, as was confirmed by XRD (data not shown).

Thermogravimetric analysis coupled with mass spectrometry (TGA-MS).—To investigate changes of the CAM surface induced by the above described storage conditions, the samples are analyzed by TGA-MS using a Mettler Toledo TGA/DSC 1 (Mettler Toledo, Switzerland) coupled to a Thermostar MS (Pfeiffer Vacuum, Germany). All samples are held at 25°C for 10 min and then heated from 25 to 1125°C at a rate of 10 K/min under Ar at a flow rate of 60 ml/min, and the associated weight loss together with the corresponding mass signals of evolved gases are recorded. It should be noted that the first ten minutes of the mass traces were used to fit a baseline. In addition to the CAM samples, also lithium reference compounds (Li_2O, LiOH, and Li_2CO_3; purity >97% for all compounds, Sigma-Aldrich, Germany) and transition metal carbonate hydrate reference compounds ($MnCO_3 \cdot xH_2O$, $CoCO_3 \cdot xH_2O$, and $NiCO_3 \cdot 2Ni(OH)_2 \cdot xH_2O$; purity >99.9% for all compounds, Sigma-Aldrich, Germany) are investigated using the same protocol. The NCM811 sample is subjected to a second testing protocol, which comprises four steps: First the CAM in "dry" condition is heated from 25 to 525°C at 10 K/min under Ar at a flow rate of 60 ml/min (step 1). After cooling down to 25°C under Ar, the same procedure is repeated without interim removal of the sample from the instrument, i.e., without air exposure, thus mimicking the analysis of a "calcined" sample (step 2). Subsequently, the sample is removed from the instrument, stored for one week at ambient air conditions and then re-measured (step 3). This resembles the analysis of a "wet" sample. Finally, the sample is exposed for only 20 min to ambient air conditions and measured again to evaluate the changes induced by the estimated minimum exposure time during material processing for electrode fabrication outside of a glove box, viz., on the order of 20 min (step 4).

Diffuse reflectance infrared fourier transform spectroscopy (DRIFTS).—Infrared spectroscopy in diffusive reflectance mode (DRIFTS) is sensitive to infrared active species at the surface of particulate materials. DRIFTS spectra are recorded by an IR spectrometer (Cary 670, Agilent, USA) with mirror optics mounted in a Praying Mantis configuration (Harricks, USA) that allows to collect diffuse IR radiation scattered from the particle surface. Mixtures of NCM811 powder in conditions "wet", "dry", and "calcined" (see Figure 2) were prepared at 1 wt% of sample in finely ground KBr (FTIR-grade, Sigma-Aldrich, Germany, dried at 120°C under vacuum overnight prior to use) to characterize carbonate and hydroxide groups on the particle surface. The sample/KBr mixture was prepared in an Ar-filled glove box and the mixture was put in an air-tight chamber

Table I. BET surface area of CAMs in the as-received condition ("dry") and after calcination in a tube furnace under Ar flow at 625°C for NCM111 or 525°C for NCM811, aimed toward removing surface contaminants ("calcined"). Measurements were conducted with 10 g of CAM.

Active material	A_{BET} "dry" [m^2/g]	Heat treatment	A_{BET} "calcined" [m^2/g]	ΔA_{BET} [m^2/g]	ΔA_{BET} [%]
NCM111	0.31	625°C	0.24	−0.06	−23
NCM811	0.30	525°C	0.25	−0.05	−17

with IR-transparent windows (HT reaction chamber, Harricks, UK). The intensity of DRIFTS spectra (sample in KBr) is calculated versus a reference (KBr only) and given in Kubelka-Munk units: Intensity $[KM] = (1 - R_\infty)^2/(2\ R_\infty)$ with $R_\infty = I_{sample}/I_{reference}$. The DRIFTS spectra are compared with spectra obtained by regular Fourier transform infrared (FTIR) spectroscopy in transmission mode. For the latter, pellets are prepared in an Ar-filled glove box at the same KBr to sample weight ratio using a manual KBr pellet press (Pike Technologies, USA). In addition, DRIFTS and transmission spectra are compared to FTIR spectra in attenuated total reflection mode (ATR). The ATR-FTIR spectra are obtained using a diamond ATR crystal and an IR spectrometer (Spectrum Two, Perkin Elmer, USA) inside the glove box (<0.1 ppm H_2O and CO_2).

On-line mass spectrometry (OMS).—To test the reactivity of the CAM samples exposed to the different treatment conditions with ethylene carbonate (EC) containing electrolyte, 1.03 g of CAM are mixed with 240 µl of 1.5 M $LiClO_4$ EC electrolyte (≡ 0.36 g) in our previously developed OEMS (on-line electrochemical mass spectrometry) cell hardware,[31] mimicking a realistic electrolyte to CAM mass ratio of 0.35:1 in commercial battery cells.[36] We use the EC-only electrolyte as a probe for the amount and reactivity of surface contaminants present on the particle surface and thus selected an electrolyte salt that does not react with hydroxide, carbonate, or hydrate surface groups. E.g., it has been shown by Ellis et al. that surface carbonates react with $LiPF_6$ to form CO_2 (equation 9 in Ref. 37). While not a commercially relevant salt, $LiClO_4$ is useful as a substitute for $LiPF_6$ to enable such diagnostic tests without competing reactions of the salt. This was also shown in a previous study of our group, investigating the hydrolysis and associated gas generation of ethylene carbonate.

Before cell assembly, all cell hardware is dried for at least 12 h at 70°C in a vacuum oven (Thermo Scientific, USA). The sealed cell containing the CAM/electrolyte mixture is placed into a programmable temperature-controlled chamber (KB 23, Binder, Germany), and connected to the mass spectrometer via a crimped capillary leak (~1 µl/min gas flow rate into the mass spectrometer).[38] First the cell is held at 10°C for 5 h to record a stable baseline for all ion current signals (m/z = 1 to 128). After that, the temperature is raised to 60°C and the corresponding gas evolution is recorded for 12 h (mimicking storage of a lithium-ion cell at elevated temperature). The cell temperature is recorded with a thermocouple positioned in a 1 cm deep hole drilled into the stainless steel cell body. For translation of the OMS ion current signals I_z into units of [ppm], the temperature is set back to 25°C and the cell is purged with a calibration gas containing H_2, CO, O_2, and CO_2 (the respective concentration of the gases is 2000 ppm in Ar, Westfalen, Germany). With the calibration gas we can quantify the concentrations of H_2 (m/z = 2), CO (m/z = 28), O_2 (m/z = 32), and CO_2 (m/z = 44) in the cell head space (for details on the calibration, see reference 31).

Electrode preparation and cycling.—NCM811 electrodes were prepared by mixing 96 wt% of the cathode active material (HED NCM811, BASF, Germany) with 2 wt% conductive carbon (Super C65, Timcal, Switzerland) and 2 wt% polyvinylidene fluoride binder (PVDF, Kynar HSV 900, Arkema, France) using N-methylpyrrolidone (NMP) as dispersant. The powders were weighed in the glove box (O_2 and H_2O < 0.1 ppm, Glovebox Systemtechnik, Germany). Subsequently, 0.67 g of N-methylpyrrolidone (NMP, Sigma-Aldrich, Germany) per gram of solid (60 wt% solid content) are added in several steps and the mixture is stirred with a planetary orbital mixer (Thinky, Japan) until a highly viscous, lump-free paste is obtained. The above paste is applied on an 18 µm thick aluminum foil (MTI, USA) with a 100 µm four-edge-blade (Erichsen, Germany). The coated foil is dried overnight in a convection oven at 50°C. Disc-shaped cathodes with a diameter of 11 mm are punched out of the foil and compressed at 1 t for 20 s.

The cathodes are then weighed, dried overnight in a vacuum oven at 120°C, and introduced into an Ar glove box without exposure to the ambient. For the "calcined" CAM powder, the entire process of slurry preparation, coating, drying, punching, and compressing is carried out under inert conditions in an Ar-filled glove box, with conductive carbon and PVdF pre-dried at 120°C overnight in a vacuum oven. The areal loading of the NCM811 cathodes after drying is 7.5 mg_{NCM811}/cm^2, corresponding to an areal capacity of 1.5 mAh/cm^2 when using a specific capacity of 200 mAh/g_{NCM811}.

The graphite anodes are prepared with a composition of 95 wt% T311 (SGL Carbon, Germany) and 5 wt% PVdF (Kynar HSV900, Arkema, France) under addition of 0.69 g of NMP per gram of solids (59 wt% solid content) in the same sequential mixing process as for the cathodes. The resultant ink is applied onto a 12 µm thick copper foil (MTI, USA) with a 100 µm four-edge-blade (Erichsen, Germany). The coated foil is dried overnight in a convection oven at 50°C. Disc-shaped electrodes with a diameter of 11 mm are punched out of the foil and compressed at 0.5 t for 20 s. The anodes are then weighed, dried overnight in a vacuum oven at 120°C, and introduced into an Ar glove box without exposure to the ambient. The areal loading of the graphite anodes after drying is 5.3 mg_{T311}/cm^2, corresponding to an areal capacity of 1.8 mAh/cm^2 when using a specific capacity of 340 mAh/g_{T311}. Consequently, the balancing of the NCM811:graphite full-cells is 1:1.2 in units of mAh/cm^2, if referenced to the 1st charge capacity of the cells.

Electrochemical testing is conducted in Swagelok T-cells at 45°C with 60 µl of LP572 electrolyte (1 M $LiPF_6$ in EC:EMC 3:7 (w:w) plus 2 vol% VC, BASF, Germany). Anode (counter electrode) and cathode (working electrode) are separated by two glass fiber separators (glass microfiber filter #691, VWR, Germany) with 11 mm diameter. Lithium metal (Rockwood lithium, USA) was taken as reference electrode by utilizing a 3-electrode setup in the T-cell. The cycling protocol was as follows: the cells were cycled between cell voltages of 3.0–4.2 V, starting with two formation cycles at C/10, and followed by 300 cycles at 1 C. Every charge (1C) was performed in constant current – constant voltage (CC-CV) mode with a C/10 current cutoff at 4.2 V. All discharge cycles were carried out in constant current (CC) mode only. The cells were cycled at 45°C (including the formation cycles) with a battery cycler (Series 4000, Maccor, USA).

Results

Quantification of surface contaminants.—Thermogravimetric analysis with coupled mass spectrometry (TGA-MS) is used to quantify the amount of surface species on the two different cathode active materials used in this study as a function of the storage conditions. Figure 3 shows the TGA-MS analyses for "dry" and "wet" samples of NCM111 (Figures 3a and 3b and NCM811 (Figures 3c and 3d with their weight loss upon heating to 1125°C (upper panels) and the corresponding mass traces of evolved gases (lower panels).

For all samples, three distinct regions can be identified upon heating: (i) In the temperature range from 25 to 125°C (region I), an increase of the H_2O baseline MS signal is observed for all samples. This can be explained by a continuous desorption of minor H_2O traces from cold spots of the MS capillary coupled to the TGA. In addition, the desorption of physisorbed H_2O from the samples has to be considered, however, this effect seems to be small since no measurable weight loss is observed in that temperature range for any of the samples. Physisorbed H_2O may stem from the unavoidable short term exposure of the samples to ambient air during transfer from the glove box to the TGA (<2 min exposure time). (ii) In the temperature range from 125 to 625°C for NCM111 and to 525°C for NCM811 (region II, marked by the yellow area in Figure 3), a mass loss concomitant with a characteristic H_2O and CO_2 fingerprint is observed for all samples. Since the thermal decomposition of NCMs at such low temperatures can be excluded,[3] we associate this weight loss with the thermal decomposition of surface contaminants. In contrast to oven Karl-Fischer titration, which is described in the literature[39] to assess the amount of physisorbed water on cathode active materials, thermogravimetric analysis serves to assess the amount of physisorbed water (below 125°C, i.e., segment (i)) and of chemisorbed water (above 125°C, i.e., segment (ii)) like tightly bound hydrates which co-crystallize with

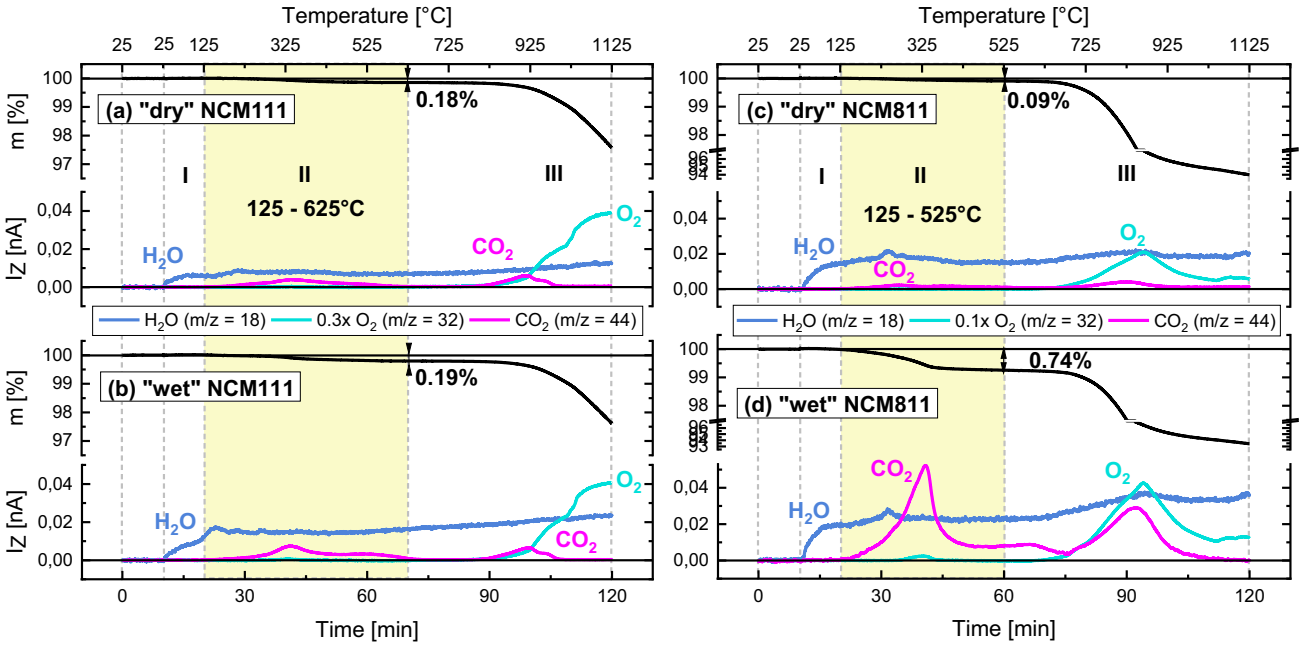

Figure 3. TGA-MS analysis under Ar of NCM111 (a and b) and NCM811 (c and d) stored under "dry" and "wet" conditions. For each sample the characteristic weight loss (upper panel) and the corresponding mass signals (lower panel) are shown for a 10 K/min temperature ramp from 25 to 1125°C. The yellow area marks the temperature range from 125 to 625°C for NCM111 and to 525°C for NCM811, where a mass loss from the thermal decomposition of the surface contaminants with its characteristic H_2O and CO_2 fingerprint is observed.

species such as $LiOH{\cdot}H_2O$. This is an important fact, since the physisorbed water will be removed by standard electrode manufacturing processes, which typically include drying at 125°C, whereas drying at these temperatures would not remove chemically bound water which we analyze in the study at hand. (iii) At temperatures above 625°C, the thermal decomposition of residual Li_2CO_3 (0.1 wt% for NCM111 according to the supplier) leads to the release of CO_2 (compare also Figure 4c) and the thermal decomposition of the NCMs under Ar flow leads to the release of O_2. As both processes overlap, a quantification of Li_2CO_3 via TGA-MS is not possible for these materials. As a side note it shall be mentioned that the thermal decomposition of NCM under Ar flow and the concomitant O_2 release is detected already at 675°C for NCM811 (compared to 825°C for NCM111), consistent with the expected lower thermal stability of Ni-rich layered oxides, clearly shown for partially delithiated NCMs.[3,40]

For NCM111 (Figures 3a and 3b), a weight loss of ~0.2% between 125 and 625°C is found for both "dry" and "wet" samples. The corresponding H_2O and CO_2 traces are more pronounced for the "wet" sample. Given the small BET surface area of ~0.3 m^2/g available for the formation of surface contaminants, the rather small weight loss is not surprising. It has to be noted that subtle differences in mass loss between the "dry" and the "wet" sample (<0.05%) may be masked by slightly varying baseline shifts of the microbalance.

A much stronger impact of the storage conditions on the amount of surface contaminants is seen for NCM811 (Figures 3c and 3d), where the weight loss of ~0.1% between 125 and 525°C for the "dry" sample is increased to ~0.7% through "wet" storage. Regarding the MS signals, this increase is mainly reflected by a higher CO_2 trace, whereas the H_2O signal remains mostly unaffected. Considering the essentially identical BET surface areas of NCM811 and NCM111 (see Table I), it is perhaps not surprising that the extent of surface contamination of the "dry" CAMs is comparable. However, NCM811 is clearly much more sensitive to "wet" storage, suggesting that the high Ni content of NCM811 seems to favor the formation of supposedly carbonate contaminants under moisture and CO_2 containing atmosphere. The exact amounts of surface contaminants can only be calculated from the measured weight losses if the chemical composition of contaminants is known. Therefore, the nature of contaminants is further investigated in the next section by comparing the above observed decomposition temperatures and evolved gases with those of reference compounds.

Comparison of surface contaminants to lithium salt references.—According to the CO_2 and H_2O fingerprint found for the NCM surface contaminants, we suggest that they consist of hydroxides, carbonates, bicarbonate species, and/or their hydrates. These species could be bound either to lithium, or to at least one of the transition metals (Ni, Mn, and/or Co).) Residual lithium from the cathode material synthesis is generally believed to be present in the form of Li_2O on the CAM particle surface after calcination,[17] since this is the thermodynamically stable high-temperature phase even under argon.[9] Several research groups reported on the reaction of Li_2O with moisture and CO_2 to yield LiOH and Li_2CO_3 on the particle surface:[17–19,23]

$$Li_2O + H_2O \rightarrow 2LiOH \quad [1]$$

$$2LiOH + CO_2 \rightarrow Li_2CO_3 + H_2O \quad [2]$$

Both reactions are equilibria, which are clearly driven to the right side as can be estimated from thermodynamic calculations. By using the standard free energy of formation values from the CRC handbook,[41] one obtains $\Delta_f G^{\ominus} \sim -84{,}7$ kJ/mol for the LiOH formation according to Equation 1 and $\Delta_f G^{\ominus} \sim -91{,}8$ kJ/mol for the Li_2CO_3 formation according to Equation 2.

In order to reveal whether the observed surface contamination can be assigned soley to lithium compounds, the TGA-MS analyses of Li_2O, LiOH, Li_2CO_3 as well as of Li_2O stored under "wet" conditions are shown in Figure 4.

As originally demonstrated in our previous work,[9] Figure 4a confirms that Li_2O does not thermally decompose in the examined temperature range of 25–1125°C, except for a minor release of H_2O at ~400°C. This coincides with onset of H_2O release upon the thermal decomposition of LiOH above ~400°C (see Figure 4b), suggesting the presence of LiOH impurities in the Li_2O reference sample. Figure 4c shows that Li_2CO_3 decomposes at temperatures higher than 725°C under the release of CO_2. Thus, Li_2O, LiOH, nor Li_2CO_3 can account

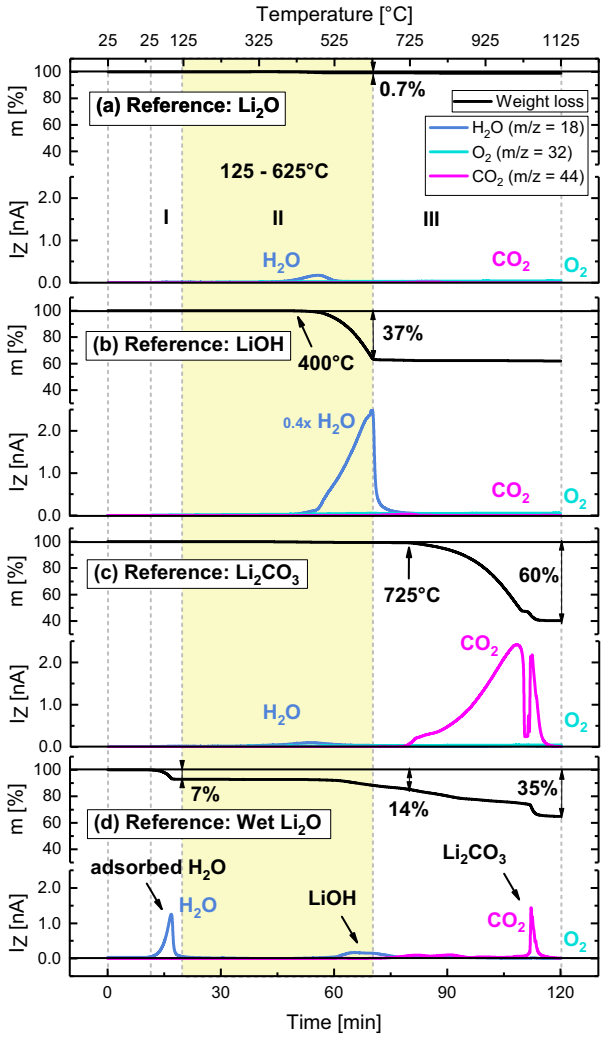

Figure 4. TGA-MS analysis of various lithium containing reference compounds: (a) Li_2O, (b) LiOH, (c) Li_2CO_3, and, (d) Li_2O stored for 1 week under "wet" conditions. For each compound the characteristic mass loss (upper panel) and corresponding mass signals (lower panel) are shown for a 10 K/min temperature ramp from 25 to 1125°C under Ar flow. Regions I, II (marked by the yellow area), and III correspond to those shown in Figure 3.

for the mass signal patterns observed between 125 and 625°C for the "dry" and "wet" CAM samples, particularly not for the observed CO_2 evolution (compare Figure 3). However, Figure 4c does confirm that the CO_2 release above 625°C that is seen for all NCM samples can indeed be assigned to Li_2CO_3 residues. Unfortunately, this process cannot be quantified from the related mass loss, as it overlaps with the mass loss due to oxygen release from the NCMs (the MS signals from the TGA-MS are only semi-quantitative). It is interesting to note that for NCM811, the Li_2CO_3-related CO_2 release concomitant with the O_2 release at high temperature is substantially increased after "wet" storage, which is not observed for NCM111. This indicates that either more residual Li_2O from the synthesis process is present on NCM811 than on NCM111, and/or that intercalated Li in the near-surface region of NCM811 is more prone to deintercalation and reaction with H_2O and CO_2. The possibility of Li_2CO_3 formation from residual Li_2O on the surface is further strengthened by a reference TGA-MS measurement with Li_2O that was stored for one week under "wet" conditions (Figure 4d): During storage, physisorbed H_2O (evidenced by H_2O evolution below 125°C) partly reacts with Li_2O to form LiOH (identified by the H_2O trace between 500 and 650°C) via Reaction 1. In addition, atmospheric CO_2 can react with Li_2O and/or previously formed LiOH (Reaction 2) to yield Li_2CO_3, the presence of which is evidenced by the CO_2 signal between 650 and 1100°C. It is important to note, however, that there is no reaction of Li_2O in ambient air that leads to compounds which exhibit a mass loss and MS signal patterns which match those observed during the thermal decomposition of NCM surface contaminants in the temperature range of 125–625°C (see Figure 3).

Therefore, it has to be concluded that lithium salts like LiOH or Li_2CO_3 cannot be the only surface contaminants on NCMs exposed to the ambient. It is important to point out that we do not negate the presence of LiOH and Li_2CO_3 on the surface of these NCM samples, and as a matter of fact Li_2CO_3 impurities are clearly detected in the TGA-MS measurements, as discussed above. However, there must be an additional type of surface contaminants originating from storage under H_2O and CO_2 containing atmosphere (e.g., ambient air) that gives rise to surface species that decompose under release of H_2O and CO_2 at temperatures as low as 125–625°C.

Comparison of surface contaminants to transition metal references.—Since Li salts cannot be the origin of surface contaminants that yield the observed CO_2 mass signals at 125–625°C, we will now consider other surface contaminants which might form upon the reaction of CO_2 and H_2O with NCM surfaces. In principle, dangling oxygen bonds at the Ni, Mn, and Co oxide surface could react to hydroxides and carbonates upon exposure of NCM with H_2O and CO_2:

$$MO + H_2O \rightarrow M(OH)_2 \quad [3]$$

$$MO + CO_2 \rightarrow MCO_3 \quad [4]$$

To evaluate this hypothesis, we investigate the TGA-MS signatures of the stable hydrates of the carbonates of Mn, Co, and the stable hydrate of the mixed carbonate hydroxide of Ni. The results are shown in Figure 5.

Figure 5a shows the thermal decomposition of the first reference compound $MnCO_3 \cdot xH_2O$, yielding H_2O and CO_2 once the temperature is increased to beyond ~320°C. While the simultaneous release of H_2O and CO_2 is also found as the characteristic fingerprint of the NCM surface contaminants (compare Figure 3), the decomposition onset temperature and the onset for CO_2 evolution (~320°C) of the $MnCO_3 \cdot xH_2O$ is significantly higher than that between ~125–200°C observed for the surface contaminants of the NCM materials, particularly of the "wet" stored materials. Consequently, hydrated manganese carbonates could be part of the contaminants, but not their only or principal component. The TGA-MS signature of the $CoCO_3 \cdot xH_2O$ reference compound (see Figure 5b) is similar to that of $MnCO_3 \cdot xH_2O$, but has a lower onset temperature (~220°C) for its decomposition and for CO_2 evolution. While the Co compound could also be part of the NCM surface contaminants, its decomposition onset temperature is still too high to explain the onset of the weight loss and CO_2 evolution for the "dry" and particularly the "wet" NCM materials at ~125–200°C. Finally, the thermal decomposition of $NiCO_3 \cdot 2Ni(OH)_2 \cdot xH_2O$ reference compound is depicted in Figure 5c. It features a weight loss onset at ~120°C, accompanied by the release of H_2O with two distinct peaks around ~125 and ~300°C as well as the onset of CO_2 evolution at ~250°C. This very much resembles the fingerprint observed for the "dry" and particularly the "wet" NCMs in Figure 3, which suggests that the nickel reference compound (or related nickel compounds, e.g., $(NiCO_3)_2 \cdot (Ni(OH)_2)_3 \cdot 4\,H_2O$)[12] is likely to represent a principal component of the NCM surface contaminants. This conclusion was also reached in a Raman spectroscopy study of surface contaminants on NCM811 stored for extended time at ambient air, which showed that simple transition metal carbonates and hydroxides were not part of the formed surface contaminants.[12] It should be noted that nickel carbonate naturally occurs in its hydrated form[42] or as a hydroxide,[43] with the exception of Gaspéite,[44] a very rare nickel carbonate mineral. The here examined nickel compound, referred to as basic nickel

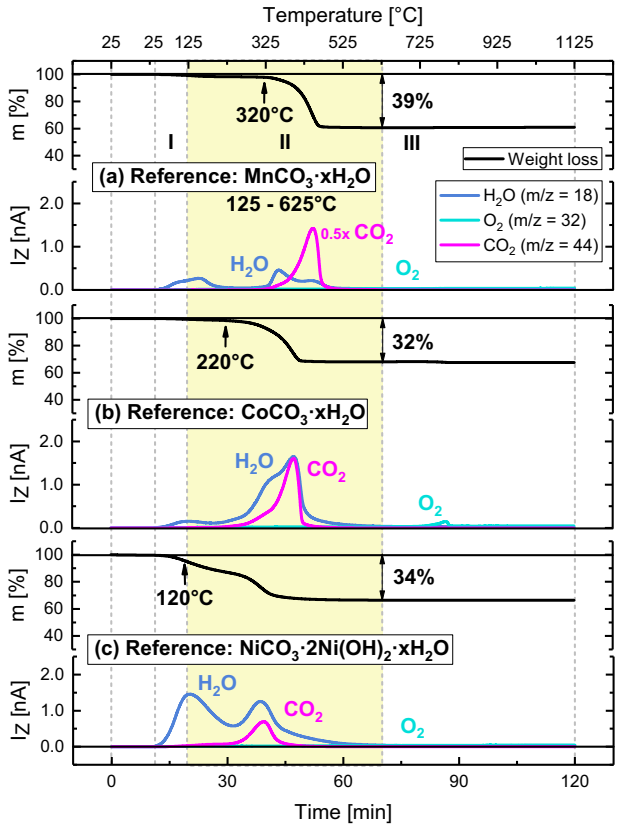

Figure 5. TGA-MS analysis of several transition metal based reference compounds: (a) $MnCO_3 \cdot xH_2O$; (b) $CoCO_3 \cdot xH_2O$; and, (c) $NiCO_3 \cdot 2Ni(OH)_2 \cdot xH_2O$ (c). For each compound the characteristic mass loss (upper panel) and corresponding mass signals (lower panel) are shown for a 10 K/min temperature ramp from 25 to 1125°C under Ar flow. Regions I, II (marked by the yellow area), and III correspond to those shown in Figure 3.

carbonate, was the only commercially available form of nickel carbonate we could find.

All in all, the thermal analysis of the transition metal carbonate (-hydroxide) hydrates suggests that the basic nickel carbonate $NiCO_3 \cdot 2Ni(OH)_2 \cdot xH_2O$ is the major surface contaminant of NCMs stored under moisture and CO_2 containing atmosphere. The reader should note that based on our TGA-MS analysis we cannot exclude the presence of other transition metal carbonates like $MnCO_3$, $CoCO_3$, and their hydrates, since the temperature ranges of thermal decomposition of these compounds overlap. However, the fact that the major weight loss already starts at ~125°C together with the observation that Ni-rich NCMs are more prone to surface contamination (see Figure 3), clearly points in the direction of $NiCO_3 \cdot 2Ni(OH)_2 \cdot xH_2O$ or related compounds. It should further be noted that on average Ni is in the oxidation state +II in pristine NCM111 and NCM811, while Co and Mn are on average in oxidation states of +III and +IV, respectively. Since the formation of transition metal carbonates and hydroxides requires the respective transition metal to be present in the oxidation state +II, it is likely that basic nickel carbonate $NiCO_3 \cdot 2Ni(OH)_2 \cdot xH_2O$ is indeed formed preferentially.

It shall be mentioned that Ni-rich materials are known to be very basic, leading to a high pH of electrode slurries (pH > 11),[17] leading to difficulties for electrode fabrication due to the gelation of the polyvinylidene fluoride (PVdF) binder in coating slurries.[3,17] In light of the above findings, these issues can be linked to the high sensitivity of Ni-rich materials toward improper storage conditions. On a final note, the TGA-MS results suggest that a thermal treatment of surface contaminated NCM under inert gas conditions at 625°C (for NCM111) or 525°C (for NCM811) should allow for the removal of all transition metal based surface contaminants as well as of LiOH contaminants (contrary to Li_2CO_3 and Li_2O surface impurities, which will remain intact at these temperatures) without degrading the NCM bulk structure or morphology (see BET results). Thus, the above-mentioned difficulties for electrode fabrication could be circumvented even for improperly stored Ni-rich NCMs by performing a heat-treatment under inert gas atmosphere prior to ink fabrication.

DRIFTS analysis of surface contaminants.—Figure 6 shows a comparison of infrared spectra of "dry" (blue line), "wet" (green line), and "calcined" (navy line) NCM811 powder taken by ATR-FTIR (a), by transmission FTIR (b), and by DRIFTS (c). This analysis was exemplarily performed for NCM811, since it is most prone to surface contamination and therefore offers the highest intensity for IR active surface species. While ATR-FTIR and transmission FTIR spectra (see Figures 6a and 6b) show a very poor sensitivity for the detection of the definitely present Li_2CO_3 with the characteristic CO_3^{2-} asymmetric stretching vibrations centered around 1470 cm^{-1} (marked by the accordingly labeled vertical dashed line in Figure 6) and out-of-plane vibrations at 850 cm^{-1},[45–47] the DRIFTS signals (see Figures 6c and 6d) which are more intense for powder samples show clearly resolved carbonate bands at 1470 cm^{-1} and a broad shoulder corresponding to hydroxide or hydrate species (OH^-/H_2O) around 3450 cm^{-1}[46] (see Figure 6c). In addition, residual sulfate traces from CAM manufacturing give rise to SO_4^{2-} stretching vibrations at 1130 cm^{-1}.[48] The peaks at 2900 cm^{-1} are artefacts from the sample preparation using polyethylene[49] weighing boats. A comparison of the DRIFTS data for the differently treated NCM811 samples (see Figures 6c and 6d), namely of the upward pointing CO_3^{2-} bands at 1470 cm^{-1} and the OH^-/H_2O bands at 3450 cm^{-1}, much more clearly reveals the impact of moisture and CO_2 on the formation of surface contaminants (note that it is currently unclear why the OH^-/H_2O band points downward rather than upward). Both, the hydroxide/hydrate and especially the carbonate content increase upon "wet" storage (green line) and decrease again by the subsequent calcination of the "wet" material at 525°C (navy line). Note that it is not surprising that the "calcined" NCM811 sample still shows a carbonate band, because in contrast to transition metal carbonates, Li_2CO_3 cannot be removed by the 525°C heat-treatment (see TGA analysis in Figures 3 and 4). While DRIFTS does not allow us to discriminate between different metal centers of the surface hydroxides and carbonates, the CO_3^{2-} and OH^-/H_2O vibrations are in agreement with the main contaminant revealed by TGA-MS, viz., basic nickel carbonate $NiCO_3 \cdot 2Ni(OH)_2 \cdot xH_2O$.

Effect of surface contaminants on electrolyte stability.—Having identified the nature and the amount of surface contaminants on NCM materials, we now want to investigate their impact on the stability of an ethylene carbonate (EC) based electrolyte at elevated temperature. The following experiment is based on our previous study,[30] where we demonstrated that catalytically active hydroxide ions (OH^-) in the presence of trace amounts of H_2O can lead to a rapid decomposition of ethylene carbonate (EC) at temperatures relevant for lithium-ion battery operation. The decomposition of EC is induced by a nucleophilic attack of OH^- and a subsequent ring opening reaction of EC under abstraction of CO_2. Concluding this past study, we had already speculated that a similar reaction can be triggered by basic surface contaminants (even though we had not yet had evidence for $NiCO_3 \cdot 2Ni(OH)_2 \cdot xH_2O$ surface species). This reaction would not only lead to the decomposition of EC-based electrolyte and accumulation of CO_2 gas in the battery cell, but likely also to a deterioration of battery performance from further reactions of the decomposition products (see Discussion Section for a detailed explanation of the electrolyte breakdown).

In order to test this hypothesis, 1.03 g of "wet", "dry", and "calcined" NCM811 are mixed with 240 µl of 1.5 M $LiClO_4$ in EC, resulting in a realistic electrolyte to CAM ratio of 0.35:1,[36] and the gas evolution from this mix is recorded by on-line mass spectrometry (OMS) during a 12 h dwell at a constant temperature of 60°C. The

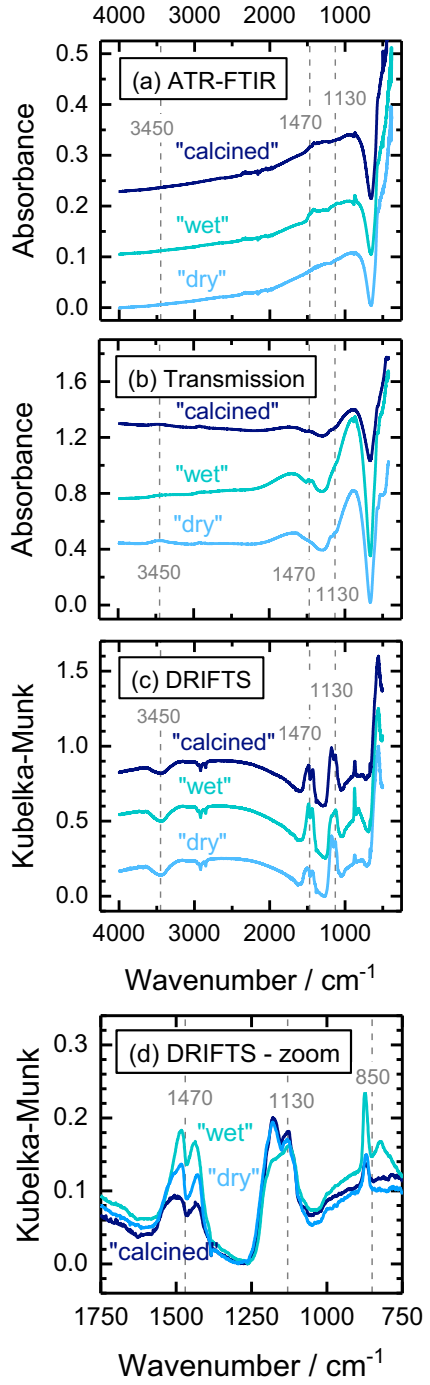

Figure 6. Infrared spectroscopic analyses of "dry" (blue lines), "wet" (green lines), and "calcined" (at 525°C under Argon, navy line) NCM811 by: (a) ATR-FTIR (undiluted NCM811) – arbitrary offset; (b) transmission FTIR (1 wt% NCM811 in KBr powder) – arbitrary offset; and, (c) DRIFTS (1 wt% NCM811 in KBr powder) – these spectra which are displayed in Kubelka-Munk units have been normalized to range between 0 and 1. The bands marked at 1130 cm^{-1} correspond to SO_4^{2-}, those at 850 and 1470 cm^{-1} correspond to CO_3^{2-}, and those at 3450 cm^{-1} correspond to OH^-/H_2O. (d) Enlarged view of the data in panel (c) without any arbitrary offset.

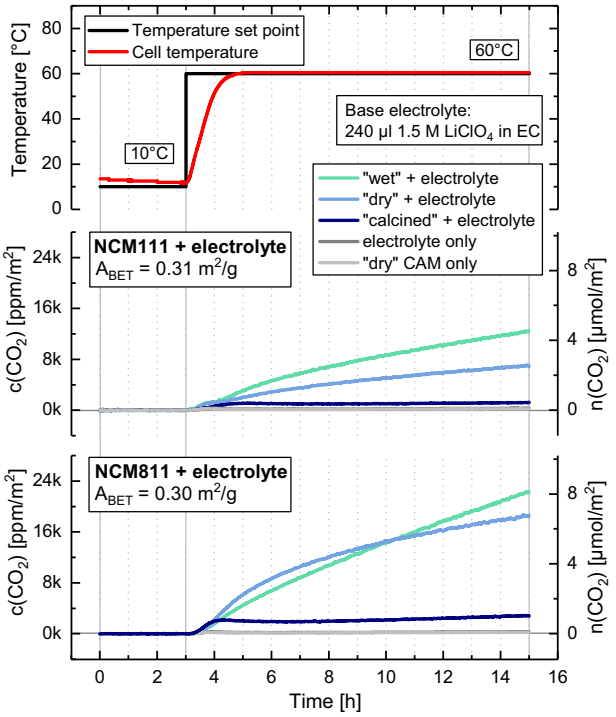

Figure 7. On-line mass spectroscopic analysis of the gas formation vs. time upon 60°C heating of mixtures of 1.5 M $LiClO_4$ in EC (240 µl, <20 ppm H_2O) with differently treated NCMs (1.03 g): "wet" (green line), "dry" (blue line) and "calcined" (navy line); background signals for pure electrolyte (dark gray) and "dry" CAM (light gray) are given for reference. The upper panel shows the temperature set point (black line) and the measured cell temperature (red line). The middle and lower panel show the corresponding evolution of the CO_2 for NCM111 and NCM811, respectively, given either in terms of the CO_2 concentration in the cell head space normalized to the BET surface area (see Table I) in [ppm/m^2] (left y-axis) or in terms of total evolved amount in [µmol/m^2] (right y-axis).

upper panel of Figure 7 depicts the temperature set point (black line) and the cell temperature (red line) vs. time for these OMS measurements.

The middle panel of Figure 7 shows the CO_2 evolution for the applied temperature profile for NCM111 mixed with the EC-containing electrolyte, given in surface area normalized units of [ppm/m^2] (left y-axis) and [µmol/m^2] (right y-axis, see Table I for BET surface areas). As in our previous study,[30] CO_2 is the only gas detected by OEMS, suggesting that indeed the hydrolysis of EC is the origin of the gassing. More electrophilic additives such as FEC or VC would probably react much faster with the nucleophilic OH groups on the CAM surface and thus decompose at much faster rate. The strongest CO_2 evolution is detected for the "wet" NCM111 sample (green line), yielding ~4 µmol/m^2 at the end of the experiment. About half of this amount of CO_2 (~2 µmol/m^2) is detected for the "dry" NCM111 sample (blue line). Interestingly, the "calcined" material (navy line) shows almost no gas evolution at all, apart from an initial increase to ~0.3 µmol/m^2 after which no further CO_2 evolution is observed. This comparison indicates a clear correlation between the extent of surface contamination and the extent of gassing caused by chemical electrolyte decomposition at elevated temperature.

For the Ni-rich NCM811, the gassing for the material in "wet" and "dry" condition (green and blue line in the middle panel of Figure 7) is twice as high as for NCM111 even in "wet" condition. The reason for the rather similar CO_2 evolution from "dry" and "wet" NCM811 is unclear at this point, but given the difference in CO_2 formation rate (slope of the green and blue line in lower panel of Figure 7), the 15 h measurement time was just not sufficient to reflect to high sensitivity of NCM811 to ambient air exposure during material packaging/handling (see Discussion Section for a quantitative assessment of this fact). Again, upon heat-treatment, surface contaminants are removed and the reactivity with the EC-based electrolyte is reduced by an order of magnitude (navy line). The substantial increase in the extent of CO_2 evolution with the Ni content of the NCM is a further strong indication that basic nickel carbonate $NiCO_3 \cdot 2Ni(OH)_2 \cdot xH_2O$ is the critical surface contaminant on NCMs, as suggested by the

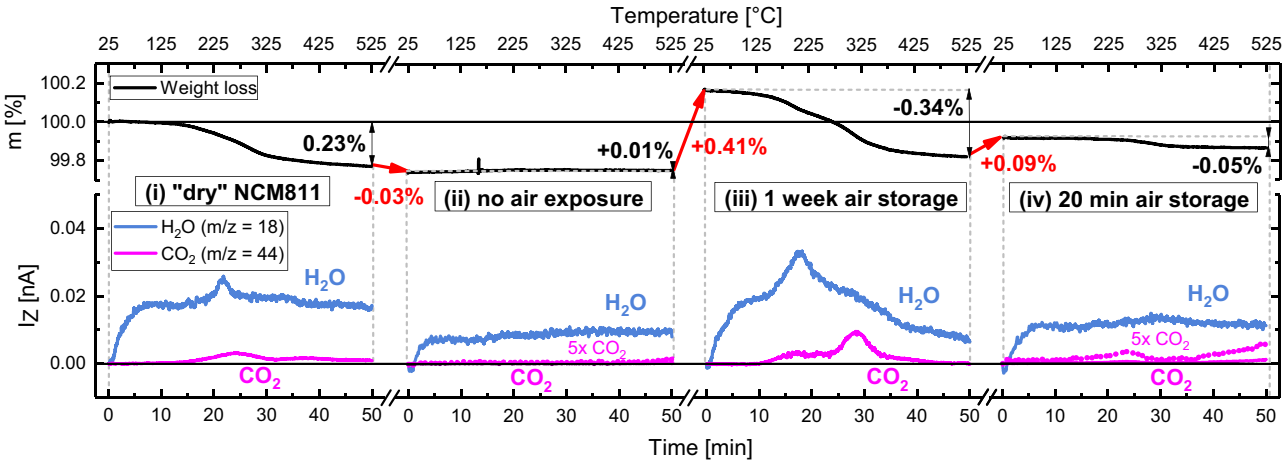

Figure 8. Four step TGA-MS measurement of one NCM811 sample showing the characteristic mass losses (upper panel) and corresponding mass signals (lower panel) during four consecutive temperature ramps from 25 to 525°C at a heating rate of 10 K/min in Ar flow. From left to right panel: (i) The sample in "dry" condition is heated to 525°C, followed by cooling to 25°C under Ar inside the closed instrument. (ii) It is then immediately heated again without interim air exposure, thus mimicking a "calcined" sample. (iii) After cooldown, the sample is removed from the instrument and stored for one week at ambient air and then heated again, thus representing a rough analogue to a sample in "wet" condition. (iv) After cooldown to 25°C, the sample is stored for only 20 min at ambient air and heated again, representing a CAM exposed to ambient air for the duration typical for battery material processing in most laboratories; a 5-fold magnification of the CO_2 signal (pink dotted line) shows CO_2 evolution between 200–300°C, contrary to the sample without air exposure in panel (ii).

TGA-MS patterns (compare Figure 3d and Figure 5c). Consequently, due care has to be taken for the storage and handling of Ni-rich cathode materials, e.g., Ni-rich NCMs and NCAs, which are considered to be among the most promising candidates for future battery electric vehicle applications.[1,4,5]

In summary, the findings in Figure 7 prove that a heat-treatment of NCMs exposed to atmospheric moisture and CO_2 can effectively remove the transition metal based surface contaminants and thereby prevent their strong effect on the decomposition of EC-based electrolyte. This finding is in excellent agreement with the TGA-MS analysis presented above, which already suggested that a heat-treatment at 625°C for NCM111 and at 525°C for NCM811 should be sufficient to remove all surface contaminants except for Li_2CO_3 and Li_2O (see Figure 4). Note that the first CO_2 release for the NCM samples in Figure 3 ceases at 625°C, indicating that all transition metal reference compounds are transformed into their stable oxide phases at that temperature (see Figure 5). Interestingly, the OMS data for NCM111 (middle panel in Figure 7) and even more though for NCM811 (lower panel in Figure 7) suggest that the "dry" NCMs already contain significant amounts of surface contaminants that can lead to considerable CO_2 evolution by EC decomposition. Again, this is in agreement with our TGA-MS analysis, since the "dry" NCMs already show noticeable weight losses (see Figures 3a and 3c) and the applied drying step at 120°C is clearly not sufficient to remove these surface contaminants. The latter is especially significant with regard to the fabrication of electrodes, which can usually not be dried at temperatures higher than 120°C due to the limited thermal stability of the PVdF binder. In consequence, nominally "dry" NCMs still contain surface contaminants that might lead to EC decomposition, CO_2 gassing, and inferior cell performance at elevated temperature.

Lastly, we would like to point out that residual Li_2O and Li_2CO_3 can definitely be excluded as the type of surface contaminants that lead to CO_2 evolution by a reaction with EC-containing electrolyte, since neither Li_2O nor Li_2CO_3 are removed by a heat-treatment at 625°C (compare Figures 4a and 4c),[9] and yet the heat treated samples show only a minimal CO_2 evolution (see Figure 7). As a matter of fact, the reactivity of Li_2CO_3 contaminants on the cathode and its implications for cell performance are currently being debated controversely in the literature: while Renfrew et al.[11] suggest that Li_2CO_3 will be electrooxidized in the first cycles, Jung et al.[12] suggest that the decomposition of Li_2CO_3 is soley due to its reaction with protic species ($Li_2CO_3 + 2\,H^+ \rightarrow 2\,Li^+ + H_2O + CO_2$) which are produced upon electrolyte oxidation at high potentials[50] and/or by side reactions related to the oxygen release from NCMs at high SOC.[51] If the latter hypothesis were true, Li_2CO_3 impurities alone should only contribute to CO_2 gassing, which would have a minor effect on battery cycle life if the Li_2CO_3 levels are sufficiently low (particularly in Swagelok T-cell or coin cell tests, where gassing induced cell bulging is less problematic). For completeness, it shall not be omitted that the base electrolyte alone (1.5 M $LiClO_4$ in EC, <20 ppm H_2O) shows a negligible amount of CO_2 evolution (dark gray line) coming from the thermal decomposition of EC at 60°C.[30]

Contaminant removal and critical exposure time.—A final TGA-MS experiment shall elucidate how different exposure times to ambient air influence the formation of surface contaminants on NCMs. Figure 8 shows a four-step TGA-MS measurement in which a single sample is subjected to four consecutive temperature ramps from 25 to 525°C. A NCM811 sample is chosen for this procedure because of its relatively high weight loss in the temperature range associated with surface contaminants compared to NCM111, which allows the more precise signal quantification.

Starting with "dry" NCM811 (panel (i) of Figure 7), the CO_2 and H_2O mass traces in the temperature window from 25 to 525°C shown Figure 3c are reproduced, however with a concomitant weight loss of 0.23% instead of 0.09%, which can be rationalized by different transfer times of the TGA sample on air. It has to be noted that according to our foregoing analysis of samples calcined at 525°C, the structural integrity of NCM811 is fully preserved during this procedure. During the subsequent cooldown to room temperature, the sample is kept within the closed TGA-MS instrument and not exposed to ambient air. It is then directly heated again to 525°C, mimicking a material that has been calcined and stored under Ar. As seen in panel (ii) of Figure 7, a negligible weight increase of 0.01% (red arrow) is monitored during cooldown between the two experiments, and this amount is lost again during the 2nd ramp at temperatures below 125°C under release of H_2O. In addition, in the corresponding mass spectrum there is virtually zero CO_2 desorption detected (dotted line in panel (ii) displays m/z = 4 4 multiplied by five). This is attributed to marginal air leakage into the closed TGA-MS, leading to the physisorption of minor amounts of H_2O on the NCM811 surface during cooldown. This again confirms that all surface contaminants are successfully removed during a heat-treatment in Ar at 525°C, which was conducted in the first step.

After the cooldown following this second temperature ramp, the sample is stored for one week at ambient air (relative humidity 35 ± 5%), which results in a weight gain of 0.41% (red arrow between

panels (ii) and (iii)) due to the renewed buildup of surface contamination on the NCM811 particles. In the subsequent third temperature ramp (panel (iii)), about the same amount is removed again, and the CO_2 and H_2O mass signal fingerprints resemble those of the "wet" NCM811 (see Figure 3d). This indicates that one week of open storage under ambient air conditions is as detrimental to the NCM811 material as our "wet" storage conditions (see Figure 2), which we had chosen deliberately to mimick extended air exposure. However, even after such a prolonged storage at ambient air, the complete removal of surface contaminants by heating up to 525°C under inert gas is feasible. In the final experiment, the "calcined" NCM811 sample obtained after the experiment shown in panel (iii) is exposed to ambient air for 20 min, which is sufficient to cause a weight-gain of 0.09% (red arrow between panels (iii) and (iv)). A subsequent fourth temperature ramp to 525°C shows a corresponding mass loss and also a weak CO_2 desorption signal (dotted red line in panel (iv)) which indicates the presence of transition metal based surface contaminants. This demonstrates that a time period that can be regarded as the minimum exposure of a CAM during electrode fabrication in most laboratories is already sufficient to build up noticeable amounts of surface contaminants on the pristine (i.e., "calcined") CAM surface. In that case, the contamination level is roughly comparable to that of the as-received ("dry") material.

Cycle life of NCM811//Graphite cells with differently conditioned NCM811.—After identifying and quantifying the surface contaminants on differently conditioned NCMs, and after demonstrating that a heat-treatment under inert gas can remove transition metal based surface contaminants, we now want to examine the impact of these contaminants on battery cell performance. For that purpose, NCM811//graphite Swagelok T-cells with 60 µl of electrolyte (LP572, BASF) are cycled with 1C between 3.0-4.2 V at an elevated temperature of 45°C, where degradation phenomena are typically more pronounced due to faster kinetics of the parasitic reactions. Figure 9a shows that the capacity retention over 250 cycles at 1C is very poor for cells with "wet" NCM811 (55%; green symbols), far inferior to those with "dry" NCM811 (85%; blue symbols). Cells with "calcined" NCM811 (navy symbols) always show the highest capacity and have the best capacity retention (92%), indicating that (i) transition metal based surface contaminants do have a detrimental effect on capacity retention, and (ii) that this effect increases with the amount of surface contaminants. After 250 cycles, there is a difference in specific discharge capacity of 16 mAh/g_{NCM811} between cells with "calcined" (176 mAh/g_{NCM811}) and "dry" NCM811 (160 mAh/g_{NCM811}), and another 66 mAh/g_{NCM811} between cells with "dry" and "wet" NCM811 (94 mAh/g_{NCM811}).

In order to gain a better understanding of the capacity fading in cells with "wet" NCM811, it is instructive to analyze the charge-averaged mean discharge voltage (see Figure 9b), a measure for the impedance buildup in lithium-ion cells. It can be obtained for every cycle by integrating the cell voltage over the discharge capacity and dividing the integral by the total discharge capacity ($\bar{V}_{discharge} = \int V_{discharge} \cdot dq_{discharge}/q_{discharge}$).[52] A low mean discharge cell voltage, especially at high rates, is indicative of a high impedance for Li^+-ion extraction from the anode material and/or Li^+-ion insertion into the cathode material. Figure 9b clearly shows that the mean discharge cell voltage after 250 cycles of cells with "wet" NCM811 is ~190 mV lower than that of cells with "dry" NCM811, which in turn is ~70 mV lower than that for cells with "calcined" NCM811 (i.e., with "wet" NCM811 after heat-treatment under inert gas at 525°C). This demonstrates that the cell impedance growth gets much more pronounced with increasing amounts of cathode surface contaminants. Thus, it can be summarized that the deliberate contamination of NCMs by "wet" storage causes a large impedance growth over cycling that leads to higher capacity fading, but that this effect can be mitigated by a subsequent heat-treatment under inert gas at 525°C. A similar effect of heat-treatment was observed for cells with NCA ($LiNi_{0.8}Co_{0.15}Al_{0.05}O_2$) stored at ambient air, showing that those cells have a large capacity fading which can be substantially reduced when annealing the ambient air exposed NCA under air at 500°C.[24]

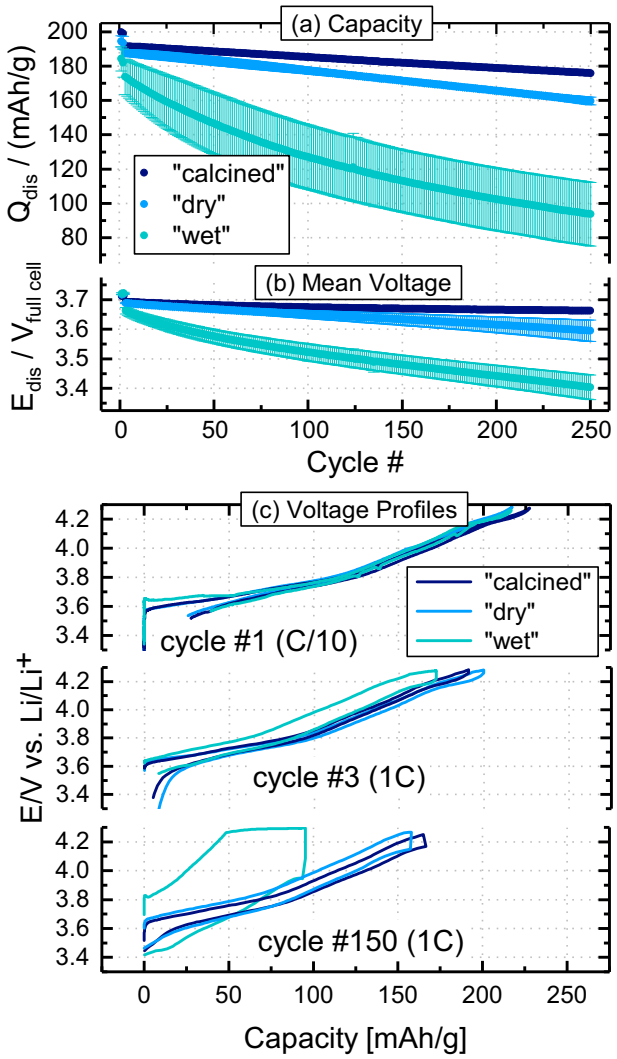

Figure 9. Charge/discharge cycling of NCM811//graphite Swagelok T-cells prepared with "dry" (blue), "wet" (green), and "calcined" (navy) NCM811, conducted between 3.0–4.2 V with 60 µl LP572 electrolyte at 45°C: (a) specific discharge capacity (left y-axis, solid spheres); (b) mean discharge cell voltage in each cycle (defined as $\bar{V}_{discharge} = \int V_{discharge} \cdot dq_{discharge} / q_{discharge}$); and, (c) the cathode voltage profiles vs. the lithium reference electrode for the first cycle at C/10 and the 3rd as well as the 150th cycle at 1C. The first two cycles were conducted at C/10, followed by cycling at 1C (CC-CV charge and CC discharge); error bars represent standard deviation of two cells.

The high overpotentials associated with an increase of internal resistance over cycling can cause the cells to reach their voltage cutoff while a considerable fraction of the cyclable lithium is still contained in the anode or cathode material. In order to elucidate whether the charge or the discharge process is more affected by increased impedance of the differently pre-trated CAMs rather than by a loss of cyclable lithium, Figure 9c displays the cathode voltage profiles versus the lithium reference for cycle #1 at C/10, for cycle #33 (1C), and for cycle #150 (1C). Figure 9c suggests that the storage condition has no influence on the cell polarization during the initial charge and discharge cycles of the different NCM811 samples, as the voltage profiles of the cells containing "wet" (green), "dry" (blue), and "calcined" material (navy) show only subtle differences for cycle #1 at 0.1C and only small differences for cycle #3 at 1C. In cycle #1, polarization of the "wet" cells is evident from the slightly increased polarization around 3.6 V. The "wet" storage, i.e., exposure to water vapor, might lead to the formation of a resistive surface layer similar as in case of washing with water,[53,54] which would lead to a reduced Li^+ conductivity

of the surface-near regions in the oxide particle. The slow C-rate, however, masks most of the polarization effects due to surface contaminants. Over prolonged cycling, the charge and discharge voltage profiles gradually drift apart, as can be seen exemplarily in Figure 9c for cycle #150, indicating increased overpotentials, as expected from the above analysis of the mean discharge cell voltage (compare Figure 9b). This is consistent with the fact that the overpotentials are much more pronounced for the cells containing "wet" NCM811 (see green lines in Figure 9c vs. blue and navy lines). Interestingly, the increased cell polarization is drastically limiting the capacity especially during charge, as the cell voltage is pushed toward the upper cutoff voltage. This polarization induced failure of the cells is different from failure mechanisms that are accompanied by low coulombic efficiency, e.g., the loss of cyclable lithium.[55,56] A mechanistic explanation for the large polarization of cells containing "wet" NCM811 is attempted at the end of the Discussion Section.

Discussion

In the study at hand, we have combined a variety of characterization techniques such as TGA-MS, OMS, DRIFTS, and electrochemical cycling to understand the nature and the origin of surface contaminants on NCM811 compared to NCM111. To further connect the findings from the individual techniques as well as to underline the relevance of surface contamination in industrial cell manufacturing, the following section presents (i) an estimation of the amount of surface contaminants based on the TGA-MS analysis, (ii) kinetic considerations regarding electrolyte breakdown by EC hydrolysis based on the gassing detected by OMS, (iii) a projection of the findings of TGA-MS and OMS on commercial battery cells, and (iv) concluding remarks of the impact of storage conditions on the cycling behavior of full cells.

Estimation of the amount of surface contaminants.—We have shown that Ni-rich materials are especially susceptible to surface contamination due to storage and handling in ambient air and that basic nickel carbonate $NiCO_3{\cdot}2Ni(OH)_2{\cdot}xH_2O$ (or varying compositions thereof)[30] rather than LiOH or Li_2CO_3 accounts for the high reactivity of contaminated samples with an EC-based electrolyte demonstrated by the OMS data in Figure 7. In the following, we want to estimate the amount of surface contaminants for "wet" NCM811 based on the 8.2 $\mu mol/m^2$ of evolved CO_2 (see lower panel of Figure 7), equating to a total amount of ~2.5 μmol of CO_2 based on the NCM811 BET area and the amount of NCM in the cell (i.e., from 8.2 $\mu mol/m^2 \times 0.30\ m^2/g_{NCM} \times 1.03\ g_{NCM}$) or to ~2.4 $\mu mol/g_{NCM}$. Comparing this to the total moles of EC in the electrolyte of 3680 μmol obtained from the electrolyte's density, the used volume, the EC mass fraction and its molecular weight (i.e., from 1.5 $g/cm^3 \times 240\ \mu l \times 0.9 \times (88\ g/mol)^{-1}$),) one can conclude that only ~0.07% of the EC that is present in the OMS cell is converted to CO_2 during the entire OMS experiment. Consequently, the reaction is not limited by the amount of EC available for reaction with the CAM surface.

Next we will examine whether the amount of the proposed critical surface contaminant on "wet" NCM811, viz., the basic nickel carbonate $NiCO_3{\cdot}2Ni(OH)_2{\cdot}xH_2O$ which decomposes between 120–525°C (see Figure 5c) would be sufficient to produce the observed amount of CO_2 in the OMS experiment (lower panel of Figure 7). However, to do so one first needs to determine the decomposition reaction and the water content (x) of $NiCO_3{\cdot}2Ni(OH)_2{\cdot}xH_2O$. Based on the TGA-MS analysis, $NiCO_3{\cdot}2Ni(OH)_2{\cdot}xH_2O$decomposes between 120–525°C with a weight loss of 34%, accompanied by the release of H_2O and CO_2, and without further changes up to 1125°C (see Figure 5c). As the thermodynamically stable high-temperature decomposition products should be NiO, CO_2, and H_2O, the following decomposition reaction is expected:

$$NiCO_3 \cdot 2Ni(OH)_2 \cdot xH_2O \rightarrow 3NiO + CO_2 \uparrow + (2+x)\,H_2O \uparrow \quad [5]$$

For this reaction, the relative weight loss Δm upon decomposition can be determined from the molecular weight of $NiCO_3{\cdot}2Ni(OH)_2{\cdot}xH_2O$ ($M_{basic\text{-}Ni} = (304 + x \times 18)$ g/mol) and that of the only remaining solid compound NiO ($M_{NiO} = 74.7$ g/mol):

$$\Delta m = (M_{basic\text{-}Ni} - 3 \times M_{NiO))/M_{basic\text{-}Ni} = (80 + x \times 18)/(304 + x \times 18) \quad [6]$$

While the water content of the basic nickel carbonate was not specified, the plausible value of two H_2O molecules per formula unit (i.e., x = 2) results in a value of Δm of 34.1%, which is in perfect agreement with the TGA-MS data in Figure 5c. Thus, our basic nickel carbonate model reference compound is $NiCO_3{\cdot}2Ni(OH)_2{\cdot}2H_2O$ with $M_{basic\text{-}Ni}$ = 340 g/mol.

Assuming that the mass loss of "wet" NCM811 of 0.74% between 120–525°C (see Figure 3d) would be entirely due to the thermal decomposition of $NiCO_3{\cdot}2Ni(OH)_2{\cdot}2H_2O$, its amount on the "wet" NCM811 would equate to ~2.2 wt% (from 0.74% divided by the mass loss Δm upon the thermal decomposition of $NiCO_3{\cdot}2Ni(OH)_2{\cdot}2H_2O$; see Figure 5c). Although we are aware that it is a crude simplification to neglect potential contributions of Mn- and Co-based surface contaminants which also decompose below 525°C, their similar mass losses (39% and 32%, see Figure 5) would not significantly change the calculated surface contaminant weight fraction; furthermore, based on the above analysis, the fraction of Mn- and Co-based surface contaminants is expected to be minor compared to that of basic nickel carbonate. Considering that the thermal decomposition of EC even at 60°C is most strongly promoted by OH^- compared to H_2O[31] we now determine the molar amount of OH^- contained in the proposed $NiCO_3{\cdot}2Ni(OH)_2{\cdot}2H_2O$ surface contaminant on "wet" NCM811: based on the above estimates of its mass fraction (~2.2 wt%), its molecular weight ($M_{basic\text{-}Ni}$ = 340 g/mol), and the fact that it contains 4 moles of OH^- per formula unit, this equates to ~260 $\mu mol_{OH^-}/g_{NCM}$. Consequently, the amount of CO_2 evolved over 8 hours at 60°C (~2.4 $\mu mol/g_{NCM}$, see above) corresponds to only ~1% of the EC that could potentially be decomposed to ethylene glycolate when using up all of the bound OH^- ions (from the previously reported reaction EC + OH- → EG^- + CO_2).[30] This analysis suggests that neither the amount of EC nor the amount the $NiCO_3{\cdot}2Ni(OH)_2{\cdot}2H_2O$ surface contaminant are limiting the overall CO_2 evolution in the OMS experiment with "wet" NCM811 (lower panel of Figure 7). This is consistent with the observation that the CO_2 evolution rate (i.e., the slope of CO_2 concentration vs. time) with "wet" NCM811 stabilizes at a constant value for a given sample after several hours at 60°C, indicating that the kinetics of the reaction is controlling the CO_2 evolution rate.

Kinetic analysis of EC decomposition.—Next we want to analyze the kinetics of the EC decomposition and discuss the implications for swelling of pouch cells. Figure 10 summarizes the CO_2 evolution rates from the reaction of the NCM samples with the EC-based electrolyte obtained from linear regression of the CO_2 evolution curves in Figure 6 during the last 3 h of the experiment (note that the rate of CO_2 evolution rates do not change much anymore at this point of the experiment). The CO_2 evolution rates are given in $[mol_{CO_2}/(s{\cdot}g_{EC})]$, which are normalized units with respect to the amount of EC in the cell for better comparability to gassing in other battery cells. It should be noted that these data are not normalized to the rather similar BET surface areas of NCM811 and NCM111 (roughly 0.3 m^2/g for the pristine materials, see Table I), as was done in Figure 7.

For both NCM111 and NCM811 samples, a clear trend in CO_2 evolution rate is visible: (i) the "wet" samples with the highest amount of surface contamination (see Figures 3b and 3d) show the highest CO_2 evolution rates; (ii) the "dry" samples which are not free of surface contaminants (see Figures 3a and 3c) show considerable CO_2 evolution rates as well and, (iii) the "calcined" samples show a quasi-zero CO_2 evolution rate, indicating that the complete removal of reactive surface species effectively prevents the decomposition of EC. The background measurements with only 240 μl of 1.5 M $LiClO_4$ in EC in the cell or with only CAM powders also show a quasi-zero CO_2 evolution rate of $<5{\cdot}10^{-12}$ $mol_{CO_2}/(s{\cdot}g_{EC})$ when compared to the rates for "wet" and "dry" samples. which are one to almost two orders of magnitude higher.

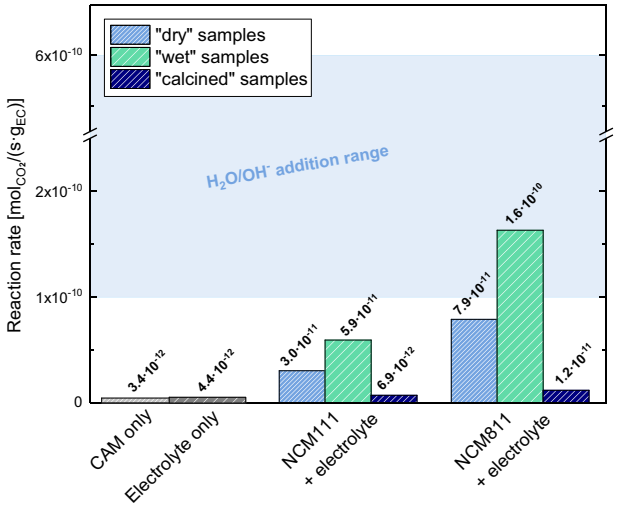

Figure 10. CO_2 evolution rates at 60°C (normalized to the mass of EC) as a measure for the EC decomposition rate, determined from a mixture of electrolyte (240 µl of 1.5 M $LiClO_4$ in EC) and "wet" (green), "dry" (blue), and "calcined" (navy) NCMs (1.03 g).) The data was extracted from the CO_2 evolution curves in Figure 7 by linear regression during the last 3 h of the 60°C temperature hold; the here used electrolyte/CAM mass ratio of 0.35/1 reflects that in commercial battery cells. The blue area represents the range of EC decomposition rates that were determined in our previous work,[30] where we directly added H_2O and OH^- to the same EC-based electrolyte, at H_2O and OH^- concentrations between ~11–280 $\mu mol/g_{electrolyte}$ with ~0.4–10 $\mu mol/g_{electrolyte}$, respectively.

The rate of gas generation from reactions with surface groups on the cathode materials would likely follow a rate equation like $r \propto m_{EC} \cdot A_{NCM}$, where m_{EC} is the total mass of EC in the cell and A_{NCM} is the total surface area of NCM cathode active material in the cell. The amount of EC would be rate limiting, since we chose an electrolyte/CAM mass ratio of 0.35/1, which reflects the ratio used in commercial battery cells. Similarly, the amount of surface groups, which clearly scales with the available surface area, is also a limiting factor.

An interesting observation is that the EC decomposition rates for "wet" and "dry" samples are remarkably close to the rates obtained for the addition of H_2O and OH^- to the same EC-based electrolyte from our previous work:[30] at 60°C, different concentrations of H_2O and OH^- ranging from 200–5000 ppm H_2O with 7–167 ppm OH^- (introduced as $TBAOH{\cdot}30H_2O$) led to CO_2 evolution rates between ~1-$^{-10}$ $mol_{CO_2}/(s{\cdot}g_{EC})$ (see blue marked area in Figure 10). As our previous study OH^- was shown to most strongly promote EC decomposition, it is interesting to compare the OH- concentrations achieved by the addition of $TBAOH{\cdot}30H_2O$ (a strong base, homogeneously distributed in the electrolyte) with the estimated amount of OH^- introduced by the NCM surface contaminants. The above given H_2O and OH^- concentrations in our previous study equate to ~11–280 $\mu mol_{H_2O}/g_{electrolyte}$ with ~0.4–10 $\mu mol_{OH\text{-}}/g_{electrolyte}$, respectively. This may be compared to the H_2O and OH^- concentrations introduced by the hypothesized $NiCO_3{\cdot}2Ni(OH)_2{\cdot}2H_2O$ surface contaminant on "wet" NCM811, which we had estimated above (~130 $\mu mol_{H_2O}/g_{NCM}$ and ~260 $\mu mol_{OH\text{-}}/g_{NCM}$), which based on the electrolyte/NCM mass ratio of 0.35/1 equates to substantially larger concentrations of ~370 $\mu mol_{H_2O}/g_{electrolyte}$ and ~740 $\mu mol_{OH\text{-}}/g_{electrolyte}$ (here we have neglected the possible additional presence of LiOH on the NCM surface). Thus, while we believe that the OH^- catalyzed EC hydrolysis reaction proceeds by the same reaction mechanism (viz., a nucleophilic attack of EC by OH^- with subsequent ring opening and CO_2),[30] independent of whether H_2O/OH^- or basic nickel carbonate surface contaminants are in contact with the electrolyte, the effectiveness of homogenously dispersed H_2O/OH^- to promote the EC decomposition is obviously higher than that of surface bound H_2O/OH^-, as illustrated here by the similar decomposition EC decomposition rate with "wet" NCM811 despite the a much higher nominal H_2O and OH^- concentration. Nevertheless, the following estimates will demonstrate that the surface contamination triggered EC decomposition rates are quite significant for commercial-size battery cells.

Implications for the storage of battery cells at elevated temperature.—The reactivity of NCM surface contaminants with alkyl carbonate electrolyte (demonstrated in Figures 7, 9, and 10) can have a pivotal influence on the storage life of lithium-ion batteries at elevated temperature. To illustrate the extent of CO_2 gassing that is to be expected during storage at 60°C, one may calculate the amount of CO_2 which would be produced over 100 h (a typical time for storage experiments) in a 3 Ah battery using the reaction rates given in Figure 10. Note that this estimate would apply for a battery in its discharged state, for which gassing and the associated cell bulging is typically lower than in the charged state. Figure 11 gives an overview of the model calculations, which are described in more detail in the following. A 3 Ah battery would contain ~20 g cathode active material (based on an NCM capacity of ~150 mAh/g) and ~7 g of electrolyte (based on ~0.35 $g_{electrolyte}/g_{CAM}$),[37] which for a typical electrolyte formulation (e.g., the here used LP572 electrolyte with ~13 wt% $LiPF_6$, ~25 wt% EC, ~60 wt% EMC and ~2 wt% VC) would correspond to ~1.75 g EC in the cell. For this cell configuration, the CO_2 evolution rate of $5.9{\cdot}10^{-11}$ $mol_{CO_2}/(s{\cdot}g_{EC})$ for "wet" NCM111 shown in Figure 10 would translate into a consumption of ~0.2% of the EC accompanied by the formation of ~0.9 cm^3 CO_2 (referenced to standard conditions of 25°C and 1 bar) over 100 h storage at 60°C. For the gas evolution rate of "wet" NCM811, that number would be ~2.4 cm^3 CO_2 (note that for this, only ~2% of the OH^- groups stored in the $NiCO_3{\cdot}2Ni(OH)_2{\cdot}2H_2O$ surface contaminant on the "wet" NCM811 would be required). Since compared to our OMS experiment, the EC content of the commercial LP572 electrolyte is three times smaller, the CAM:EC ratio is three times higher which most probably leads to an even higher CO_2 evolution. As any gas formation above 1–5 cm^3 would likely be considered significant for a 3 Ah pouch bag cell,[57] a detrimental effect on cell-life would be expected.[58]

Implications for cycling at elevated temperature.—The reduced capacity retention for T-cells with cathodes made from "wet" NCM811 powder was demonstrated in Figure 9. The capacity fading goes along with a decreasing mean discharge voltage and an increasing overall internal cell resistance that is much more pronounced for cells with contaminated NCM811 than for cells with "dry" or "calcined" NCM811. On a mechanistic level, this can be rationalized by an accumulation of unwanted reaction products in cells containing "wet" NCM811 that cause a larger impedance buildup on the anode and/or the cathode. In Figure 7 it was shown that surface contaminants lead to considerable gassing due to the decomposition of EC-based electrolytes at elevated temperature. By comparison with our previous work, we provided evidence that the EC decomposition rates triggered by surface contaminants are comparable to the OH^--driven hydrolysis of EC-based electrolyte (see Figure 10).[30] It is thus likely that during cell cycling at 45°C (see Figure 9) such hydrolysis reactions induced by basic surface groups on the contaminated NCM811 material lead to the accumulation of electrolyte decomposition products on the electrodes. Such unwanted material imposes a kinetic hindrance for Li^+-ion insertion/extraction and hence compromises efficient charge/discharge cycling.[59]

Conclusions

In this work, we attempted an in-depth analysis of the chemical composition and the quantity of surface contaminants on two different metal oxide-based cathode active materials (CAMs), the widely used $LiNi_{1/3}Mn_{1/3}Co_{1/3}O_2$ (NCM111) and the Ni-rich $LiNi_{0.8}Mn_{0.1}Co_{0.1}O_2$ (NCM811). To demonstrate the sensitivity of these materials to storage and handling in ambient air, we preconditioned the samples in three

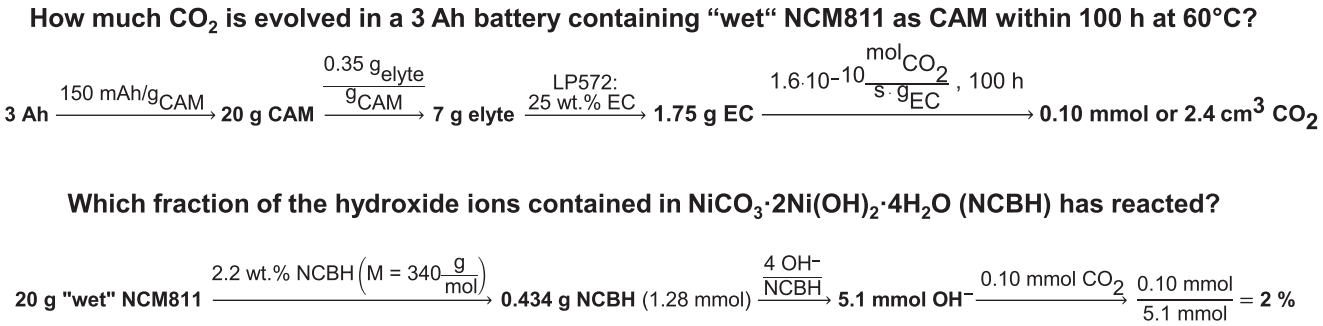

Figure 11. Overview of the model calculations of CO_2 generation due to the reactions of surface contaminants with the electrolyte component EC for a 3 Ah battery cell containing "wet" NCM811 as cathode active material.

different ways: (i) the "wet" condition is obtained by storing the CAMs under high relative humidity; (ii) the "dry" condition refers to the as-received materials dried at standard electrode fabrication temperature; and, (iii) the "calcined" condition refers to the "wet" samples subjected to a heat-treatment under inert gas at 625°C for NCM111 and at 525°C for NCM811, with the intention of removing all surface contaminants.

By TGA-MS it was shown that already the "dry" samples exhibit a significant weight loss in the temperature range from 125–625°C, accompanied by a characteristic H_2O and CO_2 evolution associated with the presence of transition metal hydroxides and carbonates on the surface. Infrared spectroscopic analysis further substantiated the presence of carbonate and hydroxide/hydrate surface species; from an experimental point of view, it was also demonstrated that the sensitivity of FTIR measurements in diffuse reflectance mode (DRIFTS) is superior compared to ATR- and transmission FTIR. The amount of the surface contaminants is increased by "wet" storage to account for a weight loss on the order of ∼1 wt% in the case of "wet" NCM811 upon heating to 525°C. Comparing the TGA-MS patterns to those of several reference samples, it was found that basic nickel carbonate $NiCO_3 \cdot 2Ni(OH)_2 \cdot 2H_2O$ is likely to be the major and the most critical surface contaminant formed upon ambient air exposure of NCMs (particularly of Ni-rich NCMs).

On-line mass spectrometry (OMS) measurements show that "wet" and "dry" NCMs exhibit a high reactivity with ethylene carbonate (EC) based electrolyte, yielding substantial amounts of CO_2 by the hydrolysis of EC with the hydroxyl groups and/or hydrates on the NCM surface. This reactivity is quasi-zero for the "calcined" samples where most basic surface contaminants are removed. Battery cells built with such "calcined", contaminant-free cathode material outperform cells with "wet" or even "dry" cathode material in extended charge/discharge cycling at 45°C due to much lower cell polarization. Against the common understanding, we show that residual Li_2CO_3 from the synthesis is not a detrimental surface contaminant, since it is still present on our "calcined" samples.

In short, our main findings are 1 that NCM811 is much more prone to surface contamination from ambient CO_2 and moisture compared to NCM111, 2 that basic nickel carbonate was identified as the major and most important surface contaminant, and 3 that the latter clearly has detrimental effects on the gassing behavior and on the cycling of full cells. We are currently investigating ways to inertize metal oxide-based cathode materials, such that storage under moisture and CO_2 containing atmosphere does not lead to surface contamination.

Acknowledgment

The authors acknowledge BASF for financial support of this research through the framework of its Scientific Network on Electrochemistry and Batteries. In particular, we thank Dr. Manuel Mendez and Dr. Heino Sommer (BASF) for fruitful discussions and helpful advice. We further thank Louis Hartmann and Christian Sedlmeier for their dedicated work and support of this project during their Bachelor's thesis and research internship, respectively.

ORCID

Johannes Sicklinger https://orcid.org/0000-0003-2815-993X
Michael Metzger https://orcid.org/0000-0002-5512-8541
Daniel Pritzl https://orcid.org/0000-0002-9029-107X
Hubert A. Gasteiger https://orcid.org/0000-0001-8199-8703

References

1. G. E. Blomgren, *J. Electrochem. Soc.*, **164**, A5019 (2017).
2. M. S. Whittingham, *Chem. Rev.*, **104**, 4271 (2004).
3. H.-J. J. Noh, S. Youn, C. S. S. Yoon, and Y.-K. K. Sun, *J. Power Sources*, **233**, 121 (2013).
4. O. Gröger, H. A. Gasteiger, and J.-P. Suchsland, *J. Electrochem. Soc.*, **162**, A2605 (2015).
5. D. Andre, S.-J. Kim, P. Lamp, S. F. Lux, F. Maglia, O. Paschos, and B. Stiaszny, *J. Mater. Chem. A*, **3**, 6709 (2015).
6. J. Paulsen, H. P. Hong, and J. D. Oh, WO 2016/055911 A1 (2016).
7. J. Paulsen, H.-K. Park, and Y. H. Kwon, US 2019/0224201 A1 (2009).
8. J. Paulsen and J. H. Kim, WO 2012/107313 A1 (2012).
9. H. Beyer, S. Meini, N. Tsiouvaras, M. Piana, and H. A. Gasteiger, *Phys. Chem. Chem. Phys.*, **15**, 11025 (2013).
10. Y. Kim, *J. Mater. Sci.*, **48**, 8547 (2013).
11. S. E. Renfrew and B. D. McCloskey, *J. Am. Chem. Soc.*, **139**, 17853 (2017).
12. R. Jung, P. Strobl, F. Maglia, C. Stinner, and H. A. Gasteiger, *J. Electrochem. Soc.*, **165**, A2869 (2018).
13. J. Kim, H. Lee, H. Cha, M. Yoon, M. Park, and J. Cho, *Adv. Energy Mater.*, **8**, 1702028 (2018).
14. J. R. Dahn, R. Fong, and U. von Sacken, US 2,264,201 (1993).
15. D.-H. Kim and J. Paulsen, United States Pat. Appl., **2016036557**, WO 2015/128722 A1 (2015).
16. J. Paulsen, H. P. Hong, and H. S. Ahn, WO 2015/036882 A2 (2015).
17. D.-H. Cho, C.-H. Jo, W. Cho, Y.-J. Kim, H. Yashiro, Y.-K. Sun, and S.-T. Myung, *J. Electrochem. Soc.*, **161**, A920 (2014).
18. J. Kim, Y. Hong, S. Ryu, M. G. Kim, and J. Cho, *Electrochem. Solid-State Lett.*, **9**, A19 (2006).
19. H. S. Liu, Z. R. Zhang, Z. L. Gong, and Y. Yang, *Electrochem. Solid-State Lett.*, **7**, A190 (2004).
20. G. V. Zhuang, G. Chen, J. Shim, X. Song, P. N. Ross, and T. J. Richardson, *J. Power Sources*, **134**, 293 (2004).
21. N. Mijung, Y. Lee, and J. Cho, *J. Electrochem. Soc.*, **153**, A935 (2006).
22. I. A. Shkrob, J. A. Gilbert, P. J. Phillips, R. Klie, R. T. Haasch, J. Bareño, and D. P. Abraham, *J. Electrochem. Soc.*, **164**, A1489 (2017).
23. H. Liu, Y. Yang, and J. Zhang, *J. Power Sources*, **162**, 644 (2006).
24. N. V. Faenza, L. Bruce, Z. W. Lebens-Higgins, I. Plitz, N. Pereira, L. F. J. Piper, and G. G. Amatucci, *J. Electrochem. Soc.*, **164**, A3727 (2017).
25. *A Dictionary of Chemistry*, 6th ed., J. Daintith, Editor, p. 330, Oxford University Press (2008).
26. B. Zhang, *thesis*, University of Pittsburgh (2012).
27. X. Zheng, X. Li, Z. Wang, H. Guo, Z. Huang, G. Yan, and D. Wang, *Electrochim. Acta*, **191**, 832 (2016).
28. R. Moshtev, P. Zlatilova, S. Vasilev, I. Bakalova, and A. Kozawa, *J. Power Sources*, **81–82**, 434 (1999).
29. R. Jung, R. Morasch, P. Karayaylali, K. Phillips, F. Maglia, C. Stinner, Y. Shao-Horn, and H. A. Gasteiger, *J. Electrochem. Soc.*, **165**, A132 (2018).
30. M. Metzger, B. Strehle, S. Solchenbach, and H. A. Gasteiger, *J. Electrochem. Soc.*, **163**, A1219 (2016).
31. M. Metzger, C. Marino, J. Sicklinger, D. Haering, and H. A. Gasteiger, *J. Electrochem. Soc.*, **162**, A1123 (2015).
32. M. Metzger, J. Sicklinger, D. Haering, C. Kavakli, C. Stinner, C. Marino, and H. A. Gasteiger, *J. Electrochem. Soc.*, **162**, A1227 (2015).
33. R. Bernhard, S. Meini, and H. A. Gasteiger, *J. Electrochem. Soc.*, **161**, A497 (2014).
34. R. Bernhard, M. Metzger, and H. A. Gasteiger, *J. Electrochem. Soc.*, **162**, A1984 (2015).

35. P. Oh, B. Song, W. Li, and A. Manthiram, *J. Mater. Chem. A*, **4**, 5839 (2016).
36. F. T. Wagner, B. Lakshmanan, and M. F. Mathias, *J. Phys. Chem. Lett.*, **1**, 2204 (2010).
37. L. D. Ellis, J. P. Allen, L. M. Thompson, J. E. Harlow, W. J. Stone, I. G. Hill, and J. R. Dahn, *Journal of The Electrochemical Society*, **164**, A3518 (2017).
38. N. Tsiouvaras, S. Meini, I. H. Buchberger, and H. A. Gasteiger, *J. Electrochem. Soc.*, **160**, A471 (2013).
39. M. Stich, N. Pandey, and A. Bund, *J. Power Sources*, **364**, 84 (2017)]
40. S.-M. Bak, E. Hu, Y. Zhou, X. Yu, S. D. Senanayake, S.-J. Cho, K.-B. Kim, K. Y. Chung, X.-Q. Yang, and K.-W. Nam, *ACS Appl. Mater. Interfaces*, **6**, 22594 (2014).
41. "Thermochemistry, Electrochemistry and Kinetics", in *CRC Handbook of Chemistry and Physics*, David R. Lide, ed., CRC Press, Boca Raton, FL, 2005.
42. T. Isaacs, *Mineral. Mag. J. Mineral. Soc.*, **33**, 663 (1963).
43. A. Van der Ven, D. Morgan, Y. S. Meng, and G. Ceder, *J. Electrochem. Soc.*, **153**, A210 (2006).
44. D. Kohls and J. Rodda, *Am. Mineral.*, **51**, 677 (1966).
45. P. Pasierb, S. Komornicki, M. Rokita, and M. Rękas, *J. Mol. Struct.*, **596**, 151 (2001).
46. W.-L. Wang, H. Jiang, Z. Liu, and X. Liu, *J. Mater. Chem.*, **15**, 1002 (2005).
47. S. Meini et al., *Phys. Chem. Chem. Phys.*, **15**, 11478 (2013).
48. F. A. Miller and C. H. Wilkins, *Anal. Chem.*, **24**, 1253 (1952).
49. N. De Geyter, R. Morent, and C. Leys, *Surf. Interface Anal.*, **40**, 608 (2008).
50. M. Metzger, B. Strehle, S. Solchenbach, and H. A. Gasteiger, *J. Electrochem. Soc.*, **163**, A798 (2016).
51. A. T. S. Freiberg, M. K. Roos, J. Wandt, R. de Vivie-Riedle, and H. A. Gasteiger, *J. Phys. Chem. A*, **122**, 8828 (2018).
52. R. Jung, M. Metzger, F. Maglia, C. Stinner, and H. A. Gasteiger, *J. Electrochem. Soc.*, **164**, A1361 (2017).
53. X. Xiong, Z. Wang, P. Yue, H. Guo, F. Wu, J. Wang, and X. Li, *J. Power Sources*, **222** 318 (2013)
54. Daniel Pritzl, Tobias Teufl, Anna T. S. Freiberg, Benjamin Strehle, Johannes Sicklinger, Heino Sommer, Pascal Hartmann, and Hubert A. Gasteiger, to be published.
55. A. J. Smith, J. C. Burns, D. Xiong, and J. R. Dahn, *J. Electrochem. Soc.*, **158**, A1136 (2011).
56. I. H. Buchberger, S. Seidlmayer, A. Pokharel, M. Piana, J. Hattendorff, P. Kudejova, R. Gilles, and H. A. Gasteiger, *J. Electrochem. Soc.*, **162**, A2737 (2015).
57. K. Wu, J. Yang, Y. Liu, Y. Zhang, C. Wang, J. Xu, F. Ning, and D. Wang, *J. Power Sources*, **237**, 285 (2013).
58. T. Bond, J. Zhou, and J. Cutler, *J. Electrochem. Soc.*, **164**, A6158 (2017).
59. J. C. Burns, A. Kassam, N. N. Sinha, L. E. Downie, L. Solnickova, B. M. Way, and J. R. Dahn, *J. Electrochem. Soc.*, **160**, A1451 (2013).

3.2.3. *In situ* DRIFTS During CO_2 and H_2O Exposure

While the previous chapter presented *ex situ* DRIFTS data as part of a combined study[47] on ambient storage-derived surface contaminants on NCM811 and NCM111, the present chapter contains the results from an *in situ* DRIFTS study on the reaction of NCM811 with CO_2 and humidity (for experimental details cf. chapter 2.2). TGA-MS and NCM811//graphite full-cell cycle-life tests were carried out in a similar way as in said study on surface contaminants and will be critically compared to the *in situ* DRIFTS data in the following.

During the *in situ* DRIFTS measurements, pure NCM811 active material powder and NCM811 electrodes were exposed to various gas mixtures containing either CO_2 in Ar, humidified Ar, or both, as explained in the experimental part (cf. chapter 2.2). As depicted in Table 5, the samples were first exposed to dry CO_2 (1000 ppm CO_2 in Ar, "segment 1" in Table 5) and then to moisture (humidified Ar, "segment 3"), before they were again exposed to dry CO_2 ("segment 5") and finally to a combination of CO_2 and moisture ("segment 6"). Extended Ar flushing was applied to remove CO_2 or residual humidity before switching between the various gas mixtures. The Ar flushing parts "segments 4" and "7" were extended to last 1 d and 2 d, respectively, in order to remove at least some of the adsorbed water from the sample surface before the final spectra were recorded.

Table 5: Experimental protocol for exposing NCM811 to moisture, CO_2, or a combination of both, with a total gas flow of 1 l/min.

Segment	Short description	Duration	Gas mixture
1	CO_2	5 d	1000 ppm CO_2 in Ar
2	Ar	3 h	Ar
3	H_2O	5 d	humidified Ar
4	Ar	1 d	Ar
5	CO_2	5 d	1000 ppm CO_2 in Ar
6	CO_2 + H_2O	5 d	1000 ppm CO_2 in humidified Ar
7	Ar	2 d	Ar

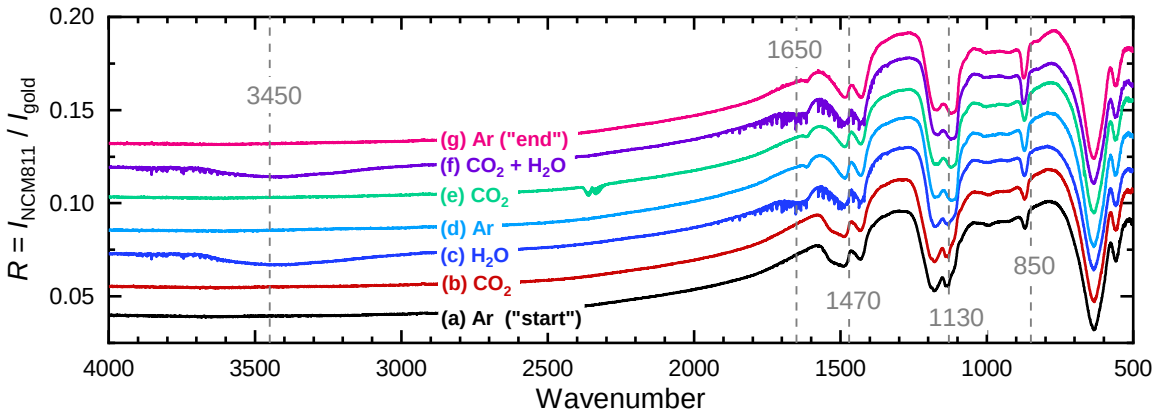

Figure 23: Selected spectra of the *in situ* DRIFTS measurement (reflectance units; arbitrary offset for better visibility) with NCM811 (pure CAM powder without any dilution medium). (a) NCM811 after calcination at 525°C in the initial state before moisture or CO_2 exposure, referred to as "start" spectrum, (b) after 5 h exposure to 1000 ppm CO_2 in Ar (10 min after the begin of segment 2, see Table 5), (c) after 5 h exposure to humidified Ar (10 min after the begin of segment 4), (d) after 1 d drying under Ar flow at room temperature (end of segment 4), (e) after 5 h exposure to 1000 ppm CO_2 in Ar (end of segment 5), after 5 h combined exposure to CO_2 and moisture (i.e., humidified Ar with 1000 ppm CO_2; 10 min after the begin of segment 7), and (g) after 2 d drying under Ar (end of segment 7), referred to as "end" spectrum.

Figure 23 is a collocation of various DRIFT spectra from the *in situ* experiment and should serve to discuss the impact of CO_2 and H_2O in the gas phase on NCM811 powder with regards to the formation of IR active surface species. In the "start" spectrum of NCM811 (panel a), typical carbonate features (sharp band above 850 cm^{-1} and doublet around 1470 cm^{-1}) as well as a sulfate band (doublet around 1130 cm^{-1}) can be observed. These carbonate and sulfate features are discussed in more detail in the study on surface contaminants of NCM811 (chapter 3.2.2).[47] Segments 1 and 3 (compare Table 5) should serve to monitor the individual effects of CO_2 or moisture on NCM811, while segment 6 comprises the simultaneous exposure to CO_2 and moisture. Comparing spectra (a) and (b) in Figure 23, no changes can be observed due to the presence of dry CO_2. Line (b) was recorded after 5 h with CO_2 in the gas mix followed by 10 min Ar flow to eliminate gas phase CO_2 signals. Similarly, line (c) was recorded after 5 h moisture exposure followed by 10 min Ar flow to minimize water vapor bands that appear between 1300 and 1800 cm^{-1} as well as between 3600 and 3900 cm^{-1} in spectrum (c) and are typical of water in the gas phase.[226] Additional features centered at ≈3450 and ≈1650 cm^{-1} are visible, both being very broad, revealing water adsorbed on oxide surfaces.[227] These signals as well as the water vapor bands have disappeared after 1 d Ar flushing as seen from line (d) in Figure 23, indicating that the dry Ar has removed most of the adsorbed water. A small feature at 1600 cm^{-1} has remained, which might be belong to a more strongly bound hydrate (H-O-H bending vibration).[228,229] Surprisingly, no hydroxide signal (e.g., from LiOH) is found. LiOH would give rise to a sharp band at ≈3700 cm^{-1} (O-H stretching vibration).[188]

As a next step in the experiment, CO_2 was flown once more through the sample chamber (segment 5) in order to investigate whether it would react with a hydrated or hydroxylated NCM811 surface to form carbonates. In the corresponding spectrum (e), the CO_2 doublet around ≈2350 cm^{-1}

appears due to the fact that there was no Ar flushing period before recording the spectrum (since there was a direct switch from dry CO_2 to humidified CO_2 as explained in Table 5), in contrast to lines (b) and (c). Apart from that, spectra (d) and (e) in Figure 24 appear to be identical and do not give any hint to additional carbonate formation. Therefore, one might hypothesize that the combined presence of CO_2 and moisture in the gas phase is a prerequisite to form carbonates on NCM811. Thus, in the following segment 6, the gas mix with 1000 ppm in CO_2 was humidified before flowing through the sample chamber. Again, the corresponding data, i.e., spectrum (f), was recorded after 10 min Ar flushing to minimize water bands. However, when comparing lines (e) and (f), the only significant changes in the spectrum are connected to water adsorption signals around 3450 and 1650 cm^{-1} as well as water vapor bands in the sample chamber. After 2 days of dry Ar flow, the water adsorption bands have disappeared again in spectrum (f). Spectra (e) and (f) are almost identical, i.e., do not reveal drastic changes of the NCM811 powder after the simultaneous exposure to CO_2 and H_2O. The carbonate signal at ≈850 cm^{-1} might have slightly increased, however the main band at ≈1470 cm^{-1} does not seem to have significantly grown in intensity.

In order to have a closer look at the carbonate band, Figure 24a compares the "start" spectrum (line (a) from Figure 23) with the final "end" spectrum after long-term exposure to CO_2 and H_2O (line (f) from Figure 23) in the lower wavenumber region (750 – 1750 cm^{-1}). In fact, the carbonate out-of-plane vibration at ≈850 cm^{-1} (CO_3 oop) has grown in intensity, however the carbonate stretching vibration at ≈1470 cm^{-1} has not increased as much, but slightly changed its shape. Taken together, this could be interpreted as a rather small increase of carbonate-based surface impurities on the NCM811, while a strong increase would have been expected after the prolonged exposure to CO_2 and H_2O. This might be a first hint that the DRIFTS sampling with undiluted CAM powder might not be sensitive enough to monitor the growth of surface species *in situ*. To test this assumption, the "end" sample was collected after the *in situ* experiment and then diluted with KBr at a CAM/KBr mass ratio of 1% (Figure 24b). Similarly, a KBr dilution of NCM811 directly after calcination at 525°C was prepared, identical to the "start" sample of the *in situ* experiment. This direct comparison finally reveals a drastic growth of both carbonate bands when comparing "start" and "end" sample in Figure 24b. Consequently, the carbonate content must have largely increased due to exposure to CO_2 and H_2O in the *in situ* DRIFTS setup. Unfortunately, only the *ex situ* DRIFTS measurement with KBr dilution seems to be sufficiently sensitive to monitor these drastic changes.

For comparison, Figure 24c displays data from the manuscript[47] (cf. chapter 3.2.2) on surface contaminants for "dry", "calcined", and "wet" NCM811. The spectra in panel (c) have been re-plotted in reflectance units instead of using a KM normalization so that it can be compared to the *in situ* measurements in panel (a) and the *ex situ* measurements of the *in situ* samples in panel (b). The comparison between (c) and (b) clearly demonstrates that the carbonate content has risen much more

strongly for the *in situ* samples ("start" and "end" in panel (b)) as compared to the ambient storage at high humidity for 1 week ("dry" and "wet" in panel (c)). One reason for this might be the higher CO_2 concentration in the *in situ* experiment (1000 ppm for 5 days) compared to the ambient storage experiment (400 ppm for 7 days). In addition, even when leaving aside the separate exposure to CO_2 or moisture in segments 1, 3, and 5 (Table 5), the simultaneous presence of moisture and CO_2 in segment 5 might have a stronger effect under gas flow conditions (10 ml/min for 5 days) in contrast to natural diffusion (for 7 days) in the ambient storage experiment.

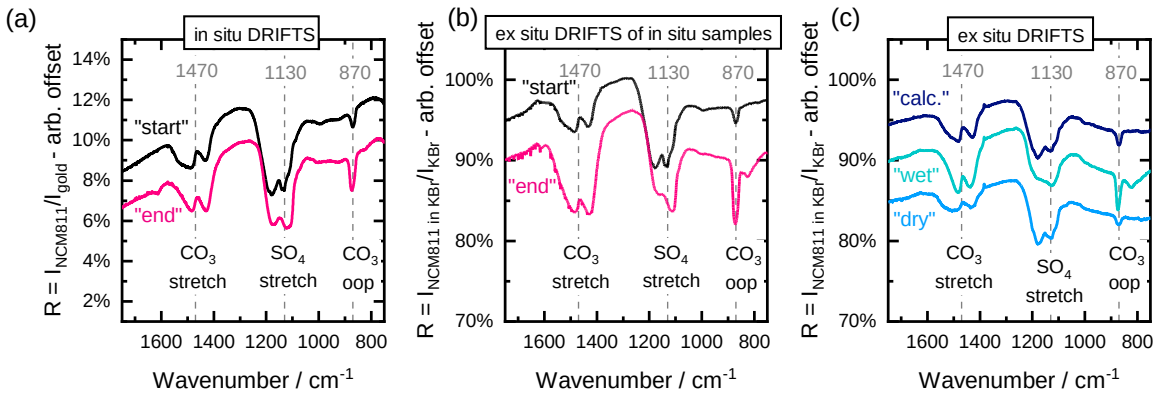

Figure 24: (a) *in situ* DRIFT spectra of NCM811 (calcined at 525°C) with "start" referring to NCM811 under Ar right before starting segment 1 (compare Table 5) and "end" referring to the last spectrum within segment 7, i.e., the final state of NCM811 after long-term exposure to CO_2 and humidity. (b) *ex situ* DRIFTS spectra of the "start" and the "end" sample (1% NCM811 powder diluted in KBr and referenced to pure KBr as background). (c) Re-plotted data from the manuscript[47] (cf. chapter 3.2.2) on surface contaminants on "dry" and "wet" NCM811 (reflectance units instead of KM normalization). The "calc." sample in panel (c) was obtained from calcining "wet" NCM811, as described in the manuscript. In contrast, the "start" samples in panel (a) and (b) were prepared by calcining "dry", i.e., pristine NCM811 (as received from the manufacturer).

From the study[47] on surface contaminants (cf. chapter 3.2.2) it is known that the cycle-life of NCM811//graphite full-cells is deteriorated after ambient storage of NCM811 at high humidity. In addition, the surface contaminants can be monitored by TGA-MS, especially the weight loss up to 525°C. The *ex situ* DRIFTS spectra of the *in situ* samples in Figure 24b revealed the formation of a carbonate amount even larger than in case of the "wet" sample from the manuscript on ambient storage (Figure 24c). Consequently, both TGA-MS data and full-cell cycle-life would have to be drastically changed under the conditions used for the *in situ* DRIFTS experiment. To check this hypothesis, two TGA-MS measurements were performed, one with the "start" sample, i.e., NCM811 calcined at 525°C and another one with the "end" sample collected after finishing the *in situ* DRIFTS experiment (Figure 25a). While the weight loss (125 – 525°C) of the "start" sample is only 0.1%, it is as high as 2.4% for the "end" sample. The almost negligible weight loss for calcined NCM811 ("start" sample) is plausible, since calcination at 525°C removes all surface contaminants apart from Li_2CO_3 (as discussed in the manuscript[47]). A drastic increase of the weight loss after prolonged exposure to CO_2 and H_2O is of course expected as well. For comparison, the "wet" sample from the ambient storage experiment described in the manuscript[47] had a weight loss of 0.74 % between 125 and 525°C. This demonstrates once more that

the increase of surface contaminants during the *in situ* DRIFTS experiment must be extremely high, considering the 2.4 % weight loss in the TGA, even though this was not reflected by the *in situ* DRIFT spectra.

Considering the findings from the manuscript on ambient storage, the even higher amount of surface contaminants formed during the *in situ* DRIFTS experiment must be detrimental for the electrochemical performance of NCM811. As described in the experimental part (cf. chapter 2.2), NCM811 electrodes were placed inside the *in situ* DRIFTS setup to be exposed to the same amounts of CO_2 and H_2O as the NCM811 powder observed by DRIFTS. Afterwards, these electrodes underwent the typical drying conditions for electrodes (120°C in vacuum for 16 h), before they were built into full-cells ("end" sample). Full-cells with NCM811 calcined at 525°C ("start" sample) were assembled for comparison. The corresponding cycling data are depicted in Figure 25b, revealing a dramatic difference between the 1C cycle-life of both samples. While the "start" sample has an initial C/10 discharge capacity of 184 mAh/g (cycle 1) and 1C discharge capacity of 172 mAh/g (cycle 3), the "end" sample starts with a value as low as 132 mAh/g at C/10 (in cycle 1) and 87 mAh/g at 1C (cycle 3). The "start" sample exhibits a moderate fade to 163 mAh/g (at 1C) after 200 cycles, while the "end" sample has almost zero capacity after only 20 cycles (4 mAh/g at 1C). Even at C/10, only 51 mAh/g discharge capacity are regained (cycle 51) in case of the "end" sample, which is only a fraction of the capacity of 176 mAh/g for the "start" sample at the same cycle. This is yet another proof that the amount of surface contaminants formed during the *in situ* DRIFTS experiment is extremely high, clearly exceeding the one after ambient storage for one week (cf. manuscript[47]).

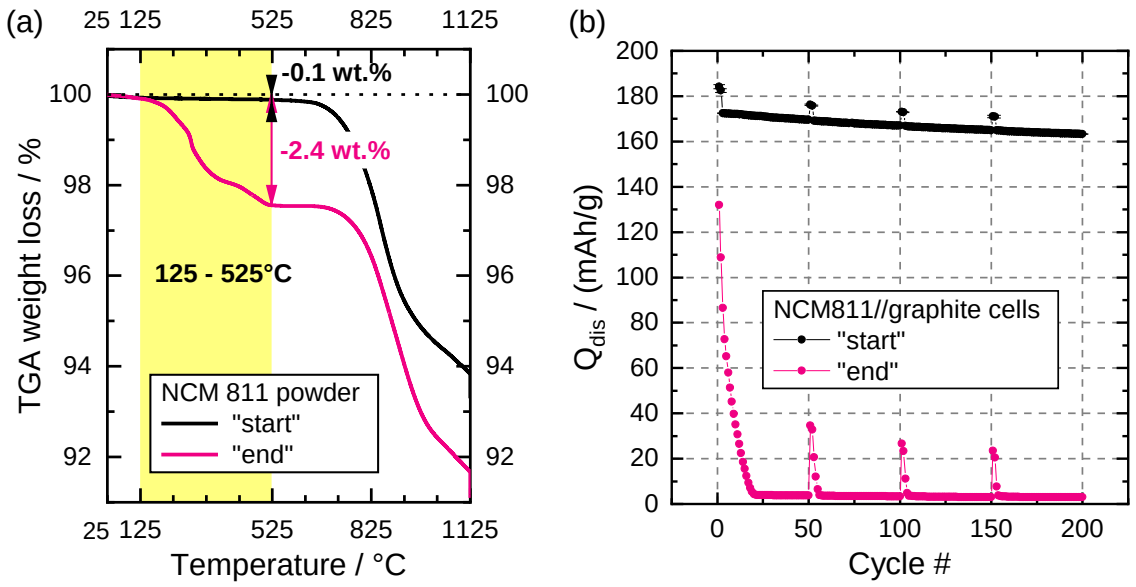

Figure 25: (a) TGA measurement (temperature ramp of 10 K/min) of NCM811 powder directly after calcination at 525°C, i.e., without any exposure ("start") and after the *in situ* DRIFTS measurement, i.e., after long-term exposure to CO_2 and humidity ("end"). (b) Corresponding Swagelok T-cell data: NCM811 electrodes were exposed under identical conditions as the NCM811 powder. NCM811/LP57-2/T311 graphite full-cells were assembled with two glass fiber separators (VWR 691), 80 µl electrolyte and 10 mm electrodes with a balancing factor of 1.1 (referenced to 200 mAh/g_{NCM811} and 340 mAh/$g_{graphite}$). Cycle life tests were performed at 25°C, alternating between two C/10 cycles and 48 1C cycles, with a CCCV charge to 4.2 V vs. graphite (C/20 or 1 h cut-off) and a CC discharge to 3.0 V vs. graphite (details in chapter 2.2). Each value represents the average of two cells each, with error bars representing maximum and minimum values.

Summarizing the above analysis, one can conclude that the DRIFTS setup used here indeed did allow for a well-defined exposure of CAM powders to controlled concentrations of CO_2 and H_2O. This was clearly proven by *ex situ* DRIFT spectra, TGA data, and NCM811//graphite full-cell cycling. However, *in situ* DRIFTS of undiluted powder samples was found to be not sensitive enough to detect the increase of surface contaminants such as carbonates, which are clearly formed on the surface of NCM811. In contrast, the *ex situ* DRIFTS data of the NCM811 samples before and after the *in situ* experiment confirmed the satisfactory sensitivity of *ex situ* DRIFT spectra of CAM samples that are diluted in KBr. Future experiments should focus on such *ex situ* DRIFTS measurements to further elucidate the reactions of NCM811 exposed to CO_2, moisture or a combination of both.

3.3. Surface Modification of Layered Oxide Cathode Active Materials

In the previous chapter it has been clearly demonstrated how sensitive Ni-rich NCM and LMR-NCM can be towards CO_2 and moisture. In the following, various surface modifications will be presented that were developed in order to optimize the stability of Ni-rich NCM and LMR-NCM not only towards CO_2 and moisture, but also in terms of electrochemical aging during full-cell cycling. In case of LMR-NCM, a thermal treatment with SO_3 was developed in order to make the material more robust versus humid ambient air (chapter 3.3.1). For this purpose, a tube furnace setup was developed including a reactor with the catalyst V_2O_5 that generates SO_3 from SO_2 and O_2. The SO_3 is directly fed into the furnace tube in order to let it react with the CAM sample placed inside. In addition, SO_3-treated material was found to have less side reactions with the electrolyte, as well as a better full-cell cycle-life, a slower resistance build-up, and a higher rate capability as compared to pristine LMR-NCM. The experimental details of the furnace setup for SO_3 treatment are described in the manuscript (chapter 3.3.1) as well as in the experimental section of this thesis (cf. chapter 2.3.1). As explained therein, the same setup could be applied to treat CAMs with SO_2 as well.

In a collaboration with the Bar-Ilan University in Israel (BIU), the thermal treatments of LMR-NCM with SO_2 was investigated for different SO_2 concentrations and temperatures. At BIU, an independent setup for the SO_2 treatment of CAMs had been developed, which is described in the experimental section of the manuscript in chapter 3.3.2. LMR-NCM was modified by SO_2 by using both setups (at TUM and BIU) and comparing the results. Even though the experimental conditions were different, in both cases the SO_2 treatment was found to have similar effect on the electrochemical performance of LMR-NCM, i.e., significantly raising its discharge capacity. These cycling results as well as an in-depth characterization of the SO_2-treated samples including surface spectroscopy (DRIFTS, XPS) and bulk analysis (X-ray and electron diffraction) will be discussed in the manuscript in chapter 3.3.2.

The SO_2 and SO_3 treatments that were originally designed for LMR-NCM were also tested for the surface modification of Ni-rich NCM (cf. chapter 3.3.3). Carbonate species could be reduced according to DRIFTS analysis, however only at a very high treatment temperature of 400°C. In contrast to LMR-NCM, the electrochemical performance could not be improved in case of Ni-rich NCM, neither in case of SO_2 nor in case of SO_3. On the one hand, lower treatment temperatures have not been tested yet and might be the next step to do in future experiments. On the other hand, the fact that the "pristine" sample already contains a significant amount of sulfate, the creation of additional surface sulfates or sulfites upon SO_2 or SO_3 treatment might even be not as relevant as in case of LMR-NCM which contains only trace amounts of sulfate amount before SO_2 or SO_3 treatment (chapter 3.3.1).[134]

As mentioned in a joint patent application by TUM, BIU, and the BASF (cf. chapter 3.3.1),[136] not only SO_2 and SO_3, but also other gases such as BF_3 are promising candidates for the modification of CAMs. F_2 is a further example, as demonstrated by the manuscript in chapter 3.3.4. In contrast to the SO_2 and SO_3 treatments, the F_2 treatment was carried out in a closed batch reactor at room temperature and not in a furnace tube with continuous gas flow at elevated temperature. The fluorination reaction was carried out by the University of Freiburg in a specially designed lab that allowed to work with elementary F_2. Since H_2O was formed inside the fluorination reactor, the CAM samples had to be calcined afterwards to remove the surface contaminants resulting from the reaction between Ni-rich NCM and H_2O. The TGA-MS and DRIFTS methods developed at TUM allowed the evaluation of surface contaminants before and after fluorination and calcination. It was further demonstrated that the fluorination of NCM811 can improve the capacity retention of NCM811//graphite full-cells. Elementary analysis of the anode after extended cycling allows the conclusion that the transition metal dissolution from the cathode can be reduced by the reaction of NCM811 with F_2. The fluorination of Ni-rich NCM samples was investigated in a collaboration within the BASF battery research network, involving the University of Freiburg, TUM, BIU, and the BASF. The detailed results of this study can be found in chapter 3.3.4.

3.3.1. SO_3 Treatment of Lithium- and Manganese-Rich NCMs for Li-Ion Batteries: Enhanced Robustness towards Humid Ambient Air and Improved Full-Cell Performance

The manuscript entitled "SO_3 Treatment of Lithium- and Manganese-Rich NCMs for Li-Ion Batteries: Enhanced Robustness towards Humid Ambient Air and Improved Full-Cell Performance" was first submitted to the peer-reviewed Journal of the Electrochemical Society on June 26, 2020. A revised version was submitted on September 1, 2020 and published online on September 18, 2020. The main findings of this paper were presented by Johannes Sicklinger at the Americas International Meeting on Electrochemistry and Solid State Science (AiMES) 2018, on October 3, 2018 in Cancún, Mexico (abstract number 235). A permanent link to this article can be found under https://doi.org/10.1149/1945-7111/abb6cb.

LMR-NCM, sometimes referred to as overlithiated NCM, can be represented with the formula $x\ Li_2MnO_3 \cdot (1-x)\ LiNi_xCo_yMn_zO_2$ and has a significantly higher capacity than stoichiometric NCMs ($LiNi_xCo_yMn_zO_2$).[2,35,88,89] However, due to its high specific surface area, LMR-NCM is prone to react with CO_2 and moisture from ambient air, forming surface contaminants.[47,134] In chapter 3.2.1, it has been demonstrated that the Li content can be a decisive factor and that surface contaminants are mainly formed if the overlithiation degree is very high. This clearly is the case for $Li_{1.42}$-LMR-NCM with the composition $0.42\ Li_2MnO_3 \cdot 0.58\ LiNi_{0.4}Co_{0.2}Mn_{0.4}O_2$, and in fact it was found to strongly react with CO_2 and moisture after storage at high humidity for one week (cf. chapter 3.2.1). In the article presented in the following, $Li_{1.42}$-LMR-NCM was used to develop a surface modification method that makes the material more robust towards CO_2 and moisture, thus avoiding surface contaminant formation upon exposure to ambient air. A special tube furnace setup was developed to generate SO_3 by SO_2 oxidation and subsequent usage of the SO_3 for thermal treatments of CAMs. The experimental details of this setup are described in the manuscript as well as in the experimental section of this thesis (cf. chapter 2.3.1). The effect of SO_3 treatment on LMR-NCM is described in the following, while the impact of SO_2 treatment will be discussed in chapter 3.3.2.

The thermal treatment with a reactive gas enables well-defined conditions to modify the surface composition of layered oxides. The amount of soluble bases on the particle surface is reduced and sulfates are formed. In contrast to typical wet chemical approaches described in the literature,[230–232] the thermal treatment with SO_3 gas might offer a better scalability to be implemented in industrial CAM manufacturing processes. For this reason, treatments with SO_3, SO_2, and further reactive gases have been suggested in a patent application by M. Metzger, H. Beyer, J. Sicklinger et al. in a collaboration between Technical University of Munich, Bar-Ilan University in Israel, and the BASF SE in

Ludwigshafen.[136] Within the manuscript on SO_3 treatment on LMR-NCM, the impact of this chemical surface modification is investigated by surface spectroscopy (DRIFTS and XPS), mass spectrometry to monitor CO_2 gassing from the reaction between electrolyte and CAM powder (OMS) as well as by electrochemical cycle-life tests in LMR-NCM//graphite coin cells. The robustness vs. CO_2 and moisture is tested by a storage experiment at ambient air with high humidity. A similar combined analysis approach has been introduced in the study on ambient storage derived surface contamination of NCM811 and NCM111 (chapter 3.2.2).[47] In the following it will be demonstrated that different to untreated $Li_{1.42}$-LMR-NCM, the SO_3-treated material is very robust towards CO_2 and moisture and thus has superior properties with regards to side reactions with the electrolyte, full-cell cycle-life, resistance build-up, and rate capability.

Author contributions

H. B. and J. S. developed the tube furnace setup to treat CAMs with SO_2 and SO_3. J. S. and L. H. performed the DRIFTS measurements; J. S. evaluated the DRIFTS data. J. S., L. H., C. S., and F. R. carried out the OMS experiments, J. S. calculated the CO_2 evolution rates. H. B. and L. H. carried out XPS measurements and XPS data analysis. J. S., L. H., C. S. and F. R. prepared electrodes and assembled full-cells to perform electrochemical cycling tests. J. S. evaluated and interpreted the cycling test results. J. S., H. B., and H. A. G wrote the manuscript. All authors discussed the data and commented on the manuscript.

Journal of The Electrochemical Society, 2020 **167** 130507

SO_3 Treatment of Lithium- and Manganese-Rich NCMs for Li-Ion Batteries: Enhanced Robustness towards Humid Ambient Air and Improved Full-Cell Performance

Johannes Sicklinger,[*] Hans Beyer,[z] Louis Hartmann,[*] Felix Riewald, Christian Sedlmeier, and Hubert A. Gasteiger[**]

Chair of Technical Electrochemistry, Department of Chemistry and Catalysis Research Center, Technische Universität München, D-85748 Garching, Germany

To increase the specific capacity of layered transition metal oxide based cathode active materials (CAMs) for Li-ion batteries such as NCMs ($Li(Ni_xCo_yMn_z)O_2$, with $x + y + z = 1$), two major strategies are pursued: (i) increasing the Ni content (beyond, e.g., NCM811 with $x = 0.8$ and $y = z = 0.1$) or (ii) using Li- and Mn-rich NCMs (LMR-NCMs) which can be represented by the formula $x\ Li_2MnO_3 \cdot (1-x)\ LiNi_xCo_yMn_zO_2$. Unfortunately, these materials strongly react with CO_2 and moisture in the ambient: Ni-rich NCMs due to the high reactivity of nickel, and LMR-NCMs due to their ≈10-fold higher specific surface area. Here we present a novel surface stabilization approach via SO_3 thermal treatment of LMR-NCM suitable to be implemented in CAM manufacturing. Infrared spectroscopy and X-ray photoelectron spectroscopy prove that SO_3 treatment results in a sulfate surface layer, which reduces the formation of surface carbonates and hydroxides during ambient air storage. In contrast to untreated LMR-NCM, the SO_3-treated material is very robust towards exposure to ambient air at high relative humidity, as demonstrated by its lower reactivity with ethylene carbonate based electrolyte (determined via on-line mass spectrometry) and by its reduced impedance build-up and improved rate capability in full-cell cycling experiments.

 [DOI: 10.1149/1945-7111/abb6cb]

Manuscript submitted June 26, 2020; revised manuscript received September 1, 2020. Published September 18, 2020. *This was paper 235 presented at the Cancun, Mexico, Meeting of the Society, September 30-October 4, 2018.*

Supplementary material for this article is available online

Li-ion battery cathode active materials (CAMs) currently considered for battery electric vehicle applications include NCA (e.g., $LiNi_{0.80}Co_{0.15}Al_{0.05}O_2$) and NCMs ($Li(Ni_xCo_yMn_z)O_2$, with $x + y + z = 1$). [1] Two of the main strategies to further increase their specific energy density are increasing the nickel as well as the development of lithium- and manganese-rich NCMs (LMR-NCMs) with the composition $xLi_2MnO_3 \cdot (1-x)LiNi_xCo_yMn_zO_2$, whereby the advantage of the latter would not only be its lower cost (due to a low nickel content) but also its significantly higher capacity.[1–4] One drawback of higher nickel contents is the increased reactivity with moisture and CO_2 from ambient air, as described in several studies in the literature.[5–9] In case of LMR-NCMs, their typically ≈10-fold higher specific surface area compared to NCMs[10] gives rise to a large number of reactive surface sites forming surface contaminants when exposed to ambient air. Recently, there has been a number of studies on the surface contamination of NCM cathode materials.[9,11–13] The reactivity of layered transition metal oxides such as $LiNiO_2$ and $LiNi_{0.5}Co_{0.5}O_2$ with moisture and CO_2 has already been discussed in earlier studies[8,14] as well as in the patent literature.[15–20] When Ni-rich or LMR-NCM are exposed to ambient atmosphere, CO_2 and H_2O readily react with the particle surface forming carbonates, hydroxides and hydrates.[7,8,13,21,22] These surface species lead to electrolyte decomposition, gassing, impedance buildup, and ultimately deteriorated cycle-life.[1,5,7,8,11–13,21–25] In addition, these basic species can trigger gelation[26] of NMP-based slurries, which complicates the electrode coating process. The most straightforward strategy to prevent such adverse effects is to avoid any exposure to moisture and CO_2 after material synthesis, which, however, is challenging in a large-scale industrial process. Thus it would be highly advantageous to add a step to the CAM manufacturing process which makes them robust against exposure to ambient atmosphere in order to facilitate storage, large-scale ink processing, and electrode manufacturing. For this, the reactive sites on the surface of nickel-rich NCMs or on LMR-NCMs with very high specific surface areas which react with CO_2 and/or H_2O must be removed prior to any potential exposure of the materials to ambient atmosphere.

Several approaches to stabilize the surface of layered transition metal oxides have been explored in the literature. These are, for example, wet chemical processes to produce spinel surface coatings on LMR-NCM[27] as well as on NCM[28] or surface modifications of LMR-NCMs by TiO_2, Al_2O_3, or AlF_3 coatings.[29,30] None of these studies, however discuss the impact of these modifications on the chemical stability of the modified CAMs towards CO_2 and moisture. In our here presented study, we aim to convert the reactive surface groups of LMR-NMC into less reactive sulfate species in order to induce chemical stability of the CAM particles towards ambient air. The generation of a Na_2SO_4 surface layer has been reported using sodium dodecyl sulfate as a precursor, however without investigating the ambient storage stability.[31] In the patent literature, the addition of sodium thiosulfate and sodium dodecyl sulfate to an aqueous washing solution in order to reduce gas generation in pouch cells was reported for NCA.[32] An alternative route to surface sulfation is mixing the cathode active material with $Na_2S_2O_8$ powder, either in the dry state or by spray coating, as described in the patent literature.[19] Yet another approach found in the literature is covering the surface of NCM811 particles with sulfated zirconia, which is demonstrated to have a positive impact on cycling, again without investigating the stability of the material upon exposure to ambient air.[33] In addition, Chae and Yim[34] reported the generation of an SO_x-immobilized surface layer on Ni-rich NCM particles via a wet-chemical approach based on a sulfate surfactant. The improved cycling performance of the coated particles was explained by the mitigation of side reactions with the electrolyte. The drawback of all these surface coating approaches is that they are batch treatments with limited scalability, while for industrial CAM manufacturing a continuous process would be advantageous. In the study at hand we present a novel approach for surface sulfation of layered transition metal oxides, i.e., a thermal treatment with SO_3 gas. Recently, we

*Electrochemical Society Student Member.
**Electrochemical Society Fellow.
[z]E-mail: hans.beyer@tum.de

have also studied surface passivation with SO_2 gas[35] in collaboration with the Aurbach group at Bar-Ilan University in Israel. Treatments of cathode active materials with various reactive gases including SO_2 and SO_3 are also described in our recent patent application[36] in collaboration with Bar-Ilan University and BASF. Therein, SO_2 was shown to enhance full-cell cycling performance of LMR-NCM as well as reduce CO_2 gassing by forming sulfur species on the CAM particle surface.[36] A prior patent application by Watanabe and Deguchi describes the reactive gas treatment of calendared NCM-based cathode sheets and claims that Li_2SO_4 formed due to the SO_2 treatment can lower the CO_2 gas generation from the decomposition reactions of the electrolyte solution.[37]

Here, we explore a chemical surface modification by an SO_3 gas treatment that would be well-suited for implementation in an industrial manufacturing process for layered transition metal oxide based CAMs, as schematically shown in Fig. 1. The synthesis of NCM or LMR-NCM was discussed in greater detail in our recent study on surface contaminants.[13] In brief, transition metal precursors, mixed transition metal sulfates or nitrates,[16,17] are mixed with a lithium precursor (Li_2CO_3 or a $LiOH{\cdot}H_2O$).[15,16] The mixture is subsequently calcined under O_2-containing atmosphere, e.g., in a pusher kiln (step 1 in Fig. 1) to form the desired layered transition metal oxide CAM. During hydroxide or carbonate decomposition, H_2O and CO_2 are formed; during the subsequent cool-down (step 2), dry atmosphere is supplied to remove this H_2O and CO_2, which would otherwise lead to the formation of surface hydroxides and carbonates. Our proposed surface passivation procedure could easily be added to this established process as step 3: after cool-down to the desired treatment temperature of 160 °C or 200 °C, 0.5% SO_3 is added to a dry carrier-gas stream to react with the layered oxide particle surface, converting reactive species such as residual lithium ($LiOH$, $LiOH \cdot H_2O$, Li_2CO_3) or nickel carbonate-hydroxides (such as $(NiCO_3)_2 \bullet (Ni(OH)_2)_3 \bullet 4\ H_2O$)[13] on the surface of the LMR-NCM or its oxide surface groups into passivating sulfate species. The goal of this surface modification approach is to enable the subsequent exposure of LMR-NCM to CO_2 and H_2O (step 4) without forming surface contaminants.

To mimic the proposed surface modification approach on the lab scale, we re-calcine the as-received LMR-NCM at 625 °C in O_2/Ar atmosphere inside a tube furnace with controlled gas flow to remove any contaminants that may have formed unintentionally during shipping and storage. After cool-down to 160 °C or 200 °C, we add 0.5% SO_3 to the gas stream. The reactive SO_3 gas is continuously generated by the so-called contact process, viz., by SO_2 oxidation at elevated temperature in a fixed-bed tube reactor filled with a V_2O_5 catalyst (see experimental section for details). We use Diffusive Reflectance Infrared Fourier Transform Spectroscopy (DRIFTS) and X-ray Photoelectron Spectroscopy (XPS) to demonstrate that this treatment leads to the formation of surface sulfates. Furthermore, we study the chemical reactivity of LMR-NCM at 60 °C with ethylene carbonate (EC) based electrolyte by On-line Mass Spectrometry (OMS), comparing SO_3-treated and untreated LMR-NCM. To assess the practical implications of our surface modification approach on full-cell cycling, we test LMR-NCM//graphite coin cells at an elevated temperature of 45 °C. In our previous work,[13] we already demonstrated that the combined DRIFTS, XPS, OMS and electrochemical analysis represents a powerful toolbox to assess surface contamination of layered transition metal oxides. In this work, we extend the use of this toolbox to characterize SO_3-treated LMR-NCM surfaces and their behavior during ambient storage at high-humidity.

Experimental

Processing of cathode active materials.—LMR-NCM was provided by BASF, shipped under inert packaging, and stored in an Ar-filled glovebox (O_2, $H_2O < 0.1$ ppm, MBraun, Germany). As in previous studies from our group,[10,38] $Li_{1.17}[Ni_{0.22}Co_{0.12}Mn_{0.66}]_{0.83}O_2$, which can also be written as $0.42\ li_2MnO_3 \cdot 0.58\ li[Ni_{0.38}Co_{0.21}Mn_{0.41}]O_2$ was used for all experiments in this study (with a BET area of ≈6.5 $m^2\ g^{-1}$). To establish a well-defined initial state of the LMR-NCM material, the as-received material was dried using the same conditions as for electrodes, i.e., 12 h at 120 °C under dynamic vacuum in a glass oven (Büchi, Switzerland). This sample is referred to as "dry" (see Fig. 2, gray box). The "calcined" sample (black box) was obtained by heat treatment of the "dry" material in a tube furnace (Carbolite, Germany) for 1 h at 625 °C (ramp: 10 K min^{-1}) in a mixture of 30% O_2 and 70% Ar (99.999% purity, Westfalen, Germany) with a controlled gas flow of 1 l min^{-1}. This calcination method was also included as a first step in our surface modification procedure (orange

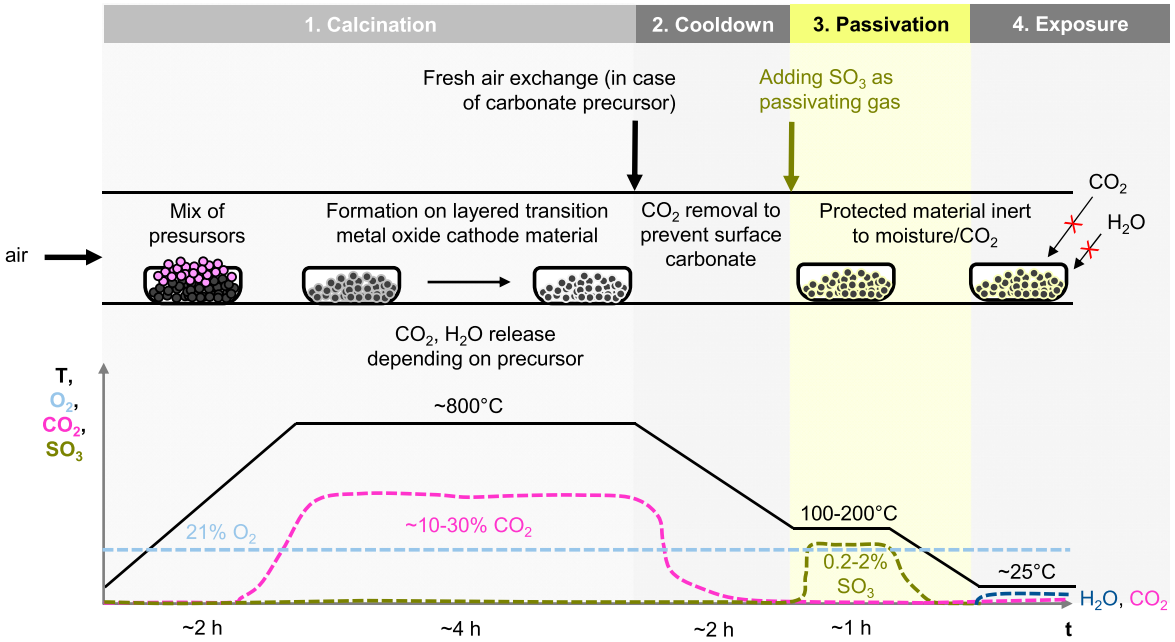

Figure 1. Process scheme for industrial manufacturing of LMR-NCMs. The precursor mix consists of LiOH or Li_2CO_3 salt mixed with transition metal carbonates (similar scheme can be found in our recent article on NCM811 and NCM111).[13] The here proposed surface passivation step (step 3) is highlighted in yellow, while the subsequent exposure test to ambient air at high relative humidity is sketched in step 4.

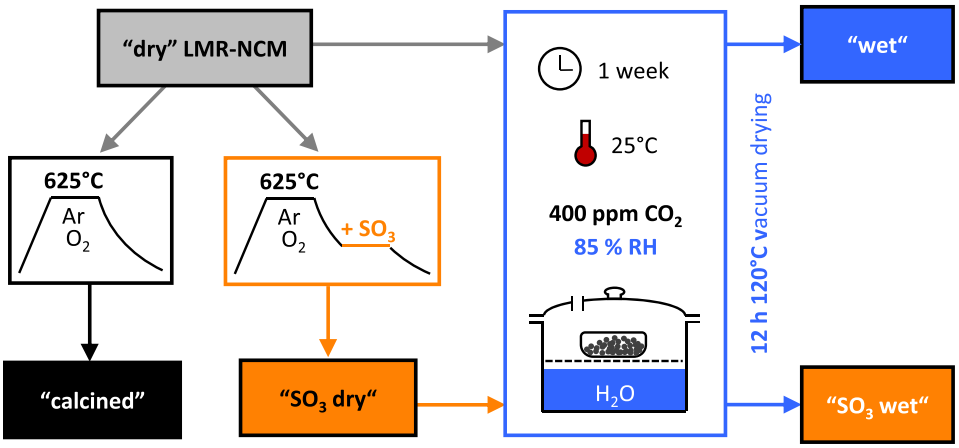

Figure 2. Depiction of the various treatments applied to the LMR-NCM material and labeling scheme of the differently treated samples that is used throughout this manuscript: i) "dry" refers to the as-received LMR-NCM material after 12 h drying under dynamic vacuum at 120 °C; ii) "calcined" refers to this material after calcination in 30% O_2/Ar at 625 °C for 1 h; iii) "SO_3 dry" refers to LMR-NCM after calcination and subsequent treatment with 0.5% SO_3 at 160 °C or 200 °C; iv) "wet" and "SO_3 wet" refers to the "dry" and "SO_3 dry" LMR-NCM materials, respectively, after they had been stored at high-humidity ambient air.

box): first, the sample was calcined in 30% O_2/Ar at 625 °C as for the "calcined" sample; then, after cool-down to the desired SO_3 treatment temperature, the sample was treated for 1 h at either 160 °C or 200 °C by adding 0.5% SO_3 to the 30% O_2/Ar gas mixture. These SO_3-treated (referred to as "SO_3 dry") as well as the "calcined" samples were transferred to the glovebox under inert conditions after cool down in 30% O_2/Ar (1 l min^{-1}).

SO_3 was produced by oxidation of SO_2 via the industrially established contact process[39,40] conducted in a vertically aligned tube reactor made in-house. As mentioned in the introduction, SO_2 had been investigated in a previous study,[35] while the paper at hand discusses the impact of SO_3 treatment on LMR-NCM. The reactor consists of a ceramic tube (l = 1100 mm, $\varnothing_i$ = 12 mm, $\varnothing_o$ = 16 mm, made of Degussit AL23, Friatec, Germany), jacketed by a wound electric heating wire (l = 3,0 m, P = 350 W, Horst, Germany) that results in a heated tube length of 50 cm, a temperature sensor (Horst, Germany), and several layers of insulating ceramic fiber mats (Carbolite, Germany). The heated section of the reactor was filled with a V_2O_5 catalyst (Katalysator O4-111, BASF, Germany, original star-shaped pellets that were crushed to fit into the reactor tube) and preheated to 430 °C in an Ar (99.999%, Westfalen, Germany) flow. At 430 °C, a gas mixture of 0.5% SO_2 (99.98% purity, with <10 ppmv H_2SO_4 and <50 ppmv H_2O, Air Liquide, Germany) 30% O_2 (99.999%, Westfalen, Germany), and 69.5% Ar was fed to the reactor from the bottom end at a space velocity of 11/h corresponding to a total flow rate of 1 l min^{-1} when assuming a space filling of 50% by the catalyst. These conditions are recommended by the catalyst manufacturer to achieve a maximum conversion of SO_2 to SO_3. According to the directions for use provided by the catalyst manufacturer, the conversion from SO_2 to SO_3 is >97% at the given conditions. From the top end of the reactor, the product gas mixture (consisting of SO_3, O_2, Ar, and residual traces of SO_2) was fed to the above-described tube furnace containing the sample via a stainless steel gas line (Swagelok, USA). The overall setup to conduct the here described SO_3 treatment procedure is illustrated in Fig. 3.

The LMR-NCM samples referred to as "wet" and "SO_3 wet" in Fig. 2 (right-hand-side) were obtained by storing the "dry" and the "SO_3 dry" LMR-NCM samples, respectively, for one week in ambient air that was humidified over a water bath at 25 °C, thus exposing them to moisture (relative humidity of 85 ± 5%, as determined by a relative humidity sensor) and the typical concentration of ≈400 ppm CO_2 in air (analogous to our previous study on the formation of surface contaminants[13]). In more detail, the water bath was covered with a lid with a small hole to ensure moisture saturation on the one hand and to allow for the diffusion of CO_2 from the ambient air into the vessel. After "wet" storage, the samples were dried in a glass oven (Büchi, Switzerland) for 12 h at 120 °C under dynamic vacuum in order to remove physisorbed H_2O; subsequently, they were stored in an Ar-filled glovebox (<0.1 ppm O_2 and H_2O, MBraun, Germany) without exposure to ambient air after drying.

We have refrained from conducting wet storage experiments with the as-received LMR-NCM (referred to as "dry") after a subsequent calcination (marked as "calcined" in the black box of Fig. 2), as we believe that the effect of wet storage is essentially identical for the as-received "dry" LMR-NCM as it would be for the "calcined" LMR-NCM, since the as-received material has already undergone calcination at ⩾800°C during manufacturing, which still does not prevent it from rapidly accumulating surface contaminants (as will be shown below).

Diffuse reflectance infrared fourier transform spectroscopy (DRIFTS).—Infrared spectroscopy in diffusive reflectance mode (DRIFTS) is sensitive to infrared active species at the surface of particulate materials. DRIFTS spectra were recorded by an IR spectrometer (Cary 670, Agilent, USA) using the Praying Mantis (Harricks, USA) mirror optics that collects diffusively scattered IR radiation from the sample. Mixtures of treated and untreated LMR-NCM were prepared with 1 wt% of sample dispersed in finely ground KBr (FTIR-grade, Sigma-Aldrich, Germany, dried at 120 °C under vacuum prior to use) to characterize surface species. The sample/KBr mixture was prepared in an Ar-filled glovebox and the mixture was put in an air-tight chamber (HT reaction chamber, Harricks, UK) with IR-transparent windows (KBr single crystals, Korth Kristalle GmbH, Germany). The spectra evaluation is described in more detail in the supporting information (Fig. S1 available online at stacks.iop.org/JES/167/130507/mmedia).

X-ray photoelectron spectroscopy (XPS).—The powders were pressed to pellets ($\varnothing$ = 3 mm) inside an argon-filled glovebox using a hand press with a 3 mm die set (PIKE Technologies, USA) and mounted on an electrically insulated sample holder, which can be transferred from the glovebox into the XPS system without any air exposure using a Kratos sample transfer chamber. Samples were kept in the XPS antechamber until a pressure of ≈10^{-8} Torr was reached and were then transferred to the sample analysis chamber where the pressure was always kept below ≈10^{-9} Torr during the whole measurement period. Spectra were acquired using

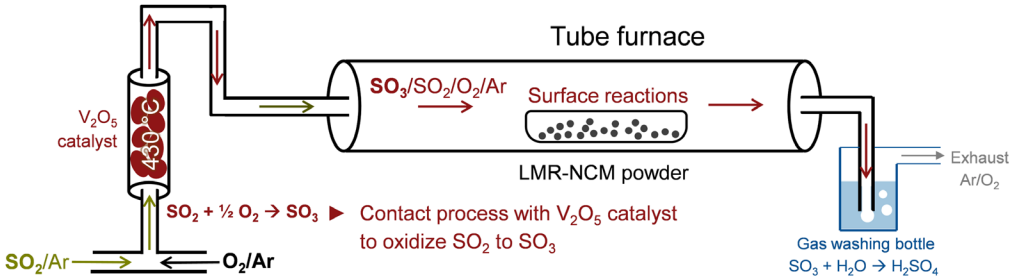

Figure 3. Detailed scheme of the tube furnace setup for the SO_3 treatment of LMR-NCM samples. On the left hand side, the contact process, i.e., the oxidation of SO_2 with O_2 over a V_2O_5 as catalyst is depicted, using a feed gas composition of 0.5% SO_2, 30% O_2, and 69.5% Ar (the latter serves as carrier gas) at a space velocity of 11/h. The gas mixture exiting the reactor and containing the highly reactive gas SO_3 then flows through the heated tube furnace, where the LMR-NCM sample is placed and where the desired reaction between SO_3 and the LMR-NCM surface takes place. The exhaust gases are quenched by a water washing bottle (on the right hand side) to avoid the emission of hazardous and corrosive SO_3.

monochromated Al Kα radiation (1486.6 eV) with an emission current of 15 mA. Survey spectra were recorded for all samples with a step size of 0.5 eV and at a pass energy of 160 eV. Detail spectra of were recorded with a step size of 0.1 eV, a pass energy of 20 eV and an emission current of 20 mA. For all measurements, a charge neutralizer was used, and the spectra were energy-calibrated to the adventitious carbon peak with a binding energy (BE) of 284.8 eV. In addition to the LMR-NCM, also the reference samples $LiSO_4$, $NiSO_4$, $NiSO_4 \cdot 6\ H_2O$, LiOH, and Li_2CO_3 (purity $>$ 98% for all compounds, Sigma-Aldrich, Germany) were measured. A Shirley background was subtracted from all spectra. A detailed overview over the applied fitting parameters and reference spectra can be found in the supporting information.

On-line mass spectrometry (OMS).—To test the reactivity of the cathode active material with the electrolyte,[41] 515 mg of cathode active material (dried at 120 °C in vacuum overnight) were mixed with 120 μl of a model electrolyte consisting of ethylene carbonate (EC) and 1.5 M $LiClO_4$ in our OMS cell hardware,[42] resulting in an industrially relevant electrolyte to CAM mass ratio of 0.35:1.[43] For the untreated "dry" and "calcined" samples, the amounts of electrolyte and CAM were doubled. As discussed in our previous work,[13] we use the thermal decomposition of EC as a probe for the amount and the reactivity of surface contaminants present on the CAM particles, and thus selected $LiClO_4$ as an electrolyte salt that does not react with hydroxide, carbonate, or hydrate surface groups. In contrast to that, $LiPF_6$ was suggested to react with carbonates forming CO_2.[44] We are aware that our "EC-only" electrolyte is quite different to commercial electrolytes, however we have demonstrated that it is well suited model electrolyte to probe the amount of surface contaminants on NCM-based cathode active materials.[13]

Before cell assembly, all cell hardware was dried for at least 12 h at 70 °C in a vacuum oven (Thermo Scientific, USA). The sealed cell containing the CAM/electrolyte mixture was placed into a programmable controlled-temperature chamber (KB 23, Binder, Germany), and then connected to the OMS system via a crimped capillary leak ($\approx$1 μl min^{-1} gas flux into the mass spectrometer).[45] First the cell was held at 10 °C for 5 h to record a stable baseline for all ion current signals (m/z = 1 to 128). After that, the temperature was raised to 60 °C and the corresponding gas evolution was recorded for 12 h (similar to storing a lithium-ion cell at elevated temperature). The cell temperature was recorded with a thermocouple positioned in a 1 cm deep channel drilled into the stainless steel cell body. For translation of the OMS ion current signals I_z into units of [ppm], the temperature was set back to 25 °C and the cell was purged with a calibration gas containing H_2, CO, O_2, and CO_2(each at a concentration of 2000 ppm in Ar, Westfalen, Germany), by these means, one can quantify the concentrations of H_2 (m/z = 2), CO (m/z = 28), O_2 (m/z = 32), and CO_2 (m/z = 44) in the cell head space.[46]

Electrode preparation and cycling.—The cathode coating slurry was produced under inert conditions analogous to our previous study on surface contaminants,[13] i.e., mixing of the solid constituents, NMP addition, and slurry preparation were carried out in an Ar-filled glovebox inside a mixing vessel which was sealed to be air-tight before transfer out of the glovebox. To produce LMR-NCM cathodes for cycling, the following ingredients were blended together: 92.5 wt% of CAM, 4 wt% carbon black (Super C65, Timcal, Switzerland), and 3.5 wt% polyvinylidene difluoride (PVdF, Solef 5130, Solvay, Belgium). Carbon black and PVdF had been vacuum dried at 120 °C for 3 days before transfer to the glovebox. After powder mixing, 0.84 g of N-methylpyrrolidone (NMP, Sigma-Aldrich, Germany) per gram of solid (54 wt% solid content) were added in several steps, in between of which the slurry was mixed with a planetary orbital mixer (Thinky, Japan) in a sealed mixing vessel until a highly viscous, lump-free coating slurry was obtained (note that the NMP addition steps were conducted in the glovebox). The final slurry was applied onto an 18 μm thick aluminum foil (MTI, USA) with a 100 μm four-edge-blade (Erichsen, Germany) inside the glovebox and then dried overnight. Disk-shaped cathodes with a diameter of 14 mm were punched out of the foil inside the glovebox and compressed at 2.5 t for 20 s outside the glovebox. Assembly and disassembly of the compression tool were carried out inside the glovebox to keep the total time of slight air exposure below one minute. In addition, the compression tool was wrapped twice with plastic bags before transferring out of the glovebox to minimize the eventual air contact of the electrodes. After compression, the cathodes were then weighed inside the glovebox, dried overnight in a vacuum oven at 120 °C, and introduced into an Ar glovebox without exposure to ambient air. The areal loading of the LMR-NCM cathodes after drying was 5.0 ± 1.0 $mg_{LMR\text{-}NCM}/cm^2$, corresponding to an areal capacity of 1.6 ± 0.3 mAh cm^{-2} when referenced to the specific charge capacity of 320 $mAh/g_{LMR\text{-}NCM}$ for the activation in the 1st cycle. Note that the reversible capacity after activation is around 250 $mAh/g_{LMR\text{-}NCM}$.

The graphite anodes were prepared with a composition of 95 wt% T311 (SGL Carbon, Germany) and 5 wt% PVdF (Kynar HSV900, Arkema, France) under addition of 0.69 g of NMP per gram of solids (59 wt% solid content) in the same sequential mixing process as for the cathodes. The resultant coating slurry was applied onto a 12 μm thick copper foil (MTI, USA) with a 100 μm four-edge-blade (Erichsen, Germany) and then dried overnight in a convection oven at 50 °C. Disk-shaped electrodes with a diameter of 16 mm were punched out of the foil and compressed at 0.5 t for 20 s. The anodes were then weighed, dried overnight in a vacuum oven at 120 °C, and introduced into an Ar glovebox without exposure to ambient air. The areal loading of the graphite anodes after drying was 6 ± 1 $mg_{graphite}$ cm^{-2}, corresponding to an areal capacity of 1.9 ± 0.3 mAh cm^{-2} based on a specific capacity of 340 $mAh/g_{graphite}$ (corresponding to 1.5 ± 0.25 mAh cm^{-2} when referenced to the reversible LMR-NCM capacity after activation of 250 $mAh/g_{LMR\text{-}NCM}$). The thereby achieved balancing of the LMR-NCM//graphite full-cells ranges from 1:1.2 to 1:1.3 in units of [mAh cm^{-2}] referenced to the 1st charge capacity of the cells.

Electrochemical testing was conducted in CR2032 type coin cells at 45 °C with 30 μl of an electrolyte containing fluoroethylene carbonate (FEC) which already had been applied in a previous study from BASF and our group,[47] viz., FEC:DEC (12:64 v:v) with 1 M $LiPF_6$ and 24 vol% of an additional fluorinated co-solvent to improve full-cell cycling stability (BASF, Germany). Anode and cathode are separated by one polyolefin separator (Celgard H2013, USA) with 17 mm diameter. The cycling protocol is summarized in Table I and consists of the following sequence: i) a constant-current (CC) activation cycle at C/15 (segment 1), which is required to obtain the full capacity of the LMR-NCM cathode[48]; ii) three cycles at slow rate of C/10 (CC) (segment 2); iii) a DCIR (direct current internal resistance) pulse, which is a 10 s discharge pulse (C/5) at 40% SOC (state-of-charge) with simultaneous recording of the cell voltage to calculate the internal resistance (sum of all resistance contributions) using Ohm's law (segment 3); iv) three cycles at fast rate of 3 C with CCCV charging (CC charge followed by a constant-voltage hold until the current drops below C/10) and CC discharging (segment 4); and, v) 33 standard cycles with C/2 (CC) charging and 1 C (CCCV) discharging (segment 5). Segments 2–5 are repeated several times. Note that C-rates are referenced the reversible capacity of LMR-NCM after activation of 250 mAh g^{-1}.

Results

Identification of surface species on pristine and SO_3-treated LMR-NCM.—Infrared spectroscopy provides qualitative understanding of how the SO_3 treatment impacts the LMR-NCM particle surface. While Fourier Transform infrared spectroscopy (FTIR) in transmission mode is not very sensitive to surface groups on the oxide particles, Diffusive Reflectance Infrared Fourier Transform Spectroscopy (DRIFTS) is very sensitive even to low amounts of IR-active species on the particle surface, as demonstrated in our recent study on surface contaminants.[13] As described in the supporting information, all spectra are normalized to the oxide band at 570 cm^{-1}. Figure 4 contains spectra of the as-received and dried ("dry") and the SO_3-treated ("SO_3 dry") LMR-NCM. For the detailed band assignment, see Table II.

The "dry" reference sample (black line; lower-most line in Fig. 4) contains a significant amount of carbonate impurities, as indicated by the band around 1470 cm^{-1}. This asymmetrical CO_3 stretching is split into two bands due two lower symmetry of the carbonate anion at the surface compared to carbonate anions in the bulk of pure Li_2CO_3.[50] Even in case of the LMR-NCM samples that were not treated with SO_3 gas ("dry," "wet" and "calcined"; left panel), a trace amount of sulfate is detected (SO_4 stretch around 1130 cm^{-1}), which accounts for trace impurities of transition metal sulfates typically used as dissolved salts in the precipitation process to prepare the precursor in the LMR-NCM manufacturing process. Since there are no characteristic features of the sulfite ion detected, i.e., no strong band at ca. 1000 or 950 cm^{-1}(see Table II), this DRIFTS analysis gives a first hint that in contrast to sulfates, no sulfites have been formed. This is supported by the XPS analysis that will be discussed later, where we will find that SO_3 treatment exclusively leads to sulfate formation.

Since the first step of our thermal gas treatment procedure is the calcination at 625 °C, the calcined sample represents the best reference for a comparison with the SO_3-treated LMR-NCM. Indeed, after calcination (black line), the carbonate band has nearly vanished due to thermal decomposition of all surface impurities except Li_2CO_3, which in its bulk form decomposes above ≈700 °C.[65] This is of course in great contrast to "wet" LMR-NCM (turquoise line in Fig. 4), where a negative band is observed for the hydrate/hydroxide region between 2500 and 3600 cm^{-1} (minimum at 3450 cm^{-1}), which seems counterintuitive, since one would expect an upward pointing feature for infrared absorbing species. A very high concentration of surface contaminants would explain the negative shaped hydrate/hydroxide region in case of "wet" LMR-NCM.[13] In case of the carbonate band around 1470 cm^{-1}, an also frequently observed phenomenon is observed, namely a derivative shape of the DRIFTS signal, which is known to occur for highly concentrated species in DRIFTS spectroscopy.[66] "Derivative shape" means that the peak does not exclusively point in one direction, but that it is distorted in such way that it contains upward as well as downward pointing parts (best illustrated by the feature of the turquoise line near 1470 cm^{-1} in the left panel of Fig. 4), which clearly is the case for the carbonate signal of "wet" LMR-NCM. Consequently, it is safe to say that the "wet" LMR-NCM sample must have a much higher carbonate content than the "dry" and the "calcined" samples. The latter one does only have an extremely weak carbonate band and no hydroxide/hydrate signal at all.

In case of the SO_3 gas treated LMR-NCM materials, namely the "SO_3 160 °C dry" and the "SO_3 200 °C dry" samples, the intense sulfate signals at 1130 cm^{-1} including the shoulder/side band at 1160 cm^{-1} clearly prove the formation of surface sulfates over the course of the SO_3 treatment (Table II). The sulfate band intensity for the "SO_3 200 °C dry" sample is even higher compared to the "SO_3 160 °C dry" sample, indicating a higher amount of sulfate at higher SO_3 gas treatment temperature. This is consistent with XPS data, as will be discussed in the following section. The side bands at 1300 cm^{-1} and 820 cm^{-1} are likely due to either pyrosulfate groups[51–53,55–60]or to vibrational features caused by the interaction of neighboring sulfate groups on the oxide surface.

After storage of the LMR-NCM samples at ambient air with high relative humidity, both of the SO_3-treated samples ("SO_3 160 °C wet" and "SO_3 200 °C wet") exclusively exhibit upward pointing, i.e., purely absorptive bands in both the carbonate and the hydrate/hydroxide region (right panels in Fig. 4). While a derivative shape of the carbonate band around 1470 cm^{-1} was observed for the "wet" sample that was not treated with SO_3 (turquoise line in the left panel of Fig. 4), no such behavior is observed for the SO_3-treated samples after exposure to humid air ("SO_3 160 °C wet" and "SO_3 200 °C wet"), which clearly indicates that these samples contain much less hydrate and hydroxide species compared to untreated "wet" LMR-NCM, demonstrating their superior robustness against exposure to moisture. Interestingly, the sulfate stretching vibrations at

Table I. Cycling protocol for LMR-NCM//graphite coin cells at 45 °C with 30 μl of electrolyte (FEC:DEC (12:64 v:v) with 1 M $LiPF_6$ and 24 vol% of an additional fluorinated co-solvent), and one polyolefin separator (Celgard H2013, USA). Segments 2–5 are repeated 4 times and C-rates are referenced to 250 mAh/$g_{LMR-NCM}$; CC (constant-current), CCCV (constant-current constant-voltage with C/10 lower current limit), DCIR (direct current internal resistance) measurement at 40% SOC (state-of-charge), with "SOC" referring to the last discharge capacity of segment 2. The partial charge and discharge cycle directly before/after the DCIR pulse was carried out at C/10. Before the DCIR pulse (at a current corresponding to C/5) was applied, the cell was allowed to rest for 1 h in OCV mode.

	Segment	Potential range [V vs Li/Li^+]	Charge rate	Discharge rate	Cycles	Repeats
1	Activation	4.8−2.0	C/15 (CC)	C/15 (CC)	1	0
2	Slow cycling	4.7−2.0	C/10 (CC)	C/10 (CC)	3	4 (start of loop)
3	DCIR	After C/10 charge to 40% SOC and 1 h OCV	—	C/5 pulse	1	4
4	Fast cycling	4.7−2.0	C/2 (CCCV)	3 C (CC)	3	4
5	Standard cycling	4.7−2.0	C/2 (CCCV)	1 C (CC)	33	4 (end of loop)

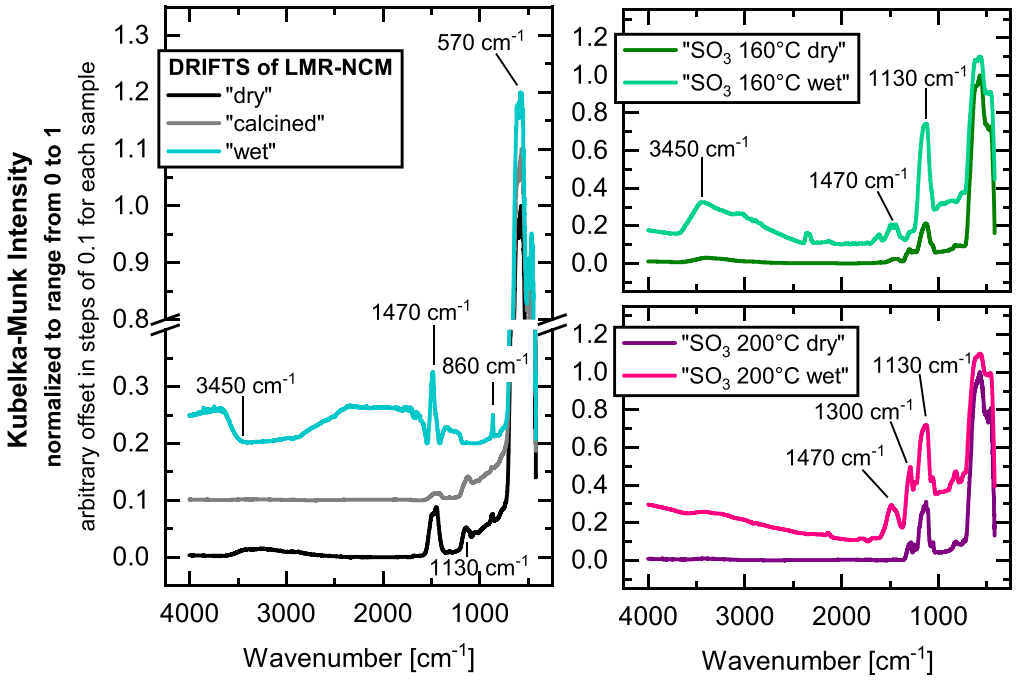

Figure 4. DRIFT spectra of the differently treated LMR-NCM samples, with the Kubelka-Munk intensity normalized to the oxide band at 570 cm^{-1} (see supporting information); the spectra are offset arbitrarily along the y-axis for better visibility. Left panel: as-received and dried LMR-NCM ("dry") as well as after calcination of the "dry" sample ("calcined") or after its wet storage ("wet"). Upper right panel: LMR-NCM treated with SO_3 at 160 °C ("SO_3 160 °C dry") and after its wet storage ("SO_3 160 °C wet"). Bottom right panel: LMR-NCM treated with SO_3 at 200 °C ("SO_3 200 °C dry") and after its wet storage ("SO_3 200 °C wet").

1130 cm^{-1} are significantly enhanced when comparing "wet" stored SO_3-treated samples to "dry" SO_3-treated samples. This could either point to an increased absorption coefficient of hydrated or protonated sulfate anions versus "free" sulfate anions or to surface rearrangements. In other words, this might indicate that SO_3 treated LMR-NCM with sulfate surface groups can still get hydrated when exposed to humidity.

The impact of SO_3 gas treatment on the surface modification of LMR-NCM and on the vulnerability of the material to "wet" storage will be discussed further in the upcoming XPS section.

In Fig. 5, S 2p spectra of pristine and SO_3-treated LMR-NCM samples can be seen. The main figure displays the data for the "200 °C SO_3" sample. According to the literature[67,68] and our reference measurements of sulfates in the supporting information (see Fig. S2), the S $2p_{3/2}$ signal of sulfates (labelled as "M-SO_4") is found at 168.7 ± 0.2 eV and is clearly detected at that position for the "200 °C SO_3" sample, while no sulfite (labelled at "M-SO_3," with S $2p_{3/2}$ at 166.8 ± 0.2 eV) or sulfide (labelled as "M-S," with S $2p_{3/2}$ at 163.0 ± 1.0 eV) can be found.[67,68] Thus it is clear that SO_3 treatment exclusively leads to the formation of sulfate groups, as was already indicated by the above DRIFTS analysis. The impact of SO_3 treatment temperature is demonstrated by the comparison of three LMR-NCM samples in the inset of Fig. 5. In case of the as-received and dried LMR-NCM ("dry"), no significant peak is visible in the S 2p spectrum, i.e., the sulfate impurities in pristine LMR-NCM, which were discussed above on the basis of the DRIFTS data, must be a rather minor amount. The LMR-NCM treated in SO_3 at 160 °C ("SO_3 160 °C dry") already exhibits a clearly marked "M-SO_4" signal, with a high peak of high intensity, which is doubled for the "SO_3 200 °C dry" sample. This clearly indicates that an increase in SO_3 treatment temperature leads to a higher amount of sulfate formed on the LMR-NCM surface. Note that we had also explored the treatment of LMR-NCM with SO_3 at a lower temperature of 120 °C, but that the M-SO_4 XPS signals in this case were so low that we decided to not examine it any further.

In the following, we will continue to discuss the surface composition of the untreated and SO_3-treated LMR-NCM samples on the basis of the XPS O 1 s data (Fig. 6).

Peak fitting of the O 1s region was performed based on literature data,[69–72] as well as reference data, i.e., O 1s spectra of Li_2SO_4, $NiSO_4$ and $NiSO_4 \cdot 6\ H_2O$ (see Fig. S2). For "dry" LMR-NCM, two distinct features can be seen, the lattice oxygen (529.2 ± 0.2 eV) labelled as 'Lattice O^{2-}' as well as hydroxide/carbonate impurities (531.3 ± 0.2 eV) labelled as "M-OH/CO_3"; details on these binding energy assignments are given in the "XPS reference data" section of the supporting information.

For the "SO_3 160 °C dry" sample, a sulfate O 1s peak labelled as "M-SO_4" appears in addition to the hydroxide/carbonate/hydroxide impurity peak, which is in line with the S 2p data. It has to be noted that the apparent increase of the "M-OH/CO_3" component in the XPS fit of the "SO_3 160 °C dry" compared to the "dry" LMR-NCM is likely due to some uncertainty in the quantitative differentiation between the hydroxide/carbonate impurities (531.3 ± 0.2 eV) and sulfate (532.0 ± 0.2 eV) signals rather than to an increase of surface impurities after the SO_3 treatment; a more quantitative analysis is unfortunately impossible, since the peak maxima are only 0.3–-0.8 eV apart from each other. This leaves two options to explain the "M-OH/CO_3" component in case of "SO_3 160 °C dry": (i) OH/CO_3 is increased compared to untreated "dry" LMR-NCM, but we cannot use the data as a proof of an increase, since the uncertainty is too big; (ii) the amount of OH/CO_3 is not increased and the signal change only reveals the uncertainty of the method. While we cannot exclude a tiny contamination with ambient air, we did not deliberately expose "SO_3 160 °C dry" LMR-NCM to ambient air or moisture, so we believe that option (ii) is more likely.

In case of the "SO_3 200 °C dry" sample, the "M-SO_4" fraction is drastically increased, which is again in line with the S 2p data shown in Fig. 5. The hydroxide/carbonate impurity peak appears to have vanished, which should again not be interpreted in a quantitative manner due to the above-mentioned uncertainty of the fit, but as a trend it is consistent with the decrease of the carbonate and hydroxide bands after SO_3 treatment observed by DRIFTS (Fig. 4).

Table II. Assignment of vibrational frequencies of the relevant species with strong (s), medium (m), weak (w) intensity or shoulder (sh).

Frequency	Assignment	Comments/literature references
Region around 3450 cm^{-1} (2500 to 3600 cm^{-1})	OH^-/H_2O	OH^- stretching vibration[49] at 3575 cm^{-1} Stretching vibration of the hydrate H_2O molecule[49] at 2965 cm^{-1}
1470 cm^{-1} (s)	CO_3^{2-}, HCO_3^-	CO_3 asymmetric stretch[50–54]
1300 cm^{-1} (s)	$S_2O_7^{2-}$	52, 53, 55, 56
1130 cm^{-1}(s)	SO_4^{2-}	SO_4 stretch[51–53,57–60]
1060 cm^{-1} (sh)	SO_4^{2-}, $S_2O_7^{2-}$	51–53, 55–60
1002 (m)	SO_3^{2-}	51, 52, 61
954 (s)	SO_3^{2-}	51, 52, 61
860 cm^{-1}	CO_3^{2-}	CO_3 bending out of plane vibrations[50–53]
820 cm^{-1} (w-m)	$S_2O_7^{2-}$	52, 53, 55, 56
632 (w)	SO_3^{2-}	51, 52, 61
570 cm^{-1} (s)	$Li_{1+x}M_{1-x}O_2$	MO_6 stretch[62–64]

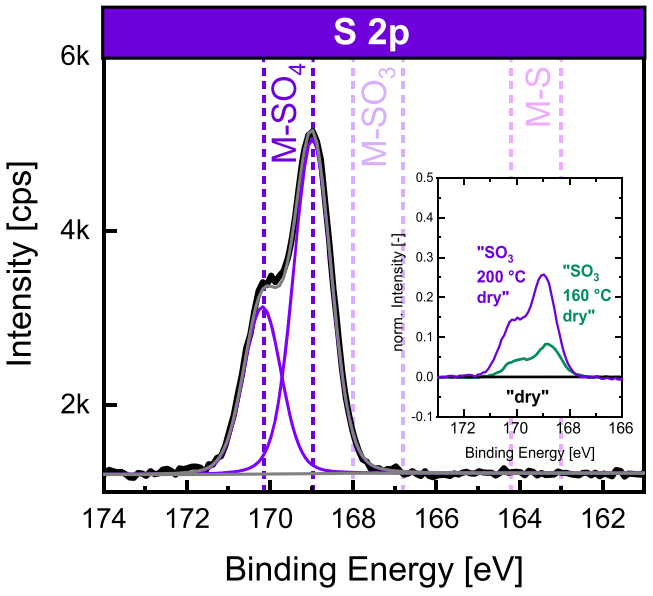

Figure 5. Analysis of the S 2p XPS data of the LMR-NCM material treated in SO_3 gas at 200 °C ("SO_3 200 °C dry"; main figure), with the *y*-axis given in counts per second (cps). Inset: Comparative signal intensities of the dried as-received LMR-NCM ("dry") and of the samples treated with SO_3 gas at different temperatures ("SO_3 160° dry" and "SO_3 200 °C dry") normalized to the intensity at 1200 eV. Background subtraction (data in the inset) was done after normalization.

Impact of wet storage on the surface composition.—We now want to elucidate the effects of LMR-NCM material storage at high relative humidity ambient air ("wet" storage) by additional XPS data. Figure 7 thus depicts O 1s spectra of as-received "calcined" and "wet" LMR-NCM samples in comparison to LMR-NCM treated with SO_3 at 160 °C in "dry" state (same data as mid panel in Fig. 6) as well as after "wet" storage.

When comparing as-received "calcined" and "wet" LMR-NCM (Fig. 7, left panel), the peak representing hydroxide/carbonate impurities is more pronounced after storage of the material at high relative humidity ambient air, which is in line with DRIFTS data (Fig. 4). Comparing the SO_3-treated samples in "dry" and "wet" condition (Fig. 7, right panel), changes in hydroxide/carbonate and sulfate content are within the uncertainty of the fit, so that it is not possible to determine whether the amount of hydroxide/carbonate species has increased upon wet storage. The only significant difference between the two spectra is the appearance of an additional peak at ≈533 eV appearing after "wet" storage (labelled as "misc."), which either points to the formation of a hydrated sulfate or to sodium contamination, as detailed in the supporting information: A comparison of anhydrous nickel sulfate with its hydrate $NiSO_4 \cdot 6\,H_2O$ reveals a signal at ≈533.5 eV for the hydrate (Fig. S2 and Table SI). On the other hand, the XPS survey scan of the "SO_3 160 °C dry" sample clearly shows evidence for the presence of sodium (Fig. S3), presumably from the synthesis process, so that the peak at ≈533 eV could also correspond to the Na_{KLL} Auger line at 533 eV.[73] It is unclear, if both effects play a role or if only one of them causes the additional peak at ≈533 eV for "wet" stored SO_3-treated LMR-NCM.

Effect of surface contaminants on electrolyte stability.—Having discussed the surface composition of SO_3-treated LMR-NCM via DRIFTS and XPS analysis, we now want to investigate the impact of the different LMR-NCM surfaces on the stability of an ethylene carbonate (EC) based electrolyte in contact with the cathode active material at elevated temperature. The following experiment is based on our previous study,[41] where we demonstrated that catalytically active hydroxide ions (OH^-) in the presence of trace amounts of

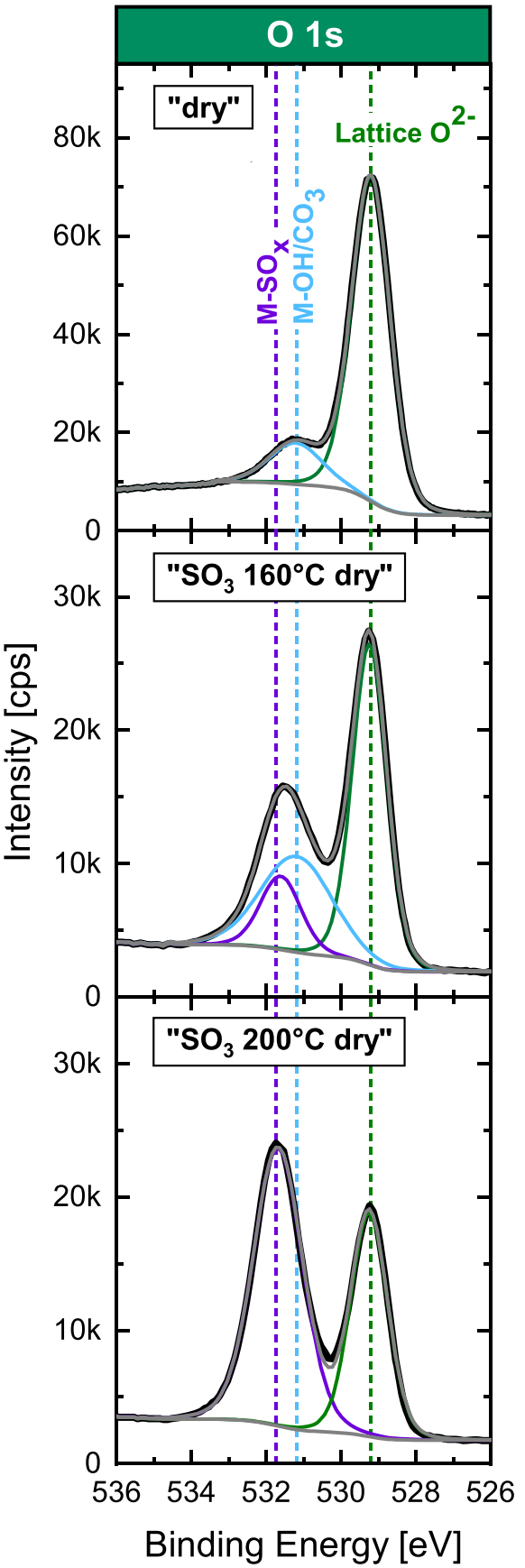

Figure 6. XPS O 1s region for the LMR-NCM samples "dry," "SO_3 160 °C dry" and "SO_3 200 °C dry" (same samples for which the S 2p data are shown in Fig. 5).

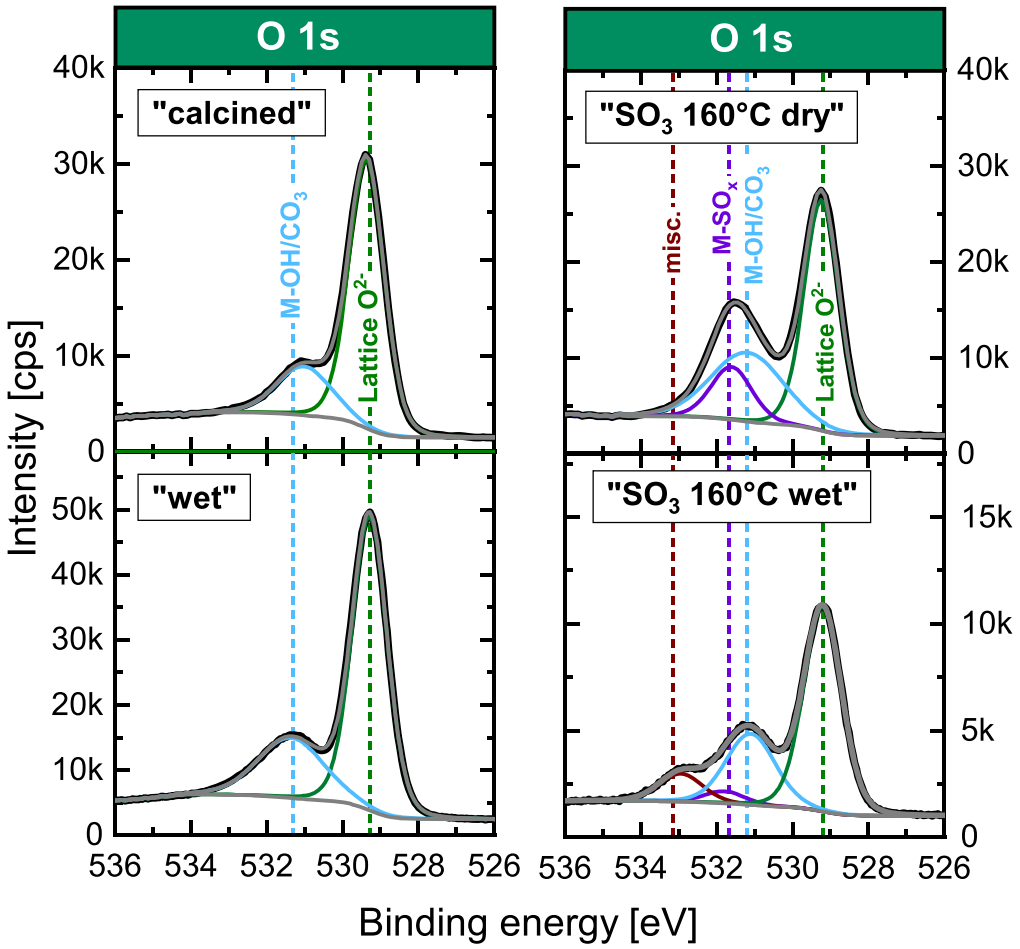

Figure 7. Effect of LMR-NCM material storage at high relative humidity ambient air ("wet" storage, see Fig. 2). O 1 s XPS of as-received "calcined" and "wet" LMR-NCM (left panel) compared to the sample treated with SO_3 at 160 °C without and after exposure to high humidity ambient air ("SO_3 160 °C dry" and "SO_3 160 °C wet," respectively; right panel).

H_2O can lead to a rapid decomposition of EC at the approximately upper temperature limit for lithium-ion battery operation. The decomposition of EC is induced by a nucleophilic attack of OH^-, and a subsequent ring opening reaction of EC under abstraction of CO_2. In a more recent study,[13] we demonstrated that a similar reaction can be triggered by basic surface contaminants like $NiCO_3 \cdot 2\,Ni(OH)_2 \cdot x\,H_2O$. We also showed that this reaction not only leads to the decomposition of EC-based electrolyte and accumulation of CO_2 gas in the battery cell, but also to a deterioration of battery performance.

For this purpose we conducted an on-line mass spectrometry (OMS) test analogous to our previous work,[13,41] exposing a mixture of cathode active material to EC-only electrolyte (EC + 1.5 M $LiClO_4$) at a realistic mass ratio[24] of 0.35:1 at an elevated temperature of 60 °C and following the evolution of CO_2 over time. This EC decomposition experiment only accounts for hydroxide based impurities,[13,41] but not for carbonates such as Li_2CO_3, which does not react with the organic carbonate solvent itself.[74] We mixed 515 mg LMR-NCM with 120 μl EC-only electrolyte; in case of the untreated "calcined" and "dry" samples, 1.03 g cathode active material and 240 μl electrolyte were used to enhance the sensitivity for the expected much smaller amounts of evolved CO_2. The impact of wet storage on gassing was investigated for untreated as well as SO_3-treated LMR-NCM (Fig. 8).

Figure 8a illustrates the cell temperature set points (black line) and the cell temperature profile (red line) in the OMS experiment. First, the CO_2 baseline signal is recorded at 10 °C for 3 h and subsequently a step to 60 °C is applied to trigger the EC decomposition reaction. After 12 h at 60 °C, the total amount of CO_2 has reached ≈56 $\mu mol/g_{EC}$ for the untreated LMR-NCM after a 1 week storage at high relative humidity air ("wet," see Fig. 8b) compared to ≈27 $\mu mol/g_{EC}$ for as-received and dried LMR-NCM ("dry"), which corresponds to an increase by a factor of two. However, with the as-received and calcined LMR-NCM ("calcined"), the CO_2 evolution is drastically reduced, leading to the formation of only ≈9 $\mu mol/g_{EC}$ after 12 h at 60 °C, which is ≈3-fold less than observed for the "dry" sample. It should be noted that for the "dry" sample a different temperature chamber was used which needed slightly more time to reach the 60 °C setpoint temperature (data not shown), so that the initial CO_2 increase is a bit more delayed compared to the other samples. When determining the CO_2 evolution rates from the CO_2 concentration increase over the last hour of the experiment (Fig. 8d), the differences become even more drastic, with an essentially negligible CO_2 evolution rate of $\approx 6.6 \cdot 10^{-13}$ $mol_{CO2}/(s \cdot g_{EC})$ for the "calcined" LMR-NCN sample compared to $\approx 1.7 \cdot 10^{-10}$ and $\approx 3.7 \cdot 10^{-10}$ $mol_{CO2}/(s \cdot g_{EC})$ for the "dry" and the "wet" samples. The impact of wet storage of cathode active materials on the EC decomposition at elevated temperatures as well as the much reduced degradation after a complete removal of surface contaminants by are-calcination of cathode active materials in combination with a strict avoidance of air exposure has already been described in our previous study with NCM811.[13]

Figure 8c shows the same CO_2 gassing analysis for the LMR-NCM material treated with SO_3 at 160 °C before and after wet storage ("SO_3 160 °C dry" and "SO_3 160 °C wet," respectively). For both cases, the total amount of evolved CO_2 over 12 h at 60 °C is identical (≈7 $\mu mol/g_{EC}$) and also quite similar to the "calcined" sample that was not treated with SO_3 (≈9 $\mu mol/g_{EC}$). Furthermore,

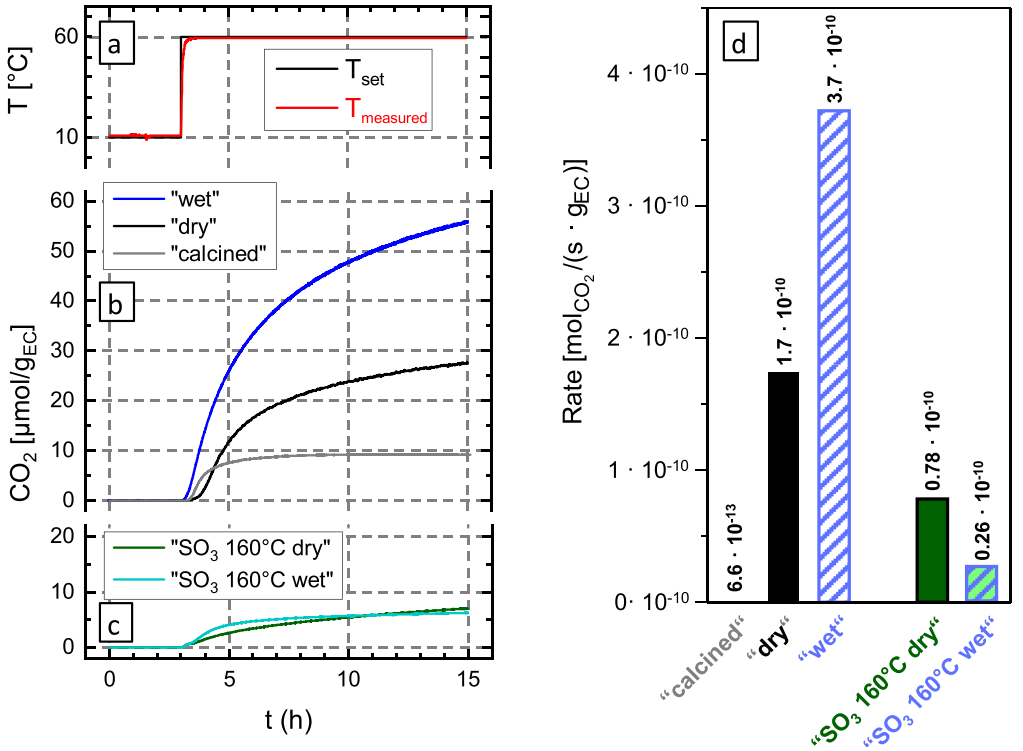

Figure 8. (a) Temperature set point and cell temperature vs time during (b) OMS measurements with mixtures of 120 μl of EC-only electrolyte (1.5 M $LiClO_4$ in EC) with 515 mg of untreated cathode active material in the conditions "wet" (blue line), "dry" (black line) and "calcined" (grey line). The total CO_2 amount is normalized to the mass of electrolyte [$\mu mol_{CO2}/g_{EC}$] (y-axis). (c) The green lines show the CO_2 evolution of LMR-NCM treated with SO_3 at 160 °C before and after wet storage ("SO_3 160 °C dry" and "SO_3 160 °C wet," respectively). (d) The CO_2 evolution rate is determined from the slope (linear fit) of the CO_2 signal in the last hour of the measurement.

the CO_2 evolution rate (Fig. 8d) of the "wet" SO_3-treated sample, appears to be slightly lower than the one of "dry" SO_3-treated material ($\approx 0.26 \cdot 10^{-10}$ compared to $\approx 0.78 \cdot 10^{-10}$ $mol_{CO2}/(s \cdot g_{EC})$), which might be a deviation within the error margin of the method. In summary, the EC hydrolysis experiments demonstrate that the SO_3 treatment leads to a preservation of the low level of hydroxide-based surface contaminants achieved by the prior calcination, even if exposed to excessive moisture.

Cycling of LMR-NCM//graphite cells.—LMR-NCM//graphite coin cells with 30 μl of electrolyte (BASF) using differently pre-treated LMR-NCM samples were subjected to extensive cycling at an elevated temperature of 45 °C. The voltage profiles of the first activation cycle at C/15 are displayed in Fig. 9. The characteristic features, namely the sloping plateau between 3 and 4.4 V as well as the activation plateau at 4.5 V are similar for SO_3-treated as well as untreated LMR-NCM samples, while the first cycle charge and discharge capacities vary. First, the calcination of the as-received LMR-NCM ("calcined") positively impacts the activation charge capacity, resulting in an increased capacity of 365 mAh g^{-1} compared to 340 mAh g^{-1} for as-received and dried LMR-NCM ("dry"). This might be explained by a re-intercalation of lithium from surface impurities into the layered oxide lattice during calcination under oxygen, as reported previously for NCM622.[22]

In contrast, the SO_3-treated samples exhibit a lower capacity of 319 mAh g^{-1} during the first charge. The same holds true for the first discharge, with 252–254 mAh g^{-1} for the SO_3-treated samples compared to 271 mAh g^{-1} for the untreated material and 274 mAh g^{-1} for the calcined one. However, this difference in initial discharge capacity may not be relevant for the practical performance of a battery cell with regards to cycle-life and rate capability, which will be discussed in the following.

From Fig. 10a it can be seen that the 1 C cycling capacity retention is rather similar for the "dry," "calcined," and the 160 °C

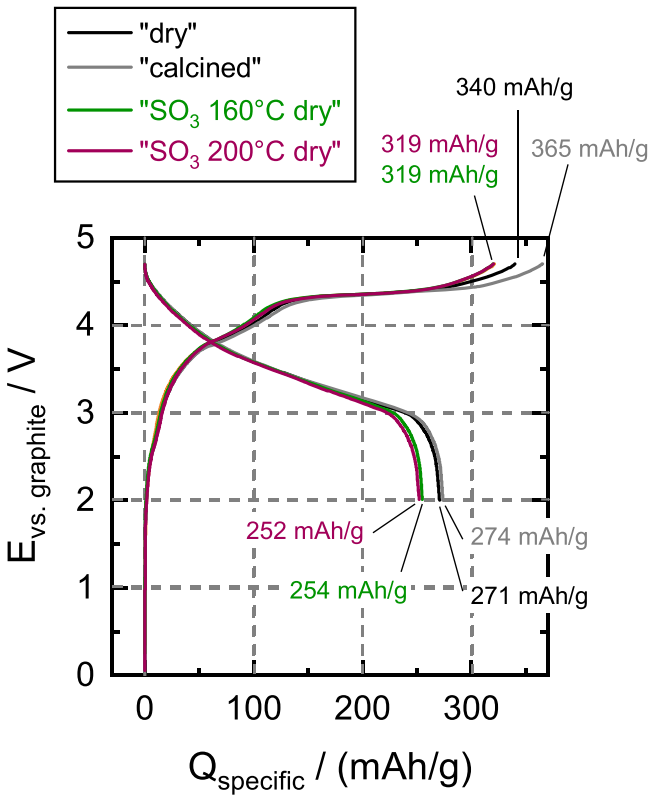

Figure 9. Voltage profiles of LMR-NCM//graphite coin cells for the first activation cycle at 45 °C (4.8 V–2.0 V at C/15). Comparison of SO_3-treated and untreated LMR-NCM. Cell setup and cycling protocol are described in Table I.

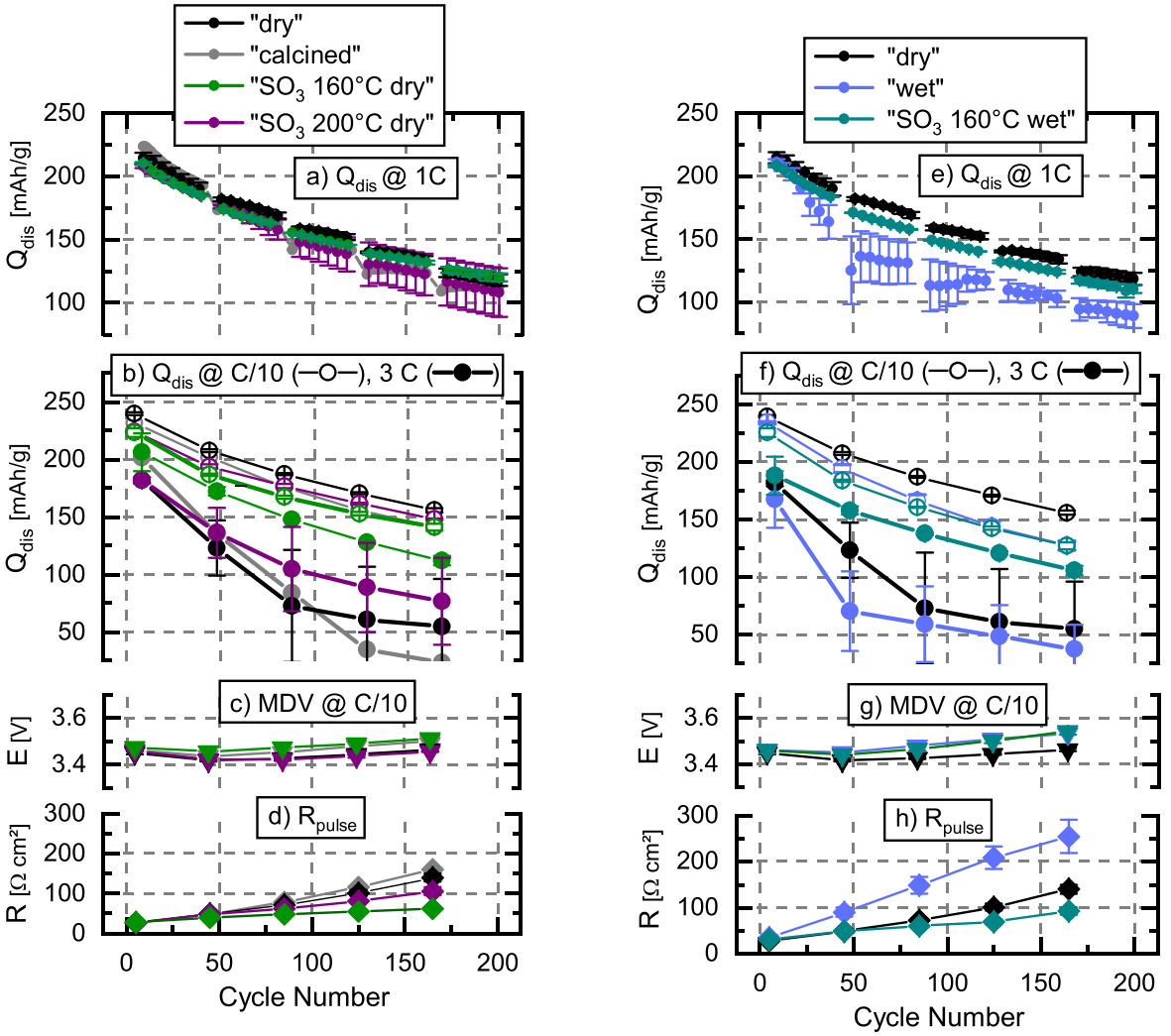

Figure 10. (a)–(d) Impact of SO_3 treatment on full-cell performance of LMR-NCM//graphite coin cells with differently pre-treated LMR-NCMs at 45 °C (average of two cells each, with error bars representing maximum and minimum values). (e)–(f) Effect of a one week long storage at high relative humidity air on SO_3-treated and untreated LMR-NCM materials ("dry" data are the same as in panels (a)–(d)). The various panels show: (a), (e) Discharge capacity (Q_{dis}) at 1 C (only every fifth cycle is displayed for the sake of better visibility); (b), (f) discharge capacity at intermittent cycles at C/10 and 3 C (the last one of the three cycles for every rate is displayed); (c), (g) mean discharge cell voltage (MDV) at C/10; and, (d), (h) DCIR pulse resistance (R) after charge to 40% SOC. The detailed cell setup and cycling protocol are given in the Experimental section and in Table I.

SO_3-treated LMR-NCM materials, while the capacity retention and the cell-to-cell deviation is slightly worse for the "SO_3 200 °C dry" sample, which suggests that the SO_3 treatment at 200 °C is perhaps too harsh. Overall, the discharge capacity at C/10 (Fig. 10b, open circles) is slightly higher for untreated LMR-NCM ("dry" and "calcined") compared to the SO_3-treated samples, which is consistent with a minor loss of active lithium due to sulfation as evidenced by the first-cycle discharge capacity (see Fig. 9). However, while the 3 C rate performance (b, solid circles) of "dry" and "calcined" LMR-NCM is comparable, it is drastically improved by the SO_3 treatment, particularly for the LMR-NCM material treated in SO_3 at 160 °C ("SO_3 160 °C dry"), again indicating that the higher SO_3 treatment temperature and the thus higher extent of M-SO_4 surface groups (see Fig. 5) is disadvantageous. For this reason, the LMR-NCM material treated in SO_3 at 160 °C was chosen for the above OMS experiments to investigate the impact of wet storage on the decomposition rate of EC at 60 °C.

The mean discharge voltage of the LMR-NCM//graphite cells is similar for all LMR-NCM samples (Fig. 10c), which means that the SO_3 treatment did not significantly influence the electrochemical bulk properties and bulk charge/discharge characteristics of the LMR-NCM samples. In contrast, the internal resistance build-up during cycling (measured from 10 s DCIR pulses at 40% SOC) is drastically reduced by the SO_3 treatment (Fig. 10d). In fact, the trend of the thus obtained resistance values is consistent with that observed for the 3 C rate performance (Fig. 10b, solid circles): The "SO_3 160 °C dry" sample has the lowest resistance build-up and consequently the best rate capability.

The key question to be answered in this work is, whether the sulfated LMR-NCM material is more robust against wet storage conditions, as was indicated by the above DRIFTS, XPS, and OMS analysis, and whether this indeed would be reflected in a superior cycling performance after wet storage. The comparison of the extended charge/discharge performance of LMR-NCM//graphite cells with the untreated "dry" and "wet" LMR-NCM samples in Fig. 10 clearly illustrates the adverse effect of wet storage conditions on untreated LMR-NCM in terms of cycle-life (Fig. 10e), rate performance (Fig. 10f), and resistance build-up (Fig. 10h). Only the mean discharge voltage (Fig. 10g) is unaffected by wet storage conditions, which means that surface contaminants do not significantly influence the electrochemical bulk charge/discharge characteristics of the LMR-NCM material. This observation is supported by the electrochemical charge/discharge profiles of the first C/15 cycle shown in Fig. S4 in the supporting information. These voltage

profiles are rather similar for "dry" and "wet" LMR-NCM, independent of whether they have been SO_3 treated or not prior to exposure to ambient air at high relative humidity.

In contrast to untreated LMR-NCM, the cycling performance of the SO_3-treated sample is not significantly affected by the wet storage. The capacity retention of the "SO_3 160 °C wet" sample (Fig. 10e, green symbols) is similar to untreated "dry" LMR-NCM (black symbols), which means it is also similar to the "SO_3 160 °C dry" material (compare Fig. 10e). Moreover, the rate capability of the "SO_3 160 °C wet" material is even better than the one of untreated LMR-NCM in dry condition (Fig. 10f), and again similar to the "SO_3 160 °C dry" material (compare Fig. 10f). Finally, the "160 °C SO_3 wet" material has a similar resistance build-up as the "dry" LMR-NCM (Fig. 10h), which is only slightly higher than for the "SO_3 160 °C dry" material (compare Fig. 10d). This dramatic improvement of the storage stability due to SO_3 treatment becomes even more apparent when comparing the resistance build-up of untreated vs 160 °C SO_3-treated LMR-NCM, both in "wet" condition (Fig. 10h).

In summary, the SO_3 treatment at 160 °C renders the LMR-NCM material robust against extended storage at high relative humidity in terms of cycling performance and gassing. It therefore is a powerful protection method for cathode active material particles to allow their storage and handling in ambient atmosphere.

Conclusions

In this study we present a novel, continuous, and scalable procedure for the surface sulfation of LMR-NCM cathode active materials, which can be integrated into the industrial manufacturing process of LMR-NCM and other cathode active materials. It combines SO_3 formation by the established contact process with the subsequent SO_3 treatment of LMR-NCM in a tube furnace directly after the removal of surface contaminants by calcination, or alternatively directly integrated into the cool-down step in the production of LMR-NCM.

We show that this surface treatment leads to the formation of surface sulfate groups. We further demonstrate the positive impact of this surface sulfation on the electrochemical performance of LMR-NCM in full-cells as well as on its robustness towards ambient storage and handling.

In the SO_3 treatment at 160 °C or 200 °C, sulfates are formed on the surface of LMR-NCM, as shown by the surface sensitive spectroscopic analysis techniques DRIFTS and XPS. This sulfate formation is accompanied by a minor loss of active lithium that is evident from the first-cycle charge capacity, which is however overcompensated by positive effects such as increased rate capability, reduced resistance build-up, less gassing, and enhanced storage stability.

We showcase the superior robustness of SO_3-treated LMR-NCM to ambient storage and handling by storing it for one week at high relative humidity ambient air. Finally, measurements with LMR-NCM//graphite full-cells demonstrate that there is no performance loss after wet storage of SO_3-treated LMR-NCM, in contrast to untreated LMR-NCM, which suffers from significant capacity fading if subjected to the same wet storage conditions. Another important aspect is the drastically reduced internal resistance build-up for SO_3-treated LMR-NCM material. In summary, our surface modification approach demonstrated for LMR-NCM is a powerful tool not only to induce robustness against atmospheric moisture and CO_2, but also to enhance the rate capability and thus the power density of layered oxides.

Acknowledgments

The authors thank BASF for financial support of this research through the framework of its Scientific Network on Electrochemistry and Batteries. In particular, we thank Dr. Manuel Mendez, Dr. Markus Hölzle, and Dr. Pascal Hartmann (BASF) for fruitful discussions and helpful advice. We further thank Maximilian Pöverlein for his dedicated work and support of this project during his Bachelor's thesis.

ORCID

Johannes Sicklinger https://orcid.org/0000-0003-2815-993X
Louis Hartmann https://orcid.org/0000-0002-3964-1935
Hubert A. Gasteiger https://orcid.org/0000-0001-8199-8703

References

1. G. E. Blomgren, *J. Electrochem. Soc.*, **164**, A5019 (2017).
2. O. Gröger, H. A. Gasteiger, and J.-P. Suchsland, *J. Electrochem. Soc.*, **162**, A2605 (2015).
3. D. Andre, S.-J. Kim, P. Lamp, S. F. Lux, F. Maglia, O. Paschos, and B. Stiaszny, *J. Mater. Chem. A*, **3**, 6709 (2015).
4. K. G. Gallagher, S. Goebel, T. Greszler, M. Mathias, L. Berkeley, W. Oelerich, D. Eroglu, and V. Srinivasan, *Energy Environ. Sci.*, **7**, 1555 (2014).
5. D.-H. Cho, C.-H. Jo, W. Cho, Y.-J. Kim, H. Yashiro, Y.-K. Sun, and S.-T. Myung, *J. Electrochem. Soc.*, **161**, A920 (2014).
6. J. Kim, Y. Hong, K. S. Ryu, M. G. Kim, and J. Cho, *Electrochem. Solid-State Lett.*, **9**, A19 (2006).
7. H. S. Liu, Z. R. Zhang, Z. L. Gong, and Y. Yang, *Electrochem. Solid-State Lett.*, **7**, A190 (2004).
8. H. Liu, Y. Yang, and J. Zhang, *J. Power Sources*, **162**, 644 (2006).
9. R. Jung, R. Morasch, P. Karayaylali, K. Phillips, F. Maglia, C. Stinner, Y. Shao-Horn, and H. A. Gasteiger, *J. Electrochem. Soc.*, **165**, A132 (2018).
10. T. Teufl, B. Strehle, P. Müller, H. A. Gasteiger, and M. A. Mendez, *J. Electrochem. Soc.*, **165**, A2718 (2018).
11. I. A. Shkrob, J. A. Gilbert, P. J. Phillips, R. Klie, R. T. Haasch, J. Bareño, and D. P. Abraham, *J. Electrochem. Soc.*, **164**, A1489 (2017).
12. S. E. Renfrew and B. D. McCloskey, *J. Am. Chem. Soc.*, **139**, 17853 (2017).
13. J. Sicklinger, M. Metzger, H. Beyer, D. Pritzl, and H. A. Gasteiger, *J. Electrochem. Soc.*, **166**, A2322 (2019).
14. R. Moshtev, P. Zlatilova, S. Vasilev, I. Bakalova, and A. Kozawa, *J. Power Sources*, **81–82**, 434 (1999).
15. J. Paulsen and J. H. Kim, *Patent Application*, WO 2012/107313 A1 (2012).
16. J. Paulsen, H.-K. Park, and Y. H. Kwon, *Patent Application*, US 2019/0224201 A1 (2009).
17. J. Paulsen, H. P. Hong, and J. D. Oh, *Patent Application*, WO 2016/055911 A1 (2016).
18. J. R. Dahn, R. Fong, and U. von Sacken, Pat.US 2,264,201 (1993).
19. D.-H. Kim and J. Paulsen, *Patent Application*, WO 2015/128722 A1 (2015).
20. J. Paulsen, H. P. Hong, and H. S. Ahn, *Patent Application*, WO 2015/036882 A2 (2015).
21. N. V. Faenza, L. Bruce, Z. W. Lebens-Higgins, I. Plitz, N. Pereira, L. F. J. Piper, and G. G. Amatucci, *J. Electrochem. Soc.*, **164**, A3727 (2017).
22. Z. Chen, J. Wang, J. Huang, T. Fu, G. Sun, S. Lai, R. Zhou, K. Li, and J. Zhao, *J. Power Sources*, **363**, 168 (2017).
23. R. Jung, P. Strobl, F. Maglia, C. Stinner, and H. A. Gasteiger, *J. Electrochem. Soc.*, **165**, A2869 (2018).
24. J. Kim, H. Lee, H. Cha, M. Yoon, M. Park, and J. Cho, *Adv. Energy Mater.*, **8**, 1702028 (2018).
25. G. V. Zhuang, G. Chen, J. Shim, X. Song, P. N. Ross, and T. J. Richardson, *J. Power Sources*, **134**, 293 (2004).
26. H.-J. J. Noh, S. Youn, C. S. S. Yoon, and Y.-K. K. Sun, *J. Power Sources*, **233**, 121 (2013).
27. X.-D. Zhang, J.-L. Shi, J.-Y. Liang, Y.-X. Yin, J.-N. Zhang, X.-Q. Yu, and Y.-G. Guo, *Adv. Mater.*, **30**, 1801751 (2018).
28. P. Oh, B. Song, W. Li, and A. Manthiram, *J. Mater. Chem. A*, **4**, 5839 (2016).
29. S. F. Amalraj et al., *Electrochim. Acta*, **97**, 259 (2013).
30. X. Zhang, I. Belharouak, L. Li, Y. Lei, J. W. Elam, A. Nie, X. Chen, R. S. Yassar, and R. L. Axelbaum, *Adv. Energy Mater.*, **3**, 1299 (2013).
31. J. Choi, J. Kim, K.-T. Lee, J. Lim, J. Lee, and Y. S. Yun, *Adv. Mater. Interfaces*, **3**, 4 (2016).
32. T. Shinpuku, H. Tani, R. Otterstedt, and K. Kanao, *Patent Application*, WO/2018/172272 (2018).
33. S.-G. Woo, J.-H. Han, K. J. Kim, J.-H. Kim, J.-S. Yu, and Y.-J. Kim, *Electrochim. Acta*, **153**, 115 (2015).
34. B.-J. Chae and T. Yim, *Mater. Chem. Phys.*, **214**, 66 (2018).
35. H. Sclar et al., *J. Electrochem. Soc.*, **167**, 110563 (2020).
36. M. Metzger et al., *WIPO Pat. Appl. No.*, WO2019002116 (2018).
37. K. Watanabe and M. Deguchi, *Patent Application*, US 2011/0117437 A1 (2011).
38. B. Strehle, K. Kleiner, R. Jung, F. Chesneau, M. Mendez, H. A. Gasteiger, and M. Piana, *J. Electrochem. Soc.*, **164**, A400 (2017).
39. O. B. Lapina, B. S. Bal'zhinimaev, S. Boghosian, K. M. Eriksen, and R. Fehrmann, *Catal. Today*, **51**, 469 (1999).
40. A. F. W. Hollemann and N. Wiberg, "Schwefelsäure H_2SO_4 und Dischwefelsäure $H_2S_2O_7$." *Lehrbuch der Anorganischen Chemie* (de Gruyter, Berlin) p. 583 (2008).
41. M. Metzger, B. Strehle, S. Solchenbach, and H. A. Gasteiger, *J. Electrochem. Soc.*, **163**, A1219 (2016).
42. M. Metzger, C. Marino, J. Sicklinger, D. Haering, and H. A. Gasteiger, *J. Electrochem. Soc.*, **162**, A1123 (2015).
43. F. T. Wagner, B. Lakshmanan, and M. F. Mathias, *J. Phys. Chem. Lett.*, **1**, 2204 (2010).

44. L. D. Ellis, J. P. Allen, L. M. Thompson, J. E. Harlow, W. J. Stone, I. G. Hill, and J. R. Dahn, *J. Electrochem. Soc.*, **164**, A3518 (2017).
45. N. Tsiouvaras, S. Meini, I. H. Buchberger, and H. A. Gasteiger, *J. Electrochem. Soc.*, **160**, A471 (2013).
46. M. Metzger, C. Marino, J. Sicklinger, D. Haering, and H. A. H. A. A. Gasteiger, *J. Electrochem. Soc.*, **162**, A1123 (2015).
47. T. Teufl, D. Pritzl, S. Solchenbach, H. A. Gasteiger, and M. A. Mendez, *J. Electrochem. Soc.*, **166**, A1275 (2019).
48. M. M. Thackeray, C. S. Johnson, J. T. Vaughey, N. Li, and S. A. Hackney, *J. Mater. Chem.*, **15**, 2257 (2005).
49. I. Gennick and K. M. Harmon, *Inorg. Chem.*, **14**, 2214 (1975).
50. P. Pasierb, S. Komornicki, M. Rokita, and M. Rękas, *J. Mol. Struct.*, **596**, 151 (2001).
51. F. A. Miller and C. H. Wilkins, *Anal. Chem.*, **24**, 1253 (1952).
52. R. A. Nyquist and R. O. Kagel, *Handbook of Infrared and Raman Spectra of Inorganic Compounds and Organic Salts: Infrared Spectra of Inorganic Compounds* (New York: Academic, New York) (2012).
53. G. Socrates, *Infrared and Raman Characteristic Group Frequencies: Tables and Charts* (John Wiley & Sons, Inc, New York) (2001).
54. S. Meini, N. Tsiouvaras, K. U. Schwenke, M. Piana, H. Beyer, L. Lange, and H. A. Gasteiger, *Phys. Chem. Chem. Phys.*, **15**, 11478 (2013).
55. R. G. Brown and S. D. Ross, *Spectrochim. Acta Part A Mol. Spectrosc.*, **28**, 1263 (1972).
56. A. Simon and H. Wagner, *Zeitschrift für Anorg. und Allg. Chemie*, **311**, 102 (1961).
57. M. Tatsumisago, H. Narita, T. Minami, and M. Tanaka, *J. Am. Ceram. Soc.*, **66**, c210 (1983).
58. T. Sato, A. Ueno, N. Todo, M. Kurita, H. Hagiwara, A. Nishijima, and Y. Kiyozumi, *Bull. Chem. Soc. Jpn.*, **54**, 3347 (1981).
59. H. Tai and A. L. Underwood, *Anal. Chem.*, **29**, 1430 (1957).
60. S. M. Teleb, *Thermochim. Acta*, **228**, 131 (1993).
61. J. C. Evans and H. C. Bernstein, *Can. J. Chem.*, **33**, 1270 (1955).
62. S. Dasgupta and A. P. B. Sinha, *Trans. Faraday Soc.*, **53**, 909 (1957).
63. R. K. Moore and W. B. White, *J. Am. Ceram. Soc.*, **53**, 679 (1970).
64. C. Julien, *Solid State Ionics*, **135**, 121 (2000).
65. H. Beyer, S. Meini, N. Tsiouvaras, M. Piana, and H. A. Gasteiger, *Phys. Chem. Chem. Phys.*, **15**, 11025 (2013).
66. B. C. Smith, "Diffusive reflectance (DRIFTS)." in*Fourier Transform Infrared Spectroscopy* (CRC Press, Boca Raton, FL) pp. 110 (1996).
67. N. Andreu, D. Flahaut, R. Dedryvère, M. Minvielle, H. Martinez, and D. Gonbeau, *ACS Appl. Mater. Interfaces*, **7**, 6629 (2015).
68. P. van der Heide, "Spectral interpretation." in*X-ray Photoelectron Spectroscopy : An Introduction to Principles and Practices*, ed. P. van der Heide (John Wiley & Sons, Inc, Hoboken, NJ, United States of America) pp. 101 (2011).
69. M. C. Biesinger, B. P. Payne, A. P. Grosvenor, L. W. M. Lau, A. R. Gerson, and R. S. C. Smart, *Appl. Surf. Sci.*, **257**, 2717 (2011).
70. A. R. Gonzalez-Elipe, J. P. Espinos, A. Fernandez, and G. Munuera, *Appl. Surf. Sci.*, **45**, 103 (1990).
71. M. C. Biesinger, B. P. Payne, L. W. M. Lau, A. Gerson, and R. S. C. Smart, *Surf. Interface Anal.*, **41**, 324 (2009).
72. J.-C. Dupin, D. Gonbeau, P. Vinatier, and A. Levasseur, *Phys. Chem. Chem. Phys.*, **2**, 1319 (2000).
73. A. Gutierrez, M. He, B. T. Yonemoto, Z. Yang, J. Wang, H. M. Meyer, M. M. Thackeray, and J. R. Croy, *J. Electrochem. Soc.*, **166**, A3896 (2019).
74. A. T. S. Freiberg, J. Sicklinger, S. Solchenbach, and H. A. Gasteiger, *Electrochim. Acta*, **346**, 136271 (2020).

SO_3 Treatment of Lithium- and Manganese-Rich NCMs for Li-Ion Batteries: Enhanced Robustness Towards Humid Ambient Air and Improved Full-Cell Performance

Johannes Sicklinger, Hans Beyer[z], Louis Hartmann, Felix Riewald, Christian Sedlmeier and Hubert A. Gasteiger

Chair of Technical Electrochemistry, Department of Chemistry and Catalysis Research Center, Technische Universität München, D-85748 Garching, Germany

Supporting Information

DRIFT Spectra Normalization.— The data treatment of FTIR spectra is exemplarily demonstrated for "dry" as well as SO_3 treated LMR-NCM ("SO_3 160°C dry") (Figure S1).

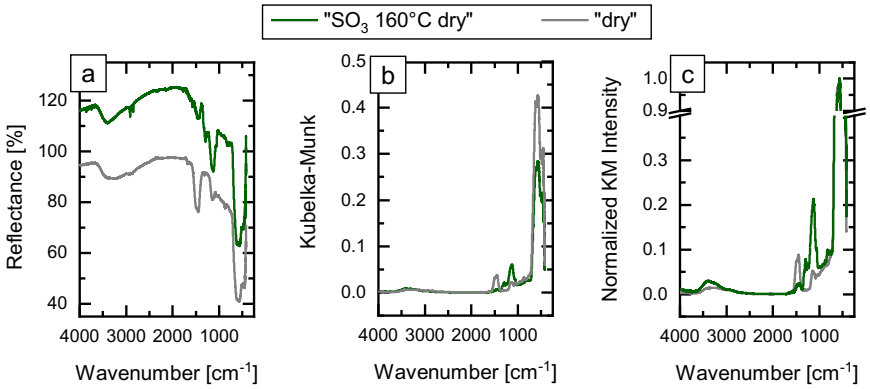

Figure S1: DRIFT spectra of SO_3 treated LMR-NCM ("SO_3 160°C dry") compared to as-received and dried LMR-NCM ("dry"). The spectra can be displayed in **(a)** Reflectance or **(b)** Kubelka-Munk (KM) units. **(c)** In the study at hand, the KM spectra were normalized to the oxide band at 570 cm^{-1}. Note that the spectra are offset arbitrarily along the y-axis for better visibility.

The intensity of DRIFTS spectra of 1 % active material diluted in KBR is first calculated versus KBr as reference in reflectance units according to $R = I_{sample}/I_{reference}$ (Figure S1a) and then

[z] E-Mail of corresponding author: hans.beyer@tum.de

converted to Kubelka-Munk units $KM = (1 - R)^2/(2R)$ (Figure S1b). The sample preparation is described in more detail in the experimental part of the main manuscript. In Reflectance units, surface species give rise to downward pointing signals due to absorption of IR radiation. After conversion to Kubelka-Munk units, absorption bands are represented by upward pointing features. The KM band intensity is roughly proportional to the concentration of IR-active species, as described by Kubelka-Munk theory. To compare the relative amounts of surface species, the spectra were normalized to the oxide band at 570 cm^{-1}, which corresponds to the maximum KM intensity for all spectra (Figure S1c). The band assignment is discussed in greater detail in the Results section of the main manuscript (Table 2).[1–3]

XPS Reference Data.—Li_2SO_4, $NiSO_4$, and $NiSO_4 \cdot 6\ H_2O$ (Figure S2) were used as model compounds for sulfate to determine the fitting parameters for the S 2p spectra relating to the "M-SO_4" component of SO_3 gas treated LMR-NCM (left panel). With a binding energy value of 168.7 (±0.2) eV for the S $2p_{3/2}$ signal and a separation of 1.0 – 1.3 eV between the $p_{3/2}$ and $p_{1/2}$ features (intensity ratio of 2:1), they are in agreement with the literature values of sulfate S 2p spectra as already mentioned in the main manuscript.[4,5] The deviation of the peak maxima positions (e.g. ±0.2 eV for the S $2p_{3/2}$ signal) of these metal sulfate reference samples was used as the constrained deviation for the measurement of the LMR-NCM samples.

In the O 1s of the sulfate salts, the "M-SO_4" signal is found at 532.0 (±0.2) eV for Li_2SO_4, $NiSO_4$, and $NiSO_4 \cdot 6\ H_2O$. In addition, a hydrate signal is obtained at 533.5(±0.2) eV for $NiSO_4 \cdot 6\ H_2O$ (Figure S2), which gives a hint for the possible formation of hydrate upon "wet" storage of the SO_3 gas treated LMR-NCM sample, i.e., the shoulder above 533 eV (see "SO_3 160°C wet" in the right bottom panel of Figure 7). An alternative explanation for this additional feature might be Na signals, as will be explained below.

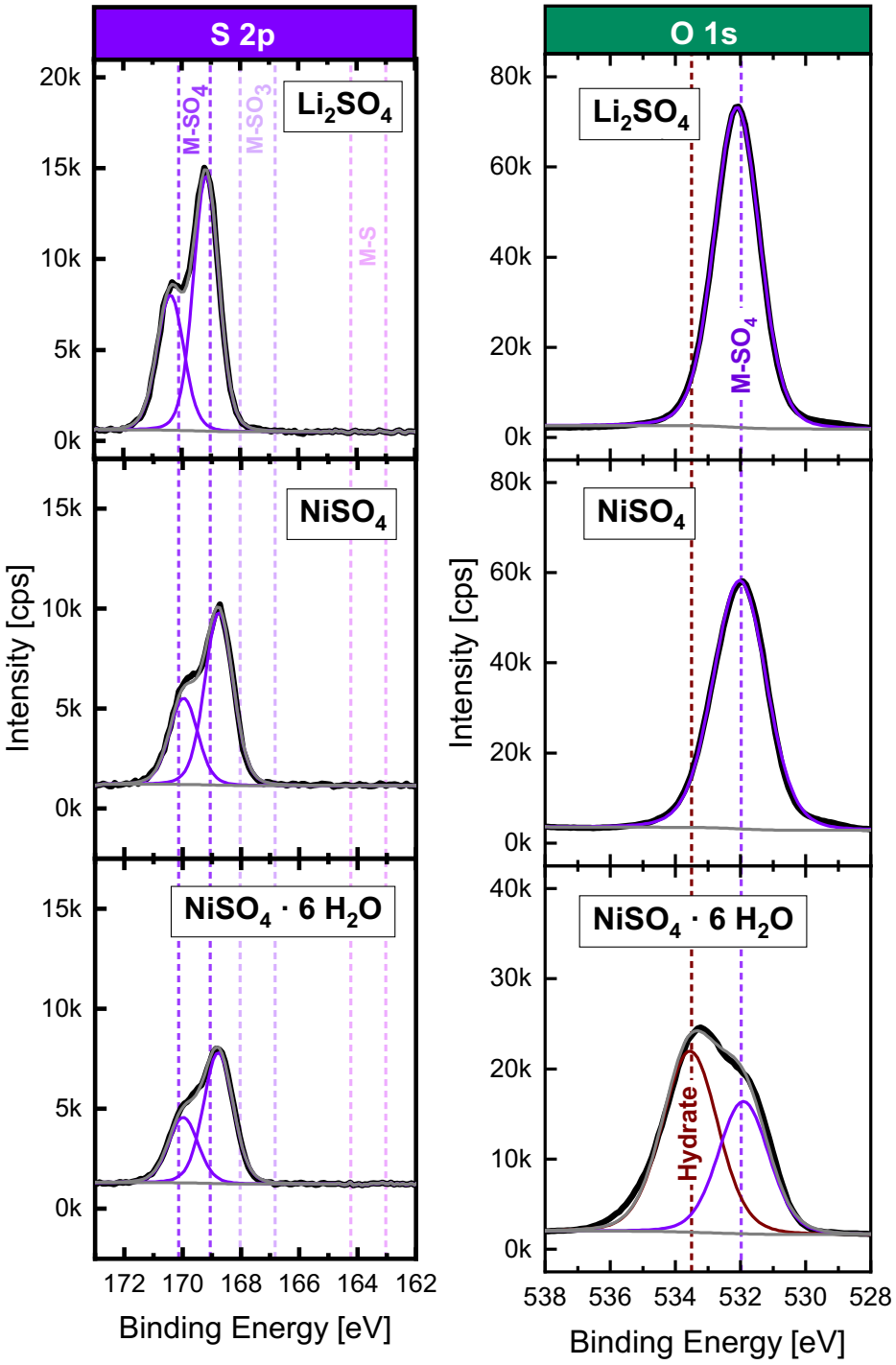

Figure S2: S 2p (left panels) and O 1s XPS (right panels) of metal sulfate reference samples Li_2SO_4 (upper panels), anhydrous $NiSO_4$ (middle panels), and $NiSO_4 \cdot 6\ H_2O$ (lower panels) including the fitted species for surface sulfates ("M-SO_4"), i.e., oxygen and sulfur in the sulfate anion (SO_4^{2-}) as well as "hydrate", i.e. the oxygen in the water molecule of metal sulfate hydrates ($M_xSO_4 \cdot y\ H_2O$).

In addition, reference values for the O 1s features of the lattice oxygen in layered transition metal oxides observed for NCM811 samples were taken from a recently conducted XPS study by our group.[6] There, the O 1s peak position of the lattice oxygen in layered NCM811 and in a

MnO_2 reference sample was observed at 529.2 eV;[6] oxygen-depleted oxide species such as in spinel and rock salt structures were assigned to 529.6 eV (for an Mn_3O_4 reference) and 529.7 eV (for an MnO reference), respectively.[6]

Based on these considerations, the O 1s spectra of treated and untreated LMR-NCM samples were fitted considering values of 532.0 (±0.2) eV and of 529.2 (±0.2) eV for the O 1s signals of the "M-SO_4" component and of the layered oxide component, respectively. The value of 531.8 eV obtained from the "SO_3 200°C dry" sample (Figure 6, lower panel) lies within the BE range of 532.0 (±0.2) eV found from the reference samples in Figure S2. The rationale behind determining the sulfate BE value from the LMR-NCM sample "SO_3 200°C dry" is that all carbonate and hydroxide surface species (referred to as "M-OH/CO_3") were removed by the SO_3 gas treatment at 200°C. While it cannot be excluded that minor amounts of oxygen-depleted surface species (spinel and rock salt at 529.6 eV and 529.7 eV, respectively) are present in the near-surface region of the LMR-NCM sample, they were not considered in the fitting procedure since the fit quality could not be improved by including these oxygen species in addition to the layered oxide peak at 529.2 eV.

The O 1s peak positions of the hydroxide/carbonate surface species ("M-OH/CO_3") were determined from untreated "wet" LMR-NCM, since it contains a negligible amount of sulfate and has the highest contaminant peak of all of the studied HE-NCM samples (Figure 7, lower left panel). The obtained value of 531.3 eV was taken as reference for the "M-OH/CO_3" peak in all of the discussed LMR-NCM O 1s spectra (Figures 6 and 7). While this BE value is slightly lower than the 531.9 eV found by Friedrich et al. in 2019 for NCM811,[6] it is quite likely that these species on the nickel-rich surface are somewhat different on the manganese-rich surface of the LMR-NCM and that the ratio of M-OH to M-CO_3 is different for the two different materials. The here used fitting parameters for the binding energy and the full-width at half-maximum (FWHM) ranges are listed below in Table S1.

Table S1: XPS peak fitting parameters used for identification and quantification of the surface species of the various untreated and SO_3 gas treated LMR-NCM samples. Binding energy and FWHM fitting parameters for the S 2p and O 1s signals of metal sulfate surface species ("M-SO_4") including the O 1s signal for hydrated $NiSO_4 \cdot 6\ H_2O$ ("Hydrate") were determined from the measurements displayed in Figure S2. All other parameters for O 1s fitting, i.e., for the layered oxide peak ("Lattice O^{2-}"), and the metal hydroxide and metal carbonate peak ("M-OH/CO_3") were taken from the other study in our group.[6]

Element/region	Assigned Species	Binding energy [eV] (constrained deviation)	FWHM [eV] constrained range
Sulfur S 2p	"M-SO_4"	A: 168.7 (±0.2) ($p_{3/2}$)	A: 1.0-1.3
		B: A+1.2 eV ($p_{1/2}$)	B: 1 · FWHM(A)
Oxygen O 1s	"Lattice O^{2-}" (green)	529.2 (±0.2)	1.0-1.15
	"M-OH/CO_3" (blue)	531.3 (±0.2)	1.5- 2.25
	"M-SO_4" (orange)	532.0 (±0.2)	1.5-2.0
	Hydrate/misc.	533.5(±0.2)	0.8-1.2

To more easily understand the growth of sulfur-containing species after SO_3-treatment, the data in the inset of Figure 5 in the main manuscript were normalized to the absolute intensity values of their respective survey-spectra at 1200 eV. After normalization, the Shirley background was subtracted from the spectra in the inset in Figure 5.

It cannot be excluded that Na signals as seen from the survey scan of the LMR-NCM sample "SO_3 160°C wet" in Figure S3 might possibly interfere with the O 1s signals of the LMR-NCM samples. The Na_{KLL} Auger line which was reported in the literature to be approximately at 533 eV[7] could in principle overlay with the above mentioned hydrate signal above 533 eV. It is crucial to notice that the Na_{KLL} Auger line at 533 eV cannot be deconvoluted from the O 1s signal at 529 eV in the survey scan, but Na 1s and Na 2s prove the presence of Na impurities on the LMR-NCM surface. In sum, it is currently unclear whether the additional shoulder for SO_3 gas treated LMR-NCM after wet storage ("SO_3 160°C wet") is mainly caused by the formation of a sulfate hydrate species or by the redistribution of Na^+ trace impurities in LMR-NCM upon "wet" storage.

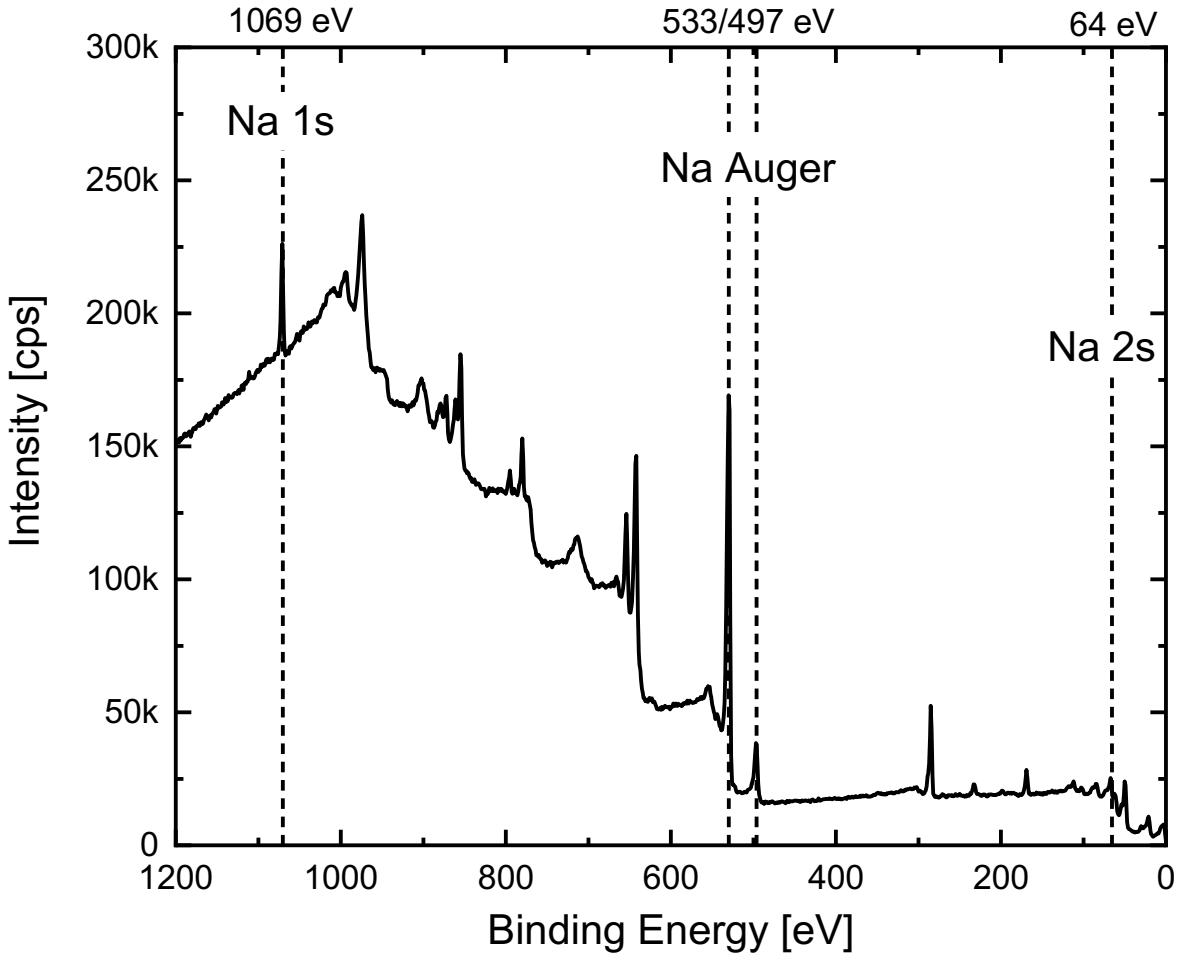

Figure S3: XPS survey scan of the LMR-NCM sample "SO_3 200°C dry" recorded with a step size of 0.5 eV and at a pass energy of 160 eV. The Na 1s and Na 2s binding energies as well as the Na_{KLL} Auger lines are marked.

Impact of "Wet" Storage on the First Cycle of LMR-NCM//Graphite Cells.— As mentioned in the main paper, LMR-NCM//graphite coin cells were cycled at 45°C. The voltage profiles of the first activation cycle at C/15 of several samples are displayed in Figure 9 in the main paper. As discussed there, the characteristic curves are similar for SO_3-treated as well as untreated LMR-NCM samples, while the first cycle charge and discharge capacities vary. The same holds true for the comparison of "wet" stored and "dry" samples (Figure S4). For untreated "wet" LMR-NCM, the charge capacity is slightly bigger than the one of "dry" LMR-NCM (352 vs. 340 mAh/g, Figure S4a). Similarly, "SO_3 160°C wet" has a bigger charge capacity than "SO_3 160°C dry" (329 vs. 319 mAh/g, Figure S4b), while "SO_3 160°C wet" has a slightly smaller charge capacity than "SO_3 200°C dry" (309 vs. 319 mAh/g, Figure S4c). However, the discharge capacities do not differ as much for the "wet" stored versus "dry" samples for both, SO_3 treated and untreated LMR-NCM (max. 6 mAh/g difference, Figure S4a-c). All in all, the long-term cycle life (Figure 10e-h in the main paper) really reveals the impact of "wet" storage on full-cell performance, while the side reactions caused by surface contaminants do not drastically impact the first cycle performed at the rather slow rate of C/15. This is consistent with the fact that rate capability and resistance build-up were really affected by surface contaminants, e.g., in case of "wet" vs. "dry" LMR-NCM, while the C/10 cycling capacity did not deteriorate as much upon "wet" storage.

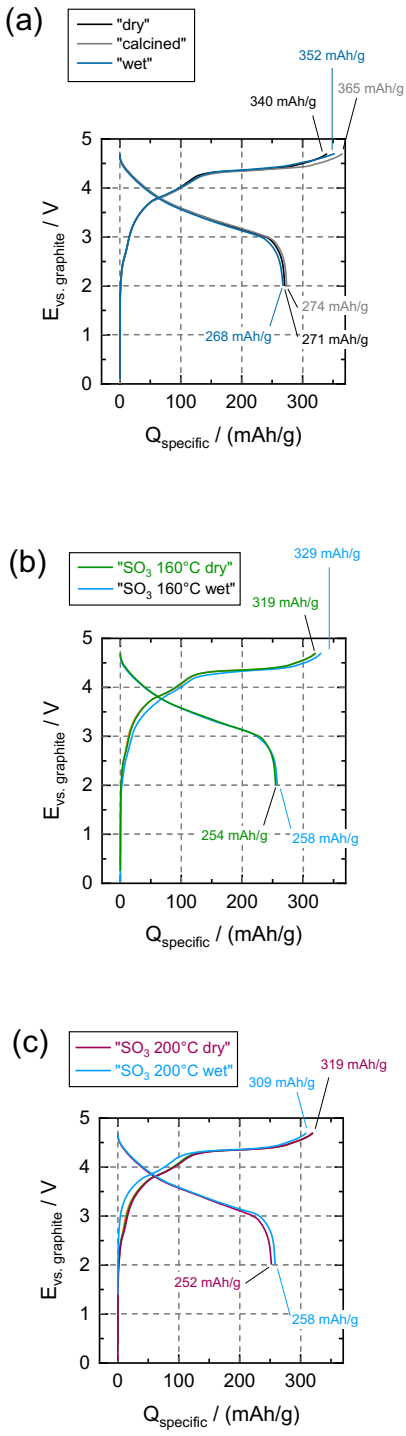

Figure S4: Voltage profiles of LMR-NCM//graphite coin cells for the first activation cycle at 45°C (4.8 V – 2.0 V at C/15). Comparison of SO_3-treated and untreated LMR-NCM. The experimental details are described in the main paper (experimental section).

References

1. P. R. Griffiths and J. A. de Haseth, "Diffusive Reflectance Spectrometry", in *Fourier Transform Infrared Spectroscopy*, pp. 349–362, John Wiley & Sons, Inc., New York (1986).

2. S. R. Culler, "Diffusive Reflectance Infrared Spectroscopy: Sampling Techniques for Qualitative/Quantitative Analysis of Solids", in *Practical Sampling Techniques for Infrared Analysis*, P. B. Coleman, Editor, pp. 94–104, CRC Press, Boca Raton (1993).

3. B. C. Smith, "Diffusive Reflectance (DRIFTS)", in *Fourier Transform Infrared Spectroscopy*, pp. 110–137, CRC Press, Boca Raton (1996).

4. N. Andreu, D. Flahaut, R. Dedryvère, M. Minvielle, H. Martinez, and D. Gonbeau, *ACS Appl. Mater. Interfaces*, **7**, 6629–6636 (2015).

5. P. van der Heide, "Spectral Interpretation", in *X-ray photoelectron spectroscopy : an introduction to principles and practices*, pp. 101–140, John Wiley & Sons, Inc., Hoboken, NJ, USA (2011).

6. F. Friedrich, B. Strehle, A. T. S. Freiberg, K. Kleiner, S. J. Day, C. Erk, M. Piana, and H. A. Gasteiger, *J. Electrochem. Soc.*, **166**, A3760–A3774 (2019).

7. A. Gutierrez, M. He, B. T. Yonemoto, Z. Yang, J. Wang, H. M. Meyer, M. M. Thackeray, and J. R. Croy, *J. Electrochem. Soc.* , **166**, A3896–A3907 (2019).

3.3.2. Enhancement of Electrochemical Performance of Lithium and Manganese-Rich Cathode Materials via Thermal Treatment with SO_2

The manuscript entitled "Enhancement of Electrochemical Performance of Lithium and Manganese-Rich Cathode Materials via Thermal Treatment with SO_2" was first submitted to the peer-reviewed Journal of the Electrochemical Society on May 17, 2020. A revised version was submitted on July 15, 2020 and published online July 31, 2020. This paper is republished with permission of IOP Publishing Ltd, from "Enhancement of Electrochemical Performance of Lithium and Manganese-Rich Cathode Materials via Thermal Treatment with SO_2", H. Sclar, J. Sicklinger, E. M. Erickson, S. Maiti, J. Grinblat, M. Talianker, F. Amalraj Susai, L. Burstein, H. Beyer, L. Hartmann, G. Avruschenko, H. A. Gasteiger, B. Markovsky, and D. Aurbach, *Journal of the Electrochemical Society*, **167** (2020); permission conveyed through Copyright Clearance Center, Inc. under a non-exclusive and non-transferable license (ID 1140838-1, August 16, 2021. A permanent link to this article can be found under https://doi.org/10.1149/1945-7111/aba6cb.

While the SO_3 treatment described in the previous chapter exclusively lead to the formation of metal sulfates, the SO_2 treatment described in the following can create a mixture of metal sulfates and sulfites depending on the specific treatment conditions, as found from XPS analysis. In the study on SO_2 gas treatment, LMR-NCM with the composition $0.35\,Li_2MnO_3 \cdot 0.65\,LiNi_{0.35}Mn_{0.45}Co_{0.20}O_2$ was investigated. Half-cell tests at 25°C and 30°C showed an initial increase of the discharge capacity by at least 20 mAh/g for SO_2 treated samples without altering the first activation charge capacity. The enhanced discharge capacity was preserved after 100 cycles. While surface sensitive spectroscopy (XPS and DRIFTS) studies clearly proved the formation of sulfates and sulfites, high resolution transmission electron microscopy (HR-TEM), electron diffraction, and X-ray diffraction (XRD) analyses gave no hint of any significant change in the LMR-NCM bulk structure after SO_2 treatment.

As indicated above, for one of the treatment conditions (0.5% SO_2 in Ar for 1 h at 200°C), a mixture of sulfites and sulfate were formed according to high-resolution XPS S 2p spectra. In SO_2, sulfur has the oxidation state +IV. The formation of sulfites ($^{+IV}SO_3^{2-}$) thus would be possible without any redox activity of SO_2 on the surface LMR-NCM. However, in order to form sulfates, ($^{+VI}SO_4^{2-}$), SO_2 would have to release 2 e^-, provoking a reduction of at least one of the species on the LMR-NCM surface. While the precise reaction mechanism cannot be completely proven by the tools used in the study, still several possible reaction pathways are suggested in the section "Possible mechanism of SO_2 gas treatment of HE-NCM materials".

Regardless of the question which model describes the reaction between SO_2 and LMR-NCM best, the study could clearly highlight the benefits of the performed novel treatments on the

electrochemical performance of the tested LMR-NCM. Similar to the SO_3 treatment described in the previous chapter, the thermal treatment with SO_2 might be of high practical relevance for industrial CAM manufacturing and thus is part of the previously mentioned patent application (cf. chapter 3.3.1), too.[136]

Author contributions

This article presents the results of a collaboration between the Technical University of Munich (TUM) and the Bar-Ilan University in Israel (BIU). Thermal treatments with SO_2 were performed by J. S., L. H. and H. B. at TUM as well as by H. S. and B. M. at BIU. J. S., L. H., H. S., B. M., and F. A. S. prepared electrodes and performed electrochemical analysis in coin cells. E. M. E., S. M., J. G., M. T., F. A. S., L. B., G. A., and B. M. carried out material characterization of the LMR-NCM that was SO_2-treated at BIU, including ICP, SEM, HR-TEM, Raman, XPS, and DSC analysis. J. S., H. B., and L. H. carried out XPS analysis of the LMR-NCM that was SO_2-treated at TUM. J. S. performed the DRIFTS analysis. B. M. and H. S. suggested chemical reactions mechanisms for LMR-NCM during SO_2-treatment. H. S., J. S., H. B., H. A. G., and D. A. wrote the manuscript. All authors discussed the data and commented on the manuscript.

Journal of The Electrochemical Society, 2020 **167** 110563
1945-7111/2020/167(11)/110563/14/$40.00 © 2020 The Electrochemical Society ("ECS"). Published on behalf of ECS by IOP Publishing Limited

Enhancement of Electrochemical Performance of Lithium and Manganese-Rich Cathode Materials via Thermal Treatment with SO_2

Hadar Sclar,[1,=] Johannes Sicklinger,[2,=,*] Evan M. Erickson,[1,a] Sandipan Maiti,[1] Judith Grinblat,[1] Michael Talianker,[3] Francis Amalraj Susai,[1] Larisa Burstein,[4] Hans Beyer,[2,z] Louis Hartmann,[2,*] Gregory Avruschenko,[1] Hubert A. Gasteiger,[2,] Boris Markovsky,[1,***] and Doron Aurbach[1,**,z]**

[1]*Department of Chemistry, Bar-Ilan University, Ramat-Gan 5290002, Israel*
[2]*Department of Chemistry and Catalysis Research Center, Technische Universität, München, D-85748 Garching, Germany*
[3]*Department of Materials Engineering, Ben-Gurion University of the Negev, Beer-Sheva 84105, Israel*
[4]*Wolfson Applied Materials Research Center, Tel-Aviv University, Tel-Aviv 69978, Israel*

In this study, we present a novel surface modification approach via SO_2 gas treatment at 200 °C–400 °C to enhance the electrochemical performance of Li and Mn-rich cathode materials $0.35Li_2MnO_3{\cdot}0.65LiNi_{0.35}Mn_{0.45}Co_{0.20}O_2$ (HE-NCM) for advanced lithium-ion batteries. It was established by X-ray photoelectron spectroscopy that the SO_2 treatment leads to the formation of surface sulfates and sulfites on the material, while the bulk remains unaffected, as confirmed by X-ray and electron diffraction studies. Based on the results obtained, we proposed possible mechanisms of the SO_2 thermal treatment that include partial reduction of manganese (however, we could not find any substantial evidence for it in the XPS data) and oxidation of sulfur. The electrochemical performance was evaluated by testing the materials as cathodes in coin-type half-cells with metallic lithium anodes at 25 °C and 30 °C. The main findings are as follows: the SO_2-treated materials demonstrate ~10% higher capacity at all C-rates and lower the voltage hysteresis during prolonged cycling compared to the untreated samples. The proposed approach to modify the surface of HE-NCM materials by SO_2 treatment is demonstrated to be a promising method to enhance the electrochemical performance of these cathodes.
 [DOI: 10.1149/1945-7111/aba6cb]

Manuscript submitted May 17, 2020; revised manuscript received July 15, 2020. Published July 31, 2020.

Supplementary material for this article is available online

With the evolvement of the energy demands in the modern world, there is a growing need for novel advanced high-power and high-energy lithium-ion batteries (LIBs) to facilitate future technologies for energy storage, especially for electric mobility. Promising candidates as cathodes for next-generation of Li-ion batteries are Li and Mn-rich high-energy materials (abbreviated in this paper as HE-NCM), with the formula of $xLi_2MnO_3{\cdot}(1-x)LiMO_2$ (M = Mn, Ni, Co) due to their high practical capacity of >250 mAh g^{-1}.[1] However, problems such as voltage fade, large voltage hysteresis, and capacity fade during cycling must be solved to make HE-NCM applicable for practical batteries.[2–5] Along with structural transformations in bulk during extended cycling,[6] rearrangements in the surface-near region concomitant with O_2 release in the first cycles seem to be responsible for the performance loss of HE-NCM electrodes.[2,7,8] Many studies have been conducted to solve these problems and to stabilize the above-mentioned performance losses of these cathode materials. There are several approaches considered in the literature for their bulk and/or surface stabilization:

Coating the materials with a protective layer using Atomic Layer Deposition (ALD) of metal oxides[9–13] and chemical coatings.[14–18] It should be noted that surface coatings can reduce the oxygen release and mitigate the voltage fade of the above cathode materials.[18]

Cationic or anionic doping or partial substitution of transition metals (TMs) in HE-NCM materials during synthesis, for instance, with foreign cations[19–23] cation/anion co-doping. For instance, both sodium and fluorine doping into Li and Mn-rich materials enhances the stability by suppressing the phase transformation from layered to spinel structure and increases the rate performance through decreasing resistance of Li diffusion and the electrons migration.[24] Integration of the surface coating and anionic doping of HE-NCM materials, for instance by fluorine-doped Li_2SnO_3 layer was also proposed.[25]

Modification of electrolyte solutions with additives, for instance, lithium-bis-oxalato borate LiBoB[26] and trimethyl phosphite[12] that can react with the electrode surface during cycling and form a stabilized solid electrolyte interphase (SEI) on the cathode.

Surface gas treatments using reactive gases like F_2,[27–29] NH_3,[30,31] or CO_2.[32] Our recent research on NH_3 gas treatment of HE-NCM materials at 400 °C demonstrated an enhanced electrode capacity and limited average voltage fade during prolonged cycling.[33] There are only a few reports in the literature,[34–36] discussing SO_2 adsorption on cathode active material surfaces, whereby SO_2 is used as a probe molecule for surface adsorption sites. For instance, Andreu et al. have shown that upon the treatment, SO_2 can be adsorbed on $LiCoO_2$ or mixed transition metal oxides $LiNi_xMn_xCo_{1-2x}O_2$ ($0.33 \leqslant x \leqslant 0.5$) at 353 K. The authors suggest that SO_2 acts as a donor or acceptor but that it can also be oxidized or reduced with electron transfer. Sulfur can also interact with surface oxygen, forming sulfite species SO_3^{2-} without changing the oxygen oxidation state. Sulfates can be formed if sulfur reacts with two surface oxygen ions, while its reaction with a metal from the surface (by dissociative mechanism) may result in the formation of a sulfide species (S^{2-}).[34] These works, as well as our study on the NH_3 gas treatment of HE-NCM materials, inspired us to investigate the impact of gaseous SO_2 on composite cathode materials enriched with Li and Mn and on those $Li[Ni_xCo_yMn_z]O_2$ (x + y + z = 1) materials enriched with nickel (Ni > 80 at.%). Both these two families of materials are considered highly promising as cathodes in lithium-ion batteries for electric vehicle applications.[37–39] To the best of our knowledge, the questions on the SO_2 thermal treatment of the above-lithiated transition metal oxides have not been studied yet. Therefore, in our recent work,[40] we have demonstrated that the SO_2 treatment of high-nickel content $LiNi_{0.85}Co_{0.10}Mn_{0.05}O_2$ material (NCM85) resulted in a remarkably stable cycling performance of

[=]These authors contributed equally to this work.
*Electrochemical Society Student Member.
**Electrochemical Society Fellow.
***Electrochemical Society Member.
[a]Present address: Department of Mechanical Engineering, University of Texas at Austin, Austin, Texas, USA.
[z]E-mail: hans.beyer@tum.de; aurbach@mail.biu.ac.il

cathodes and lesser voltage hysteresis upon cycling compared to untreated NCM85 cathodes. Besides, the SO_2-treated NCM85 material exhibited significant thermal stability, demonstrating lower (by ~12%−20%) heat evolution upon reactions with battery solutions compared to the untreated material.

The present investigation is dedicated to the surface modification via SO_2 gas thermal treatment of HE-NCM cathode materials, viz., $0.35Li_2MnO_3{\cdot}0.65LiNi_{0.35}Mn_{0.45}Co_{0.20}O_2$, demonstrating its positive effect on electrochemical cycling behavior in Li/HE-NCM half-cells. The electrochemical performance was evaluated by testing HE-NCM cathodes in coin-type cells with lithium anodes in EC-EMC/1 M $LiPF_6$ electrolyte as well as in an EC-free, FEC/DEC-based electrolyte with a highly fluorinated ether as co-solvent (BASF, Germany) with 1 M $LiPF_6$. It was established that SO_2 treatment results in the formation of surface sulfates and sulfites (detected by XPS), while the bulk of the material remains unaffected. The discharge capacity was shown to be ~10% higher over prolonged cycling at various rates (for instance, C/3, 1 C), and the average voltage hysteresis was shown to decrease from ~1.3 mV per cycle for the untreated HE-NCM materials to ~0.9 mV per cycle for the SO_2 treated ones. Importantly to note is that experiments on SO_2 treatments of the $0.35Li_2MnO_3{\cdot}0.65LiNi_{0.35}Mn_{0.45}Co_{0.20}O_2$ material and the related surface and bulk analytical studies were performed independently in two labs working in close cooperation: in the Electrochemistry Group at Bar-Ilan University (BIU) and in the Technical Electrochemistry Group at the Technical University of Munich (TUM). We demonstrate in this paper that the beneficial effect of the SO_2 treatment on the cycling behavior observed by our groups was quite similar, even though the SO_2 treatment temperature and duration, the cycling protocol, and the used electrolytes for electrochemical testing were different. Our studies provide strong evidence that SO_2 gas treatment of Li and Mn-rich HE-NCM and Ni-rich NCM materials[40] is an effective method for improving the long-term cycling, lowering the voltage hysteresis and impedance built-up during cycling, as well as for increased thermal stability with solution species of these promising cathodes for advanced Li-ion batteries.

Experimental

Thermal SO_2 gas treatment of HE-NCM.—Li and Mn-rich cathode active material with the composition $0.35Li_2MnO_3{\cdot}0.65LiNi_{0.35}Mn_{0.45}Co_{0.20}O_2$ (designated as High-Energy Nickel-Cobalt-Manganese—HE-NCM) was obtained from BASF and treated as follows by the two groups. At Bar-Ilan University (BIU), the material was treated with a gas mixture of 2% SO_2 and 98% of pure nitrogen at 400 °C for 1, 2, or 4 h in a modified "Rotovap" oven (Fig. S1 is available online at stacks.iop.org/JES/167/110563/mmedia) provided by BASF, Germany. The gas flow was adjusted to be ~0.015 l h^{-1} measured by flow-meter from Alical Scientific. We used 2 glass flasks of ~80 and ~250 cm^3 for the SO_2 treatment of 15 and 50 g of HE-NCM material, respectively. Note that before and after the exposure to SO_2, the HE-NCM material was left for 0.5 h under pure N_2 at 400 °C before cooling, so that the cathode material could continue reacting with the SO_2 that remained in the reactor. At the Technical University of Munich (TUM), SO_2-treated material was prepared by applying a mixture of 0.5% SO_2 in argon (5.0) in a tube furnace at 200 °C for 1 h with a gas flow rate of ~1 l min^{-1}. Before this SO_2 treatment (considered as "mild" due to the lower SO_2 concentration and treatment temperature compared to those applied in BIU), HE-NCM samples had been calcined at 625 °C for 1 h under a gas mixture containing 30% O_2 and 70% argon (gas flow 1 l min^{-1}) to remove surface contaminants from HE-NCM materials.[41]

Characterization of the materials.—Chemical analysis of the materials was performed by the Inductively Coupled Plasma technique (SPECTRO ARCOS ICP-OES Multi-view FHX22), and the results are presented in Table SI. Morphological characteristics were analyzed by Scanning Electron Microscopy (SEM) using Ouanta FEG 250, FEI. For structural characterization, we used X-ray diffraction (Bruker D8 Advanced X-ray diffractometer, CuKα radiation) and the intensities were recorded from powder samples in the range of $2\theta = 10°–80°$, with steps of ~0.0194 deg min^{-1}. The unit cell parameters were obtained from the data by a standard least square refinement procedure implemented in the program PowderCell (v.2.4)[42]. The quality of refinement was evaluated following the R-values of fitting the experimental and calculated profile plots.

High-Resolution Transmission Electron Microscopy (HR-TEM) studies were carried out with a LaB_6-200 kV Jeol-2100 instrument operated at 200 kV. These studies were performed in TEM mode using conventional selected area diffraction (SAED) and Convergent Beam Electron Diffraction (CBED) technique. The local structure of the nano-particles was probed using a convergent beam of electrons from an area of ~7 nm (CBED technique). Samples for the TEM studies were prepared by dispersing and sonicating the powdered HE-NCM in ethanol and adding a few drops of the resulting suspension to a TEM copper grid.

Raman spectra were measured from powders using a 50× objective lens to focus the incident beam and an 1800 lines mm-grating. The Raman spectrometer from Renishaw in Via (UK) was equipped with a 514 nm laser, a CCD camera, and an optical Leica microscope. Results from Raman spectroscopy studies are presented in Fig. S2.

At BIU, surface studies were performed by X-ray Photoelectron Spectroscopy (XPS) in UHV (2.5×10^{-10} Torr base pressure) using 5600 Multi-Technique System (PHI, USA). The samples were irradiated with an Al K_α monochromated source (1486.6 eV), and the outcoming electrons were analyzed by a Spherical Capacitor Analyzer using the slit aperture of 0.8 mm, with a pass energy of 11.750 eV. C 1s peak at 285 eV was used as the energy reference. These measurements were performed on the SO_2-treated materials by transferring them to the instrument under the argon atmosphere in a special vessel without exposure to the ambient atmosphere.

At TUM, powder samples for XPS measurements were pressed into pellets (∅ = 3 mm) inside an argon-filled glovebox using a hand press with a 3 mm die set (PIKE Technologies, USA). Pellets were mounted floating onto a stainless steel stub (∅ = 15 mm), which was then transferred from the glovebox into the load-lock of the XPS system without air exposure, using a transfer vessel (Kratos, UK). High-resolution XPS spectra were recorded with an Axis Supra system (Kratos, UK) using monochromatic Al K_α radiation (1486.6 eV) at a base pressure of $<3{\cdot}10^{-8}$ torr, a pass energy of 20 eV, a step size of 0.1 eV, and a dwell time of 200 ms; spectra were averaged from 8 scans. The measured spot size was 800 × 300 μm, in hybrid lens mode with the instrument's charge neutralizer turned on. The obtained spectra were fitted using the Kratos ESCApe software (version 1.1). Binding energies (BE) were corrected based on the C–C/C–H peak of adventitious carbon at 284.8 eV in the C 1s spectrum. A mixture of 30% Laurentzian and 70% Gaussian functions was used for the least-squares curves fitting procedure, utilizing a Shirley background subtraction. O 1s and S 2p spectra were fitted according to Table SIII.

Results and Discussion

Structural and morphological characterization.—Figure 1 compares XRD patterns of Li and Mn-rich materials before and after SO_2 thermal treatment with 2% SO_2 at 400 °C over 2 h, showing clear reflections of the monoclinic (space group C2/m) and rhombohedral (space group R-3 m) phases. As it follows from these results and the calculated lattice parameters of untreated and SO_2-treated samples (Table I), there were no significant changes in cell parameters, implying thus the integrity of the bulk structure. An additional phase of lithium sulfate was formed as detected by XRD and XPS studies of the SO_2-treated materials. The XRD patterns of these materials typically contain a weak peak at $2\theta = ~23°$ (marked with an arrow

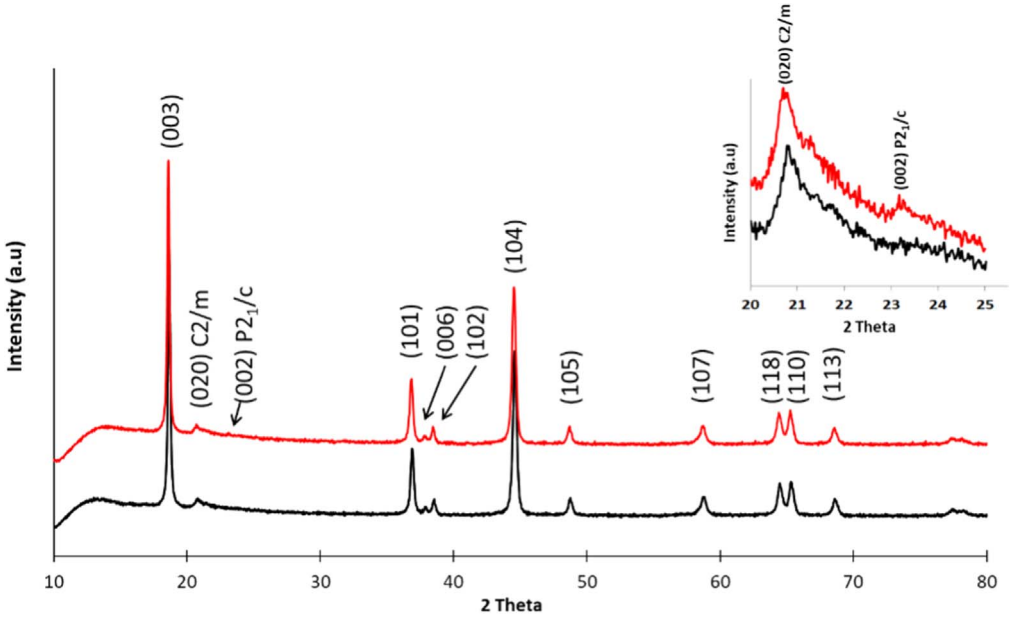

Figure 1. XRD patterns of untreated HE-NCM and the material treated with 2% SO_2 gas at 400 °C for 2 h (black and red profiles, respectively). The insert shows an enlarged peak at $2\theta = \sim 23°$ assigned to the Li_2SO_4 monoclinic phase (space group $P2_1/c$).

Table I. Lattice parameters calculated from XRD patterns of the monoclinic (C2/m) and rhombohedral (R-3m) phases of HE-NCM untreated and SO_2-treated materials.

Material	Monoclinic phase Li_2MnO_3	Rhombohedral phase Li(Mn–Ni-Co) O_2 (in terms of the hexagonal cell)	R_p
HE-NCM untreated	a = 4.929(4) Å b = 8.522(9) Å c = 5.029(0) Å β = 109.189°	a = 2.857(3) Å c = 14.259(6) Å	2.79%
HE-NCM, 2% SO_2 treatment at 400 °C, 2 h	a = 4.935(6) Å b = 8.570(5) Å c = 5.006(2) Å β = 109.46°	a = 2.854(2) Å c = 14.258(7) Å	2.42%

and shown in the Insert to Fig. 1) assigned to the strongest reflection of the Li_2SO_4 monoclinic phase, space group $P2_1/c$ [14].[43]

We have established that even for the more extreme treatment conditions used in BIU, scanning electron microscopy measurements conducted at BIU on the BIU material revealed no morphological changes after the SO_2 thermal gas treatment of the HE-NCM material comparing to the untreated one (Fig. 2). From studies of the specific surface area (S, $m^2\ g^{-1}$) of the above samples

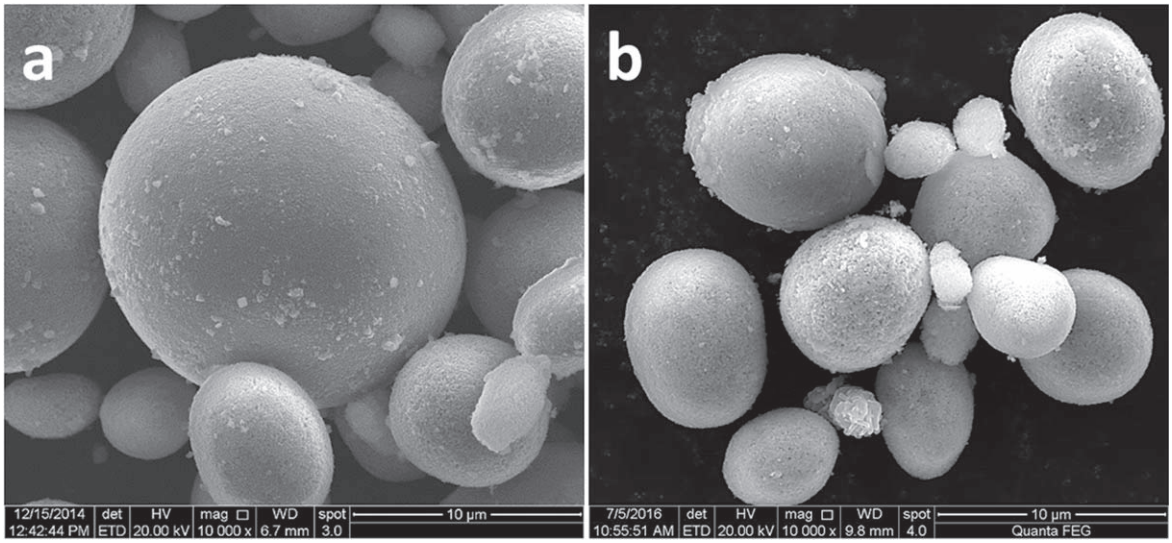

Figure 2. Typical SEM images of (a) untreated HE-NCM, and (b) 2% SO_2 treated material (400 °C, 2 h).

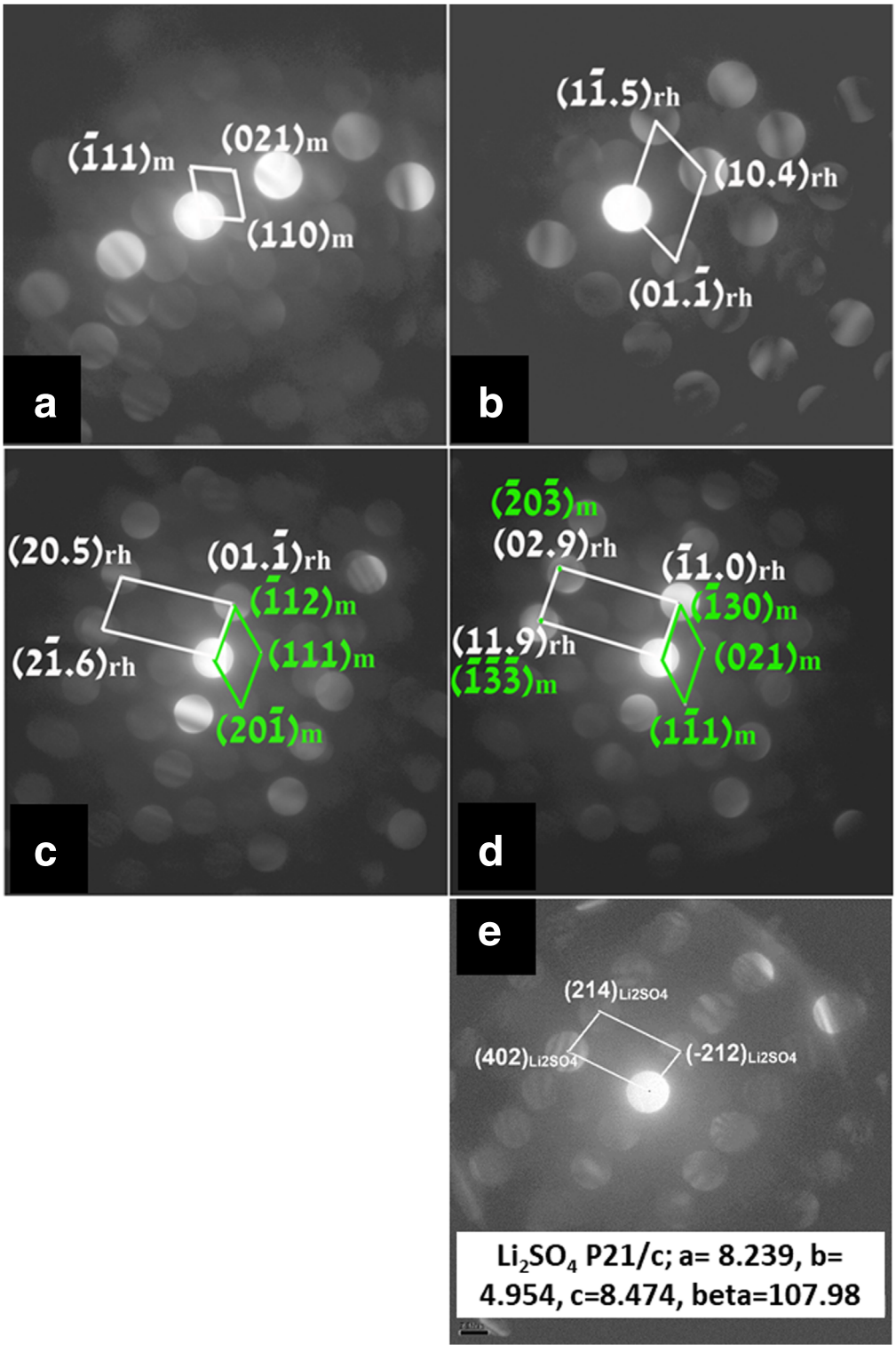

Figure 3. Nano-beam electron diffraction (NBED) patterns recorded with the probe size of ~7 nm and indexed in terms of monoclinic (m) and rhombohedral (R) phases. (a), (b) taken from particles of untreated HE-NCM, (c), (d) taken from 2% SO_2 treated material (400 °C, 2 h), and containing two reflection zones: one is associated with the monoclinic phase, and another is ascribed to the rhombohedral component. (e) CBED pattern shows the presence of Li_2SO_4 monoclinic phase (space group $P2_1/c$).

measured by the BET method, we obtained the following values: S = 6.1 m^2 g^{-1} and S = 5.6 m^2 g^{-1} for HE-NCM untreated material and the 2% SO_2-treated one (2 h at 400 °C), respectively. HE-NCM materials from BASF are ball-shaped secondary agglomerates of micron size comprising submicron primary particles. Thus, these materials can be considered as non-porous; some nano-sized pores can be possibly detected in secondary particles; however, SO_2 treatment will not significantly influence the increasing number and size. Additionally, one may suggest that Li_2SO_4 formed upon the SO_2 treatment can partially block the pores. However, the effects are tiny, and they were beyond our studies.

Analysis of TEM results.—Nano-beam electron diffraction (ED) patterns were recorded from randomly distributed 10–15 particles of Li-rich untreated and 2% SO_2-treated (400 °C, 2 h) materials. All the patterns were indexed based on either monoclinic or rhombohedral components. Among the analyzed particles, no additional phases that could have formed in untreated or SO_2-processed materials were observed. The examples of indexed micro-beam electron diffraction patterns are shown in Fig. 3. Figures 3a, 3b demonstrates patterns indexed in terms of monoclinic (m) phase and rhombohedral phase (R), respectively, of the untreated material. Figures 3c and 3d illustrate diffraction patterns obtained from the 2% SO_2-treated material (400 °C, 2 h). These patterns show two superimposed reflection zones: one is associated with the monoclinic phase, and another is ascribed to the rhombohedral component. The CBED pattern in Fig. 3e demonstrates the presence of the Li_2SO_4 phase (monoclinic, $P2_1/c$) on HE-NCM particle.

Surface studies by XPS.—Figure 4a shows S 2s and S 2p XPS spectra of untreated HE-NCM and 2% SO_2-treated samples (400 °C, 2 h), red and blue curves, respectively. It is important to emphasize that the spectrum of the untreated sample does not exhibit sulfur on the surface. Figure 4b shows Mn 3s spectra of untreated and 2% SO_2-treated (2 h, 400 °C) HE-NCM materials. The Mn 3s peak is split due to a coupling with the 3d valence band.[44–46] One may speculate that the spectrum of Mn 3s demonstrates a small increase of 0.25 eV in its energy splitting (from 4.35 to 4.60 eV) for the SO_2 processed sample. Although the obtained splitting is still lower than that characteristic of trivalent manganese Mn (ca. 5.5 eV), the increase of the splitting after the SO_2 treatment could point to the appearance of some reduced manganese species with valence state less than 4+ in addition to Mn^{4+} in HE-NCM.[33,47] A shoulder at ~90 eV (Fig. 4b) related to the SO_2-treated material indicates an even higher value of splitting compared to the untreated material revealing thus that partially Mn remains in the trivalent state as shown in the inserted table in Fig. 4. Note that in this table, the numbers without brackets were taken from Ref. 44 while those in brackets from Ref. 45. While the absolute values of the observed peak splitting do not provide unambiguous evidence for partial Mn^{4+} reduction, one should note that the latter would be expected upon the formation of surface sulfates from the SO_2 gas. The partial reduction of Mn was also shown in our previous research on ammonia thermal gas treatment of HE-NCM cathode materials.[33] In Fig. 4c, we present the O 1s spectra of untreated HE-NCM and SO_2-treated materials. The results clearly show that the peak at ~529.6 eV related to the lattice oxygen of the HE-NCM material is higher in the untreated material, while the peak at 532–531 eV is higher after the SO_2 treatment. This observation can point to the SO_2 reaction with the lattice oxygen resulting in the formation of M-SO_x species.

We have found from the XPS studies of the 0.5% SO_2-treated sample at 200 °C for 1 h (Fig. 5) that mostly sulfate was formed and that only a small fraction of sulfite was present after this mild SO_2 treatment. The doublet in Fig. 5a is a characteristic feature of the S 2p

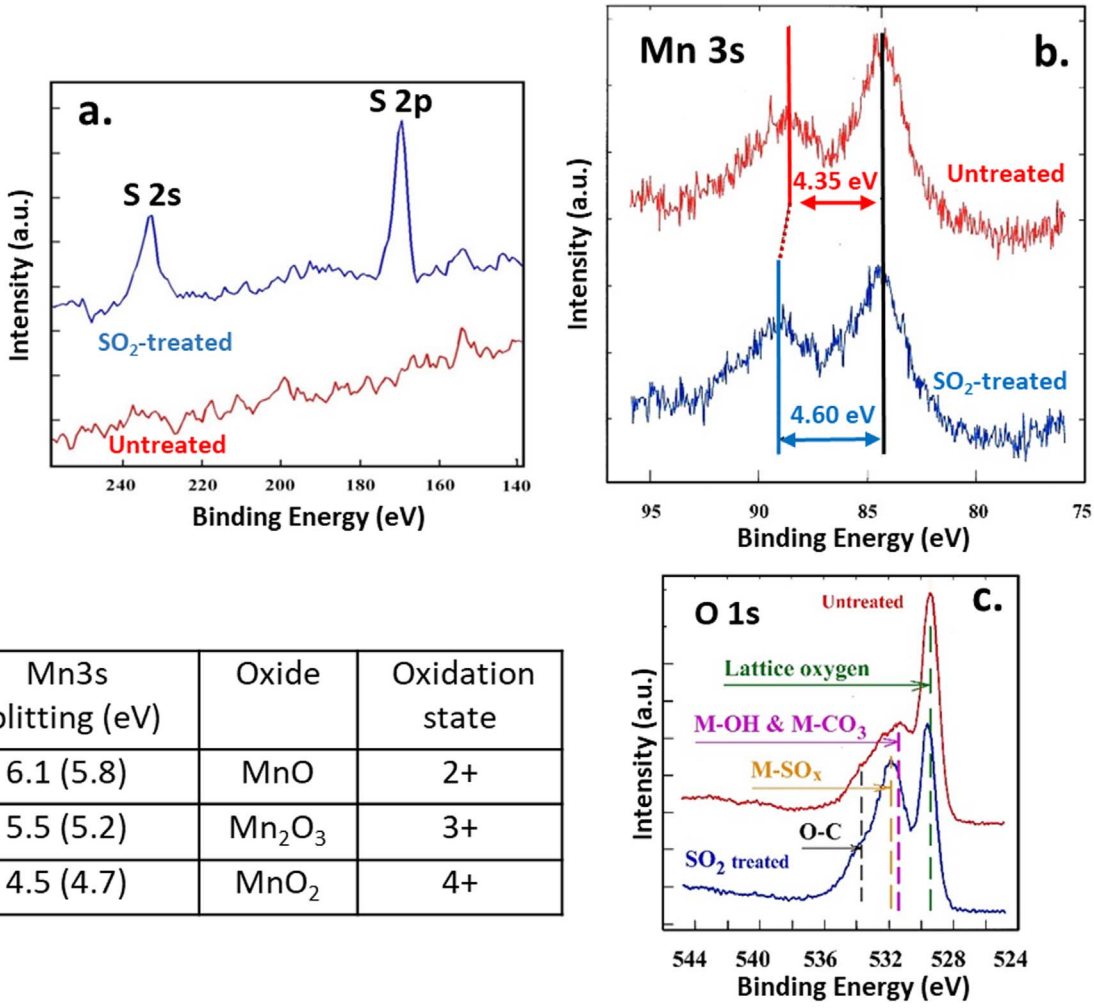

Mn3s Splitting (eV)	Oxide	Oxidation state
6.1 (5.8)	MnO	2+
5.5 (5.2)	Mn_2O_3	3+
4.5 (4.7)	MnO_2	4+

Figure 4. (a) XPS spectra of untreated HE-NCM material (red curve) and the 2% SO_2-treated one (400 °C, 1 h) (blue curve), (b). Typical XPS spectrum of Mn 3s measured from the SO_2-treated material (400 °C, 1 h), and (c) XPS spectra of O 1s measured from untreated and SO_2-treated HE-NCM materials. The inserted table shows the relation between Mn 3s splitting value (in eV) and the oxidation state of Mn.

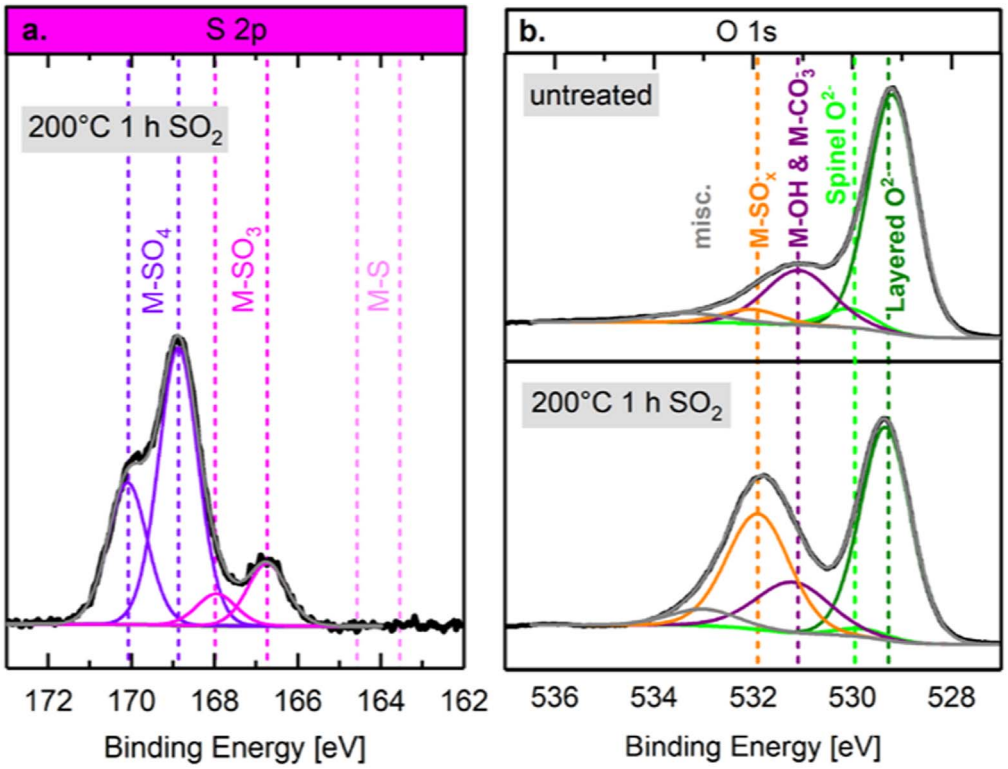

Figure 5. (a) XPS spectra of S 2p recorded after 0.5% SO_2 thermal treatment of HE-NCM material (200 °C, 1 h). (b) O 1s spectra measured from untreated and SO_2-treated HE-NCM samples, as indicated.

peak with the theoretically predicted peak area ratio between the S $2p_{3/2}$ and the S $2p_{1/2}$ peaks equal to 2:1.[48] It is important to notice that the binding energies related to sulfur in sulfate (SO_4^{2-}) are roughly 2 eV higher than in sulfite (SO_3^{2-}),[34] which in turn are roughly 4 eV higher than in sulfides (S^{2-}), as is shown in Table SIII. The XPS spectra in Fig. 5a unambiguously prove that sulfides were formed during SO_2 treatment. Further insight into the structural implications of SO_2 treatment on the oxide surface is provided by O 1s spectra, as shown in Figs. 5b and 5c. The possible mechanisms of sulfate and sulfite formation will be considered further in more detail in this section.

Peak fitting of the O 1s region was performed based on literature data[44,49–51] for appropriate reference compounds such as oxides, hydroxides, carbonates, and sulfates of Li, Ni, Co, and Mn (Table SIII). Peaks associated with lattice oxygen can be split into contributions from the original layered oxide lattice of HE-NCM and a spinel-type lattice that is formed in the near-surface region of specific samples by oxygen release from the near-surface region.[8] Peaks associated with hydroxide and carbonate surface groups can be distinguished from sulfate and sulfite surface groups, although the similarity of the chemical shifts and the relatively high FWHM values of 1.6–1.8 eV (Table SIII) due to the presence of more than one single chemical species contributing to the spectrum may cause some uncertainty in the fit. This is illustrated by the fact that pristine untreated HE-NCM, which contains only minimal traces of residual sulfur from the synthesis, does show a small contribution of M-SO_x species when the fitting parameters are applied (see orange lines in Fig. 5b). While metal sulfates M-SO_4 can be differentiated from metal sulfites M-SO_3 in the S 2p spectra, the O 1s signal for both species is identical.[34] This can be rationalized by taking into account the oxidation state of oxygen in sulfites and sulfates being the same (−II), while the valence state of sulfur differs, being +IV in sulfites and +VI in sulfates.[52]

Studies of the electrochemical behavior of untreated and SO_2-treated HE-NCM.—In this section, we discuss the impact of SO_2 treatment of the HE-NCM material on the electrochemical performance of electrodes, considering the formation of sulfate and sulfite surface species.

From the voltage profiles (Fig. 6), we conclude that both untreated and SO_2-treated materials show the typical features of HE-NCM electrodes upon charging, i.e., the sloping part in the range from 3.7 to 4 V and the high-voltage plateau at 4.5 V, as well as the slope upon discharge from 4.6 to 3 V. Many works of literature, reports state that the reaction upon charging to 4.4 V in the 1st cycle is associated predominantly with the lithium extraction from the Li(TM)O_2 rhombohedral R-3m component and the nickel oxidation to tetravalent state ($Ni^{2+} \rightarrow Ni^{4+}$). The Li_2MnO_3 component is electrochemically inactive up to 4.4 V, while in the reaction between 4.4 V and 4.7 V, lithium is extracted, and the oxygen ions are oxidized. At this stage, some authors suggest that an irreversible removal of oxygen from the near-surface of the HE-NCM material would occur,[6–8] while others suggest the partially reversible removal of oxygen from the bulk of the structure.[51] The role of the oxygen ions in the electrochemical processes during the initial and subsequent redox reactions of HE-NCM electrodes is complicated. Muhammad et al. suggest that upon charging to higher potentials oxygen can be oxidized to per-oxo species ($O^{2-} \leftrightarrow O_2^{2-}$) and then released as oxygen gas (O_2), a process which is stated to be reflected by the sharp anodic peaks at 4.5–4.6 V in the differential capacity plots in Figs. 6a, 6d. Moreover, these authors suggest that the per-oxo species and/or O_2 can undergo interfacial reactions with the EC and EMC solvents of the battery solutions or with neighboring TM ions.[53] Meanwhile, however, it is perhaps the more accepted view that the release of oxygen gas is limited to the near-surface region of the HE-NCM particles.[6–8]

It is evident from the results shown in Fig. 6 that the SO_2 treatment does not impact the characteristic features of the first charge significantly, while the first discharge is extended for both, the "400 °C, 2 h SO_2" and the "200 °C, 1 h SO_2" materials compared to the untreated HE-NCM. In more detail, the "400 °C, 2 h SO_2" treatment leads to a slightly increased discharge capacity of the first cycle at a C/15 rate, from 281 to 295 mAh g^{-1}, although charge

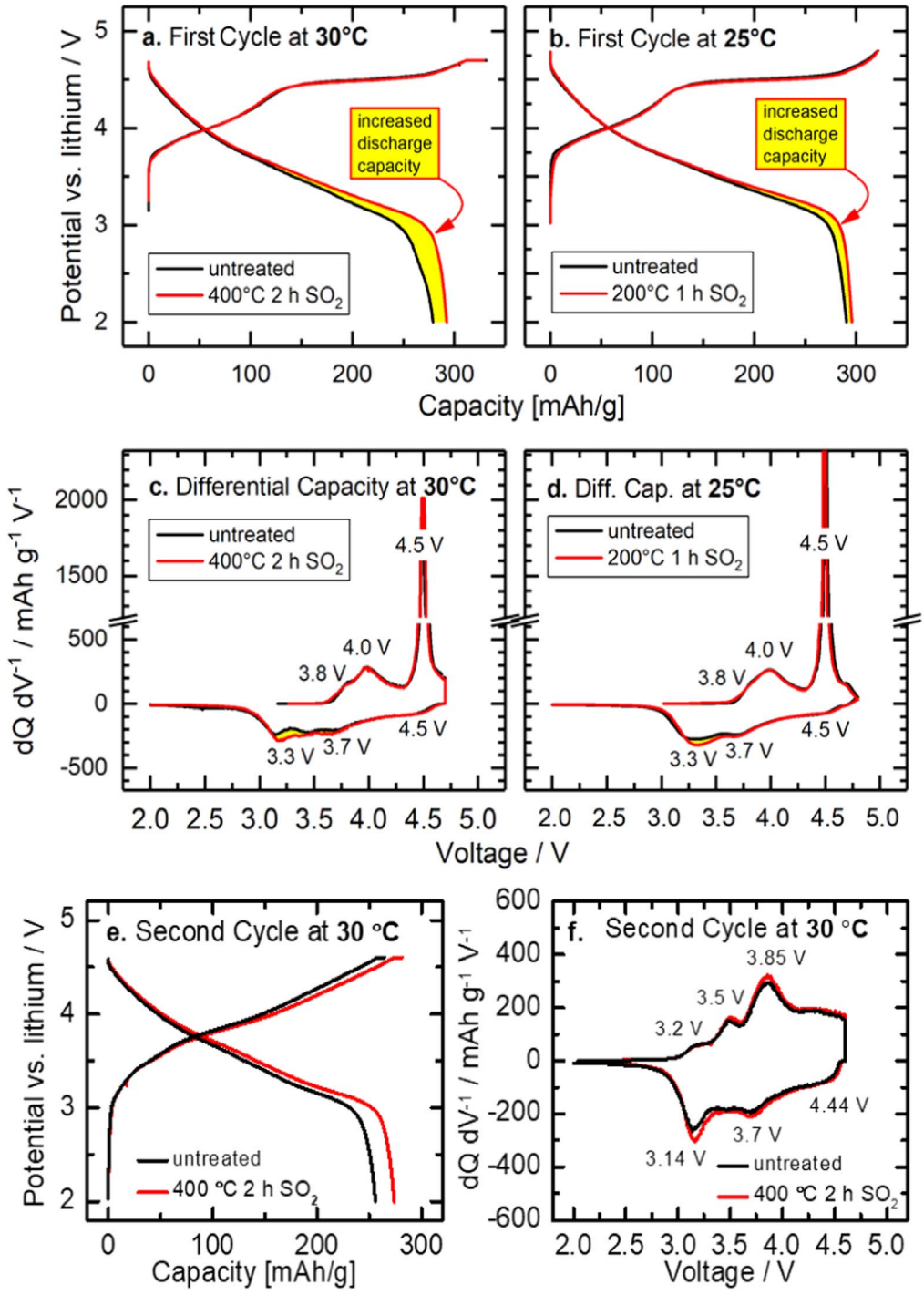

Figure 6. Voltage profiles of the first activation cycle at C/15 of Li/HE-NCM half-cells (coin cells) with untreated and SO_2-treated HE NCM. (a) Measurements at BIU with electrodes containing either the untreated or the 2% SO_2-treated (400 °C, 2 h) HE NCM, conducted in LP57 electrolyte at 30 °C (first-charge cut-off at 4.7 V, followed by a CV step). (b) Measurements at TUM with electrodes containing either the untreated or the 0.5% SO_2-treated (200 °C, 1 h) HE-NCM, conducted at 25 °C in FEC/DEC-based electrolyte with a highly fluorinated ether as co-solvent and with 1 M $LiPF_6$ (first-cycle cut-off at 4.8 V, no CV step). In both cases, the discharge cut-off was 2.0 V. (c) Differential capacity vs V plots for the data in panel (a). (d) Differential capacity vs V plot for the data in panel (b). (e)–(f) The second cycle voltage profile and differential capacity vs V plots of untreated and SO_2-treated (400 °C, 2 h) cathodes. Note that capacity values are averaged from two (measured at TUM) and three (measured at BIU) electrochemical cells studied in parallel.

capacities are rather similar (Fig. 6a and Table SIV). In this test, the Coulombic efficiency increases from 84.5% to 87.7%. Note that these values are averaged from three cells. Similar behavior is obtained for the "200 °C, 1 h SO_2" sample. In this case, the first cycle charge capacity of 321 mAh g^{-1} was not altered at all by the treatment (Fig. 6b and Table SIV), while the discharge capacity was increased slightly. The results obtained demonstrate lower irreversible capacity loss in the 1st cycle of SO_2-treated HE-NCMs both for "400 °C, 2 h SO_2" and the "200 °C, 1 h SO_2" samples compared to the untreated one. This may indicate lesser side reactions of the SO_2-treated electrode materials with contaminants of EC-EMC/$LiPF_6$ solutions (HF, PF_5, H_2O, etc.). This is supposedly due to the presence of the surface species, like Li-sulfites and TM-sulfites, which can react with traces of HF and PF_5 (strong Lewis

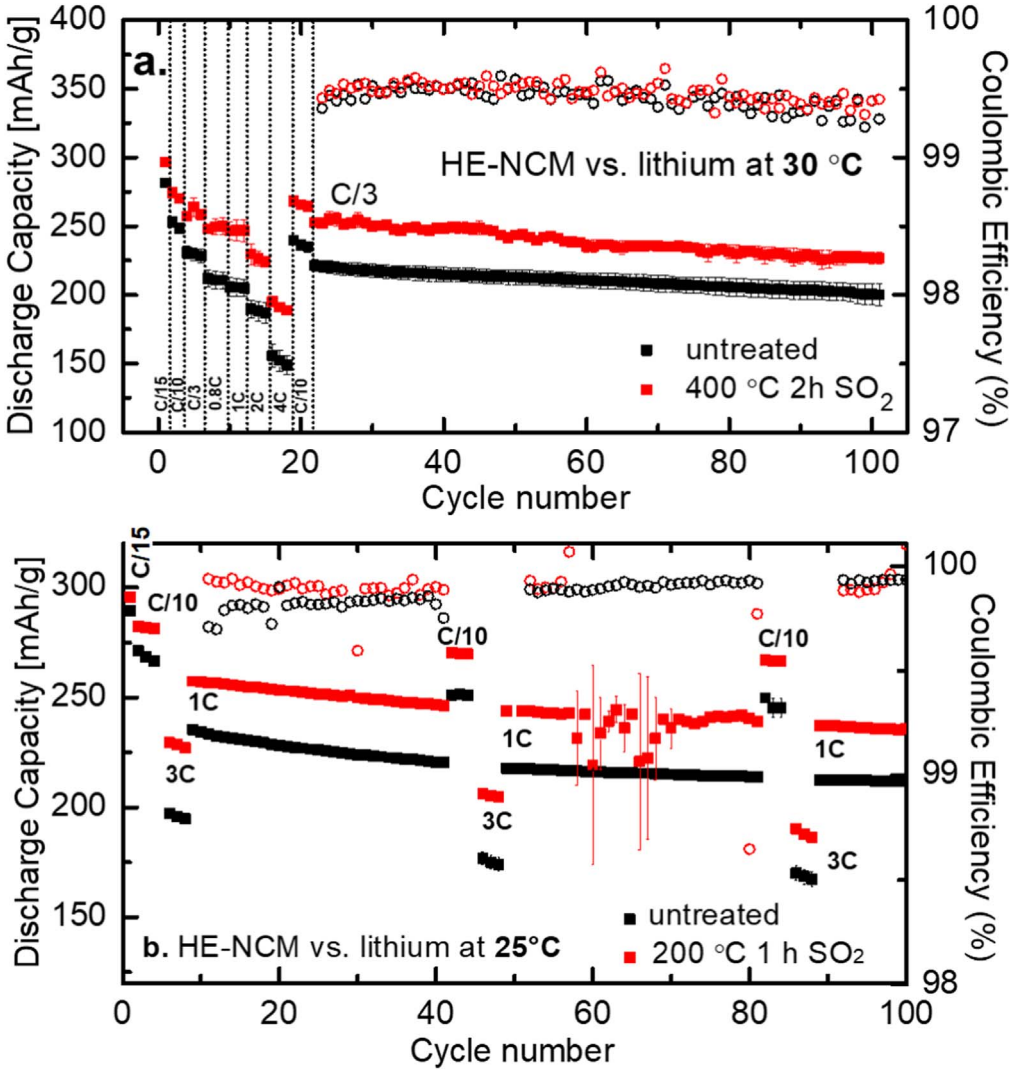

Figure 7. Discharge capacity vs cycle number of Li/HE-NCM half-cells with pristine untreated HE-NCM and with SO_2-treated HE-NCM, using the same cells for which the first-cycle activation is shown in Fig. 6. (a) Measurements conducted at BIU show the discharge capacity and the corresponding Coulombic efficiency (CE) at 30 °C during activation of electrode, rate capability studies and cycling at a C/3 rate (constant current - constant voltage mode CCCV in charge to 4.6 V and discharge to 2.0 V) for untreated HE-NCM (black) and the 2% SO_2-treated (400 °C, 2 h) HE-NCM (red) samples. (b) Measurements conducted at TUM showing the discharge capacity vs cycle number and the corresponding Coulombic efficiency (CE) at 25 °C between 4.7 and 2.0 V at C/10 rate (with a C/10 charge) and 3 C and 1 C (with a C/2 charge) for the untreated (black) and the 0.5% SO_2-treated (200 °C, 1 h) HE-NCM (red) materials.

acid) in solutions, thus reducing direct interactions with lithiated oxides at the interface, for instance: Li_2SO_3 (s) + 2HF (sol) → 2LiF (s) + H_2O + ↑SO_2 (g) and Li_2SO_3 (s) + PF_5 (sol) → 2LiF (s) + ↑POF_3 (gas) + ↑SO_2 (gas). It should be noted that these two hypothetical reaction equations are based on chemical intuition, without yet any experimental proof. Similar reactions at the surface of HE-NCMs were detected with lithium carbonate impurity, which in $LiPF_6$-containing solutions demonstrates the exothermal processes at ∼60 °C–80 °C according to our previous DSC measurements.[54]

It should be noted that the initial portions of the first-cycle discharge curves (from the upper cut-off potential to ∼3.5 V) are congruent for treated and untreated materials, however, towards the end of discharge (above approximately 150 mAh g^{-1}), the discharge voltage of the SO_2-treated materials slightly increases compared to the untreated ones (highlighted by yellow in Fig. 6). This is an important indication for the lower over-potentials, specifically at low SOC, i.e., close to the end of lithiation. The second cycle voltage profiles and differential capacity vs V plots of untreated and SO_2-treated (400 °C, 2 h) cathodes also confirm the reversibility (Figs. 6e–6f). The SO_2-treated cathodes showed Coulombic efficiency (CE) around 97% in the 2nd cycle.

Now we discuss the impact of SO_2 treatment on the rate performance and cycle life of HE-NCM electrodes. Figures 7 and S3 present the discharge capacity as a function of cycle number and selective voltage profiles measured at cycles 25, 50, and 75. We conclude from these results that both types of SO_2 treatment, viz., "400 °C, 2 h SO_2" at BIU (Fig. 7a) and "200 °C, 1 h SO_2" at TUM (Fig. 7b), substantially increase the discharge capacity of HE-NCM electrodes by ∼20–25 mAh g^{-1} during the cycle life test at all of the C-rates examined and demonstrated in Fig. 7. It was established, however, that the capacity retention is not affected by the SO_2 treatment, as is quite apparent by comparing Figs. 7a and 7b, and as is shown more quantitatively in Table SVI. Figures 7 & 8 and Table SV also contain the results of the rate capability measurements of untreated and both SO_2-treated samples. Interestingly, the capacity at any given rate is increased by the same ∼20–25 mAh g^{-1}, so that one can conclude that the rate-capability of the SO_2-treated materials is only affected indirectly, namely simply by the fact that its capacity, at any rate, is higher by the same value than that of the untreated HE-NCM.

One of the disadvantages of HE-NCM electrodes is a significant difference ΔV between the mean voltage in charge, and the mean

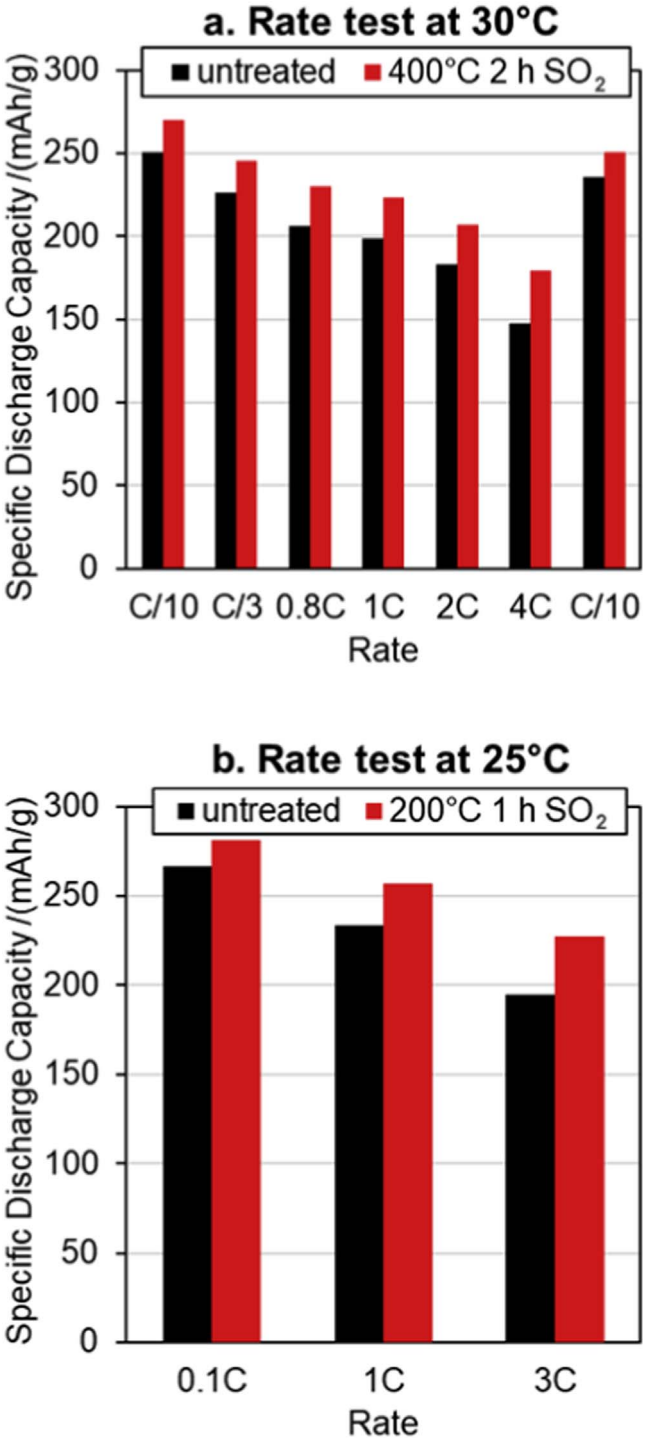

Figure 8. Discharge capacity measured during rate capability tests of SO_2-treated and untreated HE-NCM materials, in Li/HE-NCM half-cells (coin-type configuration) conducted at BIU and TUM. (a) Measurements conducted at BIU with untreated and 2% SO_2 (400 °C, 2 h)-treated HE-NCM at 30 °C after the first-cycle activation (Fig. 6a) and before the cycle-life test (Fig. 7a). (b) Measurements conducted at TUM with untreated and 0.5% SO_2 (200 °C, 1 h)-treated HE-NCM at 25 °C materials after the first-cycle activation (Fig. 6b). Cycling behavior at C/10, 1 C, and 3 C rates is shown in Fig. 7b.

voltage in discharge $\Delta V = V_{ch}\text{-}V_{disch}$ upon cycling, the so-called voltage hysteresis. This parameter should be stabilized to improve the performance of Li and Mn-rich high energy cathodes in Li-ion batteries.[55,56] We have established that average charge voltage and voltage hysteresis, both are significantly lower for the SO_2-treated materials compared to untreated ones, as it is shown in Figs. 9a–9b. The evolution of the voltage hysteresis with cycling is also lower for the treated sample (0.9 mV per cycle) compared to that of the untreated one (1.3 mV per cycle). Similar results were obtained for the half-cells tested at 25 °C. For the comparison of the voltage hysteresis, the slow rate of C/3 of the two datasets has been chosen. Thus, the depicted voltage hysteresis is caused not only by cell polarization but also by the lithium (de-)insertion kinetics during cycling. Along with the lower the voltage hysteresis of the treated samples, we have also established lower total cell impedance ($R_{cell} = R_{cathode} + R_{anode}$) registered as Nyquist plots from Li-cells with cathodes comprising SO_2-treated HE-NCM materials. Typical results are shown in Fig. S4 and Table SVII (fitted data), which indicate, for instance, that the resistance of the electrode surface layer (R_{sl}) is much lower for the latter cells measured after 100 cycles at a C/3 rate. Assuming that R_{sl} relates mainly to the cathode side, we suggest the lithium depletion from the surface layer as well as the redox processes during the SO_2 treatment might lead to a subtle restructuring of the near-surface layers and the formation of a few nanometer-thick layers (Fig. S6) comprising Li-sulfate, Li-sulfite, and TM-sulfates as established by XPS studies. We suggest that nano-sized Li_2SO_4 surface species may act as Li-ion conductive domains[57,58] enhancing thus the lithium-ion transport through the near-surface region into the bulk of the oxide. We propose that the higher discharge capacity of SO_2-treated HE-NCM during the first activation cycle, as well as its enhanced capacity during cycling, might be explained by the *"non-electrochemical" activation* of the Li_2MnO_3 domains (as discussed below) and by the enhanced the lithium-ion transport through the near-surface region into the oxide bulk.

In Fig. 10, we present differential capacity dQ/dV vs V plots and voltage profiles for untreated and SO_2-treated ("400 °C, 2 h SO_2") HE-NCM cathode materials registered from cycles 25, 50, 75, and 100. They demonstrate typical results related to the extraction of Li^+ from the Li^+ layer that is usually accompanied with oxidation processes, like $Mn^{3+/4+}$ (~3 V), $Ni^{2+/4+}$ and $Co^{3+/4+}$ (~3.8 V–4.1 V) of the NCM component.[51,53]

From the dQ/dV curves of untreated and SO_2-treated HE-NCM materials shown in Fig. 10, we observe a shifting of the main oxidation peak from 3.84 V to 3.97 V of the untreated material. The peaks become broader as the cycling continues, indicating sluggish electrochemical kinetics. However, in the SO_2-treated material, the peak position remains unaffected (~3.83 V), and this peak's width doesn't change upon cycling in contrast to the untreated material. A peak below 3.0 V (marked with the black arrow in Fig. 10a) may indicate the formation of spinel or spinel-like phase.[56]

Interactions of HE-NCM materials with battery solutions studied by DSC.—The DSC profiles for the untreated and treated materials are presented in Fig. S5. The 1st minor peak at ~80 °C for both materials corresponds to the reactions between the electrolyte and surface Li_2CO_3 species.[54] The onset temperature for untreated and treated materials was found to be 183 °C and 217 °C, respectively. The DSC profile for the untreated material with the LP57 solution shows four major exothermic peaks, positioned around 202, 229, 251, and 272 °C. The exothermic heat release for the temperature zones **(I)** and **(II)** is typically related to the reaction between the released oxygen from the HE-NCM lattice and EC and EMC solvents, while the heat release for the temperature zone **(III)** and **(IV)** corresponds to the combustion reaction of these solvents with the HE-NCM material.[59–61] The specific total heat released was determined to be $Q_t = 287 \pm 5$ and $Q_t = 258 \pm 3$ J g^{-1} for the untreated and SO_2-treated materials, respectively. The lower Q_t value measured for the treated HE-NCM can be attributed partially to lesser surface reactions of this material with solution species by interactions of the lithium sulfate or lithium sulfite formed, for example, with HF, as shown above. Surprisingly, the

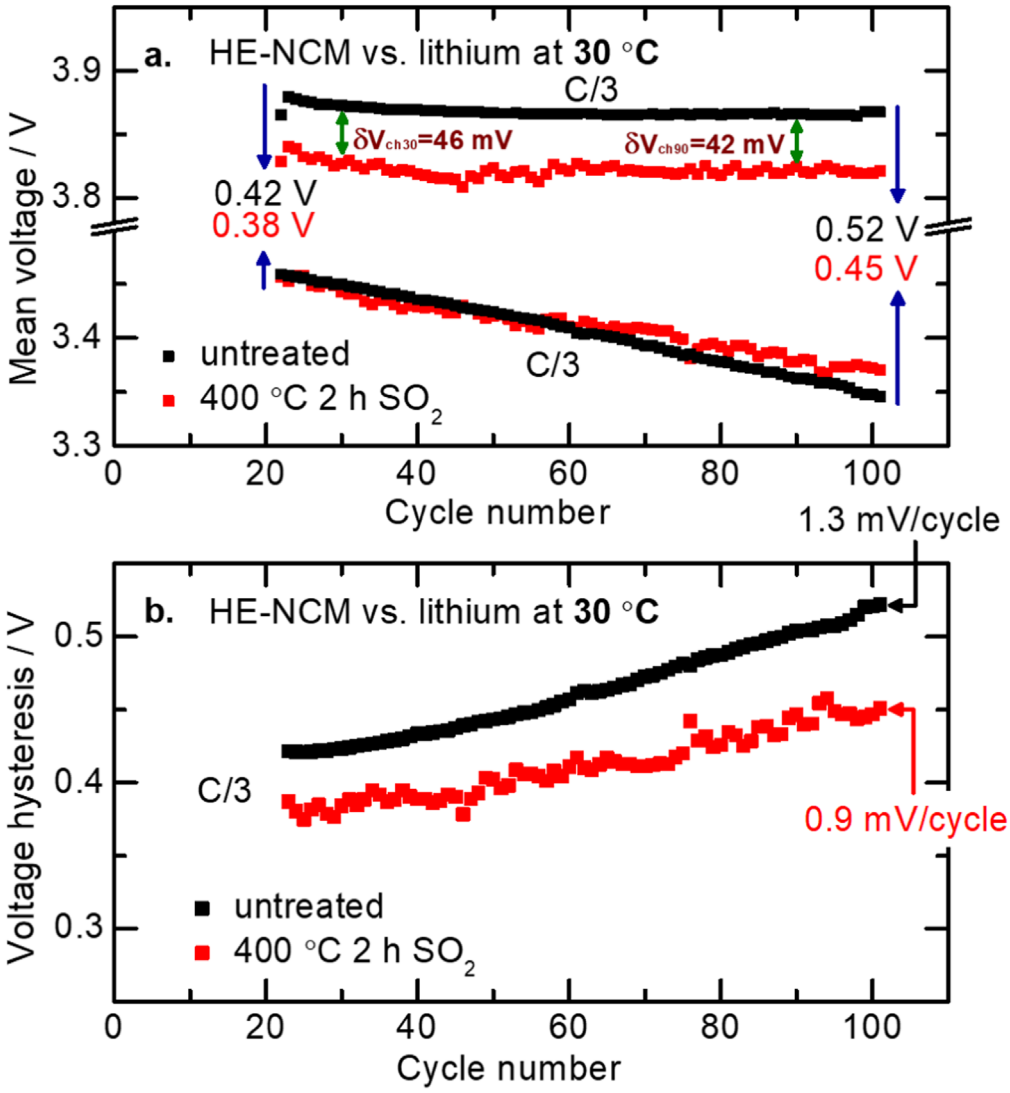

Figure 9. (a) Average voltage and (b) Voltage hysteresis calculated as the difference between mean charge and discharge voltages for untreated HE-NCM electrode compared to the electrode comprising the material treated with 2% SO_2 (400 °C, 2 h). The green arrows in (a) indicate that the mean voltage in charge is ~42–46 mV lower for the SO_2 treated sample. These data are extracted from Fig. 7a.

temperature zone **(I)** is not visible, and the other temperature zones are shifted to higher temperatures for the treated material, as follows from Fig. S5. The heat evolution due to the reaction between the HE-NCM material and EC and EMC species was also found to be lessened after SO_2 treatment. This may be due to the presence of Li_2SO_4 nano-sized layer, which was formed on the material (Fig. S6) during thermal SO_2 treatment.

Structural analysis of cycled HE-NCM electrodes.—Post mortem analysis of the cycled SO_2-treated HE-NCM electrode ("400 °C, 2 h") was performed after the 100 cycles. Transmission Electron Microscopy (TEM) studies provided detailed structural information. As expected, we observed the presence of the layered rhombohedral phase of the $LiNiO_2$ type (*R-3m*) and the monoclinic phase Li_2MnO_3 described by space group *C2/m* (see electron diffraction patterns in Figs. 11a–11b). As demonstrated in Fig. 11c, the Li_2SO_4 phase, which was detected in the uncycled SO_2-treated samples by XRD (Fig. 1), retains its stability and still exists on the cycled electrodes (after 100 cycles). Besides, the cubic spinel (*Fd-3m*), was also detected in the cycled samples (see Fig. 11d). It was formed by a layered-to-spinel transformation mechanism in the course of prolonged cycling. This observation correlates well with the electrochemical data, which also indicated the formation of a spinel phase (Fig. 10).

Possible mechanism of SO_2 gas treatment of HE-NCM materials.—Based on the results obtained, we suggest that mechanism of the surface thermal treatment of $0.35Li_2MnO_3{\cdot}0.65LiNi_{0.35}Mn_{0.45}Co_{0.20}O_2$ with SO_2 at 200 °C–400 °C may include first the chemisorption of SO_2 on the active sites of the lithiated oxide, followed by chemical interactions, for instance with the Li_2MnO_3 component (nano-domains) as shown in scheme (1):

$$2\,Li_2MnO_3 + SO_2 \rightarrow Li_2SO_4 + 2LiMn^{(3+\alpha)}O_{(2-\beta)} + \beta O_2 \quad \alpha < 1,\ \beta = \alpha/2 \qquad [1]$$

In this solid-gas reaction between Li_2MnO_3 domains and SO_2 at high enough temperature, the sulfur is observed to get oxidized from S^{4+} (in SO_2) to S^{6+} (in the surface sulfate species detected by XPS), accompanied with a partial reduction of manganese from Mn^{4+} to a valence state lower than 4+, $Mn^{(3+\alpha)}$, as suggested by the scheme (1). While minor changes occur in the manganese XPS spectra upon SO_2 treatment, they, unfortunately, do not provide unambiguous confirmation of scheme (1). Additionally, the lattice oxygen can be

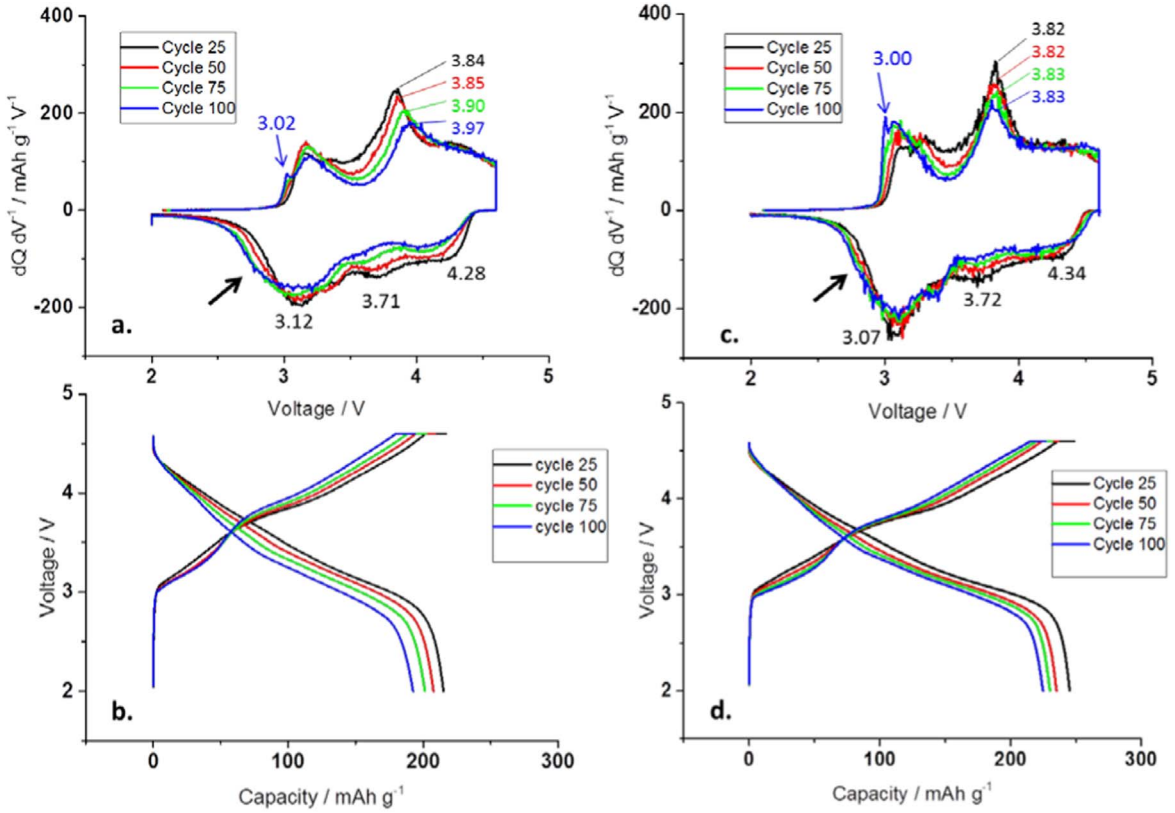

Figure 10. Differential capacity dQ/dV vs V plots (a), (c) and voltage profiles (b), (d) recorded from cycles 25, 50, 75, and 100 of HE-NCM untreated material (a), (b) and HE-NCM treated with 2% SO_2 during 2 h at 400 °C (c), (d). Coin-type cells with Li anodes cycled in LP57 electrolyte solution at 30 °C (same cells as in Figs. 6 and 7). Numbers in dQ/dV plots show the potentials of the red-ox peaks.

involved in this reaction on the surface, forming manganese oxide, lithium oxide Li_2O, as follows:

$$Li_2Mn^{IV}O_3 + SO_2 + (1-\beta)O_{lattice} \rightarrow Li_2O + Mn^{(3+\alpha)}O_{(2-\beta)} + SO_3\uparrow \quad [2]$$

Our XPS results demonstrate the decrease in oxygen with SO_2 treatment from 50.3% to 36.2% (O 1s spectra in Fig. 5b). This can be an indication of lattice oxygen participation in the above reaction, although the formation of the screening sulfate layer on the surface cannot be ruled out as well.

Lithium peroxide was not detected in our XPS measurements (its band signal typically appears at ~531 eV in the Oxygen spectra) likely due to its transformation to $Li_2O_{2-\delta}$ or lithia and oxygen at temperatures of 280 °C and higher,[62] or due to a negligible amount of Li_2O_2 remained and masked by sulfate, sulfite and carbonate species. One more reaction can be considered of $LiMn^{(3+\alpha)}O_{(2-\beta)}$ decomposition to spinel $LiMn_2O_4$ (cubic) and Li_2MnO_3 at temperatures $T > 350$ °C.[63] Spinel (tetragonal) and lithium peroxide can also be formed via the following reaction:

$$2Li_2MnO_3 + SO_2 + 2O_{lattice} \rightarrow Li_2Mn_2O_4 + Li_2O + SO_3\uparrow \quad [2a]$$

It should be noted that the processes described above represent feasible reactions, which however we could not prove unambiguously by XPS analysis. Note also that possible formation of some surface species due to the SO_2-treatment and their detection by XPS should be considered as relevant only to some degree in the context of "integrated" $0.35Li_2MnO_3{\cdot}0.65LiNi_{0.35}Mn_{0.45}Co_{0.20}O_2$ material. We suggest that the spectroscopic results measured from this SO_2-treated material should be taken with great caution since they reflect interactions of SO_2 with nano-sized domains of monoclinic Li_2MnO_3 and rhombohedral $Li(TM)O_2$ structures, respectively interconnected at the atomic level[53,64,65] and not with "single" Li_2MnO_3 and $LiNi_{0.35}Mn_{0.45}Co_{0.20}O_2$ materials. An important assumption can be deduced from the discussion of possible interactions of HE-NCM material with SO_2: since manganese is reduced to $Mn^{(3+\alpha)}$ valence state ($\alpha < 1$) and Li^+ is extracted in the form of sulfate and oxides according to reactions 1, 2, and 2a, we consider that Li_2MnO_3 domains on the *surface* of the HE-NCM undergo *"chemical"* or *"non-electrochemical" activation.* These processes resemble the Li_2MnO_3 electrochemical activation upon the initial charge of HE-NCM electrodes up to 4.7–4.8 V in lithium cells with the Li^+ extraction, formation of MnO_2 and oxygen removal from the bulk, which had been proposed in the past[66]:

$$Li_2MnO_3 \rightarrow 2Li^+ + 2e^- + MnO_2 + 1/2O_2\uparrow \quad [2b]$$

In regard of the O_2 removal during the 1st charge, it was revealed, however in a very recent study by Strehle et al.[8] that the overall amount of released oxygen from HE-NCM electrodes (evolved toward the end of the activation plateau at ~4.5 V) only corresponds to roughly 10% of what be required for a bulk conversion according to reaction 2b. This provided strong evidence that oxygen is only released from a several nm thick near-surface layer, which was confirmed later on by high-resolution transmission electron microscopy.[67] These authors suggest that structural rearrangement, such as the formation of a spinel-like "near-surface region," occurs on the surface of the HE-NCM material. We propose that in the case of the SO_2-treated $0.35Li_2MnO_3{\cdot}0.65LiNi_{0.35}Mn_{0.45}Co_{0.20}O_2$ material, reactions 1, 2 and 2a reflect possible surface structural rearrangements considered as *"chemical" activation.* Therefore, after being treated with SO_2, HE-NCM materials comprise the Li_2MnO_3 domains *already activated at the surface,* while the *bulk* of the material remains unchanged. This is confirmed by analytical

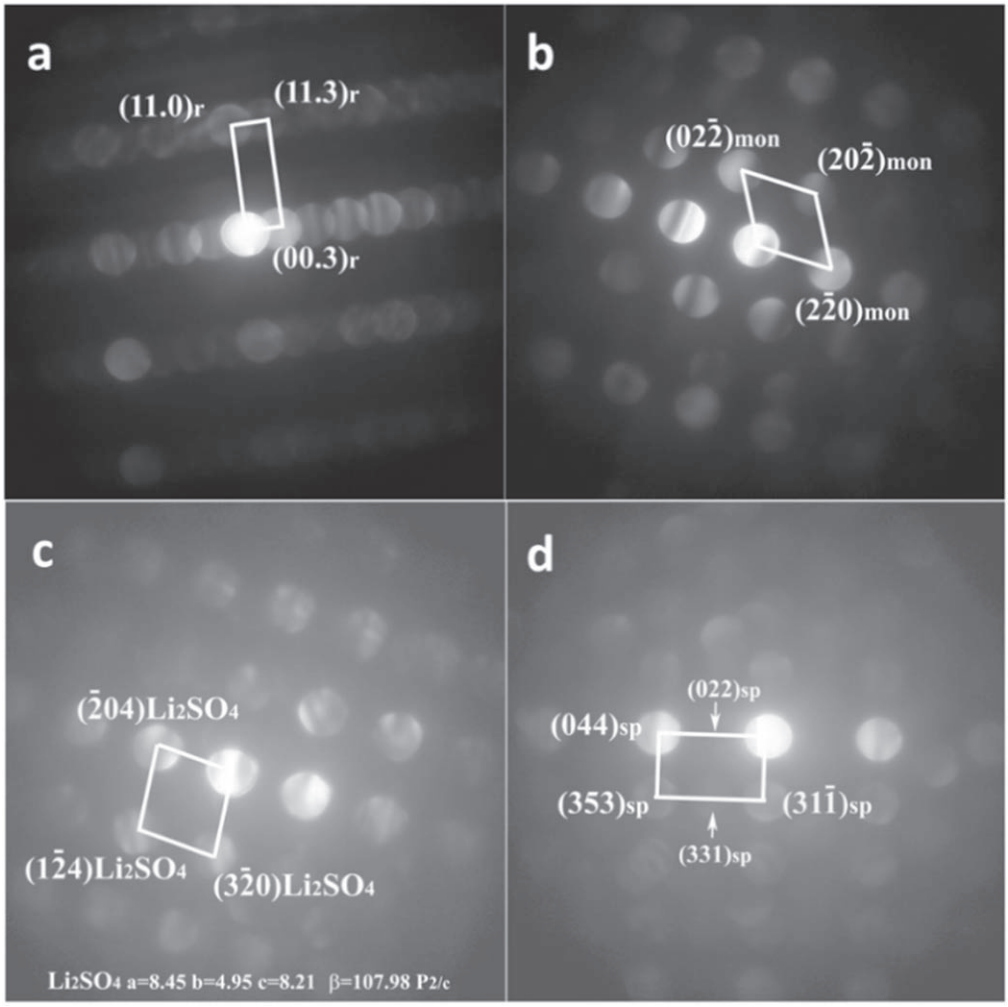

Figure 11. (a) and (b) Convergent Beam Electron Diffraction (CBED) patterns taken from the 2% SO_2-treated HE-NCM (400 °C, 2 h) after 100 cycles in coin-type Li-cells showing the presence of rhombohedral (r) and monoclinic (m) phases, respectively and (c), (d) the presence of Li_2SO_4 and cubic spinel phases, respectively.

structural data, revealing no changes in the unit cell parameters values of untreated and SO_2-treated samples measured by XRD (Fig. 1 and Table I). We also conclude from the results of the electrochemical studies that voltage profiles measured in the 1st charging of untreated $0.35Li_2MnO_3{\cdot}0.65LiNi_{0.35}Mn_{0.45}Co_{0.20}O_2$ and SO_2-treated materials exhibit the same activation potential of ~4.5 V, the same extent of the voltage plateau corresponding to a capacity of ~130 mAh g^{-1} (Fig. 6), thus implying similarity in their bulk activation processes. However, the slightly increased discharge capacities in the 1st cycle and ~20–25 mAh g^{-1} higher specific capacities of the SO_2-treated HE-NCM over extended cycling and at all C-rates may be due to the contribution from the above hypothesized $Mn^{(3+\alpha)}/Mn^{4+}$ red-ox and lithiated $LiMn^{(3+\alpha)}O_{(2-\beta)}$ species formed due to the non-electrochemical activation of Li_2MnO_3.

Further, the mechanism of the SO_2 treatment includes interactions of $LiMnO_2$ (or more accurately $LiMn^{(3+\alpha)}O_{(2-\beta)}$) formed in the reaction 1 with SO_2 via schemes (3) and (4), resulting in the formation of both Li-sulfite and Li-sulfate and transition metal sulfites and sulfates:

$$2LiMnO_2 + 3SO_2 \rightarrow Li_2SO_3 + MnSO_3 + MnSO_4 \quad [3]$$

$$2LiMnO_2 + 3SO_2 \rightarrow Li_2SO_4 + 2MnSO_3 \quad [4]$$

Li_2SO_4 and Li_2SO_3 remain stable on the surface since the temperatures of their decomposition are higher than 400 °C (melting point is 860 °C).[68] The presence of the crystalline lithium sulfate was unequivocally detected in this study by XRD measurements (Fig. 1) and after prolonged cycling by TEM (Fig. 11c).

The reaction of the $Li(TM)O_2$ component of HE-NCM layered oxide with SO_2 may result in the formation of Li_2SO_4 and transition metal sulfites associated with partial reduction of the valence state of transition metals (mainly Mn and Co) in agreement with the paper by Andreu et al.[34] showing that these TMs can be reduced during SO_2 adsorption process:

$$2Li(TM)O_2 + 3SO_2 \rightarrow Li_2SO_4 + 2(TM)SO_3 \quad [5]$$

One would also expect a chemical reaction between lithiated transition metal oxide and SO_2 to form Li_2SO_3 and sulfites of transition metals, as follows:

$$2Li(TM)O_2 + 4SO_2 \rightarrow Li_2SO_3 + (TM)_2(SO_3)_3 \quad [6]$$

It can be supposed that the species like Li_2SO_4, Li_2SO_3 and $(TM)_2(SO_3)_3$ formed on the surface (Figs. 1 and 11) protect partly the cathodes comprising SO_2-treated $0.35Li_2MnO_3{\cdot}0.65LiNi_{0.35}Mn_{0.45}Co_{0.20}O_2$ materials from interactions with solution species, decreasing thus the irreversible capacity loss compared to electrodes comprising untreated materials (Fig. 6 and Table SIV). Moreover, Li_2SO_4 formed due to the SO_2 treatment can lower the CO_2 gas generation from the decomposition reactions of the electrolyte solution.[69]

Conclusions

We proposed in this work a surface modification approach to enhance the electrochemical performance of HE-NCM cathode materials $0.35Li_2MnO_3{\cdot}0.65LiNi_{0.35}Mn_{0.45}Co_{0.20}O_2$ via their treatment with SO_2 gas at 200 °C–400 °C. First, we concluded that the SO_2 treatment resulted in the oxidation of sulfur to S^{6+} valence state, partial reduction of manganese, and the formation of sulfates and sulfites on the surface. An important conclusion is that the bulk of the material remained unchanged, as confirmed by X-ray and electron diffraction studies. The main findings of this research can be formulated as follows: the discharge capacity of the SO_2-treated samples increases by ∼20–25 mAh g^{-1} even over extended cycling and at all examined C-rates, and the evolution of the voltage hysteresis is lower compared to the untreated ones.

It is suggested that the enhancement of the electrochemical performance of the electrodes comprising SO_2-treated materials may be ascribed to the contribution from the hypothesized $Mn^{(3+\alpha)}/Mn^{4+}$ red-ox and lithiated $LiMn^{(3+\alpha)}O_{(2-\beta)}$ species formed due to the "*non-electrochemical activation*" of the Li_2MnO_3 component. We thus propose that $0.35Li_2MnO_3{\cdot}0.65LiNi_{0.35}Mn_{0.45}Co_{0.20}O_2$ electrodes in Li-cells comprise this component (nano-domains) *as already surface-activated* due to the SO_2-treatment. The positive effect of the increased specific capacities can be attributed partially to the modified interface comprising Li-ions conductive nano-sized phase Li_2SO_4 formed upon SO_2 interactions with the cathode material. We speculate that the lower heat evolved upon chemical reactions of the SO_2-treated HE-NCM material with EC-EMC/$LiPF_6$ solution species may also relate to the presence of Li_2SO_4 (and other sulfates) on the surface. It can be concluded from the post-cycling structural analysis by TEM that the Li_2SO_4 phase retains its stability and still exists on the cycled electrodes. Thus, we conclude that the formation of this stable surface phase is an important result of the SO_2 treatment that affects the electrochemical and thermal behavior of HE-NCM electrodes.

The proposed methodology to modify the surface of Li and Mn-rich materials by SO_2 treatment and to enhance thus their electrochemical performance can also be used for other cathodes, for instance, comprising high-capacity Ni-rich layered-type materials considered as the most promising in LIBs for electro-mobility applications.

Acknowledgments

A part of the work discussed here is funded by BASF, Germany, under the framework of the project for electro-mobility; by the Israeli Prime Minister's Office; and by the Israeli Committee for Higher Education within the framework of the INREP project.

ORCID

Johannes Sicklinger https://orcid.org/0000-0003-2815-993X
Sandipan Maiti https://orcid.org/0000-0001-9661-7037
Louis Hartmann https://orcid.org/0000-0002-3964-1935

References

1. M. M. Thackeray, C. S. Johnson, J. T. Vaughey, N. Li, and S. A. Hackney, *J. Mater. Chem.*, **15**, 2257 (2005).
2. P. K. Nayak, E. M. Erickson, F. Schipper, T. R. Penki, N. Munichandraiah, P. Adelhelm, H. Sclar, F. Amalraj, B. Markovsky, and D. Aurbach, *Adv. Energy Mater.*, **8**, 1702397 (2018).
3. F. Amalraj et al., *J. Electrochem. Soc.*, **160**, A324 (2013).
4. E. M. Erickson, F. Schipper, T. R. Penki, J.-Y. Shin, C. Erk, F.-F. Chesneau, B. Markovsky, and D. Aurbach, *J. Electrochem. Soc.*, **164**, A6341 (2017).
5. J. Zheng, S. Myeong, W. Cho, P. Yan, J. Xiao, C. Wang, J. Cho, and J. Zhang, *Adv. Energy Mater.*, **7**, 1601284 (2017).
6. K. Kleiner, B. Strehle, A. R. Baker, S. J. Day, C. C. Tang, I. Buchberger, F. F. Chesneau, H. A. Gasteiger, and M. Piana, *Chem. Mater.*, **30**, 3656 (2018).
7. R. Jung, M. Metzger, F. Maglia, C. Stinner, and H. A. Gasteiger, *J. Electrochem. Soc.*, **164**, A1361 (2017).
8. B. Strehle, K. Kleiner, R. Jung, F. Chesneau, M. Mendez, H. A. Gasteiger, and M. Piana, *J. Electrochem. Soc.*, **164**, A400 (2017).
9. X. Zhang, I. Belharouak, L. Li, Y. Lei, J. W. Elam, A. Nie, X. Chen, R. S. Yassar, and R. L. Axelbaum, *Adv. Energy Mater.*, **3**, 1299 (2013).
10. Y. S. Jung, A. S. Cavanagh, L. Gedvilas, N. E. Widjonarko, I. D. Scott, S. H. Lee, G. H. Kim, S. M. George, and A. C. Dillon, *Adv. Energy Mater.*, **2**, 1022 (2012).
11. F. Amalraj et al., *J. Electrochem. Soc.*, **160**, A2220 (2013).
12. Z. D. Li, Y. C. Zhang, H. F. Xiang, X. H. Ma, Q. F. Yuan, Q. S. Wang, and C. H. Chen, *J. Power Sources*, **240**, 471 (2013).
13. J. Xie et al., *ACS Nano*, **11**, 7019 (2017).
14. K. Gao, S.-X. Zhao, S.-T. Guo, and C.-W. Nan, *Electrochim. Acta*, **206**, 1 (2016).
15. X.-D. Zhang, J. Shi, J. Liang, Y. Yin, J. Zhang, X. Yu, and Y.-G. Guo, *Adv. Mater.*, **30**, 1801751 (2018).
16. X. Guan, B. Ding, X. Liu, J. Zhu, C. Mi, and X. Zhang, *J. Solid State Electrochem.*, **17**, 2087 (2013).
17. F. Yu, L. Que, C. Xu, M.-J. Wang, G. Sun, J. Duh, and Z. Wang, *Nano Energy*, **59**, 527 (2019).
18. E. Hu et al., *Nat. Energy*, **3**, 690 (2018).
19. P. K. Nayak, J. Grinblat, M. Levi, E. Levi, S. Kim, J. W. Choi, and D. Aurbach, *Adv. Energy Mater.*, **6**, 1502398 (2016).
20. P. K. Nayak, J. Grinblat, M. Levi, O. Haik, E. Levi, and D. Aurbach, *J. Solid State Electrochem.*, **19**, 2781 (2015).
21. P. K. Nayak, J. Grinblat, E. Levi, M. Levi, B. Markovsky, and D. Aurbach, *Phys. Chem. Chem. Phys.*, **19**, 6142 (2017).
22. M. N. Ates, Q. Jia, A. Shah, A. Busnaina, S. Mukerjee, and K. M. Abraham, *J. Electrochem. Soc.*, **161**, A290 (2014).
23. G. Chen et al., *Nano Energy*, **57**, 157 (2019).
24. D. Liu, X. Fan, Z. Li, T. Liu, M. Sun, C. Qian, M. Ling, Y. Liu, and C. Liang, *Nano Energy*, **58**, 786 (2019).
25. D. Wang, T. Xu, Y. Li, D. Pan, X. Lu, Y.-S. Hu, S. Dai, and Y. Bai, *ACS Appl. Mater. Interfaces*, **10**, 41802 (2018).
26. P. K. Nayak, J. Grinblat, M. Levi, and D. Aurbach, *J. Electrochem. Soc.*, **162**, A596 (2015).
27. M. Ueda, M. Ohe, J.-H. Kim, S. Yonezawa, and M. Takashima, *J. Fluor. Chem.*, **149**, 88 (2013).
28. S. Yonezawa, M. Yamasaki, and M. Takashima, *J. Fluor. Chem.*, **125**, 1657 (2004).
29. U. Breddemann et al., *ChemElectroChem*, **6**, 3337 (2019).
30. J.-S. Kim, C. S. Johnson, J. T. Vaughey, and M. M. Thackeray, *J. Power Sources*, **153**, 258 (2006).
31. M. N. Richard, E. W. Fuller, and J. R. Dahn, *Solid State Ionics*, **73**, 81 (1994).
32. Y. Ji, R. Li, D. Mu, S. Sun, C. Dai, and F. Ding, *J. Electrochem. Soc.*, **165**, A2880 (2018).
33. E. M. Erickson et al., *Adv. Energy Mater.*, **7**, 1700708 (2017).
34. N. Andreu, D. Flahaut, R. Dedryvère, M. Minvielle, H. Martinez, and D. Gonbeau, *ACS Appl. Mater. Interfaces*, **7**, 6629 (2015).
35. G. Vallverdu, M. Minvielle, N. Andreu, D. Gonbeau, and I. Baraille, *Surf. Sci.*, **649**, 46 (2016).
36. N. Andreu, I. Baraille, H. Martinez, R. Dedryvère, M. Loudet, and D. Gonbeau, *J. Phys. Chem. C*, **116**, 20332 (2012).
37. C. S. Yoon, K.-J. Park, U.-H. Kim, K. H. Kang, H.-H. Ryu, and Y.-K. Sun, *Chem. Mater.*, **29**, 10436 (2017).
38. U. Kim, H. Ryu, J. Kim, R. Mücke, P. Kaghazchi, C. S. Yoon, and Y. Sun, *Adv. Energy Mater.*, **9**, 1803902 (2019).
39. J. Lu, Z. Chen, F. Pan, L. A. Curtiss, and K. Amine, *Nat. Nanotechnol.*, **11**, 1031 (2016).
40. F. A. Susai et al., *ACS Appl. Energy Mater.*, **3**, 3609 (2020).
41. J. Sicklinger, M. Metzger, H. A. Gasteiger, H. Beyer, and D. Pritzl, *J. Eletrochemical Soc.*, **166**, 2322 (2019).
42. W. Kraus and G. Nolze, *J. Appl. Crystallogr.*, **29**, 301 (1996).
43. N. W. Alcock, D. A. Evans, and H. D. B. Jenkins, *Acta Crystallographica B*, **29**, 360 (1973).
44. M. C. Biesinger, B. P. Payne, A. P. Grosvenor, L. W. M. Lau, A. R. Gerson, and R. S. C. Smart, *Appl. Surf. Sci.*, **257**, 2717 (2011).
45. M. Kantcheva, M. U. Kucukkal, and S. Suzer, *J. Mol. Struct.*, **483**, 19 (1999).
46. J. H. Lee, Y. J. Sa, T. K. Kim, H. R. Moon, and S. H. Joo, *J. Mater. Chem. A*, **2**, 10435 (2014).
47. Rosy, H. Sclar, E. Evenstein, S. Haber, S. Maiti, T. Sharabani, M. Leskes, and M. Noked, *Chem. Mater.*, **31**, 3840 (2019).
48. P. van der Heide, *X-ray Photoelectron Spectrosc : An Introduction to Principles and Practices* (John Wiley & Sons, Inc, Hoboken, NJ, United States of America) 9781118162897 (2011).
49. A. R. Gonzalez-Elope, J. P. Espinos, A. Femandez, and G. Munuera, *Appl. Surf. Sci.*, **45**, 103 (1990).
50. M. C. Biesinger, B. P. Payne, L. W. M. Lau, A. Gerson, and R. S. C. Smart, *Surf. Interface Anal.*, **41**, 324 (2009).
51. N. S. McIntyre and M. G. Cook, *Anal. Chem.*, **47**, 2208 (1975).
52. Y. Cai, Y. Pan, J. Xue, Q. Sun, G. Su, and X. Li, *Appl. Surf. Sci.*, **255**, 8750 (2009).
53. S. Muhammad et al., *Nano Energy*, **21**, 172 (2016).
54. O. Haik, N. Leifer, Z. Samuk-Fromovich, E. Zinigrad, B. Markovsky, L. Larush, Y. Goffer, G. Goobes, and D. Aurbach, *J. Electrochem. Soc.*, **157**, A1099 (2010).
55. J. R. Croy, K. G. Gallagher, M. Balasubramanian, B. R. Long, and M. M. Thackeray, *J. Electrochem. Soc.*, **161**, A318 (2014).
56. K. G. Gallagher, J. R. Croy, M. Balasubramanian, M. Bettge, D. P. Abraham, A. K. Burrell, and M. M. Thackeray, *Electrochem. Commun.*, **33**, 96 (2013).
57. N. Kimura and M. Greenblatt, *Mater. Res. Bull.*, **19**, 1653 (1984).
58. C. Julien and G. A. Nazri, *Solid State Batteries: Materials Design and Optimization* (Kluwer Academic Publishers, Norwell, United States of America) (1994).
59. T. Inoue and K. Mukai, *ACS Appl. Mater. Interfaces*, **9**, 1507 (2017).

60. O. Haik et al., *J. Solid State Electrochem.*, **18**, 2333 (2014).
61. K. Mukai and T. Inoue, *Electrochem. Commun.*, **88**, 101 (2018).
62. K. P. C. Yao, D. G. Kwabi, R. A. Quinlan, A. N. Mansour, A. Grimaud, Y.-L. Lee, Y.-C. Lu, and Y. Shao-Horn, *J. Electrochem. Soc.*, **160**, A824 (2013).
63. J. Molenda, M. Ziemnicki, M. Molenda, M. Bucko, and J. Marzec, *Mater. Sci. Pol.*, **24**, 75 (2006).
64. M. M. Thackeray, S.-H. Kang, C. S. Johnson, J. T. Vaughey, R. Benedek, and S. A. Hackney, *J. Mater. Chem.*, **17**, 3112 (2007).
65. J. Bareño, M. Balasubramanian, S. H. Kang, J. G. Wen, C. H. Lei, S. V. Pol, I. Petrov, and D. P. Abraham, *Chem. Mater.*, **23**, 2039 (2011).
66. J.-S. Kim, C. S. Johnson, J. T. Vaughey, M. M. Thackeray, S. A. Hackney, W. Yoon, and C. P. Grey, *Chem. Mater.*, **16**, 1996 (2004).
67. T. Teufl, B. Strehle, P. Müller, H. A. Gasteiger, and M. A. Mendez, *J. Electrochem. Soc.*, **165**, A2718 (2018).
68. G. E. Tobón-Zapata, E. G. Ferret, S. B. Etcheverry, and E. J. Baran, *J. Therm. Anal. Calorim.*, **61**, 29 (2000).
69. K. Watanabe and M. Deguchi, *Positiveelectrode for nonaqueous electrolyte secondary battery, method for fabricating the same, and nonaqueous electrolyte secondary battery*, US 2011/0117437 A1 (2011), https://patents.google.com/patent/US20110117437A1/en?oq=US+2011%2f0117437+A1.

Supporting Information

Enhancement of Electrochemical Performance of Lithium and Manganese-Rich Cathode Materials *via* Thermal Treatment with SO_2

Hadar Sclar,[1,=] Johannes Sicklinger,[2,=] Evan M. Erickson,[1,a] Sandipan Maiti,[1] Judith Grinblat,[1] Michael Talianker,[3] Francis Amalraj Susai,[1] Larisa Burstein,[4] Hans Beyer,[2,z] Louis Hartmann,[2] Gregory Avruschenko,[1] Hubert A. Gasteiger,[2] Boris Markovsky,[1] Doron Aurbach,[1,z]

[1]Department of Chemistry, Bar-llan University, Ramat-Gan 5290002, Israel

[2]Department of Chemistry and Catalysis Research Center, Technische Universität, M¨unchen, D-85748 Garching, Germany

[3]Department of Materials Engineering, Ben-Gurion University of the Negev, Beer-Sheva 84105, Israel

[4]Wolfson Applied Materials Research Center, Tel-Aviv University, Tel-Aviv 69978, Israel

[=]Authors contributed equally to this work

[a]Present address: Department of Mechanical Engineering, University of Texas at Austin, Austin, TX, USA

[z]E-mail: aurbach@mail.biu.ac.il; hans.beyer@tum.de

Contents

Electrode preparation, cell assembly, and cell testing at BIU

Electrodes for electrochemical studies were prepared using 80 wt. % HE-NCM active material, 5 wt. % Super P carbon black, 5 wt. % KS6 graphite and 10 wt. % PVDF (Solef 5130) dispersed in N-methyl-2-pyrrolidone (NMP, Sigma-Aldrich). Electrode loading was ~1.6-2.4 mg_{HE-NCM}/cm^2. We used EC-EMC (3:7) /1M $LiPF_6$ electrolyte solution LP-57 from BASF and Celgard 2500 polypropylene separator in electrochemical cells.

The composition of HE-NCM material was determined at BASF by ICP analysis and the calculated ratios of TMs to Li are presented in Table S1. The ratios of TM/Li calculated for untreated and SO_2-treated samples are close to those of the pristine (as-received) material.

Table S1: Formula of the as-received HE-NCM material (BASF) calculated based on ICP analysis and calculated ratios TM/Li for untreated and "SO_2 2h 400℃" treated HE-NCM materials

Materials	Co/Li	Ni/Li	Mn/Li
Calculated formula $Li_{1.35}[Mn_{0.6425}Ni_{0.2275}Co_{0.13}]O_{2+\delta}$	0.096	0.168	0.470
Untreated HE-NCM	0.093	0.165	0.449
HE-NCM treated SO_2 (2 h 400 °C)	0.096	0.171	0.457

Electrochemical testing of untreated HE-NCM and the "400 °C 2 h SO_2" treated material was carried out by galvanostatic cycling in half-cells of coin-type 2325 (Li metal foil as a counter electrode). All cells were subjected to cycling at 30°C, as follows: the first cycle was performed from OCV to 4.7 V in charging and to 2.0 V in discharging, at a C/15 rate, C defined as 250 mAh g^{-1} (corresponding to 0.40 – 0.50 mAh/cm^2). including CC-CV (constant current-constant voltage) protocol. All subsequent cycles were performed from 2.0 to 4.6 V. For the first cycle, a constant voltage step of 3 h was applied at the anodic limit; all subsequent constant voltage steps were for 30 min. After the initial C/15 formation cycle, two cycles at C/10 were performed, followed by three cycles at C/3, 0.8C, 1C, 2C, 4C, and 0.1C rates, after which 80 cycles were performed at C/3 and then the cycling was terminated.

Electrode preparation, cell assembly, and cell testing at TUM

The cathode slurry for the "200°C 1 h SO_2" and the untreated reference sample was produced under inert conditions, i.e., powder mixing and NMP addition was carried out under argon. To produce HE-NMC cathodes, the following ingredients were blended: 92.5 wt. % of HE-NCM

active material, 4 wt. % carbon black (Super C65, Timcal, Switzerland), and 3.5 wt. % polyvinylidene difluoride (PVdF, Solef 5130, Solvay, Belgium). Carbon black and PVDF had been vacuum dried at 120°C for 3 days before transfer to the glovebox, where the powders were mixed. After powder mixing, 0.84 g of N-methyl-2-pyrrolidone (NMP, Sigma-Aldrich, Germany) per gram of solid (≡54 wt. % solid content) was added step-wise and the mixture was stirred with a planetary orbital mixer (Thinky, Japan) until a highly viscous, lump-free paste is obtained. It was then applied onto an 18 µm thick aluminum foil (MTI, USA) with a 100 µm four-edge-blade (Erichsen, Germany) and subsequently dried overnight inside the glovebox. Disc-shaped cathodes with a diameter of 14 mm were punched out of the coated foil and compressed at 2.5 t for 20 s. The cathodes were then weighed, dried overnight in a vacuum oven at 120°C, and introduced into an Ar glovebox without exposure to ambient air. The areal loading of the HE-NMC cathodes after drying was 6.0 ± 1.0 $mg_{HE\text{-}NCM}/cm^2$, corresponding to an areal capacity of 1.50 ± 0.25 mAh/cm^2 when using a reversible specific capacity of 250 $mAh/g_{HE\text{-}NCM}$ (the latter is also used for the definition of the C-rate). Coin cells were assembled with a metallic lithium counter electrode, with two glass fiber separators (VWR 691) with 16 mm diameter, and with 80 µL of electrolyte. The latter was an EC-free, FEC/DEC-based electrolyte with a highly fluorinated ether as co-solvent (BASF, Germany) and with 1 M $LiPF_6$.

For the 200°C, 1 h SO_2-treated sample, a different cycling procedure at a constant temperature of 25°C was used. The first charging at C/15 was carried out to 4.8 V and up to 4.7 V in the subsequent cycles. Furthermore, instead of the extended rate capability test at the beginning, we examined the rate capability at discharge rates of 0.1C and 3C, which were carried out after every forty cycles. The lifetime test was performed with 1C discharge rates instead of C/3. All the details of the cycling procedure are specified in Table S2.

Table S2: Cycling protocol for coin-type half-cells comprising HE-NCM cathodes and metallic lithium anodes. Segments 2 - 5 were repeated 4 times. The C-rate is referenced to 250 mAh/$g_{HE\text{-}NCM}$; CC (constant current), CC-CV (constant current-constant voltage) mode with C/10 lower current limit, DCIR (direct current internal resistance) measurement at 40% SOC (state-of-charge).

	Segment	Potential range [V vs. Li/Li^+]	Charge rate	Discharge rate	Cycles	Repeats
1	Activation	4.8 - 2.0	C/15 (CC)	C/15 (CC)	1	0
2	Slow cycling	4.7 - 2.0	C/10 (CC)	C/10 (CC)	3	
3	DCIR	at 40% SOC	-	-	1	
4	Fast cycling	4.7 - 2.0	C/2 (CCCV)	3C (CC)	3	4
5	Standard cycling	4.7 - 2.0	C/2 (CCCV)	1C (CC)	33	

Impedance measurements

The electrochemical impedance measurements of the HE-NCM/Li cells were performed using a frequency response analyzer FRA (model 1255 from Solartron) coupled with a battery test unit model 1470, Inc. (driven by Corrware and ZPlot software from Scribner Associates, Inc.). The alternating voltage amplitude in impedance measurements was 3 mV and the frequency ranged from 100 kHz to 5 mHz. All the potentials in this paper are given *vs.* Li^+/Li.

Differential scanning calorimetry measurements

The DSC analyses were carried out in the range between room temperature and 350 °C (DSC 3+ STAR^e System, METTLER TOLEDO) using closed reusable high pressure gold-plated stainless steel crucibles (30 µl in volume). The weight ratio between the electrode material and the electrolyte solution for the experiment was kept at 1:1. For individual DSC test, ~3 mg each of the cathode material and electrolyte solution was used. The initial and final weights of the loaded crucibles were measured using a microbalance (Mettler Toledo AB135-S/FACT). All the weighing measurements were performed inside an argon-filled glove-box.

Surface area measurements

Specific surface area measurements of HE-NCM materials were carried out by the Brunauer−Emmett−Teller (BET) method at 77.3 K using a Nova 3200e (Quantachrome, USA) surface area analyzer.

Experimental setup for SO_2 treatment at BIU

Figure S1: Modified roto-evaporator provided by BASF

Analysis of XPS data

For the peak deconvolution shown in Figure 5, the following peak assignments, binding energy and FWHM ranges, and peak area ratios were used.

Table S3: Data fitting for XPS spectra of untreated and SO_2 treated (200°C, 1 h) HE-NCM materials, used in the analysis of the data shown in Figure 5.

O 1s region						
assigned structure	layered oxide lattice	spinel oxide lattice	M-OH & M-CO_3	M-SO_x	misc.	
BE [eV]	529.2 ± 0.2	530.0 ± 0.2	531.1 ± 0.1	532.0 ± 0.2	533.2 ± 0.2	
FWHM [eV]	1.0 – 1.2	1.0 – 1.2	1.6 – 1.8	1.4 – 1.5	1.6 – 1.8	
S 2p region						
assigned structure	M-SO_4 $2p_{3/2}$	M-SO_4 $2p_{1/2}$	M-SO_3 $2p_{3/2}$	M-SO_3 $2p_{1/2}$	M-S $2p_{3/2}$	M-S $2p_{1/2}$
BE [eV]	168.7 ± 0.2	168.7 + 1.2	166.8 ± 0.2	166.8 + 1.2	163.0 ± 1.0	163 + 1.2
FWHM [eV]	1.0 – 1.3	1.0 – 1.3	1.0 – 1.3	1.0 – 1.3	1.0 – 1.3	1.0 – 1.3
integrated peak area		A×0.5		C×0.5		E×0.5

Capacities obtained during activation and cycling in Li/HE-NCM half-cells

The capacities extracted from the first-cycle activation (Figure 6), the extended cycling test (Figure 7), and the rate capability test (Figure 7 and 8) are given in Tables S4-6.

Table S4: Specific charge and discharge capacities measured in the first (activation) cycle at a C/15 rate in Li/HE-NCM half-cells with untreated and SO_2 treated HE-NCM for experiments conducted at BIU or TUM (see Figure 5). BIU: Electrodes containing either the untreated or the "400°C, 2 h SO_2" treated HE-NCM, conducted in LP57 electrolyte at 30°C (first-charge cut-off at 4.7 V, followed by a CV step; average and a maximum deviation of three cells per sample). TUM: Electrodes containing either the untreated or the "200°C, 1 h SO_2" treated HE-NCM, conducted at 25°C in FEC/DEC-based electrolyte with a highly fluorinated ether as co-solvent and with 1 M LiPF6 (first-cycle cut-off at 4.8 V, no CV step; average and a maximum deviation of two cells per sample). In both cases, the discharge cut-off was 2.0 V. Note approximately 5 % higher Coulombic efficiency measured from untreated HE-NCM electrodes in FEC/DEC/1.0 M $LiPF_6$ electrolyte with a highly fluorinated ether as co-solvent. This may relate, to some extent, to less side reactions of electrodes with this solution species, as well as due to the higher stability of FEC upon anodic polarization comparing to that of EC.

Sample	1st Charging	1st Discharging	Coulombic Efficiency
	mAh/g	mAh/g	%
Untreated HE-NCM (BASF)	332.5 ± 1	281.2 ± 3	84.5
400°C, 2 h SO_2 treated sample (BIU)	336.1 ± 2	294.8 ± 3	87.7
Untreated HE-NCM (BASF)	320.6 ± 0.8	289.0 ± 1	90.1
200°C, 1 h SO_2 treated sample (TUM)	321.2 ± 0.1	295.9 ± 0.1	92.1

Table S5: Specific discharge capacities (mAh/g) obtained during cycling at various C-rates. These tests were carried out after the 1st cycle (activation) shown in Figure 6 and are extracted from Figure 7 and 8 for the measurements conducted at BIU (black text) and TUM (blue text). The numbers in brackets indicate the increase in capacity (%) of the SO_2-treated samples. Average and standard deviation is based on three cells per sample for BIU and two cells for TUM.

Sample	0.1C	0.33C	0.8C	1C	2C	3C	*1C/0.1C (%)*
Untreated HE-NCM (BASF)	249 ± 2	236 ± 3	221 ± 3	214.7 ± 3	190 ± 5	-	*86.0*
400°C, 2 h SO_2 treated sample	263 ± 3 (5.6 %)	257 ± 2 (8.9 %)	241 ± 5 (9.0 %)	238 ± 2 (10.7 %)	220 ± 2 (15.6 %)	-	*90.5*
Untreated HE-NCM (BASF)	266.5 ± 0.3 (cycle 4)	-	-	233.3 ± 0.5 (cycle 11)	-	195.0 ± 2 (cycle 8)	*87.5*
200°C, 1 h SO_2 treated sample	281.2 ± 0.1 (5.6 %) (cycle 4)	-	-	256.7 ± 0.1 (10.3 %) (cycle 11)	-	227.0 ± 1 (16.4 %) (cycle 8)	*91.3*

Table S6: Specific discharge capacities obtained over extended cycling extracted from the data shown in Figure 7, namely at C/3 and 30 °C at BIU (black text, see Figure 7a) and at 1C and 25 °C at TUM (blue text, see Figure 7b). The average and maximum deviation are based on three cells per sample. At BIU and on two cells per sample at TUM.

Sample	1st	10th	25th	50th	80th	100th	*Q100/Q25*
	mAh/g	mAh/g	mAh/g	mAh/g	mAh/g	mAh/g	*%*
Untreated HE-NCM (BASF)	226.0 ± 3	221.0 ± 3	220 ± 5	207.0 ± 4	188.0 ± 6	200 ± 8	*90.9*
400°C, 2 h SO_2 treated sample	253.0 ± 1.6	249.0 ± 1.4	243 ± 2	236.0 ± 3	220.0 ± 7	220 ± 5	*90.5*
Untreated HE-NCM (BASF)	-	234.2 ± 0.4	226 ± 0.5	217.6 ± 0.9	214.0 ± 1	212 ± 2	*93.8*
200°C, 1 h SO_2 treated sample	-	257.1 ± 0.2	252 ± 0.1	238.0 ± 5	240.0 ± 1	236 ± 0	*93.7*

Raman spectroscopy studies

From the results of Raman spectroscopy studies shown in Figure S2, we suggest that SO_2 treatment has no substantial effect on the vibrational modes of the Li-rich material. Mainly, all the Raman active modes of the pristine sample (peak locations, the appearance of an additional feature at 620 cm^{-1}) remain unchanged upon this treatment.

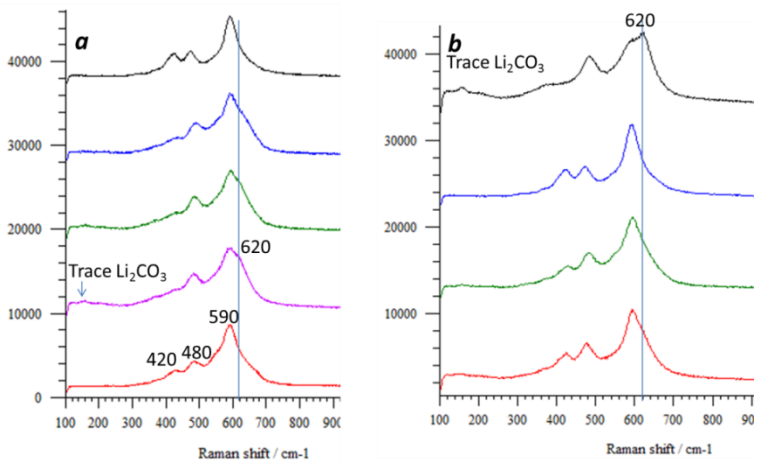

Figure S2: Raman spectra were taken from several locations of a) untreated HE-NCM material and b) HE-NCM material treated with SO_2 during 2 hours at 400 °C

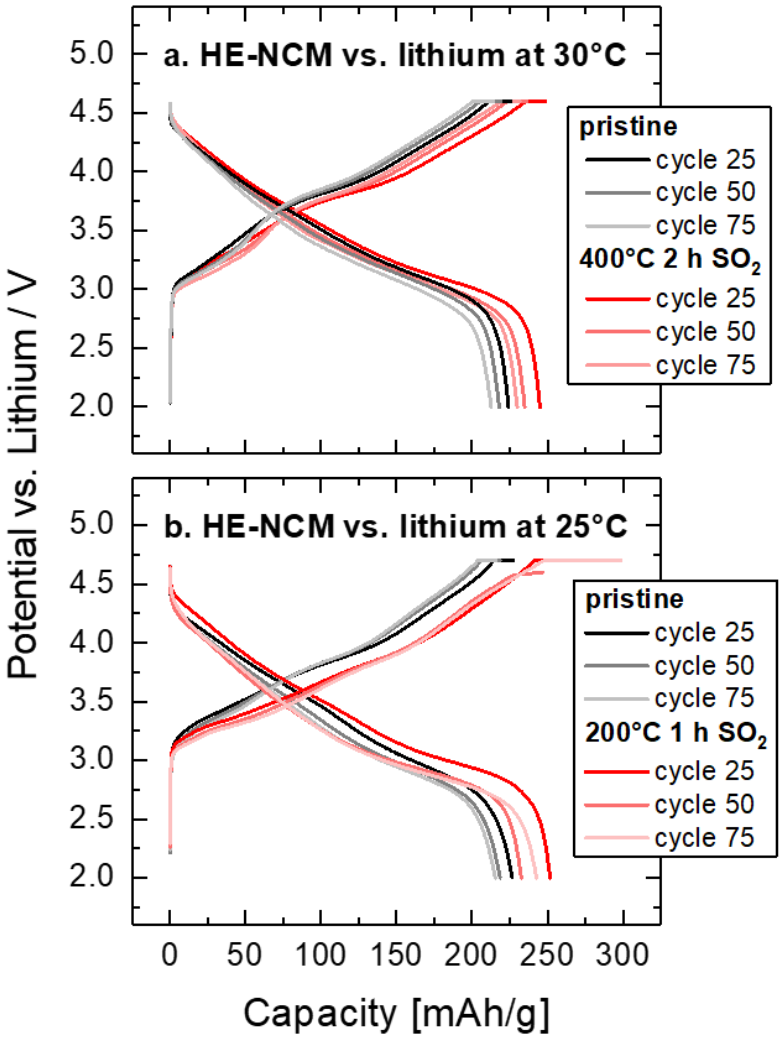

Figure S3: Voltage profiles recorded for electrodes containing untreated (pristine) and SO_2-treated HE-NCM materials (as indicated) during cycles 25, 50, and 75 in coin-type cells with Li-anodes, at 25 °C (a) and 30 °C (b).

Electrochemical Impedance Spectroscopy (EIS) studies

In Figure S4, we demonstrate typical impedance spectra (Nyquist plots) measured from Li-cells with cathodes comprising untreated and SO_2-treated HE-NCM materials, respectively, and LP57 solution. Lower contact resistance and surface-film resistance values were measured both at the beginning of their cycle life (15 cycles) and after prolonged cycling (100 times at C/3 rate) for the cells comprising SO_2-treated cathode and this observation may be related to some extent to the restructuring of the material's surface by SO_2-treatment. This suggestion is also supported by DSC thermal studies of untreated and SO_2-treated HE-NCM samples in reactions with EC-EMC/$LiPF_6$ 1M solutions (LP57). As the EIS measurements were conducted in half coin-type cells (*vs.* Li/Li^+) configuration, contributions from both HE-NCM cathodes and Li-anodes are associated with the electrical circuit parameters. Thus we define the cell impedance as follows: $R_{cell} = R_{cathode} + R_{anode}$.

Electrical equivalent circuit models were adopted to fit the experimental Nyquist plots (Figure S4) and the assignment of the circuit parameters[1] was addressed according to their values in Table S7.

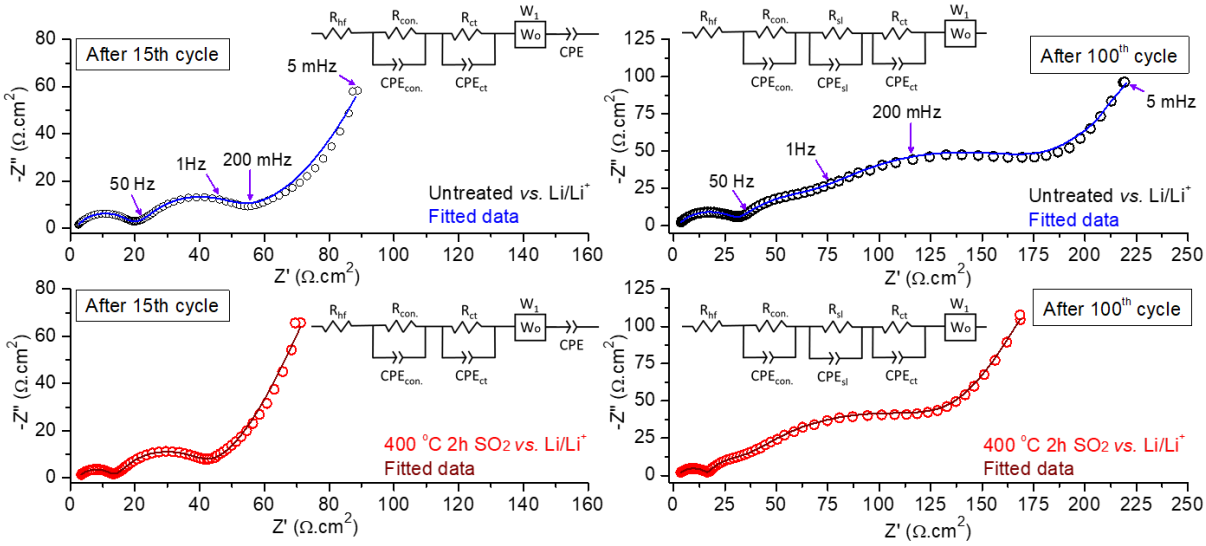

Figure S4: Impedance spectra (Nyquist plots) measured during the charge at 4.0 V after 15th and 100th charge/discharge cycles from Li/HE-NCM half-cells with cathodes comprising HE-NCM untreated (black curve) and SO_2 treated material (400 ˚C 2 h, red curve). Coin-type cells *vs.* Li anodes, EC-EMC (3:7 v/v)/$LiPF_6$ 1M solutions, at 30 ˚C. The equivalent circuit models are presented as insets in each plot.

Table S7: Fitted data for impedance spectra measured during the charging process (Li-ions extraction) at 4.0 V, after 15th and 100th cycles in half-cells comprising Li-anodes and HE-NCM untreated and SO_2-treated cathode materials. The corresponding impedance spectra of these cells are presented in Figure S4. In this Table, R_{hf}, R_{con}, R_{sl}, and R_{ct} relate respectively, to the solution resistance measured at high-frequencies, contact resistance of the cathode, the resistance of the Li^+ migration through the surface layer formed on the cathode, and interfacial charge-transfer resistance representing a contribution from both the electrodes (cathode and anode) in Li-cells.

Cycle Number	**Electrochemical cell configuration**							
	Untreated HE-NCM vs. Li/Li^+				SO_2 treated (at 400 °C, 2 h) HE-NCM vs. Li/Li^+			
	R_{hf} ($\Omega.cm^2$)	$R_{con.}$ ($\Omega.cm^2$)	R_{sl} ($\Omega.cm^2$)	R_{ct} ($\Omega.cm^2$)	R_{hf} ($\Omega.cm^2$)	$R_{con.}$ ($\Omega.cm^2$)	R_{sl} ($\Omega.cm^2$)	R_{ct} ($\Omega.cm^2$)
15th Cycle	1.6	13.7	-	18.5	1.9	8.5	-	19.7
100th Cycle	2.1	29.6	42.9	103.1	2.4	14.2	19.2	97

Results of DSC studies and TEM images of the SO_2 treated HE-NCM material

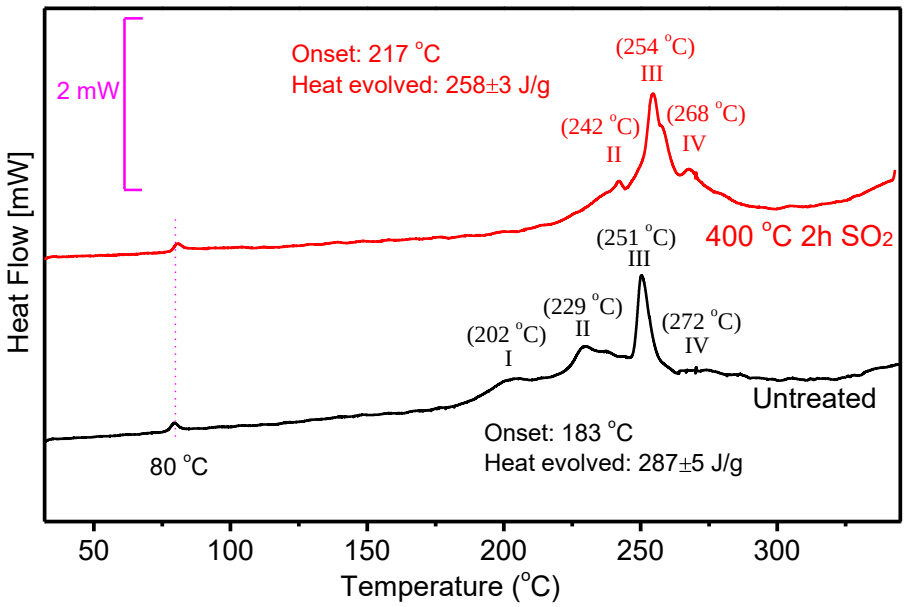

Figure S5: Results of the DSC measurements of untreated (black) and SO_2 treated HE-NCM (red) powders in EC-EMC (3:7 v/v)/$LiPF_6$ 1.0 M solution (LP57).

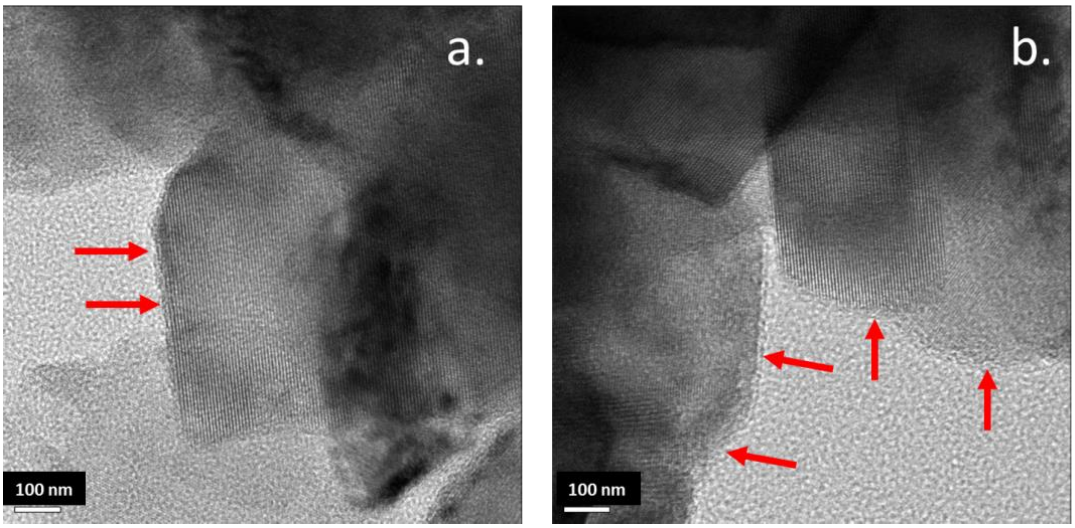

Figure S6: (a, b) TEM bright-field images of the SO_2 treated HE-NCM material demonstrating the coating of a few nanometers thick over the primary particles. According to the XPS analysis, the surface coating comprises Li_2SO_4 and TM-sulfates, as discussed in the main text.

Reference:

1. T. Teufl, D. Pritzl, S. Solchenbach, H. A. Gasteiger, M. A. Mendez, *J. Electrochem. Soc.*, **166**, A1275 (2019).

3.3.3. Thermal Treatment of Ni-rich NCM with the Reactive Gases SO_2 and SO_3

Having learned about the positive impact that SO_2 and SO_3 treatment can have on LMR-NCM from the previous two chapters (3.3.1 and 3.3.2), in the following it will be discussed how the SO_2 and SO_3 can be adapted to Ni-rich NCM. As described in the experimental part (chapter 2.3.1), NCM851005 was treated with SO_2 at 200°C and with SO_3 at 160°C after a calcination step at 525 °C in both cases (cf. left panel of Figure 26). In a second set of experiments (cf. right panel of Figure 26), this pre-calcination step was omitted and NCM851005 powder was directly heated to a 300 °C temperature plateau in the first case and to a 400 °C plateau in an additional experiment, both for a duration of 1 h under Ar flow. While keeping the temperature constant, the gas feed was then changed to 0.5% SO_2 in Ar for a 1 h SO_2 treatment while holding the temperature at 300°C or at 400°C, respectively. Furthermore, an SO_3 treatment was performed with 0.5% SO_3 and 30% O_2 in Ar for 1 h at 300°C (after a 1 h temperature hold at 300°C under Ar flow). To assess the reactivity of Ni-rich NCM with SO_2 and SO_3, the CAM powders were characterized by DRIFTS of 1% CAM samples in KBr, analogous to the study on LMR-NCM samples presented in the publication[134] in chapter 3.3.1. All the spectra for the two sets of experiments as well as the corresponding experimental protocols for SO_2 and SO_3 treatment are depicted in Figure 26.

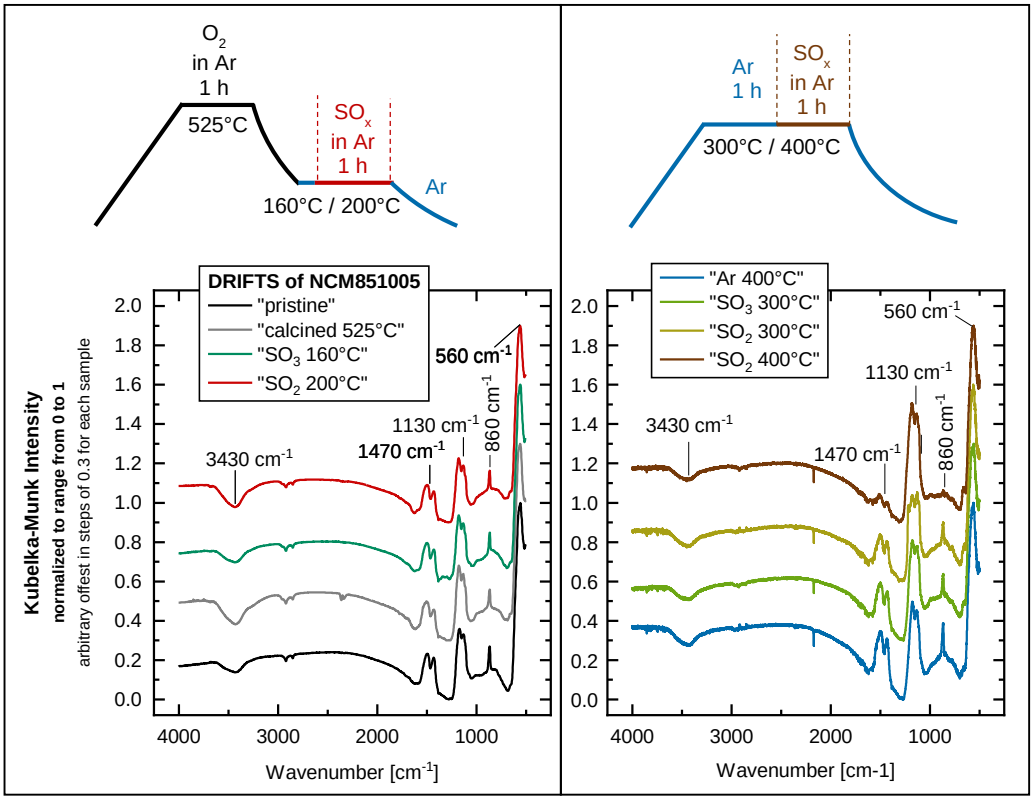

Figure 26: DRIFTS spectra of the NCM851005 samples for two sets of experiments that are schematically explained for the SO_2 treatment as an example. The Kubelka-Munk intensity has been normalized to the oxide band at 560 cm^{-1} and the spectra have been offset arbitrarily on the y-axis for better visibility. Left panel: as-received NCM851005 ("pristine"), after calcination at 525°C under 30% O_2 in Ar ("calcined"), after treatment with 0.5% SO_3 and 30% O_2 in Ar for 1 h at 160°C ("SO_3 160 °C) as well as after treatment with 0.5% SO_2 in Ar for 1 h at 200 °C ("SO_2 200°C"). Right panel: Second set of experiments with NCM851005 samples heated for 2 h at 400°C under Ar ("Ar 400°C"), heated at 300°C for 2 h, first under Ar for 1 h and then under 0.5% SO_3 and 30% O_2 in Ar for 1 h ("SO_3 300°C"), heated at 300°C for 2 h, first under Ar for 1 h and then under 0.5% SO_2 in Ar for 1 h ("SO_2 300°C") as well as heated at 400°C for 2 h, first under Ar for 1 h and then under 0.5% SO_2 in Ar for 1 h ("SO_2 400°C").

All DRIFTS spectra in Figure 26 reveal the characteristic surface groups of NCM851005 particles. Similar to the LMR-NCM samples discussed in Figure 4 of the publication[134] presented in chapter 3.3.1, the downward pointing signal at the region around 3430 cm^{-1} indicates surface hydrates and hydroxide ions (H_2O/OH^-), the doublet around 1470 cm^{-1} and the sharp band at 860 cm^{-1} are typical features of the carbonate anion (CO_3^{2-}). Taken together, e.g., the "pristine" NCM851005 sample must contain a significant fraction of the typical surface contaminants[47,48,161] such as LiOH, Li_2CO_3 and the basic nickel carbonate hydrate $NiCO_3 \cdot 2Ni(OH)_2 \cdot x\ H_2O$ (NCBH). The same holds true for most of the other samples such as the "calcined 525 °C", the "SO_3 160 °C" and "SO_2 200°C" sample as well as in case of "Ar 400 °C", "SO_3 300 °C", and "SO_2 300 °C". Only the harshest condition, i.e., SO_2 treatment at 400 °C appears to have reduced the carbonate fraction in the sample as revealed by clearly decreased carbonate bands at 1470 and 860 cm^{-1} in case of "SO_2 400 °C" (brown line in the right panel of Figure 26). However, also in this case the hydroxide/hydrate region around 3430 cm^{-1} is not much reduced in

intensity as compared to all the other samples. Interestingly, none of the samples in Figure 26 shows any change of the sulfate band (SO_4^{2-}) at 1130 cm^{-1} as compared to the pristine sample, which itself exhibits a rather intense sulfate signal. This indicates a significant sulfate content already in the "pristine" sample and the SO_2 or SO_3 treatment possibly do not further increase the total sulfate content (sum of bulk and surface sulfates) significantly. Sulfites (SO_3^{2-}) would give rise to bands at 1002 and 954 cm^{-1} (Table II within the publication[134] in chapter 3.3.1) which however cannot be seen in any of the spectra in Figure 26. In short, the only significant change observed after SO_2 treatment of NCM851005 at 400 °C according to the interpretation of the DRIFT spectra seems to be the reduction of the amount of carbonates such as Li_2CO_3 or basic nickel carbonate hydrate. This would be an advantage in case of Li_2CO_3 which be removed by calcination step at 525°C, for instance, as discussed in the paper on surface contamination of NCM811 (chapter 3.2.2).[47]

To reveal whether this reduction of the amount of carbonates affects electrochemical cycling, coin cells with NCM851005 versus lithium have been tested for "pristine" NCM851005, for "SO_2 400 °C", and for "Ar 400 °C" as baseline for the SO_2 treatment of NCM851005 at 400 °C (compare Figure 27). The half-cell tests were performed at 25 °C. Similar to the LMR-NCM study[134] described in chapter 3.3.1, the cycling protocol consisted of longer 1 C segments (33 cycles) and shorter C/10 and 3 C segments (3 cycles each); further details can be found in the experimental section of this thesis (chapter 2.3.2). The cycling results for NCM851005 can be seen from Figure 27. The initial 1 C capacities (panel a) are 187 mAh/g for the "pristine" sample, 178 mAh/g for the "Ar 400°C" baseline, and 161 mAh/g for "SO_2 400 °C". The aging behavior, i.e., the capacity decrease over 200 cycles of all three samples is rather similar. It is clearly visible from Figure 27a that the SO_2 treatment at 400°C has led to reduced capacity during 1 C cycling. This capacity loss can also be observed at C/10 (panel b) and 3 C (panel c) when comparing "SO_2 400 °C" to the other two samples. The initial pulse resistance of "SO_2 400 °C" (panel c) is not drastically increased as compared to "pristine" NCM851005, however during cycle-life the resistance growth is much bigger for "SO_2 400 °C" versus "pristine" NCM851005. The observations for the baseline sample "Ar 400 °C" are different to both of the other samples: While the C/10 capacity of "Ar 400 °C" (panel b) is even slightly bigger than the one of "pristine" NCM851005, the 3 C capacity (panel c) is clearly decreased, similar to "SO_2 400 °C". In addition, the resistance growth is more pronounced for "Ar 400 °C" versus "pristine" NCM851005, even exceeding the one of "SO_2 400 °C" (panel d). Especially in case of the SO_2 treatment at 400°C, but also in case of the Ar baseline experiment at 400°C, a resistive surface layer seems to have formed.

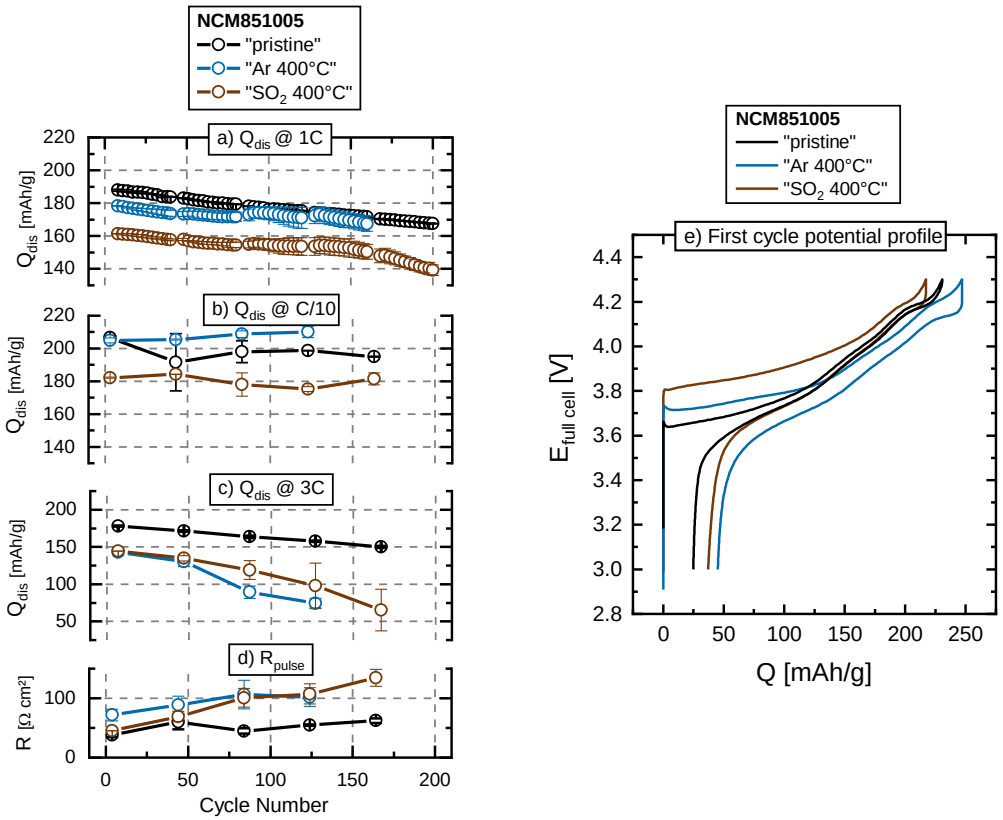

Figure 27: Impact of SO_2 and SO_3 treatment on the performance of half-cells, i.e., NCM851005/LP572/lithium coin cells at 25°C. Each value represents the average of two cells each, with error bars representing maximum and minimum values. Untreated "pristine" NCM851005 is compared to SO_2 treated NCM851005 ("SO_2 400 °C), with "Ar 400°C" as baseline for the impact of the temperature (400°C) itself. In case of "Ar 400°C", only 160 cycles have been recorded. (a) Discharge capacity (Q_{dis}) at 1 C (only every third cycle is displayed for the sake of better visibility). (b) Discharge capacity of the same cells at intermittent cycles at C/10. (c) Discharge capacity of the same cells at intermittent cycles at 3C. In panels (b) and (d) the last one of the three cycles for the corresponding rate is displayed. (d) DCIR pulse resistance (R_{pulse}) after charge to 40% SOC. (e) Voltage profiles of the first formation cycle at 25°C (3.0 – 4.3 V at C/10, one cell per sample). The detailed cell setup and cycling protocol are given in the experimental section (chapter 2.3.2).

As discussed above in the context of the DRIFT spectra (Figure 26), the "pristine" NCM851005 most probably contains a significant fraction of surface contaminants in the form of hydroxides or hydrates. This is consistent with TGA data (not shown), according to which "pristine" NCM851005 loses 0.08 wt% between 120 and 450°C (same TGA measurement protocol as for $Li_{1.33}$-LMR-NCM depicted in Figure 22), while the "Ar 400°C" sample has a negligible mass loss of only 0.01 wt%. The type of hydroxide or hydrate cannot be assessed from the DRIFTS data, i.e., LiOH cannot be differentiated from Ni-based hydroxides, for example. As it is known from a study on washing of NCM851005, MOOH-like structures caused by exposure to water are converted to rocksalt-like structures above ≈250 °C, which might explain the high resistance of the "Ar 400 °C" sample.[233] This would be consistent with the observation from the voltage profiles of the first (formation) cycle at C/10, which are displayed in Figure 27e. In case of "pristine" NCM851005, the voltage curve reflects the sloping plateau typical of layered oxides. The charge contains an initial voltage spike above 3.6 V, which could be explained by the presence of surface contaminants[47,48]. This finding would be in accordance

with the above discussed interpretation of the DRIFT spectra in Figure 26. Apart from the initial charge polarization at 3.6 V, only a slight hysteresis between the charge and the discharge curve can be observed for "pristine" NCM851005. In contrast, the "Ar 400 °C" sample and the "SO_2 400 °C" samples both reveal a clearly visible hysteresis between charge and discharge. In case of "SO_2 400 °C", this hysteresis probably covers the spike from the initial charge polarization. The "SO_2 400 °C" sample shows the highest polarization and the lowest amount of active lithium, which is assessed via the initial charge capacity (217 mAh/g), while in case of "Ar 400 °C" the initial charge capacities (241 mAh/g) are slightly higher than the one of the pristine sample (231 mAh/g). This is consistent with a capacity increase for the "Ar 400 °C" sample during cycling at C/10 (Figure 27b). As discussed above, a highly resistive surface layer might be the explanation for the increased polarization after heating under Ar at 400 °C and the even more pronounced polarization after SO_2 treatment at 400 °C.

Taken together, the SO_2 treatment at 400 °C on the one hand led to removal of surface carbonates according to DRIFTS, on the other hand the poor electrochemical performance impedes the practical application of such a treatment method. Future experiments should focus on lower treatment temperatures such as the SO_2 treatment at 200 °C or the SO_3 treatment at 160 °C, although eventual surface changes could not be proven by DRIFTS. Possibly, the fact that the "pristine" sample already contains a significant amount of sulfate, the creation of surface sulfates or sulfites upon SO_2 or SO_3 is not as relevant as in case of LMR-NCM, where the formation of sulfate and sulfite groups on the particle surface was clearly demonstrated to have a positive effect on the surface stability as well as on electrochemical cycling (chapter 3.3.1).[134]

3.3.4. Fluorination of Ni-Rich Lithium-Ion Battery Cathode Materials by Fluorine Gas: Chemistry, Characterization, and Electrochemical Performance in Full-cells

In chapters 3.3.1-3.3.3, so far the impact of SO_2 and SO_3 thermal treatments of LMR-NCM and Ni-rich NCM have been discussed. As already mentioned in the patent application (cf. chapter 3.3.1),[136] there are further gases that are known to be highly reactive and thus are potential candidates to modify layered oxide CAMs. BF_3 is such an example and is mentioned in the patent application, NH_3 was used in a study by Erickson et al.,[133] F_2 is a further example and will be discussed in detail in the manuscript on the fluorination of Ni-rich NCM, which is presented within this chapter. In contrast to the SO_2 and SO_3 treatments, the F_2 treatment was carried out in a closed batch reactor at room temperature and not in a furnace tube with continuous gas flow at elevated temperature. The experimental details of the fluorination setup are described in more detail at the beginning of the Supporting Information (Figure S1). The reaction between the layered oxide samples and F_2 most likely leads to the formation of H_2O inside the reactor vessel, which was chemically bound to the CAM surface, thus increasing the amount of surface contaminants. Luckily, a calcination at 450°C for several hours allowed to remove these additional surface hydrates and hydroxides, similar to the calcination procedure that has already demonstrated in the study on surface contaminants (chapter 3.2.2).[47] Also in case of the F_2 study, TGA-MS and DRIFTS allowed the quantitative and qualitative assessment of surface contamination on NCM851005 before and after fluorination and calcination.

One key question discussed within this manuscript is whether F_2 treatment of Ni-rich NCM (NCM811 and NCM811005) would preferably lead to surface fluorination or to bulk anion doping. While powder XRD gave no indication of bulk anion doping, ^{7}Li an ^{19}F Magic Angle Spinning Nuclear magnetic resonance (MAS-NMR) revealed the formation of LiF on the surface of the CAM particles. Despite a reduced electrical conductivity as compared to pristine material, fluorinated NCM811 had a slightly improved capacity retention after 500 cycles during electrochemical cycling tests in full-cells vs. graphite at 30°C and at 45°C. With the help of inductively coupled plasma mass spectrometry (ICP-MS) of the anode after 500 cycles, it was demonstrated that transition metal dissolution from the cathode

during cycling was clearly reduced for fluorinated NCM811, with the strongest impact on Mn and Co cross-talk. Apparently, the LiF film on the CAM has protective properties that not only stabilize the material, but also positively influence the cycle-life of NCM811.

Author contributions

This article describes the result of a collaboration within the BASF battery research network, involving the Technical University of Munich (TUM), University of Freiburg (UoF), Bar-Ilan University (BIU), Israel, and BASF in Ludwigshafen. U. B. set up the fluorination reactor at a specially equipped lab at UoF. J. S. and K. H. carried out TGA-MS measurements, DRIFTS analysis, and the calcination of fluorinated NCM851005 at TUM. C. E., F. S., E. M. E., and B. M. performed full-cell assembly and electrochemical cycling analysis. U. B., V. D., A. F., M. D., and A. H. carried out an in-depth material characterization including ICP-MS, fluorine-selective electrode measurements (FSE), ATR-FTIR spectroscopy, powder XRD, MAS-NMR, SEM, conductivity and press density measurements, TGA, and differential thermal analysis (DTA). U. B., J. S., F. S., D. A., H. A. G., and I. K. wrote the manuscript. All authors discussed the data and commented on the manuscript.

Chemistry Europe
European Chemical Societies Publishing

VIP *Very Important Paper*

Fluorination of Ni-Rich Lithium-Ion Battery Cathode Materials by Fluorine Gas: Chemistry, Characterization, and Electrochemical Performance in Full-cells

Ulf Breddemann[+],[a] Johannes Sicklinger[+],[b] Florian Schipper[+],[c] Victoria Davis,[a] Anna Fischer,[a] Korbinian Huber,[b] Evan M. Erickson,[c] Michael Daub,[a] Anke Hoffmann,[a] Christoph Erk,[d] Boris Markovsky,[c] Doron Aurbach,*[c] Hubert A. Gasteiger,*[b] and Ingo Krossing*[a]

The mild fluorination of Ni-rich NCM CAMs (NCM = nickel-cobalt-manganese oxide; CAM = cathode active material) with a few hundred mbar of elementary fluorine gas (F_2) at room temperature was systematically studied. The resulting fluorinated CAMs were fully analyzed and compared to the pristine ones. Fluorination at room temperature converts part of the soluble basic species on the CAM-surface into a protecting thin and amorphous LiF film. No formation of a metal fluoride other than LiF was detected. SEM images revealed a smoothened CAM surface upon fluorination, possibly due to the LiF film formation. Apparently due to this protecting, but insulating LiF-film, the fluorinated material has a reduced electrical conductivity in comparison to the pristine material. Yet, all fluorinated Ni-rich NCM CAMs showed a considerably higher press density than the pristine material, which in addition increased with higher fluoride concentrations. In addition, fluorination of the Ni-rich CAMs led to the chemically induced formation of small amounts of water, which according to TGA-MS-measurements can be removed by heating the material to 450 °C for a few hours. Overall, the tested fluorinated NCM 811 samples showed improved electrochemical performance over the pristine samples in full-cells with graphite anodes at 30 °C and 45 °C after 500 cycles. Moreover, the fluorination apparently reduces Mn and Co cross talk from the CAM to the anode active material (AAM) through the electrolyte during charge/discharge.

1. Introduction

The most traditional cathode active material (CAM) for lithium ion batteries (LIBs) is $LiCoO_2$ (LCO) with a reversible capacity of $\approx$140 mAh g^{-1} and good cycling stability.[1] Yet, cobalt is a critical raw material due to its toxicity and rising cost. Thus, its replacement is one of the driving forces to develop other CAMs for LIBs.[2] LCO has a layered oxide structure in which Co can be substituted with Ni and Mn giving lithium nickel cobalt manganese oxide (NCM) materials with the general composition $Li_{1+w}(Ni_xCo_yMn_z)_{1-w}O_2$ ($x+y+z=1$). Examples include NCM 111 or NCM 523; the three numbers *x*,*y*,*z* present the stoichiometric ratio of Ni:Co:Mn.[3,4,5] To increase the energy density, Li- and Mn-rich NCM materials, often referred to as "overlithiated" NCM or "high-energy NCM (HE-NCM)" were developed.[6] Alternatively, the nickel content may be increased and Ni-rich CAMs such as NCM 622 or NCM 811 are more and more being commercialized due to their higher energy density, lower cobalt concentration, and reduced cost when compared to lithium cobalt oxide (LCO) or NCM 111.[7] NCM 811 and beyond (NCM 851005 or 900505) offer practical capacities up to $\approx$200 mAh g^{-1}[8–10] in a layered α-$NaFeO_2$ structure (space group $R\bar{3}m$).[4,8–12] However, the materials have poorer thermal stability and performance at higher temperatures,[7,13] including faster capacity fading and shorter lifetime in comparison to NCM 111.[9,12,14] The high Ni content is challenging:[15] Upon cycling, reactive Ni^{3+} and Ni^{4+} ions form from trace HF (=> moisture

[a] *U. Breddemann,[+] V. Davis, A. Fischer, M. Daub, A. Hoffmann, Prof. Dr. I. Krossing*
Institut für Anorganische und Analytische Chemie, Cluster of Excellence livMatS, University of Freiburg (VD, AF, IK) and Freiburger Materialforschungszentrum (FMF)
Universität Freiburg
Albertstr. 21, 79104 Freiburg, Germany
E-mail: krossing@uni-freiburg.de
[b] *J. Sicklinger,[+] K. Huber, Prof. Dr. H. A. Gasteiger*
Chair of Technical Electrochemistry
Technische Universität München
Lichtenbergstrasse 4, 85748 Garching, Germany
E-mail: hubert.gasteiger@tum.de
[c] *F. Schipper,[+] E. M. Erickson, B. Markovsky, Prof. Dr. D. Aurbach*
Department of Chemistry
Bar-Ilan University
Ramat-Gan 5290002, Israel
E-mail: aurbach@mail.biu.ac.il
[d] *C. Erk*
BASF SE
Carl-Bosch-Str. 38, 67056 Ludwigshafen, Germany
[+] *These authors contributed equally to this work.*

Supporting information for this article is available on the WWW under https://doi.org/10.1002/batt.202000202

or electrolyte oxidation) on the Ni-rich material surface, degrading battery performance.[16,17] CAMs suffer from increased mechanical strain due to an extended unit cell volume change upon Ni^{2+}/Li^{+} cation mixing and structural degradation during cycling including particle cracking.[11,18] Ni-rich NCMs have a more reactive surface compared to e.g. NCM 111,[19] due to an increased basicity leading to a comparatively high (surface) soluble base content (SBC).[20] Thus, the amount of basic Li residuals, including $LiOH \cdot H_2O$ from synthesis and its calcination product Li_2O, on the surface of Ni-rich materials increase with the Ni content.[19] As a consequence, storage of any Ni-rich NCM CAM at higher humidity and/or elevated temperatures modifies the SBC surface layer by H_2O and CO_2 uptake to give LiOH and Li_2CO_3.[21–24] Storing the material at ambient conditions or higher humidity and/or elevated temperatures, leads to the additional development of basic nickel carbonate $NiCO_3 \cdot 2\ Ni(OH)_2 \cdot 4\ H_2O$ (NCBH) as surface impurity.[19,25] By contrast, NCM 111 is not sensitive to SBC surface layer modification even upon storage at 30 °C and 80% relative humidity for one month or longer.[19,24] Thus, on the surface of the NCM 811 CAM, a comparably high tendency to form these basic surface species in the mixed SBC/NCBH layer during storage is present.[19,21,23–25]

1.1. Surface Modification vs. Bulk Doping[7]

One possibility to stabilize Ni-rich NCM CAMs is surface modification with organic or inorganic surface coatings, e.g., polysiloxane,[26] Li_3PO_4,[27] Al_2O_3,[28] Co_3O_4,[29] TiO_2,[30] ZrO_2,[31] AlF_3,[32,33] polypyrrole,[34] sodium dodecyl sulfate,[35] or carbon.[36] An alternative strategy is cation doping with Mo,[37] Al,[32,38,39] Sn,[39,40] Fe,[39,41] and Zr[42] or even co-doping with several cations.[43] Also fluoride-modification (Review: Ref. [44]) was disclosed in the literature to improve the cycling stability of Ni-rich NCM, e.g., as F^{-} anion doping from F-sources like $[NH_4]F$, i.e. fluoride[13,45,46] and poly-tetrafluoro-ethylene (PTFE).[7] In addition, treatments e.g. with LiF,[47,48] NiF_2,[48] and $NH_4F \cdot HF$[15] may induce LiF formation on the CAM-surface, but are discussed as coating rather than bulk anion substitution. In any event, this LiF surface modification probably changes the local composition of the electrode-electrolyte interface/-phase and can be beneficial to obtain a better cycling stability, for instance, through a minimization of the electrolyte degradation at its surface.[48] Also, the change of the particle size and the surface of the CAMs when adding LiF to the lithiation step of CAM precursors allows the electrolyte solution to circulate into the microsphere, providing a good contact between the electrode material and the electrolyte.[49] For $NH_4F \cdot HF$,[14] as an example, this was explained by a synergistic stabilizing effect of surface fluorides and formation of rock-salt type NiO in the surface-near region of the oxide particles. In addition, SBC Li-residues, especially Li_2CO_3, were removed during fluoride modification as demonstrated by diffuse-reflectance infrared Fourier transform spectroscopy (DRIFTS) and X-ray photoelectron spectroscopy (XPS). Most likely this was induced through the acidic intermediate HF produced from heating $NH_4F \cdot HF$.[14]

We have recently reported on a complementary approach to the above-described acid-base or metal-fluoride impregnation methods: oxidative fluorination of CAMs at room temperature with low pressures of pure F_2 gas in a PFA vessel (PFA = perfluoroalkoxy-polymer). Extending from our account on the positive effects upon treating Li- and Mn- rich HE-NCM material with low amounts of F_2 gas,[50] here we oxidatively fluorinated NCM 811 or 851005 CAMs and fully characterized them including full-cell electrochemical cycling experiments of (fluorinated) NCM 811 CAM. To the best of our knowledge, reports using elementary fluorine gas to modify Ni-rich NCM CAMs are hitherto unknown.

Experimental Section

Full experimental details on methods, materials, procedures and measurements are deposited in the Supporting Information (SI). We concentrate here on sections relevant to the discussion and refer the reader to the SI for the rest.

Fluorination of Ni-rich CAMs with F_2 Gas

Ni-rich NCM 811 and NCM 851005 CAMs were obtained from BASF and samples were mildly fluorinated with F_2 gas. Therefore, a Monel Schlenk line of volume 66 mL (SI, Figure S1) was filled with F_2 gas at pressures between 32 to 2200 mbar (or 0.1 to 5.5 mmol). This F_2 volume was expanded into an evacuated transparent 120 mL batch PFA-reactor (SI, Figure S1) containing the CAMs at room temperature (7 g ± 0.04 g; see SI, Figure S2). This process reduces the total pressure in the system to 10 to 800 mbar. Immediately after exposure of the solid CAMs to the fluorine gas, the pressure began to drop, but stabilized within a few minutes, depending on the F_2 amount added. This indicates that the majority of the reaction is over and about 7–8 to 500 mbar pressure is left in the system. To allow for completion of the reaction, the vessel was backfilled with dry nitrogen gas to a total pressure of 1100 mbar. After a total reaction time of 1 hour, the remaining possibly reactive gas was pumped out of the reactor vessel and neutralized in a soda lime tower. The closed setup was transferred into a solvent free dry box, opened, and the fluorinated material was transferred into a storage container until further use.

Li and F Content of the Fluorinated Ni-Rich NCM Materials

To measure the water-soluble lithium (Li) and fluoride (F) concentration of the samples, ion chromatography (IC) studies were carried out for the (non-)fluorinated Ni-rich NCM CAMs. Note that LiF has a low, but reasonable solubility of 1.3 $g\,L^{-1}$ in water. Thus, 0.2 to 1.0 g fractions of the fluorinated CAMs were eluted with 250 mL ultrapure water, filtered and the fluoride and lithium contents in the filtrate were investigated. As a control, the bulk fluoride concentration of several samples was also verified by analysis after thermal CAM digestion with a fluoride selective electrode (FSE) (Figure 1, SI: Tables S1 and S2 and Figures S3 and S4).

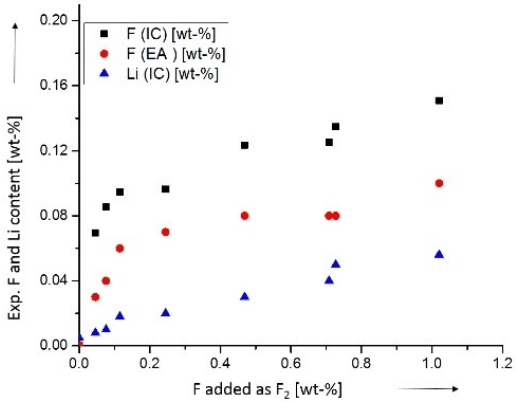

Figure 1. Plots of the fluoride and Li content of the treated NCM 811 CAMs in wt-% as a function of the applied amount of fluorine in wt-%. IC stands for ion chromatography only examining the water-soluble fraction and EA for fluoride selective electrode (FSE) determination investigating the bulk CAMs. The control pristine NCM 811 sample did not contain fluoride.

Full-Cell Battery Measurements

Electrodes were fabricated as described elsewhere.[51] Briefly, 80% (fluorinated) NCM 811 CAM (pristine batch from BASF SE, Germany) was mixed with 5% Super C65 conductive carbon (Imerys, MTI corp. USA), 5% TIMREX KS-6 graphite (Imerys, France) and 10% Solef 5130 polyvinylidenedifluoride (PVDF) binder (Solev5130 from Solvay) in *N*-methylpyrrolidone (NMP), and cast onto an Al foil (Strem Chemicals Inc., USA) current collector at a loading of ~4.3 mg cm^{-2}. Single layer pouch full-cells were fabricated with graphite anodes at a loading of ~2.8 mg cm^{-2} with 20% excess capacity (negative to positive electrodes areal capacity ratio of N/P = 1.2), using Celgard PP 2500 separators and 350 µL of BASF LP57 electrolyte (1 M $LiPF_6$ ethylene carbonate: ethyl methyl carbonate, 3:7). Areal capacity of the full-cell: ~0.7 mAh cm^{-2}, active electrode area: ~11.5 cm^2, absolute pouch cell capacity: ~8 mAh. The 1 C rate for NCM 811 was set to correspond to 180 mAh g^{-1}. All cells were prepared in triplicate and the results were averaged. Formation procedure for cells: 1 cycle at C/15 followed by 4 cycles at C/10 at 30 °C. For the continuous cycling between 2.0 and 4.2 V, the cells were measured at 30 and 45 °C with a 0.5 C charge and 1 C discharge current and a 30 minutes CV-step at 4.2 V. Every 50 cycles, one cycle was measured during charge and discharge at 0.1 C. Electrochemical impedance spectra were measured using a Solartron battery test unit model 1470 coupled with the frequency response analyzer FRA-1250 from Solartron in the frequency range from 5 mHz to 0.1 MHz with 10 points per decade. Impedance spectra were collected during charge at 4.0 V after formation, 250 and 500 cycles of the continuous cycling test.

ICP-MS Measurements of the Transition metals on the AAM

The graphite electrode from graphite/NCM 811 full-cells was separated from the separator as well as the cathode and freed from electrolyte by washing with DMC. This cleaned graphite electrode was dissolved in hydrochloric acid and filtered. With inductively coupled plasma mass spectrometry (ICP-MS) measurements of the filtrate, the Ni, Co and Mn concentration localized/deposited on the AAM was measured after 500 cycles at 30 °C and 45 °C (Table 2).

2. Results

Full-cell cycling and impedance measurements of the fluorinated vs. the pristine NCM 811 CAMs revealed considerably improved performance shown below (Figures 9 and 10). To understand this effect, the fluoride-uptake to CAMs, its consequences for structure, properties and morphology are described first, before turning to full-cell cycling and impedance measurements including post mortem analyses and continuing to the discussion section for a comprehensive analysis.

2.1. Li and F Content

To investigate if oxidative fluorination with F_2 gas led to fluoride uptake, a series of fluorinated NCM 811 CAMs with theoretically expected F content up to 1 wt.-% were examined in addition to a pristine control sample. The fluoride content of these samples was independently measured by IC as well as FSE and is shown in Figure 1. Note that IC only used aqueous extracts for fluoride determination, while in the FSE approach, the fluoride containing CAMs were thermally digested at 1100 °C in a combustion unit. The resulting hydrogen fluoride was absorbed in a total ionic strength adjustment buffer as absorption solution and determined by means of a fluoride selective electrode. Thus, this method evaluates the total fluoride concentration taken up by the CAM. Since both methods agree reasonably, we suggest that through the aqueous extraction procedure, the full fluoride content of the CAMs is accessible by IC. Turning to the ratio of F added as F_2 in comparison to the measured F content: Especially the lower applied F_2 amounts up to roughly 0.1 wt.-% F, are taken up by the CAMs more efficiently. From this applied F_2 amount on, the system integrates further fluoride at a slower rate. Thus, the reactions targeting at 1 wt-% F only led to an uptake of about 0.1 to 0.15 wt-% F (Figure 1). The observed lithium concentration measured by IC as a function of the applied gaseous F_2 amount runs rather parallel to, but lower than the F-concentrations and also increases with increasing applied F_2-amount. IC and FSE measurements behave similar for the (non-)fluorinated NCM 851005 material (SI, Table S2 and Figure S3 & S4).

2.2. Thermodynamics of F_2 Gas Reactions with CAM Components

Possibly, several reactions of F_2 with the CAM can take place at the same time: the surface SBC layer with compounds such as Li_2O, LiOH and Li_2CO_3 is likely to react with F_2, but also the NCBH layer or the layered oxide itself. Based on the thermodynamic data from Ref. [52], we have worked out the possibly underlying standard reaction enthalpies $\Delta_r H°$ in Schemes 1 and 2. Overall, water (adsorbed to the surface of the material) may react with F_2 gas to HF and O_2 [Eq. (1)]. In addition, the reactions Eqs. (2)–(4) of the SBC constituent's Li_2CO_3, LiOH and

H_2O (l) + F_2 (g)	⟶	2 HF (g) + ½ O_2 (g)	(1)
−285.8 0		−275.4 0	**−265.0**
Li_2CO_3 (s) + F_2 (g)	⟶	2 LiF (s) + CO_2 (g) + ½ O_2 (g)	(2)
−1132.1 0		−587.7 −394.4 0	**−437.7**
LiOH (s) + F_2 (g)	⟶	LiF (s) + HF (g) + ½ O_2 (g)	(3)
−441.5 0		−587.7 −275.4 0	**−421.6**
Li_2O (s) + F_2 (g)	⟶	2 LiF (s) + ½ O_2 (g)	(4)
−561.2 0		−587.7 0	**−614.2**
Li_2CO_3 (s) + 2 HF (g)	⟶	2 LiF (s) + H_2O (l) + CO_2 (g)	(5)
−1132.1 −275.4		−587.7 −285.8 −394.4	**−172.7**
LiOH (s) + HF (g)	⟶	LiF (s) + H_2O (l)	(6)
−441.5 −275.4		−587.7 −285.8	**−156.6**
Li_2O (s) + HF (g)	⟶	LiF (s) + LiOH (s)	(7)
−561.2 −275.4		−587.7 −441.5	**−192.6**

Scheme 1. Thermodynamic data to establish the enthalpies of reaction of elementary F_2 gas with H_2O, Li_2CO_3, LiOH, and Li_2O to give LiF, HF, O_2, and CO_2. In addition, reactions of secondarily formed HF [Eqs. (1), (3)] with Li_2CO_3, LiOH and Li_2O to give LiF, H_2O, LiOH, and CO_2 were investigated. Below a substance its enthalpy of formation $\Delta_f H°$ is given in kJ mol^{-1} and at the end, below the equation label, the overall resulting reaction enthalpy $\Delta_r H°$ is given in bold green if exothermic in kJ mol^{-1}.

CoO (s) + F_2 (g)	⟶	CoF_2 (s) + ½ O_2 (g)	(8)
−237.9 0		−671.5 0	**−433.6 (Ni:−411.4;Mn:−469.8)**
Co_3O_4 (s) + 4 F_2 (g)	⟶	CoF_2 (s) + 2 CoF_3 (s) + 2 O_2 (g)	(9)
−891.0 0		−671.5 −790.4 0	**−1361.3 (−453.8 per Co)**
$Co(OH)_2$ (s) + 2 F_2 (g)	⟶	CoF_2 (s) + 2 HF (g) + ½ O_2 (g)	(10)
−539.7 0		−671.5 −275.4 0	**−682.6 (Ni: −664,2)**
$CoCO_3$ (s) + F_2 (g)	⟶	2 CoF_2 (s) + CO_2 (g) + ½ O_2 (g)	(11)
−713.0 0		−671.5 −394.4 0	**−352.9**
CoO (s) + 2 HF (g)	⟶	CoF_2 (s) + H_2O (l)	(12)
−237.9 −275.4		−671.5 −285.8	**−168.7**
$Co(OH)_2$ (s) + 2 HF (g)	⟶	CoF_2 (s) + H_2O (l)	(13)
−539.7 −275.4		−671.5 −285.8	**+133.1 (Ni: +151,6)**
$CoCO_3$ (s) + 2 HF (g)	⟶	CoF_2 (s) + H_2O (l) + CO_2 (g)	(14)
−713.0 −275.4		−671.5 −285.8 −394.4	**−88.0 (Mn: −90.3)**

Scheme 2. Exemplarily collected thermodynamic data for the reaction of F_2 or intermediately formed HF gas with CoO, Co_3O_4, $Co(OH)_2$, and $CoCO_3$ to give $CoF_{2/3}$ and other plausible products. Below a substance its enthalpy of formation $\Delta_f H°$ is given in kJ mol^{-1} and at the end, below the equation label, the overall resulting reaction enthalpy $\Delta_r H°$ is given in bold green if exothermic and in bold red, if endothermic [in kJ mol^{-1}]. Where available, the data for the respective reaction with Ni-and Mn-compounds are included in parentheses (Ni: XXX; Mn: XXX).

Li_2O with F_2 gas to give LiF, CO_2, O_2 and HF are exothermic (Scheme 1). Scheme 1 also suggests the possible interplay of several follow up reactions, e.g. the intermediately in Eqs. (1) and (3) formed HF could react with the SBC as in Eqs. (5), (6), and (7). Overall, virtually all SBC constituting materials may be transformed on thermodynamic grounds in the exothermic reactions Eqs. (2)–(7) into LiF. It should be noted that also the layered oxide itself or the hydroxide and carbonate ions in $NiCO_3 \cdot 2\ Ni(OH)_2 \cdot 4\ H_2O$ (NCBH)[19,25] could likely react with F_2. However, no complete thermodynamic reference data was found for all thinkable compounds of this material class; the most complete data set is available for the element Co and thus relevant reactions of a representative set of Co-compounds, possibly present within the CAM or its surface, with F_2 and with intermediately formed HF are included in Scheme 2. Where available, the data for the respective reaction with Ni- and Mn-compounds are included in parentheses ($\Delta_f H°$ values in SI).

The reactions included with Scheme 1 and 2 are in agreement with the IC- and FSE-measurements and the above noted pressure drop. The latter agrees with the oxidation of oxide ions being the main reaction as in $F_2 + O^{2-} \rightarrow 2\ F^- + {}^1/_2\ O_2$. Apparently intermediately formed HF will react further. In addition, carbonates [cf. Eqs. (2), (5), (11) and (14)] cannot be the main partner, as else, pressure would have remained the same or even increased as a consequence of reaction stoichiometry. Yet, it is impossible to assign a preferential oxidation site only based on the thermodynamics. Thus, further analytics was performed.

2.3. Powder X-Ray Diffraction (pXRD)

To elucidate if crystalline metal fluorides were formed, pXRD measurements were carried out for the pristine and the two fluorinated NCM 811 CAMs (Figure 2 and Table 1). pXRD data of both fluorinated samples (F_m: 0.108 wt-% and F_x: 0.126 wt-%)

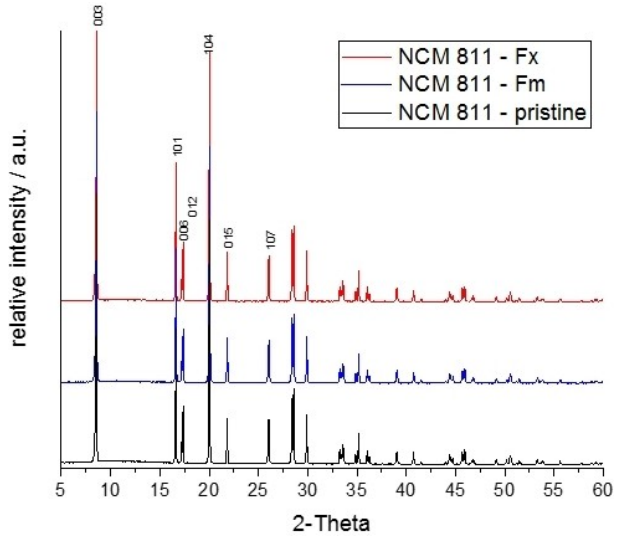

Figure 2. pXRD data of (non-)fluorinated NCM 811 CAM, measured with α Mo–$K_{\alpha1}$ radiation. Miller indices [HKL] assigned to reflexes up to 30° 2θ (F_m: 0.108 wt-% and F_x: 0.126 wt-%) are indicated.

Table 1. pXRD data analysis (Mo–$K_{\alpha1}$ radiation) and STOE fitting of the (non-)fluorinated Ni-rich NCM 811 CAM.

Cell parameters	pristine	0.105 [wt-%] label: F_m	0.126 [wt-%] label: F_x
a [Å]	2.8716(3)	2.87124(23)	2.8719(3)
c [Å]	14.2076(13)	14.2007(11)	14.2035(12)
c/*a*	4.9476	4.9458	4.9457
V [Å^3]	101.458(13)	101.387(11)	101.454(12)

showed almost identical powder diffractograms and the lattice parameters are within three times the standard deviation identical to that of the rhombohedral cell (space group $R\bar{3}m$) of pristine NCM 811 material (see SI, Figure S5 and Table S3). pXRD measurements of the (non-)fluorinated NCM 851005 showed similar results (see SI, Figure S5 and Table S3). Apparently, all the formed metal fluorides are amorphous. We note that there is no obvious change of the ratios of the relevant peak intensities of the hkl-reflections with the indices 003/104 and [(012) + (006)]/101 for pristine and fluorinated samples and thus no evidence for anion doping (cf. SI, Figures S6 and S7).

2.4. Infrared Spectroscopy (IR)

Classical ATR-IR-spectroscopy of the pristine and fluorinated Ni-rich CAMs showed no changes after exposure to F_2 gas – regardless of the applied fluorine concentration. Since LiF is invisible by IR, no direct indication for the formation of any other (bulk) metal fluoride compounds MF_2 or MF_3 with expected M–F (M=Ni, Co, Mn) stretches around 600 ± 100 cm^{-1} is evident.[53] All obtained IR spectra appeared to be identical, showing the typical characteristic bands for Ni-rich NCM materials SI, Table S4 & S5 and Figure S8 & S9) and were, therefore, omitted in the main text. However, this might be due to the low concentration of fluoride containing IR active compounds. Therefore, we switched to surface sensitive DRIFT spectroscopy.

2.5. Diffuse Reflectance Infrared Fourier Transform (DRIFT) Spectroscopy

DRIFT spectroscopy is very sensitive to surface groups on oxide particles and even detects the IR-active species such as CO_3^{2-} and SO_4^{2-} at very low concentrations.[25] To investigate, if IR active M–F bonds are present at the surface, DRIFT analyses were carried out for the uncycled NCM 851005 material.[1] However, no terminal M–F stretches were evident from the spectra shown in Figure 3. Only the expected and known signatures of surface CO_3^{2-} and SO_4^{2-} are visible.[25]

Only for the highest applied F_2 pressure of 2200 mbar (labelled F_2 max mbar), the intensity of the carbonate bands is slightly reduced compared to pristine NCM 851005 material. This suggests that Eq. (2), the reaction of F_2 with Li_2CO_3, is of lower importance for the surface chemistry. In addition, the reactions of a transition metal oxide/hydroxide or carbonate collected in Scheme 2 appear not to be prevailing either.

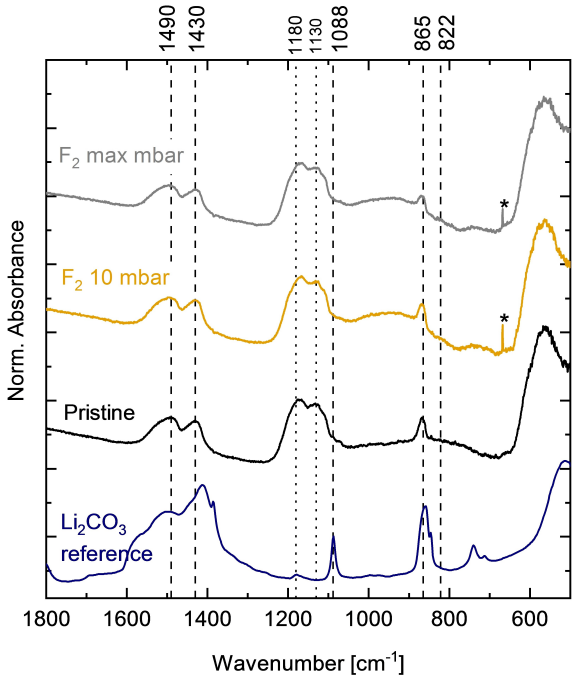

Figure 3. DRIFT spectra of Li_2CO_3 (reference material), pristine, and two fluorinated NCM 851005 CAMs (F_2 10 mbar = 0.011 wt-% F and F_2 max mbar = 2200 mbar or 0.24 wt-% F). The bands marked at 1130/1180 cm^{-1} correspond to SO_4^{2-} (from the co-precipitation process of precursor preparation), those at 865 and 1430/1490 cm^{-1} correspond to CO_3^{2-}.[25] At the bottom a batch of Li_2CO_3 is shown as reference. The signals at 670 cm^{-1} marked with an asterisk represent artefacts due to fluctuating amounts of atmospheric CO_2 in the spectrometer.

[1] Since we ran out of the pristine NCM 811 material, DRIFT spectroscopy measurements were carried out with the closely related (non-)fluorinated NCM 851005 CAM.

2.6. ^{7}Li and ^{19}F MAS-NMR Studies

Magic angle spinning nuclear magnetic resonance (MAS-NMR) of (non-)fluorinated NCM 811 CAMs were carried out to obtain direct proof for the presence of the in Eqs. (2)–(7) proposed LiF as the most likely metal fluoride in pristine, middle (0.108 wt-% F), and higher (0.126 wt-% F) fluorinated NCM CAMs (Figure 4). The ^{19}F rotor-synchronized Hahn-Echo MAS NMR spectra of all fluorinated NCM samples show a signal at an isotropic shift of −204.0 ppm that fits very well to the signal of neat solid LiF at −204.5 ppm (SI, Figure S12). There is a second very small signal at −123 ppm originating from traces of PTFE in the samples (probably from the stir bar).

The distortion of the spectra around −100 to −200 ppm results from incomplete subtraction of the background signal originating from the PTFE parts of the MAS probe (SI, Figure S14). In the rotor synchronized solid-echo ^{7}Li spectra recorded at 30 kHz MAS, a sharp signal with well resolved spinning sidebands was observed for all samples, fluorinated or not. Its isotropic shift is identical to that of neat LiF at −0.3 ppm, yet it also would match the position[54] in neat Li_2O, Li_2CO_3 or LiOH and thus is rather insensitive to the nature of the counterion (Figure 4; SI, Figure S15 and S16). Additionally, in all the ^{7}Li spectra, a very broad signal that does not split into spinning sidebands with a width of about −500 to +1000 ppm is present. It was assigned to the lithium atoms in the bulk of the Ni-rich material with the highest spatial proximity to the unpaired electrons. Furthermore, it is shifted by more than +300 ppm, if compared to neat LiF, due to the unpaired electron spin density transferred from the neighbored layered Ni-rich NCM oxide to the nucleus (Fermi contact shift). Its linewidth originates from nucleus-electron dipolar interactions as well as a distribution of Fermi contact shifts.[50] The observed chemical shifts in both the ^{19}F and ^{7}Li spectra perfectly match the ones observed for neat LiF and thus were assigned to arise from LiF. However, the spinning sidebands envelope of both, the ^{7}Li and ^{19}F signal, is strikingly broadened in comparison to that of neat LiF (about 150 kHz for ^{7}Li and 200 kHz for ^{19}F, cf. Figures S15 and S16). As the dipole-dipole coupling of ^{7}Li and ^{19}F should be comparable to that in neat LiF and should in general not exceed 100 kHz, the line broadening can only be explained by dipole-dipole interaction of the observed nuclei with the electron spin of the Ni-rich NCM oxide materials. This interaction requests a close spatial proximity. However, since the lines have isotropic shifts identical to neat solid LiF (i.e. no Fermi contact shift is observed), the LiF causing this line is not present within the bulk, but rather coating the Ni-rich NCM material.[50] In addition, ^{7}Li and ^{19}F MAS NMR studies were carried out for the (non-)fluorinated NCM 851005 CAMs and they behave similarly (SI, Figures S15 and S16).

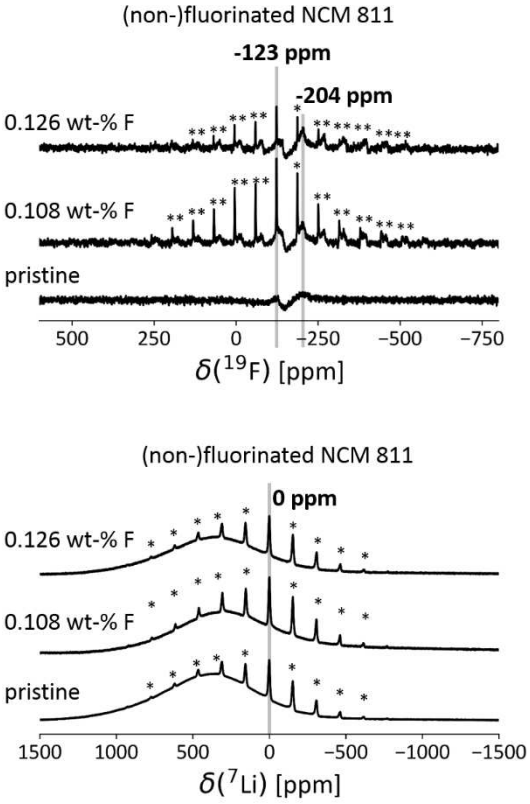

Figure 4. ^{19}F and ^{7}Li MAS NMR studies of pristine, low (0.108 wt-% F) and high (0.126 wt-% F) fluorinated NCM 811 CAMs (lower panel: ^{7}Li MAS NMR: 30 kHz spinning; upper panel: ^{19}F MAS NMR: 30 kHz spinning and ^{19}F background subtracted for NCM). Spinning sidebands are marked by '*'.

2.7. Scanning Electron Microscopy Measurements

The (non-)fluorinated NCM 851005 CAMs were characterized by scanning electron microscopy (SEM) to study the impact of fluorination on their morphology. The CAMs consist of regular spheroidal particles with a Gaussian distribution of the particle size of around 5–15 μm (Figure 5a, d and g). Pristine material showed an inhomogeneous surface (Figure 5b and c) in comparison to the smoother, more homogenous fluorinated samples (Figure 5e, f, h and i). Yet, overall there is little morphology change upon oxidative fluorination.

2.8. Thermal Stability of Ni-rich NCM CAMs after Fluorination

Thermogravimetric analysis (TGA) and differential thermal analysis (DTA) measurements were carried out at temperatures up to 650 °C by heating with 10 °C min^{-1} under a flow of nitrogen gas. For the (non-)fluorinated NCM 811 and 851005 CAMs a mass loss between 0.16 to 0.81 % (811) or 0.1 to 1.0 % (851005) was observed by TGA. In addition, DTA measurements revealed no change in thermal stability (SI, Figure S10, Table S11).

2.9. TGA Coupled with Mass Spectrometric Analysis (TGA-MS)

Published TGA-MS measurements of the fluoride containing $LiVPO_4F_{0.45}O_{0.55}$ CAM material[55] showed the release of small amounts of hydrogen fluoride during heating ($HF => m/z =$ 20). Thus, we investigated this possibility by TGA-MS analysis of

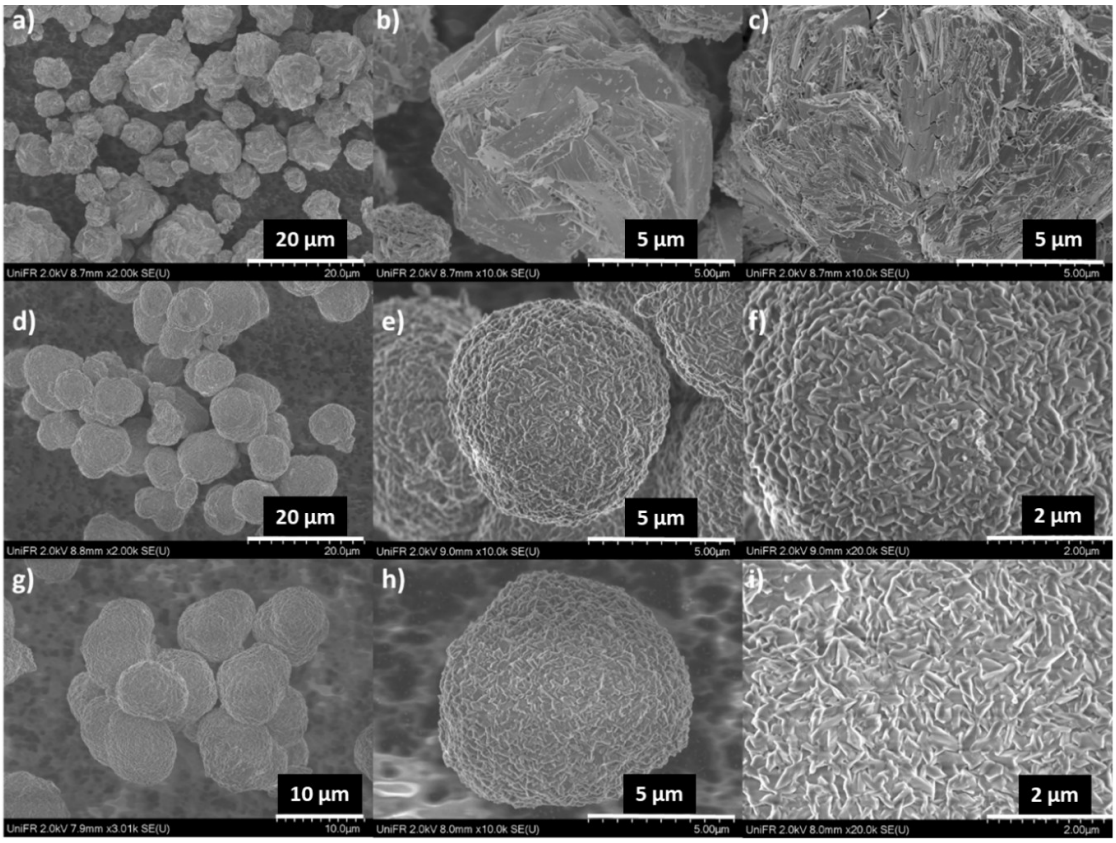

Figure 5. SEM images of pristine NCM 851005 CAM material (a, b, c); CAM with 0.162 wt.-% F (d, e, f); and CAM with 0.240 wt.-% F (g, h, i).

the pristine and two fluorinated NCM 851005 CAMs (0.007 wt-% F and 0.240 wt-% F) to detect any amount of HF, H_2O, O_2 and CO_2 formed during heating the material. TGA-MS measurements in argon were carried out up to 1125 °C for the as received as well as for materials, heated prior in argon to 400 or 450 °C (Figure 6). Due to the loss of absorbed water (m/z = 18), the as received material had a mass loss of 0.08 % in the temperature range between 120 and 450 °C (Figure 6A). In agreement with the expectation, the material heated prior to 400 °C had a mass loss of only 0.01 % between 120 and 450 °C (Figure 6D). A significant further mass loss occurs when heating to 1125 °C (adding up to a total mass loss of 7.19 % and 7.30 % for as received and heated material). This is assigned to the bulk decomposition of the material, clearly indicated by the release of O_2 ($m/z = 32$, Figure 6AD). These measurements confirmed the presence of small amounts of water on the surface of the pristine NCM 851005. The fluorinated samples measured without further treatment showed a higher mass loss (0.26 % $_{(0.007\ wt\text{-}\%\ F)}$/0.21 % $_{(0.240\ wt\text{-}\%\ F}$; Figure 6BE) in comparison to the pristine material (0.08 %; Figure 6A) in the temperature range between 120 and 450 °C. The mass spectra indicate that this increased mass loss is accompanied by the release of little CO_2 ($m/z = 44$) and more H_2O ($m/z = 18$). The total mass loss of these fluorinated samples after heating to 1125 °C is slightly higher compared to the pristine materials (7.48 % $_{(0.007\ wt\text{-}\%\ F)}$ and 7.42 % $_{(0.240\ wt\text{-}\%\ F)}$), due to slightly higher water content (Figure 6BE). Therefore, TGA-MS data confirmed the thermodynamic proposition in Schemes 1 and 2 that the reaction of F_2 gas with Ni-rich NCM finally leads to the formation of water (Figure 6BE). However, TGA-MS gives absolutely no indication for the release of HF ($m/z = 20$). In addition, TGA-MS measurements were taken on the 0.054 wt-% F fluorinated NCM 851005 CAM, untreated or heated to 450 °C after fluorination and prior to TGA-MS analysis (Figure 6CF). The mass loss between 120 and 450 °C was lowered from 0.23 % (Figure 7C, **no** preheating) to 0.05 % (Figure 7F, preheating the fluorinated sample to 450 °C). Thus, fluorinated Ni-rich NCM CAMs should be heated to 450 °C for 5 h prior to use in battery cells, to minimize the amount of water introduced to the system during oxidative fluorination.

2.10. Conductivity Measurements of the Ni-rich CAMs

Conductivity measurements were carried out for the pristine and two fluorinated NCM 811 CAMs. All investigated CAMs show a linear increase of the conductivity in the range of the pressure applied from 2 MPa to 20 MPa (Figure 7). However, in contrast to the samples cited in Refs. [56] and [57–59], the pristine NCM811 material always showed highest conductivities (for the individual values: SI, Table S6 and Figure S17). Furthermore, conductivity measurements were also carried out for the (non-)fluorinated NCM 851005 CAMs and the materials behave similarly (SI, Table S6 and Figure S17).

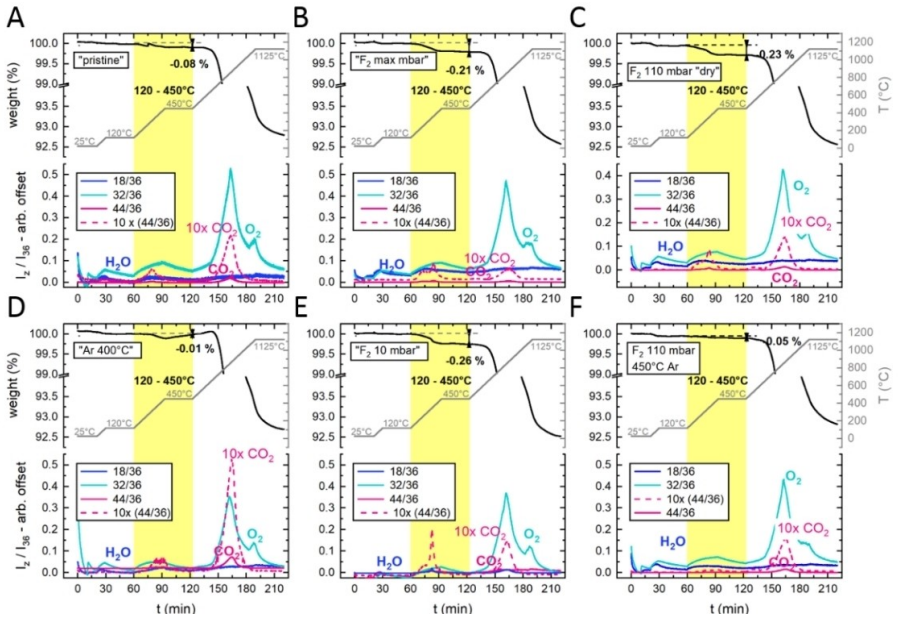

Figure 6. TGA-MS measurements of several NCM 851005 CAMs. A) pristine material measured directly. B) Material exposed to 1400 mbar F_2 pressure, labelled "F_2 max mbar" (=0.24 wt-% F). C) Material exposed to 110 mbar F_2 pressure, labelled "F_2 110 mbar (dry)" (=0.054 wt-% F). D) pristine material heated to 400 °C in Argon prior to measurement; labelled "Ar 400 °C". E) Material exposed to 10 mbar F_2 pressure, labelled "F_2 10 mbar" (=0.011 wt-% F) and F) Material exposed to 110 mbar F_2 pressure and heated to 450 °C in Argon prior to measurement, labelled "F_2 110 mbar, 450 °C Ar)" (=0.054 wt-% F). For each sample, the characteristic weight loss (upper half of each panel) and the corresponding mass spectrometric signals (lower half of each panel) are shown for a 10 K min^{-1} temperature ramp from 25 to 1125 °C with isothermal segments at 25, 120, 450 and 1125 °C. The yellow area points out the decomposition temperature of the surface contaminant species LiOH and NCBH.[25] Their decomposition is accompanied by characteristic CO_2 and H_2O fingerprints.

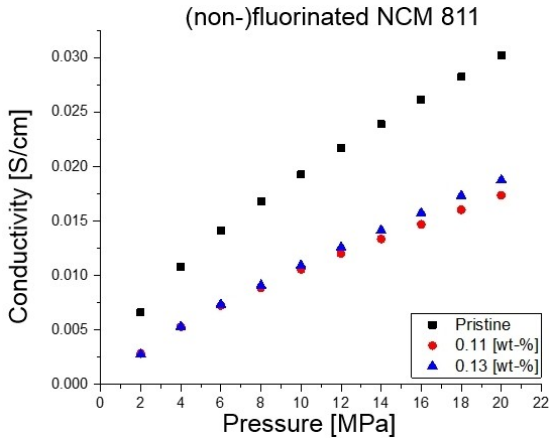

Figure 7. Conductivity measurements of (non-)fluorinated NCM 811 materials.

2.11. Press Density Measurements of the Ni-rich NCM CAMs

Measurements were carried out for the pristine and two fluorinated NCM 811 (Figure 8) and 851005 CAMs. All samples show a linear increase of the density with increasing pressure. Both fluorinated NCM 811 CAMs showed similar press densities that are up to 5% higher than that of the pristine material (for the individual values: SI, Table S7 and Figure S18 for NCM 851005).

2.12. Cycling Behavior of Pristine and Fluorinated Ni-rich NCM 811 CAMs in Full-Cells

The electrochemical performance of the (non-)fluorinated Ni-rich NCM 811 was studied in graphite/NCM 811 pouch full-cells of 8 mAh capacity with LP57 electrolyte. Two different fluoride concentrations, a middle (0.108 wt.-% F) and a higher concentration (0.126 wt-% F) were investigated together with the pristine material. Figure 9 shows the cycling data and the corresponding average charge and discharge voltages measured at 30 °C (left) and 45 °C (right). The middle fluorinated NCM 811 CAMs (0.108 wt-% F, labelled NCM811 Fm in Figure 9) showed for both temperatures the best battery performance after 500 cycles and a clear improvement over the pristine CAM. Still, even the higher fluorinated material (labelled NCM811 Fx) showed for both temperatures an improved stable cycling performance in comparison to the pristine material (Figure 9). At both temperatures, the average charge and discharge voltages calculated from the constant current cycling showed superior results for the middle-fluorinated material NCM811 Fm in comparison to the higher fluorinated NCM811 Fx and the pristine NCM811 materials. The higher fluorinated and pristine materials have rather similar average charge and discharge voltages at 30 °C. However, at 45 °C they differ visibly during discharge and even the higher fluorinated material showed a slower decrease of the average discharge voltage and a lower voltage hysteresis upon cycling compared to the pristine material (Figure 9). Yet, best performance was achieved for the middle-fluorinated material containing 0.108 wt-% F.

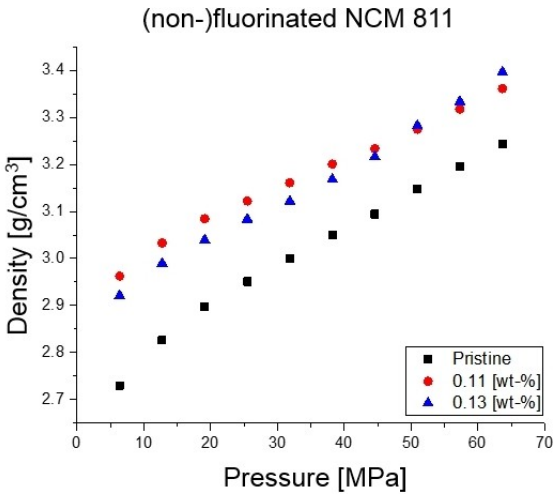

Figure 8. Press density measurements of (non-)fluorinated NCM 811.

2.13. Impedance Measurements

Figure 10 shows Nyquist plots of electrodes including (non-) fluorinated NCM 811 CAMs after 250 cycles (closed symbols) and after 500 cycles (open symbols) at 30 °C (Figure 10a) and 45 °C (Figure 10b), measured during charge at 4.0 V from 5 mHz to 0.1 MHz. In agreement with the improved cycling behavior, the middle-fluorinated material NCM 811 Fm showed for both temperatures the lowest surface film resistance throughout cycling. The higher fluorinated NCM 811 Fx and pristine NCM 811 CAMs had similar, but considerably higher values for both temperatures. In Fig 10c, the resistances calculated from the middle-to-low frequency semicircles are plotted against the number of cycles; they were fitted with Z-view. Again, the middle-fluorinated material NCM 811 Fm showed for both temperatures the best values and the higher fluorinated NCM 811 Fx as well as the pristine NCM 811 CAMs showed similar, but inferior values for both temperatures, with slightly lower resistance for the higher fluorinated CAM.

2.14. Transition Metal Leaching from the CAM and Migration to the Anode Active Material (AAM)

The dissolution of transition metals from the CAM into the electrolyte solution upon prolonged cycling with possible deposition on the AAM is detrimental to battery performance.[5,60] To investigate the effect of oxidative fluorination on the metal leaching, cells with pristine and fluorinated (0.108 wt-% F and 0.126 wt-% F) NCM 811 were disassembled after 500 cycles and the nickel, cobalt, and manganese concentration localized/deposited on the AAM after 500 cycles at 30 °C and 45 °C was determined by ICP-MS (Table 2).

Apparently, the Ni leaching is little affected by the fluorination. However, the ICP-MS measurements showed the

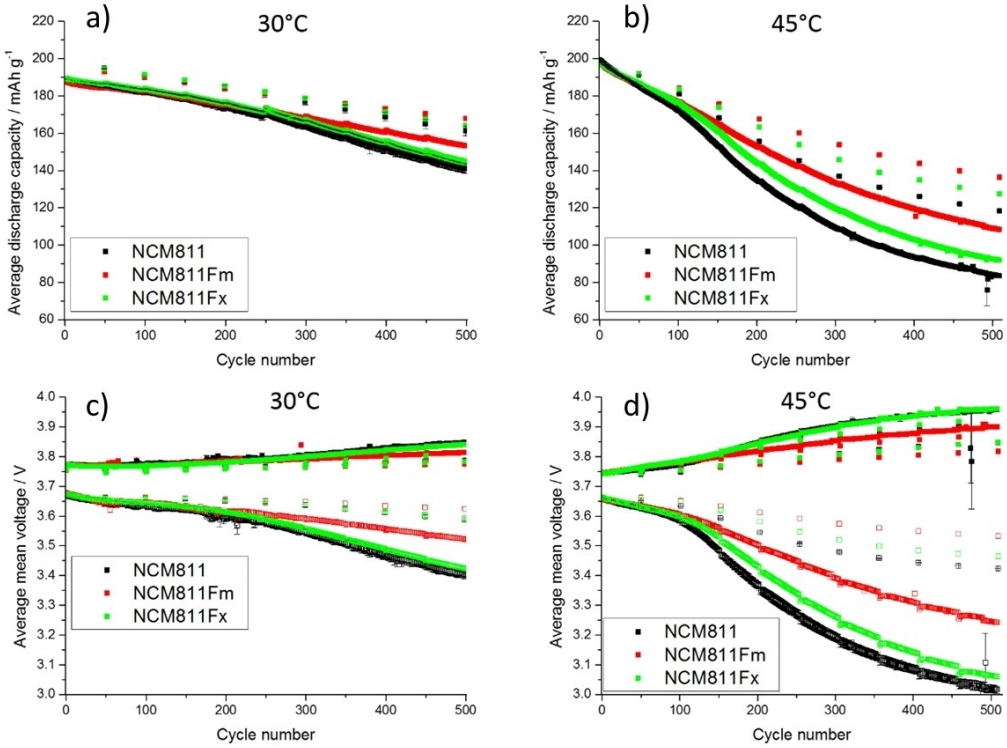

Figure 9. Full-cell cycling data (triplicate measurements including the standard deviation as error bars) of the (non-)fluorinated NCM 811 CAMs measured in full-cells at 30 °C (a, left) and 45 °C (b, right) with LP57 electrolyte. Fm stands for 0.108 wt-% F and Fx for 0.126 wt-% F. For the continuous cycling between 2.0 and 4.2 V and after the five formation cycles (omitted), the cells were measured with a 0.5 C charge and 1 C discharge current and a 30 minutes CV-step at 4.2 V. Every 50 cycles, one cycle was measured at 0.1 C for charge and discharge. c, d) Average charge and discharge voltages upon cycling, omitting the first five formation cycles, as shown in (a, b). Fm stands for 0.108 wt-% F and Fx for 0.126 wt-% F.

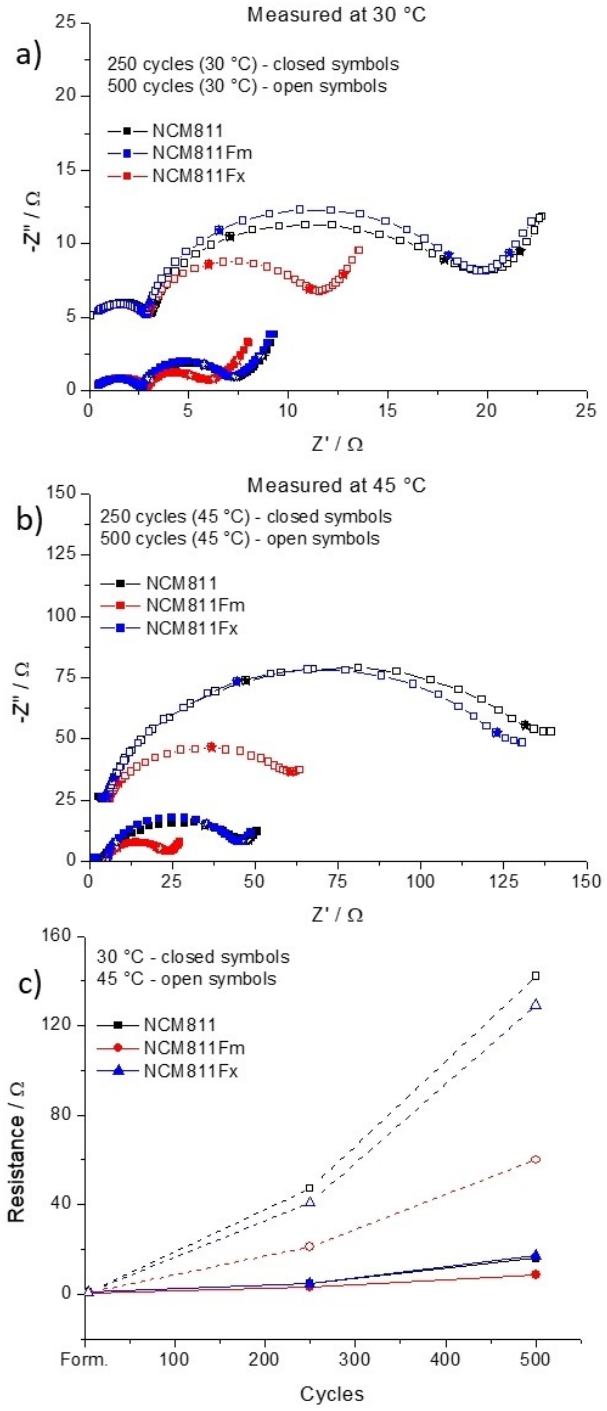

Figure 10. Nyquist plots of cells comprising (non-)fluorinated NCM 811 CAMs after 250 cycles (closed symbol) and 500 cycles (open symbol) at 30 °C (a) and 45 °C (b). Fm stands for 0.108 wt-% F and Fx for 0.126 wt-% F. For each of the plots, the impedance at 500 cycles was offset in the imaginary impedance by −5 ohms at 30 °C, and −25 ohms at 45 °C. The results have not been normalized by multiplying the geometric area of the electrode or the loading. Yet, the comparison is valid, since the electrode loading, as well as their geometric and electrochemical surface area were the same between each of the 6 cells. Impedance measured at 10, 1, 0.1 and 0.01 Hz is indicated by stars. The resistance measured from the middle-to-low frequency semi-circles are plotted against cycles, fitted with Z-view (c).

highest concentrations of Co and Mn in AAMs dissolved from the pristine material. The cells with the middle and higher fluorinated CAMs, showed a large reduction of the leaching to about one-half of the pristine (for Co), or even to one-third of the pristine materials (Mn at 45 °C). Thus, the fluorination apparently reduces transition metal cross talk for Co and Mn from the CAM to the AAM through the electrolyte solution.

3. Discussion

Earlier work showed that exposure of CAMs to higher F_2 pressures at elevated temperatures only diminished[50] subsequent discharge capacities in battery cycling.[61] This capacity reduction is in agreement with an oxidation of the transition metal octahedral network, delithiation, and formation of larger amounts of amorphous LiF according to Eq. (15).

$$\mathrm{Li[MO_2]} + x(^1/_2\ \mathrm{F_2}) \rightarrow \mathrm{Li_{1-x}[MO_2]} + x\ \mathrm{LiF} \quad (\mathrm{M{=}Co,\ Ni,\ Mn}) \tag{15}$$

Therefore, we concentrated here on the effect of mild room temperature (surface) fluorination of Ni-rich NCM material. Our main idea was to convert the SBC, i.e. Li_2O, LiOH, Li_2CO_3 and eventually the NCBH surface phase[18–23] into harmless phases for the electrochemical performance in full-cells.

3.1. Effects of Fluorine Gas Treatments on the Electrochemical Performance of Ni-rich NCM 811

Both fluorinated samples showed enhanced electrochemical performance after 500 cycles at 30 °C and 45 °C, and a clear improvement over the pristine CAM (Figure 9). At both temperatures, the middle-fluorinated sample (0.108 wt.-% F) showed superior battery performance, more stable average charge/discharge voltages, and the lowest surface film resistance throughout cycling (at 250 and 500 cycles). In the following, we attempt to rationalize these observations.

3.2. Reduction of the SBC Content by Fluorination

Apparently, the room temperature reaction with low F_2 pressures produces a thin LiF layer on the CAM. This agrees with the thermodynamics of the reactions shown in Scheme 1, Eqs. (2)–(7) as well as the direct observation of LiF in the MAS-NMR. Yet, the DRIFT spectra showed that the Li_2CO_3 surface content is only slightly diminished. Support comes from thermodynamics: the reaction of Li_2CO_3 with F_2 [Eq. (2)] is by 176 kJ mol^{-1} **less favored** in $\Delta_r H°$ than Eq. (4), the reaction of F_2 with Li_2O. Therefore, Eq. (4) could be the major oxidative fluorination path. In addition, this fits with the observed pressure drop after fluorination: in Eq. (4), one equivalent F_2 gas only releases half an equivalent O_2 gas. Since the fluorine molecule F_2 is gaseous and very small, this gas molecule can in principle reach every pore of a solid structure. Advantageously, it was expanded within seconds to the evacuated reactor vessel with the porous CAM. Thus, despite its high reactivity, we

Table 2. Results of ICP-MS measurements of the hydrochloric acid extracts to determine the nickel, cobalt, and manganese concentration in wt-% localized on the AAM after 500 cycles at 30 °C or 45 °C and dissolution of metals in hydrochloric acid.

NCM 811 CAM	Ni [%] at 30 °C	Co [%] at 30 °C	Mn [%] at 30 °C	Ni [%] at 45 °C	Co [%] at 45 °C	Mn [% at 45 °C
pristine	0.067	0.052	0.259	0.076	0.062	0.617
0.108 wt-% F	0.073	0.029	0.152	0.065	0.032	0.178
0.126 wt-% F	0.058	0.025	0.144	0.065	0.031	0.209

expect that it did immerse into every pore of the material. Already earlier work[50,62] showed that thin LiF surface films on CAMs have positive effects on the performance of the battery. The transformation of parts of the surface accessible basic compounds into chemically neutral and in the electrolyte solution insoluble LiF presumably reduced the SBC and thereby led to less degradation of the electrolyte during cycling resulting in reduced impedance built-up.

3.3. Limited Fluoride Uptake

For the screening fluorination reactions performed, the fluoride content of the nickel-rich NCM CAMs after room temperature oxidative fluorination was always lower than 0.25 wt-% F, although gas pressures targeting up to an ideal fluoride uptake of up to 1.0 wt.-% (NCM 811) and for NCM 851005 even up to 3.0 wt.-% were applied (Figure 1; Figure S3, Table S1). Thus, a certain amount of self-levelling of the fluoride uptake by oxidative fluorination appears to occur. This may be induced by the action of the protecting LiF layer, which is inert towards further oxidation with F_2.

3.4. How Does Fluorination Reduce Co and Mn Leaching from the CAM?

The transition metal dissolution from closely related pristine NCM 622 and their migration to the graphite anode was earlier investigated: at high potentials Ni, Mn, and Co dissolved in the electrolyte and deposited nearly stoichiometrically on the AAM.[17] Our ICP-MS measurements of the Ni, Co and Mn concentration on the graphite AAM after 500 cycles at 30 °C and 45 °C (Table 2) indicate that Ni leaching is slightly reduced by fluorination. By contrast, a large leaching-reduction to about one-half of the pristine (for Co), or even to one-third of the pristine materials (Mn at 45 °C) was observed. We discuss some background first before turning to this observation.

3.5. On the Oxidation State of TMs in NCM CAMs

Recent analyses showed that in pristine discharged NCM CAMs the Ni ions are present in three different oxidation states, mainly 2+, but also 3+, and 4+. Co ions adopt the 3+ oxidation state and Mn ions exist as 4+.[63] The amount of Ni^{3+} ions increases with increasing Ni content in NCMs, while that of Ni^{2+} ion decreases. Ni^{4+} is only found in Ni-rich NCM CAMs such as NCM 811.[63] The valence state of the redox ions present[25,64] depends on the charge state/composition and follows for $Li_{1-x}Ni_{1/3}Co_{1/3}Mn_{1/3}O_2$ the amount of x present: Ni^{2+}/Ni^{3+} for $0 \leq x \leq 1/3$, Ni^{3+}/Ni^{4+} for $1/3 \leq x \leq 2/3$, and Co^{3+}/Co^{4+} for $2/3 \leq x 1$.[65]

3.6. Structural Instability Induced by the Jahn-Teller Effect

Both LCO and NCM CAMs have a layered structure, in which the metal atoms are octahedrally coordinated by oxygen atoms and the lithium ions are localized in-between the MO_6 layer (M=Ni, Co, and Mn).[66] In such an environment, the *d*-orbitals of the transition metals are split into an e_g set (d_{x2-y2}; d_{z2}) and a t_{2g} set (d_{xy}; d_{xz}; d_{yz}). The Jahn-Teller-(JT-)effect describes a further splitting of the *d*-orbitals with a d^{4-9} configuration to remove degeneracies. This leads either to *compressed* or *elongated* structures (both with local D_{4h} symmetry). Hence, the JT-effect can produce structural instabilities in the CAM during charge and discharge, which may lead to the preferential dissolution of the lattice metal JT-ion into the electrolyte, facilitated by traces of HF in the electrolyte.[67] Ions with strong JT-effect are those, in which the degenerate e_g set is unevenly distributed, i.e. d^4 high spin (Mn^{3+}) and d^7 low spin (Co^{2+}; Ni^{3+}). Thus, it is expected that ions in these configurations will, due to the structural JT-instability, more easily leach into the electrolyte and finally deposit on the AAM.

Yet, the presence of accessible, presumably surface bound Co^{2+} as well as Mn^{3+} is against the conventional wisdom (see above). However, support for this hypothesis comes from the investigation[68] of the related $Na_{2/3}Co_{2/3}Mn_{1/3}O_2$ prepared by a coprecipitation method. The sodium intercalation in P2–$Na_{2/3}Co_{2/3}Mn_{1/3}O_2$ was investigated by X-ray absorption spectroscopy (XAS). The oxidation states in pristine $Na_{2/3}Co_{2/3}Mn_{1/3}O_2$ were assigned as Co^{3+} and Mn^{4+}. Important features of Co^{2+} and Mn^{3+}, for example, energy shifts and bond distances, were observed using XAS and indicate that both redox couples Co^{3+}/Co^{2+} and Mn^{4+}/Mn^{3+} are to some extent simultaneously present in the discharged state.[68] Therefore, we suggest that also in the Ni-rich $Li_{1+w}(Ni_xCo_yMn_z)_{1-w}O_2$ phases some of the cobalt could exist in the divalent state together with reduced Mn^{3+}.

3.7. Effect of Oxidative Fluorination on Co and Mn Leaching

In the pristine NCM 811 CAM used in this study, the leaching of all three metals, potentially as the JT-ions Mn^{3+}, Co^{2+} and Ni^{3+} with structural instability, is similar. Upon fluorination, the Ni leaching is only slightly diminished. The reason could be that

Ni^{3+} is the "natural" oxidation state of Ni in the discharged NCM CAM and more difficult to oxidize than the JT-ions with lower oxidation state (Co^{2+}) or the easier to oxidize Mn^{3+}. Thus, low oxidation state surface Co^{2+} and Mn^{3+} ions present in the pristine material could, in addition to SBC, be preferentially oxidized by the gaseous reagent F_2 to the non-leachable Co^{3+}/Mn^{4+} ions that are immediately covered by a concomitantly formed LiF surface film insoluble in the electrolyte. Apparently, this does not lead to Co–F or Mn–F bond formation (cf. DRIFTS), but rather would include for example the exothermic oxidation of surface $Co^{II}(OH)_2$ to $Co^{III}O(OH)$ as in Eq. (16),

$$Co^{II}(OH)_{2\,(s)} + \tfrac{1}{2}\,F_{2\,(g)} \rightarrow Co^{III}O(OH)_{(s)} + HF_{(g)} \qquad (16)$$

−539.7 0 −456.0 −275.4 **−191.7**

delivering HF, which immediately reacts further with other basic surface sites according to Schemes 1 and 2. Eq. (16) is exothermic by −191.7 kJ mol^{-1} (bold **green**; $\Delta_f H°$ of all components[52,69] is given below the substances). $Co^{III}O(OH)$ formation is already induced by oxygen in alkaline solution,[70] and thus appears sensible to work with F_2 as oxidant. Mn^{3+} would similarly be converted according to Eq. (15) with M=Mn to MnO_2. Thus, the amount of redox accessible low oxidation state surface Co^{2+} and Mn^{3+} ions susceptible to leaching could be lowered by the oxidative gas phase fluorination. Consequently, Co and Mn leaching would be strongly diminished, but Ni leaching is little changed. However, all ions are slightly protected from leaching by formation of an amorphous and protecting LiF surface film. This would also account for the slight reduction of Ni leaching observed in 3 out of 4 cases for the fluorinated NCM 811 CAMs (Table 2).

3.8. Secondary Effects of Fluorination

3.8.1. Formation of Trace Water

TGA-MS analysis showed for the fluorinated samples slightly higher mass loss in comparison to the pristine material in the temperature range between 120 °C and 450 °C. This agrees with the chemical formation of water as a consequence of the fluorination as given in Eq. 5 and 6 in Scheme 1. pXRD data showed a tiny influence of the fluorination on the unit cell parameters, in which the pristine material had the smallest unit cell (Figure S7, Table S3). This might be consistent with the incorporation of H_2O in the material during the reaction of fluorine gas with the Ni-rich NCM CAMs. However, heating for a few hours at 450 °C did remove these small water amounts effectively according to the TGA-MS analysis. In agreement, the material, heated to 450 °C for 5 h had the smallest unit cell of all samples. Thus, for an improved battery performance, an intermediate drying step at 450 °C is recommended, if CAMs exposed to oxidative fluorination are to be used in LIBs.

3.8.2. Reduced Conductivity, but Increased Press Density

Electronic conductivities of CAMs measured with a four-point conductivity test method may increase upon fluoride uptake, i.e. the conductivity of vanadium phosphates improved from $Li_3V_2(PO_4)_3$ (3.7×10^{-7} S cm^{-1}) over fluorinated $Li_3V_2(PO_4)_{2.95}F_{0.05}$ (1.2×10^{-6} S cm^{-1}) to $Li_3V_2(PO_4)_{2.90}F_{010}$ (7.2×10^{-6} S cm^{-1}), but again decreased for highest F-content in $Li_3V_2(PO_4)_{2.85}F_{0.15}$ (9.2×10^{-7} S cm^{-1}).[56] Similarly, fluorinated lithium iron fluorophosphates have a higher conductivity ($LiFePO_4F$: $\approx1\times10^{-7}$ S cm^{-1} at 300 K) than non-fluorinated $LiFePO_4$ ($\approx1\times10^{-9}$ S cm^{-1} at 300 K).[57–59] However, in our case the conductivities decreased, but instead the press densities increased. To account for this observation, one should note that typically inorganic fluorides such as LiF do act as fluxing reagents. Thus, LiF is most widely used as a flux in the production of ceramics, such as enamels, glasses and glazes. The pXRD analyses of our fluorinated Ni-rich CAMs showed that the LiF formed is probably amorphous. In addition, SEM-images showed for the non-treated material a rougher surface in comparison to both fluorinated samples with smoothened surfaces. Apparently, this – possibly through the amorphous character improved – fluxing property of the homogeneous LiF-surface may facilitate sintering and increases densities of the fluorinated CAM powders upon pressurization. The rough trend is that higher fluoride concentrations led to higher press densities. This might be related to the reduction of the SBC layer by fluorination to give LiF. However, LiF is an electrical insulator and therefore fluorinated NCM 811 (and also NCM 851005) has a reduced conductivity in comparison to the pristine material.

4. Conclusions

The treatment of Ni-rich NCM CAM with low pressures (a few hundred mbar) of fluorine gas at room temperature lowers the SBC concentration on the surface of the material, producing a thin LiF film. DRIFT spectra suggest that the main reaction partner within the SBC is Li_2O and the less favored reaction of F_2 with Li_2CO_3 only occurs to a small degree. In addition, no formation of metal fluorides other than LiF was detected. SEM images revealed a smooth coating of the fluorinated CAM particles, possibly due to a LiF film. This X-ray amorphous LiF film may have a fluxing property and, favorably, all fluorinated Ni-rich NCM CAMs showed a considerably higher press density than the pristine material. However, apparently due to this insulating LiF-film, the fluorinated material has a reduced conductivity in comparison to the pristine one. As a co-product, fluorination of the Ni-rich CAM leads to the chemical formation of small amounts of water, which according to TG-MS-measurements can be removed by heating the material to 450 °C for a few hours. Overall, the tested fluorinated NCM 811 samples showed enhanced electrochemical performance in full-cells at 30 °C as well as 45 °C after 500 cycles and a clear improvement over the pristine NCM 811 CAM. At both temperatures, the middle-fluorinated sample (0.108 wt-% F) showed the superior battery performance, much more stable average charge and

discharge voltages and the lowest built-up of surface film resistance after 250 and 500 cycles. These improvements may result from diminished electrolyte decomposition during cycling leading to reduced impedance built-up. Possibly, this reduction is induced by reduction of the SBC content and formation of the protecting thin amorphous surface LiF-film. Further improving the electrochemical performance, Mn and Co leaching from the CAM and their subsequent deposition on the AAM is reduced after 500 cycles at 30 °C and 45 °C. While the Ni dissolution is almost unaffected, the cells with the fluorinated CAMs showed a large leaching-reduction to about one-half of the pristine (Co), or even to one-third of the pristine materials (Mn at 45 °C). Thus, the fluorination apparently reduces Co and Mn cross talk from the CAM to the AAM through the electrolyte solution during charge/discharge. This may tentatively be assigned to the oxidative fluorination, which suppresses the preferential leaching of the surface bound strong Jahn-Teller ions Co^{2+} (d^7) and Mn^{3+} (d^4) in the pristine material by oxidizing them to non-leachable Co^{3+} (e.g., as CoO(OH)) and Mn^{4+} (e.g., as MnO_2) imbedded into the protecting and insoluble surface LiF film on the CAM.

Acknowledgements

This work was supported by the [Albert-Ludwigs-Universität Freiburg], by the Deutsche Forschungsgemeinschaft (DFG, German Research Foundation) under Germany's Excellence Strategy – EXC-2193/1 – 390951807 and by BASF SE in the Battery Materials Network. The use of the SEM-EDX set up, acquired through the BMBF project EDELKAT (FKZ 03X5524), is gratefully acknowledged. We would like to thank Anita Becherer for support in obtaining SEM-EDX measurements and Mr. Andreas Warmbold for executing the TGA/DTA measurements. Finally, we would also like to thank Hans Beyer for valuable suggestions. Open access funding enabled and organized by Projekt DEAL.

Conflict of Interest

The authors declare no conflict of interest.

Keywords: Lithium-ion batteries · Ni-rich cathode materials · mild surface fluorination · fluorine gas · electrochemical testing.

[1] a) V. Etacheri, R. Marom, R. Elazari, G. Salitra, D. Aurbach, *Energy Environ. Sci.* **2011**, *4*, 3243; b) J. B. Goodenough, Y. Kim, *Chem. Mater.* **2010**, *22*, 587; c) U. Kasavajjula, C. Wang, A. J. Appleby, *J. Power Sources* **2007**, *163*, 1003; d) M. Winter, J. O. Besenhard, *Solid-State Electron.* **1999**, *45*, 31; e) P. N. Kumta, D. Gallet, A. Waghray, G. E. Blomgren, M. P. Setter, *J. Power Sources* **1998**, *72*, 91.

[2] L. Leyssens, B. Vinck, C. van der Straeten, F. Wuyts, L. Maes, *Toxicology* **2017**, *387*, 43.

[3] a) Y.-H. Cho, D. Jang, J. Yoon, H. Kim, T. K. Ahn, K.-W. Nam, Y.-E. Sung, W.-S. Kim, Y.-S. Lee, X.-Q. Yang, et al., *J. Alloys Compd.* **2013**, *562*, 219; b) P. Hou, X. Wang, D. Song, X. Shi, L. Zhang, J. Guo, J. Zhang, *J. Power Sources* **2014**, *265*, 174; c) K. Wu, F. Wang, L. Gao, M.-R. Li, L. Xiao, L. Zhao, S. Hu, X. Wang, Z. Xu, Q. Wu, *Solid-State Electron.* **2012**, *75*, 393; d) C.-C. Yang, Z.-Y. Lian, S. J. Lin, J.-Y. Shih, W.-H. Chen, *Solid-State Electron.* **2014**, *134*, 258; e) H. Kaneda, *Int. J. Electrochem. Sci.* **2017**, 4640; f) S. Li, X. Fu, J. Zhou, Y. Han, P. Qi, X. Gao, X. Feng, B. Wang, *J. Mater. Chem. A* **2016**, *4*, 5823; g) R. Koerver, I. Aygün, T. Leichtweiß, C. Dietrich, W. Zhang, J. O. Binder, P. Hartmann, W. G. Zeier, J. Janek, *Chem. Mater.* **2017**, *29*, 5574; h) F. Schipper, M. Dixit, D. Kovacheva, M. Talianker, O. Haik, J. Grinblat, E. M. Erickson, C. Ghanty, D. T. Major, B. Markovsky, et al., *J. Mater. Chem. A* **2016**, *4*, 16073; i) D.-C. Li, T. Muta, L.-Q. Zhang, M. Yoshio, H. Noguchi, *J. Power Sources* **2004**, *132*, 150; j) J. Oh, J. Kim, Y. M. Lee, D. O. Shin, J. Y. Kim, Y.-G. Lee, K. M. Kim, *Mater. Chem. Phys.* **2019**, *222*, 1; k) Y. Sun, Z. Zhang, H. Li, T. Yang, H. Zhang, X. Shi, D. Song, L. Zhang, *Dalton Trans.* **2018**, *47*, 16651; l) B.-J. Chae, J. H. Park, H. J. Song, S. H. Jang, K. Jung, Y. D. Park, T. Yim, *Solid-State Electron.* **2018**, *290*, 465; m) G. Li, L. Qi, P. Xiao, Y. Yu, X. Chen, W. Yang, *Solid-State Electron.* **2018**, *270*, 319; n) M. A. Mezaal, L. Qu, G. Li, W. Liu, X. Zhao, K. Zhang, R. Zhang, L. Lei, *Solid-State Electron.* **2017**, *21*, 145.

[4] Y. Xi, Y. Liu, D. Zhang, S. Jin, R. Zhang, M. Jin, *Solid State Ionics* **2018**, *327*, 27.

[5] M. Evertz, F. Horsthemke, J. Kasnatscheew, M. Börner, M. Winter, S. Nowak, *J. Power Sources* **2016**, *329*, 364.

[6] a) E. M. Erickson, F. Schipper, T. R. Penki, J.-Y. Shin, C. Erk, F.-F. Chesneau, B. Markovsky, D. Aurbach, *J. Electrochem. Soc.* **2017**, *164*, A6341–A6348; b) E. M. Erickson, C. Ghanty, D. Aurbach, *J. Phys. Chem. Lett.* **2014**, *5*, 3313; c) P. Rozier, J. M. Tarascon, *J. Electrochem. Soc.* **2015**, *162*, A2490–A2499; d) V. A. Godbole, J.-F. Colin, P. Novák, *J. Electrochem. Soc.* **2011**, *158*, A1005; e) C. Villevieille, J. L. Gomez-Camer, M. Hess, P. Novak, *J. Electrochem. Soc.* **2014**, *161*, A871-A874; f) A. Guéguen, D. Streich, M. He, M. Mendez, F. F. Chesneau, P. Novák, E. J. Berg, *J. Electrochem. Soc.* **2016**, *163*, A1095–A1100; g) L. Boulet-Roblin, M. E. Kazzi, P. Novak, C. Villevieille, *J. Electrochem. Soc.* **2015**, *162*, A1297–A1300; h) B. Strehle, K. Kleiner, R. Jung, F. Chesneau, M. Mendez, H. A. Gasteiger, M. Piana, *J. Electrochem. Soc.* **2017**, *164*, A400–A406; i) D. Streich, A. Guéguen, M. Mendez, F. Chesneau, P. Novák, E. J. Berg, *J. Electrochem. Soc.* **2016**, *163*, A964–A970; j) C. Villevieille, P. Lanz, C. Bünzli, P. Novák, *J. Mater. Chem. A* **2014**, *2*, 6488; k) M. M. Thackeray, C. S. Johnson, J. T. Vaughey, N. Li, S. A. Hackney, *J. Mater. Chem.* **2005**, *15*, 2257; l) E. J. Berg, C. Villevieille, D. Streich, S. Trabesinger, P. Novák, *J. Electrochem. Soc.* **2015**, *162*, A2468–A2475; m) J. Yan, X. Liu, B. Li, *RSC Adv.* **2014**, *4*, 63268.

[7] S. Zhou, G. Wang, W. Tang, Y. Xiao, K. Yan, *Solid-State Electron.* **2018**, *261*, 565.

[8] J. Yang, Y. Xia, *J. Electrochem. Soc.* **2016**, *163*, A2665–A2672.

[9] H.-J. Noh, S. Youn, C. S. Yoon, Y.-K. Sun, *J. Power Sources* **2013**, *233*, 121.

[10] J. Li, L. E. Downie, L. Ma, W. Qiu, J. R. Dahn, *J. Electrochem. Soc.* **2015**, *162*, A1401–A1408.

[11] L. de Biasi, A. O. Kondrakov, H. Geßwein, T. Brezesinski, P. Hartmann, J. Janek, *J. Phys. Chem. C* **2017**, *121*, 26163.

[12] J. Zheng, W. H. Kan, A. Manthiram, *ACS Appl. Mater. Interfaces* **2015**, *7*, 6926.

[13] S.-U. Woo, B.-C. Park, C. S. Yoon, S.-T. Myung, J. Prakash, Y.-K. Sun, *J. Electrochem. Soc.* **2007**, *154*, A649.

[14] W. Liu, P. Oh, X. Liu, M.-J. Lee, W. Cho, S. Chae, Y. Kim, J. Cho, *Angew. Chem. Int. Ed.* **2015**, *54*, 4440.

[15] J. Wang, C. Du, C. Yan, X. Xu, X. He, G. Yin, P. Zuo, X. Cheng, Y. Ma, Y. Gao, *RSC Adv.* **2016**, *6*, 26307.

[16] a) X. Xiong, Z. Wang, X. Yin, H. Guo, X. Li, *Mater. Lett.* **2013**, *110*, 4; b) S. Solchenbach, G. Hong, A. T. S. Freiberg, R. Jung, H. A. Gasteiger, *J. Electrochem. Soc.* **2018**, *165*, A3304–A3312.

[17] R. Jung, F. Linsenmann, R. Thomas, J. Wandt, S. Solchenbach, F. Maglia, C. Stinner, M. Tromp, H. A. Gasteiger, *J. Electrochem. Soc.* **2019**, *166*, A378–A389.

[18] H.-H. Sun, A. Manthiram, *Chem. Mater.* **2017**, *29*, 8486.

[19] R. Jung, R. Morasch, P. Karayaylali, K. Phillips, F. Maglia, C. Stinner, Y. Shao-Horn, H. A. Gasteiger, *J. Electrochem. Soc.* **2018**, *165*, A132–A141.

[20] J. Paulsen, J. H. Kim, US2014/0054495A1.

[21] Z. Chen, J. Wang, J. Huang, T. Fu, G. Sun, S. Lai, R. Zhou, K. Li, J. Zhao, *J. Power Sources* **2017**, *363*, 168.

[22] a) N. V. Faenza, L. Bruce, Z. W. Lebens-Higgins, I. Plitz, N. Pereira, L. F. J. Piper, G. G. Amatucci, *J. Electrochem. Soc.* **2017**, *164*, A3727–A3741; b) H. S. Liu, Z. R. Zhang, Z. L. Gong, Y. Yang, *Electrochem. Solid-State Lett.* **2004**, *7*, A190; c) I. A. Shkrob, J. A. Gilbert, P. J. Phillips, R. Klie, R. T. Haasch, J. Bareño, D. P. Abraham, *J. Electrochem. Soc.* **2017**, *164*, A1489–A1498.

[23] K. Matsumoto, R. Kuzuo, K. Takeya, A. Yamanaka, *J. Power Sources* **1999**, *81–82*, 558.

[24] K. Shizuka, C. Kiyohara, K. Shima, Y. Takeda, *J. Power Sources* **2007**, *166*, 233.
[25] J. Sicklinger, M. Metzger, H. Beyer, D. Pritzl, H. A. Gasteiger, *J. Electrochem. Soc.* **2019**, *166*, A2322–A2335.
[26] H. Wang, W. Ge, W. Li, F. Wang, W. Liu, M.-Z. Qu, G. Peng, *ACS Appl. Mater. Interfaces* **2016**, *8*, 18439.
[27] S.-W. Lee, M.-S. Kim, J. H. Jeong, D.-H. Kim, K. Y. Chung, K. C. Roh, K.-B. Kim, *J. Power Sources* **2017**, *360*, 206.
[28] a) Y.-Y. Sun, S. Liu, Y.-K. Hou, G.-R. Li, X.-P. Gao, *J. Power Sources* **2019**, *410–411*, 115; b) J. Wang, C. Du, C. Yan, X. He, B. Song, G. Yin, P. Zuo, X. Cheng, *Solid-State Electron.* **2015**, *174*, 1185; c) K. S. Yoo, Y. H. Kang, K. R. Im, C.-S. Kim, *Materials* **2017**, *10*.
[29] K. Min, K. Park, S. Y. Park, S.-W. Seo, B. Choi, E. Cho, *J. Electrochem. Soc.* **2018**, *165*, A79–A85.
[30] a) H. Gao, X. Zeng, Y. Hu, V. Tileli, L. Li, Y. Ren, X. Meng, F. Maglia, P. Lamp, S.-J. Kim, et al., *ACS Appl. Mater. Interfaces* **2018**, *1*, 2254; b) C. Qin, J. Cao, J. Chen, G. Dai, T. Wu, Y. Chen, Y. Tang, A. Li, Y. Chen, *Dalton Trans.* **2016**, *45*, 9669.
[31] F. Schipper, H. Bouzaglo, M. Dixit, E. M. Erickson, T. Weigel, M. Talianker, J. Grinblat, L. Burstein, M. Schmidt, J. Lampert, et al., *Adv. Energy Mater.* **2018**, *8*, 1701682.
[32] D. Aurbach, O. Srur-Lavi, C. Ghanty, M. Dixit, O. Haik, M. Talianker, Y. Grinblat, N. Leifer, R. Lavi, D. T. Major, et al., *J. Electrochem. Soc.* **2015**, *162*, A1014–A1027.
[33] H.-H. Sun, J.-Y. Hwang, C. S. Yoon, A. Heller, C. B. Mullins, *ACS Nano* **2018**.
[34] Q. Ran, H. Zhao, Y. Hu, Q. Shen, W. Liu, J. Liu, X. Shu, M. Zhang, S. Liu, M. Tan, et al., *Solid-State Electron.* **2018**, *289*, 82.
[35] B.-J. Chae, T. Yim, *Mater. Chem. Phys.* **2018**, *214*, 66.
[36] H. Dong, G. Liu, S. Li, S. Deng, Y. Cui, H. Liu, H. Liu, X. Sun, *ACS Appl. Mater. Interfaces* **2018**.
[37] a) Y. Zhang, Z.-B. Wang, F.-D. Yu, L.-F. Que, M.-J. Wang, Y.-F. Xia, Y. Xue, J. Wu, *J. Power Sources* **2017**, *358*, 1; b) O. Breuer, A. Chakraborty, J. Liu, T. Kravchuk, L. Burstein, J. Grinblat, Y. Kauffman, A. Gladkih, P. Nayak, M. Tsubery, et al., *ACS Appl. Mater. Interfaces* **2018**, *10*, 29608; c) B. Pişkin, C. Savaş Uygur, M. K. Aydınol, *Int. J. Energy Res.* **2018**, *42*, 3888.
[38] M. Dixit, B. Markovsky, D. Aurbach, D. T. Major, *J. Electrochem. Soc.* **2017**, *164*, A6359–A6365.
[39] M. Eilers-Rethwisch, M. Winter, F. M. Schappacher, *J. Power Sources* **2018**, *387*, 101.
[40] a) M. Eilers-Rethwisch, S. Hildebrand, M. Evertz, L. Ibing, T. Dagger, M. Winter, F. M. Schappacher, *J. Power Sources* **2018**, *397*, 68; b) G. Kang, K. Lee, K. Kwon, J. Song, *Metals* **2017**, *7*, 395.
[41] L. Liu, J. Li, Y. Xiao, W. Sun, B. Yue, *J. Mater. Sci. Mater. Electron.* **2018**, *29*, 21213.
[42] a) B. Han, S. Xu, S. Zhao, G. Lin, Y. Feng, L. Chen, D. G. Ivey, P. Wang, W. Wei, *ACS Appl. Mater. Interfaces* **2018**, *10*, 39599; b) X. Li, K. Zhang, M. Wang, Y. Liu, M. Qu, W. Zhao, J. Zheng, *Sustain. Energy Fuels* **2018**, *2*, 413.
[43] R. Zhao, J. Liang, J. Huang, R. Zeng, J. Zhang, H. Chen, G. Shi, *J. Alloys Compd.* **2017**, *724*, 1109.
[44] U. Breddemann, I. Krossing, *ChemElectroChem* **2020**, *7*, 1389.
[45] P. Yue, Z. Wang, H. Guo, X. Xiong, X. Li, *Solid-State Electron.* **2013**, *92*, 1.
[46] P. Yue, Z. Wang, J. Wang, H. Guo, X. Xiong, X. Li, *Powder Technol.* **2013**, *237*, 623.
[47] M. Ménétrier, J. Bains, L. Croguennec, A. Flambard, E. Bekaert, C. Jordy, P. Biensan, C. Delmas, *J. Solid State Chem.* **2008**, *181*, 3303.
[48] L. Croguennec, J. Bains, M. Ménétrier, A. Flambard, E. Bekaert, C. Jordy, P. Biensan, C. Delmas, *J. Electrochem. Soc.* **2009**, *156*, A349.
[49] L. Li, B. H. Song, Y. L. Chang, H. Xia, J. R. Yang, K. S. Lee, L. Lu, *J. Power Sources* **2015**, *283*, 162.
[50] U. Breddemann, E. M. Erickson, V. Davis, F. Schipper, M. Ellwanger, M. Daub, A. Hoffmann, C. Erk, B. Markovsky, D. Aurbach, et al., *ChemElectroChem* **2019**.
[51] a) E. M. Erickson, H. Sclar, F. Schipper, J. Liu, R. Tian, C. Ghanty, L. Burstein, N. Leifer, J. Grinblat, M. Talianker, et al., *Adv. Energy Mater.* **2017**, *26*, 1700708; b) E. M. Erickson, F. Schipper, R. Tian, J.-Y. Shin, C. Erk, F. F. Chesneau, J. K. Lampert, B. Markovsky, D. Aurbach, *RSC Adv.* **2017**, *7*, 7116; c) F. Amalraj, M. Talianker, B. Markovsky, L. Burlaka, N. Leifer, G. Goobes, E. M. Erickson, O. Haik, J. Grinblat, E. Zinigrad, et al., *J. Electrochem. Soc.* **2013**, *160*, A2220–A2233.
[52] D. R. Lide (Ed.) *CRC handbook of chemistry and physics. A ready-reference book of chemical and physical data*, CRC Press, Boca Raton, Fla., **1997**.
[53] K. Nakamoto, *Infrared and Raman spectra of inorganic and coordination compounds. Part A: Theory and applications in inorganic chemistry*, Wiley, Hoboken, N.J, **2009**.
[54] N. Dupre, M. Cuisinier, D. Guyomard, *Interface* **2011**, *20*, 61.
[55] E. Boivin, R. David, J.-N. Chotard, T. Bamine, A. Iadecola, L. Bourgeois, E. Suard, F. Fauth, D. Carlier, C. Masquelier, et al., *Chem. Mater.* **2018**.
[56] S. Zhong, L. Liu, J. Liu, J. Wang, J. Yang, *Solid State Commun.* **2009**, *149*, 1679.
[57] Y. Zhang, Q. Liang, C. Huang, P. Gao, H. Shu, X. Zhang, X. Yang, L. Liu, X. Wang, *Solid-State Electron.* **2018**, *22*, 1995.
[58] P. F. Xiao, M. O. Lai, L. Lu, *Solid State Ionics* **2013**, *242*, 10.
[59] D. Chen, G.-Q. Shao, B. Li, G.-G. Zhao, J. Li, J.-H. Liu, Z.-S. Gao, H.-F. Zhang, *Solid-State Electron.* **2014**, *147*, 663.
[60] a) D. R. Gallus, R. Schmitz, R. Wagner, B. Hoffmann, S. Nowak, I. Cekic-Laskovic, R. W. Schmitz, M. Winter, *Electrochim. Acta* **2014**, *134*, 393; b) H. Zheng, Q. Sun, G. Liu, X. Song, V. S. Battaglia, *J. Power Sources* **2012**, *207*, 134.
[61] S. Yonezawa, M. Yamasaki, M. Takashima, *J. Fluorine Chem.* **2004**, *125*, 1657.
[62] M. Ueda, M. Ohe, J.-H. Kim, S. Yonezawa, M. Takashima, *J. Fluorine Chem.* **2013**, *149*, 88.
[63] A. Chakraborty, S. Kunnikuruvan, M. Dixit, D. T. Major, *Isr. J. Chem.* **2020**, *25*, 71.
[64] a) Y. W. Tsai, B. J. Hwang, G. Ceder, H. S. Sheu, D. G. Liu, J. F. Lee, *Chem. Mater.* **2005**, *17*, 3191; b) W.-S. Yoon, M. Balasubramanian, K. Y. Chung, X.-Q. Yang, J. McBreen, C. P. Grey, D. A. Fischer, *J. Am. Chem. Soc.* **2005**, *127*, 17479; c) M. Dixit, B. Markovsky, F. Schipper, D. Aurbach, D. T. Major, *J. Phys. Chem. C* **2017**, *121*, 22628.
[65] a) J.-M. Kim, H.-T. Chung, *Solid-State Electron.* **2004**, *49*, 937; b) Y. Koyama, I. Tanaka, H. Adachi, Y. Makimura, T. Ohzuku, *J. Power Sources* **2003**, *119–121*, 644; c) B. J. Hwang, Y. W. Tsai, D. Carlier, G. Ceder, *Chem. Mater.* **2003**, *15*, 3676; d) A. Deb, U. Bergmann, S. P. Cramer, E. J. Cairns, *J. Electrochem. Soc.* **2005**, *97*, 113523; e) M. Dixit, M. Kosa, O. S. Lavi, B. Markovsky, D. Aurbach, D. T. Major, *Phys. Chem. Chem. Phys.* **2016**, *18*, 6799; f) K.-W. Nam, S.-M. Bak, E. Hu, X. Yu, Y. Zhou, X. Wang, L. Wu, Y. Zhu, K.-Y. Chung, X.-Q. Yang, *Adv. Funct. Mater.* **2013**, *23*, 1047.
[66] Y. Shao-Horn, L. Croguennec, C. Delmas, E. C. Nelson, M. A. O'Keefe, *Nat. Mater.* **2003**, *2*, 464.
[67] a) W. Xu, *Int. J. Electrochem. Sci.* **2017**, 9758; b) J. Lu, K. S. Lee, *Mater. Technol.* **2016**, *31*, 628.
[68] J.-H. Cheng, C.-J. Pan, J.-F. Lee, J.-M. Chen, M. Guignard, C. Delmas, D. Carlier, B.-J. Hwang, *Chem. Mater.* **2014**, *26*, 1219.
[69] D. Petzold, *J. Therm. Anal.* **1985**, *30*, 391.
[70] V. Pralong, A. Delahaye-Vidal, B. Beaudoin, B. Gérand, J.-M. Tarascon, *J. Mater. Chem.* **1999**, *9*, 955

Manuscript received: August 28, 2020
Revised manuscript received: November 23, 2020
Accepted manuscript online: December 4, 2020
Version of record online: December 21, 2020

Batteries & Supercaps

Supporting Information

Fluorination of Ni-Rich Lithium-Ion Battery Cathode Materials by Fluorine Gas: Chemistry, Characterization, and Electrochemical Performance in Full-cells

Ulf Breddemann[+], Johannes Sicklinger[+], Florian Schipper[+], Victoria Davis, Anna Fischer, Korbinian Huber, Evan M. Erickson, Michael Daub, Anke Hoffmann, Christoph Erk, Boris Markovsky, Doron Aurbach,* Hubert A. Gasteiger,* and Ingo Krossing*

Contents

Experimental Section

Chemicals

99.98 % fluorine gas was donated by Solvay Fluor GmbH, Germany, and the Ni-NCM (NCM 811 and NCM 851005) CAMs were contributed by BASF SE, Germany. **Attention!** Safety glasses, lab coat, and protective gloves must be worn at all times. **Caution!** Fluorine gas is an extremely hazardous material and should only be handled by trained personnel. All reactions should be carried out in a well-ventilated fume hood.

Materials and Equipment

The fluorine fume hood

The fluorine fume hood is a modified standard fume hood with its own discharge shaft and with an exhaust flow rate of 1200 m^3/h. All of the walls in the fume hood as well as the full ventilation system are made of V4 A stainless steel. Fluorine gas is used from a 5 L fluorine gas bottle and stored inside the fume hood. For safety purposes, it is positioned in an additional V4 A stainless steel box coupled with a pressure regulator valve (Matheson Valves & Fittings Ltd.). One end of the pressure regulator valve is attached to the fluorine bottle using special O- Rings. The other end travels to the back of the fume hood and is connected to a *Monel vacuum line*, which can handle fluorine gas. All valves within the additional *V4 A stainless steel* box are equipped with length extended levers for easy access from outside of the box. There are three valves: the main bottle valve, the pressure-regulating valve, and a needle valve. (Figure S1).

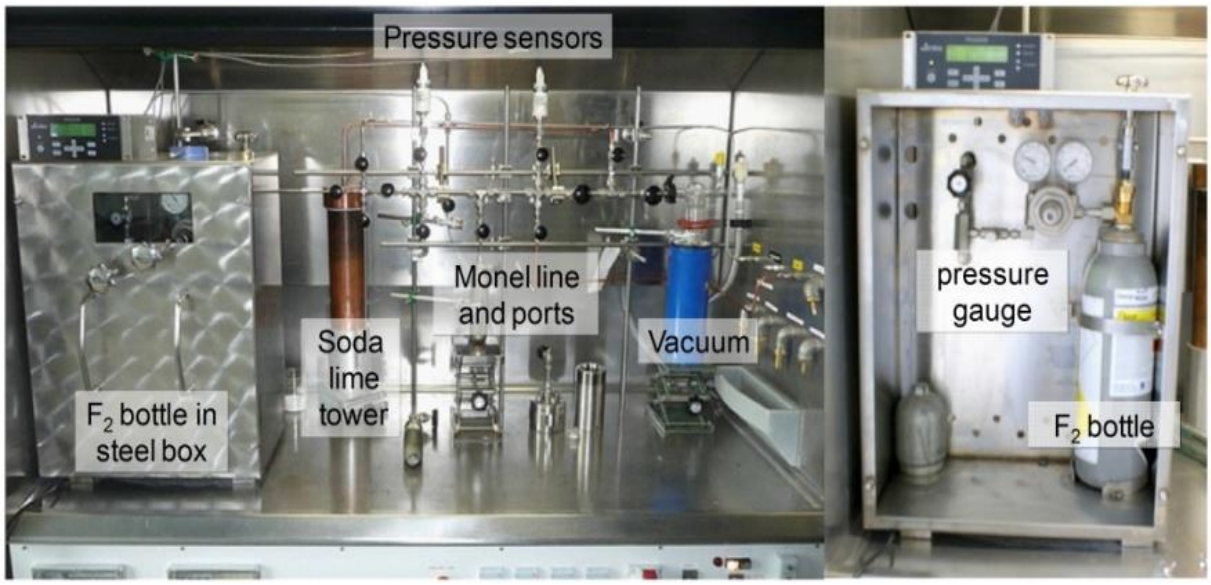

Figure S1: Left) Fluorine fume hood with the Monel vacuum line. Right) Inside of the fluorine bottle box.

Ion Chromatography (IC)

IC measurements were carried out by *822 Compact IC plus from Metrohm* unit with a Metrosep A Supp 5 – 250/4.0 high-performance separation anion column from *Metrohm* with a 1 mmol L^{-1} $NaHCO_3$ and 3 mmol $NaCO_3$ in 10/90 % acetone/ultrapure water solution used as eluent. A *Metrosep C 4 - 100/4.0* high separation efficiency universal standard cation column from *Metrohm* were used with an eluent of 0.7 mmol 2,6-pyridinedicarboxylic acid and a 1.7 mmol nitric acid.

Ultrapure water

Ultrapure water was product by PURELAB flex from the company Veolia Water Solutions & Technologies.

Fluoride selective electrode (FSE)

The fluoride containing CAMs were thermally digested in an oxygen-steam stream at 1100 °C using a combustion unit (AQF-2100H, a1 envirotech). The resulting hydrogen fluoride was absorbed in an absorption solution (total ionic strength adjustment buffer, TISAB) and detected by means of a fluoride selective electrode (ISE 6.0502.150, Metrohm).

FT-IR spectroscopy (IR)

IR measurements were measured on a Bruker alpha Fourier transform IR spectrometer arranged in an argon-filled glove box using a diamond ATR unit. The spectra were recorded in the range of 375 – 4000 cm^{-1} and analyzed with the OPUS software package.

Powder X-Ray Diffraction (pXRD)

pXRD data were collected with a Stoe Stadi P Powder diffractometer equipped with Mo-$K_{\alpha1}$ radiation, a Ge(111) monochromator, and a silicon microstrip detector (Mythen 1k). The WinXPow package (STOE) was used for analysis and unit cell refinement. LeBail refinements were carried out with the program GSAS.[1],[2]

Magic Angle Spinning – Nuclear Magnetic Resonance Spectroscopy (MAS-NMR)

^{7}Li and ^{19}F magic angle spinning nuclear magnetic resonance experiments were performed on a Bruker DSX 500 solid-state NMR spectrometer running at a Larmor frequency of 194.40 MHz and 470.65 MHz for ^{7}Li and ^{19}F, respectively. The rotor synchronized Hahn Echo and rotor synchronized solid state Echo experiments were performed under magic angle spinning rates of 20 kHz to 30 kHz using a 2.5 mm MAS probe with an $\omega_1/2\pi$ frequency of 125 kHz (i.e. a 90° pulse duration of 2 µs). and relaxation delays of 5 s (^{7}Li) and 30 s (^{19}F). All spectra were measured at room temperature, leading to sample temperatures of 300 K to 325 K, due to frictional heating of the magic angle spinning.

Scanning electron microscopy (SEM)

SEM was performed on a Field Emission Gun-High Resolution Scattering Electron Microscope (FEG-HRSEM) SU8220 (Hitachi) with a Transmission Electrons (TE), Back Scattering Electrons (BSE), Secondary Electrons (SE), and and 2 EDX detectors (Bruker).

Conductivity and Press Density measurements

Conductivity and Press Density measurements were carried out on a "*Loresta resistivity measurement unit"* from *Mitsubishi Chemical Analytech*.

Thermo-gravimetric analyses (TGA) and Differential Thermal Analysis (DTA)

TGA and DTA was performed under nitrogen atmosphere on a STA 409 from the company *Netzsch*.

Electrochemical testing (Copy from Main Text, to have all data in one file)

Full-Cell (triplicate) Measurements: Electrodes were fabricated as described elsewhere.[*] Briefly, 80 % active cathode active material (pristine batch obtained from BASF SE, Germany) was mixed with 5 % Super C65 conductive carbon (Imerys, MTI corp. USA), 5 % TIMREX KS-6 graphite (Imerys, France) and 10 % Solef 5130 polyvinylidenedifluoride (PVDF) binder (Solev5130 from Solvay) in N-methylpyrrolidone (NMP), and cast onto an Al foil (Strem Chemicals Inc., USA) current collector at a loading of ~4.3 mg cm^{-2}. Single layer pouch full-cells were fabricated with graphite anodes at a loading of ~2.8 mg cm^{-2} with 20% excess capacity (negative to positive electrodes areal capacity ratio of N/P = 1.2), using Celgard PP 2500 separators and 350 µL of BASF LP57 electrolyte (1 M $LiPF_6$ ethylene carbonate: ethyl methyl carbonate, 3:7). Areal capacity of the full-cell: ~0.7 mAh cm^{-2}, active electrode area: ~11.5 cm^2, absolute pouch cell capacity: ~8 mAh. The 1C rate for NCM 811 was set to correspond to 180 mAh g^{-1}. All cells were prepared in triplicate and the results were averaged. Formation procedure for cells: 1 cycle at C/15 followed by 4 cycles at C/10 at 30 °C. For the continuous cycling between 2.0 and 4.2 V, the cells were measured at 30 and 45 °C with a 0.5 C charge and 1 C discharge current and a 30 minutes CV-step at 4.2 V. Every 50 cycles, one cycle was measured during charge and discharge at 0.1 C. Electrochemical impedance spectra were measured using a Solartron battery test unit model 1470 coupled with the frequency response analyzer FRA-1250 from Solartron in the frequency range from 5 mHz to 0.1 MHz. Impedance spectra were collected during charge at 4.0 V after formation, 250 and 500 cycles of the continuous cycling test.

[*] i.e., a) E. M. Erickson, H. Sclar, F. Schipper, J. Liu, R. Tian, C. Ghanty, L. Burstein, N. Leifer, J. Grinblat, M. Talianker et al., *Adv. Energy. Mater.* **2017**, *26*, 1700708; b) E. M. Erickson, F. Schipper, R. Tian, J.-Y. Shin, C. Erk, F. F. Chesneau, J. K. Lampert, B. Markovsky, D. Aurbach, *RSC Adv* **2017**, *7*, 7116; c) F. Amalraj, M. Talianker, B. Markovsky, L. Burlaka, N. Leifer, G. Goobes, E. M. Erickson, O. Haik, J. Grinblat, E. Zinigrad et al., *J. Electrochem. Soc.* **2013**, *160*, A2220-A2233.

Experimental Procedure of Ni-NCM Fluorination

Direct Fluorination Setup for Ni-NCM materials

The setup consists of a 120 mL low pressure PFA (perfluoropolyether) batch reactor vessel equipped with a ¼‘‘end cup fitting, a Stainless Steel *Swagelok* Tee-Type with a 0.5 µm particle filter (connect to the end cup), and a Kel-F valve[3] (connected to the filter). These parts were assembled and connected to a *Monel* vacuum line of volume 66 mL (Figure S1) and checked for leaks (Figure S2). The reactor was evacuated and then filled with elemental fluorine gas at a total pressure of 1.1 bar for one hour to achieve equipment passivation. Once passivation was completed, the reactor was evacuated and the remaining reactive gases were neutralized over a soda lime tower. The setup was transferred into a solvent free dry box. In the dry box, the reactor vessel was opened and 7 g (±0.04 g) of Ni-NCM material (along with a Teflon-coated stir bar) was transferred into the batch reactor. The setup was removed from the dry box, connected to the *Monel* vacuum line to ensure the absence of any leaks and the inert gas in the PFA reactor vessel was pumped out. Next, the Monel Schlenk line was filled with F_2 gas at pressures between 32 to 2200 mbar (or 0.1 to 5.5 mmol F_2; cf. **Table S*1*** and **Table S*2*** for the pressure) and afterwards the valve to the evacuated PFA reactor vessel was opened and the gas expanded to a total pressure of 10 to 800 mbar. Immediately after exposure of the CAMs to the fluorine gas, the pressure began to drop, and stabilized within a few minutes indicating that the reaction was over. When the pressure stabilized (depending on the F_2 amount added: at about 7-8 to 500 mbar), the vessel was backfilled with dry nitrogen gas until a total pressure of 1100 mbar was observed. After a reaction time of 1 hour, the remaining reactive gas was pumped out of the reactor vessel and neutralized in a soda lime tower. The closed setup was transferred into a solvent free dry box, opened, and the fluorinated material was transferred into a storage container until further use.

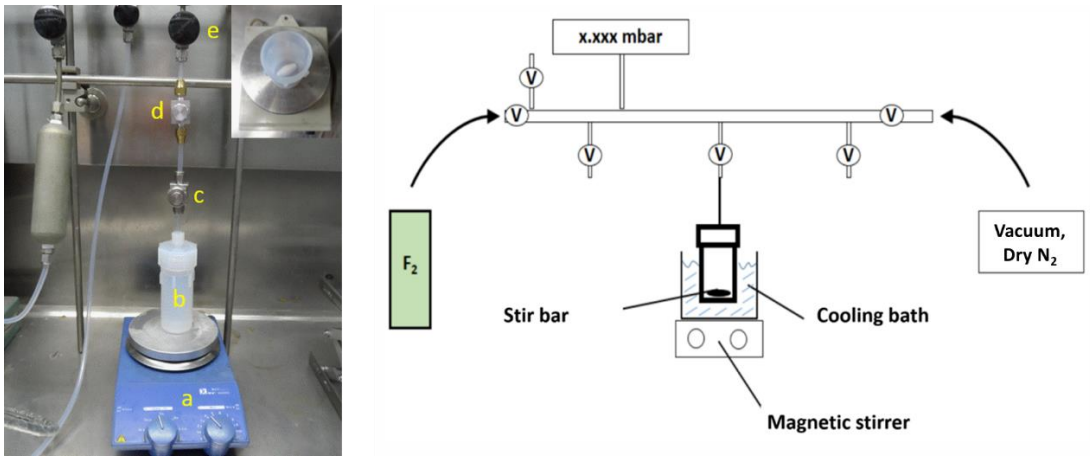

Figure S2: Left: The setup consists of a magnetic stirrer (a), a 120 mL low pressure PFA (perfluoroether) batch reactor vessel equipped with a ¼‘‘end cup fitting (b), a Stainless Steel Swagelok Tee-Type with a 0.5 µm particle filter (c), and a Kel-F valve (c). The vessel is connected to the Monel vacuum line (e). The top right inset picture shows the stir bar inside the vessel.

Right: Schematic drawing of the setup. The pre-passivated vacuum line has a volume of 66 mL and was filled with 32 to 2200 mbar F_2-pressure.

Analytics of the prepared fluorinated Ni-NCM CAM

Ion Chromatography (IC)

IC measurements were carried out to determine the lithium and fluorine concentrations of the pristine and fluorinated Ni-NCM samples. A high purity multi-element ion chromatography cation and anion standard solution was used (Sigma-Aldrich) to assign the measured element and its concentration with precision. It is believed that after fluorination a LiF film forms at the surface of the cathode material as well as a possible formation of a metal fluorides such as NiF_2, CoF_2, and MnF_2. The LiF film and the metal fluorides are soluble (in small amount) in water.[4],[5],[6],[7],[8],[9],[10],[11],[12],[13] The pristine and fluorinated samples were stored in a solvent free, argon filled dry box. In this dry box, an amount between 200 and 1000 mg fraction of the fluorinated samples was transferred into a PFA (perfluoroether) volumetric flask and transferred out of the box. The material was eluted with 250 mL ultrapure water, filtered (hydrophobic PTFE, 0.45 µm) before measurement.

Li and F content of the Fluorinated Ni-NCM materials

To measure the water-soluble lithium (Li) and fluoride (F) concentration of the samples, ion chromatography (IC) studies were carried out for the (non-)fluorinated Ni-rich NCM CAMs. The presumably mainly formed LiF (v.i.) has a low, but reasonable solubility of 1.3 g L^{-1} water. Thus, 0.2 to 1.0 g fractions of the fluorinated CAMs were eluted with 250 mL ultrapure water, filtered and the fluoride and lithium contents in the filtrate were investigated. The fluoride concentration of several samples was also verified by fluoride selective electrode (EA or FSE) analysis (labelled ‘EA’, Figure S3, Figure S4, Table S1, and Table S2).

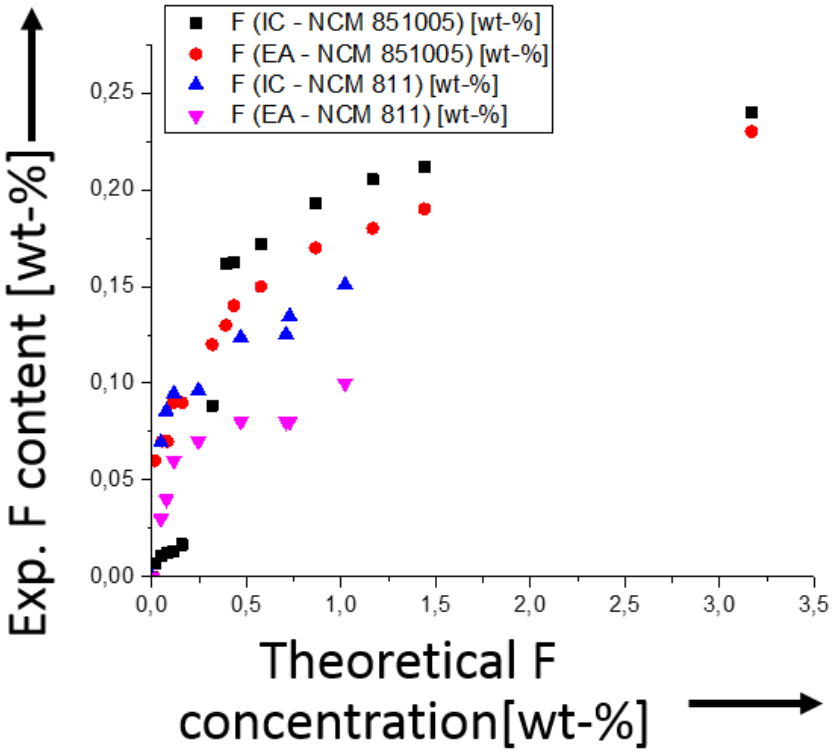

Figure S3: Plots of the water-soluble fluoride content of the treated CAMs in wt-% as a function of the applied amount of fluoride in wt-%. IC stands for ion chromatography and EA for a FSE determination.

First, one needs to note that the independent fluoride determinations by IC as well as FSE agree reasonably, so that we may suggest that through the aqueous extraction procedure, the full fluoride content is accessible. In general, one may state that especially lower fluorine amounts up to roughly 0.25 wt-% applied F are taken up by the CAMs more efficiently. Interestingly, the fluoride contents of NCM 811 and NCM 851005 develop differently as a function of the added F_2 amount at F-contents larger than about 0.25 wt-% (theoretical uptake). On the NCM 811 CAM, from this applied F_2 amount on, the system takes up further fluoride at a much slower rate. By contrast, the NCM 851005 system exhibits an almost asymptotic behavior approaching an apparently limiting fluoride content of about 0.24 wt-% (exp. fluoride content). This limiting F-content of the CAM is lower for NCM 811 by about 0.15 wt-%. Thus, apparently NCM 851005 contains a larger amount of the soluble base content (Li_2O, LiOH, $LiOH{\cdot}H_2O$, Li_2CO_3) that we expect to react preferentially with the F_2 gas giving LiF as the main and relevant product.

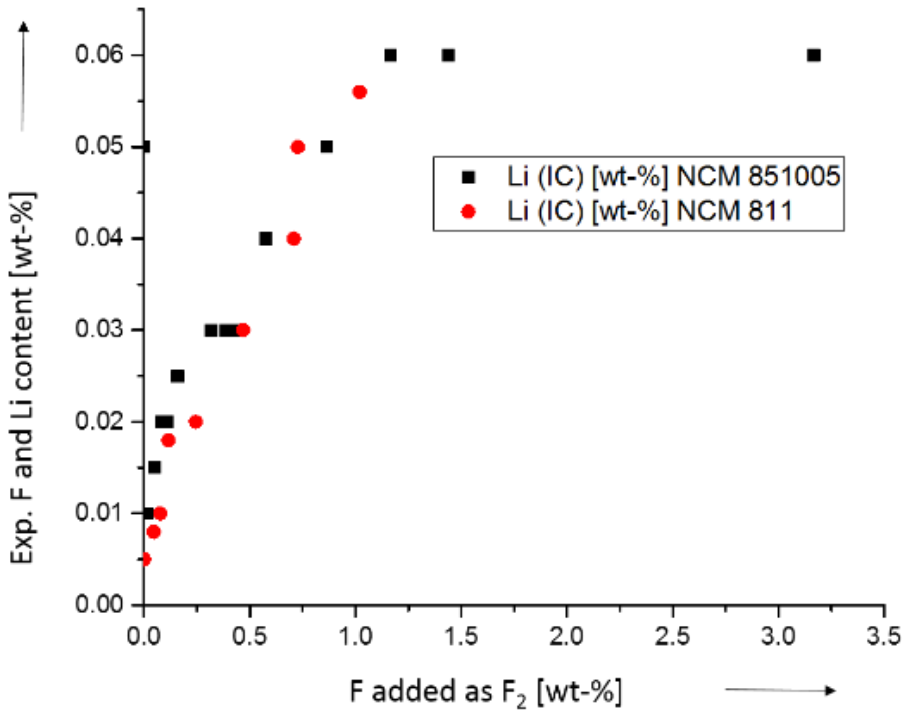

Figure S4: Plots of the water-soluble lithium content of the treated CAMs in wt-% as a function of the applied amount of fluoride in wt-%. IC stands for ion chromatography.

Lithium concentrations measured by IC showed comparable results. A strong increase of the observed lithium concentration as a function of the applied gaseous fluorine amount (theoretical F conc. in wt-%) was observed, until a limiting uptake of about 0.06 wt-% lithium was reached (exp. Li content).

Table S1: Ion chromatography (IC)[a] and fluoride selective electrode (FSE)[b] measurements for the (non-)fluorinated NCM 811 materials.

Numeration of samples	p(F_2) [mbar]	n F_2 [mmol]	Theoretical F concentration [wt-%]	IC[a] Amount of F [wt-%]	FSE[b] Amount of F [wt-%]	IC[a] Amount of Li [wt-%]
1	0	0.0	0	0	0	0.005
2	32	0.1	0.046	0.070	0.030	0.08
3	53	0.1	0.076	0.086	0.040	0.01
4	80	0.2	0.115	0.095	0.060	0.018
5	170	0.5	0.245	0.096	0.070	0.02
6	326	0.9	0.469	0.124	0.080	0.03
7	492	1.3	0.708	0.125	0.080	0.04
8	505	1.4	0.727	0.135	0.080	0.05
9	707	1.9	1.02	0.151	0.100	0.06

[a] Since LiF has a solubility of 1.3 g L^{-1} water, a between 200 and 1000 mg fraction of the fluorinated samples were eluted with 250 mL ultrapure water and the fluoride and lithium contents in the water were investigated by IC. [b] As control experiments, selected fluorinated Ni-NCM 811 materials were tested for the fluoride content by fluoride selective electrode (FSE) after a complete work up for the analysis (here labelled FSE).

Table S2: Ion chromatograph (IC)[a)] and fluoride selective electrode (FSE)[b)] measurements for the (non-)fluorinated NCM 851005 materials.

Numeration of samples	p(F_2) [mbar]	n F_2 [mmol]	Theoretical F concentration [wt-%]	IC[a)] Amount of F [wt-%]	FSE[b)] Amount of F [wt-%]	IC[a)] Amount of Li [wt-%]
1	0	0.0	0	0	0	0.05
2	10	0.0	0.014	0.007	0.06	0.01
3	36	0.1	0.052	0.011	0.07	0.015
4	56	0.2	0.081	0.013	0.07	0.02
5	76	0.2	0.109	0.013	0.09	0.02
6	110	0.3	0.158	0.017	0.09	0.025
7	220	0.6	0.317	0.088	0.12	0.03
8	270	0.7	0.389	0.162	0.13	0.03
9	300	0.8	0.432	0.162	0.14	0.03
10	400	1.1	0.576	0.172	0.15	0.04
11	600	1.6	0.864	0.193	0.17	0.05
12	810	2.2	1.166	0.205	0.18	0.06
13	1000	2.7	1.440	0.212	0.19	0.06
14	2200	5.9	3.168	0.240	0.23	0.06

[a)] Since LiF has a solubility of 1.3 g L^{-1} water, a between 200 and 1000 mg fraction of the fluorinated samples were eluted with 250 mL ultrapure water and the fluoride and lithium contents in the water were investigated by IC. [b)] As control experiments, selected fluorinated Ni-NCM 851005 materials were tested for the fluoride content by fluoride selective electrode (FSE) after a complete work up for the analysis (here labelled FSE).

Powder X-Ray Diffraction (pXRD)

pXRD data of (non-)Fluorinated NMC 811 and 851005 CAM

In a dry box, the material was transferred into a capillary (length: 80 mm, outside-diameter: 0.3 mm, and a wall thickness: 0.01 mm), then air-tight sealed and transferred out of the dry box for further sealing (with a lighter) of the capillary until an average length of 2 cm.

pXRD measurements were carried out for the pristine and the few fluorinated NCM 811 and 851005 samples (Figure S5 and Table S3). pXRD data for the low and high fluorinated NCM 811 and 851005 materials showed almost identical powder diffractograms and LeBail fittings (only 851005 CAMs) suggested lattice parameters very close to that of the rhombohedral cell (space group $R\bar{3}m$) of pristine NCM 811 and 851005 material (see below).

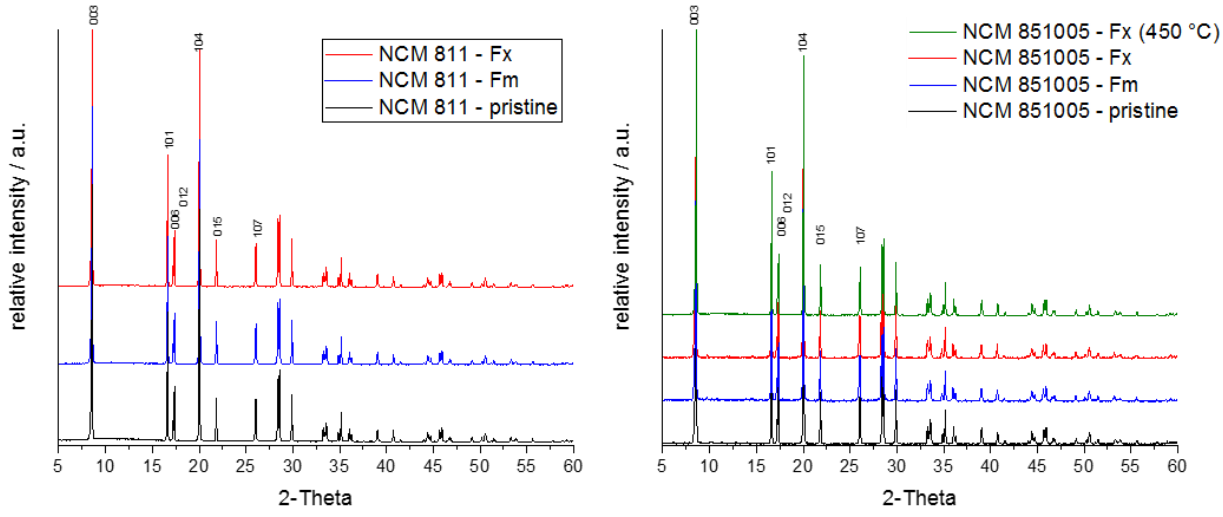

Figure S5: pXRD data of (non-)fluorinated Ni-NCM CAM, measured with α Mo-$K_{\alpha 1}$ radiation with full powder traces with Miller indices [HKL] assigned to reflexes up to 30° 2θ. Left) NCM 811 CAM and right) NCM 851005 CAM.

Table S3: pXRD data analysis (Mo-$K_{\alpha 1}$ radiation) and LeBail fitting of the (non-)fluorinated Ni-rich CAMs.

Method	Cell parameters	NCM 811 pristine	NCM 811 0.105 wt-% label: F_m	NCM 811 0.126 wt-% label: F_x	NCM 851005 pristine	NCM 851005 0.06 wt-% label: F_m	NCM 851005 0.23 wt-% label: F_x	NCM 851005 0.23 wt-% heated to 450 °C label: F (450 °C)
STOE	*a* [Å]	2.8716(3)	2.87124(23)	2.8719(3)	2.8715(3)	2.8707(4)	2.8710(3)	2.87181(24)
STOE	*c* [Å]	14.2076(13)	14.2007(11)	14.2035(12)	14.1911(14)	14.2258(18)	14.2318(15)	14.1832(10)
STOE	*c*/*a*	4.9476	4.9458	4.9457	4.9421	4.9556	4.9571	4.9388
STOE	*V* [Å^3]	101.458(13)	101.387(11)	101.454(12)	101.335(12)	101.527(17)	101.594(15)	101.301(11)
LeBail	*a* [Å]	no Data			2.87186(3)	2.87177(3)	2.87180(4)	2.871728(17)
LeBail	*c* [Å]	no Data			14.1959(2)	14.2296(3)	14.2331(3)	14.18333(14)
LeBail	*c*/*a*	no Data			4.9431	4.9550	4.9562	4.9390
LeBail	*V* [Å^3]	no Data			101.396(2)	101.626(2)	101.657(3)	101.297(1)

pXRD was carried out for the pristine and few selected fluorinated Ni-NCM materials. pXRD data for the low and high fluorinated NCM 811 materials showed almost identical powder diffractograms and LeBail fitting suggested lattice parameters very close to that of the rhombohedral cell (space group $R\bar{3}m$) of pristine NCM 851005 material (Figure S6 and Figure S7).

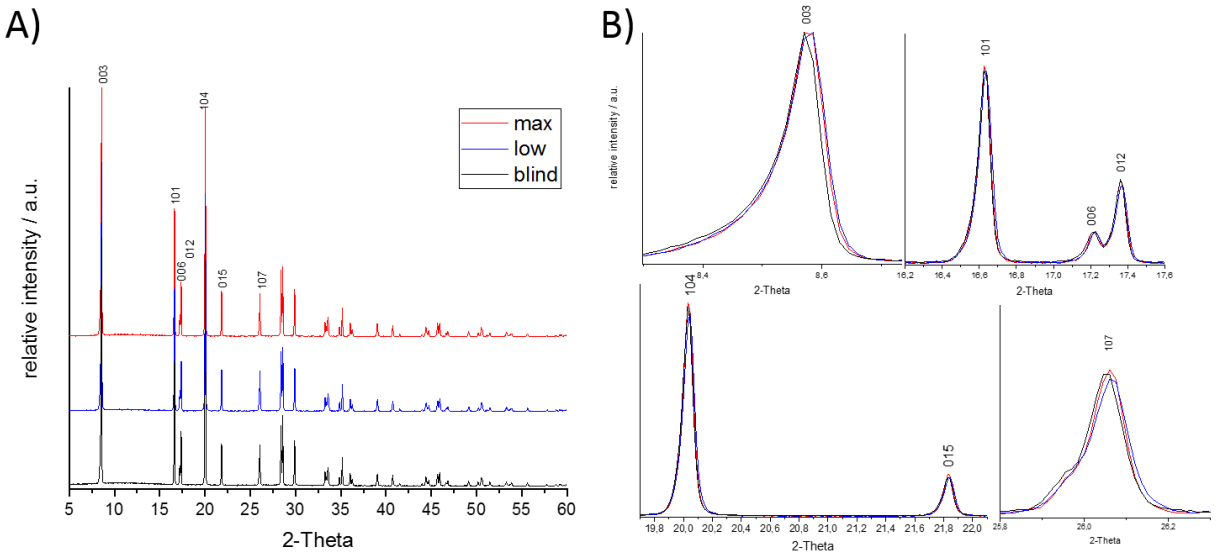

Figure S6: pXRD traces of (non-)fluorinated NCM 811 CAM, measured with Mo-K$_{\alpha 1}$ radiation. A) Full powder traces with Miller indices [hkl] assigned to reflexes up to 30° 2θ; B) detail between 8.2 to 8.8, 16.0 to 17.6, 19.7 to 22.2, and 25.8 to 26.3° 2θ.

pXRD data of (non-)fluorinated NCM 851005 CAM showed for all materials the same a-axis value. The c-axis showed for the fluorinated samples the same value, where the value of the pristine and high fluorinated and over calcination material showed almost identical lattice parameters (Figure S7).

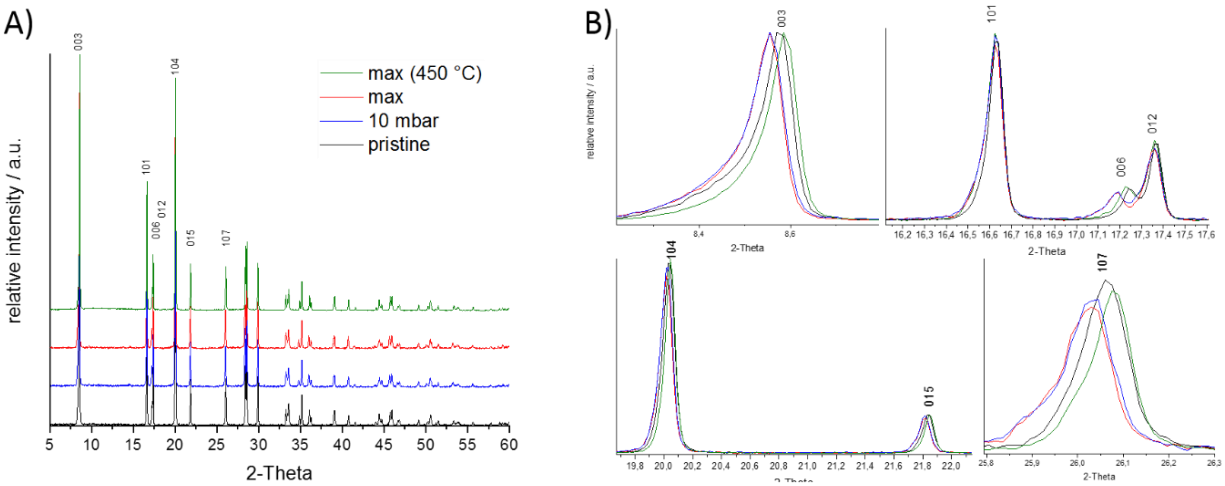

Figure S7: pXRD traces of (non-)fluorinated NCM 851005 CAM, measured with Mo-K$_{\alpha 1}$ radiation. A) Full powder traces with Miller indices [HKL] assigned to reflexes up to 30° 2θ; B) detail between 8.2 to 8.8, 16.0 to 17.6, 19.7 to 22.2, and 25.8 to 26.3° 2θ.

Infrared spectroscopy (IR) of (non-)NCM 811 and (non-)NCM 851005

ATR-IR spectra of the bulk (non-)fluorinated NCM 811 and (non-)NMC 851005 CAMs indicated no formation of metal fluorine compounds.[14] All obtained IR spectra appeared to be identical showing the typical characteristic bands for NCM 811 and NCM 851005 CAMs.

Table S4: Experimental IR frequencies (range 350 cm^{-1} to 4000 cm^{-1}) of (non-)fluorinated NCM 811 materials. The samples are ordered by increasing theoretical F-content. The samples 270 mbar and 400 mbar were not measured.

Pristine	0.05 wt-% F (lable: 23-32)	0.06 wt-% F (lable: 38-53)	0.07 wt-% F (lable: 505)	0.11 wt-% F (lable: 57)	0.11 wt-% F (lable: 122)	0.11 wt-% F (lable: 363)
			961 (13)			
			938 (17)			
	903 (10)		903 (22)		901 (12)	
860 (21)	863 (28)	868 (28)	865 (35)	861 (18)	868 (26)	
	856 (28)	860 (28)	854 (37)		859 (26)	859 (16)
						848 (18)
	836 (32)	839 (32)	837 (37)	839 (18)		
828 (27)				828 (20)	825 (34)	823 (21)
	817 (36)		810 (41)	816 (24)	809 (38)	
			800 (41)			802 (26)
	798 (40)	796 (38)			792 (40)	792 (26)
	782 (42)	787 (38)	782 (41)			784 (29)
774 (42)		778 (40)			775 (42)	
	773 (42)	772 (40)		771 (33)		
763 (40)		761 (40)		763 (33)	762 (40)	762 (29)
		755 (40)				
569 (100)	571 (100)	569 (100)	572 (100)	569 (100)	569 (100)	570 (100)
541 (90)	544 (84)	545 (87)	540 (89)	543 (82)	543 (86)	544 (87)
534 (89)		535 (87)		537 (82)	536 (88)	
			528 (83)	529 (84)		
		501 (64)		510 (76)		
				497 (64)		
				487 (60)		482 (47)
476 (44)	477 (46)	471 (43)	476 (48)		473 (48)	
	466 (42)		462 (43)	465 (47)		
		457 (32)		456 (40)		457 (32)
444 (29)	449 (30)	443 (28)		448 (40)		441 (24)
434 (25)	438 (28)	436 (26)		437 (38)	435 (34)	430 (24)
424 (19)	424 (24)		427 (28)	430 (33)	425 (26)	419 (16)
	414 (18)	409 (19)	410 (22)	411 (22)		410 (18)
						404 (16)

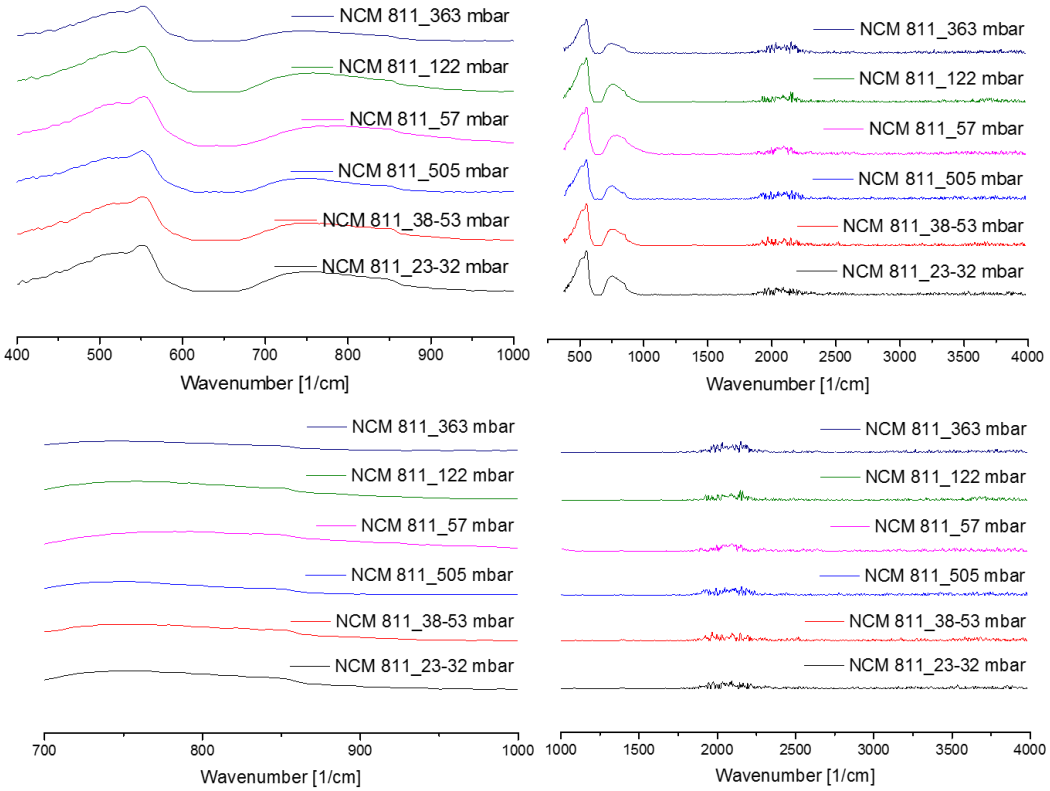

Figure S8: ATR-IR Spectra of the pristine and fluorinated NCM 811 materials (with a baseline correction), where 32-32 (0.05 wt-%), 38-53 (0.06 wt-% F), 505 (0.07 wt-% F), 57 (0.11 wt-% F), 122 (0.11 wt-% F), and 363 (0.11 wt-% F).

Table S5: Experimental IR frequencies (range 350 cm^{-1} to 4000 cm^{-1}) of (non-)fluorinated NCM 851005 materials. The samples are ordered by increasing theoretical F-content. The sample 270 mbar and 400 mbar were not measured.

pristine	0.06 wt-% F	0.11 wt-% F	0.013 wt-% F	0.013 wt-% F	0.017 wt-% F	0.088 wt-% F	300 wt-% F	0.162 wt-% F	0.205 wt-% F	0.212 wt-% F	0.240 wt-% F
3705 (23)	3705 (23)	3704 (23)	3706 (23)	3706 (23)	3705 (23)	3705 (23)	3706 (23)	3705 (23)	3705 (23)	3705 (22)	3705 (23)
3677 (16)	3677 (17)	3676 (15)	3676 (16)	3676 (16)	3676 (16)	3677 (16)	3674 (15)	3676 (16)	3677 (16)	3676 (16)	3677 (17)
///	3664 (10)	3666 (8)	///	///	///	///	///	///	///	///	///
///	1614 (10)	1620 (8)	///	///	///	///	///	///	///	///	///
1368 (22)	1368 (23)	1368 (22)	1368 (22)	1368 (22)	1367 (22)	1368 (22)	1367 (22)	1368 (21)	1368 (22)	1368 (22)	1367 (23)
1286 (28)	1282 (30)	1286 (28)	1287 (28)	1285 (28)	1285 (28)	1286 (29)	1286 (29)	1387 (22)	1285 (28)	1285 (28)	1285 (29)
///	///	///	///	///	///	///	///	1286 (28)	///	///	///
1175 (41)	///	///	///	///	///	///	///	///	///	///	///
1158 (43)	///	///	///	///	///	///	///	///	///	///	///
1124 (24)	1227 (25)	1227 (24)	1227 (24)	1226 (24)	1226 (24)	1226 (24)	1226 (24)	1226 (24)	1226 (24)	1225 (24)	1227 (24)
///	1173 (42)	1175 (42)	1174 (42)	1174 (42)	1173 (41)	1174 (42)	1175 (42)	1173 (42)	1174 (42)	1173 (42)	1175 (42)
///	1159 (44)	1158 (43)	1158 (43)	1160 (43)	1158 (43)	1157 (43)	1156 (43)	1158 (42)	1158 (43)	1158 (43)	1159 (43)
1086 (46)	1086 (47)	1086 (46)	1088 (46)	1087 (46)	1086 (46)	1085 (46)	1085 (46)	1087 (46)	1086 (46)	1086 (46)	1086 (46)
///	1075 (sh)	1074 (sh)	1074 (sh)	1075 (sh)	1074 (sh)	///	1075 (sh)	///	1076 (sh)	1076 (sh)	1076 (sh)
1064 (sh)	1062 (sh)	1062 (sh)	1060 (sh)	1066 (sh)	///	1065 (sh)	///	///	///	///	///
///	///	///	///	1055 (sh)	1055 (sh)	///	///	1053 (sh)	///	///	///
///	///	1030 (sh)	///	///	///	///	1038 (sh)	///	///	1041 (sh)	1047 (sh)
918 (8)	920 (9)	918 (8)	920 (8)	921 (8)	919 (8)	920 (8)	918 (8)	919 (8)	919 (8)	917 (8)	920 (8)
883 (27)	883 (28)	884 (27)	884 (27)	884 (27)	885 (27)	884 (27)	882 (27)	883 (27)	884 (27)	884 (27)	883 (27)
858 (sh)	861 (sh)	859 (sh)	859 (sh)	859 (sh)	858 (sh)	859 (48)	860 (48)	857 (sh)	858 (sh)	860 (sh)	858 (sh)
847 (60)	846 (60)	846 (60)	849 (59)	847 (59)	846 (60)	847 (60)	848 (60)	858 (59)	846 (59)	846 (60)	848 (60)
816 (35)	817 (37)	817 (35)	815 (35)	818 (36)	817 (35)	818 (36)	819 (36)	816 (35)	816 (35)	818 (35)	816 (36)
803 (34)	808 (35)	808 (34)	807 (33)	807 (33)	807 (34)	806 (34)	807 (34)	808 (34)	807 (34)	807 (36)	807 (34)
///	///	///	///	///	///	799 (29)	///	///	///	///	///
759 (60)	760 (61)	759 (59)	759 (59)	759 (60)	760 (60)	759 (60)	759 (60)	759 (60)	759 (60)	759 (60)	758 (60)
742 (48)	742 (49)	742 (47)	741 (47)	741 (47)	742 (47)	742 (48)	740 (47)	740 (48)	741 (48)	741 (48)	742 (48)

719 (38)	720 (40)	720 (38)	719 (40)	720 (38)	718 (39)	719 (39)	718 (38)	719 (38)	721 (38)	719 (38)	718 (39)
///	///	705 (sh)	706 (sh)	708 (sh)	711 (sh)	708 (33)	709 (sh)	707 (32)	708 (33)	707 (sh)	708 (sh)
680 (20)	680 (21)	680 (20)	680 (20)	680 (20)	681 (20)	681 (20)	///	680 (20)	679 (20)	680 (20)	680 (20)
///	///	///	///	///	///	///	669 (17)	///	///	///	///
568 (100)	567 (100)	569 (100)	569 (100)	568 (100)	568 (100)	568 (100)	567 (100)	567 (100)	567 (100)	566 (100)	567 (100)
///	///	///	///	///	///	///	557 (sh)	///	558 (sh)	///	552 (90)
532 (83)	532 (83)	532 (83)	531 (83)	531 (83)	531 (83)	531 (83)	531 (83)	533 (83)	532 (83)	531 (84)	531 (83)
522 (75)	519 (76)	519 (75)	517 (75)	517 (75)	518 (75)	517 (75)	517 (75)	520 (76)	518 (75)	518 (75)	517 (75)
///	///	///	///			499 (sh)	508 (sh)		503 (sh)	509 (70)	509 (sh)
487 (57)	487 (58)	486 (57)	486 (56)	485 (57)	485 (57)	486 (6)	487 (57)	485 (57)	486 (57)	485 (57)	485 (57)
461 (42)	464 (43)	464 (41)	463 (42)	464 (41)	463 (41)	462 (41)	462 (41)	463 (41)	465 (42)	463 (42)	463 (42)
///	///	///	461 (sh)	///	///	///	///	///	///	///	///
///	454 (sh)	///	///	///	452 (sh)	453 (sh)	451 (sh)	///	450 (sh)	453 (sh)	451 (sh)
///	444 (sh)	439 (sh)	438 (sh)	439 (sh)	439 (sh)	439 (sh)	439 (sh)	439 (sh)	438 (sh)	437 (sh)	437 (sh)
426 (26)	425 (28)	424 (27)	426 (26)	426 (26)	424 (27)	424 (26)	426 (26)	425 (26)	424 (26)	425 (26)	425 (27)
411 (15)	415 (22)	415 (21)	415 (21)	414 (22)	414 (21)	413 (21)	414 (21)	413 (21)	416 (21)	414 (21)	414 (21)
///	398 (10)	399 (9)	///	399 (9)	///	///	///	///	///	///	///

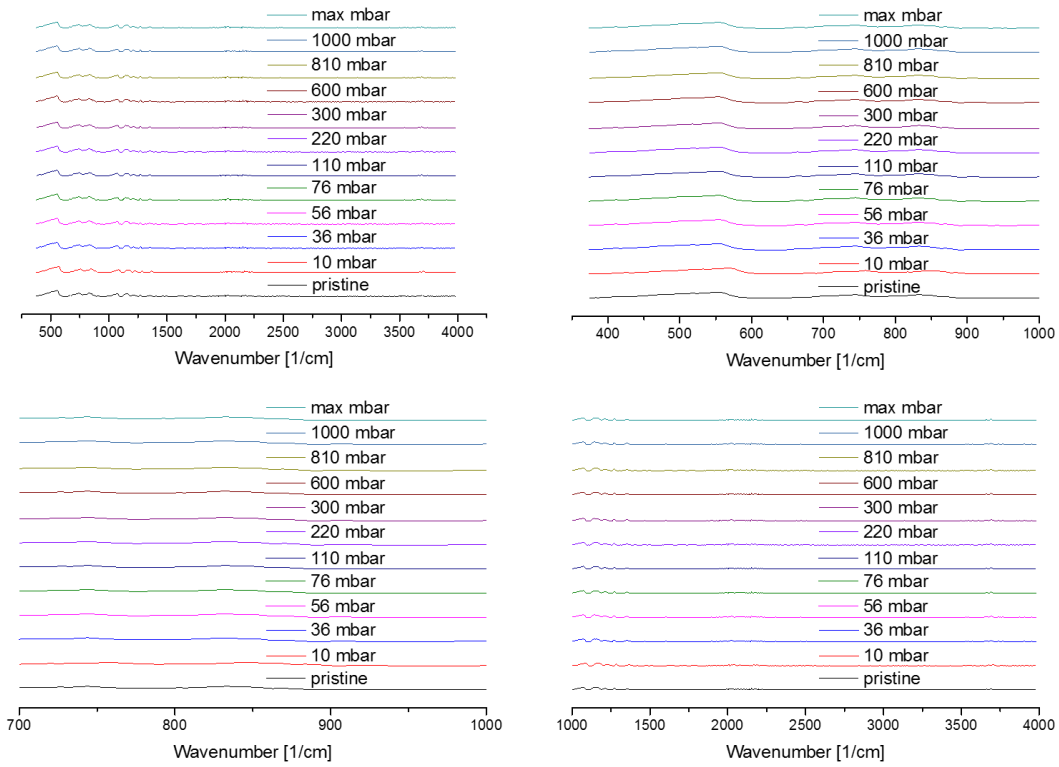

Figure S9: ATR-IR Spectra of the pristine and fluorinated NCM 851005 materials (with a baseline correction), where 10 mbar (0.06 wt-% F), 36 mbar (0.11 wt-% F), 56 mbar (0.013 wt-% F), 76 mbar (0.013 wt-% F), 110 mbar (0.017 wt-% F), 220 mbar (0.088 wt-% F), 300 mbar (300 wt-% F), 600 mbar (0.162 wt-% F), 810 mbar (0.205 wt-% F), 1000 mbar (0.212 wt-% F), and max mbar (0.240 wt-% F).

Thermogravimetric analyses (TGA) and Differential Thermal Analysis (DTA)

Does Fluorination alter the Thermal stability of Ni-rich NCM CAMs…? The thermal stability of the (non-) fluorinated Ni-rich NCM CAMs is crucial for a long battery lifetime. To study the thermal stability, thermogravimetric analysis (TGA) and differential thermal analysis (DTA) measurements were carried out. The materials were placed in a thermogravimetric analyser and heated to 650 °C at 10 °C/min under nitrogen gas. The pristine material was also characterized under the same conditions. TGA measurements showed for the (non-)fluorinated NCM 811 CAM a mass loss between 0.16 to 0.81 % (Figure S10), where the DTA measurements shown no change in thermal stability (Figure S10). TGA measurements showed for the (non-)fluorinated NCM 851005 CAM a mass loss between 0.1 to 1.0 % (Figure S11), where the DTA measurements shown no change in thermal stability (Figure S11).

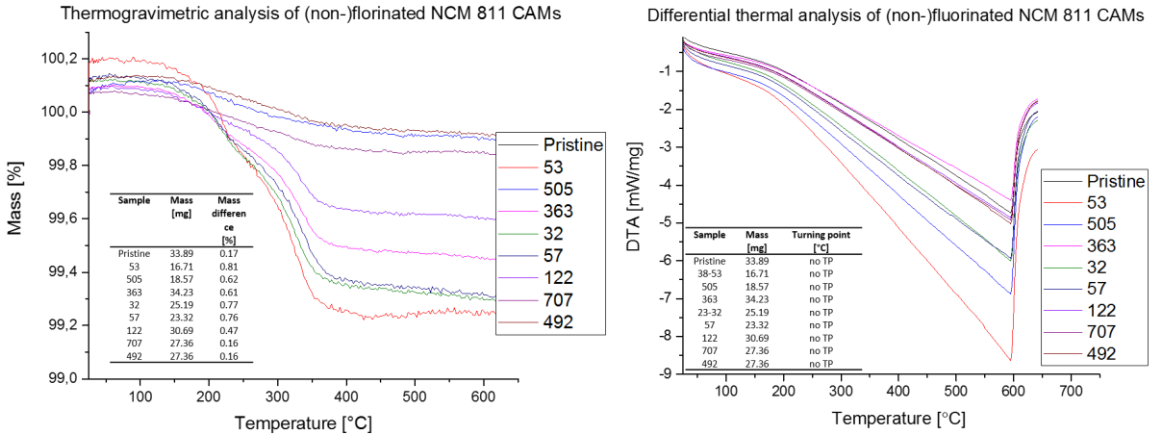

Figure S10: TGA and DTA results of (non-) fluorinated Ni-rich NCM 811 CAMs.

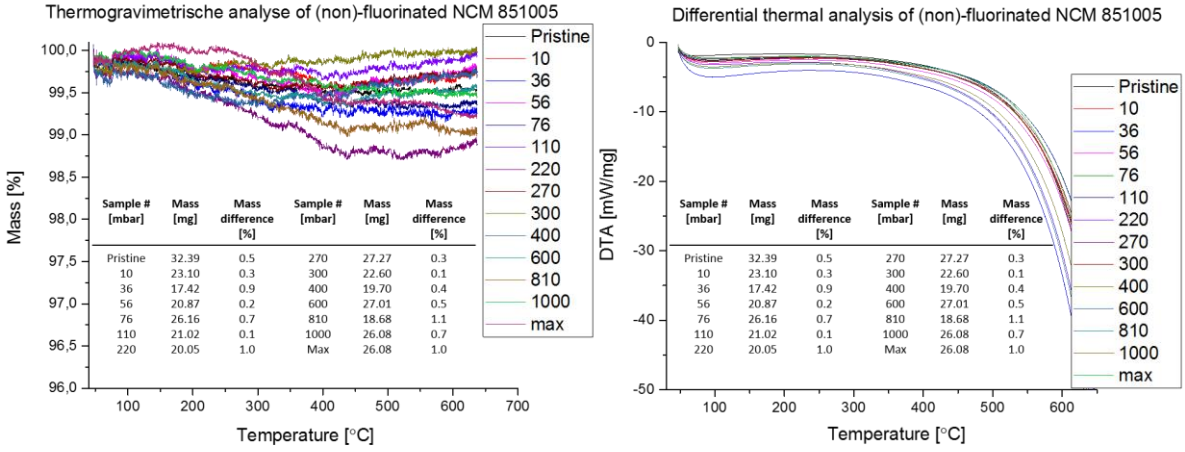

Figure S11: TGA and DTA results of (non-) fluorinated NCM 851005 CAMs, , where 10 mbar (0.06 wt-% F), 36 mbar (0.11 wt-% F), 56 mbar (0.013 wt-% F), 76 mbar (0.013 wt-% F), 110 mbar (0.017 wt-% F), 220 mbar (0.088 wt-% F), 300 mbar (300 wt-% F), 600 mbar (0.162 wt-% F), 810 mbar (0.205 wt-% F), 1000 mbar (0.212 wt-% F), and max mbar (0.240 wt-% F).

Thermogravimetric Analysis coupled with Mass Spectrometry (TGA-MS)

To analyze thermally labile surface species on the materials, the samples were analyzed by TGA-MS using a Mettler Toledo TGA/DSC 1 (*Mettler Toledo*, Switzerland) coupled to a Thermostar MS (*Pfeiffer Vacuum*, Germany). Inside the glovebox, 30 mg to 35 mg of the sample were filled into a 150 µl aluminum oxide crucible and transported to the device inside an airtight glass bottle. The sample was at pace inserted into the device (exposure time to ambient air less than 1 min) and heated stepwise at a rate of 10 K min^{-1} to 1125 °C under argon. This temperature was retained for another 30 min. At 120 °C and 450 °C the temperature was hold constant for 30 min to ensure a clear separation of the desorbing phases. The temperature profile, which contains further isothermal steps at 25 and 1125°C, is illustrated in the TGA-MS results. A constant Ar flow of 60 ml min^{-1} forces the desorption products to the MS. The weight loss and the associated mass signals are recorded.

Subsequent calcination/heat treatment

The effect of a calcination under Ar at 400 °C and 450 °C was investigated. These conditions are from now on referred to as “Ar 400 °C” and “Ar 450 °C”. The total gas flow was 1 L min^{-1}. In each case, the target temperature was held for 1 h.

Magic Angle Spinning – Nuclear Magnetic Resonance Spectroscopy (MAS-NMR)

^{7}Li and ^{19}F MAS NMR Studies of (non-)Fluorinated NMC 811 and 851005 CAMs

^{7}Li and ^{19}F MAS NMR Studies were carried out for (non-)fluorinated NMC 811 and 851005 CAMs for the pristine, low (average F-concentration: 0.108 wt-%$_{(NCM811)}$/0.0335 wt-%$_{(NCM\ 851005)}$), and high (average F-concentration: 0.126 wt-%$_{(NCM\ 811)}$/0.24 wt-%$_{(NCM\ 851005)}$) fluorinated NCM CAMs (Figure ***S12***).

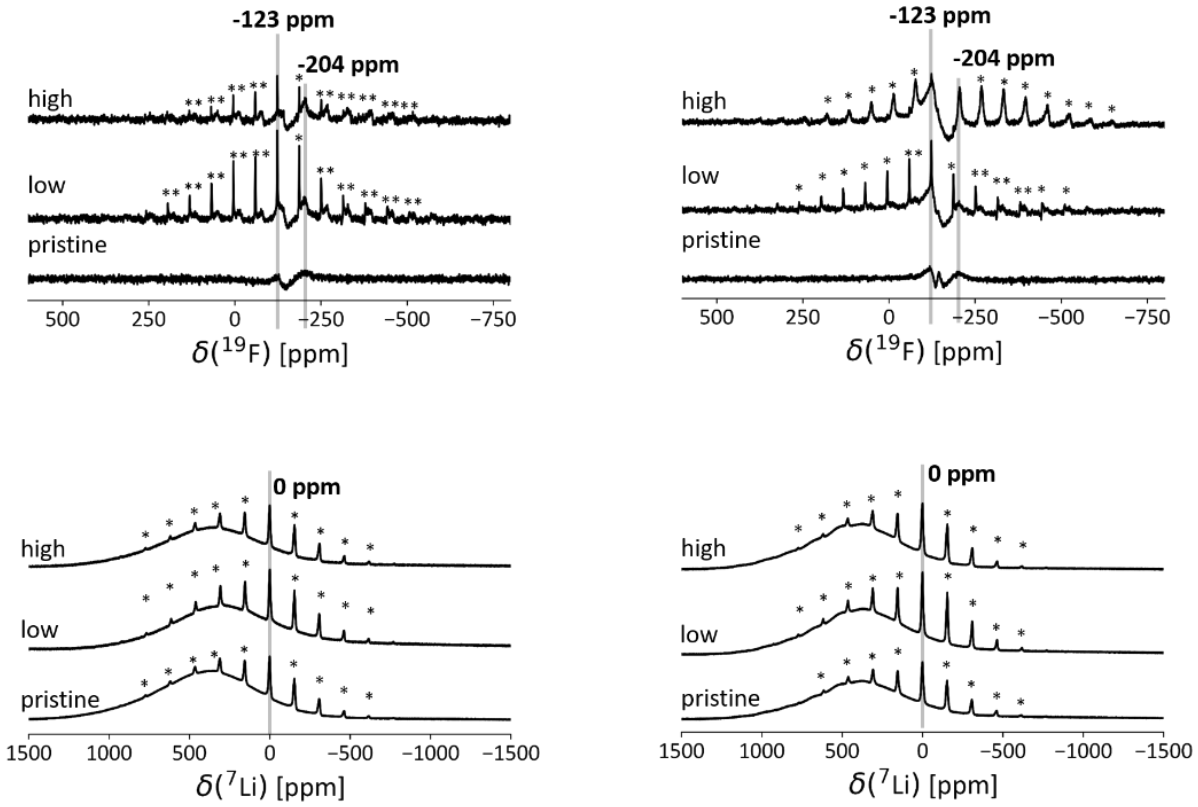

Figure S12: ^{19}F and ^{7}Li MAS NMR (30 kHz spinning, ^{19}F background subtracted); left) (non-)fluorinated NCM 811 and right) (non-)fluorinated NCM 851005 of pristine, low and high fluorinated NCM CAMs. Spinning sidebands are marked by*.

The ^{19}F rotor-synchronized Hahn-Echo MAS NMR spectra of all fluorinated NCM samples show a signal at an isotropic shift of –204.0 ppm that fits very well to the signal of neat solid LiF at –204.5 ppm (Figure S15). There is a second very small signal at –123 ppm originating from traces of PTFE (–123 ppm) in the samples (probably from the stir bar). The distortion of the spectra around –100 to –200 ppm results from incomplete subtraction of the background signal originating from the PTFE parts of the MAS probe (Figure S14).

In the rotor synchronized solid-echo ^{7}Li spectra recorded at 30 KHz MAS a sharp signal with well resolved spinning sidebands is observed for all fluorinated samples. Its isotropic shift is identical to that of neat LiF at –0.3 ppm (Figure S12 and Figure S16). Additionally, in all the ^{7}Li spectra a very broad signal that does not split into spinning sidebands with a width of about –500 to +1000 ppm

could be found. It was assigned to the lithium atoms in the bulk material of the Ni-rich material with the highest spatial proximity to the unpaired electrons.

Furthermore, it is shifted by more than 300 ppm as compared to neat LiF due to the unpaired electron spin density transferred from the neigh bored layered Ni-rich NCM oxide to the nucleus (Fermi contact shift). Its linewidth originates from nucleus-electron dipolar interactions as well as a distribution of Fermi contact shifts.[15]

The observed chemical shifts in both the ^{19}F and ^{7}Li spectra perfectly match the ones observed for neat LiF and thus were assigned to arise from LiF.

However, the spinning sidebands envelope of both, the ^{7}Li and ^{19}F signal, is strikingly broadened in comparison to that of neat LiF (about 150 kHz for ^{7}Li and 200 kHz for ^{19}F). As the dipole-dipole coupling of ^{7}Li and ^{19}F should be comparable to that in neat LiF and should in general not exceed 100 kHz, the line broadening can only be explained by dipole-dipole interaction of the observed nuclei with the electron spin of the Ni-rich NCM oxide materials. This interaction requests a close spatial proximity. However, since the lines have isotropic shifts identical to neat solid LiF (i. e. no Fermi contact shift is observed) the LiF causing this line is not present within the bulk but rather coating the Ni-rich NCM material.[32]

Further Information on the ^{7}Li and ^{19}F MAS NMR Studies

Identification of LiF by MAS-NMR Spectroscopy: The ^{19}F Hahn-Echo MAS-NMR spectra (Figure ***S13***) of low and high fluorinated CAMs were measured at a spinning frequency of 30 kHz. There is a large background signal originating from the PTFE, which is far outside the NMR coil and hence experiences smaller pulse angles than the sample. It is thus not well refocused by the Echo experiment- However, its signal is not entirely suppressed and its phasing is not compatible with that of the sample. Thus, the background signal was recorded separately and subtracted (as shown for high fluorinated NCM 811 in Figure S14). Unfortunately, the actual shape slightly changes as the sample is removed, leading to a visible distortion of the spectra around –100 ppm to –200 ppm (Figure S13). The spectra of all samples show a signal with an isotropic shift of –204.0 ppm, which very well fits to the signal of neat LiF at –204 ppm that was recorded for comparison. The FWHM (full width at half maximum) of the spinning sidebands envelope is about 200 kHz, when measured at 470.65 MHz. This is a significantly increased value when compared to the spinning sidebands envelope of neat LiF, as easily is seen in the comparison of both spectra in Figure ***S15***. The origin of this increased width will be discussed jointly with the lithium spectra. The spectra also show traces of PTFE (–123 ppm) contained in the sample (likely from the stir bar used), which could be identified by its chemical shift and its very sharp signal.

The ^{7}Li solid-state Echo MAS-NMR spectra of the high fluorinated samples are shown in Figure ***S16*** and compared to a spectrum of neat LiF, showing an isotropic shift of –1.4 ppm. Both samples exhibit a sharp signal at an identical isotropic shift. The spinning sidebands envelope of this signal was also strikingly broadened in comparison to neat LiF to about 150 kHz.

A pristine sample of the Ni-rich NCM CAM (Figure S12) also showed a similar sharp signal in the same region that could be assigned to Li_2CO_3. The existence of a Li_2CO_3 layer is commonly known for NCM cathode materials.[16] Already by qualitative comparison of the intensities, the amount of the coating lithium species was easily found to be significantly increased in all measured fluoridated samples. As the observed chemical shifts in both the ^{19}F and ^{7}Li spectra perfectly match the ones observed for neat LiF and both lines exhibit the same broadening of the sideband pattern they were assigned to arise from LiF.

Additionally, a very broad signal that does not split into spinning sidebands with a width of about 200 kHz to 300 kHz could be found in every ^{7}Li MAS NMR spectrum. Due to the broadness, the lack of splitting into spinning sidebands and its huge integral value, it was assigned to the lithium atoms in the bulk material of the Ni-rich NCM CAMs with the highest spatial proximity to the unpaired electron spins. Furthermore, it is shifted by more than 300 ppm as compared to neat LiF due to the unpaired electron spin density transferred from the neighboured layered Ni-rich NCM oxide to the nucleus (Fermi contact shift). Its linewidth originates from nucleus-electron dipolar interactions as well as a distribution of Fermi contact shifts.[17]

The huge increase in the width of the spinning sideband patterns observed in ^{7}Li and ^{19}F spectra of all samples cannot be explained by dipole-dipole coupling of ^{7}Li and ^{19}F, as this should be comparable to the one in neat LiF and should in general not exceed 100 kHz. It can only be explained by interaction of the observed nuclei with the electron spin of the layered Ni-rich NCM oxide. This interaction requests a close spatial proximity. However, the lines have isotropic shifts identical to neat solid LiF, i.e. no Fermi contact shift is observed as would be expected for material within the bulk. Hence, the LiF causing this line is not present within the bulk but rather coating the Ni-rich NCM material as likewise reported by Ménétrier et. al. and Murakami et. al.[17],[18]

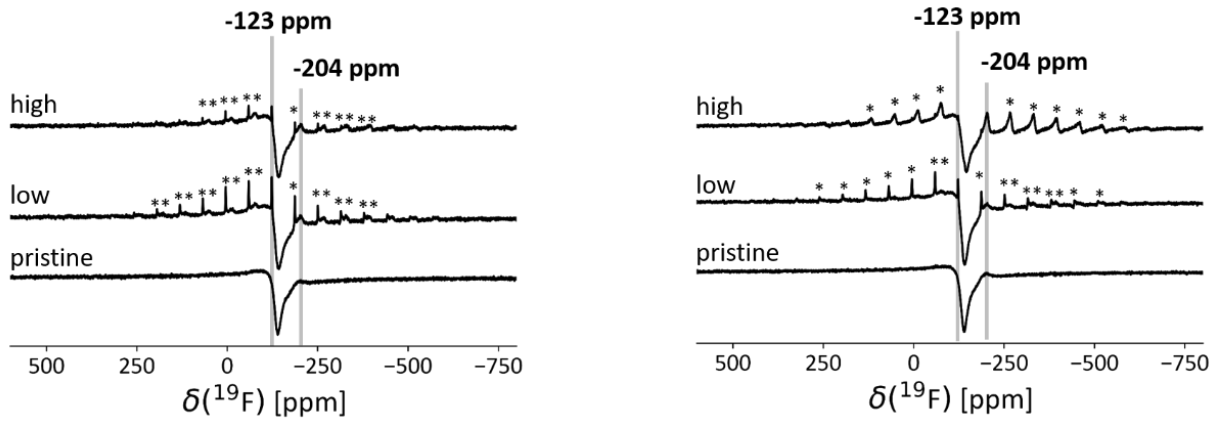

Figure S13: ^{19}F MAS NMR; left) (non-)fluorinated NCM 811 and right) (non-)fluorinated NCM 851005 of pristine, low and high fluorinated NCM CAMs. Spinning sidebands are marked by *.

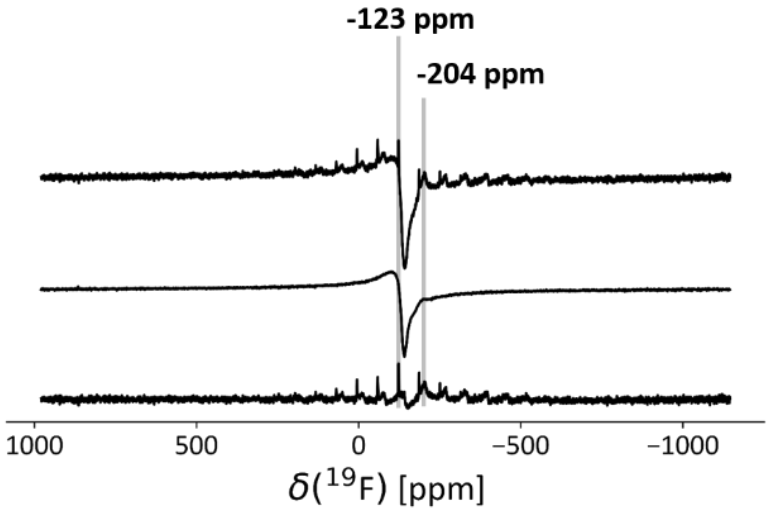

Figure S14: ^{19}F Hahn Echo MAS-NMR spectrum of high fluorinated NCM 811 (30 kHz spinning, r.t., 2.5 mm rotor, 470.65 MHz). The top spectrum shows the signal as recorded, the middle spectrum the background signal arising from PTFE parts of the probe and the bottom spectrum is the difference of the two.

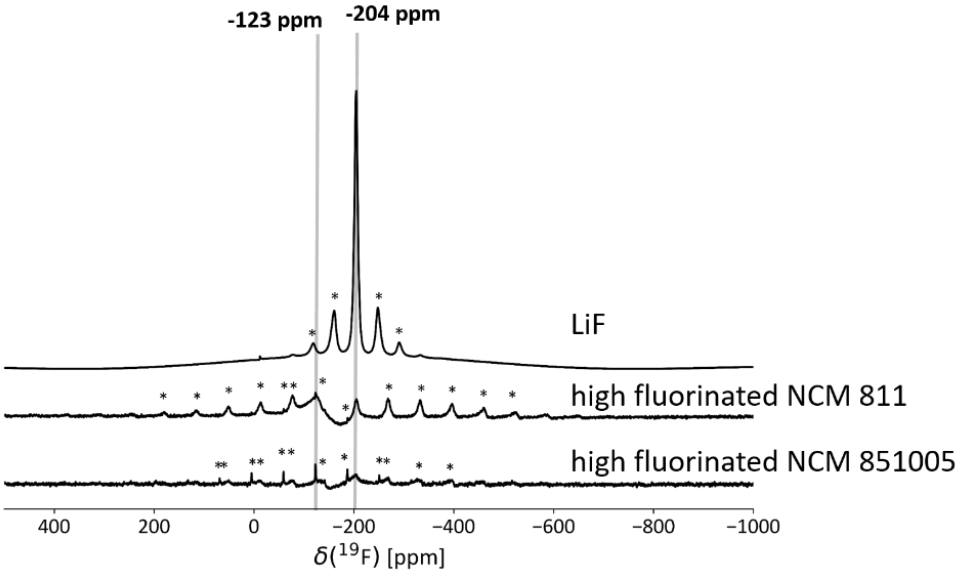

Figure S15: ^{19}F Hahn Echo MAS-NMR spectra of LiF (20 kHz spinning) and high fluorinated Ni-rich NCM materials (30 kHz spinning, background subtracted). Spinning sidebands are marked by *.

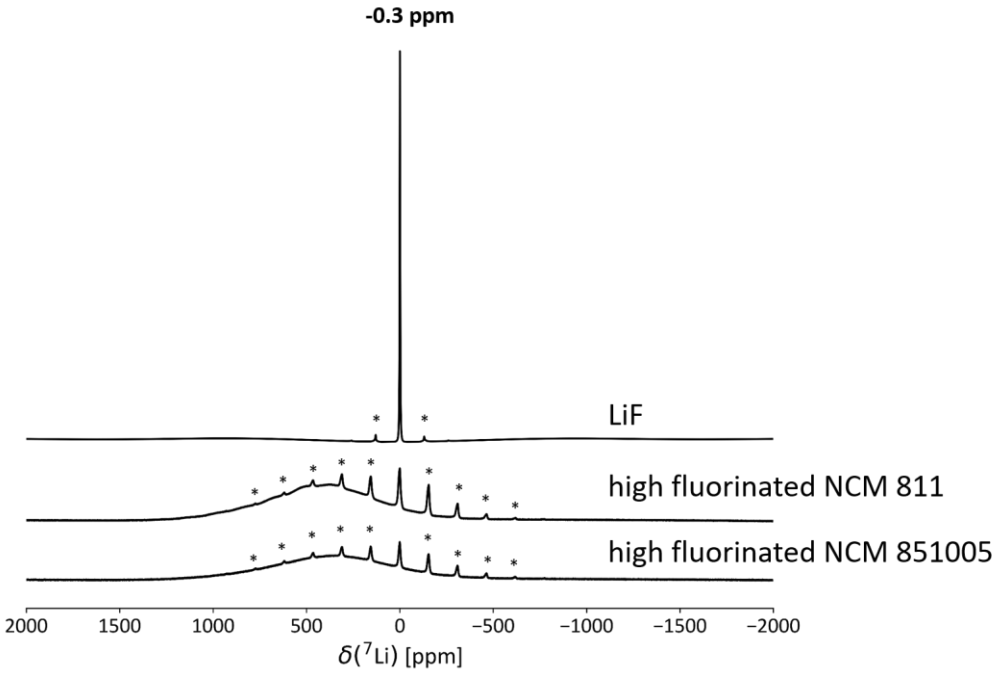

Figure S16: ^{7}Li solid-echo MAS NMR spectra of LiF (20 kHz spinning) and high fluorinated Ni-rich NCM Material (30 kHz spinning). Spinning sidebands are marked by *.

Conductivity measurements of the Ni-rich materials

These measurements were carried out for the pristine and the little fluorinated NCM 811 and NCM 851005 CAMs (Figure S17 and Table S6). For the NCM 811 material: all three samples (pristine, 0.11 wt-% F, and 0.13 wt-% F) show a linear increasing of the conductivity from 2 MPa to 20 MPa. Both fluorinated samples show almost identical results (conductivity vs. pressure), yet the pristine material showed the highest overall conductivities result. The (non-)fluorinated NCM 851005 CAMs

shown almost the same conductivity at 2 MPa with a linear increase of the conductivity vs. pressure until at 20 MPa for all samples. The pristine material showed the best result, followed by the 1.17 wt-% fluorinated material. The results of the four fluorinated samples (0.05 wt-%, 0.58 wt-%, 0.86 wt-%, and 1.44 wt-%) are almost identical.

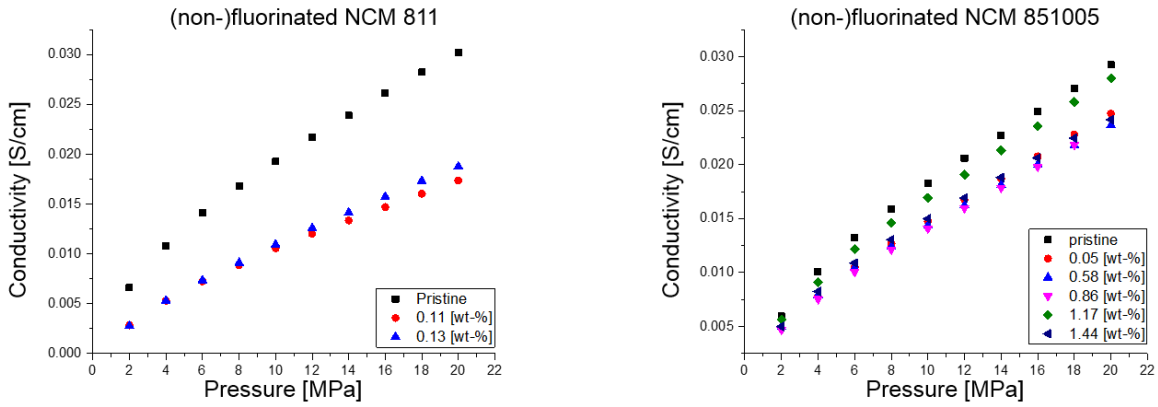

Figure S17: Conductivity measurements of (non-)fluorinated Ni-rich materials, left) NCM 811 and right) NCM 851005.

Table S6: Conductivity measurements of (non-)fluorinated Ni-rich materials.

	(non-)fluorinated NCM 811			(non-)fluorinated NCM 851005					
Pressure [MPa]	**Pristine [S/cm]**	**0.11 wt-% F [S/cm]**	**0.13 wt-% F [S/cm]**	**Pristine [S/cm]**	**0.05 wt-% F [S/cm]**	**0.58 wt-% F [S/cm]**	**0.86 wt-% F [S/cm]**	**1.17 wt-% F [S/cm]**	**1.44 wt-% F [S/cm]**
2	0.00663	0.00285	0.00278	0.00595	0.00483	0.00495	0.00469	0.00565	0.005
4	0.01079	0.00529	0.00531	0.01008	0.00779	0.00789	0.00755	0.00911	0.00825
6	0.01409	0.00723	0.00736	0.01323	0.01052	0.01043	0.01005	0.01219	0.01089
8	0.01681	0.00885	0.00911	0.0159	0.01268	0.01241	0.01213	0.01462	0.01306
10	0.01927	0.01056	0.01095	0.01829	0.01475	0.01436	0.01407	0.01692	0.01499
12	0.02168	0.01201	0.01259	0.0206	0.01674	0.0162	0.01597	0.01905	0.01692
14	0.02388	0.01334	0.01416	0.02271	0.0187	0.01812	0.01786	0.02133	0.01882
16	0.02614	0.01469	0.01575	0.02491	0.02076	0.01996	0.0198	0.02356	0.02062
18	0.02822	0.01603	0.01733	0.02706	0.02279	0.02179	0.02184	0.02581	0.02245
20	0.03021	0.01736	0.01877	0.02924	0.02472	0.02365	no data	0.028	0.02417

Press density measurements of the Ni-rich NCM CAMs

These measurements were carried out for several (non-)fluorinated NCM 811 and NCM 851005 samples (Figure S18 and Table S7). All samples show a linear increase of the density with increasing pressure. Yet, all fluorinated samples show consistently higher Press densities at all pressures than the pristine material. The fluorinated NCM 851005 sample with the fluorine concentration of 1.17 wt-% showed the highest Press density values, followed by the 1.44 wt-% fluorinated sample. The best Press densities are by up to 34 % higher than those of the pristine material (Table S7). The

lower fluorinated samples (0.05…0.86 %) showed considerably lower, but still better densities than the pristine material.

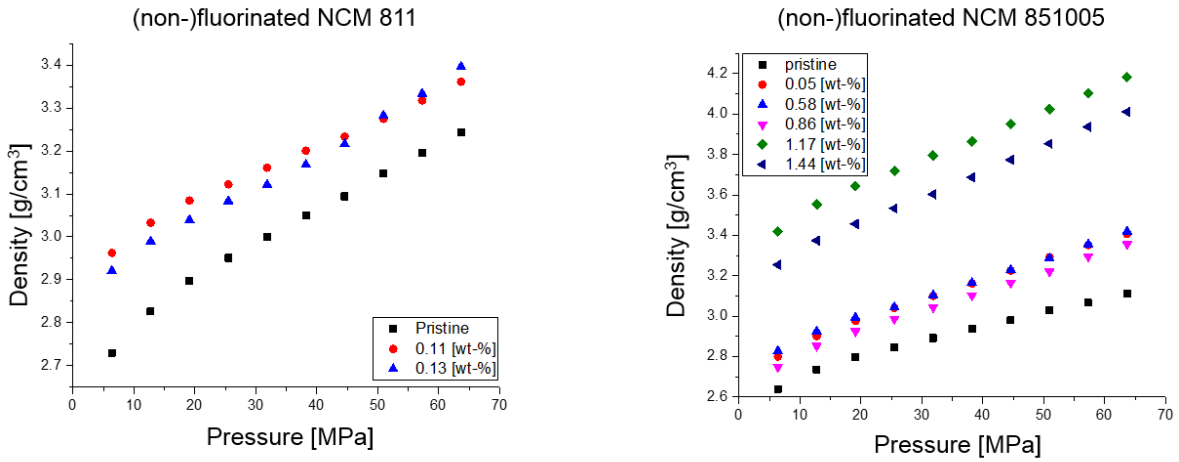

Figure S18: Press density measurements of (non-)fluorinated NCM 811 (left) and NCM 851005 (right).

Table S7: Press density measurements of (non-)fluorinated NCM 811 and NCM 851005.

	(non-)fluorinated NCM 811			(non-)fluorinated NCM 851005					
Pressure [MPa]	**Pristine [g/cm³]**	**0.11 wt-% F [g/cm³]**	**0.13 wt-% F [g/cm³]**	**Pristine [g/cm³]**	**0.05 wt-% F [g/cm³]**	**0.58 wt-% F [g/cm³]**	**0.86 wt-% F [g/cm³]**	**1.17 wt-% F [g/cm³]**	**1.44 wt-% F [g/cm³]**
6.3662	2.72983	2.9625	2.921	2.63959	2.79973	2.82809	2.74817	3.41841	3.25374
12.7324	2.82668	3.03304	2.98957	2.7361	2.90177	2.92538	2.85268	3.55209	3.37425
19.09859	2.89734	3.08445	3.03952	2.79623	2.97635	2.99406	2.92465	3.64369	3.45655
25.46479	2.951	3.12225	3.08368	2.84627	3.04028	3.04408	2.9863	3.71827	3.53315
31.83099	2.9996	3.16098	3.12147	2.89156	3.09946	3.10333	3.04332	3.79596	3.60302
38.19719	3.04984	3.20069	3.16805	2.9383	3.16098	3.16493	3.10255	3.86519	3.68632
44.56338	3.09425	3.23319	3.21606	2.97959	3.225	3.22903	3.16414	3.94922	3.77357
50.92958	3.14773	3.27475	3.28237	3.02925	3.29167	3.28729	3.22007	4.0242	3.85338
57.29578	3.19507	3.31739	3.33392	3.06575	3.35231	3.35649	3.29496	4.10209	3.93663
63.66198	3.24385	3.36115	3.39615	3.11072	3.40609	3.41948	3.35566	4.18305	4.0109

Thermodynamics of Fluoride Uptake

Reaction equations 1 to 16 in the main text showed the evaluated thermodynamic data for the analysis of the enthalpies of reaction of elementary fluorine gas with the NCBH and SBC layer as well as their side reactions. Below we include the enthalpies of formation $\Delta_f H^0$ are given in kJ mol^{-1}. This data shows that fluorine gas can react thermodynamically with the NCBH and SBC layer, which both are localized on the surface of the material.

Enthalpies of Formation $\Delta_f H^0$ and $\Delta_f S^0$ from Ref. [8] or the National Institute of Standards and Technology Website at https://webbook.nist.gov/chemistry/name-ser/

Compound	$\Delta_f H^0$ [kJ/mol]	$\Delta_f S^0$ [J/K mol]	Compound	$\Delta_f H^0$ [kJ/mol]	$\Delta_f S^0$ [J/K mol]
NiO(s)	–240.0	43.7	LiOH(s)	–441.5	
CoO(s)	–237.9	53.0	Li_2O(s)	–561.2	
MnO(s)	–385.2	59.7	Li_2CO_3(s)	–1132.	
Mn_2O_3(s)	–959.0	110.5	LiF(s)	–587.7	
MnO_2(s)	–520.0	53.1	F_2(g)	0.0	202.8
Ni_2O_3(s)	–489.5		O_2(g)	0.0	205.2
$Ni(OH)_2$(s)	–538.0	79.0	HF(g)	–275.4	173.8
$Co(OH)_2$(s)	–539.7	79.0	H_2O(l)	–285.8	70.0
Co_3O_4(s)	–891.0	102.5	H_2O(g)	–241.8	188.8
$CoCO_3$(s)	–713.0	91.7	CO_2(g)	–394.4	213.8
$MnCO_3$(s)	–894.1	85.8	MnF_2(s)	–855.0[a)]	
NiF_2(s)	–651.4	73.6			
CoF_2(s)	–671.5	82.0			
CoF_3(s)	–790.4	94.5			

[a)] From Jacob, K. T.; Hajra, J. P. (1987): Measurement of Gibbs energies of formation of CoF_2 and MnF_2 using a new composite dispersed solid electrolyte. In: Bull. Mater. Sci. 9 (1), S. 37–46. DOI: 10.1007/BF02744391.

References

[1] A.C. Larson and R.B. Von Dreele, *General Structure Analysis System (GSAS)*. *Los Alamos National Laboratory Report LAUR 86-748*, **2004**.

[2] B. H. Toby, *J Appl Crystallogr* **2001**, *34*, 210.

[3] E. G. Reilly, *Review of Scientific Instruments* **1953**, *24*, 875.

[4] Acros Organics, "Material Safety Data Sheet of MnF_3".

[5] Alfa Aesar, "Sicherheitsdatenblatt (Material Safety Data Sheet) of LiF", **2013**.

[6] Alfa Aesar, "Sicherheitsdatenblatt (Material Safety Data Sheet) of NiF_2", **2014**.

[7] Carl Roth, "Sicherheitsdatenblatt (Material Safety Data Sheet) of LiF", **2015**.

[8] D. R. Lide (Ed.) *CRC handbook of chemistry and physics*. *A ready-reference book of chemical and physical data*, CRC Press, Boca Raton, Fla., **1997**.

[9] Merck Group, "Sicherheitsdatenblatt (Material Safety Data Sheet) of LiF", **2015**.

[10] SCS GmbH, "Sicherheitsdatenblatt (Material Safety Data Sheet) of LiF", **2012**.

[11] SIGMA-ALDRICH, "Sicherheitsdatenblatt (Material Safety Data Sheet) of LiF", **2016**.

[12] SIGMA-ALDRICH, "Sicherheitsdatenblatt (Material Safety Data Sheet) of NiF_2", **2016**.

[13] Thermo Fisher Scientific, "Sicherheitsdatenblätter (Material Safety Data Sheet) of MnF_3", **2017**.

[14] K. Nakamoto, *Infrared and Raman spectra of inorganic and coordination compounds*. *Part A: Theory and applications in inorganic chemistry*, Wiley, Hoboken, N.J, **2009**.

[15] U. Breddemann, E. M. Erickson, V. Davis, F. Schipper, M. Ellwanger, M. Daub, A. Hoffmann, C. Erk, B. Markovsky, D. Aurbach et al., *ChemElectroChem* **2019**.

[16] M. Murakami, H. Yamashige, H. Arai, Y. Uchimoto, Z. Ogumi, *Electrochem. Solid-State Lett.* **2011**, *14*, A134.

[17] M. Ménétrier, J. Bains, L. Croguennec, A. Flambard, E. Bekaert, C. Jordy, P. Biensan, C. Delmas, *J. Solid State Chem.* **2008**, *181*, 3303.

[18] N. Dupré, J.-F. Martin, D. Guyomard, A. Yamada, R. Kanno, *J. Power Sources* **2009**, *189*, 557.

4. Conclusion and Outlook

Electrolyte stability and surface reactivity of cathode materials are decisive factors for the cycle-life of Li-ion battery cells. First, the oxidative and the reductive stability of the electrolyte components VC, EC, and $LiPF_6$ were investigated by a newly developed method, i.e., *operando* DRIFTS. Second, quantity and nature of surface contaminants on Ni-rich NCM and LMR-NCM have been studied before and after exposure to moisture and CO_2. Third, reactive gas treatments with SO_2, SO_3, and F_2 were developed to make the CAM surfaces more stable and thus improve their electrochemical cycling performance.

To investigate the stability of electrolyte components, an *operando* DRIFTS cell was developed in order to monitor the working electrode during electrochemical cycling as well as the formation of IR active gases. Using reductive and oxidative scans, electrolyte solvents such as EC and VC and the commonly used electrolyte salt $LiPF_6$ were investigated. In a first set of experiments, the baseline of DRIFT spectra was found to change simultaneous to the lithiation of graphite. In a second set of experiments, LFP was used for reductive scans in order to avoid such baseline effects. However, there were no infrared signals observed that would belong to typical SEI species such as LEDC, indicating an insufficient surface sensitivity of the developed *operando* DRIFTS method. In a third set of experiments, the evolution of infrared active gases such as POF_3, CO_2, and PF_5 could be observed during the oxidation of a VC/$LiPF_6$ electrolyte on an LTO working electrode. The oxidative decomposition of electrolyte species is a relevant side reaction when using CAMs such as LNMO or LMR-NCM that need cut-off potentials as high as 4.4 V vs. graphite.

In case of LMR-NCM, the electrolyte is not only decomposed by oxidation, but also by a chemical reaction with basic surface species. Ni-rich NCMs suffer from the same problem, i.e., hydrates, hydroxides, carbonates, and mixtures of those[48,136,161] are formed when these CAMs are exposed to CO_2 and H_2O, e.g., from ambient air exposure. Within this thesis, a storage experiment was developed that exposed CAMs deliberately to atmospheric atmosphere at high humidity. The formed surface contaminants were then analyzed via DRIFTS, thermogravimetric analysis coupled with mass spectrometry (TGA-MS), on-line mass spectrometry (OMS), and full-cell cycling. TGA-MS experiments with NCM811 and reference salts revealed that basic nickel carbonate hydrate $NiCO_3 \cdot 2Ni(OH)_2 \cdot x\,H_2O$ (NCBH) is the major surface contaminant. The presence of carbonate was confirmed by *ex situ* DRIFTS measurements of CAM powder diluted with KBr. This *ex situ* DRIFTS characterization was found to be very sensitive to surface species on CAM powders (such as CO_3^{2-}, OH^-/H_2O), in great contrast to the above mentioned *operando* DRIFTS method (trying to observe electrolyte reduction products). Calcination at elevated temperature was demonstrated to remove most of the formed contaminants and is thus suggested as a mitigation strategy for both Ni-rich NCM and LMR-NCM. OMS and coin cell tests demonstrated how such a calcination helps to avoid gassing problems

and to improve the full-cell cycle-life. In addition to the mentioned *ex situ* DRIFTS measurements, an *in situ* method was developed to monitor the chemical reaction between NCM811 and CO_2, H_2O, or a combination of both. However, similar to *operando* DRIFTS of electrolyte reduction, *in situ* DRIFTS of NCM811 reacting with CO_2 and H_2O failed to detect the reaction products, i.e., surface contaminants formed on the surface of NCM811. In great contrast, *ex situ* DRIFTS data of the same samples clearly proved the presence of carbonates and hydroxides/hydrates after the exposure of NCM811 to CO_2 and moisture. TGA-MS and full-cell cycling with a graphite anode clearly proved the formation of a large amount of surface contaminants. For this reason, it is suggested that future experiments should focus on *ex situ* DRIFTS characterization of NCM811 in order to further elucidate the reaction mechanisms of the CAM surface with CO_2 and H_2O that generate surface contaminants.

Not only calcination, but also reactive gases modifying the CAM surface can help to avoid problems derived from surface contaminants. In a study with LMR-NCM, a thermal treatment with SO_3 was demonstrated as a method to make the material more robust versus humid ambient air. The reaction of SO_3 with LMR-NCM was carried out in a specially developed tube furnace. The setup included a reactor with the catalyst V_2O_5, generating SO_3 from SO_2 oxidation. After the SO_3 treatment, sulfate formation was found from XPS and DRIFTS analysis. SO_3-treated LMR-NCM exhibited reduced CO_2 gassing when stored with electrolyte at 60°C, as well as an improved full-cell cycle-life, lower pulse resistance, and an enhanced rate capability as compared to pristine LMR-NCM. In another study, LMR-NCM was modified by SO_2, which lead to an increased discharge capacity. DRIFTS and XPS proved the formation of sulfites and sulfates on the LMR-NCM surface. The higher robustness and superior cycling performance of LMR-NCM after SO_2 and SO_3 treatment makes these reactive gases promising candidates for optimizing CAMs on an industrial scale.[136] In case of NCM851005, the cycling performance could not be improved after SO_2 or SO_3 treatment. Possibly this could be achieved by further optimization of the experimental parameters for the thermal treatment. However, the sulfate content of pristine NCM851005 was found to be much higher compared to LMR-NCM, thus an additional surface sulfation via SO_2 or SO_3 treatment might not be very effective to optimize its surface properties. F_2 is a further reactive gas that was used to modify NCM811 and NCM851005. The treatment was carried out at room temperature with elementary F_2 in a closed reactor vessel. During fluorination, H_2O was formed from the reaction with the NCM. Therefore, the fluorinated CAM samples were calcined in order to remove the surface contaminants formed during the reaction. The fluorination of NCM811 improved the capacity retention of full-cells, most probably due the formation of a protective LiF layer that reduces transition metal leaching from the cathode during cycling.

Taking into account the current trends in the industry to increase the specific energy density of battery cells by using NCA, NCM811, or CAMs with even higher Ni content, the detailed knowledge about the formation of surface contaminants during material handling and electrode manufacturing is

becoming increasingly important. The thesis at hand clearly demonstrated that the exposure of CAMs to CO_2 and H_2O must be avoided as much as possible. While the current work focused on showcasing the difference between extreme cases, i.e., storing CAMs in moisture saturated ambient air ("wet" storage) vs. handling CAMs under inert conditions ("dry" and "calcined" samples), for future work it might be of interest to reveal the impact of practically relevant humidity values of conditioned lab atmospheres or controlled environments typical of a cell manufacturing factory. At the same time, the tuning of CAM surfaces will play an important role to make Ni-rich NCM or LMR-NCM less sensitive to ambient air and moisture. The thesis at hand focused on reactive gas treatments that promise to be well scalable for industrial CAM manufacturing. Further methods such as ALD coatings can be expected to be optimized for larger scales as well.[164] Independent of the choice of method, for present and future cathode chemistries it is vital to ensure a robust surface chemistry in order to meet the cycle-life targets for practical applications.

References

1. G. Zubi, R. Dufo-López, M. Carvalho, and G. Pasaoglu, The lithium-ion battery: State of the art and future perspectives, *Renew. Sustain. Energy Rev.*, **89**, 292–308 (2018).
2. G. E. Blomgren, The Development and Future of Lithium Ion Batteries, *J. Electrochem. Soc.*, **164**, A5019–A5025 (2017).
3. Wacker Neuson, *Emissionsfrei, leise und leistungsstark – Die Elektro-Minibagger EZ17e und EZ26e*, https://www.wackerneuson.de/de/aktuelles/news/ez17e/ (accessed: March 31, 2020).
4. A. Chinchane and O. Sumant, *Battery Power Tools Market [...]: Global Opportunity Analysis and Industry Forecast, 2019-2026*, https://www.alliedmarketresearch.com/battery-power-tools-market (accessed: March 31, 2020).
5. A. Ahlswede, *Absatz von E-Bikes in Deutschland bis 2019*, https://de.statista.com/statistik/daten/studie/152721/umfrage/absatz-von-e-bikes-in-deutschland/ (accessed: March 31, 2020).
6. A. Ahlswede, *Anzahl der E-Scooter in Deutschland nach ausgewählten Städten im Jahr 2019*, https://de.statista.com/statistik/daten/studie/1031136/umfrage/anzahl-der-e-scooter-in-deutschland-nach-ausgewaehlten-staedten/ (accessed: March 31, 2020).
7. B. Madapur, S. Madangopal, and M. N. Chandrashekar, Micro-Mobility Infrastructure for Redefining Urban Mobility, *Eur. J. Eng. Sci. Technol.*, **3**, 71–85 (2020).
8. M. Pagliaro and F. Meneguzzo, Electric Bus: A Critical Overview on the Dawn of Its Widespread Uptake, *Adv. Sustain. Syst.*, **3**, 1800151 (2019).
9. M. Lienkamp, *Status Elektromobilität 2016 oder wie Tesla nicht gewinnen wird*, https://www.researchgate.net/publication/304247929 (accessed: June 23, 2016).
10. I. Wagner, *Energy demand for electric vehicle charging worldwide in 2030, by key market*, https://www.statista.com/statistics/972072/electric-vehicle-charging-energy-demand-worldwide-by-market/ (accessed: March 31, 2020).
11. K. Naughton, *Japan's hybrid cars (int'l edition)*, https://web.archive.org/web/20110628194634/http://www.businessweek.com/archives/1997/b3557013.arc.htm (accessed: April 1, 2020).
12. A. Lidl, *Tesla Roadster Sport 2.5*, https://www.autozeitung.de/tesla/roadster/1-generation (accessed: March 31, 2020).
13. N. Tajitsu and N. Shirouzu, *Warming to lithium-ion, Toyota charges up its battery options*, https://www.reuters.com/article/us-toyota-batteries/warming-to-lithium-ion-toyota-charges-

up-its-battery-options-idUSKBN12U0ZH (accessed: March 30, 2020).

14. ecomento UG, *Neues Tesla Model S 100D mit 632 Kilometern Reichweite*, https://ecomento.de/2017/01/20/tesla-model-s-100d-632-kilometer-reichweite-model-x-100d-565-kilometer/ (accessed: April 2, 2020).

15. C. Riley, *The great electric car race is just beginning*, https://edition.cnn.com/2019/08/14/perspectives/batteries-lithium-ion-innovation/index.html (accessed: April 2, 2020).

16. W. Rudschies, *Tesla Model 3: Setzt Maßstäbe, trotz Schwächen*, https://www.adac.de/rund-ums-fahrzeug/autokatalog/marken-modelle/tesla/tesla-model-3/ (accessed: December 27, 2020).

17. J. Wieler and T. Geiger, *VW ID.3: Das Volks-Elektroauto im ADAC Test*, https://www.adac.de/rund-ums-fahrzeug/autokatalog/marken-modelle/vw/vw-id-3/ (accessed: December 27, 2020).

18. Volkswagen Aktiengesellschaft, *Der e-up! UNITED*, https://www.volkswagen.de/de/modelle-und-konfigurator/e-up-united.html (accessed: April 2, 2020).

19. BMW AG, *Technische Daten des BMW i3*, https://www.bmw.de/de/neufahrzeuge/bmw-i/i3/2020/bmw-i3-technische-daten.html#tab-0 (accessed: April 2, 2020).

20. P. Z. Lévay, Y. Drossinos, and C. Thiel, The effect of fiscal incentives on market penetration of electric vehicles: A pairwise comparison of total cost of ownership, *Energy Policy*, **105**, 524–533 (2017).

21. N. Hooftman, M. Messagie, J. Van Mierlo, and T. Coosemans, A review of the European passenger car regulations – Real driving emissions vs local air quality, *Renew. Sustain. Energy Rev.*, **86**, 1–21 (2018).

22. A. Boretti, Dependent performance of South Australian wind energy facilities with respect to resource and grid availability, *Energy Storage*, **1**, e97 (2019).

23. R. Schlögl, Energiewende 2.0, *Angew. Chemie*, **127**, 4512–4516 (2015).

24. O. Saritas, D. Meissner, and A. Sokolov, A Transition Management Roadmap for Fuel Cell Electric Vehicles (FCEVs), *J. Knowl. Econ.*, **10**, 1183–1203 (2019).

25. I. Staffell, D. Scamman, A. Velazquez Abad, P. Balcombe, P. E. Dodds, P. Ekins, N. Shah, and K. R. Ward, The role of hydrogen and fuel cells in the global energy system, *Energy Environ. Sci.*, **12**, 463–491 (2019).

26. B. G. Pollet, S. S. Kocha, and I. Staffell, Current status of automotive fuel cells for sustainable transport, *Curr. Opin. Electrochem.*, **16**, 90–95 (2019).

27. M. Miotti, J. Hofer, and C. Bauer, Integrated environmental and economic assessment of current

and future fuel cell vehicles, *Int. J. Life Cycle Assess.*, **22**, 94–110 (2017).

28. Nobel Media AB, *Press release: The Nobel Prize in Chemistry 2019*, https://www.nobelprize.org/prizes/chemistry/2019/press-release/ (accessed: April 3, 2020).

29. M. S. Whittingham, Electrical Energy Storage and Intercalation Chemistry, *Science*, **192**, 1126–1127 (1976).

30. N. Pereira, G. G. Amatucci, M. S. Whittingham, and R. Hamlen, Lithium–titanium disulfide rechargeable cell performance after 35 years of storage, *J. Power Sources*, **280**, 18–22 (2015).

31. K. Mizushima, P. C. Jones, P. J. Wiseman, and J. B. Goodenough, Li_xCoO_2 (0<x<-1): A new cathode material for batteries of high energy density, *Mater. Res. Bull.*, **15**, 783–789 (1980).

32. A. Yoshino, K. Sanechika, and T. Nakajima, Secondary Battery, *Patent*, US 466859 (1987).

33. A. Yoshino, K. Sanechika, and T. Nakajima, Secondary Battery, *Patent*, JP 1989293 (1985).

34. Y. Nishi, The development of lithium ion secondary batteries, *Chem. Rec.*, **1**, 406–413 (2001).

35. D. Andre, S.-J. Kim, P. Lamp, S. F. Lux, F. Maglia, O. Paschos, and B. Stiaszny, Future generations of cathode materials: an automotive industry perspective, *J. Mater. Chem. A*, **3**, 6709–6732 (2015).

36. D. A. Thielmann, D. C. Neef, D. T. Hettesheimer, D. H. Döscher, P. D. M. Wietschel, and P. D. J. Tübke, *Energiespeicher-Roadmap (Update 2017)*, http://www.isi.fraunhofer.de/isi-de/t/projekte/%0Aat-bema2020-batterie2020.php (accessed: April 3, 2020).

37. H. Li, M. Cormier, N. Zhang, J. Inglis, J. Li, and J. R. Dahn, Is Cobalt Needed in Ni-Rich Positive Electrode Materials for Lithium Ion Batteries?, *J. Electrochem. Soc.*, **166**, A429–A439 (2019).

38. J. E. Harlow, X. Ma, J. Li, E. Logan, Y. Liu, N. Zhang, L. Ma, S. L. Glazier, M. M. E. Cormier, M. Genovese, S. Buteau, A. Cameron, J. E. Stark, and J. R. Dahn, A Wide Range of Testing Results on an Excellent Lithium-Ion Cell Chemistry to be used as Benchmarks for New Battery Technologies, *J. Electrochem. Soc.*, **166**, A3031–A3044 (2019).

39. K. Xu, Nonaqueous Liquid Electrolytes for Lithium-Based Rechargeable Batteries, *Chem. Rev.*, **104**, 4303–4418 (2004).

40. M. B. Armand, in D. W. Murphy, J. Broadhead, and B. C. H. Steele, Editors, p. 145–161, Springer US, Boston, MA (1980).

41. P. Rozier and J. M. Tarascon, Review—Li-Rich Layered Oxide Cathodes for Next-Generation Li-Ion Batteries: Chances and Challenges, *J. Electrochem. Soc.*, **162**, A2490–A2499 (2015).

42. U. Müller and C. E. Mortimer, Eds., *Elektrochemie*, in: Chemie., p. 357–359, Georg Thieme Verlag, (2010).

43. J. B. Goodenough and K. S. Park, The Li-ion rechargeable battery: A perspective, *J. Am. Chem. Soc.*, **135**, 1167–1176 (2013).

44. R. Fong, U. van Sacken, and J. R. Dahn, Studies of Lithium Intercalation into Carbons Using Nonaqueous Electrochemical Cells, *J. Electrochem. Soc.*, **137**, 2009–2013 (1990).

45. T. Ohzuku, Zero-Strain Insertion Material of Li $[Li_{1/3}Ti_{5/3}]O_4$ for Rechargeable Lithium Cells, *J. Electrochem. Soc.*, **142**, 1431–1435 (1995).

46. C. P. Sandhya, B. John, and C. Gouri, Lithium titanate as anode material for lithium-ion cells: a review, *Ionics*, **20**, 601–620 (2014).

47. J. Sicklinger, M. Metzger, H. Beyer, D. Pritzl, and H. A. Gasteiger, Ambient Storage Derived Surface Contamination of NCM811 and NCM111: Performance Implications and Mitigation Strategies, *J. Electrochem. Soc.*, **166**, A2322–A2335 (2019).

48. R. Jung, R. Morasch, P. Karayaylali, K. Phillips, F. Maglia, C. Stinner, Y. Shao-Horn, and H. A. Gasteiger, Effect of Ambient Storage on the Degradation of Ni-Rich Positive Electrode Materials (NMC811) for Li-Ion Batteries, *J. Electrochem. Soc.*, **165**, A132–A141 (2018).

49. A. K. Padhi, K. S. Nanjundaswamy, C. Masquelier, S. Okada, and J. B. Goodenough, Effect of Structure on the Fe^{3+}/Fe^{2+} Redox Couple in Iron Phosphates, *J. Electrochem. Soc.*, **144**, 1609–1613 (1997).

50. W.-J. Zhang, Structure and performance of $LiFePO_4$ cathode materials: A review, *J. Power Sources*, **196**, 2962–2970 (2011).

51. P. Verma, P. Maire, and P. Novák, A review of the features and analysis of the solid electrolyte interphase in Li-ion batteries, *Electrochim. Acta*, **55**, 6332–6341 (2010).

52. E. Peled and S. Menkin, Review—SEI: Past, Present and Future, *J. Electrochem. Soc.*, **164**, A1703–A1719 (2017).

53. M. Nie, D. Chalasani, D. P. Abraham, Y. Chen, A. Bose, and B. L. Lucht, Lithium ion battery graphite solid electrolyte interphase revealed by microscopy and spectroscopy, *J. Phys. Chem. C*, **117**, 1257–1267 (2013).

54. S. K. Heiskanen, J. Kim, and B. L. Lucht, Generation and Evolution of the Solid Electrolyte Interphase of Lithium-Ion Batteries, *Joule*, **3**, 2322–2333 (2019).

55. R. Petibon, C. P. Aiken, N. N. Sinha, J. C. Burns, H. Ye, C. M. Vanelzen, G. Jain, S. Trussler, J. R. Dahn, C. P. Aiken, H. Ye, C. M. Vanelzen, G. Jain, S. Trussler, and J. R. Dahn, Comparative study of electrolyte additives using electrochemical impedance spectroscopy on symmetric cells, *J. Power Sources*, **160**, A117–A124 (2014).

56. S. Pérez-Villar, P. Lanz, H. Schneider, and P. Novák, Characterization of a model solid

electrolyte interphase/carbon interface by combined in situ Raman/Fourier transform infrared microscopy, *Electrochim. Acta*, **106**, 506–515 (2013).

57. K. U. Schwenke, S. Solchenbach, J. Demeaux, B. L. Lucht, and H. A. Gasteiger, The Impact of CO_2 Evolved from VC and FEC during Formation of Graphite Anodes in Lithium-Ion Batteries, *J. Electrochem. Soc.*, **166**, A2035–A2047 (2019).

58. M. Metzger, J. Sicklinger, D. Haering, C. Kavakli, C. Stinner, C. Marino, and H. A. Gasteiger, Carbon Coating Stability on High-Voltage Cathode Materials in H_2O-Free and H_2O-Containing Electrolyte, *J. Electrochem. Soc.*, **162**, A1227–A1235 (2015).

59. M. Wetjen, D. Pritzl, R. Jung, S. Solchenbach, R. Ghadimi, and H. A. Gasteiger, Differentiating the Degradation Phenomena in Silicon-Graphite Electrodes for Lithium-Ion Batteries, *J. Electrochem. Soc.*, **164**, A2840–A2852 (2017).

60. M. Metzger, B. Strehle, S. Solchenbach, and H. A. Gasteiger, Analysis of Vinylene Carbonate (VC) as Additive in Graphite/$LiNi_{0.5}Mn_{1.5}O_4$ Cells, *J. Electrochem. Soc.*, **163**, A798–A809 (2016).

61. B. Zhang, M. Metzger, S. Solchenbach, M. Payne, S. Meini, H. A. Gasteiger, A. Garsuch, and B. L. Lucht, Role of 1,3-propane sultone and vinylene carbonate in solid electrolyte interface formation and gas generation, *J. Phys. Chem. C*, **119**, 11337–11348 (2015).

62. C. Xu, F. Lindgren, B. Philippe, M. Gorgoi, F. Björefors, K. Edström, and T. Gustafsson, Improved Performance of the Silicon Anode for Li-Ion Batteries: Understanding the Surface Modification Mechanism of Fluoroethylene Carbonate as an Effective Electrolyte Additive, *Chem. Mater.*, **27**, 2591–2599 (2015).

63. R. Jung, M. Metzger, D. Haering, S. Solchenbach, C. Marino, N. Tsiouvaras, C. Stinner, and H. A. Gasteiger, Consumption of Fluoroethylene Carbonate (FEC) on Si-C Composite Electrodes for Li-Ion Batteries, *J. Electrochem. Soc.*, **163**, A1705–A1716 (2016).

64. B. Strehle, S. Solchenbach, M. Metzger, K. U. Schwenke, and H. A. Gasteiger, The Effect of CO_2 on Alkyl Carbonate Trans-Esterification during Formation of Graphite Electrodes in Li-Ion Batteries, *J. Electrochem. Soc.*, **164**, A2513–A2526 (2017).

65. E. Markevich, G. Salitra, K. Fridman, R. Sharabi, G. Gershinsky, A. Garsuch, G. Semrau, M. A. Schmidt, and D. Aurbach, Fluoroethylene Carbonate as an Important Component in Electrolyte Solutions for High-Voltage Lithium Batteries: Role of Surface Chemistry on the Cathode, *Langmuir*, **30**, 7414–7424 (2014).

66. D. Pritzl, S. Solchenbach, M. Wetjen, and H. A. Gasteiger, Analysis of Vinylene Carbonate (VC) as Additive in Graphite/$LiNi_{0.5}Mn_{1.5}O_4$ Cells, *J. Electrochem. Soc.*, **164**, A2625–A2635 (2017).

67. T. Teufl, D. Pritzl, P. Krieg, B. Strehle, M. A. Mendez, and H. A. Gasteiger, Operating EC-

based Electrolytes with Li- and Mn-Rich NCMs: The Role of O_2-Release on the Choice of the Cyclic Carbonate, *J. Electrochem. Soc.*, **167**, 110505 (2020).

68. L. Ma, S. L. Glazier, R. Petibon, J. Xia, J. M. Peters, Q. Liu, J. Allen, R. N. C. Doig, and J. R. Dahn, A Guide to Ethylene Carbonate-Free Electrolyte Making for Li-Ion Cells, *J. Electrochem. Soc.*, **164**, A5008–A5018 (2016).

69. Y.-M. Song, J.-G. Han, S. Park, K. T. Lee, and N.-S. Choi, A multifunctional phosphite-containing electrolyte for 5 V-class $LiNi_{0.5}Mn_{1.5}O_4$ cathodes with superior electrochemical performance, *J. Mater. Chem. A*, **2**, 9506–9513 (2014).

70. Y. Dong, J. Demeaux, and B. L. Lucht, Investigation of the Effect of Added Methylene Ethylene Carbonate (MEC) and Vinylene Carbonate (VC) on $LiNi_{0.5}Mn_{1.5}O_4$/Graphite Cell Performance, *J. Electrochem. Soc.*, **163**, A2413–A2417 (2016).

71. R. Jung, M. Metzger, F. Maglia, C. Stinner, and H. A. Gasteiger, Oxygen Release and Its Effect on the Cycling Stability of $LiNi_xMn_yCo_zO_2$ (NMC) Cathode Materials for Li-Ion Batteries, *J. Electrochem. Soc.*, **164**, A1361–A1377 (2017).

72. R. Jung, M. Metzger, F. Maglia, C. Stinner, and H. A. Gasteiger, Chemical versus Electrochemical Electrolyte Oxidation on NMC111, NMC622, NMC811, LNMO, and Conductive Carbon, *J. Phys. Chem. Lett.*, **8**, 4820–4825 (2017).

73. L. E. Downie, S. R. Hyatt, and J. R. Dahn, The Impact of Electrolyte Composition on Parasitic Reactions in Lithium Ion Cells Charged to 4.7 V Determined Using Isothermal Microcalorimetry, *J. Electrochem. Soc.*, **163**, A35–A42 (2015).

74. T. Teufl, D. Pritzl, S. Solchenbach, M. A. Mendez, and H. A. Gasteiger, Thermal Stability of FEC-Based Electrolytes for High-Voltage Li-Ion Batteries, *to be published*.

75. B. Aktekin, R. Younesi, W. Zipprich, C. Tengstedt, D. Brandell, and K. Edström, The Effect of the Fluoroethylene Carbonate Additive in $LiNi_{0.5}Mn_{1.5O4}$ - $Li_4Ti_5O_{12}$ Lithium-Ion Cells, *J. Electrochem. Soc.*, **164**, A942–A948 (2017).

76. T. Teulf, D. Pritzl, S. Solchenbach, H. A. Gasteiger, and M. Mendez, Thermal Stability of Fluoroethylene Carbonate (FEC) Containing Electrolytes Using $LiPF_6$ As Conductive Salt, *ECS Meeting Abstracts*, **MA2018-02**, 456 (2018).

77. W. Xu, J. Wang, F. Ding, X. Chen, E. Nasybulin, Y. Zhang, and J.-G. Zhang, Lithium metal anodes for rechargeable batteries, *Energy Environ. Sci.*, **7**, 513–537 (2014).

78. J. Wandt, C. Marino, H. A. Gasteiger, P. Jakes, R.-A. Eichel, and J. Granwehr, Operando electron paramagnetic resonance spectroscopy – formation of mossy lithium on lithium anodes during charge–discharge cycling, *Energy Environ. Sci.*, **8**, 1358–1367 (2015).

79. D. Lu, Y. Shao, T. Lozano, W. D. Bennett, G. L. Graff, B. Polzin, J. Zhang, M. H. Engelhard, N. T. Saenz, W. A. Henderson, P. Bhattacharya, J. Liu, and J. Xiao, Failure Mechanism for Fast-Charged Lithium Metal Batteries with Liquid Electrolytes, *Adv. Energy Mater.*, **5**, 1400993 (2015).

80. D. Ma, Z. Cao, and A. Hu, Si-Based Anode Materials for Li-Ion Batteries: A Mini Review, *Nano-Micro Lett.*, **6**, 347–358 (2014).

81. M. N. Obrovac, L. Christensen, D. B. Le, and J. R. Dahn, Alloy Design for Lithium-Ion Battery Anodes, *J. Electrochem. Soc.*, **154**, A849 (2007).

82. T. Krauskopf, B. Mogwitz, C. Rosenbach, W. G. Zeier, and J. Janek, Diffusion Limitation of Lithium Metal and Li–Mg Alloy Anodes on LLZO Type Solid Electrolytes as a Function of Temperature and Pressure, *Adv. Energy Mater.*, **9**, 1902568 (2019).

83. Y. Kato, R. Saito, M. Sakano, A. Mitsui, M. Hirayama, and R. Kanno, Synthesis, structure and lithium ionic conductivity of solid solutions of $Li_{10}(Ge_{1-x}M_x)P_2S_{12}$ (M = Si, Sn), *J. Power Sources*, **271**, 60–64 (2014).

84. T. Krauskopf, F. H. Richter, W. G. Zeier, and J. Janek, Physicochemical Concepts of the Lithium Metal Anode in Solid-State Batteries, *Chem. Rev.*, **120**, 7745–7794 (2020).

85. D. Aurbach, B. D. McCloskey, L. F. Nazar, and P. G. Bruce, Advances in understanding mechanisms underpinning lithium-air batteries, *Nat. Energy*, **1**, 16128 (2016).

86. Y.-C. Lu, H. A. Gasteiger, M. C. Parent, V. Chiloyan, and Y. Shao-Horn, The Influence of Catalysts on Discharge and Charge Voltages of Rechargeable Li–Oxygen Batteries, *Electrochem. Solid-State Lett.*, **13**, A69–A72 (2010).

87. H. Beyer, S. Meini, N. Tsiouvaras, M. Piana, and H. A. Gasteiger, Thermal and electrochemical decomposition of lithium peroxide in non-catalyzed carbon cathodes for Li–air batteries, *Phys. Chem. Chem. Phys.*, **15**, 11025–11037 (2013).

88. K. G. Gallagher, S. Goebel, T. Greszler, M. Mathias, L. Berkeley, W. Oelerich, D. Eroglu, and V. Srinivasan, Quantifying the promise of lithium–air batteries for electric vehicles, *Energy Environ. Sci.*, **7**, 1555–1563 (2014).

89. O. Gröger, H. A. Gasteiger, and J.-P. Suchsland, Review—Electromobility: Batteries or Fuel Cells?, *J. Electrochem. Soc.*, **162**, A2605–A2622 (2015).

90. M. N. Obrovac and V. L. Chevrier, Alloy Negative Electrodes for Li-Ion Batteries, *Chem. Rev.*, **114**, 11444–11502 (2014).

91. Y. Jin, B. Zhu, Z. Lu, N. Liu, and J. Zhu, Challenges and Recent Progress in the Development of Si Anodes for Lithium-Ion Battery, *Adv. Energy Mater.*, **7**, 1700715 (2017).

92. R. Petibon, V. L. Chevrier, C. P. Aiken, D. S. Hall, S. R. Hyatt, R. Shunmugasundaram, and J. R. Dahn, Studies of the Capacity Fade Mechanisms of $LiCoO_2$/Si-Alloy: Graphite Cells, *J. Electrochem. Soc.*, **163**, A1146–A1156 (2016).

93. J. Lyubina, Phase transformations and hysteresis in Si-based anode materials, *Appl. Phys. Lett.*, **118**, 90501 (2021).

94. Y. Jiang, G. Offer, J. Jiang, M. Marinescu, and H. Wang, Voltage Hysteresis Model for Silicon Electrodes for Lithium Ion Batteries, Including Multi-Step Phase Transformations, Crystallization and Amorphization, *J. Electrochem. Soc.*, **167**, 130533 (2020).

95. M. M. Thackeray, S.-H. Kang, C. S. Johnson, J. T. Vaughey, R. Benedek, and S. A. Hackney, Li_2MnO_3-stabilized $LiMO_2$ (M = Mn, Ni, Co) electrodes for lithium-ion batteries, *J. Mater. Chem.*, **17**, 3112 (2007).

96. R. Schmuch, R. Wagner, G. Hörpel, T. Placke, and M. Winter, Performance and cost of materials for lithium-based rechargeable automotive batteries, *Nat. Energy*, **3**, 267–278 (2018).

97. K. Amine, Olivine $LiCoPO_4$ as 4.8 V Electrode Material for Lithium Batteries, *Electrochem. Solid-State Lett.*, **3**, 178 (1999).

98. A. Mauger and C. M. Julien, Olivine Positive Electrodes for Li-Ion Batteries: Status and Perspectives, *Batteries*, **4**, 1–32 (2018).

99. S. Solchenbach, M. Wetjen, D. Pritzl, K. U. Schwenke, and H. A. Gasteiger, Lithium Oxalate as Capacity and Cycle-Life Enhancer in LNMO/Graphite and LNMO/SiG Full Cells, *J. Electrochem. Soc.*, **165**, A512–A524 (2018).

100. T.-F. Yi, J. Mei, and Y.-R. Zhu, Key strategies for enhancing the cycling stability and rate capacity of $LiNi_{0.5}Mn_{1.5}O_4$ as high-voltage cathode materials for high power lithium-ion batteries, *J. Power Sources*, **316**, 85–105 (2016).

101. G. Liang, V. K. Peterson, K. W. See, Z. Guo, and W. K. Pang, Developing high-voltage spinel $LiNi_{0.5}Mn_{1.5}O_4$ cathodes for high-energy-density lithium-ion batteries: current achievements and future prospects, *J. Mater. Chem. A*, **8**, 15373–15398 (2020).

102. J. R. Croy, M. Balasubramanian, K. G. Gallagher, and A. K. Burrell, Review of the U.S. Department of Energy's "Deep Dive" Effort to Understand Voltage Fade in Li- and Mn-Rich Cathodes, *Acc. Chem. Res.*, **48**, 2813–2821 (2015).

103. Z. Zou, H. Xu, H. Zhang, Y. Tang, and G. Cui, Electrolyte Therapy for Improving the Performance of $LiNi_{0.5}Mn_{1.5}O_4$ Cathodes Assembled Lithium–Ion Batteries, *ACS Appl. Mater. Interfaces*, **12**, 21368–21385 (2020).

104. J. R. Croy, K. G. Gallagher, M. Balasubramanian, B. R. Long, and M. M. Thackeray,

Quantifying Hysteresis and Voltage Fade in $xLi_2MnO_3 \cdot (1-x)LiMn_{0.5}Ni_{0.5}O_2$ Electrodes as a Function of Li_2MnO_3 Content, *J. Electrochem. Soc.*, **161**, A318–A325 (2013).

105. A. Boulineau, L. Simonin, J.-F. Colin, E. Canévet, L. Daniel, and S. Patoux, Evolutions of $Li_{1.2}Mn_{0.61}Ni_{0.18}Mg_{0.01}O_2$ during the Initial Charge/Discharge Cycle Studied by Advanced Electron Microscopy, *Chem. Mater.*, **24**, 3558–3566 (2012).

106. B. Zeuner, An Obsolescing Bargain in a Rentier State: Multinationals, Artisanal Miners, and Cobalt in the Democratic Republic of Congo, *Front. Energy Res.*, **6**, 123 (2018).

107. L. Kraft, T. Zünd, D. Schreiner, R. Wilhelm, F. J. Günter, G. Reinhart, H. A. Gasteiger, and A. Jossen, Comparative Evaluation of LMR-NCM and NCA Cathode Active Materials in Multilayer Lithium-Ion Pouch Cells: Part II. Rate Capability, Long-Term Stability, and Thermal Behavior, *J. Electrochem. Soc.*, **168**, 020537 (2021).

108. A. R. Armstrong, M. Holzapfel, P. Novák, C. S. Johnson, S.-H. Kang, M. M. Thackeray, and P. G. Bruce, Demonstrating Oxygen Loss and Associated Structural Reorganization in the Lithium Battery Cathode $Li[Ni_{0.2}Li_{0.2}Mn_{0.6}]O_2$, *J. Am. Chem. Soc.*, **128**, 8694–8698 (2006).

109. F. La Mantia, F. Rosciano, N. Tran, and P. Novák, Direct evidence of oxygen evolution from $Li_{1+x}(Ni_{1/3}Mn_{1/3}Co_{1/3})_{1-x}O_2$ at high potentials, *J. Appl. Electrochem.*, **38**, 893–896 (2008).

110. P. Lanz, H. Sommer, M. Schulz-Dobrick, and P. Novák, Oxygen release from high-energy $xLi_2MnO_3 \cdot (1-x)LiMO_2$ (M = Mn, Ni, Co): Electrochemical, differential electrochemical mass spectrometric, in situ pressure, and in situ temperature characterization, *Electrochim. Acta*, **93**, 114–119 (2013).

111. B. Strehle, K. Kleiner, R. Jung, F. Chesneau, M. Mendez, H. A. Gasteiger, and M. Piana, The Role of Oxygen Release from Li- and Mn-Rich Layered Oxides during the First Cycles Investigated by On-Line Electrochemical Mass Spectrometry, *J. Electrochem. Soc.*, **164**, A400–A406 (2017).

112. Z. Lu, L. Y. Beaulieu, R. A. Donaberger, C. L. Thomas, and J. R. Dahn, Synthesis, Structure, and Electrochemical Behavior of $Li[Ni_xLi_{1/3-2x/3}Mn_{2/3-x/3}]O_2$, *J. Electrochem. Soc.*, **149**, A778 (2002).

113. Z. Lu and J. R. Dahn, Understanding the Anomalous Capacity of $Li/Li[Ni_xLi_{(1/3-2x/3)}Mn_{(2/3-x/3)}]O_2$ Cells Using In Situ X-Ray Diffraction and Electrochemical Studies, *J. Electrochem. Soc.*, **149**, A815 (2002).

114. D. Mohanty, J. Li, S. C. Nagpure, D. L. Wood, and C. Daniel, Understanding the structure and structural degradation mechanisms in high-voltage, lithium-manganese–rich lithium-ion battery cathode oxides: A review of materials diagnostics, *MRS Energy Sustain.*, **2**, E15 (2015).

115. N. Yabuuchi, K. Yoshii, S. T. Myung, I. Nakai, and S. Komaba, Detailed studies of a high-

capacity electrode material for rechargeable batteries, Li_2MnO_3-$LiCo_{1/3}Ni_{1/3}Mn_{1/3}O_2$, *J. Am. Chem. Soc.*, **133**, 4404–4419 (2011).

116. H. Koga, L. Croguennec, M. Menetrier, K. Douhil, S. Belin, L. Bourgeois, E. Suard, F. Weill, and C. Delmas, Reversible Oxygen Participation to the Redox Processes Revealed for $Li_{1.20}Mn_{0.54}Co_{0.13}Ni_{0.13}O_2$, *J. Electrochem. Soc.*, **160**, A786–A792 (2013).

117. E. McCalla, A. M. Abakumov, M. Saubanère, D. Foix, E. J. Berg, G. Rousse, M.-L. Doublet, D. Gonbeau, P. Novák, G. Van Tendeloo, R. Dominko, and J.-M. Tarascon, Visualization of O-O peroxo-like dimers in high-capacity layered oxides for Li-ion batteries, *Science*, **350**, 1516–1521 (2015).

118. H. Koga, L. Croguennec, M. Ménétrier, P. Mannessiez, F. Weill, and C. Delmas, Different oxygen redox participation for bulk and surface: A possible global explanation for the cycling mechanism of $Li_{1.20}Mn_{0.54}Co_{0.13}Ni_{0.13}O_2$, *J. Power Sources*, **236**, 250–258 (2013).

119. D.-H. Seo, J. Lee, A. Urban, R. Malik, S. Kang, and G. Ceder, The structural and chemical origin of the oxygen redox activity in layered and cation-disordered Li-excess cathode materials, *Nat. Chem.*, **8**, 692–697 (2016).

120. W. E. Gent, K. Lim, Y. Liang, Q. Li, T. Barnes, S.-J. Ahn, K. H. Stone, M. McIntire, J. Hong, J. H. Song, Y. Li, A. Mehta, S. Ermon, T. Tyliszczak, D. Kilcoyne, D. Vine, J.-H. Park, and S.-K. Doo, M. F. Toney, W. Yang, D. Prendergast, W. C. Chueh, Coupling between oxygen redox and cation migration explains unusual electrochemistry in lithium-rich layered oxides, *Nat. Commun.*, **8**, 2091 (2017).

121. S. Zhao, K. Yan, J. Zhang, B. Sun, and G. Wang, Reaction Mechanisms of Layered Lithium-Rich Cathode Materials for High-Energy Lithium-Ion Batteries, *Angew. Chemie Int. Ed.*, **60**, 2208–2220 (2021).

122. S. R. Gowda, D. W. Dees, A. N. Jansen, and K. G. Gallagher, Examining the Electrochemical Impedance at Low States of Charge in Lithium- and Manganese-Rich Layered Transition-Metal Oxide Electrodes, *J. Electrochem. Soc.*, **162**, A1374–A1381 (2015).

123. T. Teufl, D. Pritzl, S. Solchenbach, H. A. Gasteiger, and M. A. Mendez, Editors' Choice—State of Charge Dependent Resistance Build-Up in Li- and Mn-Rich Layered Oxides during Lithium Extraction and Insertion, *J. Electrochem. Soc.* , **166**, A1275–A1284 (2019).

124. S. Solchenbach, G. Hong, A. T. S. Freiberg, R. Jung, and H. A. Gasteiger, Electrolyte and SEI Decomposition Reactions of Transition Metal Ions Investigated by On-Line Electrochemical Mass Spectrometry, *J. Electrochem. Soc.*, **165**, A3304–A3312 (2018).

125. H. Zheng, Q. Sun, G. Liu, X. Song, and V. S. Battaglia, Correlation between dissolution behavior and electrochemical cycling performance for $LiNi_{1/3}Co_{1/3}Mn_{1/3}O_2$-based cells, *J.*

Power Sources, **207**, 134–140 (2012).

126. K. Amine, Z. Chen, Z. Zhang, J. Liu, W. Lu, Y. Qin, J. Lu, L. Curtis, and Y.-K. Sun, Mechanism of capacity fade of MCMB/$Li_{1.1}[Ni_{1/3}Mn_{1/3}Co_{1/3}]_{0.9}O_2$cell at elevated temperature and additives to improve its cycle life, *J. Mater. Chem.*, **21**, 17754–17759 (2011).

127. F. Friedrich, B. Strehle, A. T. S. Freiberg, K. Kleiner, S. J. Day, C. Erk, M. Piana, and H. A. Gasteiger, Editors' Choice—Capacity Fading Mechanisms of NCM-811 Cathodes in Lithium-Ion Batteries Studied by X-ray Diffraction and Other Diagnostics, *J. Electrochem. Soc.*, **166**, A3760–A3774 (2019).

128. T. Teufl, B. Strehle, P. Müller, H. A. Gasteiger, and M. A. Mendez, Oxygen Release and Surface Degradation of Li- and Mn-Rich Layered Oxides in Variation of the Li_2MnO_3 Content, *J. Electrochem. Soc.*, **165**, A2718–A2731 (2018).

129. J. Zheng, X. Wu, and Y. Yang, Improved electrochemical performance of $Li[Li_{0.2}Mn_{0.54}Ni_{0.13}Co_{0.13}]O_2$ cathode material by fluorine incorporation, *Electrochim. Acta*, **105**, 200–208 (2013).

130. S. Krishna Kumar, S. Ghosh, and S. K. Martha, Synergistic effect of magnesium and fluorine doping on the electrochemical performance of lithium-manganese rich (LMR)-based Ni-Mn-Co-oxide (NMC) cathodes for lithium-ion batteries, *Ionics*, **23**, 1655–1662 (2017).

131. X. Feng, Y. Gao, L. Ben, Z. Yang, Z. Wang, and L. Chen, Enhanced electrochemical performance of Ti-doped $Li_{1.2}Mn_{0.54}Co_{0.13}Ni_{0.13}O_2$ for lithium-ion batteries, *J. Power Sources*, **317**, 74–80 (2016).

132. U. Breddemann, E. M. Erickson, V. Davis, F. Schipper, M. Ellwanger, M. Daub, A. Hoffmann, C. Erk, B. Markovsky, D. Aurbach, and I. Krossing, Fluorination of Li-Rich Lithium-Ion-Battery Cathode Materials by Fluorine Gas: Chemistry, Characterization, and Electrochemical Performance in Half Cells, *ChemElectroChem*, **6**, 3337–3349 (2019).

133. E. M. Erickson, H. Sclar, F. Schipper, J. Liu, R. Tian, C. Ghanty, L. Burstein, N. Leifer, J. Grinblat, M. Talianker, J. Y. Shin, J. K. Lampert, B. Markovsky, A. I. Frenkel, and D. Aurbach, High-Temperature Treatment of Li-Rich Cathode Materials with Ammonia: Improved Capacity and Mean Voltage Stability during Cycling, *Adv. Energy Mater.*, **7**, 1700708 (2017).

134. J. Sicklinger, H. Beyer, L. Hartmann, F. Riewald, C. Sedlmeier, and H. A. Gasteiger, SO_3 Treatment of Lithium- and Manganese-Rich NCMs for Li-Ion Batteries: Enhanced Robustness towards Humid Ambient Air and Improved Full-Cell Performance, *J. Electrochem. Soc.*, **167**, 130507 (2020).

135. H. Sclar, J. Sicklinger, E. M. Erickson, S. Maiti, J. Grinblat, M. Talianker, F. Amalraj Susai, L. Burstein, H. Beyer, L. Hartmann, G. Avruschenko, H. A. Gasteiger, B. Markovsky, and D.

Aurbach, Enhancement of Electrochemical Performance of Lithium and Manganese-Rich Cathode Materials via Thermal Treatment with SO_2, *J. Electrochem. Soc.*, **167**, 110563 (2020).

136. M. Metzger, H. Beyer, J. Sicklinger, D. Pritzl, B. Strehle, H. Gasteiger, H. Sclar, E. Erickson, F. A. Susai, J. Grinblat, D. Aurbach, and B. Markovsky, Process for making a cathode active material for a lithium ion battery, *Patent Application*, WO/2019/002116A1 (2019).

137. J. Zheng, M. Gu, J. Xiao, B. J. Polzin, P. Yan, X. Chen, C. Wang, and J.-G. Zhang, Functioning Mechanism of AlF_3 Coating on the Li- and Mn-Rich Cathode Materials, *Chem. Mater.*, **26**, 6320–6327 (2014).

138. X.-D. Zhang, J.-L. Shi, J.-Y. Liang, Y.-X. Yin, J.-N. Zhang, X.-Q. Yu, and Y.-G. Guo, Suppressing Surface Lattice Oxygen Release of Li-Rich Cathode Materials via Heterostructured Spinel $Li_4Mn_5O_{12}$ Coating, *Adv. Mater.*, **30**, 1801751 (2018).

139. P. Oh, B. Song, W. Li, and A. Manthiram, Overcoming the chemical instability on exposure to air of Ni-rich layered oxide cathodes by coating with spinel $LiMn_{1.9}Al_{0.1}O_4$, *J. Mater. Chem. A*, **4**, 5839–5841 (2016).

140. J. Helbig, T. Beuse, V. Siozios, T. Placke, M. Winter, and R. Schmuch, Li/Mn-Rich Cathode Materials with Low-Cobalt Content and Core-Shell Particle Design for High-Energy Lithium Ion Batteries, *J. Electrochem. Soc.*, **167**, 60519 (2020).

141. J. Li, R. Doig, H. Liu, G. Botton, and J. R. Dahn, The Effect of Interdiffusion on the Properties of Lithium-Rich Core-Shell Cathodes, *J. Electrochem. Soc.*, **163**, A2841–A2848 (2016).

142. H. Li, N. Zhang, J. Li, and J. R. Dahn, Updating the Structure and Electrochemistry of Li_xNiO_2 for $0 \leq x \leq 1$, *J. Electrochem. Soc.*, **165**, A2985–A2993 (2018).

143. M. Bianchini, M. Roca-Ayats, P. Hartmann, T. Brezesinski, and J. Janek, There and Back Again—The Journey of $LiNiO_2$ as a Cathode Active Material, *Angew. Chemie Int. Ed.*, **58**, 10434–10458 (2019).

144. H.-J. J. Noh, S. Youn, C. S. S. Yoon, and Y.-K. K. Sun, Comparison of the structural and electrochemical properties of layered $Li[Ni_xCo_yMn_z]O_2$ (x = 1/3, 0.5, 0.6, 0.7, 0.8 and 0.85) cathode material for lithium-ion batteries, *J. Power Sources*, **233**, 121–130 (2013).

145. H. Gabrisch, T. Yi, and R. Yazami, Transmission Electron Microscope Studies of $LiNi_{1/3}Mn_{1/3}Co_{1/3}O_2$ before and after Long-Term Aging at 70°C, *Electrochem. Solid-State Lett.*, **11**, A119–A124 (2008).

146. S.-K. Jung, H. Gwon, J. Hong, K.-Y. Park, D.-H. Seo, H. Kim, J. Hyun, W. Yang, and K. Kang, Understanding the Degradation Mechanisms of $LiNi_{0.5}Co_{0.2}Mn_{0.3}O_2$ Cathode Material in Lithium Ion Batteries, *Adv. Energy Mater.*, **4**, 1300787 (2014).

147. R. Jung, M. Metzger, F. Maglia, C. Stinner, and H. A. Gasteiger, Oxygen Release and Its Effect on the Cycling Stability of $LiNi_xMn_yCo_zO_2$(NMC) Cathode Materials for Li-Ion Batteries, *J. Electrochem. Soc.*, **164**, A1361–A1377 (2017).

148. H. Li, A. Liu, N. Zhang, Y. Wang, S. Yin, H. Wu, and J. R. Dahn, An Unavoidable Challenge for Ni-Rich Positive Electrode Materials for Lithium-Ion Batteries, *Chem. Mater.*, **31**, 7574–7583 (2019).

149. C. M. Julien and A. Mauger, NCA, NCM811, and the Route to Ni-Richer Lithium-Ion Batteries, *Energies*, **13**, 1–46 (2020).

150. E. Talaie, P. Bonnick, X. Sun, Q. Pang, X. Liang, and L. F. Nazar, Methods and protocols for electrochemical energy storage materials research, *Chem. Mater.*, **29**, 90–105 (2017).

151. L. de Biasi, A. O. Kondrakov, H. Geßwein, T. Brezesinski, P. Hartmann, and J. Janek, Between Scylla and Charybdis – Balancing Among Structural Stability and Energy Density of Layered NCM Cathode Materials for Advanced Lithium-Ion Batteries, *J. Phys. Chem. C*, **121**, 26163–26171 (2017).

152. M. M. Besli, S. Xia, S. Kuppan, Y. Huang, M. Metzger, A. K. Shukla, G. Schneider, S. Hellstrom, J. Christensen, M. M. Doeff, and Y. Liu, Mesoscale Chemomechanical Interplay of the $LiNi_{0.8}Co_{0.15}Al_{0.05}O_2$ Cathode in Solid-State Polymer Batteries, *Chem. Mater.*, **31**, 491–501 (2019).

153. S.-M. Bak, K.-W. Nam, W. Chang, X. Yu, E. Hu, S. Hwang, E. A. Stach, K.-B. Kim, K. Y. Chung, and X.-Q. Yang, Correlating Structural Changes and Gas Evolution during the Thermal Decomposition of Charged $LixNi_{0.8}Co_{0.15}Al_{0.05}O_2$ Cathode Materials, *Chem. Mater.*, **25**, 337–351 (2013).

154. S.-M. Bak, E. Hu, Y. Zhou, X. Yu, S. D. Senanayake, S.-J. Cho, K.-B. Kim, K. Y. Chung, X.-Q. Yang, and K.-W. Nam, Structural Changes and Thermal Stability of Charged $LiNi_xMn_yCo_zO_2$ Cathode Materials Studied by Combined In Situ Time-Resolved XRD and Mass Spectroscopy, *ACS Appl. Mater. Interfaces*, **6**, 22594–22601 (2014).

155. R. Jung, P. Strobl, F. Maglia, C. Stinner, and H. A. Gasteiger, Temperature Dependence of Oxygen Release from $LiNi_{0.6}Mn_{0.2}Co_{0.2}O_2$ (NMC622) Cathode Materials for Li-Ion Batteries, *J. Electrochem. Soc.*, **165**, A2869–A2879 (2018).

156. L. Ma, M. Nie, J. Xia, and J. R. Dahn, A systematic study on the reactivity of different grades of charged $Li[Ni_xMn_yCo_z]O_2$ with electrolyte at elevated temperatures using accelerating rate calorimetry, *J. Power Sources*, **327**, 145–150 (2016).

157. L. Kong, C. Li, J. Jiang, and M. Pecht, Li-Ion Battery Fire Hazards and Safety Strategies, *Energies*, **11**, 2191 (2018).

158. J. Wandt, A. T. S. Freiberg, A. Ogrodnik, and H. A. Gasteiger, Singlet oxygen evolution from layered transition metal oxide cathode materials and its implications for lithium-ion batteries, *Mater. Today*, **21**, 825–833 (2018).

159. A. T. S. Freiberg, M. K. Roos, J. Wandt, R. de Vivie-Riedle, and H. A. Gasteiger, Singlet Oxygen Reactivity with Carbonate Solvents Used for Li-Ion Battery Electrolytes, *J. Phys. Chem. A*, **122**, 8828–8839 (2018).

160. J. Xia, R. Petibon, D. Xiong, L. Ma, and J. R. Dahn, Enabling linear alkyl carbonate electrolytes for high voltage Li-ion cells, *J. Power Sources*, **328**, 124–135 (2016).

161. N. V. Faenza, L. Bruce, Z. W. Lebens-Higgins, I. Plitz, N. Pereira, L. F. J. Piper, and G. G. Amatucci, Editors' Choice—Growth of Ambient Induced Surface Impurity Species on Layered Positive Electrode Materials and Impact on Electrochemical Performance, *J. Electrochem. Soc.*, **164**, A3727–A3741 (2017).

162. F. A. Susai, H. Sclar, S. Maiti, L. Burstein, O. Perkal, J. Grinblat, M. Talianker, S. Ruthstein, C. Erk, P. Hartmann, B. Markovsky, and D. Aurbach, Stabilized Behavior of $LiNi_{0.85}Co_{0.10}Mn_{0.05}O_2$ Cathode Materials Induced by Their Treatment with SO_2, *ACS Appl. Energy Mater.*, **3**, 3609–3618 (2020).

163. U. Breddemann, J. Sicklinger, F. Schipper, V. Davis, A. Fischer, K. Huber, E. M. Erickson, M. Daub, A. Hoffmann, C. Erk, B. Markovsky, D. Aurbach, H. A. Gasteiger, and I. Krossing, Fluorination of Ni-Rich Lithium-Ion Battery Cathode Materials by Fluorine Gas: Chemistry, Characterization, and Electrochemical Performance in Full-cells, *Batter. Supercaps*, **4**, 632–645 (2021).

164. S. Neudeck, A. Mazilkin, C. Reitz, P. Hartmann, J. Janek, and T. Brezesinski, Effect of Low-Temperature Al_2O_3 ALD Coating on Ni-Rich Layered Oxide Composite Cathode on the Long-Term Cycling Performance of Lithium-Ion Batteries, *Sci. Rep.*, **9**, 5328 (2019).

165. S.-T. Myung, H.-J. Noh, S.-J. Yoon, E.-J. Lee, and Y.-K. Sun, Progress in High-Capacity Core–Shell Cathode Materials for Rechargeable Lithium Batteries, *J. Phys. Chem. Lett.*, **5**, 671–679 (2014).

166. D.-W. Jun, C. S. Yoon, U.-H. Kim, and Y.-K. Sun, High-Energy Density Core–Shell Structured $Li[Ni_{0.95}Co_{0.025}Mn_{0.025}]O_2$ Cathode for Lithium-Ion Batteries, *Chem. Mater.*, **29**, 5048–5052 (2017).

167. F. Schipper, H. Bouzaglo, M. Dixit, E. M. Erickson, T. Weigel, M. Talianker, J. Grinblat, L. Burstein, M. Schmidt, J. Lampert, C. Erk, B. Markovsky, D. T. Major, and D. Aurbach, From Surface ZrO_2 Coating to Bulk Zr Doping by High Temperature Annealing of Nickel-Rich Lithiated Oxides and Their Enhanced Electrochemical Performance in Lithium Ion Batteries,

Adv. Energy Mater., **8**, 1701682 (2018).

168. A. Liu, N. Zhang, H. Li, J. Inglis, Y. Wang, S. Yin, H. Wu, and J. R. Dahn, Investigating the Effects of Magnesium Doping in Various Ni-Rich Positive Electrode Materials for Lithium Ion Batteries, *J. Electrochem. Soc.*, **166**, A4025–A4033 (2019).

169. M. Metzger, H. Beyer, J. Sicklinger, D. Pritzl, B. Strehle, H. Gasteiger, H. Sclar, E. Erickson, F. A. Susai, J. Grinblat, D. Aurbach, and B. Markovsky, Process for making a cathode active material for a lithium ion battery, *WIPO Pat. No. WO 2019/002116 A1* (2019).

170. I. A. Shkrob, J. A. Gilbert, P. J. Phillips, R. Klie, R. T. Haasch, J. Bareño, and D. P. Abraham, Chemical Weathering of Layered Ni-Rich Oxide Electrode Materials: Evidence for Cation Exchange, *J. Electrochem. Soc.*, **164**, A1489–A1498 (2017).

171. P. Novák, F. Joho, R. Imhof, J. Panitz, and O. Haas, In situ investigation of the interaction between graphite and electrolyte solutions, *J. Power Sources*, **81**–**82**, 212–216 (1999).

172. H. Ota, Y. Sakata, A. Inoue, and S. Yamaguchi, Analysis of Vinylene Carbonate Derived SEI Layers on Graphite Anode, *J. Electrochem. Soc.*, **151**, A1659–A1669 (2004).

173. R. Bernhard, M. Metzger, and H. A. Gasteiger, Gas Evolution at Graphite Anodes Depending on Electrolyte Water Content and SEI Quality Studied by On-Line Electrochemical Mass Spectrometry, *J. Electrochem. Soc.*, **162**, A1984–A1989 (2015).

174. M. Nie, D. Chalasani, D. P. Abraham, Y. Chen, A. Bose, and B. L. Lucht, Lithium Ion Battery Graphite Solid Electrolyte Interphase Revealed by Microscopy and Spectroscopy, *J. Phys. Chem. C*, **117**, 1257–1267 (2013).

175. G. V Zhuang, H. Yang, B. Blizanac, and P. N. Ross, A Study of Electrochemical Reduction of Ethylene and Propylene Carbonate Electrolytes on Graphite Using ATR-FTIR Spectroscopy, *Electrochem. Solid-State Lett.*, **8**, A441–A445 (2005).

176. C. M. Burba and R. Frech, Raman and FTIR Spectroscopic Study of Li_xFePO_4 ($0 \leq x \leq 1$), *J. Electrochem. Soc.*, **151**, A1032 (2004).

177. Y. B. Yohannes, S. D. Lin, N.-L. Wu, and B.-J. Hwang, SEI Grown on MCMB-Electrode with Fluoroethylene Carbonate and Vinylene Carbonate Additives as Probed by In Situ DRIFTS, *J. Electrochem. Soc.*, **166**, A2741–A2748 (2019).

178. Y. Ein-Eli, B. Markovsky, D. Aurbach, Y. Carmeli, H. Yamin, and S. Luski, The dependence of the performance of Li-C intercalation anodes for Li-ion secondary batteries on the electrolyte solution composition, *Electrochim. Acta*, **39**, 2559–2569 (1994).

179. K. U. Schwenke, Analysis of electrolyte stability and the effect of contaminants in aprotic Li-O_2 cells, Ph.D. thesis, Techical University of Munich (2015).

180. S. R. Culler, *Diffusive Reflectance Infrared Spectroscopy: Sampling Techniques for Qualitative/Quantitative Analysis of Solids, in: Practical Sampling Techniques for Infrared Analysis* P. B. Coleman, Editor, 1st ed., p. 94–104, CRC Press, Boca Raton, (1993).

181. F. Joho and P. Novák, SNIFTIRS investigation of the oxidative decomposition of organic-carbonate-based electrolytes for lithium-ion cells, *Electrochim. Acta*, **45**, 3589–3599 (2000).

182. M. Matsui, S. Deguchi, H. Kuwata, and N. Imanishi, In-operando FTIR Spectroscopy for Composite Electrodes of Lithium-ion Batteries, *Electrochemistry*, **83**, 874–878 (2015).

183. A. M. Haregewoin, T.-D. Shie, S. D. Lin, B.-J. Hwang, and F.-M. Wang, An Effective In situ DRIFTS Analysis of the Solid Electrolyte Interface in Lithium Ion Battery Atetegeb Meazah Haregewoin, *ECS Trans.*, **53**, 23–32 (2013).

184. S.-T. Myung and H. Yashiro, Electrochemical stability of aluminum current collector in alkyl carbonate electrolytes containing lithium bis(pentafluoroethylsulfonyl)imide for lithium-ion batteries, *J. Power Sources*, **271**, 167–173 (2014).

185. S.-T. Myung, Y. Sasaki, S. Sakurada, Y.-K. Sun, and H. Yashiro, Electrochemical behavior of current collectors for lithium batteries in non-aqueous alkyl carbonate solution and surface analysis by ToF-SIMS, *Electrochim. Acta*, **55**, 288–297 (2009).

186. P. Pasierb, S. Komornicki, M. Rokita, and M. Rękas, Structural properties of Li_2CO_3–$BaCO_3$ system derived from IR and Raman spectroscopy, *J. Mol. Struct.*, **596**, 151–156 (2001).

187. W.-L. Wang, H. Jiang, Z. Liu, and X. Liu, Effects of base concentration and cation on hydrothermal processes of cetyltrimethylammonium permanganate in various aqueous media, *J. Mater. Chem.*, **15**, 1002–1010 (2005).

188. S. Meini, N. Tsiouvaras, K. U. Schwenke, M. Piana, H. Beyer, L. Lange, and H. A. Gasteiger, Rechargeability of Li–air cathodes pre-filled with discharge products using an ether-based electrolyte solution: implications for cycle-life of Li–air cells, *Phys. Chem. Chem. Phys.*, **15**, 11478–11493 (2013).

189. C. M. Sedlmeier, An In Situ DRIFTS Study of Surface Contaminants on Overlithiated Nickel-Cobalt-Manganese-Oxide, M.Sc. thesis, Technical University of Munich (2018).

190. J. Sirita, S. Phanichphant, and F. C. Meunier, Quantitative Analysis of Adsorbate Concentrations by Diffuse Reflectance FT-IR, *Anal. Chem.*, **79**, 3912–3918 (2007).

191. E. Peled and H. Yamin, Solid Electrolyte Interphase (SEI) Electrodes. Part 1. The Kinetics of Lithium in $LiAlCl_4$-$SOCl_2$, *Isr. J. Chem.*, **18**, 131–135 (1979).

192. D. R. Gallus, R. Schmitz, R. Wagner, B. Hoffmann, S. Nowak, I. Cekic-Laskovic, R. W. Schmitz, and M. Winter, The influence of different conducting salts on the metal dissolution

and capacity fading of NCM cathode material, *Electrochim. Acta*, **134**, 393–398 (2014).

193. I. Buchberger, S. Seidlmayer, A. Pokharel, M. Piana, J. Hattendorff, P. Kudejova, R. Gilles, and H. A. Gasteiger, Aging Analysis of Graphite/$LiNi_{1/3}Mn_{1/3}Co_{1/3}O_2$ Cells Using XRD, PGAA, and AC Impedance, *J. Electrochem. Soc.*, **162**, A2737–A2746 (2015).

194. J. Wandt, A. Freiberg, R. Thomas, Y. Gorlin, A. Siebel, R. Jung, H. A. Gasteiger, and M. Tromp, Transition metal dissolution and deposition in Li-ion batteries investigated by operando X-ray absorption spectroscopy, *J. Mater. Chem. A*, **4**, 18300–18305 (2016).

195. C. Yan, R. Xu, Y. Xiao, J.-F. Ding, L. Xu, B.-Q. Li, and J.-Q. Huang, Toward Critical Electrode/Electrolyte Interfaces in Rechargeable Batteries, *Adv. Funct. Mater.*, **30**, 1909887 (2020).

196. R. Imhof, In Situ Investigation of the Electrochemical Reduction of Carbonate Electrolyte Solutions at Graphite Electrodes, *J. Electrochem. Soc.*, **145**, 1081–1087 (1998).

197. M. Masia, M. Probst, and R. Rey, Ethylene Carbonate−Li^+: A Theoretical Study of Structural and Vibrational Properties in Gas and Liquid Phases, *J. Phys. Chem. B*, **108**, 2016–2027 (2004).

198. F. A. Miller and C. H. Wilkins, Infrared Spectra and Characteristic Frequencies of Inorganic Ions, *Anal. Chem.*, **24**, 1253–1294 (1952).

199. C. Hu, J. Liu, J. Wang, Z. Gu, C. Li, Q. Li, Y. Li, S. Zhang, C. Bi, X. Fan, and W. Zheng, New design for highly durable infrared-reflective coatings, *Light Sci. Appl.*, **7**, 17175 (2018).

200. A. Ghannoum, R. C. Norris, K. Iyer, L. Zdravkova, A. Yu, and P. Nieva, Optical Characterization of Commercial Lithiated Graphite Battery Electrodes and in Situ Fiber Optic Evanescent Wave Spectroscopy, *ACS Appl. Mater. Interfaces*, **8**, 18763–18769 (2016).

201. R. Black, S. H. Oh, J.-H. Lee, T. Yim, B. Adams, and L. F. Nazar, Screening for Superoxide Reactivity in Li-O_2 Batteries: Effect on Li_2O_2/LiOH Crystallization, *J. Am. Chem. Soc.*, **134**, 2902–2905 (2012).

202. Y. Peng and P. Wu, A two dimensional infrared correlation spectroscopic study on the structure changes of PVDF during the melting process, *Polymer (Guildf).*, **45**, 5295–5299 (2004).

203. C. M. Julien, K. Zaghib, A. Mauger, M. Massot, A. Ait-Salah, M. Selmane, and F. Gendron, Characterization of the carbon coating onto $LiFePO_4$ particles used in lithium batteries, *J. Appl. Phys.*, **100**, 063511 (2006).

204. A. Ait-Salah, J. Dodd, A. Mauger, R. Yazami, F. Gendron, and C. M. Julien, Structural and magnetic properties of $LiFePO_4$ and lithium extraction effects, *Zeitschrift fur Anorg. und Allg. Chemie*, **632**, 1598–1605 (2006).

205. H. Yang, G. V. Zhuang, and P. N. Ross, Thermal stability of $LiPF_6$ salt and Li-ion battery

electrolytes containing $LiPF_6$, *J. Power Sources*, **161**, 573–579 (2006).

206. G. V. Zhuang, K. Xu, H. Yang, T. R. Jow, and P. N. Ross, Lithium ethylene dicarbonate identified as the primary product of chemical and electrochemical reduction of EC in 1.2 M $LiPF_6$/EC:EMC electrolyte, *J. Phys. Chem. B*, **109**, 17567–17573 (2005).

207. J. P. Pemsler and W. G. Planet, Infrared Spectrum of PF_5, *J. Chem. Phys.*, **24**, 920–921 (1956).

208. H. S. Gutowsky and A. D. Liehr, The Infrared Spectra of PF_3, POF_3, and PF_5, *J. Chem. Phys.*, **20**, 1652–1653 (1952).

209. K. L. Dorris, J. E. Boggs, A. Danti, and L. L. Altpeter, Infrared and Raman Spectra of Vinylene Carbonate, *J. Chem. Phys.*, **46**, 1191–1193 (1967).

210. M. Falk and A. G. Miller, Infrared spectrum of carbon dioxide in aqueous solution, *Vib. Spectrosc.*, **4**, 105–108 (1992).

211. P. Andersson, P. Blomqvist, A. Lorén, and F. Larsson, Using Fourier transform infrared spectroscopy to determine toxic gases in fires with lithium-ion batteries, *Fire Mater.*, **40**, 999–1015 (2016).

212. S. Solchenbach, M. Metzger, M. Egawa, H. Beyer, and H. A. Gasteiger, Quantification of PF_5 and POF_3 from Side Reactions of $LiPF_6$ in Li-Ion Batteries, *J. Electrochem. Soc.*, **165**, A3022–A3028 (2018).

213. H. Beyer, M. Metzger, J. Sicklinger, X. Wu, K. U. Schwenke, and H. A. Gasteiger, Antimony doped tin Oxide–synthesis, characterization and application as cathode material in Li-O_2 cells: Implications on the prospect of Carbon-free cathodes for rechargeable Lithium-air batteries, *J. Electrochem. Soc.*, **164**, A1026–A1036 (2017).

214. D. R. Lide, Ed., *CRC Handbook of Chemistry and Physics*, 86th ed., CRC Press, (2005).

215. M. Metzger, B. Strehle, S. Solchenbach, and H. A. Gasteiger, Hydrolysis of Ethylene Carbonate with Water and Hydroxide under Battery Operating Conditions, *J. Electrochem. Soc.*, **163**, A1219–A1225 (2016).

216. P. Andersson, P. Blomqvist, A. Lorén, and F. Larsson, *Investigation of fire emissions from Li-ion batteries*, SP Report., p. 15–18, Forskningsinstitut SP Technical Research, Borås, (2013).

217. S. Solchenbach, M. Metzger, and H. A. Gasteiger, A Comparative Study of the Anodic and Cathodic Decomposition of Ethylene Carbonate, Vinylene Carbonate and Fluoroethylene Carbonate, *ECS Meeting Abstracts*, **MA2015-02**, 362 (2015).

218. D. Pritzl, T. Teufl, A. T. S. S. Freiberg, B. Strehle, J. Sicklinger, H. Sommer, P. Hartmann, and H. A. Gasteiger, Washing of nickel-rich cathode materials for lithium-ion batteries – Towards a mechanistic understanding, *J. Electrochem. Soc.*, **166**, A4056–A4066 (2020).

219. J. Paulsen, H. P. Hong, and J. D. Oh, Impurity Containing Cathode Material With Preferred Morphology And Method To Preprare From Impurity Containing Metal Carbonate, *Patent Application*, WO 2016/055911 A1 (2016).

220. J. Paulsen, H.-K. Park, and Y. H. Kwon, Process Of Making Cathode Material Containing Ni-Based Lithium Transition Metal Oxide, *Patent Application*, US 2019/0224201 A1 (2009).

221. J. Paulsen and J. H. Kim, High Nickel Cathode Material Having Low Soluble Base Content, *Patent Application*, WO 2012/107313 A1 (2012).

222. J. R. Dahn, R. Fong, and U. von Sacken, Lithiated Nickel Dioxide And Secondary Cells Prepared Therefrom, *Patent*, US 2,264,201 (1993).

223. D.-H. Kim and J. Paulsen, Sulfate Containing Rechargeable Battery Cathode With Oxidized Surface, *Patent Application*, WO 2015/128722 A1 (2015).

224. J. Paulsen, H. P. Hong, and H. S. Ahn, Water Based Cathode Slurry For A Lithium Ion Battery, *Patent Application*, WO 2015/036882 A2 (2015).

225. L. Zou, Y. He, Z. Liu, H. Jia, J. Zhu, J. Zheng, G. Wang, X. Li, J. Xiao, J. Liu, J.-G. Zhang, G. Chen, and C. Wang, Unlocking the passivation nature of the cathode–air interfacial reactions in lithium ion batteries, *Nat. Commun.*, **11**, 3204 (2020).

226. T. Hakkarainen, E. Mikkola, J. Laperre, F. Gensous, P. Fardell, Y. Le Tallec, C. Baiocchi, K. Paul, M. Simonson, C. Deleu, and E. Metcalfe, Smoke gas analysis by Fourier transform infrared spectroscopy – summary of the SAFIR project results, *Fire Mater.*, **24**, 101–112 (2000).

227. M. Takeuchi, G. Martra, S. Coluccia, and M. Anpo, Evaluation of the Adsorption States of H_2O on Oxide Surfaces by Vibrational Absorption: Near- and Mid-Infrared Spectroscopy, *J. Near Infrared Spectrosc.*, **17**, 373–384 (2009).

228. Ö. Cizer, C. Rodriguez-Navarro, E. Ruiz-Agudo, J. Elsen, D. Van Gemert, and K. Van Balen, Phase and morphology evolution of calcium carbonate precipitated by carbonation of hydrated lime, *J. Mater. Sci.*, **47**, 6151–6165 (2012).

229. S. F. Parker, K. Refson, R. I. Bewley, and G. Dent, Assignment of the vibrational spectra of lithium hydroxide monohydrate, $LiOH{\cdot}H_2O$, *J. Chem. Phys.*, **134**, 84503 (2011).

230. J. Choi, J. Kim, K.-T. Lee, J. Lim, J. Lee, and Y. S. Yun, Effect of Na_2SO_4 Coating layer on Nickel-Rich $Li(Ni_xCo_yMn_z)O_2$ Cathode Materials for Lithium-Ion Batteries, *Adv. Mater. Interfaces*, **3**, 4–9 (2016).

231. T. Shinpuku, H. Tani, R. Otterstedt, and K. Kanao, Lithium Metal Composite Oxide Powder with Suppressed Gas Generation, *Patent Application*, WO/2018/172272 (2018).

232. B.-J. Chae and T. Yim, Effect of surface modification using a sulfate-based surfactant on the

electrochemical performance of Ni-rich cathode materials, *Mater. Chem. Phys.*, **214**, 66–72 (2018).

233. D. Pritzl, T. Teufl, A. T. S. Freiberg, B. Strehle, J. Sicklinger, H. Sommer, P. Hartmann, and H. A. Gasteiger, Editors' Choice—Washing of Nickel-Rich Cathode Materials for Lithium-Ion Batteries: Towards a Mechanistic Understanding, *J. Electrochem. Soc.*, **166**, A4056–A4066 (2019).

List of Figures

Scientific Contributions

Articles

U. Breddemann,[=] **J. Sicklinger**,[=] F. Schipper,[=] V. Davis, A. Fischer, K. Huber, E. M. Erickson, M. Daub, A. Hoffmann, C. Erk, B. Markovsky, D. Aurbach, H. A. Gasteiger, and I. Krossing, Fluorination of Ni-Rich Lithium-Ion Battery Cathode Materials by Fluorine Gas: Chemistry, Characterization, and Electrochemical Performance in Full-cells, *Batteries & Supercaps*, **4**, 632–645 (2021).

J. Sicklinger, H. Beyer, L. Hartmann, F. Riewald, C. Sedlmeier, and H. A. Gasteiger, SO_3 Treatment of Lithium- and Manganese-Rich NCMs for Li-Ion Batteries: Enhanced Robustness towards Humid Ambient Air and Improved Full-Cell Performance, *Journal of the Electrochemical Society*, **167**, 130507 (2020).

D. Pritzl, T. Teufl, A. T. S. S. Freiberg, B. Strehle, **J. Sicklinger**, H. Sommer, P. Hartmann, and H. A. Gasteiger, Editor's Choice—Washing of nickel-rich cathode materials for lithium-ion batteries – Towards a mechanistic understanding, *Journal of the Electrochemical Society*, **166**, A4056–A4066 (2020).

H. Sclar,[=] **J. Sicklinger**,[=] E. M. Erickson, S. Maiti, J. Grinblat, M. Talianker, F. Amalraj Susai, L. Burstein, H. Beyer, L. Hartmann, G. Avruschenko, H. A. Gasteiger, B. Markovsky, and D. Aurbach, Enhancement of Electrochemical Performance of Lithium and Manganese-Rich Cathode Materials via Thermal Treatment with SO_2, *Journal of the Electrochemical Society*, **167**, 110563 (2020).

A. T. S. Freiberg, **J. Sicklinger**, S. Solchenbach, and H. A. Gasteiger, Li_2CO_3 decomposition in Li-ion batteries induced by the electrochemical oxidation of the electrolyte and of electrolyte impurities, *Electrochimica Acta*, **346**, 136271 (2020).

J. Sicklinger,[=] M. Metzger,[=] H. Beyer, D. Pritzl, and H. A. Gasteiger, Ambient Storage Derived Surface Contamination of NCM811 and NCM111: Performance Implications and Mitigation Strategies, *Journal of the Electrochemical Society*, **166**, A2322–A2335 (2019).

H. Beyer, M. Metzger, **J. Sicklinger**, X. Wu, K. U. Schwenke, H. A. Gasteiger, Antimony Doped Tin Oxide–Synthesis, Characterization and Application as Cathode Material in Li-O_2 Cells: Implications on the Prospect of Carbon-Free Cathodes for Rechargeable Lithium-Air Batteries, *Journal of the Electrochemical Society*, **164**, A1026 - A1036 (2017).

M. Metzger, **J. Sicklinger**, D. Haering, C. Kavakli, C. Stinner, C. Marino, H. A. Gasteiger, Carbon Coating Stability on High-Voltage Cathode Materials in H_2O-Free and H_2O Containing Electrolyte, *Journal of the Electrochemical Society*, **162**, A1227-A1235 (2015).

M. Metzger, C. Marino, **J. Sicklinger,** D. Haering, H. A. Gasteiger, Anodic Oxidation of Conductive Carbon and Ethylene Carbonate in High-Voltage Li-Ion Batteries Quantified by On-Line Electrochemical Mass Spectrometry, *Journal of the Electrochemical Society*, **162**, A1123-A1134 (2015).

S. Wuttke, S. Braig, T. Preiß, A. Zimpel, **J. Sicklinger**, C. Bellomo, J. O. Rädler, A. M. Vollmar, and T. Bein, MOF nanoparticles coated by lipid bilayers and their uptake by cancer cells, *Chemical Communications*, **51**, 15752-15755 (2015).

K. Fominykh, P. Chernev, I. Zaharieva, **J. Sicklinger**, G. Stefanic, M. Döblinger, A. Müller, A. Pokharel, S. Böcklein, C. Scheu, T. Bein, and D. Fattakhova-Rohlfing, Iron-doped nickel oxide nanocrystals as highly efficient electrocatalysts for alkaline water splitting, *ACS Nano*, **9**, 5180-5188 (2015).

K. Fominykh, J. M. J. M. Feckl, **J. Sicklinger**, M. Döblinger, S. Böcklein, J. Ziegler, L. Peter, J. Rathousky, E.-W. E.-W. Scheidt, T. Bein, and D. Fattakhova-Rohlfing, Water Splitting: Ultrasmall Dispersible Crystalline Nickel Oxide Nanoparticles as High-Performance Catalysts for Electrochemical Water Splitting, *Advanced Functional Materials*, **24**, 3105–3105 (2014).

S. Böcklein, S. Günther, R. Reichelt, R. Wyrwich, M. Joas, C. Hettstedt, M. Ehrensperger, **J. Sicklinger**, and J. Wintterlin, Detection and quantification of steady-state ethylene oxide formation over an Ag(111) single crystal, *Journal of Catalysis*, **299**, 129–136 (2013).

[=]These authors contributed equally to this work.

Patent Application

M. Metzger, H. Beyer, **J. Sicklinger**, D. Pritzl, B. Strehle, H. Gasteiger, H. Sclar, E. Erickson, F. A. Susai, J. Grinblat, D. Aurbach, and B. Markovsky, Process for making a cathode active material for a lithium ion battery, *International Patent Application*, WO/2019/002116 (2019).

Oral Presentations

J. Sicklinger, H. Beyer, L. Hartmann, C: Sedlmeier, D. Pritzl, F. Riewald, H. A. Gasteiger, Reactivity of Layered Oxides with CO_2 and Moisture, Americas International Meeting on Electrochemistry and Solid State Science (AiMES), Cancún, Mexiko, 30th September – 4th October 2018 (abstract number 235), supported by travel scholarships from the German Academic Exchange Service (DAAD) and the German Chemical Society (GDCh)

J. Sicklinger, H. Beyer, L. Hartmann, C. Sedlmeier, D. Pritzl, F. Riewald, H. A. Gasteiger, Reaktivität von Schichtoxiden mit CO_2 und Feuchtigkeit, Außerordentliches Anorganisch-Chemisches Seminar, Albert-Ludwigs-Universität Freiburg, 21.02.2019, invitation from Prof. Dr. Ingo Krossing

Poster Presentations

J. Sicklinger, H. Beyer, L. Hartmann, C. Sedlmeier, D. Pritzl, F. Riewald, H. A. Gasteiger, Reactivity of Layered Oxides with CO_2 and Moisture, 16th Ulm ElectroChemical Talks (UECT), Ulm, November 13-14, 2018 (1st Price of the Poster Award)

J. Sicklinger, K. U. Schwenke, N. Zensen, H. A. Gasteiger, Single-Solvent Electrolytes for Lithium-Ion Batteries Studied By Operando Diffusive Reflectance Infrared Fourier Transform Spectroscopy, 18th International Meeting on Lithium Batteries, Chicago, Illinois, USA, 19.-24. Juli 2016